Les Rencontres de Physique de la Vallée d'Aoste

Results and Perspectives in Particle Physics

FRASCATI PHYSICS SERIES

Series Editor
Stefano Bianco

Technical Editor
Luigina Invidia

Volume XXX Special Issue

Istituto Nazionale di Fisica Nucleare – Laboratori Nazionali di Frascati
Divisione Ricerca – SIS – Ufficio Pubblicazioni
P.O. Box 13, I–00044 Frascati (Roma) Italy
email: invidia@lnf.infn.it

FRASCATI PHYSICS SERIES

Les Rencontres de Physique de la Vallée d'Aoste

RESULTS AND PERSPECTIVES IN PARTICLE PHYSICS

ISBN 88-86409-38-9

Printed in Italy by Poligrafica Luziale, P.le della Stazione 1, 00044 Frascati

FRASCATI PHYSICS SERIES

Volume XXX

Les Rencontres de Physique de la Vallée d'Aoste

Results and Perspectives in Particle Physics

Editor
Mario Greco

La Thuile, Aosta Valley, March 9-15, 2003

Conference Organizers

Giorgio Bellettini	*Pisa*
Giorgio Chiarelli	*Pisa*
Mario Greco	*Roma III*

List of Chairpersons

Franco Bedeschi	*INFN Pisa*
Giorgio Bellettini	*Pisa*
Matteo Cacciari	*Parma*
Giorgio Chiarelli	*INFN Pisa*
Giordano Diambrini-Palazzi	*Roma I*
Al Goshaw	*FNAL*
Mario Greco	*Roma III*
Clemens Heusch	*Santa Cruz*
Maurizio Lusignoli	*Roma I*
Giampaolo Mannocchi	*CNR/LNF*
Peter Minkowski	*Berne*
Victor Novikov	*ITEP*
Ornella Palamara	*LNGS*
Avi Yagil	*FNAL*

FOREWORD

The 2003 Rencontres de Physique de la Vallée d'Aoste were held at the Planibel Hotel of La Thuile, Aosta Valley, on March 9–15 with the seventeenth edition of "Results and Perspectives in Particle Physics".

The physics programme included various topics in particle physics, also in connection with present and future experimental facilities, as cosmology, astrophysics and neutrino physics, CP violation and rare decays, electroweak and hadron physics with e^+e^- and hadron colliders, heavy flavours and prospects at future facilities.

The non-physics programme included special colloquia on the role and the strategies of Science Communication, on Quantum Computation and on Nuclear Terrorist Threats.

Giorgio Bellettini, Giorgio Chiarelli and I should like to warmly thank the session chairpersons and the speakers for their contribution to the success of the meeting.

The regional government of the Aosta Valley, in particular through the Minister of Public Education Ennio Pastoret, has been very pleased to offer its financial support and hospitality to the Rencontres of La Thuile. Also on behalf of the participants, representatives of some major Laboratories and Institutes in the world, we would like to thank all the Regional Authorities. Special thanks are also due to Bruno Baschiera, local coordinator of the Rencontres.

We are grateful to the President of INFN Enzo Iarocci, the Directors of INFN Laboratori Nazionali di Frascati, Sergio Bertolucci and INFN Sezione di Pisa, Marcello Giorgi, for the support in the organization of the Rencontres. We would like to thank also Paolo Caponera, Lucia Lilli, Rossana Morani, Claudia Tofani, and Paolo Villani for their help in both planning and running the meeting. We are also grateful to Alessandra Miletto for her valuable contribution to the local organization of the meeting. The excellent assistance provided by Giovanni Nicoletti and Mauro Giannini made it possible to set up the computer link to the international network. Special thanks are due to Luigina Invidia for valuable help in the technical editing of the Proceedings.

Finally we would like to thank the Mayor Gilberto Roullet and the local authorities of La Thuile and the "Azienda di Promozione Turistica del Monte Bianco" for their warm hospitality, and the Planibel Hotel staff for providing us an enjoyable atmosphere.

September 2003 Mario Greco

CONTENTS

Foreword VII

SESSION I – ASTROPHYSICS AND COSMOLOGY 1

R.Wayne Springer — Observing Ultra High Energy Cosmic Rays with the High Resolution Fly's Eye Detector 3
Eugenio Coccia* — Coincidence of Gravitational Waves Detectors 17
Alexander Dolgov — Magnetic Fields in Cosmology 19
Michail I. Vysotsky — $c/\sqrt{3}$: Critical Velocity Relativity 33
Alvaro de Rujula* — Gamma Ray Bursts and the Sociology of Science 41

SESSION II - NEUTRINO PHYSICS 43

Paolo Desiati — Neutrino Astronomy at the South Pole: Status of the AMANDA Experiment 45
Phil Adamson* — The Running-in of MINOS 63
Yoshi Uchida — First Results from the KamLAND 65
Larry Sulak* — Results from SuperKamiokande 77
Taku Ishida — Indications of Neutrino Oscillation in the K2K Neutrino Oscillation Experiment 79
Andrew Hime* — Results from SNO 95
Jonathan M. Link — Status of MiniBooNE, a Short Baseline Neutrini Oscillation Experiment 97
Francesco Vissani — Perspectives in Neutrino Physics 103

SESSION III - HEAVY FLAVOUR PHYSICS 145

Takayuki Kawamura — CHORUS Results on Charm Physics 147
Wenfeng F. Wang — Recent $\psi(2s)$ Results from BES 155
Roy A. Briere — CLEO $|V_{ub}|$ and $|V_{cb}|$ Results and Plans of CLEO-C 165
Ivan K. Furić — Charm Physics in CDF II 175
Mikhail Danilov* — Mysteries in Charmonium Production 183

Matt Herndon	B Physics at CDF	185
Franco Simonetto	B Meson Decay Properties at BaBar	193
Nick Hastings	High Precision Measurements of B-Decay Final States with the Belle Detector	205
Heriberto Castilla*	Recent Results on B physics at D0	217

SESSION IV - HEAVY IONS PHYSICS **219**

Sebastian White	Recent Results from the Heavy Ion Collider Program at RHIC	221
Vladimir R. Zoller	Decorrelation of Forward Dijets in DIS off Nuclei	229

SESSION V – ELECTROWEAK AND TOP QUARK PHYSICS **241**

Andrea Venturi	W Mass at LEP and Electronweak Fit Results	243
Thomas Schöner-Sadenius	LEP1 Heavy Flavour Electroweak Physics and 2–Fermion Process at LEP2	255
Bob Kehoe	Recent Run II Electroweak and Physics QCD Results from and DØ	269
Anyes Taffard	Electroweak and Top Physics at CDF in Run II	285
Marumi Kado	Recent Top Quark Physics Results from DØ	297
Boris I. Ermolaev	Forward-Backward Charge Asymmetry at Very High Energies	311
Charles A. Nelson	Consequences of a Large Top-quark Chiral Weak–Moment	319

SESSION VI – CP VIOLATION AND RARE DECAYS **329**

Takeo Higuchi	Measurements of the Unitarity Triangle by Belle	331
Sandrine Laplace	Rare B decays and Direct CP Violation at BaBar	357
Riccardo Faccini	Measurements of CP Violation in Mixing with the BaBar Experiment at PEP-II	373
Alexei Drutskoy	Direct CP Violation Searches at Belle	385
Gino Isidori	New Physics in $B_d - \overline{B}_d$ Mixing and CKM Fits	393

Ivan Mikulec	CP Violation and Rare Decays in the K Sector at NA48	405
Eugeny Shabalin	Semi-Phenomenological Approach to the Estimate of CP–Effects in $K\pm \to 3\pi$ Decays	417
Giancarlo D'Ambrosio	Theory of Rare Kaon Decays	427
SESSION VII – QCD		**445**
Marco Contalbrigo	A First Measurement of the Tensor Structure Function b_1^d	447
Luca Passalacqua	Recent Results from the KLOE Experiment	455
Jörg Pretz	COMPASS – Status and Perspective	471
Robert Snihur*	Jet studies at CDF in Run 2	483
Igor Dremin	Jet physics at LEP and QCD	485
Harald Fritzsch	A Time Variation of the QCD Coupling Constant	497
SESSION VIII – SEARCH FOR PHYSICS BEYOND THE SM		**505**
Philip Bambade	Four–Fermion Production and Limits on Anomalous Couplings at LEP–2	507
Pablo Garcia*	Higgs Results and Searches for New Physics at LEP	529
Lorenzo Bellagamba	Searches for New Physics at HERA	531
Emmanuel Sauvan	Lepton Production in ep Collisions at HERA	539
Luca Scodellaro	Searches for New Phenomena in CDF	547
Wyatt Merritt	Recent New Phenomena Results from the Searches at D0 Experiment	557
Victor Novikov	Z-Lineshape versus 4th Generation Masses	571
SESSION IX – FUTURE EXPERIMENTS AND PROJECTS		**583**
Makoto Tomoto	Prospects for DØ Higgs Search	585
Marco Grassi*	A Sensitive Search for the $\mu \to e\gamma$ Decay: the MEG Experiment	565
Massimo Masera	Perspectives of the ALICE Experiment	597

SPECIAL SESSION – PHYSICS AND SOCIETY **609**

Judith Jackson — Global Communication Strategies for a Global Community 611

Francesco De Martini* — Trends and Perspectives in Quantum Information and Computation 615

Massimiliano Russo* — The Nuclear Terrorist Threats: Reality and Countermeasures 617

Giovanni Bignami* — Future Missions in Space 619

Participants 621

* The trasparencies of the missing contributions are available on the web site http://www.pi.infn.it/lathuile/lathuile_2003.html

SESSION I – ASTROPHYSICS AND COSMOLOGY

R.Wayne Springer	Observing Ultra High Energy Cosmic Rays with the High Resolution Fly's Eye Detector
Eugenio Coccia*	Coincidence of Gravitational Waves Detectors
Alexander Dolgov	Magnetic Fields in Cosmology
Michail I. Vysotsky	$c/\sqrt{3}$: Critical Velocity Relativity
Alvaro de Rujula*	Gamma Ray Bursts and the Sociology of Science

* The trasparencies of the missing contributions are available on the web site http://www.pi.infn.it/lathuile/lathuile_2003.html

OBSERVING ULTRA HIGH ENERGY COSMIC RAYS WITH THE HIGH RESOLUTION FLY'S EYE DETECTOR

R. Wayne Springer
for the High Resolution Fly's Eye Collaboration
Department of Physics , University of Utah, Salt Lake City, Utah 84112

Abstract

The High Resolution Fly's Eye Detector (HiRes) detects and measures properties of ultra high energy, $E > 10^{18} eV$, cosmic rays. The HiRes detector exploits what is known as the "Air Fluorescence" technique that uses the atmosphere as a calorimeter. A brief description of this technique and how it is used by the HiRes detector will be given in this paper.

Introduction

The properties of Ultra High Energy Cosmic Rays (UHECR) measured by the HiRes detector are the following:

- The energy spectrum for energies above 10^{18} eV.
- Anisotropy of arrival directions.
- Average chemical composition vs. energy.

In addition to these measurements, searches for exotic phenomena such as neutrino induced air showers will also be performed. This paper will describe the technique of air fluorescence detection in general and how it has been implemented in the HiRes detector in particular.

Cosmic ray energy spectrum

The gross dependence of the flux of cosmic rays on energy is described by a power law, $flux = E^{-3}$. A spectral index of between 2.7 and 3.1 holds from energies of $10^9 eV$ up to and perhaps beyond several times 10^{19} eV. The expected integrated flux at energies above $10^{18} eV$ is only 1 particle/km^2/year. At energies above 10^{20} eV the expected integrated flux is less than 1 $particle/km^2/century$. Consequently, to study the Ultra High Energy Cosmic rays in the energy range above 10^{18} eV, one must build and operate detectors with large apertures of at least 1000 $km^2 - sr$. In the case of air fluorescence detectors, the minimum required aperture is 10,000 $km^2 - sr$. This larger aperture is necessary to compensate for the 10% duty cycle associated with the requirement for operating only on dark moonless nights.

There also appears to be "structure" in the cosmic ray spectrum. This structure appears as features such as the "knee" at $\approx 10^{15}$eV and the "ankle" at $\approx 10^{18}$ eV. One notable feature is the apparent change in spectral index at an energy of approximately $3 \times 10^{18} - 10^{19} eV$. The Fly's eye stereo result indicates a dip at 3×10^{18} eV while the AGASA result indicates a dip occurring at $10^{19} eV$.

The commonly accepted interpretation for changes in spectral index is that the change is the result of changing distributions and types of astrophysical sources. These changes in sources would modify the observed flux. It should be noted, however, that the cosmic ray spectrum is the measured flux versus the measured **observed** energy. It is therefore possible that structure in the spectrum results from changes in the properties of air showers where the fraction of observed energy changes due to new physics processes. In this manner, the study of ultra-high energy cosmic rays may be a window on particle physics processes occurring at energy scales not accessible in present-day accelerators.

It should also be noted that structure in the spectrum could be an experimental artifact. An energy dependent aperture t hat is not properly modeled could change the slope of the measured spectrum. Improper energy scales as well as tails in energy resolution could also wreak havoc with the measured energy spectrum.

Several cosmic ray particles have purportedly been observed with measured energies in excess of the so-called "GZK energy cutoff". The GZK cutoff [1] results from the interaction of the UHECR particle, presumably a proton, with photons from the 2.7 deg K cosmic microwave background radiation. The proton energy threshold for photo-pion production with these photons is $E_{GZK} = 6 \times 10^{19} eV$. Assuming that the sources of the UHECR are of extragalactic origin uniformly distributed out to cosmological distances, the flux of UHECR would be expected to abruptly drop above $E > E_{GZK}$. IF the sources are "local" $R < 50 Mpc$, the flux would continue above E_{GZK}.

Chemical composition

Another property of UHE cosmic rays that can be studied is their chemical composition. There are indications that there is a tendency toward light nuclei (i.e. protons) as energy increases above 10^{18} eV. Knowledge of the chemical composition is of fundamental importance in understanding the nature of the sources of UHECR. The HiRes detector will make a statistical determination of particle species by using the depth of shower maximum as a discriminator.

Anisotropy and Point Source Searches

At energies above the GZK cutoff the radius of curvature for the proton in the extragalactic magnetic fields may be large. This radius depends upon the strength and coherence lengths of the field. For conventionally accepted values of these magnetic fields, it is expected that the deflection of the proton would be small enough that the arrival direction of the cosmic ray proton would point back to its source. There has yet been little evidence that the arrival directions of the "Super-GZK" events point back to possible astrophysical sources such as Active Galactic Nuclei (AGN). It has recently been hypothesized, however, that the extragalactic magnetic field is strong enough to deflect the protons so that their arrival directions would no longer point back to their source. In that case, UHECR astronomy would not be possible and the lack of correlation of the arrival directions with AGNs would not rule out the possibility that the UHECR are produced in local active galactic nuclei.

Requirements and specifications for the HiRes detector

The HiRes detector was designed to have an effective detection aperture that approaches 10^4 km^2 – *steradian* for particles with an energy of 10^{20} eV. The HiRes detector was also designed to reconstruct the energy of the primary cosmic ray particle with a resolution of 20% at 10^{20} eV. The determination of depth at which the shower has its maximum, X_{max} , yields statistical information concerning the chemical composition of the cosmic rays. The HiRes detector has been designed to measure this quantity with a resolution of 20-30 g/cm^2. Finally, the HiRes detector has been designed to have an angular resolution of < 0.4 deg. This angular resolution will allow searches for point sources as well as anisotropy measurements to be performed.

Air Fluorescence Technique

The air fluorescence technique uses the atmosphere as a calorimetric detector. To reconstruct the energy of the incoming primary cosmic ray particle using this technique one must have a good understanding of the following:

1. **Shower Development.** The Primary Cosmic Ray Particle interacts with a nucleus in the upper atmosphere initiating a Hadronic Shower. Hadronic Shower develops producing mainly pions. The neutral pions decay into pairs of gamma-rays that in turn initiate electromagnetic showers. The passage of charged particles through air generates Ultraviolet Fluorescence photons. This UV fluorescence yield must be known.

2. **UV Fluorescence and Propagation of light through Atmosphere.** Ultraviolet scintillation photons are produced by Nitrogen molecules excited by the passage of the charged particles (mostly e^- and e^+) produced in the electromagnetic shower. UV photons propagate through atmosphere towards the detector. Direct and Scattered Cerenkov photons are also produced

3. **Detector Calibration.** UV photons are collected by mirror and focused onto array of photomultiplier tubes. Individual PMTs measure photon flux (vs. time or integrated) by counting photo-electrons read out by digitizing system

A cosmic ray interacting with a nucleus in the upper atmosphere will produce a cascade of secondary particles. The number of secondary particles has a roughly linear dependence on the energy of the primary particle. This relationship is what is exploited in calorimetric techniques of energy measurement. To determine the exact relationship between the number of secondary charged particles and the primary's energy, one needs to understand the physics of shower

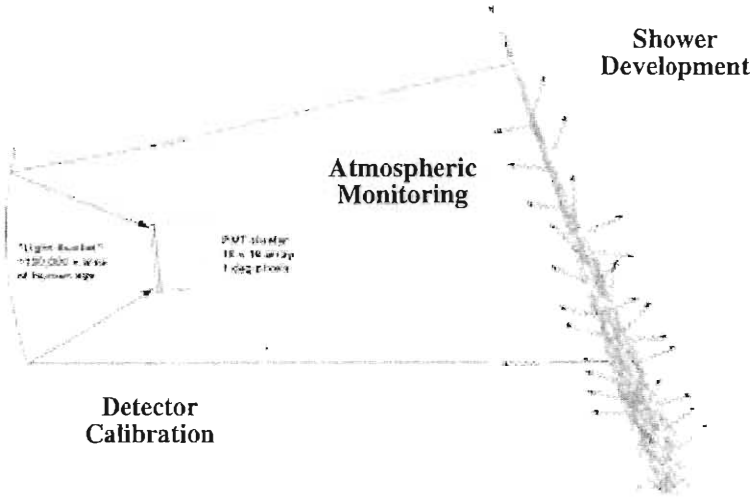

Figure 1: Schematic representation of elements of the air fluorescence technique.

development. One also needs to understand the longitudnal development of the shower to estimate the total energy in the case that one only observes a short segment of the shower. For the air fluorescence technique this is less of a problem than for a ground array that samples the number of secondary particles at only one depth in the shower.

The number of secondary charged particles can be estimated from the amount of UV scintillation light that is produced as the shower front passes through the atmosphere. This scintillation light is produced by the excitation of Nitrogen molecules by the passage of the charged particles. The amount of UV light produced by the passage of charged particles through the atmosphere is known as the Fluorescence yield. This quantity has been determined experimentally

to be approximately 4.5 photons/m/particle [2]. This UV scintillation light is emitted isotropically. As the UV photons propagate through the atmosphere they can be scattered by both molecules and aerosols. The typical attenuation length for a desert atmosphere is roughly 12 km. Given the 12.6 km separation of the HiRes detector sites the effects of atmospheric attenuation are considerable. The variation of the atmospheric attenuation length is large due to various factors including weather as well as pollution such as forest fires. Therefore it is important not only to understand the average properties of the atmosphere but monitoring of the atmosphere must also be performed.

Cerenkov light also accompanies extensive air showers. The Cerenkov light is highly beamed along the axis of the air shower. This direct Cerenkov light precludes reconstructing showers that are directed toward the fluorescence detector. Cerenkov light can be scattered by molecules and aerosols in the atmosphere to larger angles away from the shower axis. Both the direct and scattered Cerenkov light needs to be considered when reconstructing the shower with an air fluorescence detector. The atmosphere also needs to be monitored to estimate the amount of Cerenkov light that is scattered toward the detector.

Finally the detector response must be well understood. The function of the detector is to measure the **absolute** flux of photons at the mirror. To do this one needs an absolute calibration of the response of the detector chain including the following:

- Mirror reflectivity and effective area.
- Optical properties of mirror. spot size. aberrations.
- Transmission of UV lines through filter
- **Absolute** Sensitivity = Quantum efficiency × Gain of phototubes

Once these properties are understood one can convert a detector signal into a measurement of photon flux. After determination of the shower geometry (discussed in a later section) a correction for shower distance and propagation losses through the atmosphere can be made. After applying the fluorescence yield conversion, an estimate for the number of secondary particles in the shower observed by that PMT can be made. In this manner the number of secondary particles vs. shower age can be determined. By integrating this function and applying the appropriate conversion factors the energy of the cosmic ray primary can be obtained.

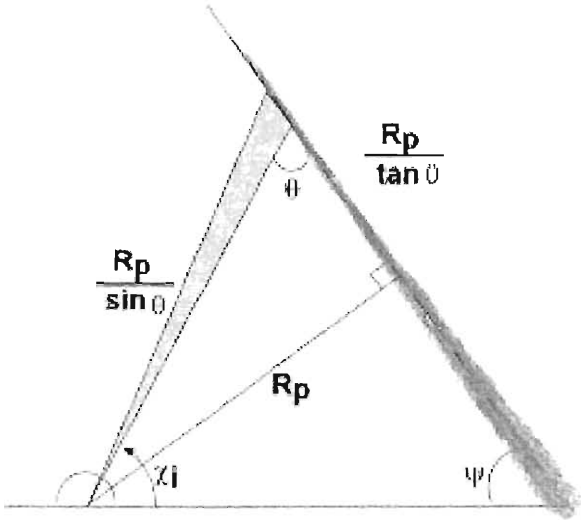

Figure 2: Monocular Timing fit determination of shower geometry.

Monocular Reconstruction Technique

Monocular reconstruction of the shower geometry is based upon the relationship between arrival times of light arriving from a particular direction in the sky. Consider the simple case where the shower axis crosses the optical axis of a detector at 90 degrees. In that case, the distance to the shower can be determined by the amount of time it takes to cross $\Delta\theta$ degrees of the sky. Assuming that the shower front is moving at the speed of light.

$$\text{distance to shower} = \frac{c\Delta t}{sin\Delta\theta}$$

There is an ambiguity between the distance to the shower and the angle with respect to the optical axis of the detector. Because of this ambiguity one

can not simply use the inverse angular speed of the shower to determine its distance. If the shower tracks are "long" (> 20 degrees) then one can use the following formula that exploits the curvature of the timing profile. This resolves the ambiguity between distance and inclination angle. Figure 2 illustrates the timing based monocular reconstruction. Using the measured arrival times of the light at each tube i. Minimization of the following equation results in the determination of both distance and inclination angle. Refer to figure 2 for definitions of the variables.

$$\chi^2_{time} = \Sigma_i \frac{1}{\sigma_i^2}(t_i - (t_0 + \frac{R_p}{c} tan(\frac{\pi - \Psi - \chi_i}{2})))^2$$

For the shorter tracks obtained in the HiRes1 monocular data an additional constraint is needed. That constraint is to assume that the shower maximum, X_{max}, occurs at a given value for X_{max} between 680 g/cm^2 and 860 g/cm^2. This additional constraint then allows one to determine the distance to the shower. Albeit at the cost of not being able to measure shower maximum to perform composition studies.

Stereo Reconstruction Technique

In the stereoscopic reconstruction method, a shower-detector plane (SDP) is found for each detector by using the pointing directions of the tubes that viewed light from the EAS to construct a plane in space. The shower axis is simply the line formed by the intersection of the two shower-detector planes. This method works well as long as the opening angle between the planes is sufficient. In the case where the opening angle is zero degrees the 2 shower detector planes are co-planar and it is no longer possible to determine where in the plane lies the shower axis. Timing information is also utilized to improve the determination of the geometry.

The geometrical determination of the location of the shower in space using the stereoscopic technique, results in greatly improved resolution in the determination of both the energy and the arrival direction of UHE cosmic rays. The energy measurement is improved due to the reduction in the uncertainty of the distance to the air shower. Assumptions about the shower profile that are sometimes necessary in the monocular reconstruction technique are no longer necessary. Therefore the stereoscopic Reconstruction technique allows the measurement of the depth of shower maximum to be performed. The measurement of the depth of shower maximum can then be used in the determination of the chemical composition of the UHE cosmic rays.

Description of the HiRes Detector

The High Resolution Fly's Eye detector consists of two air fluorescence detector sites located on Dugway Proving Grounds, Utah U.S.A. The two sites are separated by a distance of 12.6 km. Each site consists of a number of $3.8m^2$ mirrors. Each mirror is instrumented with a cluster of 256 photomultiplier tubes. The field of view for each of these mirror/PMT cluster systems extends approximately 15 deg in both elevation and azimuth. Each hexagonal PMT views approximately a 1 degree by 1 degree segment of the sky.

The HiRes 1 site has 21 mirror systems viewing elevation angles from 3 deg to 17 deg above the horizon and nearly the full azimuthal range. The HiRes 2 site is equipped with 42 mirror systems viewing elevation angles from 3 deg to 31 deg above the horizon and nearly the full azimuthal range

The electronics used to read out the PMTs at the HiRes 1 site uses a sample and hold technique where the signal is integrated with a time constant of 5 μsec. A 10 MHz FADC system [3] has been deployed at the HiRes2 site. Digitization at a rate of 10 MHz provides additional information on the development of the shower for distant tracks in the case where the light spot takes longer than 100 nsec to cross a photo-tube.

Detector Calibration

Calibration of the detector is performed to relate the electronics signal to the photon flux impinging upon the PMT cluster. At both detector sites, relative calibrations using light sources such as lasers and xenon flashers are performed periodically. Optical fibers have been installed at both sites to deliver light from a YAG laser to each of the PMT clusters. The laser calibrations have been automated and are performed on a nightly basis. The laser calibrations are used to monitor the stability of the detector calibration.

Calibrations using "standard" "roving" xenon flashers are manually performed on nearly a monthly basis. The roving "Xenon" flasher is a more stable light source than the YAG laser. Shot-to-shot variability in the intensity of the xenon flasher is less than 1%. The roving Xenon flasher is calibrated to deliver a known amount of light. Photo-electron statistics are also used to determine the number of photo-electrons delivered to the PMTs. These calibrations yield an estimate of the sensitivity of the PMTs. The PMT sensitivity is the product of the quantum efficiency multiplied by the gain.

Ultimately the PMTs need to be calibrated on an absolute scale. To achieve this absolute calibration, each of PMTs used in HiRes1 and HiRes2 were scanned using a 1mm radius light spot obtained from a YAG laser. This light spot

was scanned across the surface of each PMT in 1 mm steps. The intensity of the laser pulse was measured using NIST calibrated photo-diodes. The DC current of the tube was measured resulting in a measurement of the sensitivity, current/intensity, of the tube as a function of position. The manufacturer performed measurements of the average quantum efficiency of each tube for 355 nm light. The wavelength dependence of the quantum efficiency was also measured by the manufacturer for a subset of the PMTs. An end-to-end absolute calibration using laser shots at a distance of approximately 3 km are being performed to aid in the determination of the absolute energy scale.

Atmospheric Monitoring

To properly reconstruct energy and determine the actual detector aperture, one needs to know the transmission and scattering properties of the atmosphere. This information is required to estimate the amount of attenuation suffered by the UV light as it travels from the air shower to the detector. The ideal solution would be to populate the detector volume with calibrated light sources. This ideal solution is of course impossible to realize. What is done for the HiRes detector is to sweep a laser beam throughout the volume and measure the amount of scattered light from various segments of the laser beam. Using the measurements of this scattered light, parameters characterizing the atmosphere can be obtained.

A steerable laser system located at the site known as Fly's Eye II was in operation from prior to 1997 through summer 1999. A steerable laser system located at the HiRes2 site became operational in spring 1999. A second steerable laser system located at the HiRes1 site was installed in 2000. In addition to the fixed laser installations, a roving laser facility has been established.

Preliminary Results

Monocular Results

Preliminary results for monocular observations of UHECR with the HiRes detector were presented at the 1999 [4] and 2001 [5] International Cosmic Ray conference. These results have also been submitted to Physical Review Letters [6] for publication. The results obtained with the HiRes-I detector were based upon about 3100 hours of data. Of these 3100 hours about 2400 hours of good weather data were analyzed The profile-constrained time fit was used to obtain the geometry of the air shower for events measured by the HiRes-I detector. Using detector simulations, a monocular aperture that attains an estimated value of $9100 km^2 - sr$ at 10^{20} eV is shown in figure 3 . The cosmic ray energy spectrum as measured by the HiRes-I detector shown in figure 4 is obtained

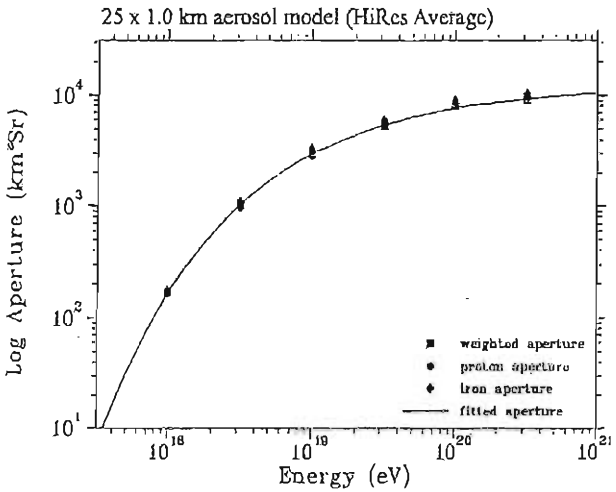

Figure 3: Monocular aperture vs. energy for average atmospheric conditions

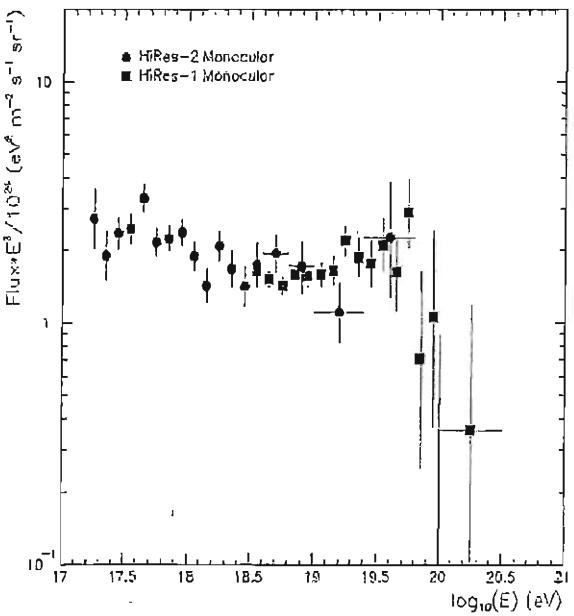

Figure 4: Energy Spectrum as measured by HiRes in monocular mode. Flux is multiplied by E^3 and plotted as a function of Energy.

using the the estimated aperture and the number of observed events. The plot in figure 4 also shows the spectrum measurement obtained in monocular mode from the HiRes-II detector. The HiRes-II detector was used to measure the energy spectrum at lower energies than was possible with the HiRes-I detector. The HiRes-II detector has a lower energy threshold due to the nearly double range of elevation angle coverage as well as the improved FADC readout system. It should be noted that the overall flux normalization of these measurements are consistent with one another. Taking these two spectrum measurements together there is an indication that the spectral index changes at an energy of approximately $3 \times 10^{18} eV$.

Stereoscopic Reconstruction

Data of good quality from December 1999 through February 2003 from both detector sites has been analyzed. This data set has been used to check relative detector calibrations between the two sites as well as for comparison studies of the monocular and stereo reconstruction techniques. In this time period HiRes1 recorded approximately 65 million triggered events while HiRes2 recorded 36 million triggered events. The vast majority of these events are noise and events associated with artificial light sources such as vertical flasher shots and steerable laser shots. One of the tasks of the data processing chain is to filter out the the noise and artificial light sources from cosmic ray candidates. An easy and effective means of eliminating noise is to require a coincidence in time between events recorded at both sites. A time window of 500 μsec was used for time matching between the sites. Most of the remaining stereo events are from artificial light sources. The next step in filtering was to remove the events from artificial light sources such as the vertical flashers and laser shots. This was done by reconstructing the events and identifying the light pulses as upward-going emanating from the known locations of the light sources. After applying this filter approximately 4000 "loose" cosmic candidates remain. Several analyses are being carried out on this data set. The search for super-GZK events is an optimization of signal over background. Better energy resolution can be obtained by making stricter quality cuts but with a corresponding loss is statistics. Another analysis looking for structure in the spectrum is also being carried out. In this analysis stringent cuts to maintain an energy resolution better than 20% are required in order to be able to observe a change in the spectral index.

A comparison of the monocular reconstruction technique to the stereo reconstruction technique was performed using this sample of stereo events. For this study the monocular reconstruction using the profile-constrained timing fit method on the HR1 data to determine geometry was compared to the stereo reconstruction method. For a subset of well measured events, the energy de-

termined through the monocular reconstruction technique agrees as expected with the energy determined using the stereo reconstruction technique.

Summary

Both sites of the HiRes detector have been operational since spring 1999 and are now collecting data of stereo-scopic observations of UHECR. We have submitted a paper [6] to Physical Review Letters describing a measurement of the energy spectrum of UHE cosmic rays using monocular analysis techniques using a data set obtained from 1997 until February 2003. A more detailed paper describing the Monocular analysis technique using the HiRes-II detector [7] has been submitted to the Astrophysical Journal. We are currently working on the measurement of the spectrum of UHE cosmic rays using the stereo-scopic technique. We hope to submit a paper describing this measurement by Fall 2003. More information concerning the HiRes Detector can be found at http://www.cosmic-ray.org/.

References

1. K.Greisen, *Phys. Rev. Lett.* **16**, 748 (1966); G.T.Zatsepin and V.A. Kuzmin, *Pisma Zh. Eksp. Teor. Fiz.***4**, 144 (1966).

2. Kakimoto et al., *Nucl. Instr. and Meth. A* **327**, 529 (1996).

3. J.Boyer et al., *NIM* **A482**, 457 (2002).

4. The HiRes Collaboration, *Proceedings of the 26 th ICRC.*

5. The HiRes Collaboration, *Proceedings of the 27 th ICRC.*

6. T. Abu Zayad et al.,Measurement of the Flux of Ultra High Energy Cosmic Rays from Monocular Observations by the High Resolution Fly's Eye Experiment,Submitted to Phys. Rev. Lett.

7. T. Abu Zayad et al.,Measurement of the Spectrum of UHE Cosmic Rays by the HiRes Experiment,Submitted to Ap. J.

COINCIDENCE OF GRAVITATIONAL WAVES DETECTORS

Eugenio Coccia
University of Rome "Tor Vergata" and INFN

Written contribution not received

MAGNETIC FIELDS IN COSMOLOGY

A.D. Dolgov
INFN, sezione di Ferrara, Via Paradiso, 12 - 44100 Ferrara, Italy
and
ITEP, Bol. Cheremushkinskaya 25, Moscow 113259, Russia

Abstract

Different mechanisms which may possibly explain existence of magnetic fields on astronomically large scales are described. A recently suggested model of magnetic fields generation slightly before hydrogen recombination is discussed in more detail.

1 Introduction

It is known from observations, mostly from Faraday effect, that there are magnetic fields in galaxies with magnitude of a few micro-Gauss and coherence length of the order of galactic size, $l_{gal} \sim$ (a few) kpc, The energy density of such fields is close to the energy density of the cosmic microwave background radiation (CMBR):

$$\rho_B = B^2/8\pi \sim \rho_\gamma \sim 10^{-4}\rho_m \approx 3 \cdot 10^{-34}\,\mathrm{g/cm^3} \qquad (1)$$

where ρ_γ is the energy density of CMBR and $\rho_m \approx 1.5$ keV/cm^3 is the total cosmological mass/energy density. Though the magnitude of such fields is small in comparison with the fields of stars or even planets (see below) it is very difficult to understand their huge coherence length. Even more puzzling is a possible existence of intergalactic magnetic fields which are 3 orders of magnitude weaker but coherent at a Megaparsec scale, for a review see ref. ?).

For comparison, magnetic field of the earth is $B_\otimes = 0.5$ G, magnetic fields of solar type stars can be as large as 10^3 G, magnetic fields of white dwarfs may reach 10^9 G, and absolute champions are neutron stars with magnetic fields at the level of 10^{13} G.

Possible creation mechanisms of large scale galactic or intergalactic fields can be roughly separated into four classes (for reviews see ref. ?):

1. Conventional (astrophysical) mechanism based on stellar ejecta of magnetic fields with subsequent magnetic lines reconnection (from different stars) to create a homogenous on large scale field component. This mechanism was reviewed recently in ref. ?)

2. Processes in the early universe which invoke inflation to stretch the characteristic scale of the field up to galactic or even larger scales. A comprehensive list of references on different versions of these mechanisms can be found in the recent paper ?).

3. Phase transitions in the early universe during which strong magnetic fields could be created but at a very small scale.

4. Relaxation of previously created inhomogeneities. In this process turbulent or laminar flow of primeval plasma with non-zero vorticity could be generated and due to different mobilities of charge carriers vortical electric currents producing magnetic fields would be created. Such mechanism may operate either in the early or relatively late universe.

All these mechanisms either generate magnetic fields at very small scales or of insufficiently large amplitude. In the first case "Brownian" type reconnection of

magnetic field lines is necessary for creation of coherent magnetic fields at large distances. The amplitude of the field in the course of reconnection decreases as $(l_{in}/l_{fin})^{3/2}$ where l_{in} and l_{fin} are the initial and final coherence lengths. Inflationary stretched fields are usually rather weak, though may have a very large coherence length. In both cases galactic dynamo [?] should amplify the seed magnetic fields up to the necessary magnitude.

2 A comment on astrophysical mechanism

The total energy of galactic magnetic field in a large galaxy, e.g. in the Milky Way, is equal to:

$$\mathcal{E}^B_{gal} = \frac{4}{3}\pi R^3_{gal}\rho_B \approx 10 M_\odot \tag{2}$$

where $M_\odot$ is the solar mass. Magnetic energy of a neutron star with radius $R_{ns} = 10^6$cm is equal to $\mathcal{E}^B_{ns} \approx 10^{-11} M_\odot (B/10^{13}G)^2$. Magnetic energy of white dwarfs with $R_{wd} = 10^9$cm is $\mathcal{E}^B_{wd} \approx 10^{-10} M_\odot (B/10^9 G)^2$. Thus about 10^{11} white dwarfs with magnetic field $B = 10^{10}$G or 10^{12} neutron stars with $B = 10^{13}$G should be in the Galaxy to feed galactic magnetic field if the energy of the field were not lost in the process of line reconnection. Since the total number of stars in the Galaxy is about $2 \cdot 10^{11}$ it is hardly possible to meet this requirement. Of course this estimate is quite rough and more accurate considerations may be not so negative but still it shows that efficiency of stellar creation of galactic magnetic field should be very high to satisfy energy constraints.

3 Generation of seed magnetic fields in the early universe

It is well known that during inflation very long gravitational waves and large scale scalar field perturbations are generated. A natural question is: "why not electromagnetic fields?" The answer is that scalars and tensor fields are not conformally invariant even in the zero mass case, while photons are. Conformal invariance means that rescaling metric with an arbitrary factor $b(t, \mathbf{r})$ and the fields by the same factor to a power depending on the spin of the field we arrive to formally the same action written in terms of new variables. According to the Parker theorem [?] conformally invariant fields are not generated in conformally flat space-time. Indeed it is known that cosmological Friedman-Robertson-Walker (FRW) background is conformally flat, i.e. after the proper coordinate choice the metric can be written in the form

$$ds^2 = a(\tau, \mathbf{x})^2 \left(d\tau^2 - d\mathbf{x}^2\right), \tag{3}$$

Thus after conformal transformation with the factor $b = a(\tau, \mathbf{x})$ to a proper power we can exclude FRW-gravity for conformally invariant fields. Fortunately, as it has been already mentioned, this cannot be done for scalar (in particular, inflaton) fields. Otherwise cosmological density perturbations would not be generated and we would not be here.

Several possible ways to break conformal invariance of electrodynamics and to create seed magnetic fields have been discussed in the literature:

1. New non-minimal interaction of electromagnetic field with gravity, possibly not gauge invariant [?] :

$$\mathcal{L} = C_1 R A_\mu A^\mu + C_2 R_{\mu\nu} A^\mu A^\nu + C_3 R_{\mu\nu\alpha\beta} F^{\mu\nu} F^{\alpha\beta} + ... \qquad (4)$$

   where A_μ is the electromagnetic vector-potential, $F^{\mu\nu}$ is the Maxwell tensor, $R_{\mu\nu\alpha\beta}$ is the Riemann tensor, $R_{\mu\nu}$ is the Ricci tensor, and R is the curvature scalar.

2. Interaction with a new hypothetical field, dilaton, θ [?]:

$$\mathcal{L} = -(1/4)\, e^{\theta}\, F_{\mu\nu} F^{\mu\nu} \qquad (5)$$

3. Quantum conformal anomaly due to famous triangle diagram which leads to non-zero trace of the energy-momentum tensor of electromagnetic field and breaks in this way conformal invariance of electrodynamics [?]:

$$T^\mu_\mu = \kappa F_{\mu\nu} F^{\mu\nu} \qquad (6)$$

   where the constant coefficient κ depends upon the rank of the gauge group and the number of charged fermions. For $SU(N)$ with N_f number of charged fermions it is: $\kappa = (\alpha/\pi)(11N/3 - 2N_f/3)$.

In all these models electromagnetic waves could be generated at inflationary stage and sufficiently large magnetic fields at very large scales would be created to serve as seeds for galactic fields, if one takes appropriate values of of coupling constants in the Lagrangians or sufficiently large number of charge particles in the third case. Unsatisfactory features of this approach are introduction of new fields or interactions, though the second case looks quite natural in string inspired theories, while the third one looks good in grand unification models especially keeping in mind that the fine structure coupling constant α becomes quite large, about 1/40, at the unification scale. The latter makes the mechanism much more efficient.

4 Generation of vorticity perturbations by cosmological inhomogeneities

There are several mechanisms which might create inhomogeneities in the primeval plasma whose relaxation could lead to generation of primordial magnetic fields:

1. First order phase transitions creating bubbles of one phase inside another [?]. Though the magnitude of magnetic fields produced on the boundaries between the phases could be very large, the characteristic scale is extremely small and it is difficult to stretch it up to galactic size.

2. Creation of stochastic inhomogeneities in cosmological charge asymmetry, either electric [?], or e.g. leptonic [?] at large scales which produce turbulent electric currents and, in turn, magnetic fields. The first of these models could be quite efficient but it demands rather unusual physics. For realization of the second model only one rather innocent assumption is necessary, namely, an existence of sterile neutrino, ν_s, very weakly mixed with active ones, $\nu_{e,\mu,\tau}$. If ν_s is lighter than ν_a and the mass difference is sufficiently large then the MSW-resonance transition between ν_s and active neutrinos would take place giving rise to a large, about 0.1, and strongly fluctuating lepton asymmetry in the active neutrino sector [?]. When the wave length of the domain with a large lepton (or anti-lepton) number crossed horizon, the neutrino or antineutrino flux from this domain would induce electric current by scattering on electrons or positrons because of different νe^-- and νe^+-cross-sections. In this process hydrodynamical flows with large Reynolds numbers would be generated and turbulent vortical currents could be produced. The characteristic wave length of the generated magnetic field is about 100 pc and chaotic line reconnection and large but not unreasonable dynamo amplification are necessary for explanation of the observed galactic fields.

3. Generation of seed magnetic fields slightly before hydrogen recombination epoch [?] through relaxation of the usual density perturbations which are known from observations to exist. This model does not demand any new physics and predicts quite promising amplitude of seed fields at galactic scales. Since the work [?] is new, not yet published, we will discuss it in the next section in some detail.

5 Generation of large scale magnetic fields at recombination epoch

We will consider the period when the universe was already quite old and cool with temperature about 1-100 eV, i.e. somewhat before hydrogen recombination. The usual cosmological density perturbations are known to exist at that

time, with rather small amplitude, $\delta\rho/\rho \sim 10^{-4}$. The motion of the cosmological plasma, or better to say fluid, under pressure forces is governed by the hydrodynamical equation (see e.g. the book [?]):

$$\rho\left(\partial_t v_i + v_k \partial_k v_i\right) = -\partial_i p + \partial_k \left[\eta\left(\partial_k v_i + \partial_i v_k - \frac{2}{3}\delta_{ik}\partial_j v_j\right) + \partial_i\left(\zeta\,\partial_j v_j\right)\right] \quad (7)$$

where v is the velocity of the fluid element, ρ and p are respectively the energy and pressure densities of the fluid, and η and ζ are the first and second viscosity coefficients. In the case of constant viscosity coefficients this equation is reduced to the well known Navier-Stokes equation. The coefficient η is related to the mean free path of particles in fluid as

$$\eta/\rho \equiv \nu = l_f \quad (8)$$

In what follows we disregard the second viscosity ζ.

The behavior of the solution to eq. (??) crucially depends upon the value of the Reynolds number

$$R_\lambda = \frac{v\lambda}{\nu} \quad (9)$$

where λ is the wavelength of the velocity perturbations. If $R \gg 1$, then the fluid motion would become turbulent and non-zero vorticity would be created by spontaneously generated turbulent eddies. In the opposite case of low R the motion is smooth and and no vorticity could be generated in the first order in $\delta\rho$. One would expect that in the case of scalar perturbations vorticity remains zero in any order in $\delta\rho$. However, this is not the case, as we will argue in what follows.

Let us first estimate the Reynolds number of the fluid motion created by the pressure gradient in eq. (??). To this end we assume that the liquid is quasi incompressible and homogeneous, so that the second term in the r.h.s. of this equation can be neglected. This is approximately correct and the obtained magnitude of the fluid velocity is sufficiently accurate. In this approximation eq. (??) reduces to a much simpler one:

$$\partial_t \mathbf{v} + (\mathbf{v}\,\nabla)\,\mathbf{v} - \nu\Delta\mathbf{v} = -\frac{\nabla p}{\rho} \quad (10)$$

A comment worth making at this stage. The complete system of equations includes also continuity equation which connects the time variation of energy density with the hydrodynamical flux (see below eq. (??)) and the Poisson equation for gravitational potential induced by density inhomogeneities. We will however neglect the gravitational force and the back reaction of the

fluid motion on the density perturbation. This approximation would give a reasonable estimate of the fluid velocity for the time intervals when acoustic oscillations are not yet developed, i.e. for $t < \lambda/v_s$, where λ is the wave length of the perturbation and v_s is the speed of sound (in the case under consideration $v_s^2 = 1/3$). In fact the wave length should be larger than the photon mean free path, to avoid diffusion damping, and the characteristic time interval, as we see below, should be somewhat larger than λ. So we may hope that our estimates of the velocity are reasonable enough. Neglecting gravitational forces, especially those induced by dark matter would result in a smaller magnitude of the fluid velocity, so the real effect should be somewhat larger.

For small velocities (or sufficiently small wavelengths) we may neglect the second term in the l.h.s. with respect to the third one. In this approximation the equation becomes linear and can be easily solved for the Fourier transformed quantities. Assuming that the parameters are time-independent (though it is not necessary) we obtain:

$$\mathrm{v_k} = -\frac{i\mathrm{k}}{3k^2\nu}\,\delta_k\,\left[1 - \exp(-\nu k^2 t)\right] \tag{11}$$

where $\delta_k = (\delta\rho/\rho)_k$ is the Fourier transform of relative density perturbations, $\delta\rho/\rho$; its natural value is $\sim 10^{-4}$, though it might be much larger at small scales. The coefficient $1/3$ comes from equation of state of relativistic gas, $p = \rho/3$.

Therefore, for the Reynolds number we obtain:

$$R_k = \frac{\delta_k}{3\,(k\,\nu)^2}\left[1 - \exp\left(-\nu k^2 t\right)\right]\,. \tag{12}$$

If δ_k is weakly dependent on k, then R_k is a monotonically rising function of the wavelength $\lambda = 2\pi/k$. For $t \ll \lambda^2/\nu$ it takes the value

$$R_k = \frac{t}{3\nu}\,\delta_k \ll 1, \tag{13}$$

so the hydrodynamical flow remains laminar and vorticity is not spontaneously generated. Dynamical generation of vorticity is governed by the equation:

$$\partial_t \Omega - \nu\Delta\,\Omega = -\nabla \times \left(\frac{\nabla p}{\rho}\right) \tag{14}$$

where $\Omega = \nabla \times \mathbf{v}$ and we assume that velocity is small so that the term quadratic in v was neglected. If the r.h.s. is non-vanishing, then Ω would be non-zero too. However usually pressure density is proportional to the energy density, $p = w\rho$, with a constant coefficient w and hence $\nabla \times (\nabla p/\rho) = 0$. We

can see that this is not so because cosmic plasma consist of different components whose motion is somewhat different. Let us assume that plasma is in local thermal equilibrium with common temperature $T(\mathbf{x})$. This assumption is justified by a large interaction rate between radiation and charged particles. If T would be the only parameter which determines the state of the medium, then vorticity would not be generated because we would have in our disposal only ∇T and it is impossible to construct non-vanishing $\nabla \times \mathbf{v}$ from the gradient of only one scalar function. However, distributions of charged particles depend upon one more function, their chemical potential:

$$f = \exp\left[-\frac{E}{T(\mathbf{x})} + \xi(\mathbf{x})\right] \tag{15}$$

where the dimensionless chemical potential ξ can be readily expressed through particle number density $n_e \approx n_B = \beta(x) n_\gamma$ with $\beta(x) = 6 \cdot 10^{-10} + \delta\beta(x)$:

$$\xi(x) = \ln \beta(x) + \text{const} \tag{16}$$

Hence we will find that the source term in the vorticity equation (??) is equal to:

$$S_k \equiv -\epsilon_{ijk}\, \partial_j \left(\frac{\partial_i p}{\rho}\right) = \epsilon_{ijk}\, \frac{\partial_i \rho_\gamma}{3\rho_{\rm tot}}\, \frac{\partial_j \beta}{\beta}\, \frac{\rho_b}{\rho_{\rm tot}} \tag{17}$$

An essential feature here is that the spatial distribution of charged particles does not repeat the distribution of photons and hence the vectors $\nabla\rho_\gamma$ and $\nabla\beta$ are not collinear. This could occur if, for the wave length corresponding to subgalactic scales, there exist baryon isocurvature fluctuations and thus $\rho(x)$ and $\beta(x)$ have different profiles. As we have mentioned above, different mean free paths of photons and charged particles would maintain such non-collinearity of the order of unity at the scales $\lambda \sim l_\gamma$. Moreover, even in the case of adiabatic perturbations a shift in the distribution of photons and charged particles could also be created because of acoustic oscillations that proceeded with different phases of radiation and matter densities. At the scales $\lambda \leq l_\gamma$ perturbations in the the plasma temperature would be erased by the diffusion damping [?], while for $\lambda \gg l_\gamma$ the diffusion processes are not efficient and one would expect self-similar perturbation leading to collinearity of $\nabla\rho_\gamma$ and $\nabla\beta$. On the other hand, when λ entered under horizon acoustic oscillations begun which destroyed the self-similarity. Thus the expected wavelengths of vorticity perturbations should be between $l_\gamma < \lambda < H^{-1}$.

Surprisingly vorticity can be also generated (and in the case under consideration even a larger one) if perturbations in plasma are determined by a single scalar function, for example, by $T(t, \mathbf{x})$ because it might be proportional to the product $\partial_i T(t, \mathbf{x})\, \partial_j T(t', \mathbf{x})$. These two gradients generally are not collinear if

taken at different time moments t and t'. To see that, let us start from the Boltzmann equation for the distribution function $f(t, \mathbf{x}, E, \mathbf{p})$ of photons:

$$\left(\frac{\partial}{\partial t} + \mathbf{V}\cdot\nabla - H\,\mathbf{p}\frac{\partial}{\partial \mathrm{p}} + \mathbf{F}\,\frac{\partial}{\partial \mathbf{p}}\right) f(t, \mathbf{x}, E, \mathbf{p}) = I_{\rm coll}\left[f_a, f_b, ...\right] \ , \qquad (18)$$

where $\mathbf{V} = \mathrm{p}/E$ is the particle velocity (not to be confused with the velocity $\mathbf{v}$ of macroscopic motion of the medium, for photons $V = 1$, while $v \ll 1$), E and $\mathbf{p}$ are respectively the particle energy and spatial momentum, H is the universe expansion rate, $\mathbf{F}$ is an external force acting on particles in question (the latter is assumed to be absent), and $I\left[f_a, f_b, ...\right]$ is the collision integral depending on the distributions f_a of all participating particles.

At temperatures in eV-range only the Thomson scattering of photons on electrons is essential, so the collision integral is dominated by the elastic term. Integrating both parts of eq. (??) over $d^3p/(2\pi)^3$ we arrive to the continuity equation:

$$\dot{n}(\mathbf{x}) + \nabla \mathrm{J} = 0 \qquad (19)$$

where $\mathbf{J}$ is the photon flux given by

$$\mathrm{J} \equiv \mathrm{v}n = \int \frac{d^3p}{(2\pi)^3}\,\frac{\mathbf{p}}{E}\,f \qquad (20)$$

and $\mathbf{v}$ is the average macroscopic velocity of the photon plasma. Using the standard arguments one can derive from eq. (??) the diffusion equation:

$$\dot{n} = D\,\Delta n \qquad (21)$$

where $D \approx l_\gamma/3$ is the diffusion coefficient. We will use this equation below to determine time evolution of the photon temperature T.

If the elastic reaction rate $\Gamma_{\rm el} = \sigma_{\rm Th} n_e X_e = 1/l_\gamma$ is sufficiently large, local thermal equilibrium would be established and the photon distribution would be approximately given by

$$f \approx f_0 = \exp\left(-E/T + \xi\right) \qquad (22)$$

where the temperature and effective chemical potential could be functions of time and space coordinates: $T = T(t, \mathbf{x})$ and $\xi = \xi(t, \mathbf{x})$, and the photon mean free path is given by $l_\gamma = 30\,\mathrm{pc}/X_e(T)T_{eV}^3$, where T_{eV} is the plasma temperature in eV and X_e is a fraction of the free electrons: $X_e(z)$ is practically 1 for $z > 1500$, and sharply decreases for smaller z's, reaching values $\sim 10^{-5}$ at $z < 1000$.

Evidently f_0 annihilates the collision integral. We can find correction to this distribution, $f = f_0 + f_1$, substituting this expression into kinetic equation (??) and approximating the collision integral in the usual way as $-\Gamma_{el} f_1$:

$$(K + \Gamma_{el})\, f_1 = -K f_0 \tag{23}$$

where K is the differential operator, $K = \partial_t + (\mathbf{V}\,\nabla)$. The solution of this equation is straightforward:

$$f_1\,(t, \mathbf{x}, E, \mathbf{V}) = -\int_0^t d\tau_1 \exp\left[-\int_0^{\tau_1} d\tau_2 \Gamma_{el}\,(t - \tau_2, \mathbf{x} - \mathbf{V}\tau_2)\right] K f_0\,(t - \tau_1, \mathbf{x} - \mathbf{V}\tau_1) \tag{24}$$

Using this result we can calculate the average macroscopic velocity of the plasma. The calculations are especially simple if elastic scattering rate is high and the integrals are dominated by small values of τ_1. In this case we obtain:

$$v_j(t, \mathbf{x}) = \frac{\int d^3p V_j f_1(t, \mathbf{x}, E. \mathbf{V})}{\int d^3p f_0(t, \mathbf{x}, E)} \tag{25}$$

and the vorticity, $\Omega_i = \epsilon_{ijk}\partial_j v_k$ is:

$$\Omega_i \approx 6\epsilon_{ijl}\, l_\gamma^2 \left(\frac{\partial_j T}{T}\right)\left(\frac{\partial_l \partial_l T}{T}\right) \tag{26}$$

To estimate time derivatives of the temperature we will use the diffusion equation (??), from which we find $\partial_l T = D\Delta T$ and finally obtain for vorticity with the wave vector $k = 2\pi/\lambda$:

$$|\Omega|_\lambda \approx 2\left(\frac{\delta T}{T}\right)_\lambda^2 l_\gamma^3\, k^4 \approx 3 \cdot 10^3 \left(\frac{\delta T}{T}\right)_\lambda^2 \frac{l_\gamma^3}{\lambda^4} \tag{27}$$

Since the photon diffusion erases temperature fluctuations at the scales $\lambda < l_\gamma$ the vorticity reaches maximum value near $\lambda \sim l_\gamma$. This magnitude of vorticity is considerably larger than found previously with the source term (??) and we will rely on it in the estimates of magnetic field presented below.

Since the conductivity of cosmic plasma is very high,

$$\kappa = (3/2\alpha)\,(n_e/n_\gamma)\,(m_e^2 T), \tag{28}$$

the generation of magnetic field by the source currents, created by the cosmological inhomogeneities, is governed by the well know equation of magnetic hydrodynamics:

$$\partial_t \mathbf{B} = \nabla \times (\mathbf{v} \times \mathbf{B}) + \frac{1}{\kappa}\nabla \times \mathbf{J} \tag{29}$$

The electric current J induced by the relaxation of the density inhomogeneities would contain two components: electronic and protonic. However the first one is surely dominant because it is much easier to drift electrons than heavier protons. This is why a non-zero current can be induced in electrically neutral medium. Of course the motion of electrons would not produce any excess of electric charge because the current could be realized by the flow of the dominant homogeneous part of electron distribution.

The solution of eq. (??) can be roughly written as

$$B \sim \int_0^t dt_1 \left(\frac{2\pi J}{\lambda \kappa}\right) e^{2\pi v t_1/\lambda} \tag{30}$$

An estimate of magnetic field without pregalactic dynamo enhancement can be easily done if the helical source current is known, $\nabla \times \mathbf{J} = en_e\Omega$. With Ω given by eq. (??) and B by eq. (??) we obtain:

$$\frac{B_0}{T^2} = 0.24 \cdot 10^3 (4\pi\alpha)^{3/2} \left(\frac{t}{\lambda}\right) \left(\frac{l_\gamma}{\lambda}\right)^3 \left(\frac{T}{m_e}\right)^2 \approx 10^{-8} T_{cV}^3 \tag{31}$$

where we took the wavelength equal to the photon mean free path, $\lambda = l_\gamma$.

If we take into account that linear compression of pregalactic medium in the process of galaxy formation is approximately $r \sim 10^2$, the seed field in a galaxy after its formation would be $r^2 B_0$, i.e. 4 orders of magnitude larger than that given by eq. (??) and, for $T = 1$ eV, a relatively mild galactic dynamo, about 10^4, is necessary to obtain the observed galactic magnetic field of a few micro-Gauss at the scale $l_B \sim (100/r)$ kpc = 1 kpc. The seed magnetic fields formed earlier (at higher T) would have larger magnitude ($\sim T^3$) but their characteristic scale would be smaller by factor $1/T^2$. Chaotic line reconnection could create magnetic field at larger, galactic scale l_{gal}, but the magnitude of this field would be suppressed by Brownian motion law - it would drop by the factor $(l_B/l_{gal})^{3/2}$. It is interesting that according to these results all scales give comparable contributions at l_{gal}. This effect may lead to an enhancement of the field but it is difficult to evaluate the latter. Let us also note that magnetic fields generated by the discussed mechanism at the cluster scale, 10 Mpc, should be not larger than 10^{-8} μG if no additional amplification took place.

Larger density perturbations could be helpful for generation of larger magnetic field for which dynamo might be unnecessary. Though much bigger δT is not formally excluded at the scale about 100 kpc, but to have them at the level $(\delta T/T)^2 \sim 10^{-4}$ seems to be too much. A natural idea is to turn to a later stage, to onset of structure formation when $\delta\rho/\rho$ becomes larger than 10^{-2}. With such density perturbations strong enough magnetic fields might be generated without dynamo amplification. However after recombination the

number density of charge carriers drops roughly by 5 orders of magnitude. Correspondingly l_γ rises by the same amount and the strength of the seed field would be 5 orders of magnitude smaller if density perturbations and the temperature of formation remained the same. However both became very much different. Density perturbations rose as scale-factor, $(\delta\rho/\rho)^2 \sim (T_{eq}/T)^2$, where $T_{eq} \sim 1$ eV is the temperature when radiation domination changed into matter domination and density perturbations started to rise. Since, $B/T^2 \sim T^3$, according to eq. (??), the net effect of going to smaller T is a decrease of B/T^2 which would be difficult to cure even by later reionization. Still, as argued in ref. [?], magnetic field generation, driven by anisotropic and inhomogeneous radiation pressure (and in this sense similar to our mechanism) at the epoch of reionization, could end up with the field of about $8 \cdot 10^{-6}\mu$G. This result is 8 orders of magnitude larger than that found in the earlier papers [?] and quite close to ours (??), though these two mechanisms operated during very different cosmological epochs and were based on different physical phenomena.

Generation of magnetic field at recombination was also considered in ref. [?] where a much weaker result was found. This difference can be possibly attributed to the following effects. We considered above an earlier period when the photon mean free path was much smaller than the horizon. It gives a factor about 10^3 in fluid velocity, eq.(??). Moreover, since in our case the electrons are tightly bound to photons the electron-photon fluid moves as a whole (while protons and ions are at rest) and the electric current induced by macroscopic motion/oscillations of plasma is noticeably larger.

6 Conclusion

Despite many suggested models, the origin of galactic magnetic fields and, especially, intergalactic, if existence of the latter is confirmed, remains mysterious. One class of models is based on known physics and do not invoke any ad hoc assumptions for the explanation of the phenomenon. The explanation based on stellar ejecta possibly encounters serious difficulties because of energy constraints. The mechanism of field generation just before hydrogen recombination looks reasonably good but probably it cannot explain both galactic and intergalactic fields within the frameworks of the standard cosmology with flat spectrum of density perturbations.

Another class of models is based on physical phenomena in the early universe and its different members are spread between inflationary stage to relatively late MeV-epoch. These models manipulate with unknown physics (except possibly the MeV one) and because of that are much less restricted in their possibilities. It is a difficult task to understand what mechanism is indeed responsible for creation of the observed magnetic fields. A critical test would be a possibility of simultaneous explanation of galactic and intergalactic fields.

To this end a confirmation of a possible existence of the latter is of primary importance.

7 Acknowledgements

The hospitality of the Research Center for the Early Universe of the University of Tokyo, where this contribution was prepared for publication, is gratefully acknowledged.

References

1. P.P. Kronberg, Rep. Prog. Phys., **57**, 325 (1994);
   R. Beck et al, Ann. Rev. Astron. Astrophys., **34**, 155 (1996).

2. D. Grasso, H.R. Rubinstein, Phys. Repts., **348**, 161 (2001);
   A.D. Dolgov, hep-ph/0110293; in Gurzadyan, V.G. (ed.) et al.: From integrable models to gauge theories, p. 143.

3. P.L. Biermann, C.F. Galea, to be published in Proc. Palermo Meeting, Sept. 2002, Eds. N. G. Sanchez et al., astro-ph/0302168.

4. K. Dimopoulos, T. Prokopec, O. Tornkvist, A. C. Davis, Phys. Rev. **D65**, 063505 (2002).

5. A.A. Ruzmaikin, A.M. Shukurov, D.D. Sokolov, "Magnetic Fields in Galaxies", Kluwer Academic Publishers, Dordrecht, 1988;
   R.M. Kulsrud, Ann. Rev. Astron. Astrophys. **37**, 37 (1999);
   L. Malyshkin, R. Kulsrud, astro-ph/0202284.

6. L. Parker, Phys. Rev. Lett. **21**, 562 (1968).

7. M.S. Turner and L.M. Widrow, Phys. Rev. **D37**, 2743 (1988).

8. B. Ratra, Astrophys. J. **391**, L1 (1992).

9. A.D. Dolgov, Phys.Rev. **D48**, 2499 (1993);
   A.D. Dolgov, Pisma Zh. Eksp. Teor. Fiz. **32**, 673 (1980);
   A.D. Dolgov, Sov. Phys. JETP, **54**, 223 (1981) [Zh. Eksp. Teor. Fiz. **81**, 417 (1981).

10. C.H. Hogan, Phys. Rev. Lett., **51**, 1488 (1983);
    T. Vachaspati, A. Vilenkin, Phys. Rev. Lett., **67**, 10 (1991).

11. A.D. Dolgov, J. Silk, Phys.Rev., **D47**, 3144 (1993).

12. A.D. Dolgov, D. Grasso, Phys. Rev. Lett. **88**, 011301 (2002).

13. P.Di Bari, Phys.Lett. **B482**, 150 (2000).

14. Z. Berezhiani, A.D. Dolgov, astro-ph/0305595.

15. L.D. Landau, E.M. Lifshits, "Gidrodinamika" (Hydrodynamics) (Moscow: Nauka, 1986) [Translated into English "Fluid Mechanics" (Oxford: Pergamon Press, 1987)].

16. J. Silk, Astrophys. J. **151**, 459 (1968).

17. M. Langer, J.-L. Puget, N. Aghanim, Phys. Rev. D67 (2003) 043505.

18. K. Subramanian, D. Narasimha, S.M. Chitre, Mon. Not. Roy. Astr. Soc. 271 (1994) L15;
N.Y. Gnedin, A. Ferrara, E.G. Zweibel, Astrophys. J. 539 (2000) 505.

19. C. Hogan, astro-ph/0005380.

$c/\sqrt{3}$: CRITICAL VELOCITY

M.I. Vysotsky
ITEP, 117218 Moscow, Russia

Abstract

We define the critical coordinate velocity v_c. A particle moving radially in Schwarzschild background with this velocity, $v_c = c/\sqrt{3}$, is neither accelerated, nor decelerated if gravitational field is weak, $r_g \ll r$, where r_g is the gravitational radius, while r is the current one. We find that the numerical coincidence of v_c with velocity of sound in ultrarelativistic plasma, u_s, is accidental, since two velocities are different if the number of spatial dimensions is not equal to 3.

This talk is based on paper [1] written in collaboration with S.I. Blinnikov and L.B. Okun.

1 Motivation

According to General Relativity (GR) clocks run slowly in the presence of gravitational field, as a result, the coordinate velocity of photons decreases. This is the reason for the delay of radar echo from inner planets predicted and measured by I. Shapiro [2]. Propagation of ultrarelativistic particles is described similarly to that of photons. That is why the retardation must take place not only for photons but also for ultrarelativistic particles. In this respect the latter drastically differ [3] from nonrelativistic bodies, velocity of which evidently increases when they are falling radially onto a gravitating body (e.g., onto the Sun). Obviously, there should be some intermediate velocity v_c which remains constant for a particle falling in gravitational field of the Sun (or another star). The numerical value $v_c = c/\sqrt{3}$ will be found in Sect. 2. When a particle moves radially with this velocity in weak field it "ignores" gravity: it is neither accelerated, nor decelerated. For nonradial trajectories gravity is never ignored: the trajectories are bent for any velocity.

It is well known that $u_s = c/\sqrt{3}$ is the speed of sound in ultrarelativistic plasma and the question arises whether the equality $u_s = v_c$ has some physical reason, or it is a numerical coincidence. To answer this question we find in Sect. 3 expressions for v_c and u_s in spaces with number of dimensions n different from 3. Since for $n \neq 3$ we get $v_c \neq u_s$ we come to the conclusion that their coincidence at $n = 3$ does not have deep physical reason.

2 Derivation of $v_c = c/\sqrt{3}$

To simplify formulas, we put light velocity $c = 1$, restoring it when it is necessary. In what follows G is gravitational constant; gravitational radius r_g of an object with mass M equals

$$r_g = 2GM \ . \tag{1}$$

Let us start from definitions used in GR. The expression for interval in the case of radial motion ($d\theta = d\varphi = 0$) has the well known Schwarzschild form:

$$ds^2 = g_{00}dt^2 - g_{rr}dr^2 \equiv d\tau^2 - dl^2 \ , \tag{2}$$

where $g_{00} = (g_{rr})^{-1} = 1 - \frac{r_g}{r}$. The local velocity v of a particle measured by a local observer at rest is:

$$v = \frac{dl}{d\tau} = \left(\frac{g_{rr}}{g_{00}}\right)^{1/2} \frac{dr}{dt} = \frac{1}{g_{00}} \frac{dr}{dt} \ , \tag{3}$$

while observer at infinity, where $g_{00}(\infty) = g_{rr}(\infty) = 1$, measures the so-called coordinate velocity at r:

$$\mathrm{v} = \frac{dr}{dt} = v\left(\frac{g_{00}}{g_{rr}}\right)^{1/2} = g_{00}v \ . \tag{4}$$

In order to determine the time of radial motion from a to b, the infinitely distant observer should calculate the integral

$$t = \int_a^b \frac{dr}{\mathrm{v}} \ , \tag{5}$$

that is why the coordinate velocity is relevant for radar echo.

For a particle moving in static gravitational field one can introduce conserved energy (see ref. [4], eq. 88.9):

$$E = \frac{m\sqrt{g_{00}}}{\sqrt{1-v^2}} \ . \tag{6}$$

The expression for E through v:

$$E = \frac{m\sqrt{g_{00}}}{\sqrt{1-(\mathrm{v}/g_{00})^2}} \tag{7}$$

allows us to determine $\mathrm{v}(r)$ from the energy conservation:

$$E(r=\infty) = E(r) \ , \tag{8}$$

$$\mathrm{v}^2 = g_{00}^2 - g_{00}^3 + g_{00}^3\mathrm{v}_\infty^2 = g_{00}^2[1 - g_{00}(1-\mathrm{v}_\infty^2)] \ . \tag{9}$$

For the local velocity v measured by a local observer we obtain:

$$v^2 = 1 - g_{00}(1-\mathrm{v}_\infty^2) \ , \tag{10}$$

so, while v always increases for a falling massive particle, reaching c at $r = r_g$, the behaviour of v is more complicated. Substituting $g_{00} = 1 - \frac{r_g}{r}$ into (9), we get for weak gravitational field ($r \gg r_g$):

$$\mathrm{v}^2 = \mathrm{v}_\infty^2 + \frac{r_g}{r}(1 - 3\mathrm{v}_\infty^2) \ . \tag{11}$$

For the motion of a nonrelativistic particle ($\mathrm{v}_\infty \ll 1$) the well-known expression is reproduced:

$$\mathrm{v}^2 = \mathrm{v}_\infty^2 + \frac{2MG}{r} \ . \tag{12}$$

For $v_\infty = v_c = 1/\sqrt{3}$ the coordinate velocity of particle does not change, while it grows for $v_\infty < v_c$ and diminishes for $v_\infty > v_c$. At $r = 3r_g$ according to eq.(11) the coordinate velocity becomes equal to v_c. However, for $r = 3r_g$ our weak field approximation fails.

Let us dispose of the assumption of the weak field. Coming back to expression (9) and substituting there $g_{00} = 1 - \frac{r_g}{r}$, we observe that for $v_\infty > v_c$ the coordinate velocity always diminishes and becomes zero at $r = r_g$, while in the case $v_\infty < v_c$ it grows up to the value

$$v^2_{max} = 4/(27(1 - v^2_\infty)^2) , \tag{13}$$

which is reached at

$$r_0 = \frac{3(1 - v^2_\infty)}{(1 - 3v^2_\infty)} r_g , \tag{14}$$

and after that diminishes to zero at $r = r_g$. It is interesting to note that the velocity v measured by local observer equals v_c at the point where $v = v_{max}$.

Thus, if the coordinate velocity is only mildly relativistic, $v_\infty > c/\sqrt{3}$, then v already decreases at the free fall.

As an example of a non-radial motion let us consider the deflection of light from a star by the Sun and compare it with the deflection of a massive particle. It is well known that the angle of deflection θ of photons grazing the Sun is given by

$$\theta_\gamma = \frac{2r_g}{R_\odot} \tag{15}$$

where $R_\odot$ is the radius of the Sun. In the case of massive particles the deflection angle is larger:

$$\theta = \theta_\gamma(1 + \beta^{-2}) , \tag{16}$$

where $\beta \equiv v_\infty/c < 1$.(See ref. [5], eq. 25.49, and ref. [6], problem 15.9, eq.13.)

3 Speed of sound u_s and critical speed v_c in n dimensions

For ultrarelativistic plasma with equation of state $P = e/3$, where P is pressure and e is energy density (including mass density), we have for the speed of sound u_s:

$$u_s^2 = c^2 \left.\frac{\partial P}{\partial e}\right|_{ad} = \frac{c^2}{3} , \tag{17}$$

We use eq. 134.14 of ref. [7], and correct misprint there, or eq. 126.9 from [8]; "ad" means adiabatic, i.e. for constant specific entropy. In order to obtain the expression for u_s in the case when $n \neq 3$, where n is the number of spatial dimensions, let us start with equation of state.

One can use a virial theorem to connect pressure P and thermal energy $\mathcal{E}$ of an ideal gas using classical equations of particle motion (cf. [9]). We have for a particle with momentum $\mathbf{p}$ and a Hamiltonian H:

$$\dot{\mathbf{p}} = -\frac{\partial H}{\partial \mathbf{q}} , \tag{18}$$

hence,

$$\mathbf{q}\dot{\mathbf{p}} = -\mathbf{q}\frac{\partial H}{\partial \mathbf{q}} = \mathbf{q}\mathbf{F} , \tag{19}$$

where $\mathbf{F}$ is the force acting on the particle. Let us average over time t:

$$\langle \ldots \rangle \equiv \frac{1}{t}\int_0^t \ldots d\bar{t} . \tag{20}$$

Integrating by parts we get:

$$\langle \mathbf{q}\dot{\mathbf{p}} \rangle = -\langle \dot{\mathbf{q}}\mathbf{p} \rangle = \langle \mathbf{q}\mathbf{F} \rangle . \tag{21}$$

For non-relativistic (NR) particles

$$\dot{\mathbf{q}}\mathbf{p} = 2E_{\mathrm{kin}} = \mathbf{p}^2/m . \tag{22}$$

For extremely relativistic (ER.) particles

$$\dot{\mathbf{q}}\mathbf{p} = E_{\mathrm{kin}} = c|\mathbf{p}| . \tag{23}$$

Now for N particles in a gas

$$-\sum_{i=1}^{N}\langle \dot{\mathbf{q}}_i\mathbf{p}_i \rangle = \sum_{i=1}^{N}\langle \mathbf{q}_i\mathbf{F}_i \rangle . \tag{24}$$

(By the way, $-\frac{1}{2}\sum_i \langle \mathbf{q}_i\mathbf{F}_i \rangle$ is called the *virial*.) If the gas is ideal (i.e. non-interacting particles), then the force $\mathbf{F}$ is non-zero only at the collision of a particle with the wall, and the virial reduces to an integral involving pressure:

$$-\sum_{i=1}^{N}\langle \dot{\mathbf{q}}\mathbf{p} \rangle = -\int P\mathbf{n}\mathbf{q}\, dS = -P\int \mathrm{div}\,\mathbf{q}\, dV = -3PV , \tag{25}$$

where $\mathbf{n}$ is a unit vector normal to the wall area element dS and the Gauss theorem is used for transforming the surface integral to the volume one. So, since the thermal energy $\mathcal{E}$ (not including mass) is just the total kinetic energy of molecules,

$$\mathrm{NR}: \quad 2\mathcal{E} = 3PV, \quad P = 2\mathcal{E}/(3V) , \tag{26}$$

$$\text{ER}: \quad \mathcal{E} = 3PV, \quad P = \mathcal{E}/(3V) \equiv e/3 \,. \tag{27}$$

The last equality holds since in extremely relativistic case $E_{\text{kin}} \gg m$. We see that 3 here is due to $\operatorname{div} \mathbf{q} = 3$, i.e. the dimension of our space.

In a space of n dimensions, following the same lines, we get $\operatorname{div} \mathbf{q} = n$, so $P = e/n$ and for ER gas we obtain:

$$u_s = c/\sqrt{n} \,. \tag{28}$$

Here we should use n-volume V_n instead of $V \equiv V_3$ and postulate the first law of thermodynamics for adiabatic processes to be $d\mathcal{E} + PdV_n = 0$, so pressure would be the force per unit V_{n-1} – the boundary of V_n.

The same equation of state follows from consideration of the stress tensor T_{ik} of ultrarelativistic plasma, which is diagonal and traceless in a rest frame of plasma: $T_{00} = e$, $T_{ii} \equiv P = e/n$.

In order to find v_c in the case $n \neq 3$ we need an $n+1$-dimensional spherically-symmetric static generalization of the $3+1$-dimensional Schwarzschild metric which was found by Tangherlini [10]. (See refs. [11] for the details of aspherical and time-dependent black holes metrics in higher dimensional spacetimes). The line element of the $n+1$-dimensional Schwarzschild metric is

$$ds^2 = \left(1 - \frac{r_{gn}^{n-2}}{r^{n-2}}\right) dt^2 - \left(1 - \frac{r_{gn}^{n-2}}{r^{n-2}}\right)^{-1} dr^2 - r^2 d\Omega_{n-1}^2, \tag{29}$$

where $d\Omega_{(n-1)}$ is the line element on the unit $(n-1)$-sphere and the gravitational radius r_{gn} is related to the black hole mass M:

$$r_{gn}^{n-2} = \frac{16\pi G_n M}{(n-1)\, A_{n-1}}. \tag{30}$$

Here A_{n-1} denotes the area of a unit $n-1$ sphere, which is $2\pi^{\frac{n}{2}}/\Gamma(\frac{n}{2})$ (for $n = 3$: $\Gamma(3/2) = \sqrt{\pi}/2$, $A_2 = 4\pi$). We consider the spaces with $n \geq 3$. The factor in the definition of r_{gn} is taken from refs. [11]. The form of the metric (29) is very easy to guess. In weak field limit, when $g_{00} \to 1 + 2\varphi$ we have

$$\varphi = -\frac{r_{gn}^{n-2}}{2r^{n-2}} \quad \text{for} \quad r \to \infty \,. \tag{31}$$

This leads in a natural way to the gravitational acceleration g with the radial component

$$g_n = -\frac{\partial \varphi}{\partial r} = -\frac{(n-2) r_{gn}^{n-2}}{2r^{n-1}} \quad \text{for} \quad r \to \infty \,, \tag{32}$$

which implies the constant flux of the acceleration g equal to

$$A_{n-1} r^{n-1} g_n = 8\pi \frac{n-2}{n-1} G_n M \tag{33}$$

through a sphere of area $A_{n-1}r^{n-1}$ at large r. It is not hard to verify that the Ricci tensor R_{ik} is zero for the metric (29), that is the metric (29) satisfies Einstein equations in vacuum and describes a spherically symmetric spacetime outside a spherical gravitating body.

One should remember that the dimension of G_n depends on n. It is clear in the weak field limit from eqs. (31) and (30), since the dimension of $[\varphi]$ is the square of velocity, i.e. zero for $c = 1$, and hence

$$[G_n] = \frac{L^{n-2}}{M}\,, \tag{34}$$

or $[G_n] = L^{n-1}$, if $[M] = L^{-1}$.

For the coordinate velocity of a radially falling particle we get from eq. (9) for weak gravitational field:

$$\mathrm{v}^2 = \mathrm{v}_\infty^2 + \left(\frac{r_{gn}}{r}\right)^{n-2}(1 - 3\mathrm{v}_\infty^2) \tag{35}$$

instead of eq. (11). We see that in the case of n-dimensional space the expression for v_c remains the same, $\mathrm{v}_c = c/\sqrt{3}$. Number "3" here is not due to the dimension of space, it is simply due to cubic polynomial in (9).

4 Conclusions and Acknowledgements

The speed of sound in relativistic, radiation dominated plasma depends on the dimension of space, while the critical velocity $\mathrm{v}_c = c/\sqrt{3}$ in the Schwarzschild metric is the same for any dimension.

I am grateful to the organizers for possibility to participate in such a useful and pleasant event.

References

1. S.I. Blinnikov, L.B. Okun, M.I. Vysotsky, Bled Workshops in Physics **2**, No.2 (2001) 116.

2. I. Shapiro, Phys. Rev. Lett. **13**, 789 (1964); see also S. Weinberg, *Gravitation and Cosmology*, Wiley, 1972.

3. L.B. Okun, Mod. Phys. Lett. **A15**, 1941 (2000).

4. L.D. Landau and E.M. Lifshits, *Teoriya Polya*, Moscow, Nauka, 1967 (in Russian); *Classical Field Theory*, Pergamon Press 1961 (in English).

5. C.W. Misner, K.S. Thorne, J.A. Wheeler, *Gravitation*, W. H. Freeman & Co., 1971.

6. A.P. Lightman, W.H. Press, R.H. Price, S.A. Teukolsky, *Problem Book in Relativity and Gravitation*, Princeton U., 1975.

7. L.D. Landau and E.M. Lifshits, *Hydrodynamics* (in Russian), Moscow, Nauka, 1986.

8. L.D. Landau and E.M. Lifshits, *Fluid Mechanics*, Oxford, Pergamon Press 1982.

9. R. Kubo, *Statistical Mechanics*, North-Holland 1965.

10. F.R. Tangherlini, Schwarzschild field in n-dimensions and the dimensionality of space problem, Nuovo Cimento, **27**, 636 (1963).

11. R.C. Myers and M.J. Perry, "Black holes in higher dimensional spaces", Ann. Phys. **172**, 304 (1986); Leong Chung Wei Bernard, "Black Holes in Higher Dimensions", http://citeseer.nj.nec.com/218539.html

GAMMA RAY BURSTS AND THE SOCIOLOGY OF SCIENCE

A. de Rujula
CERN

Written contribution not received

SESSION II - NEUTRINO PHYSICS

Paolo Desiati	Neutrino Astronomy at the South Pole: Status of the AMANDA Experiment
Phil Adamson*	The Running-in of MINOS
Yoshi Uchida	First Results from the KamLAND
Larry Sulak*	Results from SuperKamiokande
Taku Ishida	Indications of Neutrino Oscillation in the K2K Neutrino Oscillation Experiment
Andrew Hime*	Results from SNO
Jonathan M. Link	Status of MiniBooNE, a Short Baseline Neutrini Oscillation Experiment
Francesco Vissani	Perspectives in Neutrino Physics

* The trasparencies of the missing contributions are available on the web site http://www.pi.infn.it/lathuile/lathuile_2003.html

NEUTRINO ASTRONOMY AT THE SOUTH POLE STATUS OF THE AMANDA EXPERIMENT

Paolo Desiati
desiati@amanda.wisc.edu
Physics Department, University of Wisconsin, Madison, U.S.A.
for the AMANDA Collaboration*

Abstract

AMANDA (Antarctic Muon And Neutrino Detector Array) is a neutrino telescope built under the southern polar icecap, and its scope is exploring the possibility to detect high energy cosmic neutrinos generated by powerful celestial objects where acceleration mechanisms can bring protons up to 10^{20} eV. We describe the achievements and results from the AMANDA-B10 prototype and the preliminary results from the current AMANDA-II detector showing a dramatic increase in sensitivity. An outlook on IceCube will be given.

1 Introduction

Observational astronomy and astrophysics are based on the detection of information carriers to determine the properties of the emitting objects. Three types of carriers have been used so far: electromagnetic radiation, cosmic rays, and neutrinos. The electromagnetic radiation was the first to be observed. Due to their neutral charge, photons are not deflected by interstellar and intergalactic magnetic fields, therefore they point directly back to their source. Photons are emitted within the outer regions of the sources and they cannot give any information about the source internal processes. Moreover, high energy photons are affected by interactions with the microwave and infrared backgrounds (mostly through $\gamma\gamma \rightarrow e^+e^-$), as they traverse intergalactic distances. This limits the range of cosmological sources that can be observed with the highest energy photons.

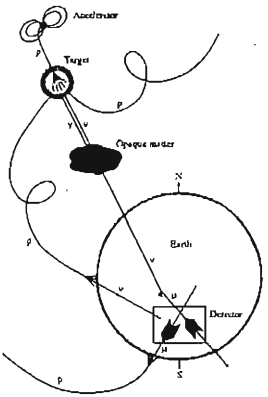

Figure 1: *High energy information carriers*

Cosmic rays are composed of charged nuclei and are deflected by magnetic fields, so they don't bring directional information and they are subject to energy loss processes during their propagation, which deforms the energy spectrum measured at the Earth with respect to the one at the source. Moreover the highest energy cosmic rays ($E \geq 5 \cdot 10^{19}$eV) are expected to be absorbed due to collisions with microwave background photons, through $p + \gamma(2.7°K) \rightarrow p + \pi^\circ$ (Greisen-Zatsepin-Kuzmin, or GZK cutoff [1]). This would generate

a degradation of proton energy after a distance of 50 Mpc [2]. Thus, while cosmic rays carry some information about the energy distribution mechanisms at their source, they cannot indicate directly where those sources are located and they cannot propagate for cosmological distances (see figure 1).

Neutrinos have no electric charge and have a low interaction cross-section with matter. They can propagate from the production sources through cosmological distances, un-deflected by magnetic fields. The distance at which the Universe can be observed with high energy neutrinos is limited only by the signal strength of the source. Thus, they can reach the Earth carrying the complete flux and spectral information about their generation mechanism. On the other hand, their low cross-section makes them difficult to detect. Very large detectors, long exposure times and sophisticated data analyses are needed to measure high energy extraterrestrial neutrino fluxes and spectra. High energy cosmic neutrinos are beleived to be produced in energetic accelerating environments through p-p or p-γ interactions via π production and decay. Such an accelerator might be the core of an active galaxy, powered by a supermassive black hole. The energy dependence of the expected neutrino spectrum is predicted to be $\sim \mathrm{E}^{-2}$.

After Greisen's 1960 review on cosmic ray showers [3], the detection of neutrinos was suggested by Markov and Zheleznikh [4] via the process

$$\nu_l(\bar{\nu}_l) + N \rightarrow l^{\pm} + X \tag{1}$$

of upward or horizontal neutrinos interacting with a nucleon N of the matter surrounding the detector. At high energy, approximately half of the neutrino energy is carried by the produced lepton and the angle between the neutrino and the lepton is, for muon flavor [5]

$$< \psi_{\nu_\mu,\mu} > \approx \left(\frac{0.7^\circ}{E_\nu/\mathrm{TeV}} \right)^{0.7} \tag{2}$$

where E_ν the neutrino energy. At sufficiently high neutrino energy the muon is collinear with the parent neutrino and the muon detection will give information on the neutrino direction. The possibility to measure the high energy cosmic neutrino direction opened the door to neutrino astrophysics. This idea started to become reality with the DUMAND project [6] in the deep Pacific Ocean near Hawaii. This pioneering effort opened the road to the realization of the

first dedicated working projects, Baikal [7] and AMANDA [8], and to the two planned projects in the Mediterranean Sea NESTOR [9] and ANTARES [10].

2 AMANDA-II Description and Operational Principles

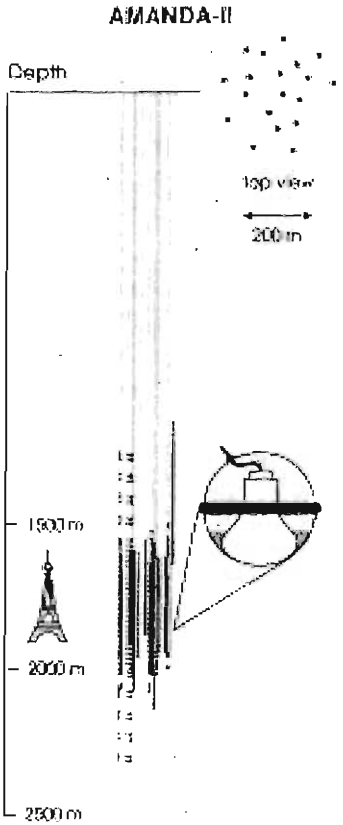

Figure 2: *AMANDA-II schematics*

AMANDA is a neutrino telescope built and operated at the Geographic South Pole. The final detector configuration, called AMANDA-II, was deployed in four South Pole campaigns between November 1995 and February 2000 [11]. The detector consists of 677 optical modules (OM) arranged on 19 vertical strings deployed at depths between 1300-2400 meters. The used instrumented volume ranges between 1500-2000 meters, and covers a cylinder of 200 meters diameter (See figure 2).
An AMANDA-II OM consists of a single 8 inch Hamamatsu R5912-2 photomultiplier tube (PMT) housed in a glass pressure vessel. The PMT is optically coupled to the glass housing by a transparent gel. Each module is connected to electronics on the surface by a dedicated electrical cable, which supplies high voltage and carries the anode signal of the PMT. For each event, the OM is read out by a peak-sensing ADC and TDC capable of registering up to eight separate pulses [12]. The first 10 strings, completed in 1997 and containing 302 OMs, are known as AMANDA-B10, with 120 m diameter.

The holes where AMANDA strings are buried, were produced with high pressure hot water ($\sim 90°C$). The drilling procedure was continuously moni-

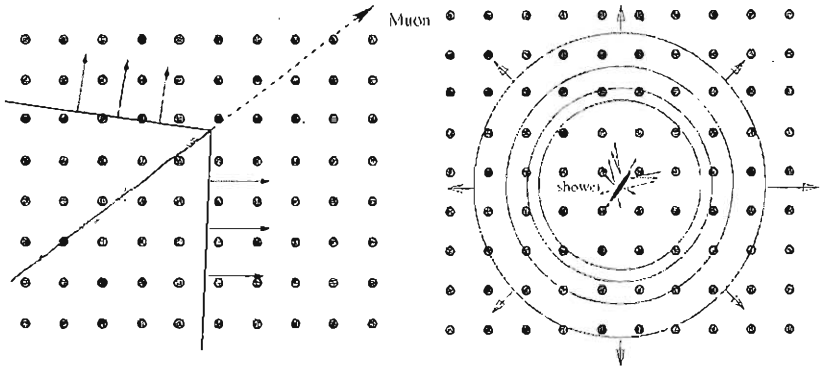

Figure 3: *Cherenkov light detection topology in the AMANDA-II array for tracks (left) and cascades (right)*

tored and the average hole diameter was approximately 50 cm over the entire hole, with a depth-variation, due to the ice temperature profile. The string deployment is done just after drilling is finished and before the hole diameter starts to shrink due to refreezing. Each OM is connected to the main cable and tested in situ at deployment time. The South Pole Air Shower Experiment (SPASE) is a surface array which measures the the shower direction and size, via the electron density [13]. The SPASE/AMANDA coincident events are used to study the cosmic ray composition above 10^{15} eV.

The channels through which neutrino telescopes detect neutrinos above energies of a few tens of GeV is by observing the Cherenkov light from relativistic leptons produced in ν_l-nucleon interactions (eq. 1) in or near the telescope. The primary channel is the ν_μ, which leads to a high energy μ track. The muons can propagate several kilometers through the ice and they can be reconstructed with reasonable precision even with a coarsely instrumented detector, provided the medium is sufficiently transparent. The time and amplitude of detected signals are used to reconstruct the path of the muon through the detector.

The other possible detection channels ν_e and ν_τ have a different behavior. An electron, produced by a ν_e, will generate an electromagnetic cascade, which is confined to a volume of a few cubic meters. It overlays the hadronic cascade of the primary interaction vertex. The size of both cascades is small compared to the OM spacing in the array and the signature is an expanding spherical shell

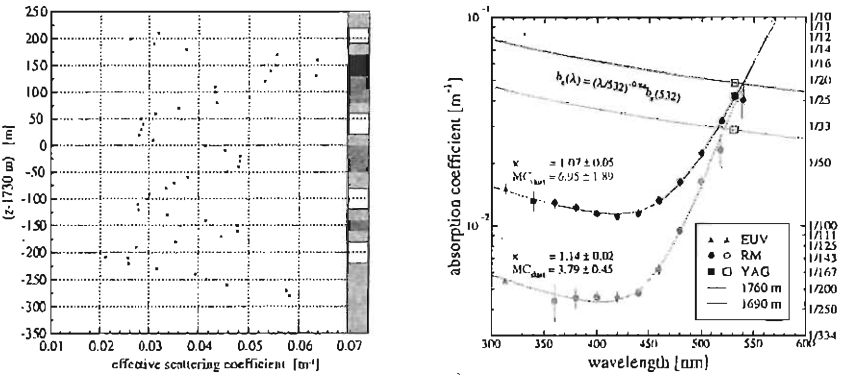

Figure 4: *Left: effective scattering coefficient as a function of depth at 532 nm wavelength. Right: absorption and effective scattering (b_e) coefficients versus wavelengths.*

of Cherenkov photons (figure 3). A τ, produced by a ν_τ, will decay immediately and generate a second hadronic cascade. However, at energies above 1 PeV the two cascades are separated by several tens of meters, connected by a single track.

A detected event corresponds to a realization of a majority trigger of a predefined hit OM channels within 2.5 μs. To ensure that the observed muons are produced by neutrinos, the Earth is used as a filter and only up-going muons are selected. This condition is used to reduce the contamination from down-going cosmic ray muon flux. The location depth in the ice serves to further minimize the flux of cosmic ray muons.

The ice surrounding AMANDA is part of the neutrino telescope and its optical properties are very important and are directly connected to the detector sensitivity. These properties were studied in detail, using in-situ light emitters located on the strings and the down-going muon flux itself. This study shows the ice is not homogeneous [14], but it can be considered as made of several horizontal layers, laid down by varying climatological conditions in the past [15]. Figure 4 shows the effective scattering length versus depth for 532 nm. The figure shows also the absorption and effective scattering lengths as a function of wavelength for 2 different depths. At 400 nm (corresponding to the maximum OM optical sensitivity) the average absorption length at AMANDA-II depth is

110 m and the average effective scattering length is 20 m [12].

The light emitters on the strings are used also as a detector time and geometry calibration system. The time calibration is a measure of the cable length and, therefore, of PMT signal time delay due to cable propagation. The overall precision on the photon arrival times is approximately 5 ns. The position calibration is performed using two sets of information: the absolute array position, obtained from drill recordings and pressure sources, and the relative positions, obtained with the measured propagation times of photons between different light emitters and receivers. The position of the OMs are determined with a precision of about 0.5 m [24].

3 Simulation and Data Processing

In order to study the detector response to the different event sources, a Monte Carlo simulation covering the complete chain from the primary particle flux interactions to the detector response, is used to evaluate the array sensitivity. The down-going muon flux is generated by using CORSIKA (v6.020) shower generator with QGSJET01 interaction model [16]; the up-going muons are generated with a program called NUSIM [17], which allows us to simulate any $\nu_{\mu,e}$ spectrum, the propagation through the Earth and their interactions. The produced muons are propagated through the ice, taking into account all the relevant energy losses [18]. The Cherenkov photon production and propagation are simulated taking into account the ice optical properties and the OM acceptance. The detector trigger simulation includes the hardware response of each OM [19]. At this stage the simulated data are treated exactly as the experimental raw data and passed through the same data processing.

The AMANDA data are passed through a standard filter which is common to all the neutrino analyses. This filtering is performed in 2 separate levels. The level 1 filter (L1) includes the OM cleaning, which excludes the channels which are dead or have odd transient behavior, performs time calibration and a first guess reconstruction. A loose angular cut on the approximate reconstructed muon track is used to filter upward moving tracks and to reduce the amount of data to be passed to the following level. The level 2 filter (L2) applies iterative likelihood reconstructions, which take into account the ice properties, and a Bayesian reconstruction [20]. A second cut on the likelihood reconstructed angle is applied to further reduce the down-going event contamination. To

study down-going muon events the same filter levels are applied but with no angular cut.

4 AMANDA-II Background Sources

4.1 Atmospheric Muons

The largest background source for AMANDA is represented by the down-going cosmic ray muon flux, which is 5 orders of magnitude larger than the total expected neutrino flux, and contributes to the detector trigger with a rate of $\sim$ 100 Hz. Selecting upward reconstructed events (sect. 3) has an important effect in removing a large fraction of these events, but due to the finite reconstruction resolution a small fraction of down-going muon events is mis-reconstructed as upward. Such events represent a background which still needs to be eliminated in any neutrino analysis. Nevertheless the large cosmic ray muon flux can be used to study the detector response, possible systematic effects and also to perform physics measurements. The cosmic ray muon angular and vertical intensities were measured in AMANDA-II and they agree well with simulation, with other experimental measurements and with theoretical calculations [21]. These measured distributions are related to the sea-level muon and primary Cosmic Ray energy spectrum. The measured spectral index of sea-level differential muon spectrum ($\gamma_\mu = 2.70 \pm 0.04$) and of primary differential cosmic ray spectrum ($\gamma_{prim} = 3.72 \pm 0.17$) are in agreement with other experimental results [22]. The down-going muon events which are in coincidence with SPASE surface array [13] were used to measure the cosmic ray mass composition as a function of the primary energy near the knee. An energy resolution of $\sim$ 7% was achieved in the energy range of 1-10 PeV and a tendency toward heavier nuclei above the knee was measured [23].

The down-going muon flux is well understood and an on-going analysis is examining the sensitivity for detecting muons from charmed meson decays in the atmosphere.

Uncorrelated, multiple atmospheric muon events represent another source of background for neutrino analyses. The expected rate of such events is very low in AMANDA-II (of the order of $\sim$ 1 Hz, higher than neutrino trigger rate) but their contamination cannot be neglected as for AMANDA-B10. The contamination of such events becomes clear at high quality cut level where

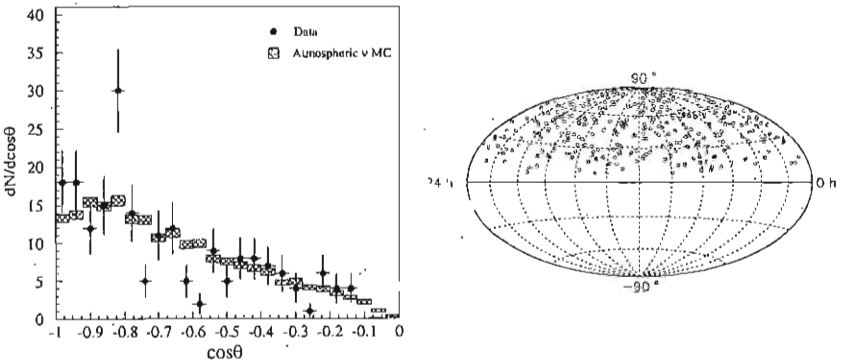

Figure 5: *Left: the zenith angle distribution of up-going reconstructed events. Monte Carlo prediction is normalized to the experimental data. Right: skyplot of the reconstructed events in equatorial coordinates.*

the bulk of atmospheric muons has been eliminated. A typical uncorrelated muon event could be a muon hitting the upper detector and one hitting the lower detector shortly before. The reconstruction tries to find the best up-going single muon track compatible with the recorded hit times. The easiest way to eliminate such a background is to require a uniform hit distribution along the reconstructed track.

4.2 Atmospheric Neutrinos

In order to measure the atmospheric neutrino component, a rejection factor of $\sim 10^5$ is needed to eliminate the cosmic ray muon background contamination. The detection of atmospheric neutrinos in AMANDA provided the first check of the detector sensitivity [24, 12].

Figure 5 shows the published result from the year 1997 of AMANDA-B10. The 130.1 days livetime analyzed gave $N_{exp} = 204$ experimental reconstructed events with a prediction of $N_{MC} = 279 \pm 3$. Normalizing the Monte Carlo simulated events to the experimental sample at high quality level gives a background contamination (i.e. a residual leakage of down-going muons reconstructed as up-going) of 5-10 %. The low neutrino acceptance close to the horizon reflects the effect of down-going muon background elimination. The track pointing resolution is $\psi = 3.2°$ and the skyplot, shown in figure 6, is consistent with

a uniform isotropic flux. The estimated energy of detected neutrino sample ranges between 66 GeV and 3.4 TeV (90 % of events) [12].

AMANDA-II detector, with its increased size, has a better sensitivity than AMANDA-B10 and its larger diameter allows us to better reconstruct the horizontal events. Thus the acceptance near the horizon is improved and the down-going muon flux rejection turns out to be an easier task than with the smaller detector. Requiring a minimum number of direct hits (i.e. hits with a small time residual with respect to the direct Cherenkov light time of propagation), a high likelihood of reconstruction value and a uniform light deposition along the reconstructed track, we record about 4 well reconstructed neutrino events per day in AMANDA-II. The preliminary unfolded ν_μ sea-level energy spectrum was determined and is in agreement with the expectation up to 10^4 GeV [25].

5 AMANDA Analyses

5.1 Diffuse Flux of ν_μ

A search for high energy neutrino flux from unresolved sources throughout the Universe was done in AMANDA-B10, using the data taken during 1997. After cleaning the experimental data sample from atmospheric muon background, the neutrino event selection was designed to retain high energy track-like events [26] in order to eliminate the lower energy atmospheric neutrino background. The energy cut is performed through the hit channel multiplicity observable.

The AMANDA-B10 sensitivity [1] was tested with respect to an assumed high energy neutrino spectrum given by $\Phi_{\nu_\mu} = 10^{-5} \cdot E^{-2}$ cm^{-2}s^{-1}sr^{-1}GeV^{-1}. This spectrum was simulated along with the atmospheric neutrinos and the detector response was studied. Optimizing the atmospheric neutrino background rejection with a suitable channel multiplicity cut, there is no excess of events with respect to the estimated background and a limit was set on the high energy flux. Figure 6 shows the effect of the energy cut on the atmospheric and high energy neutrino events (on the left) and the calculated limit (on the right). The limit, including 25% atmospheric neutrino flux systematic uncertainty, is $\Phi^{lim}_{\nu_\mu} < 8.4 \times 10^{-7} \cdot E^{-2}$ cm^{-2}s^{-1}sr^{-1}GeV^{-1}

[1] defined as 90% CL average upper limit from an ensemble of identical experiments with no signal present

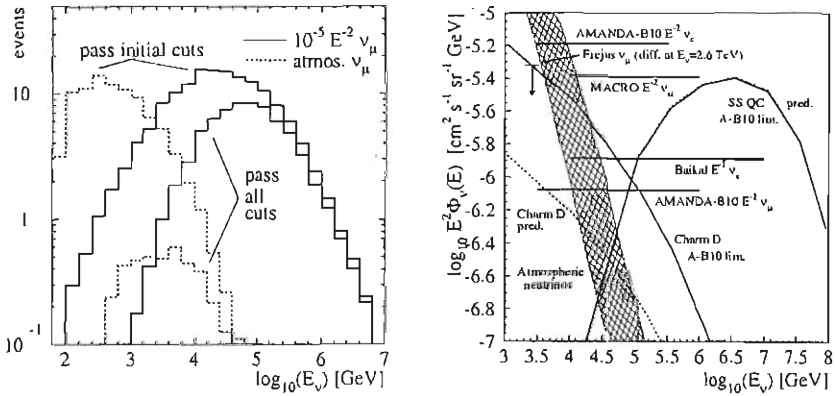

Figure 6: *Left: energy spectrum of the incident atmospheric (dashed line) and E^{-2} (solid line) neutrinos for events that pass the initial cuts, and after channel multiplicity cut. Right: Summary of experimental 90% classical confidence level flux limits from various detectors assuming an E^{-2} spectrum.*

As stated in section 4, AMANDA-II is bigger than AMANDA-B10 and the background which needs to be eliminated has larger intensity and includes the coincident uncorrelated atmospheric muon events. The tested high energy neutrino flux is $\Phi_{\nu_\mu} = 10^{-6} \cdot E^{-2}$ cm^{-2}s^{-1}sr^{-1}GeV^{-1} and the optimized energy cut selects events between 10 TeV and 10 PeV. Since 1997 about 10 times the exposure has been achieved in total with AMANDA-B10 (1997-99) and AMANDA-II (2000-present). This combined data set has a limit-setting potential more than 5 times better than the above AMANDA-B10 limit.

5.2 Point Sources of ν_μ

If the dominant extraterrestrial neutrino flux is emitted by a few particularly bright or close sources, their direction could be resolved. For that reason the 1997 data taken with AMANDA-B10 were analyzed also to search for neutrinos from point sources [27]. The sky was divided in 154 search bins, with half width of about 5°. Due to the lower background within each search bin, it is possible to relax the cuts, with respect to the search for diffuse flux of neutrinos, and thus gain a higher signal efficiency. The pointing resolution results to be $\psi = 3.9°$. The probability for the observed number of events in each search bin

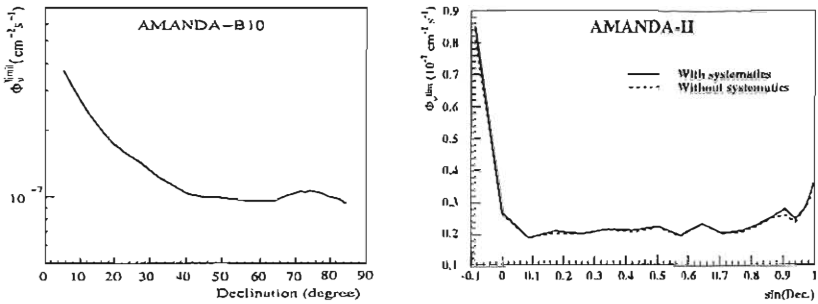

Figure 7: *Left: AMANDA-B10 upper 90% CL limit on neutrino flux as a function of declination. Right: AMANDA-II sensitivity as a function of declination.*

shows no significant excess with respect to the pure background expectation. Therefore a limit was derived. Figure 7 shows, on the left, the upper limit (90% CL) as a function of declination.

The search for high energy neutrinos from point sources was also performed in AMANDA-II using the data taken during 2000 [28]. Due to the better pointing resolution ($\psi = 2.3°$) of AMANDA-II, in this analysis the sky was divided in 300 search bins, with half width of about 3.5°. No significant excess of events was observed in any search bin. Figure 7, on the right, shows the AMANDA-II sensitivity (integrated over neutrino energies above 10 GeV) as a function of declination. It is evident that AMANDA-II has a more uniform angular sensitivity and, in average, about a factor of 5 better than AMANDA-B10.

Table 1 shows the preliminary 90% CL upper limits on a selection of candidate sources [28]. n_{obs} is the number of observed events within the search bin and n_b the number of expected background, determined by measuring the events off-source in the same declination band. These upper limits are substantially better than the limits from AMANDA-B10 [27].

5.3 Flux of ν_μ from Gamma Ray Bursts

AMANDA detector data were analyzed to search high energy neutrinos spatially and temporally coincident with 317 triggered GRBs, detected by the BATSE satellite detector, and 153 non-triggered GRBs, obtained by searching the BATSE archived data [29]. The experimental data are from AMANDA-B10

Table 1: *Preliminary 90% CL upper limits on a selection of candidate sources in AMANDA-II. The limits $\Phi^{lim}_{\mu,\nu}$ are calculated for an assumed E^{-2} spectral shape, integrated above $E_{\mu,\nu} = 10$ GeV and in units of $10^{-15} cm^{-2} s^{-1}$ and $10^{-8} cm^{-2} s^{-1}$, respectively.*

Candidate	Dec (°)	R.A. (h)	n_{obs}	n_b	Φ^{lim}_{μ}	Φ^{lim}_{ν}
SS433	5.0	19.20	0	2.38	0.8	0.6
M 87	12.4	12.51	0	0.95	1.1	0.9
Crab Nebula	22.0	5.58	2	1.76	2.1	2.1
Mkr 421	38.2	11.07	3	1.50	2.6	3.1
Mkr 501	39.8	16.90	1	1.57	1.3	1.6
Cygnus X-3	41.0	20.54	3	1.69	2.5	3.1
QSO 0219+428	42.9	2.38	1	1.63	1.1	1.4
Cassiopea A	58.8	23.39	0	1.01	0.7	1.1
QSO 0716+714	71.3	7.36	2	0.74	2.4	3.8

(taken in 1997-99) and AMANDA-II (taken in 2000) combined. The preliminary results are consistent with no GRB neutrino signal. A 4-year combined neutrino event 90% CL upper limit of 1.45 for the 317 BATSE-triggered bursts was derived.

5.4 Flux of Ultra High Energy ν_μ

AMANDA-B10 data were searched for muon neutrinos with energies above 10^{16} eV. At these energies the Earth is opaque to neutrinos and the events are concentrated at the horizon. The background is represented by the large muon bundles from down-going atmospheric events. The absence of extremely bright events in excess with respect to the expected background, allowed us to put a limit of $\Phi^{lim}_{\nu_\mu} < 7.2 \times 10^{-7} \mathrm{E}^{-2} \mathrm{cm}^{-2} \mathrm{s}^{-1} \mathrm{sr}^{-1} \mathrm{GeV}^{-1}$ in the energy range $2.5 \times 10^{15} eV < E_\nu < 5.6 \times 10^{18} eV$ [30]. The preliminary sensitivity of AMANDA-II, for one year of operation, is about a factor of three better.

5.5 Diffuse Flux of ν of all Flavors

As explained in section 2, the signature for $\nu_{e,\tau}$ is different from the one for ν_μ, therefore different fit procedures need to be used to reconstruct such events. The advantage of detecting these events is the lower atmospheric background, the better energy resolution with respect to the muon case, since the full energy

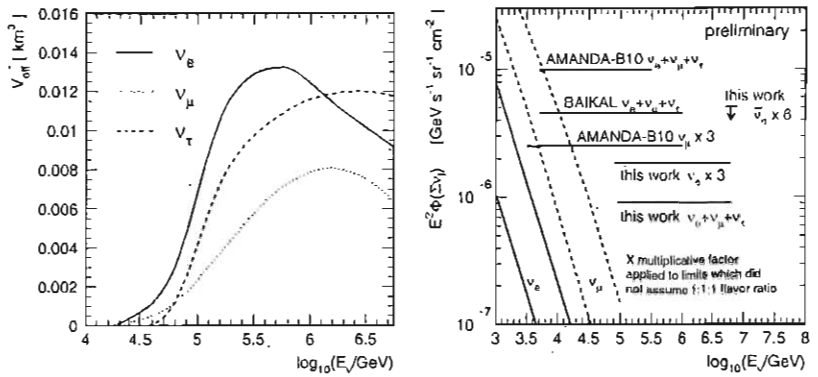

Figure 8: *Left: Effective Volume versus neutrino energy for AMANDA-II. Right: Upper 90% CL limits on the flux of cosmic neutrinos following a* E^{-2} *spectrum*

is deposited in the detector, and the sensitivity to all neutrino flavors, because of neutral current interactions. Detection of all the three flavors increases the sensitivity, since, for typical astrophysical fluxes, the ratio of neutrino flavors $\phi_{\nu_e} : \phi_{\nu_\mu} : \phi_{\nu_\tau} \approx 1 : 2 : 0$, becomes $1 : 1 : 1$ at the detection site, due to neutrino oscillations. For contained cascades, the cascade vertex position resolution is $\Delta r \sim 5$ m for both AMANDA-B10 and AMANDA-II [31] and the energy resolution is $\Delta(LogE) \sim 0.1$-0.2. The bigger AMANDA-II volume increases the sensitivity to higher cascade energies and the angular acceptance is nearly uniform over 4π [32].

Figure 8 shows the effective volume of AMANDA-II as a function of neutrino energy for all neutrino flavors, and the upper limits for AMANDA-II compared with those of AMANDA-B10. An order of magnitude improvement in sensitivity is evident from the figure.

5.6 Flux of ν_e from Supernovæ

AMANDA-B10 data were also searched for the detection of low energy ($\sim$ MeV) neutrinos from Supernovæ [33] through the process $\bar{\nu}_e + p \rightarrow n + e^+$. The e^+ track length is too short to be reconstructed, but the Cherenkov light from many such tracks can induce a correlated increase in the noise rate of the OMs that can be detected. The OM count rate was monitored continuously

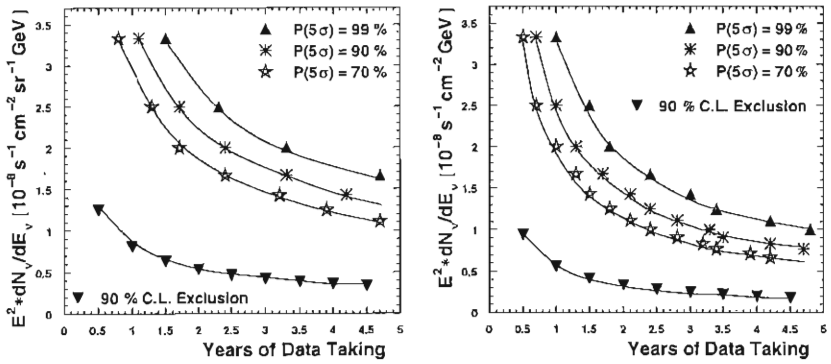

Figure 9: *IceCube sensitivity to diffuse neutrino fluxes (on the left) and to point sources of neutrinos (on the right), as a function of exposure. P(5σ)=x% means that the probability that a signal shows up as a 5 sigma effect is x%.*

in 10 s bins in search for such an excess. The analysis includes a specific OM selection criterion, which keeps only modules with very stable behavior over the years 1997-98. A stable counting rate is achieved with a moving average. AMANDA-B10 yields a 70% coverage of the Galaxy with one backgound fake per year with 90% efficiency. AMANDA-II supernova data are being analyzed now and indicate a 90% coverage of the Galaxy.

5.7 Flux of ν_μ from WIMPs

An indirect search for non-baryonic dark matter, in the form of Weakly Interacting Massive Particles, from the center of the Earth was done in AMANDA-B10 using the data taken in 1997-99 [34]. This analysis requires the selection of well reconstructed vertically up-going events. An iterative discriminant analysis retains 30% of the signal (represented by neutralino annihilations) and 0.3% of background. The observation of no excess with respect to the expected background was interpreted as a limit on the muon flux from neutralino annihilation. An upper limit of $\sim 10^3\ \mu\ km^{-2}yr^{-1}$ for $m_\chi > 10^3$ GeV, and less stringent values for smaller neutralino masses, were derived from AMANDA-B10. Preliminary analyses show that AMANDA-II has competitive sensitivity to search also for WIMPS from the Sun.

6 The Future: IceCube

IceCube is the kilometer-cubed successor of AMANDA-II. To be built starting in 2004, it will consist of 4800 10-inch PMTs enclosed in transparent pressure spheres, distributed along 80 vertical strings up to a depth of 2400 meters [35]. As a significant improvement over the AMANDA technology, each OM will also house the electronics to digitize the PMT pulses, retaining the full waveform information. The digitized information is sent to the surface processors, which form a global trigger. Triggered events will be filtered and reconstructed on-line, and the relevant information will be transmitted via satellite to the northern hemisphere.

Figure 9 shows the expected IceCube sensitivities for diffuse and point source ν_μ fluxes as a function of detector exposure.

Acknowledgments

This research was supported by the following agencies: National Science Foundation Office of Polar Programs, National Science Foundation–Physics Division, University of Wisconsin Alumni Research Foundation, USA; Swedish Research Council, Swedish Polar Research Secretariat, and Knut and Alice Wallenberg Foundation, Sweden; German Ministry for Education and Research, Deutsche Forschungsgemeinschaft (DFG), Germany; Fund for Scientific Research (FNRS-FWO), Flanders Institute to encourage scientific and technological research in industry (IWT), and Belgian Federal Office for Scientific, Technical and Cultural affairs (OSTC), Belgium.

*The AMANDA Collaboration

J. Ahrens[11], X. Bai[1], S.W. Barwick[10], T. Becka[11], J.K. Becker[2], K.-H. Becker[2], E. Bernardini[4], D. Bertrand[3], A. Biron[4], D.J. Boersma[4], S. Böser[4], O. Botner[17], A. Bouchta[17], O. Bouhali[3], T. Burgess[18], S. Carius[6], T. Castermans[13], A. Chen[15], D. Chirkin[9], B. Collin[8], J. Conrad[17], J. Cooley[15], D.F. Cowen[8], A. Davour[17], C. De Clercq[19], T. DeYoung[12], P. Desiati[15], J.-P. Dewulf[3], P. Doksus[15], P. Ekström[2], T. Feser[11], T.K. Gaisser[1], R. Ganugapati[15], H. Geenen[2], L. Gerhardt[10], K.S. Goldmann[2], A. Goldschmidt[7], A. Groß[2], A. Hallgren[17], F. Halzen[15], K. Hanson[15], R. Hardtke[15], T. Hauschildt[4], K. Helbing[7], M. Hellwig[11], P. Herquet[13], G.C. Hill[16], D. Hubert[19], B. Hughey[15], P.O. Hulth[18], K. Hultqvist[18], S. Hundertmark[18], J. Jacobsen[7], A. Karle[15], M. Kestel[8], L. Köpke[11], M. Kowalski[4], K. Kuehn[10], J.I. Lamoureux[7], H. Leich[4], M. Leuthold[4], P. Lindahl[6], I. Liubarsky[5], J. Madsen[16], K. Mandli[15], P. Marciniewski[17], H.S. Matis[7], C.P. McParland[7], T. Messarius[2], Y. Minaeva[18], P. Miočinović[9], R. Morse[15], R. Nahnhauer[4], J. Nam[10], T. Neunhöffer[11], P. Niessen[19], D.R. Nygren[7], H. Ögelman[15], Ph. Olbrechts[19], C. Pérez de los Heros[17], A.C. Pohl[18], P.B. Price[9], G.T. Przybylski[7], K. Rawlins[15], E. Resconi[4], W. Rhode[2], M. Ribordy[13], S. Richter[15], J. Rodríguez Martino[18], D. Ross[10], H.-G. Sander[11], K. Schinarakis[2], S. Schlenstedt[4], T. Schmidt[4], D. Schneider[15], R. Schwarz[15], A. Silvestri[10], M. Solarz[9], G.M. Spiczak[16], C. Spiering[4], M. Stamatikos[15], D. Steele[15], P. Steffen[4], R.G. Stokstad[7], K.-H. Sulanke[4], I. Taboada[14], L. Thollander[18], S. Tilav[1], W. Wagner[2], C. Walck[18], Y.-R. Wang[15], C.H. Wiebusch[2], C. Wiedemann[18], R. Wischnewski[4], H. Wissing[4], K. Woschnagg[9], G. Yodh[10]

(1) Bartol Research Institute, University of Delaware, Newark, DE 19716, USA
(2) Fachbereich 8 Physik, BUGH Wuppertal, D-42097 Wuppertal, Germany
(3) Université Libre de Bruxelles, Science Faculty, Brussels, Belgium
(4) DESY-Zeuthen, D-15738 Zeuthen, Germany
(5) Blackett Laboratory, Imperial College, London SW7 2BW, UK
(6) Dept. of Technology, Kalmar University, S-39182 Kalmar, Sweden
(7) Lawrence Berkeley National Laboratory, Berkeley, CA 94720, USA
(8) Dept. of Physics, Pennsylvania State Univ., University Park, PA 16802, USA
(9) Dept. of Physics, University of California, Berkeley, CA 94720, USA
(10) Dept. of Physics and Astronomy, Univ. of California, Irvine, CA 92697, USA
(11) Institute of Physics, University of Mainz, D-55099 Mainz, Germany
(12) Dept. of Physics, University of Maryland, College Park, MD 20742, USA
(13) University of Mons-Hainaut, 7000 Mons, Belgium
(14) Dept. de Física, Universidad Simón Bolívar, Caracas, 1080, Venezuela
(15) Dept. of Physics, University of Wisconsin, Madison, WI 53706, USA
(16) Physics Dept., University of Wisconsin, River Falls, WI 54022, USA
(17) Div. of High Energy Physics, Uppsala University, S-75121 Uppsala, Sweden
(18) Dept. of Physics, Stockholm University, SE-10691 Stockholm, Sweden
(19) Vrije Universiteit Brussel, Dienst ELEM, B-1050 Brussels, Belgium

References

1. M.S. Longair, *High Energy Astrophysics*, CUP (1997)
2. R.W. Springer, *et al.*, these proceedings
3. K. Greisen, Ann. Rev. Nucl. Sci. **10**, 63 (1960)
4. M.A. Markov, I.M. Zheleznykh, Nucl. Phys. **27**, 385 (1961)
5. T. Gaisser, *Cosmic Rays and Particles Physics*, CUP (1990)

6. A. Roberts, Rev. Mod. Phys. **64**, 259 (1992)
7. I.A. Belolaptikov, *et al.*, Proc. 24^{th} ICRC, Rome (1995)
8. P.A. Mock *et al.*, Proc. 24^{th} ICRC, Rome (1995)
9. E.G. Anassontzis *et al.*, NIM A **502** 150 (2003)
10. P. Amram *et al.*, Astrop. Phys. **13** 127 (2000)
11. R. Wischnewski, *et al.*, Proc. 27^{th} ICRC, Hamburg (2001)
12. E. Andrès, *et al.*, Nature **410**, 441 (2001)
    E. Andrès, *et al.*, Phys. Rev. D **66**, 012005 (2002)
13. J.E. Dickinson *et al.*, NIM A **440**, 95 (2000)
    J. Ahrens *et al.*, submitted to NIM A
14. K. Woschnagg, Proc. 26^{th} ICRC **2**, 202-203, Salt Lake City (1999)
15. B. Price *et al.*, Geophys. Res. Lett. **27**, 2129 (2000)
16. D. Heck *et al.*, Report FKZA 6019 (1998)
17. G.C. Hill, Astrop. Phys. **6**, 215 (1997)
18. D. Chirkin, W. Rhode, Proc. 27^{th} ICRC, HE220, Hamburg (2001)
19. S. Hundertmark *et al.*, DESY-PROC-1-1999 (1999)
20. J. Ahrens *et al.*, to be submitted to NIM A
21. P. Desiati, K. Bland, Proc. 28^{th} ICRC, Tsukuba (2003)
22. H. Geenen, Diploma Thesis WU-D-2002-10, BUGH, Wuppertal (2002)
23. K. Rawlins, Proc. 28^{th} ICRC, Tsukuba (2003)
    J. Ahrens *et al.*, to be submitted to Astrop. Phys.
24. E. Andrès *et al.*, Astrop. Phys. **13**, 1 (2000)
25. H. Geenen, Proc. 28^{th} ICRC, Tsukuba (2003)
26. J. Ahrens *et al.*, Phys. Rev. Lett., accepted (2003)
    G.C. Hill, M. Leuthold, J. Cooley, Proc. 28^{th} ICRC, Tsukuba (2003)
27. J. Ahrens *et al.*, Astroph. J. **583**, 1040 (2003)
28. T. Hauschildt, D. Steele, Proc. 28^{th} ICRC, Tsukuba (2003)
    J. Ahrens *et al.*, in preparation
29. R. Hardtke, K. Kuehn, M. Stamatikos, Proc. 28^{th} ICRC, Tsukuba (2003)
30. S. Hundertmark, Proc. 28^{th} ICRC, Tsukuba (2003)
31. J. Ahrens *et al.*, Phys. Rev. D **67**, 012003 (2003)
32. M. Kowalski, Proc. 28^{th} ICRC, Tsukuba (2003)
33. J. Ahrens *et al.*, Astrop. Phys. **16**, 345 (2002)
34. J. Ahrens *et al.*, Phys. Rev. D **66**, 032006 (2002)
    P. Olbrechts, Proc. 28^{th} ICRC, Tsukuba (2003)
35. J. Ahrens *et al.*, arXiv:astro-ph/0305196, submitted to Astrop. Phys.
    S. Yoshida, Proc. 28^{th} ICRC, Tsukuba (2003)

THE RUNNING-IN OF MINOS

Phil Adamson
London

Written contribution not received

FIRST RESULTS FROM KamLAND

Yoshi Uchida for the KamLAND Collaboration
Stanford University Physics Department, Stanford CA 94305, USA

Abstract

The recently published first results from the KamLAND reactor antineutrino experiment are presented. Experiments have accumulated much information about solar neutrinos over the last several years, and their results are converging on the matter-enhanced large mixing angle (MSW LMA) solution to the solar neutrino problem. KamLAND uses an entirely different approach to probe the same region of oscillation parameter space as the solar experiments, with the ability to confirm or disallow the LMA solution in a single measurement. Here, emphasis is placed on the complementary aspects of these experiments and the meaning and implications of the KamLAND results.

1 Introduction

KamLAND, the Kamioka Liquid Scintillator Antineutrino Detector [1], started taking data in early 2002, in the cavern previously occupied by the old Kamiokande experiment [2], 1 km deep in the Kamioka mine in central Japan. Weeks after Masatoshi Koshiba, who led the earlier experiment, received the 2002 Nobel Prize in Physics in conjunction with Ray Davis for opening up the field of neutrino astrophysics, KamLAND announced its first results. These results help answer the questions posed by the experiments of Koshiba and Davis and the neutrino astrophysics experiments which followed them, but using an entirely Earth-based measurement. In these proceedings, we refer to the original KamLAND publication [1] for technical details of KamLAND and its measurement of reactor antineutrinos, and instead concentrate on the context of the measurement and the implications of the new results.

2 Solar Neutrino Experiments and the Solar Neutrino Problem

The solar neutrino experiments which have been performed to date fall into one of four categories according to detection method:

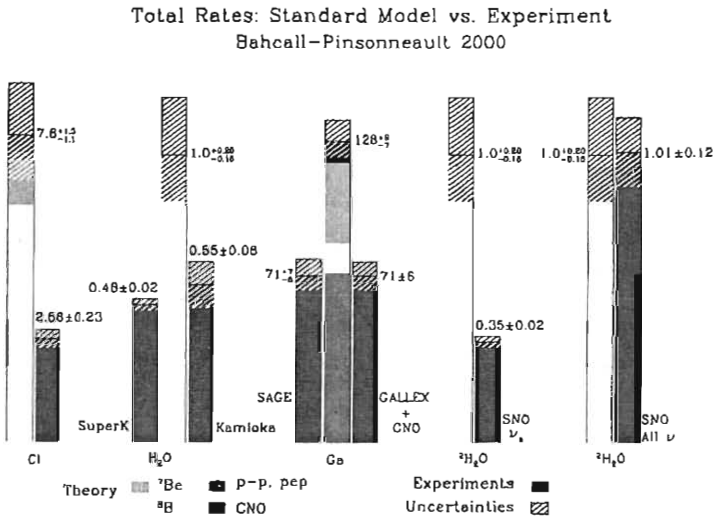

Figure 1: *Comparison of measured solar neutrino fluxes to that calculated from the Solar Standard Model. One-sigma errors are indicated by shading.* [3]

Chorine (Homestake experiment [4]) Radiochemical, counting of ν_e over integrated periods of time, low 0.814 MeV E_ν threshold

Gallium (SAGE [5], Gallex [6], GNO [7]) Radiochemical, counting of ν_e over integrated periods of time, very low 0.233 MeV threshold

Water Cerenkov (Kamiokande [2], Super-Kamiokande [8]) Real-time, mostly ν_e energy and directionality information, 5 MeV threshold

Heavy Water (SNO [9]) Real-time, separate measurements of ν_e and ν_{all}, energy and directionality information, 5 MeV threshold

These experiments employ contrasting methods and are sensitive to several different neutrino energy ranges, and all indicate a deficit in the observed rate of electron neutrinos from the Sun compared to that expected by the Solar Standard Model, by a factor of one half to two-thirds. In the SSM [10], nuclear fusion reactions which can explain the generation of light and heat in the Sun are given, and the rate at which each reaction is occurring is established, under the constraints imposed by the observed parameters of the star, such as density, dimensions, and luminosity. Each reaction produces a neutrino of a certain energy or energy distribution, and by summing these according to the reaction rates, the total expected flux and energy spectrum are obtained. The discrepancy between expectation and measurement first came to light with the results of the Homestake experiment in 1968, and the mystery, known as the solar neutrino problem, survived the continued refinement of theory and experiment until the publication of the first results from the SNO experiment in 2001.

In fig. 1 the measured fluxes are compared to the theoretical expectations. The first four columns show the rates and deficits for the ν_es, for the different sensitivity ranges of the four detection methods. The rightmost column is for the total neutrino rate measured by SNO, which shows excellent agreement with the electron neutrino rate according to the SSM.

Three possible reasons were considered in order to explain the discrepancies; experimental inaccuracies, incorrect modelling of the Sun, and neutrino propagation deviating from a straightforward $1/R^2$ dependence on distance. The first possibility became increasingly unlikely with the cross-checks provided by the different methods and continued scrutiny of the experimental methods. Consistency checks of the SSM have ruled out calculational errors that could explain the reduction in fluxes by over 50%. SNO, the only solar neutrino experiment which is sensitive to the ν_e and ν_{all} fluxes separately, published its results in 2001 and 2002. These left as the only plausible explanation that the number of neutrinos leaving the Sun is consistent with that expected by the SSM, and that neutrinos change flavour as they travel from the centre of the Sun to the Earth.

3 Mechanisms for Electron Neutrino Disappearance

Several models have been proposed for the mechanism behind the observed deficit in solar neutrinos.

Neutrino flavour oscillations can arise naturally from quantum mechanics if neutrinos are massive and there is a mass difference between the mass eigenstates in which the neutrinos propagate [11]. The nature of the oscillations depends on the mass differences between the mass eigenstates, and the rotation matrix which links these mass eigenstates with the flavour eigenstates in which the neutrinos are created and interact [12]. These two different types of mixing parameter are represented as mass-squared differences (Δm^2) and mixing angles ($\sin^2 2\theta$) which constitute the phase-spaces for describing neutrino oscillations. In terms of these parameters, in the simplified case of electron neutrinos oscillating with another flavour of neutrino, the probability of an electron neutrino of energy E_ν remaining unchanged after travelling a distance of L can be written as follows:

$$P_{\nu_e \to \nu_e}(E_\nu, L|\Delta m^2, \sin^2 2\theta) = 1 - \sin^2 2\theta \times \sin^2\left(\frac{1.27 \times \Delta m^2[\mathrm{eV}^2] \times L[\mathrm{m}]}{E_\nu[\mathrm{MeV}]}\right) \quad (1)$$

These oscillations can explain the observed deficit and dependence on baseline of atmospheric neutrinos [13] However the distance between the Sun and Earth is too long for straightforward oscillations to explain the large, energy dependent deficits observed in electron neutrinos from the Sun.

Another phenomenon arises when there are mass differences between the neutrino propagation eigenstates and they pass through dense matter such as that in the Sun. The Mikheyev, Smirnov and Wolfenstein (MSW) effect, in which the presence of matter enhances flavour oscillations [14], can cause significant changes in the flavour content away from electron neutrinos as they travel from the centre of the Sun through matter of decreasing density [15]. The effect is caused by the difference between the interactions of electron neutrinos with matter, which contains a high density of electrons, and the interactions between matter and muon and tau neutrinos. Electron neutrinos possess charged- and neutral-current interactions with electrons, as opposed to muon and tau neutrinos which only interact with electrons via the neutral-current. In terms of the quantities in eq. 1, $\sin^2 2\theta$ and the factor of 1.27 are altered as well-defined functions of the density of electrons in the matter that the neutrinos are passing through. Therefore, for any combination of the mixing parameters, the density profile of the Sun according to the SSM can be applied to obtain the flavour content of the neutrino flux as a function of energy and distance, according to the MSW model.

Over the years, as experimental data for solar neutrinos was being accumulated, the MSW effect provided different regions in mixing parameter space which were compatible with all data as solutions to the solar neutrino problem. After the latest SNO data, the large mixing angle (LMA) MSW matter-enhanced oscillation solution remains as the most strongly favoured possibility [9, 16] (fig. 7).

The solar neutrino experimental data is by nature restricted to a baseline corresponding to the distance between the Sun and the Earth, with the interpretation of the data being inseparable from the modelling of the Sun. The experimental methods also place limitations on the measurements of energy dependence of the observed flux. The observations are consistent with the MSW LMA solution, but other effects, such as non-standard MSW matter interactions [17], and neutrino magnetic moments [18] can also explain the solar neutrino deficits and be consistent with other measurements of neutrino properties [19].

Under the oscillation hypothesis, KamLAND is able to probe the same Δm^2 and $\sin^2 2\theta$ region as the MSW LMA solution indicated by the solar experiments, at a baseline near the pure vacuum oscillation length of this solution, as is discussed below.

4 Reactor Neutrino Experiments

Ever since Reines and Cowan made use of the Savannah River nuclear reactor to demonstrate the existence of neutrinos [20], nuclear rectors have been used to provide large neutrino fluxes to allow their properties to be probed [21]. Reactors operate through controlled nuclear fission chain reactions, in which the nuclei which comprise the fuel break up into unstable isotopes, which then proceed to beta decay, producing approximately six antineutrinos per initial nucleus. The observed antineutrino energy spectrum, which is a convolution of the production spectrum at reactors and the cross section at the detector as a function of energy [22], ranges between 1.8 MeV and 8 MeV, peaking near 4 MeV. Many of the later experiments were performed to search for deficits in the neutrino fluxes, but in spite of increasing baselines — up to 1 km for Palo Verde [23] and Chooz [24] — the event rates had all been consistent with a $1/R^2$ behaviour for reactor antineutrinos.

The 1 km baseline and antineutrino energy of a few MeV correspond, in oscillation phase space, to atmospheric neutrino oscillations, and the absence of a deficit puts a limit on involvement of the electron neutrino state in atmospheric neutrino oscillations. Once it was established that neutrinos do not exhibit an appreciable deficit after travelling these distances, these measurements have been used to help understand the fluxes and energy spectra of antineutrinos from reactors [25, 26].

5 KamLAND and the Reactor Antineutrino Measurement

Here we briefly summarise the detection and analysis methods; the reader is referred to the original publication for details of the detector and the reactor antineutrino measurement [1].

Fig. 2 is a map of Japan with the locations of the country's nuclear power plants indicated, together with the location of KamLAND in Gifu Prefecture. The bulk of the antineutrino flux from nuclear reactors towards Kamioka, when weighted for output

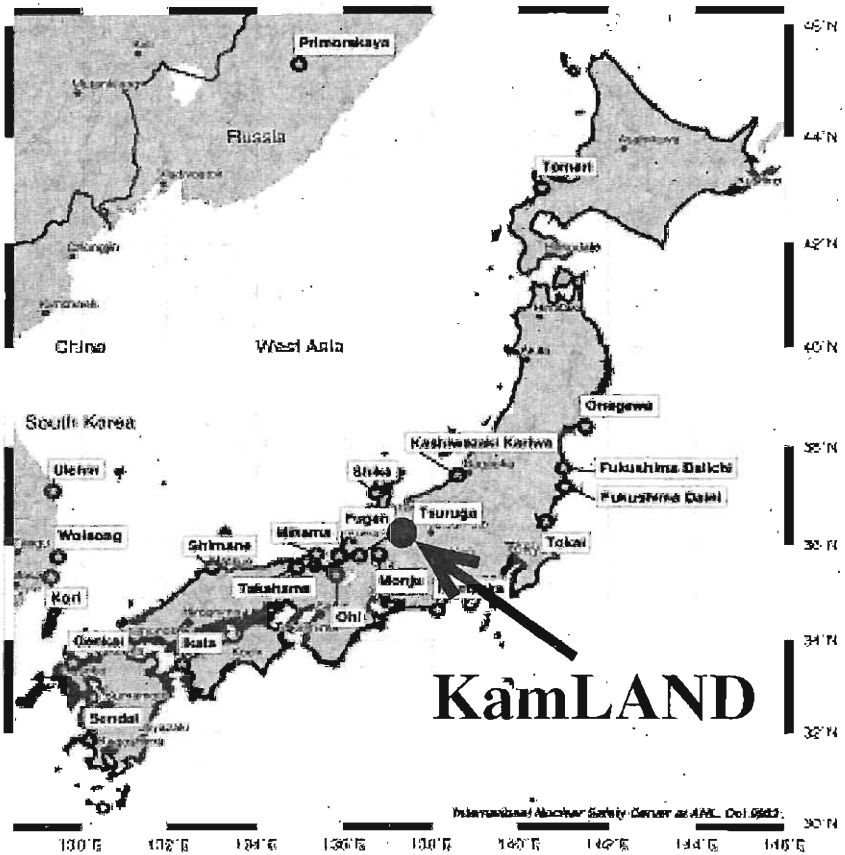

Figure 2: *The location of KamLAND, superimposed on a reactor map of Japan, from the International Nuclear Safety Center. Nuclear power reactor sites are indicated by the labelled circles. Approximately four-fifths of the antineutrino flux which arrives at Kamioka, calculated assuming $1/R^2$ dependence of the flux on distance, is from reactors within 138 to 214 kilometres of KamLAND. One-third of the flux comes from the 25 GW Kashiwazaki-Kariwa complex, 160 km to the north-east of KamLAND.*

power and distance, comes from about 180 km away, with four-fifths of the flux being from between 138 to 214 km in distance.

The detector (fig. 3) is the world's largest monolithic liquid scintillator detector,

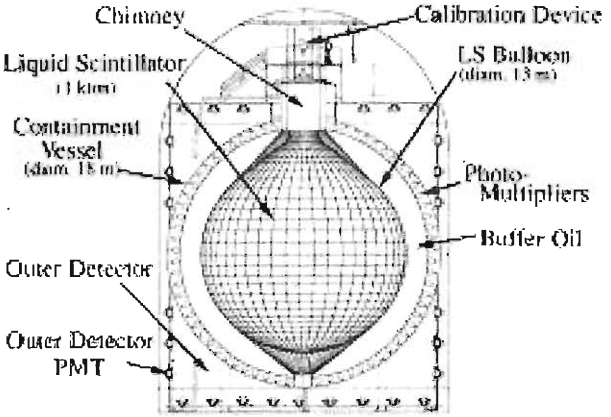

Figure 3: *The KamLAND detector.*

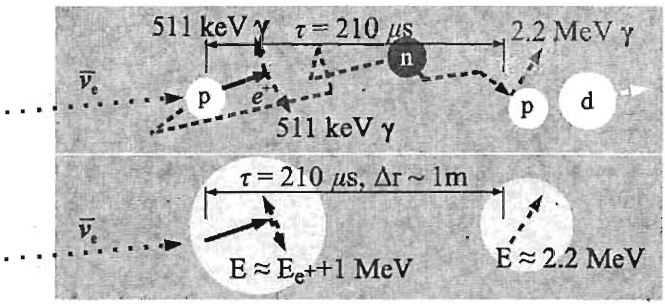

Figure 4: *The inverse beta decay signature. (top: underlying interactions, bottom: observed scintillation signal).*

consisting of a 13 m diameter balloon with 1000 tonnes of purified liquid scintillator, shielded by 2 m of inactive purified mineral oil, and viewed by almost 2,000 photomultiplier tubes. The energy resolution is $\sim 7.5\%/\sqrt{E\ (\mathrm{MeV})}$. This inner detector is contained in a water Cerenkov veto counter, and is located 1 km (2,700 m water equivalent) below the surface. The triggering threshold is just under 1 MeV, with the trigger rate averaging about 30 Hz, and the antineutrino signal to be measured is detected in the form of a specific delayed coincidence signal as shown in fig. 4. The chance of random background event mimicking this signature is very small, in spite of the low signal rate of about one event a day. Spallation products from muons, which traverse the detector every three seconds on average, introduce large correlated backgrounds, which are reduced by applying specialised timing and geometry cuts after muons.

Table 1: *Estimated systematic uncertainties (%) for the KamLAND reactor antineutrino measurement.*

Total scintillator mass	2.1	Reactor power	2.0
Fiducial mass ratio	4.1	Fuel composition	1.0
Energy threshold	2.1	Time lag	0.28
Efficiency of cuts	2.1	$\bar{\nu}$ spectra	2.5
Live time	0.07	Cross section	0.2
		Total systematic error	6.4

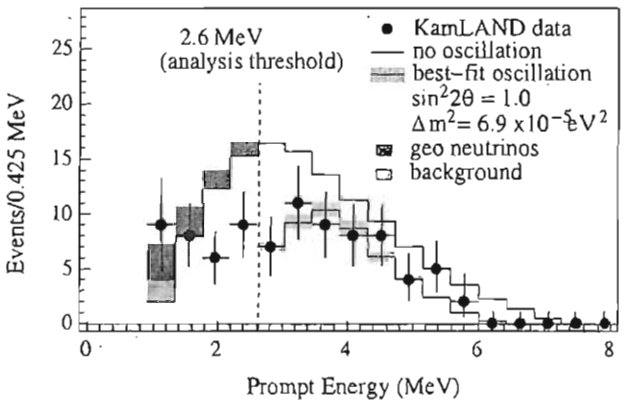

Figure 5: *The energy spectrum of the prompt part of the antineutrino events. The upper histogram is the expected spectrum in the case of a $1/R^2$ behaviour of the flux over distance, and lower histogram is that calculated for antineutrinos which oscillate according to the best-fit oscillation parameters derived from the data points above 2.6 MeV. The numerical values of these parameters are $\Delta m^2 = 6.9 \times 10^{-5} eV^2$ and $\sin^2 2\theta = 1.0$. The shaded areas below 2.6 MeV indicate the best-fit for antineutrinos from U and Th in the earth. The shaded area in the lowest bin is the contribution from background events.*

The systematic uncertainties are listed in table 1.

For the first reactor antineutrino measurement from KamLAND, 145.1 × 24 hours of data were analysed. The number of expected events, taking the reactor activity corresponding to the periods that the detector was taking data and applying a $1/R^2$ dependence of the flux on distance, was 86.8±5.6. 54 events were observed in the data, and subtracting the estimated background of 0.95 ± 0.99 events, the ratio of

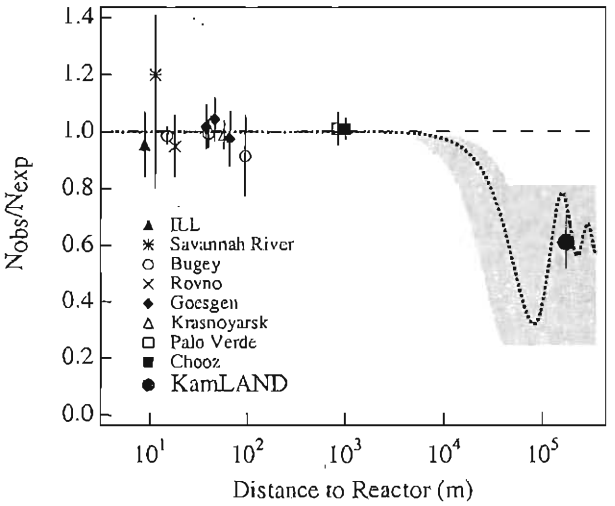

Figure 6: *The ratio of measured to expected (no-oscillation) $\bar{\nu}_e$ flux from reactor experiments. The solid circle is the KamLAND results plotted at a flux-weighted average distance of ~ 180 km. The shaded region indicates the range of flux predictions corresponding to the 95% C.L. LMA region from a global analysis of the solar neutrino data. The dotted curve is representative of the best-fit LMA prediction at* $\sin^2 2\theta = 0.833$ *and* $\Delta m^2 = 5.5 \times 10^{-5}\ eV^2$.

observed signal to the number for no deficit is $0.611 \pm 0.085 \pm 0.041$, where the errors are statistical and systematic, respectively. The energy spectrum of the observed antineutrinos is shown in fig. 5, and the event rate is compared with previous reactor experiments in fig. 6.

From the number of events seen, and the shape of the energy spectrum, fits can be made to determine the most likely parameters under the vacuum oscillation hypothesis, using eq. 1. The fit results are summarised in fig. 7, where the best fit LMA region from the solar experiments is also shown.

6 Conclusions

The mixing parameters from KamLAND and the solar experiments display remarkable agreement; here we emphasise again the contrasting nature of the measurements and oscillation hypotheses:

- Solar experiments measure neutrinos travelling 150 million km from the Sun, with oscillations being enhanced due to matter effects as neutrinos travel through the Sun.

- KamLAND measures electron antineutrinos travelling ~ 180 km, effectively in

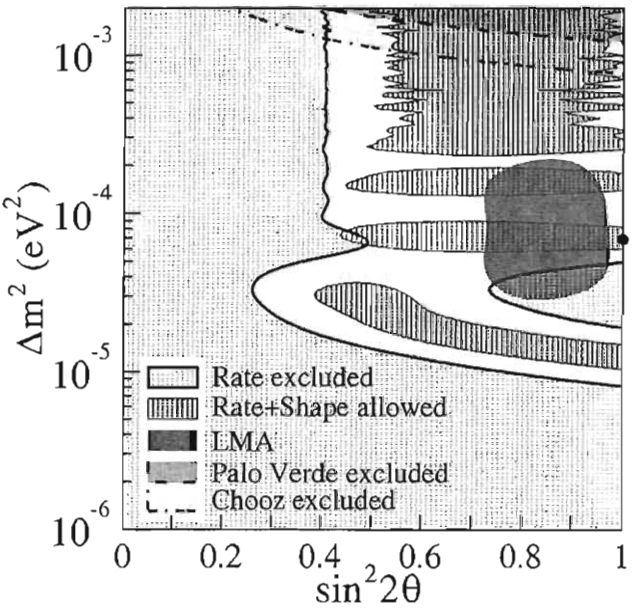

Figure 7: *Results from fits to the KamLAND data at 95% confidence level, assuming two-generation vacuum oscillations. The solid dot indicates the best-fit point ($\Delta m^2 = 6,9\times10^{-5}eV^2$, $\sin^2 2\theta = 1.0$) to the KamLAND data in the physical region. The MSW LMA solution region, according to the solar neutrino experiments, is indicated by the dark round region.*

vacuum, with any observed oscillations directly reflecting the underlying mixing parameters.

Assuming CPT conservation, ie, that neutrinos and antineutrinos have equivalent mixing properties, KamLAND rules out as leading contributions, all oscillation scenarios other than MSW LMA for solar neutrinos, and mechanisms which invoke properties of the Sun to explain the solar neutrino problem.

KamLAND is expected to run for several more years. The good energy resolution of the detector allows the energy dependence of the oscillations (eq. 1) to be measured directly. It can be seen from fig. 5 that more data needs to be accumulated in order for a clear and statistically significant oscillation signal to be observed in the energy spectrum. This will allow KamLAND to measure the mixing parameters to very good precision [27]. The same figure also shows the region in which antineutrinos from geological sources (uranium and thorium) are expected to be contributing to the spectrum. Such neutrinos have never been observed, and with further running, KamLAND should be able to measure the abundances of these elements in the region [28]. In addition, the detector is constantly on the lookout for supernovae with a dedicated trigger algorithm, and in the event of such an occurrence, reactions in the scintilla-

tor are expected to provide unique insight on the nature of the neutrinos from these events [29]. Other topics to be studied by the experiment include the measurement of higher energy antineutrino fluxes, and searches for nucleon decay.

References

1. K. Eguchi *et al.* [KamLAND Collaboration], "First results from KamLAND: Evidence for reactor anti-neutrino disappearance," Phys. Rev. Lett. **90** (2003) 021802
2. K. S. Hirata *et al.* [KAMIOKANDE-II Collaboration], "Observation Of B-8 Solar Neutrinos In The Kamiokande-Ii Detector," Phys. Rev. Lett. **63** (1989) 16.
3. J. N. Bahcall, `http://www.sns.ias.edu/~jnb`
4. B. T. Cleveland *et al.*, "Measurement Of The Solar Electron Neutrino Flux With The Homestake Chlorine Detector," Astrophys. J. **496** (1998) 505.
5. J. N. Abdurashitov *et al.* [SAGE Collaboration], "Measurement of the solar neutrino capture rate with gallium metal," Phys. Rev. C **60** (1999) 055801.
6. P. Anselmann *et al.* [GALLEX Collaboration], "Solar Neutrinos Observed By Gallex At Gran Sasso," Phys. Lett. B **285** (1992) 376.
7. M. Altmann *et al.* [GNO Collaboration], "GNO solar neutrino observations: Results for GNO I," Phys. Lett. B **490** (2000) 16
8. Y. Fukuda *et al.* [Super-Kamiokande Collaboration], "Measurements of the solar neutrino flux from Super-Kamiokande's first 300 days," Phys. Rev. Lett. **81** (1998) 1158 [Erratum-ibid. **81** (1998) 4279]
9. Q. R. Ahmad *et al.* [SNO Collaboration], "Direct evidence for neutrino flavor transformation from neutral-current interactions in the Sudbury Neutrino Observatory," Phys. Rev. Lett. **89** (2002) 011301
10. J. N. Bahcall, "Solar models: An historical overview," AAPPS Bull. **12N4** (2002) 12
11. P. Fisher, B. Kayser and K. S. McFarland, "Neutrino mass and oscillation," Ann. Rev. Nucl. Part. Sci. **49** (1999) 481
12. Z. Maki, M. Nakagawa and S. Sakata, "Remarks On The Unified Model Of Elementary Particles," Prog. Theor. Phys. **28** (1962) 870.
13. Y. Fukuda *et al.* [Super-Kamiokande Collaboration], "Evidence for oscillation of atmospheric neutrinos," Phys. Rev. Lett. **81** (1998) 1562
14. L. Wolfenstein, "Neutrino Oscillations In Matter," Phys. Rev. D **17** (1978) 2369.

15. S. P. Mikheev and A. Y. Smirnov, "Resonance Enhancement Of Oscillations In Matter And Solar Neutrino Spectroscopy," Sov. J. Nucl. Phys. **42** (1985) 913

16. M. B. Smy [Super-Kamiokande collaboration], "Solar neutrino precision measurements using all 1496 days of Super-Kamiokande-I data,"

17. J. W. Valle, "Resonant Oscillations Of Massless Neutrinos In Matter," Phys. Lett. B **199** (1987) 432.

18. A. Cisneros, "Effect Of Neutrino Magnetic Moment On Solar Neutrino Observations," Astrophys. Space Sci. **10** (1971) 87.

19. S. Pakvasa and J. W. Valle, "Neutrino properties before and after KamLAND,"

20. F. Reines and C. L. Cowan, "Detection Of The Free Neutrino," Phys. Rev. **92** (1953) 830.

21. C. Bemporad, G. Gratta and P. Vogel, "Reactor-based neutrino oscillation experiments," Rev. Mod. Phys. **74** (2002) 297

22. P. Vogel, "Analysis Of The Anti-Neutrino Capture On Protons," Phys. Rev. D **29** (1984) 1918.

23. F. Boehm *et al.*, "Final results from the Palo Verde neutrino oscillation experiment," Phys. Rev. D **64** (2001) 112001

24. M. Apollonio *et al.* [CHOOZ Collaboration], "Limits on neutrino oscillations from the CHOOZ experiment," Phys. Lett. B **466** (1999) 415

25. P. Vogel, G. K. Schenter, F. M. Mann and R. E. Schenter, "Reactor Anti-Neutrino Spectra And Their Application To Anti-Neutrino Induced Reactions. 2," Phys. Rev. C **24** (1981) 1543.

26. B. Achkar *et al.*, "Comparison of anti-neutrino reactor spectrum models with the Bugey-3 measurements," Phys. Lett. B **374** (1996) 243.

27. H. Murayama and A. Pierce, "Energy spectra of reactor neutrinos at KamLAND," Phys. Rev. D **65** (2002) 013012

28. R. S. Raghavan, S. Schonert, S. Enomoto, J. Shirai, F. Suekane and A. Suzuki, "Measuring the global radioactivity in the earth by multidetector anti-neutrino spectroscopy," Phys. Rev. Lett. **80** (1998) 635.

29. J. F. Beacom, W. M. Farr and P. Vogel, "Detection of supernova neutrinos by neutrino proton elastic scattering," Phys. Rev. D **66** (2002) 033001

RESULTS FROM SUPERKAMIOKANDE

Larry Sulak
Boston

Written contribution not received

INDICATIONS OF NEUTRINO OSCILLATION IN THE K2K NEUTRINO OSCILLATION EXPERIMENT

Taku Ishida, representing K2K collaboration
Institute for Particle and Nuclear Studies(IPNS)
High Energy Accelerator Research Organization(KEK)
1-1 Oho, Tsukuba-shi, Ibaraki 305-0801, Japan

Abstract

The indications of neutrino oscillation observed by the K2K long-baseline neutrino oscillation experiment are presented in this talk: From 1999 to 2001, 5.6×10^{19} protons on target were delivered to the experiment in 234.8 days of running. During this period there were 56 events fully contained in the Super-Kamiokande inner detector fiducial area, which was synchronized to the beam-spill timing. In the case of no oscillations, the expected number of events was $80.1^{+6.2}_{-5.4}$. Out of the 56 events, we obtained 29 events of single ring μ-like events. The neutrino energy spectrum for the events, reconstructed by assuming two-body kinematics of quasi-elastic interactions, shows a deficit in the E_ν=0.5~1GeV bin, compared with the spectrum at the production observed by the near detectors. These two facts indicate neutrino oscillation with common oscillation parameter regions. A combined oscillation analysis gives $\Delta m^2 = 1.5 \sim 3.9 \times 10^{-3}\mathrm{eV}^2$ at $sin^2 2\theta$=1.0 at the 90% confidence level, and the null oscillation probability is found to be less than 1%.

1 Introduction

The atmospheric neutrino anomaly observed by Super-Kamiokande(SK) and other recent underground experiments strongly suggest $\nu_\mu \leftrightarrow \nu_\tau$ neutrino oscillation. The allowed region of the oscillation parameters are in the range of $\Delta m^2_{atm} = 1.6 \sim 3.9 \times 10^{-3}$ eV^2 and $sin^2 2\theta_{atm} > 0.92$ at the 90% confidence level, [2] where Δm^2_{atm} is the mass-difference squared between two neutrino mass eigenstates and θ_{atm} is the mixing angle between two neutrinos. The principal goal of the K2K (*KEK-to-Kamioka*) experiment is to confirm neutrino oscillation with a man-made neutrino beam and to measure the oscillation parameters. We use the 12-GeV PS at KEK as a neutrino source, which produces a wide-band neutrino beam with an average energy of $\overline{E}_\nu$=1.3 GeV. The far detector, Super-Kamiokande, a 50 *kt* water Cherenkov detector, is located L =250km East from KEK. In order to measure the effects of oscillation we compare the total number of events and the ν_μ spectrum observed by SK to those expected from measurements by a near detector system at KEK. A deficit of ν_μ events and / or a distortion of the neutrino spectrum are evidence of neutrino oscillation. Owing to the E_ν/L value, which is in a similar range to that of atmospheric neutrinos, we have sensitivity to explore a similar mass-difference region, $\Delta m^2 \geq 2 \times 10^{-3}$eV^2.

2 The K2K experiment

Fig. 1 shows a bird's-eye view of the neutrino beam-line at KEK. The 12-GeV PS provides $\sim 6 \times 10^{12}$ protons per spill every 2.2 sec, and each spill has 9 bunches in a 1.1 μsec spill width. Protons are bent in the direction of Kamioka in the primary beam line, and are injected on aluminum target of 3cm$\phi \times$ 66cm length, embedded in the 1^{st} horn magnet. Two horn magnets [3] focus the produced positively-charged pions effectively towards the direction of Kamioka. The neutrino beam strength becomes $\times \sim 20$ larger than in the case without them. The produced pions decay into μ and ν_μ within 200m of a decay pipe filled with helium gas, and the produced ν_μ beam flys underground to the SK direction with a tilting angle of -1°. The neutrino flux and the spectrum shape at SK is expected to be the same within 3$m$rad, because the neutrino beam divergence is mainly determined by the decay kinematics of the pions. We measure the profile of muons from pion decays by ionization chambers and silicon pad detectors located behind the beam dump, which indirectly guarantees that the center of the neutrino beam profile is stable *spill-by-spill* within $\leq \pm 1m$rad. A pion monitoring gas Cherenkov counter [4] is occasionally placed in the beam axis downstream of the 2^{nd} horn. By adjusting the internal gas pressure, it can explore the momentum and angle distribution of the produced pions in $p_\pi \geq$2GeV/c, without suffering any effect from the

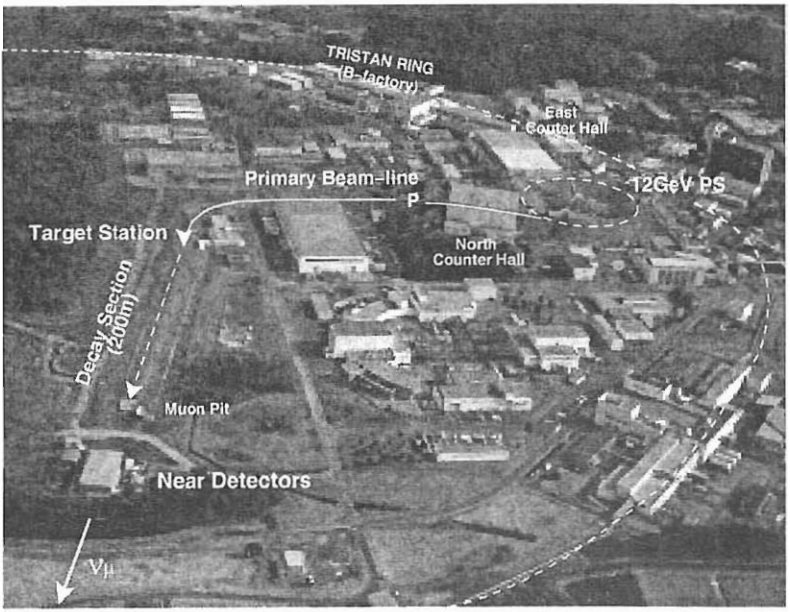

Figure 1: *Bird's-eye view of the neutrino beam-line at KEK. Each beam-line component is explained in the main text. A near detector system is located 300m downstream from the primary target, which aims to study the neutrino beam properties at the time of production.*

background of the primary 12GeV/c protons. This enables us to extrapolate the neutrino flux from the near site to the far site in the $E_\nu \geq 1$GeV region within an accuracy of $\sim \pm 10\%$.[1]

Fig. 2 shows a record of the protons on target, on which some memorial dates for the experiment are also recorded. After the success of the fast extraction of protons for the experiment on February 3^{rd} 1999, neutrino beam commissioning started on March 4^{th}. After engineering runs to study neutrino beam operations in April through May, stable data taking began in June, 1999. At that time we employed an aluminum target with $2cm\phi$ and a horn current of 200 kA. The typical proton intensity was 4.5×10^{12} *protons-per-pulse*. On June 19^{th}, we observed the first K2K signal at SK. It was the first achievement to detect an accerelator-produced neutrino at a distance of hundreds of *km*. [6]

[1] For an energy lower than 1GeV, we employ an empirical pion production model, [5] which reproduces the pion monitor measurements very well.

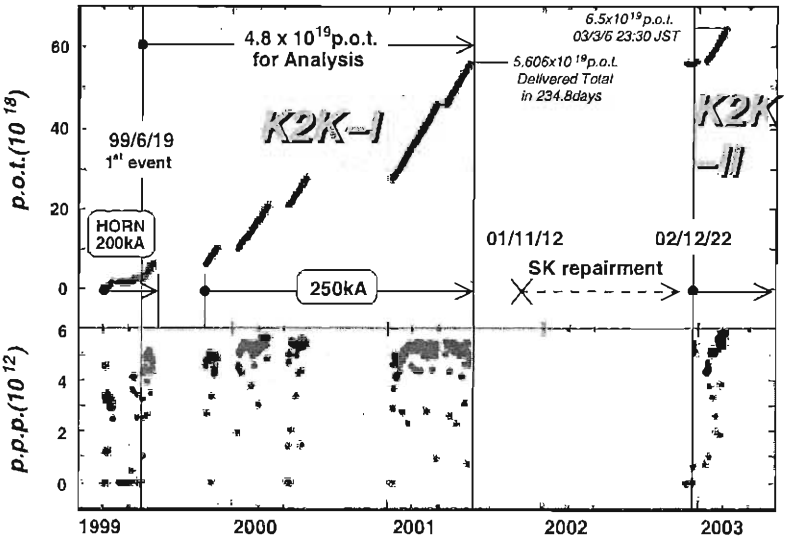

Figure 2: *Accumulated protons on target (upper) and protons per pulse at the target (lower) as function of the date from 1999 to 2003.*

After the summer shutdown, continuous data taking began again in November, with an aluminum target of $3cm\phi$ and a horn current of 250 kA. The typical proton intensity was enhanced to $5{\sim}6{\times}10^{12}$ *ppp*. After the upgrade, we successfully took data during November 1999 to June 2000, and January to July 2001. The accumulated number of protons on the target from the start of the experiment was $5.606{\times}10^{19}$ in total. Among them, we used data with stable beam operation after June, 1999, for an analysis, which corresponds to $4.8{\times}10^{19}$ *pot*. All of the results presented in this talk are based on these K2K-I data.

On November 12^{th} 2001, a severe accident broke out in SK: Due to a chain reaction of shock waves, caused by a sudden improsion of one PMT at the bottom, we lost about 60% of the 11,140 PMTs within a few seconds. Owing to a very quick decision that we try to resume the experiment within one year by rearranging the remaining and spare PMTs at half density,[2] [7] and

[2]In the relevant energy region for atmospheric neutrinos, proton decays and K2K, it is expected that the difference in the SK configurations will cause no changes to the quality of the experiments.

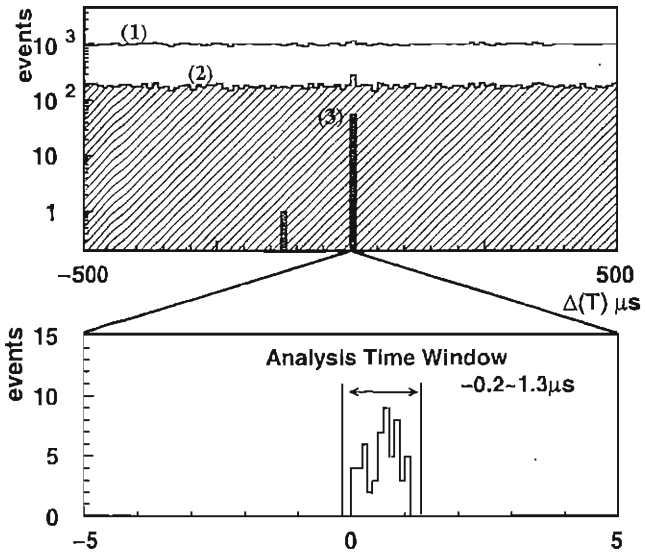

Figure 3: ΔT ($\equiv T_{SK.} - T_{KEK} - T_{T.O.F.}$) *distributions at each reduction stage at SK in* $\pm$ *500*μ*sec time window (upper) (1) high-energy trigger condition (2) no decay electron event (3) no activity in the outer detector (fully-contained, FC) and the vertex is in the fiducial volume (FV).* $\pm$ *5*μ*sec time window for FCFV events (lower).*

also owing to very great efforts to achieve that, SK started data taking again on December 22^{nd}, 2002. The K2K experiment also resumed from that day, and is accumulating data now. We call the data-taking period after the repair as K2K-II.

The GPS system is used [8] to look for events at SK, which synchronizes to the KEK PS beam pulses. Fig. 3 shows the $\Delta T \equiv T_{SK} - T_{KEK} - T_{T.O.F.}$ distributions at each reduction stage for all K2K-I data. After the final requirements that the event is fully-contained in inner detector (FC) and the neutrino interaction vertex is inside of the 22.5kt fiducial volume (FV), we admit a very clear peak, which coincides to the KEK beam pulse of 1.1μsec width. Inside of an 1.5μsec analysis timing window, which takes the resolution of the ΔT measurement (< 200 nsec) into account, we have observed 56 events in total. The atmospheric neutrino background expected for the timing window is only $\sim 10^{-3}$ events. The arrival times of the events are consistent with a Poisson distributed distribution with regards to the integrated protons on target. Among the FCFV events, 32 events are single-ring (1R) events, and 30 of the 1R events are muon-like events, which are identified by using Cherenkov ring

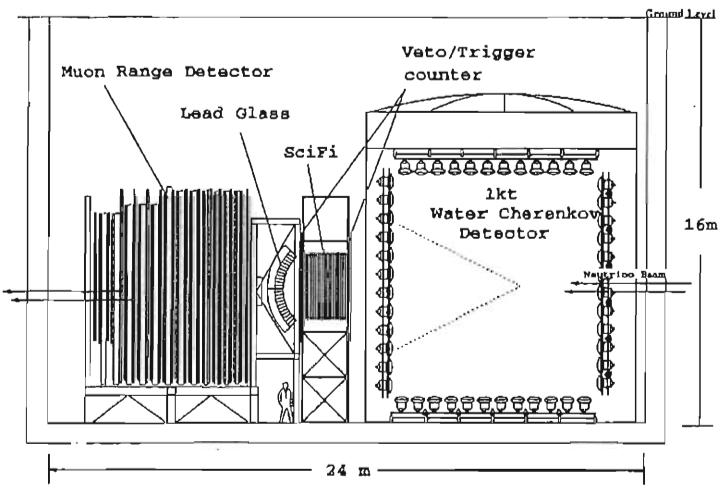

Figure 4: *K2K near detector system, 1kt (right) and FGD (left, composite of SciFi, LG, and MRD). All setups are in a 24mφ - 16m deep well-like hall, so that the neutrino beam, being tilted by about -1° towards the direction of Kamioka, will pass through the center of the detectors.*

image pattern recognition. [9] For the 1Rμ-like events, we can reconstruct the incoming neutrino energy from the muon momentum and angle by assuming a charged-current quasi-elastic interaction, $\nu_\mu + n \rightarrow \mu + P$:

$$E_\nu^{\rm rec} = \frac{m_N E_\mu - m_\mu^2/2}{m_N - E_\mu + P_\mu \cos\theta_\mu}, \qquad (1)$$

omitting the Fermi momentum and the nuclear potential. We will use the $E_\nu^{\rm rec}$ to see the distortion on the neutrino spectrum shape.

3 Reconstruction of the Neutrino Spectrum by Near Detectors

The K2K experiment employs a near-detector system located $300m$ downstream from the primary target. Fig. 4 shows a schematic view of the near-detector system. It is composed of two independent detectors: a 1 kiloton SK-like water Cherenkov detector (*1kt*) and a fine-grained detector (FGD). They provide a unique probe for detailed studies on the neutrino-nucleus (H_2O) interactions around E_ν in a few GeV region, which is not yet well understood. [10] We will reconstruct the neutrino energy spectrum at the time of production by

analyzing the momentum and angular distributions of muons observed in these two detectors. This is one of the very necessary inputs for oscillation analysis.

3.1 Water Cherenkov detector (*1kt*)

1kt is a miniature of SK with a 1/50 volume, whose data can be directly compared with the SK ones by using the same type of detector and by common analysis procedures. Inside of a $8.6m\phi$-8.6m height cylinder, 680 of 20" PMTs are arranged in the same 70cm lynning as the SK. The inner volume is 496 tons of purified water, where the event rate in the full volume is 0.2 event per spill. To choose a single interaction per spill, a flash-ADC records the analog sum of all PMTs. The interaction vertex reconstruction, Cherenkov ring counting, and μ-like / e-like ring identification of each ring are performed by the same methods as are employed in the SK. [9] For the K2K spectrum analysis, (1) FCFV-1Rμ-like samples are chosen based on the following selection criteria:

- Events with a $>1000p.e.$ ($\sim$ 100 MeV) single peak in the Flash-ADC (FADC) are chosen. It is used to extract a single interaction in a spill.
- Events with the reconstructed vertex is inside of a cylindrical volume along the beam, $-2m < z < 0m$, $r < 2m$ with a fiducial volume mass=$25t$ (FV events). By these two cuts, the efficiency for those events, which have an interaction vertex in the fiducial volume, is *eff*=75%.
- The total light yield of all PMTs should be in the range of $1000\sim20000p.e.$.
- The maximum response of the inner PMTs is less than 200 $p.e.$. It is used to extract fully contained (FC) events, with it's track endpoint inside of the inner detector (FCFV/Fid.all=75%).
- At last, events with a μ-like single ring pattern are chosen (FCFV1Rμ-like/FCFV=47%).

The characteristics of these events are good sensitivity to the large scattering angle, whereas the sensitivity is limited to the low muon momentum region (p_μ <1 GeV) due to the requirement of the 4^{th} (FC) condition. It is to be noted that in our relevant energy region a recoil proton track is usually not seen (Cherenkov threshold is $p_{thr.}$ ~1.1 GeV/c), and the CCQE interaction is identified as a single ring μ-like event. For the absolute event rate, the measurement has a 5% systematic error, of which the largest contribution comes from the vertex reconstruction uncertainty. For the spectrum measurement, the largest systematic error is an uncertainty on the energy scale. It is known to be within $^{+2}_{-3}$ %, confirmed with both cosmic-ray muons and beam-induced π^0 analysis.

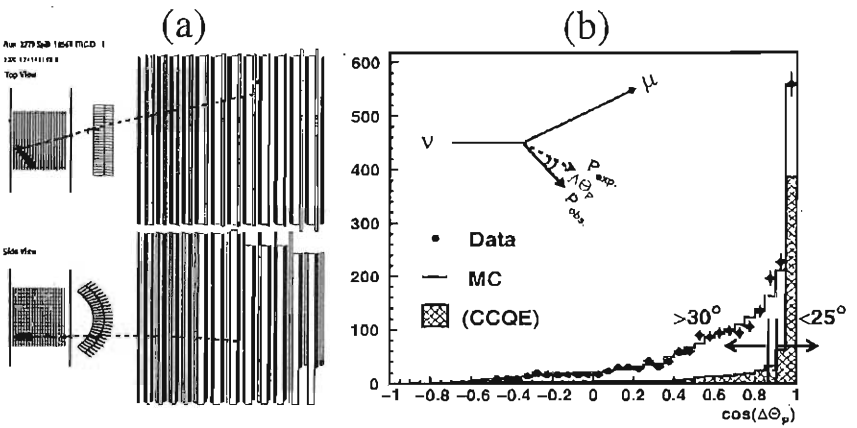

Figure 5: *(a) Typical FGD two track events with an vertex in the SciFi. Track-associated hits are represented by red circles with their size proportional to the number of pixels in the hits. (b) $cos(\Delta\theta_P)$ distribution for two-track samples. It is used to distinguish CCQE / non-QE enhanced samples.*

3.2 Fine-Grained Detector (FGD)

FGD aims to measure neutrino interactions precisely by using a tracking-type device. It consists of a scintillating fiber tracker (SciFi), plastic scintillator veto/trigger counters surrounding the SciFi, an electromagnetic calorimeter of 600 lead glass blocks (LG), and a muon range detector (MRD). The SciFi tracker [11] has a $2.6m \times 2.6m \times 1.7m$ rectangular shape. It is composed of 19 layers of $6cm$-thick water containers, sandwiched with $20\times(yy\text{-}xx)$ layers of $700\mu m\phi$ scintillating fibers. The full weight of the sensitive volume is $8.6t$. All of the fibers are bundled and attached to 24 image intensifier tubes. CCD pixel images are analyzed for hit and track reconstruction. The track finding efficiency [12] is 70% for a track passing through three layers of scintillating fiber and close to 100% for more than 5 layers. Three layers is the minimum track length required in this analysis. MRD [13] measures the momentum of a muon coming out from the SciFi by it's range. It is a sandwich of 12 iron plates ($10cm\times4$ + $20cm\times8$) with drift chambers, covering a $7.6m\times7.6m$ transverse area of the beam. The total mass is 915 tons and events contained in MRD are very important to monitor the neutrino beam stability for the rate and for the profile. For neutrino spectrum reconstruction, we choose SciFi-MRD events with the following criteria:

- A vertex with track(s) with a length $\geq$ 3 SciFi layers is reconstructed.

Table 1: *Statistics of the near-detector events for each category used in the spectrum analysis. Details of the event selection are given in the main text.*

		pot($\times 10^{19}$)†	# Events	*dof.*‡
1kt FCFV1Rμ	(1)	3.213	22,476	79
SciFi-MRD		3.970	8,393	
Single Track	(2)		5,963	44
2-track $\Delta\theta_P \leq 25°$	(3)		764	40
2-track $\Delta\theta_P > 30°$	(4)		1,288	40

† *pot* value corresponding to the part of data used for the spectrum analysis.
‡ Number of points on the (p_μ, θ_μ) plane used in the spectrum fit.

The fiducial volume is defined as a rectangle with Δx and $\Delta y \leq 1.1m$, covering the 1^{st} to 17^{th} water containers (fiducial mass= 5.9 t).

- A SciFi track should match to a hit of the downstream veto/trigger counters: This guarantees that the interaction is in a beam spill.
- The track also should match to a LG cluster, and to a MRD track and/or hit cells.

The last condition guarantees that the track passes the LG cells, and is thus a minimum-ionizing muon. At the same time, the cut limits the p_μ sensitivity in the range greater than $\sim$ 500MeV/c. With all of these cuts, the *net* efficiency in the fiducial volume is $\sim$45% for the CCQE interactions and $\sim$31% for the CC-*inclusive* interactions. The momentum of the primary muon track is measured by its range with an accuracy of 2.7%, which is a linear sum of the weight accuracy and a dE/dx uncertainty of the iron. Fig. 5(a) shows a typical FGD event with a secondary track, probably a scattered proton. It is thus a candidate of a CCQE interaction, $\nu_\mu + n \rightarrow \mu + P$. For two-track events, a kinematic variable, $\Delta\theta_P$, is defined to enhance the fraction of CCQE and non-QE interactions: Assuming a QE interaction (omitting the effect from Fermi motion), the direction of the scattered proton can be calculated from the muon momentum. We define $\Delta\theta_P$ as the difference between the observed direction of the second track and that of the expectation. Fig. 5(b) shows the $cos(\Delta\theta_P)$ distribution. CCQE events, shown by a hatched histogram, concentrate around $cos(\Delta\theta_P) = 1$, *i.e.* $\Delta\theta_P = 0$.[3] We select a CCQE enhanced sample by requiring $\Delta\theta_P$ within 25 degrees, and non-QE enhanced samples by $\Delta\theta_P$ more than 30 degrees, respectively. In the CCQE enhanced sample, 62% of the events are

[3]Proton re-scattering inside of Oxygen nuclei is taken into account. [14]

to be QE events. In the non-QE enhanced sample, 82% of events come from interactions other than CCQE. The SciFi events are divided into three event categories: (2) 1-track, (3) 2-track CCQE enhanced, and (4) 2-track non-QE enhanced samples, respectively. The observed number of events for each event category is summarized in Table 1.

3.3 Neutrino Spectrum Reconstruction

The 2-dimensional distributions of the muon momentum versus angle with respect to the beam direction of four event categories, *i.e.* (1) the *1kt* event samples and the three SciFi event samples, (2)~(4), are used to reconstruct the neutrino spectrum at the time of production. A χ^2-fitting method is used to compare these data against the MC expectation. The neutrino spectrum is divided into 8 energy bins, as defined in Table 2. During the fit, the flux in each energy bin is re-weighted relative to the values in the beam MC. These weights are normalized so that the E_ν = 1.0−1.5 GeV bin is unity, and an overall normalization is introduced as a free parameter. In addition, a parameter, R_{nqe}, is used to re-weight the ratio between the QE and non-QE cross section relative to the MC simulation for the entire E_ν region. It is to be noted that R_{nqe} is strongly constrained by the ratio between the number of events in category (3) and that in category (4). The systematic uncertainties of each detector, *i.e.* the energy scales, the track finding efficiencies, and the detector thresholds, are incorporated as fitting parameters. The spectrum measurement by the pion monitor is also used as a constraint on the flux re-weighting factors.

The best-fit results of the flux re-weighting factors, Φ_{ND}, are shown in Table 2. All of the parameters, including the detector systematics, are found to lie within their expected errors. The χ^2 is 227.2/197 d.o.f.. The muon momentum and angular distributions of each event category are overlaid with the re-weighted MC in Fig. 6. As can be seen, the fit result agrees well with the data. The errors of the fit are provided in the form of an error matrix, and correlations between the parameters are taken into account in the following oscillation analysis. The diagonal elements in the matrix, $\Delta(\Phi_{ND})$ are also given in Table 2.

3.4 Neutrino Interaction Models

The uncertainty due to neutrino interaction models is studied separately. Our MC treats neutrino-nucleus interactions through the following four branches: [15] CC Quasi elastic scattering (CCQE), CC 1π production through baryon resonances (CC1π), Coherent π production, and deep inelastic scattering:

- In CCQE scattering, the axial vector mass in the dipole formula is set to a central value of 1.1 GeV/c^2, and is varied by ±10%.

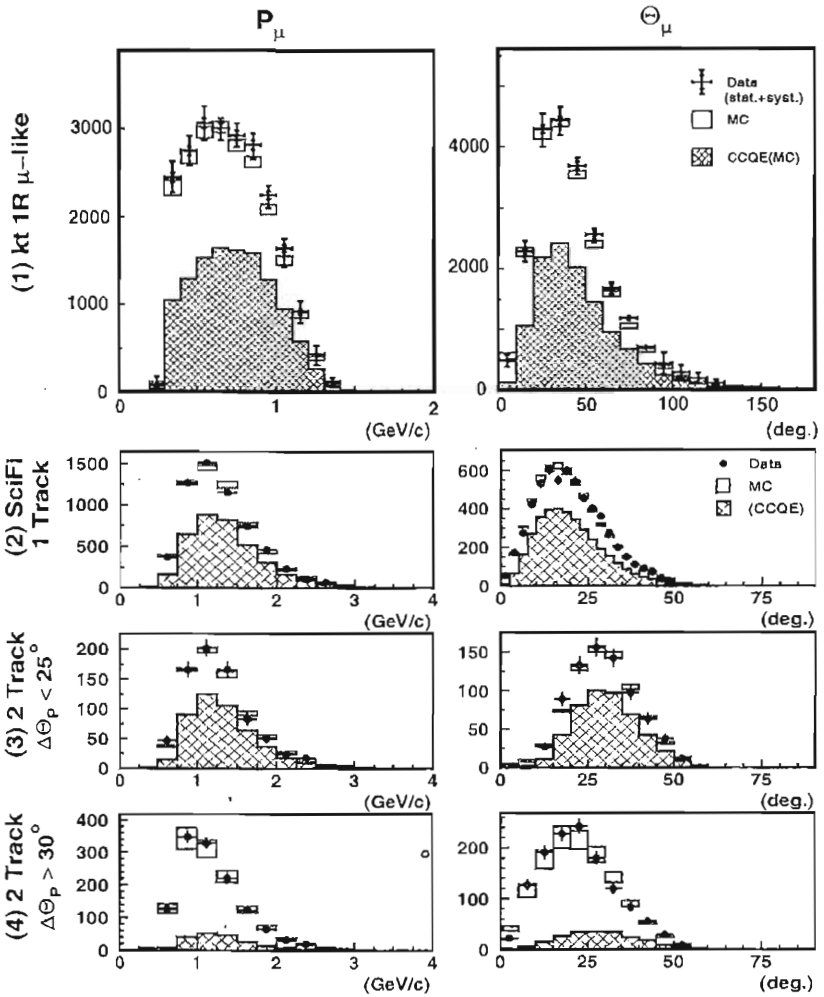

Figure 6: *Muon momentum (left) and angle (right) distributions for each event category: (1) 1kt FCFV single-ring μ-like events, (2) SciFi single-track events, (3) 2-track QE enhanced events, and (4)2-track non-QE enhanced events. The crosses are data and the boxes are MC with the best fit parameters. The errors on the MC distributions correspond to the uncertainties of each flux bin and R(nonQE/QE). The hatched histograms show the CCQE contributions.*

Table 2: *Central values of the flux re-weighting parameters for the spectrum fit at the near detectors (Φ_{ND}) and the percentage size of the energy dependent systematic errors on the re-weighting parameters ($\Delta(\Phi_{ND})$), F/N ratio, and reconstruction efficiency for 1Rμ events at SK (ϵ_{SK}). Φ_{ND}s are given relative to the 1.0−1.5 GeV energy bin.*

E_ν (GeV)	Φ_{ND}	$\Delta(\Phi_{ND})$	Δ(F/N)†	$\Delta(\epsilon_{SK})$‡
0−0.5	1.31	±49	±2.6	±8.7
0.5−0.75	1.02	±12	±4.3	±4.3
0.75−1.0	1.01	±9.1	±4.3	±4.3
1.0−1.5	≡ 1.00	—	±6.5	±8.9
1.5−2.0	0.95	±7.1	±10	±10
2.0−2.5	0.96	±8.4	±11	±9.8
2.5−3.0	1.18	±19	±12	±9.9
3.0−	1.07	±20	±12	±9.9

† Errors are quoted from the pion monitor measurement in >1 GeV, and from the uncertainties in hadron production models in <1 GeV, respectively.
‡ The error on the particle identification dominates in <0.5 GeV, and the error on ring counting dominates in >1 GeV, respectively.

- The axial mass for CC1π is set to a central value of 1.2 GeV/c^2, and is varied by ±20%. [16]
- For coherent pion production, the Rein and Sehgal model [17] and a model by Marteau [18] are compared.
- For deep inelastic scattering, GRV94 [19] and the corrected structure function by Bodek and Yang [20] are both studied.

For an oscillation analysis, the Marteau model and Bodek and Yang structure functions are employed. Varying the choice of models causes the fitted value of R_{nqe} (= 0.93) to change by ∼ 20%. In order to account for this, an additional systematic error of ±20% on R_{nqe} is added by hand. It is found that the choice of models does not affect the Φ_{ND} values, themselves, beyond the size of the fitted errors. Also, it is to be noted that the effects of the model difference on the oscillation analysis is found to be negligible, because of a cancellation between the near cite and the far cite measurements.

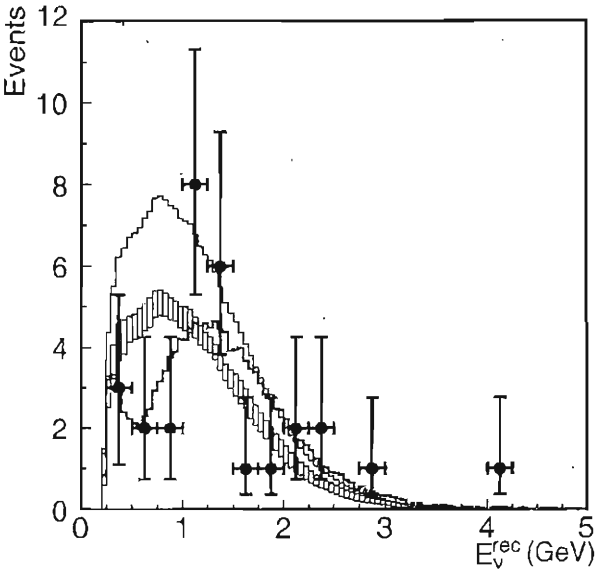

Figure 7: *Reconstructed E_ν distribution for the $1R\mu$ sample. The points with error bars are data. The box histogram is the expected spectrum without oscillations, where the height of the box is the systematic error. The thick-solid line is the best-fit spectrum. These histograms are normalized by the number of observed events, 29. In addition, the thin-solid line shows the expectation with no oscillations normalized to the expected number of events, 44.*

4 Oscillation Analysis

A two-flavor neutrino oscillation analysis with ν_μ disappearance is performed by the maximum-likelihood method. In the analysis, both the number of FCFV events (56) and the energy spectrum shape for $1R\mu$ events (29) are used.[4] The likelihood is defined as

$$\mathcal{L} = \mathcal{L}_{norm} \times \mathcal{L}_{shape}, \tag{2}$$

where the normalization term, $\mathcal{L}_{norm}(N_{obs}, N_{exp})$, is the Poisson probability to observe N_{obs} events when the expected number of events is $N_{exp}(\Delta m^2, \sin^2 2\theta, f)$. Here, the symbol f represents a set of parameters constrained by the systematic errors. They consist of the re-weighted neutrino spectrum measured at the

[4]Data taken in June 1999 are discarded for $\mathcal{L}_{shape}$, because the spectrum shape was different from that for the rest of the running period due to the different horn configuration. The data correspond to 6.5% of the total *pot*.

near detectors (Φ_{ND}), the F/N ratio, the reconstruction efficiency (ϵ_{SK}) of SK for $1R\mu$ events, the re-weighting factor for the QE/non-QE ratio (R_{nqe}), the SK energy scale (3% [9]) and the overall normalization. Note that the errors on the first 3 items depend on the energy and have correlations between each energy bin. The diagonal parts of their error matrices are summarized in Table 2. Since the *1kt* has the same kind of detector as SK, most of the systematic uncertainties on the measurement are expected to be canceled to each other. The expected number of FCFV events, N_{exp}, at SK without oscillation with an overall normalization measured by the *1kt* is estimated to be $80.1^{+6.2}_{-5.4}$, which is to be compared to $N_{obs} = 56$. The major contributions to the errors come from the uncertainties in the F/N ratio ($^{+4.9\%}_{-5.0\%}$) and the normalization (5.0%). The latter is dominated by uncertainties of the fiducial volumes due to vertex reconstruction errors at both the *1kt* and SK. On the other hand, the shape term,

$$\mathcal{L}_{shape} = \prod_{i=1}^{N_{1R\mu}} P(E_i; \Delta m^2, \sin^2 2\theta, f)_i. \qquad (3)$$

is a product of the probability for each $1R\mu$ event to be observed at $E_\nu^{\rm rec} = E_i$, where P is the normalized $E_\nu^{\rm rec}$ distribution, estimated by MC, and $N_{1R\mu}$ is the number of $1R\mu$ events. The number of $1R\mu$ events observed (excluding the data of June 1999) is 29, and the corresponding number of $1R\mu$ events expected from MC in the case of no oscillation is 44. The likelihood is calculated at each point in the Δm^2 and $\sin^2 2\theta$ space to search for the point where the likelihood is maximized.[5] As a result, the best-fit point is found to be at $(\sin^2 2\theta, \Delta m^2)$=$(1.0, 2.8\times10^{-3}\ {\rm eV}^2)$. [6] At the best-fit point the predicted total number of FCFV events is 54.2, which agrees with the observation (56) within the statistical error. The observed $E_\nu^{\rm rec}$ distribution of the $1R\mu$ sample is shown in Fig. 7 together with the expected distributions for the best-fit oscillation parameters, and the expectation without oscillations. The best-fit spectrum shape agrees with the observations. Fig. 8(a) shows the allowed regions of oscillation parameters, evaluated by calculating the likelihood ratio of each point to the best-fit point. The 90% C.L. contour crosses the $\sin^2 2\theta = 1$ axis at Δm^2=1.5 and $3.9\times10^{-3}\ {\rm eV}^2$. Fig. 8(b) shows a $-ln\mathcal{L}$ behavior at $\sin^2 2\theta = 1$ slice, which shows that the Δm^2 preferred by the total flux suppression and the energy distortions alone agree well. The probability that the observations are due to a statistical fluctuation instead of neutrino oscillation is calculated to be 0.7%. When only normalization (shape) information is used, the probabilities are estimated to be 1.3% (16%), respectively.

[5] We treat the systemtic parameters, f, as fitting parameters, with an additional constraint term in the likelihood.

[6] $(1.03, 2.8\times10^{-3}\ {\rm eV}^2)$ if the unphysical region is taken into account.

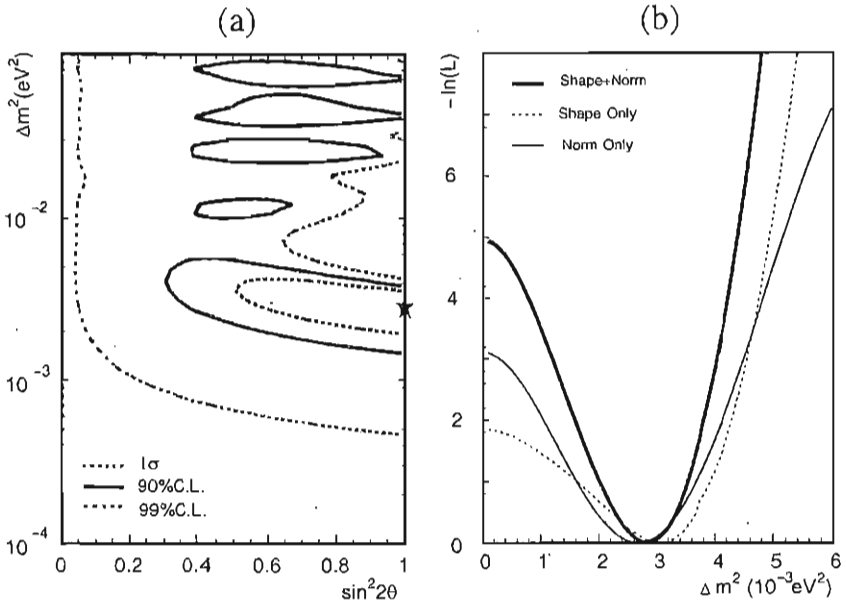

Figure 8: *(a) Allowed regions of oscillation parameters. Dashed, solid and dot-dashed lines are 68.4%, 90% and 99% C.L. contours, respectively. The best fit point is indicated by a star. (b) Behavior of negative log likelihood along $sin^2 2\theta$=1. Analysis results of number of event only (thin-solid) and shape only (dashed) are also given, which suggest mutually consistent Δm^2 values.*

5 Conclusion

The K2K experiment has collected approximately one-half of its planned 10^{20} protons on target in K2K-I. During the period of running, we have collected 56 FCFV events at SK, which should be compared to the expectation, $80.1^{+6.2}_{-5.4}$. 29 1Rμ-like events are further used to study the spectrum distortion, and both the number of FCFV events and the energy spectrum are found to be consistent with neutrino oscillation. A combined likelihood analysis gives ($\sin^2 2\theta$, Δm^2)=$(1.0, 2.8\times 10^{-3}\ \mathrm{eV}^2)$ as the best-fit values. The 90% C.L. contour crosses $\Delta m^2 = 1.5 \sim 3.9 \times 10^{-3}\mathrm{eV}^2$ at $sin^2 2\theta$=1.0, which are consistent with the ones suggested by atmospheric neutrinos. The probability that the measurements at SK can be explained by statistical fluctuation is found to be less than 1%. After the recovery from the accident at SK, we started a new phase of K2K-II, to provide sufficient statistics for a further study on neutrino oscillation.

References

1. Outline of the present talk is based on the references: M.H. Ahn *et al.* [K2K collaboration] Phys. Rev. Lett. bf 90, 041801 (2003). See also S.H. Ahn *et al.* [K2K collaboration] Phys. Lett. **B511**, 178 (2001).
2. Y. Fukuda *et al.* [Super-Kamiokande collaboration], Phys. Rev. Lett. **81**, 1562 (1998); L. Sulak, *this conference.*
3. H. Noumi *et al.*, Nucl. Instrum. Meth. **A 398**, 399 (1997).
4. T. Maruyama, Ph. D thesis, Tohoku Univ. (2000).
5. Y. Cho *et al.* Phys. Rev. **D 4**, 1967 (1971).
6. http://neutrino.kek.jp/news/990628.1stSK/index.html
7. http://neutrino.kek.jp/news/2001.11.12.html
8. H.G. Berns and R.J. Wilkes, IEEE Nucl. Sci. **47**, 340 (2000).
9. Y. Fukuda *et al.* [SK collaboration], Phys. Lett. **B433**, 9 (1998).
10. T. Ishida, in: Proc. The First International Workshop on Neutrino-Nucleus Interactions in the Few GeV Region (NuInt01), (ed. J.G. Morfin, M. Sakuda and Y. Suzuki, KEK, December 2001), Nucl. Phys. **B** (*Proc. Suppl.*) **112**, 132 (2002).
11. A. Suzuki *et al.*, Nucl. Instr. and Meth. **A 453**, 165 (2000).
12. B.J. Kim *et al*, Nucl. Instr. and Meth. **A497**, 450 (2003).
13. T. Ishii *et al.*, Nucl. Instr. and Meth. **A 482**, 244 (2002).
14. C.W. Walter, Nucl. Phys. **B** (*Proc. Suppl.*) **112**, 140 (2002).
15. Y. Hayato, Nucl. Phys. **B** (*Proc. Suppl.*) **112**, 171 (2002).
16. V. Bernard, L. Elouadrhiri, and U.G. Meissner, J. Phys. **G28**, R1 (2002).
17. D. Rein and L.M. Sehgal, Nucl. Phys. **B223**, 29 (1983).
18. J. Marteau et al., Nucl. Instrum. Meth. **A451**, 76 (2000).
19. M. Gluck, E. Reya, and A. Vogt, Z. Phys. **C67**, 433 (1995).
20. A. Bodek and U.-K. Yang, Nucl. Phys. **B** (*Proc. Suppl.*) **112**, 70 (2002).

RESULTS FROM SNO

Andrew Hime
LBNL, Los Alamos, NM 87545 USA

Written contribution not received

STATUS OF MiniBooNE, A SHORT BASELINE NEUTRINI OSCILLATION EXPERIMENT

Jonathan M. Link
Columbia University

Abstract

This report describes the state of neutrino oscillation studies in the LSND signal region (high Δm^2). Prospects for and status of the Fermilab experiment, MiniBooNE, which is intended to verify or refute the LSND signal, are discussed.

1 The LSND Result

The Liquid Scintillator Neutrino Detector (LSND) Experiment took data from 1993 to 1998 at the LANSCE accelerator at Los Alamos National Laboratory. The purpose of LSND was to look for the oscillation of $\bar{\nu}_\mu$ to $\bar{\nu}_e$. An intense beam of π^+ mesons stopped in copper was used to create a high flux of $\bar{\nu}_\mu$ (E_ν in the range of 20 to 50 MeV) at the detector resulting from the π^+, μ^+ decay chain. The detector was separated from the copper beam stop by 30 m of shielding.

Evidence for oscillations was observed with a $\bar{\nu}_e$ excess of $87.9 \pm 22.4 \pm 6.0$ events (see Fig. 1). If attributed to neutrino oscillations, this excess corresponds to an oscillation probability (averaged over the experimental energies and spatial acceptances) of $(0.264 \pm 0.067 \pm 0.045)\%$.

In the case of oscillations involving two flavors, the probability for a neutrino of one flavor to oscillate to a neutrino of the second flavor is given by

$$P = \sin^2 2\theta \sin^2(1.27\Delta m^2 L/E) \qquad (1)$$

where θ is the mixing angle, Δm^2 is the mass difference between the neutrino mass eigenstates, L is the distance traveled by the neutrino (also known as the baseline) and E is the neutrino energy. Neutrino oscillation results are typically shown graphically as the allowed region in Δm^2 and $\sin^2 2\theta$ space. The allowed region for the LSND observed excess is shown in Fig. 2.

The LSND signal ($\Delta m^2 \sim 0.1\ eV^2$) when combined with the strong evidence for oscillations from atmospheric neutrinos [2] ($\Delta m^2 \sim 10^{-3} eV^2$) and

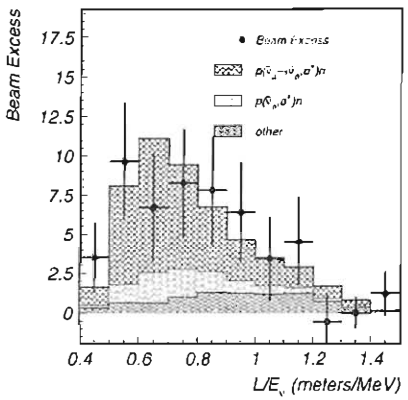

Figure 1: The LSND L/E distribution for $\bar{\nu}_e$ candidate events. The data fit the expectation for neutrino background plus oscillations.

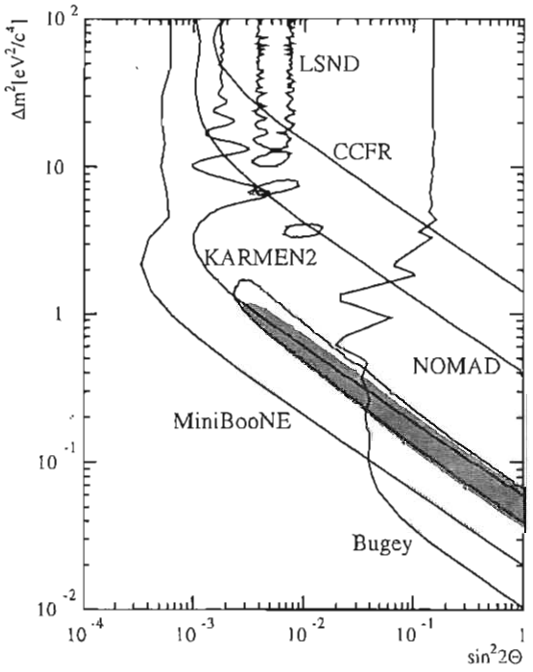

Figure 2: The allowed region (filled in) from joint LSND and KARMEN fit [1] in Δm^2 and $\sin^2 2\theta$; exclusion/allowed regions (solid lines) from several experiments; and the projected sensitivity of MiniBooNE at 90% CL.

solar neutrinos [3] ($\Delta m^2 \sim 10^{-5} eV^2$) is problematic for the standard model which has only three light neutrino flavors. With three neutrino flavors, only two independent Δm^2 scales are possible. The introduction of a fourth neutrino that does not interact via the weak force may resolve this dilemma. Another possible solution involves different Δm^2 scales for antineutrinos and neutrinos, but this clearly violates CPT [4].

In addition to these theoretical difficulties, the LSND signal is challenged by a null result from the KARMEN experiment. KARMEN also looked for $\bar{\nu}_\mu \rightarrow \bar{\nu}_e$ using $\bar{\nu}_\mu$ from the π^+, mu^+ decay chain [5]. Figure 2 shows the region allowed at 90% confidence level (CL) from a joint analysis of the LSND and KARMEN data. Although KARMEN does rule out portions of the LSND

signal region, a significant allowed region still exists.

2 The MiniBooNE Experiment

To resolve the LSND question, the Booster Neutrino Experiment (BooNE) [6] collaboration was formed. BooNE is a collaboration of about 60 scientists from 14 institutions. The goal of BooNE is to make a definitive measurement of neutrino oscillations (or lack thereof) in the LSND signal region. The first phase of BooNE, known as MiniBooNE, will cover the entire LSND region with a sensitivity to an oscillation signal of at least 5σ.

The BooNE beamline uses protons from Fermilab's Booster. The Booster is a high-intensity source of 8 GeV protons. MiniBooNE is intended to run at an average rate of 5 Hz with 5×10^{12} protons per pulse. Each Booster pulse is 1.6 μs long. The pulsed beam is important for reducing backgrounds from cosmic rays.

Protons from the primary beam strike a beryllium target, producing short-lived hadrons. The charged mesons which decay to neutrinos are focused toward the detector using a pulsed toroidal field magnet, known as a horn. The Be target is located in the focusing horn. The horn is followed by a 50 m decay region which can be reduced to 25 m in order to perform cross checks of the intrinsic ν_e flux. The resulting beam has a mean neutrino energy of about 1.0 GeV.

The MiniBooNE detector is positioned 500 m from the target (450 m of earth shielding). The detector consists of a spherical tank 6.1 m in radius. An inner structure at 5.75 m radius supports 1280 8-inch photomultiplier tubes (10% coverage) pointed inward and optically isolated from the outer region of the tank. The vessel is filled with $\sim$ 800 tons of mineral oil, resulting in a $\sim$ 450 ton fiducial volume. The outer volume, viewed by 240 phototubes, serves as a veto shield for identifying particles entering and/or exiting the detector.

3 Prospects and Status of MiniBooNE

Figure 2 shows the expected sensitivity for MiniBooNE at 90% CL assuming 1×10^{21} protons on target. The MiniBooNE expectation completely covers the LSND allowed region.

The MiniBooNE detector and beamline are now complete and data taking began in September 2002. As of this writing MiniBooNE has collected about 100,000 quasi-elastic ν_μ interactions and taken about 1×10^{20} protons on target. This represent about one tenth of the baseline goals for this run. Figure 3 and 4 illustrate the quality of the data taken thus far and the progress made at understanding the data.

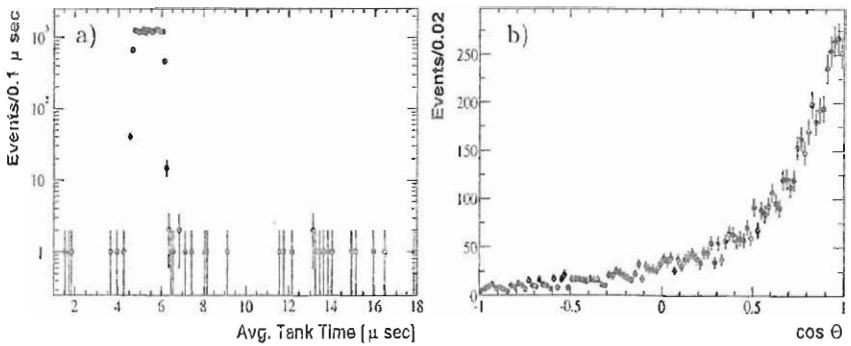

Figure 3: a) Time in the beam trigger window for events with more than 200 hits in the main tank and less than 6 hits in the veto system. The data is accumulated in the 1.6 μs of spill (from 4.5 to 6.1 μs) and outside this window there are very few events. This demonstrates that our veto system is very efficient at rejecting cosmic ray backgrounds (S/N $\simeq$ 5000). b) The distribution of $\cos\theta$ along the beam direction for the Čerenkov rings in events from inside the beam window in a). This shows that the majority of events are are in the forward direction as expected.

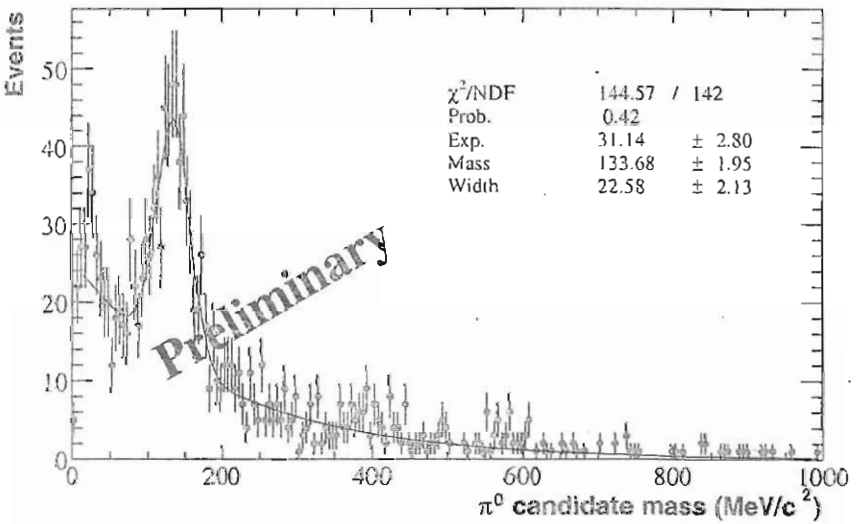

Figure 4: The reconstructed π^0 distribution for two Čerenkov ring, π^0 candidate events in the detector. This figure illustrates that the π^0 algorithm works in at least some instances and will be instrumental in removing π^0 events as a background to the oscillation sample. Further, these events provide a set of electron like Čerenkov rings independent of the ν_e candidate sample, which will be useful for testing the particle id.

In addition to the LSND oscillation search, the BooNE collaboration is exploring several other interesting physics studies. These include, neutrino cross section measurements, a search for the KARMEN timing anomaly [7], a search for the neutrino magnetic moment [8], and supernova neutrino observatory.

In the near future, the LSND question will be resolved by the MiniBooNE experiment.

References

1. E. D. Church, K. Eitel, G. B. Mills, and M. Steidl. Phys. Rev., **D66** 013001, (2002).
2. Y. Fukuda *et al.* Phys. Rev. Lett., **81** 1562–1567, (1998).
3. Q. R. Ahmad *et al.* Phys. Rev. Lett., **87** 071301, (2001).
4. G. Barenboim, L. Borissov, J. Lykken, and A. Yu Smirnov. JHEP, **10** 001, (2002).
5. B. Armbruster *et al.* Phys. Rev., **D65** 112001, (2002).
6. E. Church *et al.* A proposal for an experiment to measure muon-neutrino $\rightarrow$ electron-neutrino oscillations and muon-neutrino disappearance at the fermilab booster: Boone. Technical Report FERMILAB-P-0898, Fermilab, (1997).
7. S. Case, S. Koutsoliotas, and M. L. Novak. Phys. Rev., **D65** 077701, (2002).
8. Bonnie Fleming. *Inner Structure and Outer Limits: Precision QCD and Electroweak Tests from Neutrino Experiments.* PhD thesis, Columbia University, (2002).

PERSPECTIVES IN NEUTRINO PHYSICS

Borut Bajc,
Jožef Stefan Institute, Ljubljana, Slovenia
Fabrizio Nesti,
International School for Advanced Studies, SISSA/ISAS, Trieste, Italy
Goran Senjanović,
Abdus Salam International Centre for Theoretical Physics, Trieste, Italy
Francesco Vissani,
INFN, Laboratori Nazionali del Gran Sasso, Theory Group, Assergi, Italy

Abstract

There are mounting evidences that ν_e, ν_μ and ν_τ are superpositions of 3 mass eigenstates with large mixing angles and moderate mass hierarchy. This picture should receive a number of confirmations in the future years, perhaps enriched by new discoveries, even though major surprises are not excluded. In this scheme, we know 4 parameters of the neutrino mass matrix out of a total of 9. To progress further, we would like to infer from experiments the mixing angle θ_{13}, the neutrino mass scale, the Majorana nature of their masses, and (some of) the CP violating phases. Thus, the program of reconstruction of the neutrino masses from data will be very demanding and probably will have a limited reach for a long time. The other complementary approach is to understand neutrino masses within a well defined theoretical framework–an 'up-down' approach. After describing the limitations of a model based on U(1) flavor symmetry (mostly due to the unknown 'coefficients of order unity'), we discuss a renormalizable, supersymmetric SO(10) model where neutrino masses are connected with those of the other fermions. We also mention the most promising possibilities to use neutrinos as astrophysical probes.

1 Phenomenology, A.D. 2003

This first part is organized in three sections: the first, sec.1.1 is about oscillations, in particular in the three neutrino framework; the second, sec.1.2 on other approaches to investigate neutrino masses; the last, sec.1.3, is on the use of neutrinos as astrophysical probes.

Trying to fulfill the task assigned by the Organizers, we will recall some important steps in the history of neutrino physics. We would like to begin by reminding the actuality of the vision of Bruno Pontecorvo; for a more accurate account, the reader can profit of his recollections written 20 years ago [1]. Pontecorvo began to work on neutrino physics since the forties, even though it was common opinion (apparently even of his outstanding guide, Enrico Fermi) that neutrino investigations were undoable in practice. He introduced the idea of oscillation in 1957 using only ν_e and its 'antineutrino', by analogy with $K^0 - \bar{K}^0$ decay. He overcomed this limitation in 1967,[1] and the connection with neutrino masses was outlined. He did realize the extraordinary sensitivity to neutrino masses offered by oscillations, now universally understood. In fact, it is almost unpleasant to recall that soon after the 1967 paper on oscillations, Pontecorvo discussed the possibility that the leading contribution to double beta decay could be *not* related to neutrino mass, but to some other mechanism [6]: indeed, this seems to suggest the view that there is no hope otherwise.[2] S.Bilenky recalled to us that Pontecorvo believed that the mixing has to be either zero, or maximal [7]. This insight is again of impressive actuality for whoever is working in the field. It is a great pity that Pontecorvo passed away 10 years ago, before he could see his views becaming reality. Pontecorvo liked to introduce his investigations by carefully selected and well formulated questions: so let us conclude this account expressing the hope that there will be more Physicists, who following Pontecorvo will be able to understand which are the right questions.

---

[1] In 1962, the concept of mixed neutrinos was introduced [2], and immediately later the (2 flavor) leptonic mixing matrix in 1962 was considered, even if in the context of an incorrect model of hadrons [3]. This shortcoming was corrected one year later, by drawing the connection between the mixing matrix and the neutrino masses [4]. The leptonic mixing matrix is sometimes called MNS matrix after the authors of [3]. It should be added that, none of these authors mentioned neutrino oscillations—but presumably they did ignore Pontecorvo's papers.

[2] Even if we will show that this conclusion does not necessarily apply, we feel that such a view is all but deceiving.

1.1 Oscillations and neutrino masses

In view of the rather complete discussion on experimental evidences of oscillations we have had at this Conference [8], there are not many reasons to have a section like the present one, apart from offering a formal (useless) introduction to oscillations, and a brief (biased) summary of data. So, we kept in mind a few rather specific aims, in particular: to make explicit the recent change of perspective (strongly boosted since 1998 by the achievements of the Super-Kamiokande experiment, SK from here on), that oscillations are to be considered as a method of measuring neutrino properties.[3] It should be realized that such a point of view is supported by existing data, but only partially. Neutrinos experiments are difficult and this is *one* of the reasons why these experiments have often produced surprising and sometimes contradictory results in the past (many of us do feel that neutrinos are *really* surprising particles). Furthermore, it is true that a large number of facts can be explained assuming that the standard model/usual neutrinos are endowed with mass, but this is not sufficient to explain all anomalies, as will be recalled in the section 1.1.3. Nevertheless, in this talk we will mostly take the view that 3 neutrino oscillations occur. In summary, we believe neutrino mass models that address solar and atmospheric neutrino anomalies in terms of oscillations are still not compelling, but largely motivated by present data. However, we have to wait for the results of MINOS, CNGS and MiniBooNE to reassess (or reconsider) the validity of such a working hypothesis. In this view, we will mention which are the most appealing goals still to be achieved.

1.1.1 How well do we know neutrinos?

We know for sure that neutrinos have always been generous with surprises. Perhaps the future reserves more surprises; or maybe we are turning to a less exciting era (measurements).

We have strong hints of oscillations with the following mass scales and indicative significances (from solar, atmospheric and LSND neutrino data):

$$\Delta m^2_{\rm sol} \sim 10^{-3}\ {\rm eV}^2 \quad (\sim 16\ \sigma)$$
$$\Delta m^2_{\rm atm} \sim 10^{-1}\ {\rm eV}^2 \quad (\sim 10\ \sigma)$$
$$\Delta m^2_{\rm LSND} \sim 10^{0}\ {\rm eV}^2 \quad (\sim 3-7\ \sigma)$$

It should be noted that the strong evidence for oscillations from solar neutrinos comes from the inclusion of a lot of information (also KamLAND), while

[3] This attitude can be contrasted with another view, that oscillations are the mean for discovering and/or of proving beyond doubt that neutrino have mass. Of course these two views are complementary, but they lead to emphasize different experimental or theoretical aspects.

the atmospheric neutrino evidence for oscillations is largely lead by Super-Kamiokande. The estimation of LSND significance is unfortunately rather dependent on the statistical approach. Assuming that the errors are fairly estimated, the significance of first two evidences can be dubbed as infinite-sigma.[4] The third one certainly needs independent confirmation and this could be done with MiniBooNE.

Many people believe that in the last 5 years, neutrinos led us beyond the frontiers of the standard model (some other think that we passed from suspicion to triumphalism...)

1.1.2 The oldest case: Solar neutrinos

Since recently, there is a growing awareness that, after having quantified the effect of oscillations, we should use solar neutrinos as probes of the sun. As a matter of fact, this was the original reason for studying solar neutrinos. This motivated since the early sixties the attentions of John Bahcall see e.g. [9], and (a few years later) of Zatsepin and Kuzmin [10]. Bahcall and collaborators created and improved along the years a theoretical description of the sun that is in fact called 'the standard solar model'. However, since the late sixties the Homestake experiment has been pointing out a serious discrepancy with the predictions of the solar models, that has been confirmed by all subsequent experiments, with a variety of techniques. It took 35 years and lot of efforts to be sure that the reason for this discrepancy was the occurrence of neutrino oscillations.

With hindsight, it is fair to say that the solar neutrinos are the most complicated case of oscillations that we have. The reason is that the 'LMA solution' (confirmed in recent years by SNO, Super-Kamiokande, KamLAND) is a *transition regime*. Indeed, assuming that an electron neutrino produced in

[4] Solar neutrino experiments will produce new data in the short term (SNO neutral current data, KamLAND and Borexino). There are plans to study sub-MeV neutrinos (once again with Borexino and KamLAND, but later with new experiments) and we are coming back to the original goal of using neutrinos to study the sun (Beryllium-neutrinos, pp-neutrinos, pep, CNO cycle contribution). Atmospheric neutrino evidence has been tested at 3 sigma by K2K experiment and will be further tested at MINOS and CNGS. It should be recalled that in the meantime, we will progress on cross section relevant for solar neutrinos (e.g., with LUNA). At higher energies the HARP experiment will contribute to clarify the relevant pion-production processes and K2K should be able to improve on neutrino cross section measurements. Also important are the new generation of calculations of atmospheric neutrino fluxes, that seems to suggest larger discrepancies than expected.

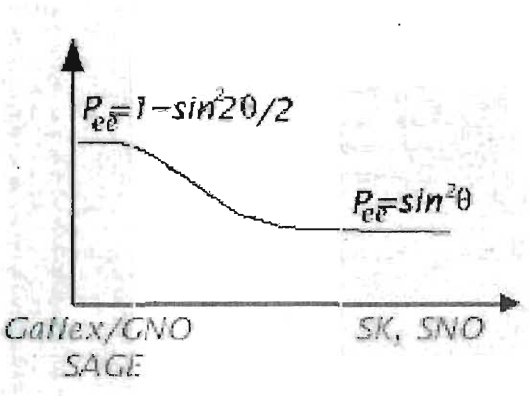

Figure 1: *An illustration of the properties of the 'LMA solution', that emphasizes the fact that in different regions of neutrino energy, different physics is involved.*

the vacuum is a superposition of two states of given mass, $\nu_e = \cos\theta\ \nu_1 + \sin\theta\ \nu_2$, a ν_e produced in the sun exits as:

$$\begin{cases} \cos\theta\ \nu_1 + \sin\theta\ \nu_2\ e^{i\infty} & \text{at low } E \\ \nu_2 & \text{at high } E \end{cases} \qquad (1)$$

The first case is the Gribov-Pontecorvo [11] vacuum oscillation regime, when ν_2 gets a large phase w.r.t. ν_1; the second case is the Mikheyev-Smirnov-Wolfestein regime, [12] when *weak interaction* phases lead ν_e to be the eigenstate of an effective hamiltonian already at production, which smoothly becomes ν_2 (this is known as 'adiabatic propagation'). From the previous equation one can easily obtain the survival probabilities quoted in fig.1. It looks simple and this is as it must be: physics looks simple *after*.

1.1.3 A 'standard' 3 neutrino interpretation

(The quotation marks for 'standard' is because we are not yet in a position to claim to have a standard model for neutrino masses, both for experimental and for theoretical limitations). In order for oscillations to occur, the neutrino fields with given flavor (that is, those in the charged leptonic current) should be superpositions of mass eigenstates:

$$\nu_\ell = U_{\ell i} \cdot \nu_i \quad \text{with } \ell = e, \mu, \tau, \quad i = 1, 2, 3 \qquad (2)$$

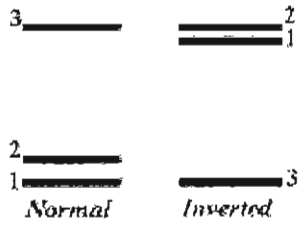

Figure 2: *Possible mass spectra and conventional numeration of the ν_i-states.*

As for the quark sector, it is most useful to have a parameterization of the mixing matrix U and for the purpose of oscillations, only four parameters are needed (more discussion later). Indeed, one can use for this purpose the same parameterization that is used for the quarks and that can be found for instance in the PDG biannual report or, at http://pdg.lbl.org. An alternative possibility is the following one (that has $U_{ei} \in R$ is $\alpha = \beta = 0$):

$$U = R_{23}(\theta_{23}) \cdot \mathrm{diag}(1, e^{i\phi}, 1) \cdot R_{13}(\theta_{13}) R_{12}(\theta_{12}) \cdot \mathrm{diag}(1, e^{i\alpha}, e^{i\beta}) \qquad (3)$$

For the moment it is enough to know that the only phase that could matter for oscillations is ϕ. The summary of the parameters is given in table1. Note that beside the mixing angles, we quote also two mass squared differences $\Delta m^2_{ij} = m^2_j - m^2_i$, whose values are in eV^2. They are very often referred to as the 'solar Δm^2', Δm^2_{12} and the 'atmospheric Δm^2', Δm^2_{23}, though the terminology is inaccurate. It should be recalled here that:
(1) only the difference squared (not some 'absolute' neutrino mass, say m_1) affect oscillations,
(2) there is a third Δm^2, namely Δm^2_{13} but it practically coincides with Δm^2_{23};
(3) while Δm^2_{12} is positive, Δm^2_{23} can be either positive or negative depending on whether the mass spectrum is 'normal' or 'inverted' (see fig.2). Present data are compatible with both possibilities and are not able to distinguish among them.

1.1.4 Goals in oscillations

⋆ The priority is to get θ_{13}, the only unknown mixing angle. There are several approved experiments that will reach few degrees sensitivity such as ICARUS or MINOS. Future projects like JHF could go below 1 degree.

⋆ Many theorists would like to know whether the atmospheric neutrino mixing angle is maximal or not. However from the point of view of the experimental investigation this will be a difficult task.

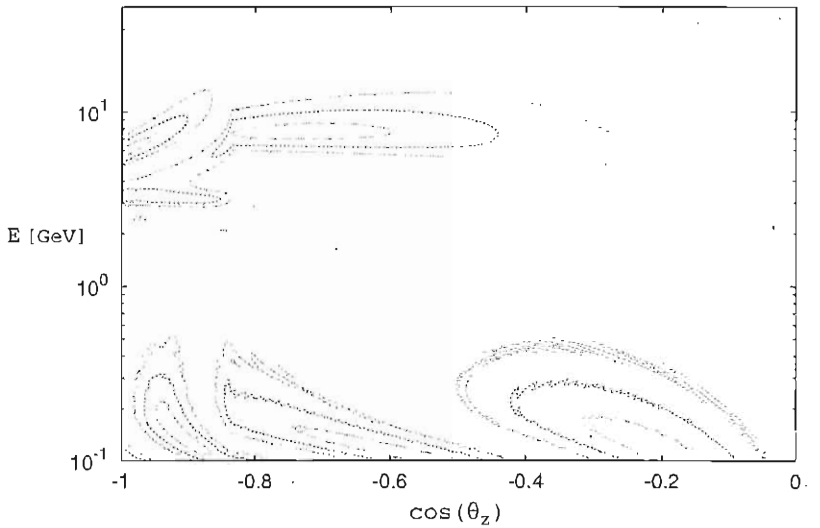

Figure 3: *A numerical calculation of the probability P_{ee}, for neutrinos produced in the atmosphere at the height of 15 km and crossing the Earth. MSW effect at $E \sim 0.1$ (~ 10) GeV corresponds to solar (atmospheric) oscillations. The structure at $\theta_Z \sim \pi$ (upward going neutrinos) and $E \sim 5$ GeV is due to MSW in Earth core. The 3 'solar islands' result from an interplay between matter effects and vacuum oscillations and the fuzzy contours are due to θ_{13} driven vacuum oscillations.*

$\star$ In the long run, we could use the *wrong sign muons* signal, to reveal the occurrence of e.g., $\nu_e \to \nu_\mu$ oscillations from the observation of μ^- (ν_e could come from $\mu^+ \to \nu_e\, e^+ \bar{\nu}_\mu$). This can be useful also to reveal leptonic $\not{C}\not{P}$

$$P(\nu_e \to \nu_\mu) - P(\bar{\nu}_e \to \bar{\nu}_\mu) \propto Im[U_{e1} U^*_{e3} U^*_{\mu 1} U_{\mu 3}] \propto \theta_{13} \sin\phi$$

This quantity is proportional to the phase ϕ but also to θ_{13}. It is essential to disentangle the MSW effect, that acts in opposite manner for ν_e and $\bar{\nu}_e$ and should be distinguished from fundamental $\not{C}\not{P}$. (Incidentally, MSW effect has been seen only with solar neutrinos).

$\star$ But, even in oscillations, surprises are not excluded. E.g., there could be appreciable oscillations into sterile neutrinos. (We will not discuss that, but interested readers may see [14].)

Table 1: *The 'oscillation parameters' known today, with the name of relevant experiments indicated* [13]. *In brackets, future experiments.*

$\theta_{23} = 45° \pm 6°$ $\lvert\Delta m^2_{23}\rvert =$ $2.7 \pm 0.4 \cdot 10^{-3}$ eV^2	$\theta_{13} < 7°$	$\theta_{12} = 34° \pm 2°$ $\Delta m^2_{12} =$ $7.1 \pm 0.6 \cdot 10^{-5}$ eV^2
KAM, IMB, SK MACRO, Soudan K2K (Minos, ICARUS, OPERA)	CHOOZ, Palo Verde (ICARUS, Minos, Krasnoyarsk, JHF...)	Homestake, KAM, SK Gallex/GNO, SAGE, SNO, KamLAND (???)

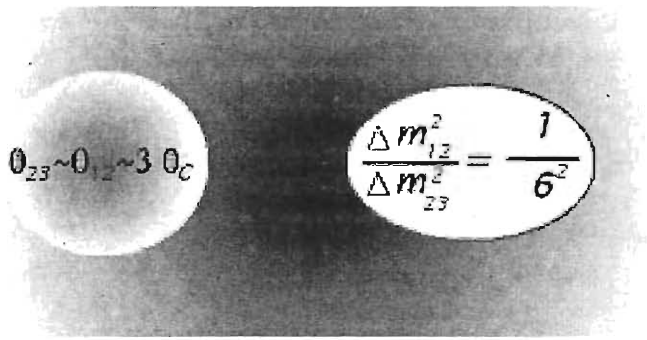

Figure 4: *An illustration of the most puzzling features of neutrino masses: large mixing angles, and weak hierarchy of masses. For comparison we used the largest quark mixing angle, $\theta_C \approx 0.22$ (the Cabibbo angle).*

1.2 Non-oscillation techniques to investigate neutrino masses

As already recalled, at this Conference we have had a complete and exhaustive discussion on oscillations. We would like to corroborate it, keeping in mind the aim of discussing massive neutrinos, with a number of remarks on the other possibilities to investigate neutrino masses: the beta decay spectra, the neutrinoless double beta decay process and cosmology. Here we will provide some introductory material and will be again somehow diffuse on historical issues.[5]

[5]The reader should be aware that any of the processes mentioned below can get other contributions beside those from massive neutrinos; however we will not discuss this possibility any further.

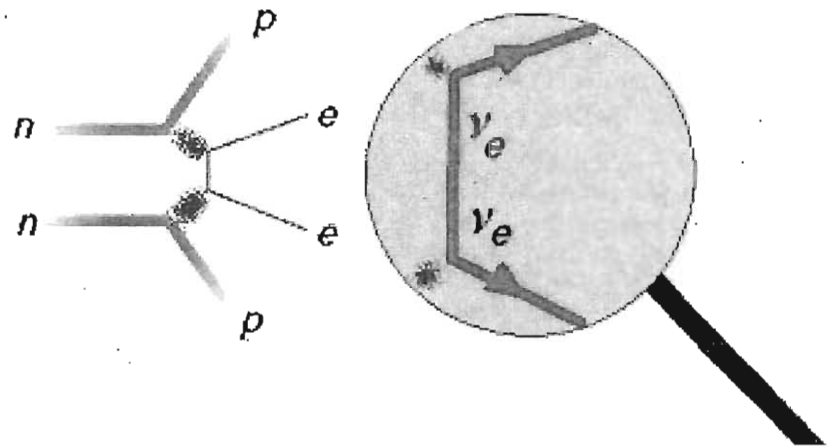

Figure 5: *A Feynman diagram for neutrinoless double beta decay. The arrows in the 2 e^- lines must change direction in the line of the (virtual) neutrino, thus its mass has to give $\Delta L_e = 2$ lepton number violation: a Majorana mass.*

1.2.1 Direct search

First we describe what is often called 'direct mass search'. In 1934, shortly after Pauli introduced the idea of neutrinos, Fermi noted that the region of the beta spectra where the energy of the neutrino E_ν is minimal (that is, where E_e is maximal, since $Q \approx E_e + E_\nu$) can be modified, due to the phase space factor $d^3p_\nu \propto E_\nu(E_\nu^2 - m^2)^{1/2}$. Indeed, knowing that there are 3 neutrinos and that they mix, we expect three such steps or kinks in the beta spectrum [15]. However, if their separation is not possible – due to limited resolution in E_e measurements – we effectively probe only the combination $m^2_{\nu_e} = \sum_i |U^2_{ei}|\, m_i^2$ [16, 17]. In practice, m_{ν_e} reduces to whichever of the neutrino masses m_1, m_2 or m_3, if the common neutrino mass scale is large in comparison to the 'oscillation scales' $(m_i^2 - m_j^2)^{1/2}$. The existing limit on m_{ν_e} at 95 % CL is 2.2 eV [19, 20], and has been obtained by the experiments MAINZ and TROITSK (however, this latter experiment has non understood features in their beta spectrum). The estimated sensitivity of future project KATRIN is around 0.25 eV [21].

1.2.2 Neutrinoless double beta decay

In 1937, very soon after Majorana explained how to describe massive neutral fermions, Racah remarked that if the neutrinos have the mass described by Majorana, lepton violating phenomena like the transition $(A, Z) \to (A, Z+2) + 2\, e^-$ (=neutrinoless double beta decay) could take place (the lepton conserving analogue $(A, Z) \to (A, Z+2) + 2\, e^- + 2\, \overline{\nu}_e$ was suggested few years before by Goppert-Mayer.) A detailed treatment of this transition, including nuclear aspects, was given by Furry in 1939. In modern language, we say that this transition is possible if the *ee-element* of the neutrino mass matrix is non-zero: $M_{ee} = \sum_i U_{ei}^2 m_i \neq 0$, see also the illustration in5. Said more explicitly, this nuclear transition gives us the chance to probe (the absolute value of) 1 element of the neutrino mass matrix; for the other matrix elements, the situation is much tougher if not impossible.

There is a small number of nuclear species that can be employed for this sake. The isotope ^{76}Ge, with natural abundance ~ 7 % was considered more than 35 years ago by Fiorini *et al.* [22]. This technique yielded the best limit we have, $|M_{ee}| < 0.38$ eV at 95 % CL in the experiment Heidelberg-Moscow at the Gran Sasso National Laboratory [23]. Some members of this collaboration reanalyzed the data and claimed for an 'evidence' [24], but the significance of the putative signal is not strong and crucially depends on the procedure of analysis. A number of future projects plan to go down with M_{ee} by more than one order of magnitude, e.g., GENIUS, MAJORANA, GEM [25] and other ones with different nuclear species, as CUORE, EXO, NEMO, *etc* [26]. This means that this observable has the best chances to improve the bounds on (or, perhaps, to dig out?) neutrino masses in laboratory.

Some theoretical remarks are in order. First, we restate that neutrino mass has to have Majorana character in order to contribute to this process, but it is not guaranteed that if the neutrino mass is Majorana, it does contribute [27]. We want to mean that if neutrinos have normal hierarchy, it is always possible to arrange the equality $M_{ee} = 0$ without contradicting what we know today on oscillations. [28, 29, 18] This is due to the fact that the contributions of the three neutrinos come with the phases α and β of eq.3 ('Majorana phases'), [30, 31] that can lead to destructive interference for a certain value of the lightest neutrino mass. Another important remark is that, despite the long history of these investigations, the nuclear uncertainties remain rather severe. This can be seen from the fact that one should quote the Heidelberg-Moscow result as $|M_{ee}| < 0.38 \times h$ eV. For the calculation of Staudt *et al.* that they use as a reference $h = 1$, but if one uses another calculation, h should range from 0.6 to 2.8, see e.g. [18]. It is possible to test these calculations with the rate of the lepton conserving (Goppert-Mayer) transition, but the relation between

the two matrix elements is not necessarily tight.

1.2.3 Cosmology

In 1966, soon after the foundation of the big-bang model, Gershtein and Zeldovich [33] realized that this model predicted that neutrinos must fill the Universe, since they are in thermal equilibrium above MeV energies. The expansion of the Universe implies that the neutrino momentum p decreases with the cosmic scale factor $p(t) \propto 1/a(t)$. Thus we can say that $T_\nu \propto 1/a$, since the neutrino occupation number is $n = 1/(\exp[p/T_\nu] + 1)$ (thus, the mass of neutrinos is always negligible in n and usually, one assumes that the leptonic asymmetry is very small). After decoupling, T_ν remains the same as the photon temperature T_γ, *modulo* episodes of entropy production like e^+e^- annihilation.

That implies $T_\nu = 1.9$ °K,[6] which is related to the temperature that anybody knows, $T_\gamma = 2.7$ °K. In this context, one can try and reveal neutrino masses of cosmological significance by studying their influence on the formation of observable structure (galaxies, clusters, voids, CMB, etc). In good approximation, this method probes the parameter $m_{cosm} = \sum_i m_i$.

Till few years ago, CMB inhomogeneities were not measured and a hot dark matter component (like the one provided by neutrino masses) was very much welcome, in order to correct the prediction of the cold dark matter 'Einstein-de Sitter' cosmology $\Omega_c = 1$. In an influential paper, it was shown [38] that the most successful blend had $\Omega_\nu \sim 0.3$ and thus $\Omega_c \sim 0.7$; low values of the Hubble constant H_0 were also required. In this model, $m_{cosm} \sim 6$ eV, so that any of the neutrinos had to have a mass of a pair of eV. Many particle physicist liked this hot+cold dark matter cosmology, because (1) it was a positive indication of neutrino masses; (2) it was possible to avoid the introduction cosmological constant (which is known to be a particularly tough issue). Indeed, this indication from cosmology stimulated lively discussions, on whether it is possible to reconcile quasi-degenerate neutrino mass spectra with some theoretical scheme or other facts, but eventually these discussions were not able either to rule out or confirm this convincingly.

However, the situation begun to change few years ago. Indeed, (a) new statistical analyses of the galaxy distribution by the 2dF collaboration revealed that the hot+dark matter picture is not in good agreement with the data,

[6] Most probably the ν-momentum distribution is non-thermal, namely their occupation number differs from $n_{th.} = 1/(\exp[E_\nu/T_\nu] + 1)$, since $m \gg T_\nu$ for neutrinos (except perhaps the lightest). However, the direct detection of these non-relativistic neutrinos seems to be exceedingly too difficult to be of any practical interest and the only chance we are left with is their gravitational interactions.

(b) precise investigations of CMB inhomogeneities (first seen by COBE) became possible (BOOMERANG, MAXIMA, DASI, Archeops, WMAP, etc.) and although they supported the expectation from inflation, $\Omega = 1$, they did not need much neutrino masses, (c) studies of type I supernovae at cosmological distances (Supernova 1a project, HST) added arguments in favor of the introduction of a cosmological constant and finally (d) the recent determinations of H_0 pointed out to larger values than indicated by hot+cold dark matter cosmology. These facts together lead to a *debacle* of the idea that neutrinos have an important role in cosmology! Indeed, the common view today is that cosmology provides a *bound* on neutrino masses. The most recent version of this bound is $m_{cosm} < 0.71$ eV at 95 % CL [39], and this is sometimes called 'WMAP bound', but for fairness and in view of the multitude of facts above recalled, we believe that it should be referred as 'cosmological bound'. It is important to recall that this relies on a set of untested hypothesis [40] and perhaps we should be cautious when comparing this number with other laboratory bounds.[7]

1.2.4 *Comparing the different masses*

To summarize things properly, let us begin by giving the formal definition of the Majorana neutrino mass matrix M. This is the set of 9 numbers[8] in the lagrangian

$$\mathcal{L}_{\nu\ mass} = \frac{1}{2}\nu_\ell(x)C^{-1}M_{\ell\ell'}P_L\nu_{\ell'}(x) + h.c. \quad \ell,\ell' = e,\mu,\tau \tag{4}$$

where C is the charge conjugation matrix and P_L is the projector on left states. As it is clear, this violates U(1) symmetries, as lepton numbers and also weak hypercharge (however, as we will see below, this violation can be ascribed to the vacuum).

From this point of view, the simplest observable is $|M_{ee}|$ as implied in neutrinoless double beta decay. To connect the mass matrix with the other observables, one introduces the unitary decomposition:

$$M_{\ell\ell'} = U^*_{\ell i}m_i U^*_{\ell' i} \tag{5}$$

[7] In a recent analysis [37] of most cosmological data, it was found a preference for a non-zero value of $m_{cosm} = 0.64^{+0.40}_{-0.28}$ eV. We are not sure how this result should be interpreted and more clearly, whether it bounces us back to the hypothesis of degenerate neutrinos! However, it certainly shows that cosmology is able to reach important sensitivities and that this field of investigation has a bright future.

[8] Indeed, this is a symmetric complex matrix and 3 phases can be absorbed in the definition of the neutrino fields.

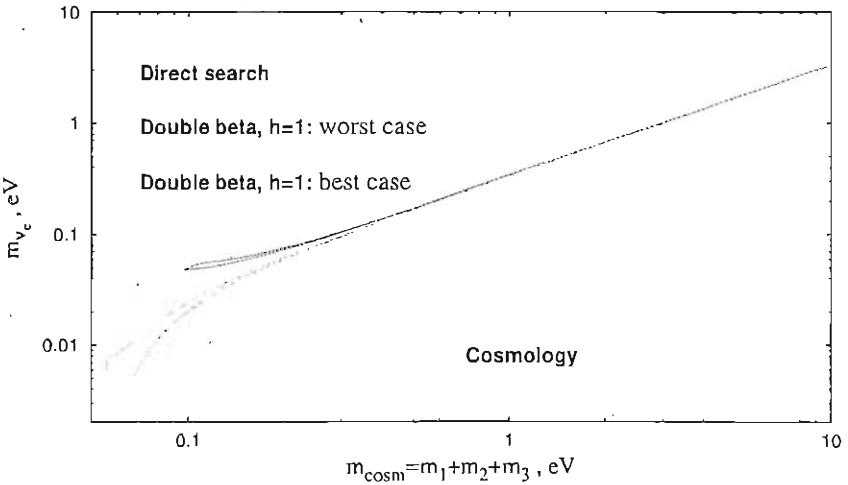

Figure 6: *Predicted regions in the plane $m_{cosm} - m_{\nu_e}$, for inverted spectrum (region above) and normal one (region below). Superimposed, the experimental limits from laboratory, direct search and from neutrinoless double beta decay (horizontal lines) and the one from cosmology (vertical line).*

where U is the mixing matrix of eq.2 already discussed and the non-negative parameters m_i are the neutrino masses. It should be noted that the massive parameter of beta decay does not depend on the phases α and β as defined in eq.2, sometimes called Majorana phases; however the same is true for oscillations [31]. One may say that 'β-decay and oscillations cannot tell Majorana from Dirac masses', but we prefer to stress here the fact that the 'Majorana phases will be very tough to measure'[9].

Even if this framework can be felt as somehow restrictive, it is well motivated by the theoretical point of view, as we will discuss later. Furthermore, within this framework we can compare the various experimental observables. For instance, we plot in fig.6 the regions of the plane $m_{cosm} - m_{\nu_e}$ (mass appearing in cosmology *versus* mass appearing in β-decay) allowed by the 1 sigma ranges of the 'oscillation parameters', for normal and inverted spectra. There, one can see that the present limit from cosmology is an order of magnitude

[9]Ref. [34] stressed which are the cases that would be ideal for experimental approach, however (even in view of present data) we believe that these are not likely and feel inclined to agree with the opinions expressed in [35, 36].

more restrictive than the limit from direct search. One sees also that a good limit on m_{ν_e} derives from the combination of oscillation data and neutrinoless double beta decay (assuming that the nuclear fudge factor h is not very far from 1).

However, the comparison is most simple in the case when neutrinos have a common large mass ('quasi degenerate neutrinos') and in this case, some approximate analytical formulae can be given: $m_{cosm}/3 \approx m_{\nu_e} \approx \max(M_{ee})$, while $\min(M_{ee}) = m_{\nu_e} \cos 2\theta_{12}$; minimal and maximal values refer to the possibility to vary the Majorana phases. These formulae are excellent, in view of the present limited sensitivity of non-oscillation experiments.

1.3 Neutrinos as astrophysical probes

In this section, we abandon for a while the main focus of the talk (=evidences, manifestations and meaning of neutrino masses) to discuss some possibilities to use neutrinos as astrophysical probes. But oscillations will reappear, in the sense that most often a proper interpretation of the neutrino signal requires to take them into account [41]. Instead, we will not discuss the kinematical methods to investigate neutrino masses: for supernova neutrinos, the sensitivity of this method is just around the tenth of eV [42] even though this neutrino source is very powerful.[10]

It is important to recall that the information from ν can be complementary to the one from γ, since not only their detection, but also their production and propagation are different (think, e.g., to our sun as an example). For more detailed accounts of the subjects touched here, see for instance [43, 44, 45, 46, 47]. Our presentation follows closely [3].

1.3.1 Chances for neutrino astronomy

This subsection has two main aims: (1) to recall what a 'neutrino telescope' is and (2) to give some discussion on possible neutrino sources. Table 2 gives a partial list of the possibilities for neutrino astronomy and the numbers indicated may be useful for a first orientation (but nothing more than that).

Let us begin describing some concepts of neutrino detector.

⋆ *One can instrument a large volume, possibly vetoing for external particle and wait for a charged particle coming apparently from nowhere—in actuality, created by a neutrino interaction.* Active volume can be a bubble chamber, a

[10] One can conceive other sources located at cosmological distances, but before discussing whether they are useful to investigate neutrino masses, one should first try to estimate their neutrino beam, as irradiated power, time- and energy-distributions. To get an idea of the uncertainties, see e.g. [44].

Table 2: *Some astrophysical sources of neutrinos.*

Site of production	Relevant process	Energy range	Experimental technique
Earth	fission	$\sim 10^6$ eV	undergr. detect.
Sun	fusion	$\sim 10^6$ eV	as above
Core-collapse supernova	non-equil. nucl. phys.(?)	$\sim 10^7$ eV	as above
AGN? GRB?	$p\gamma \to \Delta^+$	$\sim 10^{14}$ eV	large surface... km^3 detector
as above, ???	as above, ???	$\sim 10^{19}$ eV	inclined EAS, ...

scintillator, a Cherenkov radiator, a layered target. This method works from sub-MeV to several GeV energies, because it is subject to the condition that the (main part of the) event is contained in the detector. The number of events scales as the volume of the detector and these detectors are located underground to limit the effect of the background.

⋆ *One can set a muon counter and timing system underground (underwater or under-ice), for muons that originate from neutrinos-as those coming from below.* Detectors are located underground to avoid cosmic ray (CR) muons. This is the oldest method [48] and works since muons suffer of mild energy losses till ~ 500 GeV (roughly, 1 km in water). It applies from energies around a GeV till several hundred TeV; then the Earth becomes opaque even to neutrinos, see e.g. [43]. The number of events scales as the area of the detector (actual target being the Earth, the sea or the ice where the detector is located).

⋆ *By an extension of previous concept, one could use the Earth atmosphere as a target for high energy neutrinos to produce muons (inclined air showers); or, use mountains to convert almost horizontal ν_τ of very high energy into visible taus.* In this way, we could observe neutrinos of highest energies. The search of inclined air showers is just a spin-off of extensive air shower arrays research activity. Till now, however, no positive detection has been claimed.

Now we pass to describe a number of neutrino sources:

(1) Solar neutrinos [0.1-20 MeV] More than 30 years ago, Homestake begun a program of great success: a) the physics of the center of the sun ($\rho_c \sim 150$ gr/cc) was probed; b) low energy ν experiments Gallex/GNO, SAGE proved that the pp-chain (initiated by $pp \to De^+\nu_e$) is the main energy source; c) also higher energy neutrino flux obeys the predictions of solar models[11], and remarkably

[11] When oscillations into active ν are taken into account, or when 'solar model independent' observables are used–e.g., neutral currents at SNO, or the shape of the Boron spectrum at (Super-)Kamiokande.

the standard solar model. Future observations will aim at the Beryllium line (Borexino, KamLAND) and at real time pp-neutrino detection.
(2) Atmospheric neutrinos [0.05-1000 GeV] The study of CR secondaries, like gamma's, muons or atmospheric neutrinos, permits us to investigate CR spectra and their interactions with Earth atmosphere, which is not that different from the possible sites (places) where the CR are produced (even though we have not a definitive theory of CR origin). Atmospheric neutrinos are an important background to search for cosmic sources.
(3) Neutrinos from cosmic sources [unknown energies] This is a vast field and includes a large variety of approaches of observation and of objects; presumably, also unknown objects [44]. For instance, one can search for an excess of neutrino events over the expected background by selecting a solid angle–observation window–around a cosmic source (say, an active galactic nucleus) or an appropriate time window around a cosmic events (say, a gamma ray burst). The observation of point (or diffuse) sources is a very important goal: e.g., ν (and γ) astronomy above TeV can shed light on the problem of the origin of CR. Till now several experiments like LSD, MACRO, LVD, Super-Kamiokande, Baksan, AMANDA, EAS-TOP, HiRES and other ones produced upper limits on the fluxes. In future, this type of search will be conducted by AUGER, ICECUBE, NEMO, ANTARES.
(4) Supernova neutrinos [few-100 MeV] In 1987, Kamiokande II, IMB, Baksan (and perhaps Mont Blanc detector) begun extragalactic neutrino astronomy, by observing neutrinos from a supernova [49] located in the Large Magellanic Cloud (SN1987A). Many operating neutrino detectors like Super-Kamiokande, SNO, LVD, KamLAND, Baksan, AMANDA could be blessed by the next galactic supernova. Other detectors like ICARUS and Borexino will also be able to contribute to galactic supernovae monitoring in the future.

1.3.2 Neutrinos from core collapse supernovae

We would like to spend some other words on supernovae. We have three main reasons to select this source among the other ones: (1) this technique of investigation relies on established techniques (it worked for SN1987A); (2) it as big payoff in astro- and particle physics (e.g., the number of papers after SN1987A is very large) (3) however, it has enough open questions for theorists and experimentalists to enjoy it.

Some of the most relevant points on core collapse supernovae are:
• The huge amount of gravitational energy of iron core, $E_b \sim 1 - 5 \cdot 10^{53}$ erg (namely, about 20 % of the rest energy $M_{core}c^2$) is released in neutrinos of various flavors during the formation of a neutron star.
• Simulated explosions are very difficult to obtain. The conservative attitude toward this obstruction is that we need full 3D simulations. But perhaps,

Table 3: *Main phases and emitted neutrinos for SN delayed explosion*

Conventional name	Description	Duration	% of E_b
infall (early neutronization) [only ν_e]	Collapse begins. $ep \to \nu_e n$. ν-trapping increases	~ 100 millisec	less than 1 %
flash [only ν_e]	Bounce. Flash obtains when the ν-sphere is reached	few msec [$t \equiv 0$]	~ 1 %
accretion [ν_e, $\bar{\nu}_e$, ν_x?]	Shock stalls, then resumes (how?) $e^+e^- \to \nu_x\bar{\nu}_x$ begins	fraction of a second	$\sim 10 - 20$ %
cooling [all ν types]	Proto NS cools and contracts emitting ν's	till 10-100 seconds	$\sim 80 - 90$ %

some unexpected (astro)physics is involved. Or perhaps, there is nothing like a "standard explosion".

• The agreement of expectations with SN1987A neutrinos looks good, perhaps even too much. In fact, there are just $\sim$ 20 ν-events, and there are several puzzling features when one looks into the matter closely.

The dynamic of neutrino production is expected to be rather complex; we sketch in table 3 the main phases of the 'delayed explosion' scenario. However, a zeroth-order description of the (time integrated) energy distribution assumes (a) that ν_μ ν_τ and their antineutrinos are produced in very similar amount and (b) that the three neutrino types ($i = e, \bar{e}, \mu$) have a Fermi-Dirac distribution:

$$F_i^0 = \frac{f_i E_b}{4\pi D^2} \cdot \frac{n(E/T_i)}{T_i^2} \text{ with } n(x) \approx \frac{0.18x^2}{1+\exp(x)}$$

The general expectations are that $f_e \sim f_{\bar{e}} \sim f_\mu$, $T_e < T_{\bar{e}} < T_\mu$, $T_{\bar{e}} = 3 - 5$ MeV (indeed, it is almost as *imprecise* as stated here). The 3 T_ℓ's are different, since the leakage of neutrinos from the center of the star is a non-equilibrium process and more tightly coupled neutrinos decouple in cooler regions of the collapsing star (strictly speaking, these parameters are not 'temperatures').

MSW theory predicts that, after neutrinos reach densities of 10^4 gr/cc or lower, the distributions in flavors are modified -neutrinos are reshuffled. E.g., with 3 ν, 'normal' hierarchy and no MSW in Earth we have

$$\begin{aligned} \bar{\nu}_e \to \quad & \bar{\nu}_1 \Rightarrow F_{\bar{e}} = \cos^2\theta_{12}\ F_{\bar{e}}^0 + \sin^2\theta_{12}\ F_{\mu}^0 \\ \nu_e \to \begin{cases} & \nu_2 \Rightarrow F_e = \sin^2\theta_{12}\ F_e^0 + \cos^2\theta_{12}\ F_{\mu}^0 \\ & \nu_3 \Rightarrow F_e = F_{\mu}^0 \end{cases} \end{aligned}$$

(the ambiguity in the equation for ν_e flux depends on whether θ_{13} is large or small, but intermediate cases are possible). The conclusion is simply that we

should profit of *three* signals: ν_e, $\bar{\nu}_e$, $\nu_{NC} = \sum \nu_i$, not only of the chance offered by inverse beta decay signal $\bar{\nu}_e p \to n e^+$. *Possibly, we need several different reactions & detectors to exploit fully what we can learn from the neutrinos of the next (galactic, core-collapse) supernova.*

2 Toward a theory of neutrino masses

In this second part, we consider elements and issues for a theory of neutrino and fermion masses. There are three main sections, that corresponds to the questions: (1) Why neutrino masses are so small? (2) What is the structure of neutrino masses? (3) What are the expectations for fermion masses in unified models? This amount roughly to a discussion (1) of the seesaw mechanism for neutrino masses, (2) of flavor symmetries and (3) of realistic grand unified models. All three topics can be said to take the steps from the $SU(3)_c \times SU(2)_L \times U(1)_Y$ (standard) model; in fact, (1) the seesaw mechanism is in essence the manifestation of new effective operators, related to physics above the electroweak scale; (2) flavor symmetries are motivated by the structure of the most numerous family of parameter of the standard model, the fermion masses (which, to say it clearly, seem a disordered set of numbers); (3) grand unified theories are just an extension of the principles of the SM (gauge principle, Higgs mechanism) and motivations for supersymmetry is also stemming from the only untested sector of the standard model: the scalar one.

2.1 The seesaw mechanism

One usually used (and often still does) to define the minimal standard model (MSM) without a right-handed neutrino. After all, it has never been seen and furthermore, being a gauge singlet, cannot play any role in the cancelation of anomalies. At the renormalizable level neutrinos end up being massless; however there is always a possibility of higher-dimensional operators of the type [50]

$$\mathcal{L}_{eff} = f_{\ell\ell'} \nu_\ell^t \, C^{-1} \nu_{\ell'} \frac{H_0^2}{M} \,, \tag{6}$$

where H_0 is the neutral component of the Higgs doublet[12], and M a scale of new physics. If nothing else, M should naturally be of the order of the Planck scale M_{Pl}, for there is no reason for gravity to preserve global symmetries such as L or $B - L$.

Although there was hope [51, 52] that $m_\nu \approx M_W^2/M_{Pl}$ solves the solar neutrino puzzle through the so called just-so oscillations, today we know that is

[12] The SU(2) invariant form being $(\ell H)^2$, where ℓ is one of the lepton doublets, e.g. (ν_e, e).

not enough. Atmospheric neutrinos and even solar neutrinos tell us that there must be some new physics much below M_{Pl}: $M \leq 10^{16}$ GeV (though, Planck scale effects could still be relevant, see for example [53]).

2.1.1 *The hypothesis of a heavy right-handed neutrino*

The simplest possibility is to add right-handed neutrinos to the MSM and write the most general gauge-invariant Lagrangian

$$\mathcal{L}_{Yukawa}(\nu) = \overline{\nu}_R Y_D H^\dagger \ell + \nu_R^t C^{-1} M_R \nu_R + h.c.\,, \tag{7}$$

where ν_R stands for (3) right-handed neutrinos, ℓ for leptonic doublets, H for the Higgs doublet and Y_D and M_R are matrices in generation space.

In turn, upon integrating out heavy ν_R light neutrinos pick up small masses

$$m_\nu = -Y_D\ M_R^{-1}\ Y_D^t \frac{2M_W^2}{g^2}\,. \tag{8}$$

This is the celebrated see-saw mechanism [54, 55, 56], a starting point for most of the theoretical work on neutrino masses and mixings. The same mechanism offers a theory of leptogenesis and baryogenesis through the joint effect of out-of-equilibrium decays of ν_R and sphalerons [57].

It would seem that all is well and simple. Unfortunately, the see-saw mechanism by itself tells us nothing about neutrino masses (except that neutrinos are light) and mixings; it is not a theory, but a scenario. To have a theory we need information about M_R and (or) Y_D. Since it is M_R that breaks $B-L$ and on the other hand $B-L$ is anomaly free, it is natural to gauge it and attribute M_R to the scale of gauged $B-L$ breaking. This happens naturally in any L-R symmetric theory [58], such as Pati-Salam theory [59] or SO(10) GUT [60]. Both PS (see [61] for a recent analysis) and SO(10) offer information about M_R, but SO(10) is more predictive and furthermore offers a check through the proton decay.

2.1.2 *Canonical and non-canonical seesaw*

An important note is needed, regarding the nature of the see-saw mechanism. Namely, in any renormalizable L-R symmetric theory, the formula (8) must be generalized. What happens is the following: $M_R \propto \langle \Delta_R \rangle$, where Δ_R is the field that breaks $B-L$ symmetry. It is a triplet of $SU(2)_R$ symmetry and by L-R symmetry its left-handed counterpart Δ_L, an $SU(2)_L$ triplet, must also exist and furthermore it must couple to ν_L. In other words, the relevant Yukawa couplings take the form

$$\delta\mathcal{L}_Y = \ell_R^t C^{-1} f \Delta_R \ell_R + \ell_L^t C^{-1} f \Delta_L \ell_L\,, \tag{9}$$

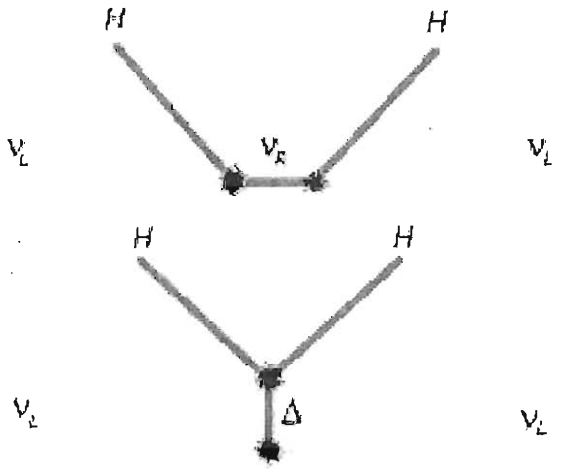

Figure 7: *Feyman diagrams for canonical and non-canonical seesaw.*

where $\ell_{R,L}$ is e.g., $(\nu_e, e)_{R,L}$.

It can be shown [55, 56] that Δ_L picks up a small VEV:

$$\langle \Delta_L \rangle \approx \frac{M_W^2}{M_R} \,. \tag{10}$$

In other words, neutrino mass becomes

$$m_\nu \approx \left(-Y_D \frac{1}{f} Y_D^t + \xi f \right) \frac{M_W^2}{M_R} \,. \tag{11}$$

The first term is the canonical see-saw, called type I and the second term is the non-canonical or type II see-saw. The size of the second term depends on the scalar potential of the theory; however both terms are "see-saw" in nature, in the sense that these contribution to neutrino masses become smaller, when the scale of new physics M_R becomes larger.

Very often, for no good reason at all, people opt for type I seesaw and then face the question as to why neutrino mixing are large. This was studied

in detail [62], where it was shown that small Yukawa and a large atmospheric mixing (θ_{atm}) requires well defined conspiracies. We would like to argue in favor of type II see-saw. As a matter of fact, it also needs a conspiracy to give a large θ_{atm}, but the conspiracy takes a very physical form: it is $b-\tau$ unification at the GUT scale [63]. We will come back to this discussion in sect.2.3.

2.2 Flavor symmetries

Quark and lepton mass matrices do not show any evident pattern; even the hierarchical structure of the mass matrices is very much different, hierarchy being stronger for up quarks, weak for neutrinos and intermediate for down quarks and charged leptons. Starting a quarter of century ago, attempts were made to postulate a symmetry or mechanism able to explain (order-of-magnitude-wise) the observed masses and mixing [64, 65]. This is what is called *horizontal* or *flavor* symmetry.

The flavor symmetry is naturally assumed to hold only at some high (unification) scale. Its breaking should account for masses and mixings relations at electroweak scale. The main problem to compare with is: for quarks, such a symmetry is violated almost uniquely by mass splittings, the CKM matrix [66] being almost identity; for leptons, it is also badly broken by mixing angles, mainly due to maximal and almost-maximal neutrino mixings. This makes family unification a tough task. Other issues are the need to distinguish between "up" and "down" components inside each family and the fact that mass generation for neutrinos may be quite different from that of charged fermions, as explained in previous section.

Models of flavor symmetry may be divided in two sets, depending on whether they use an *abelian* or *non-abelian* flavor symmetry group. We will be mostly concerned with the first (simpler) type and will give just a short account of the other type.

2.2.1 Abelian flavor symmetry

The idea that the pattern in the fermion mass matrices derives from the spontaneous breaking of an abelian symmetry was proposed back in the work of Froggatt and Nielsen [65]. They argued that 'order parameter' could be the vacuum expectation value of scalar fields called 'flavons'[13]. The effective couplings of the fermions to flavons could ultimately result in the Yukawa couplings of the standard model.

[13] These are one or more scalar fields that carry flavor charge and break the symmetry after acquiring a VEV (usually, by some unspecified mechanism).

Thus, the fermion fields that carry a charge Q with respect to the broken flavor symmetry, get a coupling suppressed by a factor ε^Q. $\varepsilon = \langle\phi\rangle/M$ is a *small* parameter, the ratio between the VEV of a breaking field (flavon) and the characteristic scale of unification.

Therefore by choosing the group and assigning suitable charges to the fermion fields, it is possible to tune the magnitude of the entries in the Yukawa couplings. Actual entries still carry undetermined numerical factors, that are reasonably *assumed* to be all of the same order and presumed not to be essential to explain the family relations.

As an example, let's choose $\mathrm{U}(1)_H$ as the flavor group and a single breaking field, i.e. a single *small* parameter ε. It plays a role similar to ϑ_C that appears to regulate the CKM matrix [67]. The *left* neutrino and charged lepton mass matrices are modified as:

$$M_{\nu_L} = \varepsilon^{\mathrm{Diag}Q_L} \cdot \mathcal{O}(1) \cdot \varepsilon^{\mathrm{Diag}Q_L} \qquad M_\ell = \varepsilon^{\mathrm{Diag}Q_L} \cdot \mathcal{O}(1) \cdot \varepsilon^{\mathrm{Diag}Q_R} . \tag{12}$$

Focusing on neutrino oscillations, we see that only charges for the left doublet fields Q_L contribute to the observed mass hierarchy, while for the mixing matrix the contribution from the diagonalization of the charged lepton matrix M_ℓ gives dependence on the right charges Q_R also.[14]

The choice of $Q_L = (1,0,0)$ leads to an interesting left neutrino mass matrix, with a μ-τ *dominant block*: [68, 69, 70, 71, 72]

$$M_{\nu_L} \propto \begin{pmatrix} \varepsilon^2 & \varepsilon & \varepsilon \\ \varepsilon & 1 & 1 \\ \varepsilon & 1 & 1 \end{pmatrix} \tag{13}$$

where it is understood that each entry carries a further $\mathcal{O}(1)$ coefficient. This *texture* has the effect of lowering one eigenvalue to be of order ε^2 and also, in the mixing matrix, to lower $\theta_{13} \simeq \varepsilon$. At the same time the atmospheric angle θ_{23} is not affected and can remain maximal, as illustrated in figure 8.

Let us explain how these numbers were calculated. There are two ingredients: the minor one, the choice of neutrino mass mechanism and, the major one, the $\mathcal{O}(1)$ coefficients of Yukawa entries. The $\mathcal{O}(1)$ coefficients are however unknown and all one can do is to hope that they are not crucial to describe the fermion masses. In fact, since the work of Froggatt-Nielsen [65] it was argued that the $\mathcal{O}(1)$ numeric coefficients may be treated as unimportant or even random. Recently, it was proposed to choose literally the $\mathcal{O}(1)$ coefficients at random [73], and to test the percentage of resulting Yukawa couplings that are

[14] The right charges Q_R entering M_ℓ are preferably chosen so as to account for the hierarchy of masses of e, μ, τ: with Q_L of the form $Q_L = (m,0,0)$ (in the text $m = 1$) one has $Q_R = (3n-m, n, 0)$ (and $\varepsilon \simeq (m_\mu/m_\tau)^{1/n}$).

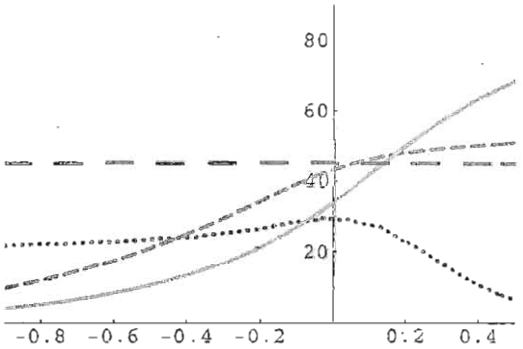

Figure 8: *Average values of the mixing angles in degrees and hierarchy factor scaled by 100 (*$100 \times h$*), as a function of* $\log \varepsilon^{Q_{L1}}$. *Random neutrino mass matrices were generated using the type I seesaw mechanism. The curves are: solid green for* θ_{13}, *short-dashed red for* θ_{12}, *long-dashed blue for* θ_{23} *and dotted for* h.

successful in reproducing the observed data for mixings and mass hierarchy inside measured ranges. In other terms, one can use random number generators, with some 'reasonable' distribution, to scan the possible $\mathcal{O}(1)$ coefficients. In this manner, one can test with a minimum bias whether textures like this can predict/accommodate measured data. The idea is that a specific choice of Froggatt-Nielsen charges should be enough to produce the right predictions. Therefore it is clear that in such a case, the percentage of successful matrices should be not too small. Since experimental ranges are narrowed as experiments get more precise results, the percentage of successful probes can quickly become very small, if the charges are not able to explain exactly all data. Nevertheless, some meaning can be extracted also from variations of percentage e.g., when ε is varied. However, small percentages of success indicate the need of additional model features (more theory).

For the charges presented above, $Q_L = (1, 0, 0)$ and choosing random coefficients of modulus one[15] the percentage of successful matrices is shown in figure 9. In figure 10 we present the effect of the individual cuts on for mixing

[15]There are several possible choices for the distribution of random coefficients. The results differ mainly for the hierarchy factor h, that is slightly spoiled if also the modulus of the $\mathcal{O}(1)$ coefficients is let to fluctuate. We will not discuss this point since there are no principles in this approach that help in discriminating among the choices.

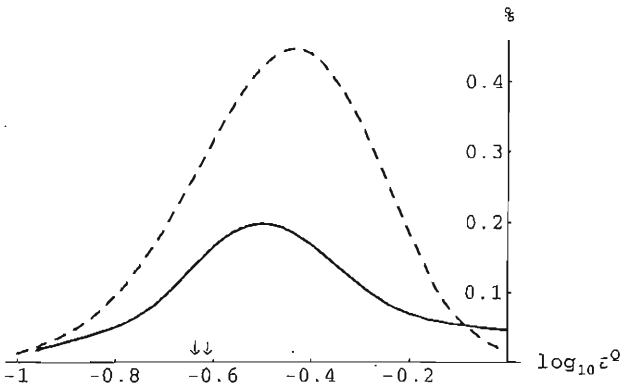

Figure 9: *Percentages of models, as a function of* $\log \varepsilon^{Q_{L1}}$, *that reproduce mixing angles and mass hierarchy within ranges* twice *those in table 1. The* dashed *line represents models that take into account only the diagonalization of the neutrino mass matrix. The* solid *line represents successful matrices considering also the basis rotation for charged leptons, but varying* Q_R *so to keep their mass ratio acceptable. Values for* $\varepsilon = \theta_C$ *and* $\sqrt{m_\mu/m_\tau}$ *are shown.*

angles and hierarchy factor, defined as

$$h = \Delta m^2_{12}/\Delta m^2_{23},$$

as a function of ε. Conclusions to be drawn from the analysis are as follows: (a) as can be noted from the absolute values in figure 9, the percentages are very low, due to more stringent cuts from experimental values. (b) Best values for ε are anyway near the Cabibbo angle or the ratio $(m_\mu/m_\tau)^{1/2}$. (c) In correspondence with these values θ_{13} is small enough to fall inside required data (conservatively, $< 15°$) but it is always nonzero. (d) The atmospheric angle θ_{23} stays nicely maximal, independently from ε (although its spread is quite high, roughly 25°). (e) The solar angle θ_{12} and the hierarchy factor h are not correctly predicted by this model (their spread is also quite high, roughly 70% of its mean for θ_{12} and 150% for h) and ask for tuning of the $\mathcal{O}(1)$ coefficients in order to come out right.[16]

[16] A remark about the so-called neutrino *anarchy* hypothesis may be in order: the limit $\varepsilon \to 1$ in figure 9 reproduces the absence of neutrino charges, advocated by some authors [73] (but see also [74]). From the analysis presented here it is evident that the tuning of $\mathcal{O}(1)$ coefficients needed in this limit is stronger than, e.g., at $\varepsilon \simeq \theta_C$. For instance, taking into account only neutri-

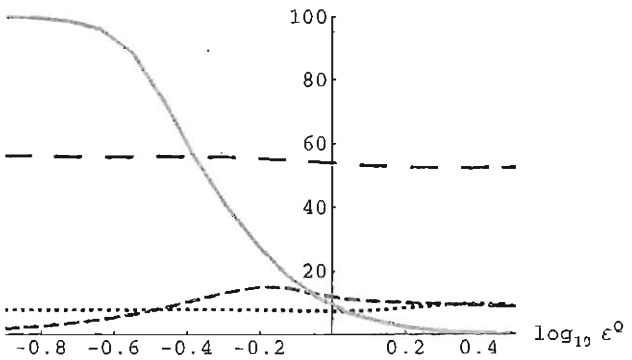

Figure 10: *Percentages of neutrino mass matrices that satisfy single cuts on angles or on the hierarchy factor h. The curves are: solid green for θ_{13}, short-dashed red for θ_{12}, long-dashed blue for θ_{23} and dotted for h.*

All this comes now with no surprise since we know that the dominant block form, eq. 13 above, was chosen exactly to accomplish the smallness of θ_{13} and the maximality of θ_{23}. The fact that we now know that neutrinos enjoy a mild hierarchy $h \simeq 1/36$ and a large $\theta_{12} \simeq 34°$, reflecting in the need to tune $\mathcal{O}(1)$ coefficients,[17] leads us to seek for more sophisticated forms that allow nontrivial hierarchy *together* with maximal θ_{23} and large θ_{12}. Thus further mechanisms of abelian flavor symmetry were formulated trying to accommodate the LMA solution together with large hierarchy and maximal atmospheric mixing (see for example [76], or [77] for a recent analysis). They are based on supersymmetry, more breaking fields, or discrete abelian groups (mainly products of $\mathbf{Z}^n$). Supersymmetry can force zeroes (*holomorphic zeroes*) to appear in the Yukawa matrices, thus leading to enhancement or suppression of eigenvalues, to arrange for nontrivial hierarchy. Using discrete abelian groups removes for some entries the suppression factor that would otherwise be present with continuous groups like U(1). More breaking fields (with opposite charges) of

nos, the probability to fulfill data is 40 times less, while with the inclusion of the charged lepton rotation matrix, the probability is 4 times less (also, in this case the charged fermions mass hierarchy had still to be assured by choosing $Q_R = (6, 2, 0)$, along with $Q_L = (0, 0, 0)$).

[17] For instance, in order for h to comply with present data ($h \simeq 1/36$) the 2-3 sub-block needs some tuning. As noted in the first of [71] and [75], it needs to satisfy the additional constraint $\mathrm{Det}_{23} \simeq \varepsilon$, for the chosen value of ε.

a single abelian group can provide anomaly cancelation and allow for more elaborated textures [78], to accommodate the required hierarchical splittings without having hierarchical masses. Other interesting studies of abelian flavor symmetries are in [79]. In summary, we feel that the limitation of these approaches is the sensible degree of arbitrariness in the choice of group, charges and particularly of the $\mathcal{O}(1)$ coefficients.

2.2.2 *Non-Abelian flavor symmetries*

Non-abelian groups of flavor symmetry are candidates for models that overcome some limitations of the previous approach. The main advantages are: (a) a breaking to abelian subgroups automatically predicts Froggatt-Nielsen charges (that were arbitrary with abelian groups) (b) the breaking chain can lead to more than one small parameter, also in hierarchical order,[18], (c) merging this mechanism with a GUT scheme can also solve the main limitation of the abelian flavour symmetry, namely the arbitrariness of the $\mathcal{O}(1)$ coefficients.

This setting seems thus quite more predictive. Several models [80, 81] have been constructed based on non-abelian groups of flavor symmetry, outside or inside a GUT scheme. We will not discuss them here and refer the reader to [82]. Most of them rely on GUT (and the most promising on SUSY GUT) so we are led, in the last part of this work, to focus on the theory of neutrino masses in a grand unified perspective.

2.3 Seesaw, SUSY and SO(10)

In this last part, we will abandon the idea of using flavor symmetry as a tool to understand fermion masses, and explore instead the capabilities of grand unification. A surprising outcome is that the minimal supersymmetric grand unified model has a potential to provide the unknown $\mathcal{O}(1)$ coefficients, in a sense that we will clarify below.

The usual hierarchy problem cries for low-energy supersymmetry and the supersymmetric SO(10), see e.g. [83]. There is another important reason to consider a supersymmetric see-saw theory based on the spontaneous breaking of $B-L$ (such as SO(10)): if renormalizable, it predicts exact R-parity at all energies both perturbative and nonperturbative [84]. This plays a profound role in having the lightest supersymmetric particle as a natural dark matter candidate. The result is based on a simple observation: R-parity violation

[18] For example $\mathrm{U}(2) \xrightarrow{\varepsilon'} \mathrm{U}(1) \xrightarrow{\varepsilon} 1$ includes an ε that can be used for a dominant block as above and a further parameter ε' available to predict e.g. the observed hierarchy.

would imply an existence of a pseudo-Majoron with a mass $M_J^2 \approx M_W^3/M_R \ll M_Z^2$ coupled to the Z-boson, ruled out by the Z-decay width. The argument parallels the impossibility of breaking spontaneously R-parity in the minimal supersymmetric standard model (MSSM). In that case $m_J = 0$, but the physical implication is the same.

In what follows we describe in some detail the minimal renormalizable supersymmetric SO(10) theory [85, 87, 86, 88] and discuss its predictions for fermion masses and mixings. We pay special attention to the neutrino sector and review our main result mentioned before: a large θ_{atm} and a small V_{cb} are intimately tied to $b - \tau$ unification [63]. This result is the product of SO(10) symmetry only; *no* new flavor symmetry whatsoever is needed. A three generation analysis shows accord with all the data and furthermore predicts $|U_{e3}| \approx 0.16$ [89].

2.3.1 *Minimal supersymmetric SO(10) grand unified theory*

There is some subtlety in defining a gauge theory, it has to do with the Higgs sector. We must find a criterion of minimality and it is subject to the following issue: should we take the smallest representation that does a particular job, or the most economical, i.e. the most predictive one? We shall opt for the second choice: *we will demand the least number of parameters* in defining the minimal theory. In this sense, the size of representations is *not* what counts; if a smaller representation has more parameters, it is less predictive and thus it cannot lead to a minimal theory. Example: a complex doublet of SU(2) (4 fields) is much more predictive than say two real singlets.

Supersymmetric SO(10) must be broken to the supersymmetric standard model. Unlike in the SU(5) case, this requires at least two Higgs supermultiplets. In the process we must break $B - L$ symmetry and here is the first dilemma: be a 16-dimensional Higgs (16_H) or a 126-dimensional (126_H) Higgs representation? In the first case one has to appeal to non-renormalizable operators of the type $16_f 16_f 16_H 16_H$ in order to give a mass to ν_R and this leads to a severe problem: (16_H) breaks R-parity at the large scale, experimentally not allowed. Thus the practitioners of this model invoke other symmetries beyond SO(10) and to us by definition it cannot be the minimal SO(10) theory. Furthermore, the superpotential has a number of parameters of the type 16_H^4. There are more problems regarding the light sector and we discuss them below.

In what follows we also choose the principle of renormalizability, i.e. we focus on the SO(10) theory with renormalizable couplings only. This makes the theory extremely predictive and it allows us to test the gauge symmetry of SO(10). Of course, there is a danger in doing this: it is like taking MSM with *no* higher-dimensional operators. This predicts massless neutrinos and stable proton, the first being manifestly wrong, but quantitatively a tiny effect and

the second still not tested. If the SO(10) theory without higher-dimensional operators turns out to be correct (see conclusions), it will tell us that the Planck scale effects are for some reason negligible; if, on the other hand, it fails we will have a window to a new physics beyond GUTs.

It is worth mentioning an argument in favor of neglecting $1/M_{Pl}$ suppressed operators. Namely, such an operator

$$c16_f16_f16_f16_f/M_{Pl} \tag{14}$$

leads to the effective B and L violating operators

$$cQQQL/M_{Pl} \quad cU^cU^cD^cE^c/M_{Pl} \tag{15}$$

which in turn give $d = 5$ proton decay. Experimental limits $\tau_p < 10^{33}$ yrs, imply $c < 10^{-6}$, contrary to a naive $c \approx \mathcal{O}(1)$ expectation when thinking of higher dimensional terms.

We wish not to be apologetic about this lengthy physical discussion; it serves us to define the minimal theory. The heavy sector, needed to break SO(10) down to SU(3)×SU(2)×U(1) needs the following multiplets:

$$\begin{array}{rl} 210_H & \text{(4 index antisymmetric)}, \\ 126_H \text{ and } \overline{126}_H & \text{(5 index antisymmetric, self and anti-self dual)}. \end{array}$$

The light Higgs supermultiplet is the minimal 10-dimensional one

$$10_H, \tag{16}$$

and we have the three families of quarks and leptons in their 16-dimensional representations

$$16_f^i \ (i = 1, 2, 3). \tag{17}$$

The Higgs superpotential is quite simple

$$\begin{aligned} W \ = \ & M_1 210_H^2 + \lambda_1 210_H^3 + M_2 126_H \overline{126}_H + \lambda_2 210_H 126_H \overline{126}_H \\ & + M_3 10_H^2 + \lambda_3 210_H 10_H 126_H + \lambda_4 210_H 10_H \overline{126}_H, \end{aligned} \tag{18}$$

only 7 parameters in total. Compare with the minimal SU(5): 4 parameters for 24_H and 5_H and $\overline{5}_H$.

There are only two Yukawa couplings (as in SU(5))

$$W_Y = 16_f Y_{10} 16_f 10_H + 16_f Y_{126} 16_f \overline{126}_H, \tag{19}$$

but unlike in SU(5) we will show that all the fermion masses and mixing are correctly accounted for.

Furthermore, there are *no* R-parity violating couplings (*no* 16_f^3 terms). The minimal SO(10) theory has less parameters than the minimal SU(5), a surprising result. Of course, you can impose R-parity in SU(5), but then you need new singlets (the right handed neutrinos) and more Yukawa's. In either case, the SU(5) theory has more parameters and, of course, it needs higher dimensional terms to fix the wrong mass relations, thus even more couplings.

The details of the superpotential and the symmetry breaking are being worked out and will be presented in a forthcoming publication. Here, let us just complete the proof that the above is the minimal theory. First, one needs both 126 and $\overline{126}$ in order to cancel the D-terms and preserve supersymmetry at the GUT scale. Thus $\langle 126_H \rangle = \langle \overline{126}_H \rangle = M_R$ with $M_R \approx M_{GUT}$. These VEVs preserve SU(5) and so more is needed. Why not choose 45_H (two index antisymmetric) instead of 210_H? It can be shown that $\langle 45_H \rangle$ also preserve SU(5) at the renormalizable level. One could also try 54_H, but then there is *no* coupling $54_H 126_H \overline{126}_H$ and one cannot trigger M_R. The minimal theory was considered to be $45_H + 54_H + 126_H + \overline{126}_H$, but it is easy to show that it contains 10 parameters.

In short, the above theory with 210_H and 126_H and $\overline{126}_H$ is truly the minimal and simplest SO(10) theory. *It is arguably the minimal consistent grand unified theory.*

2.3.2 *Symmetry breaking*

It is useful to decompose the SO(10) fields under the Pati-Salam subgroup [59], namely $SU(2)_L \times SU(2)_R \times SU(4)_C$

$$\begin{aligned}
210_H &= (1,1,15) + (1,1,1) + (1,3,15) + (3,1,15) + \\
&\quad + (2,2,6) + (2,2,10) + (2,2,\overline{10}) \\
126_H &= (1,3,\overline{10}) + (3,1,10) + (1,1,6) + (2,2,15) \\
\overline{126}_H &= (1,3,10) + (3,1,\overline{10}) + (1,1,6) + (2,2,15) \\
10_H &= (2,2,1) + (1,1,6) \\
16_f &= (2,1,4) + (1,2,\overline{4})
\end{aligned} \tag{20}$$

It is easy to see that at the supersymmetric level the following symmetry breaking takes place (we assume an approximate single-step breaking suggested by the unification of the MSSM couplings)

$$\langle (1,1,1) \rangle \approx \langle (1,1,15) \rangle \approx \langle (1,3,10) \rangle \approx \langle (1,3,\overline{10}) \rangle \approx \langle (1,3,15) \rangle \approx M_{GUT} \tag{21}$$

SO(10) gets broken to the SM symmetry. Next we discuss the MSSM symmetry breaking. It is easy to see that $(2,2,1)$ in 10 and $(2,2,15)$ fields in 126 and $\overline{126}$ mix through the couplings a and b and a large VEV $(1,1,15)$. With the usual

minimal fine-tuning this means that both $(2,2,1)$ and $(2,2,15)$ will have non-vanishing VEVs and contribute to fermion masses. In the language of SU(5) it amounts to have a 45 of Higgs as in the Georgi-Jarlskog program [90], however with an important characteristic of this minimal SO(10) which unifies these Yukawa couplings with the right-handed neutrino ones.

More precisely, all the color singlet bidoublets get the VEV

$$\begin{array}{l}\langle(2,2,10)_{210}\rangle \approx \langle(2,2,\overline{10})_{210}\rangle \approx \langle(2,2,15)_{126}\rangle \\ \approx \langle(2,2,15)_{\overline{126}}\rangle \approx \langle(2,2,1)_{10}\rangle\end{array} \tag{22}$$

Next, from

$$\begin{array}{rl} W & = \ldots\lambda_3(2,2,1)(2,2,10)(3,1,\overline{10}) + \lambda_4(2,2,1)(2,2,\overline{10})(3,1,10) \\ & + M_2(3,1,10)(3,1,\overline{10}) \end{array} \tag{23}$$

with $M \approx M_{GUT}$, it is clear that $(3,1,10$ and $(3,1,\overline{10})$ fields get small VEVs

$$\langle(3,1,10)\rangle = \frac{\lambda_3}{M_{GUT}}\langle(2,2,1)\rangle\langle(2,2,10)\rangle \approx \frac{M_W^2}{M_{GUT}} \tag{24}$$

$$\langle(3,1,\overline{10})\rangle = \frac{\lambda_4}{M_{GUT}}\langle(2,2,1)\rangle\langle(2,2,\overline{10})\rangle \approx \frac{M_W^2}{M_{GUT}} \tag{25}$$

The last equation gives the so-called type II see-saw which plays important role in neutrino masses and mixings as we discuss below.

2.3.3 *Fermion masses and mixings*

Introduce a notation

$$\langle(2,2,1)\rangle = \begin{pmatrix} v_u & 0 \\ 0 & v_d \end{pmatrix}\ ,\ \langle(2,2,15)_{\overline{126}_H}\rangle = \begin{pmatrix} \overline{v}_u & 0 \\ 0 & \overline{v}_d \end{pmatrix} \tag{26}$$

The Yukawa couplings give the following mass matrices

$$\begin{array}{ll} M_u = Y_{10}v_u + Y_{126}\overline{v}_u & M_D = Y_{10}v_u - 3Y_{126}\overline{v}_u \\ M_d = Y_{10}v_d + Y_{126}\overline{v}_d & M_e = Y_{10}v_d - 3Y_{126}\overline{v}_d \\ M_\nu \propto Y_{126}M_W^2/M_R & M_{\nu_R} = Y_{126}M_{GUT} \end{array} \tag{27}$$

The role of $(2,2,15)_{\overline{126}}$ is clear; it leads to a Georgi-Jarlskog picture where this field gives a correct relation $m_s \approx m_\mu/3$ at M_{GUT}. On the other hand, the $(2,2,1)$ field should reproduce the correct relation $m_b = m_\tau$ at M_{GUT}. Let us discuss carefully the second and the third generation; by (temporarily) ignoring the first generation we will shed light in the large atmospheric mixing

angle. Ignore, furthermore, CP violation (a reasonable assumption for the two generation case) for the time being.

What about the see-saw mechanism? In general, both type I and type II contribute and no predictions can be made. Normally the workers in the field assume for no reason whatsoever that type I dominates. This was done in the original work of Babu and Mohapatra [91] and in the absence of CP violation in the neutrino sector it leads to a small θ_{atm}. It has been argued [92] that with large CP phases the theory is consistent with all the data and furthermore that the 1-3 mixing is large: $U_{e3} \approx 0.16$.

It was shown recently, on the contrary, that the type II see-saw automatically leads to the large θ_{atm}, if there is $b-\tau$ unification at M_{GUT}: see [63]. Let us review the argument briefly. It is remarkably simple. From (27) one gets a simple relation

$$M_\nu \propto M_d - M_e \tag{28}$$

If M_d and M_e have small mixings and neglecting m_s and m_μ

$$M_\nu \propto \begin{pmatrix} 0 & 0 \\ 0 & m_b - m_\tau \end{pmatrix} \tag{29}$$

Large θ_{atm} requires $b-\tau$ unification, which is not automatically anymore due to the $(2,2,15)$ Higgs, but is quite good experimentally as the reader knows well. Actually, we can do better than that. From (27) it is easy to see that

$$M_u = aM_d + bM_e \tag{30}$$

by simply inverting Y_{10} and Y_{126} in favor of M_d and M_e, say. This gives additional information about quark mixings and in turn determines θ_{atm} as a function of θ_{bc} and quark masses. In the approximation (illustrative, but not valid numerically) of negligible second generation fermion masses as before, you get at M_{GUT}

$$\tan^2\theta_{atm} = \frac{\sin 2\theta_{cb}}{2\sin^2\theta_{cb} - (m_b - m_\tau)/m_b}\,. \tag{31}$$

This simple formula speaks elegantly for itself. Since $\theta_{cb} \approx 10^{-2}$, the only way to get a large θ_{atm} is via $b-\tau$ unification: $m_b = m_\tau$ at M_{GUT}. All you need to do next is that the running plus switching on the second generation masses does not spoil the result. We have done that and as expected these effects are small: θ_{atm} remains large. The numerical study gives for the ratio of neutrino masses $m_2/m_3 \approx 1/6$, which fits nicely with the hierarchical mass solution to the solar and atmospheric neutrino puzzle.

Recently a numerical study of the full three generation case has been performed, first without CP phases ([89]). The theory passes the test, but has θ_{atm} on the lower side; it also predicts a large 1-3 mixing: $U_{e3} \approx 0.16$. Thus,

we seem to have a robust prediction of the large 1-3 leptonic mixing as a test of the minimal supersymmetric SO(10) theory. However a complete study is still to be performed and further insight, tests and calculations would be most welcome.

3 Perspectives

Reflecting the structure of the talk, we divide the final discussion into two parts. However, as in the spirit of the talk, we hope that sometimes soon the two parts will meet and merge.

3.1 Phenomenology

To be definite, we focused our attention on a scenario with three massive neutrinos, that is able to explain several facts in terms of neutrino oscillations. The LSND anomaly however cannot be explained, and this raises doubts on the meaning of such a scheme. It is true, that other cosmological hints like big-bang nucleosynthesis seems to prefer 3 (or perhaps even less) neutrinos, which makes the life of other sterile neutrinos rather tough. This lead people to consider complicated scenarios to explain LSND observations, e.g., CPT violation, additional neutrino interactions of decay, even though it seems fair to say that there is not yet a really convincing scenario [93]. The hypothesis of three neutrinos may be considered a forerunner in view of its minimal nature, even if we should consider it provisional for the time being. In this assumptions, one expects that long baseline experiments will see signals of oscillations, whereas MiniBooNE will not[19]. Again in this assumption, one can say that 4 parameters of the neutrino mass matrix are measured (the two Δm^2 and two mixing angles) and several other ones are waiting to be discovered.

However, we went through the list of the observables we realistically have. This list suggests that the next steps will be not easy. simply because the measurements we are left with are very difficult. There is the hope that θ_{13} is not very small (the optimist would ask: why it should be so?), and one may dare to wish that neutrinos are almost mass degenerate (the pessimist would ask: why it should be so?). The latter case would be great for neutrinoless double beta experiments, cosmological measurements, perhaps direct search for mass, and could have an impact on mixing angles as well. But to be concrete, it seems to us that at best 'non-oscillation' experiments would be able to dig out 1 parameter (the neutrino mass scale) and we are still not

[19]This hypothetical sequence of events would certainly change the interpretation of LSND findings, but probably would not mean that they should be immediately rejected, especially until their significance is clearly assessed.

there. It would be great to reduce nuclear uncertainties in neutrinoless double beta decay experiments. Also it would be great if oscillation measurements would culminate in the discovery of the CP violating phase, but probably this will be not for the near future. In other terms, we feel that in the near future we could hope to measure 1, or perhaps 2 new parameters.[20]

Presumably, the best that we can do with these data without really doing theory is to make some educated guesses. E.g., suppose that the hierarchy is normal, that neutrinos have Majorana mass and that the lightest neutrino has a mass below, or not much above $(\Delta m^2_{sol})^{1/2}$. Then the structure of the neutrino mass matrix is more or less fixed on account of the maximal atmospheric mixing angle [68]:

$$M_\nu = \frac{(\Delta m^2_{atm})^{1/2}}{2} \begin{pmatrix} 0 & 0 & 0 \\ 0 & 1 & 1 \\ 0 & 1 & 1 \end{pmatrix} + \text{small}. \qquad (32)$$

Note, here 1 means 1, not $\mathcal{O}(1)$. A bit different from what one would have guessed on the basis of what we know on charged fermion masses, but at least something definite.

We briefly discussed the possibilities to use neutrinos as astrophysical probes and in particular neutrinos from core collapse supernovae. However, we recalled the large number of open questions and most remarkably the serious uncertainties in simulating the explosion. We discussed why it would be important to observe neutrinos of different flavors. Maybe it is a good idea to close this section wondering: *are we ready for the next galactic supernova?*

3.2 Theory

It is difficult to put a limit to imagination and consequently to predict what will be future theories of neutrino masses. There are a lot of promising ideas in the recent literature and many more will certainly come in the future years. Here we limited ourselves to simple and rather old ideas, that offer a hope to make sense of the neutrino masses, namely, ideas based on 'flavor symmetry' or 'grand unification'. We are not sure that what we discussed has any resemblance to what Nature has chosen, but we believe that we should first try the simplest and most motivated options, hoping at least to learn from their failures.

[20] A more complete list of questions should include: Why is the mass hierarchy is so weak? Why some leptonic mixing angles are large (when those of the quarks are small)? What is the absolute neutrino mass scale? What is the type of hierarchy? Is $\theta_{23} = 45°$? Is $\theta_{13} = 0$? Is $\theta_{12} \neq 45°$? (We expect that the neutrinos will show their devious nature by answering the above list of questions in reverse order–if at all they will answer). Today, the rough summary is $|\theta_{23} - 45°| < \theta_C/2$ (not so small), $\theta_{13} < \theta_C/2$ (not so small), $\theta_{12} \neq 45°$ at 3-4σ.

As for the flavor symmetries, we have shown that a generic *ansatz* as 'dominant block' proposed in [69] and studied in [70, 71, 94, 78, 76, 72, 75] is often insufficient to describe the data. Partly, this is due to the fact that the data are increasingly more precise, but this also happens because the structure of the neutrino mass matrix (shown in eq.32) does not agree *generically* with the ansatz with a 'dominant block' [71, 76], unless the $\mathcal{O}(1)$ coefficients satisfy very special relations. In other terms, to really improve we need to get a theory of the $\mathcal{O}(1)$ coefficients; possibly a testable one.

As for grand unification, we described the potential of the minimal supersymmetric grand unified theory as a theory of fermion masses. This theory possesses the following features:
(i) exact R-parity and thus dark matter candidate;
(ii) it can account correctly for all fermion masses and mixings;
(iii) in the case of type II see-saw it connects naturally large θ_{atm} with $b - \tau$ unification;
(iv) for pure type I or type II seesaw, it predicts quite large leptonic 1-3 mixing, close to the experimental limit;
(v) d=5 proton decay is under control, albeit being large.
The detailed predictions of this theory are being worked out at the present and will appear in a future publication. We would like to stress that this theory is rather constrained, so that it is not clear *a priori* that it will pass all experimental tests, and we are glad of that, since good theories are supposed to be falsifiable eventually.

References

1. B.M.Pontecorvo, Sov.Phys.Usp. **26** 1087 (1983).
2. Y.Katayama, K.Matumoto, S.Tanaka, E.Yamada, Prog.Theor.Phys. **28**, 675 (1962).
3. Z.Maki, M.Nakagawa, S.Sakata, Prog.Theor.Phys. **28**, 870 (1962).
4. M.Nakagawa, H.Okonogi, S.Sakata, A.Toyoda, Prog.Theor.Phys. **30**, 727 (1963).
5. See also M.Nakagawa, hep-ph/9811358
6. B.M.Pontecorvo, Phys.Lett.B **26** 230 (1968).
7. See e.g. the recent review W.M. Alberico, S.M. Bilenky, hep-ph/0306239
8. See the contributions of Y. Uchida, L. Sulak, T. Ishida, A. Hime, Ph. Adamson, J. Link.

9. See the 'Bibliography' at the web page http://www.sns.ias.edu/~jnb/

10. G.T.Zatsepin, V.A.Kuzmin, 'On the neutrino spectroscopy of the sun', ICRC London (1965) 1024

11. B. Pontecorvo, Sov.Phys. JETP **26** (1968) 984 [Zh.Eksp.Teor.Fiz. **53** (1967) 1717]. V.N. Gribov and B. Pontecorvo, Phys.Lett. B **28** (1969) 493

12. L.Wolfenstein, Phys. Rev. D **17** (1978) 2369; S.P. Mikheev and A.Yu. Smirnov, Sov. J. Nucl. Phys. **42** (1985) 913 and [18)]

13. P. Creminelli, G. Signorelli and A. Strumia, hep-ph/0102234; G.L. Fogli, G. Lettera, E. Lisi, A. Marrone, A. Palazzo and A. Rotunno, Phys. Rev. D **66** (2002) 093008 and updates presented at the Venice conference on Neutrino Telescope, 2003; M.C. Gonzalez-Garcia and C. Peña-Garay, hep-ph/0306001.

14. V. Berezinsky, M. Narayan and F. Vissani, Nucl. Phys. B **658**, 254 (2003), P.C. de Holanda and A.Yu. Smirnov, hep-ph/0211264.

15. R.E. Sbrock, Phys. Lett. **B96** (1980) 159, I.Yu. Kobzarev *et al.*, Sov. J. Nucl. Phys. **32** (1980) 823

16. B.H. McKellar, "Influence of mixing of finite mass neutrinos on beta decay spectra, Phys.Lett. B **97**, 93 (1980).

17. The connection with oscillations has been explored in M. Czakon, J. Studnik and M. Zrałek, hep-ph/0006339 and F.Vissani, Nucl.Phys.Proc.Suppl. **100** (2001) 273, and next reference. See also: Y. Farzan, O.L. Peres and A.Yu. Smirnov, Nucl. Phys. B **612** (2001) 59, Y. Farzan and A.Yu. Smirnov, Phys. Lett. B **557** (2003) 224.

18. F. Feruglio, A. Strumia and F. Vissani, "Neutrino oscillations and signals in β and $0\nu2\beta$ experiments," Nucl. Phys. B **637** (2002) 345; Addendum-ibid. B **659** (2003) 359 [hep-ph/0201291].

19. J. Bonn *et al.*, Nucl. Phys. Proc. Suppl. **91** (2001) 273;

20. V.M. Lobashev *et al.*, Nucl. Phys. Proc. Suppl. **91** (2001) 280

21. A. Osipowicz *et al.* [KATRIN Collaboration], hep-ex/0109033.

22. E. Fiorini, A. Pullia, G. Bertolini, F. Cappellani and G. Restelli, Phys. Lett. B **25** (1967) 602.

23. L. Baudis *et al.*, Phys. Rev. Lett. **83** (1999) 41; H.V. Klapdor-Kleingrothaus *et al.*, Eur. Phys. J. A **12** (2001) 147.

24. H. V. Klapdor-Kleingrothaus, A. Dietz, H. L. Harney and I. V. Krivosheina, "Evidence for neutrinoless double beta decay," Mod. Phys. Lett. A **16** (2001) 2409

25. H. V. Klapdor-Kleingrothaus, [GENIUS Collaboration] Nucl. Phys. Proc. Suppl. **110** (2002) 364; C. E. Aalseth and H. S. Miley [Majorana Collaboration], Nucl. Phys. Proc. Suppl. **110** (2002) 392; Y.G. Zdesenko, O.A. Ponkratenko and V.I. Tretyak, [GEM Collaboration] J. Phys. G **27** (2001) 2129.

26. See e.g., R. Arnold *et al.* [NEMO Collaboration], Nucl. Instrum. Meth. A **503** (2003) 649 C. Arnaboldi *et al.* [CUORE Collaboration], hep-ex/0212053 and 0302021; K. Wamba [EXO Collaboration], eConf **C020620** (2002) THAP11.

27. L. Wolfenstein, "Lepton number violation and neutrino mass", published in Neutrino 1984, Dortmund, Germany–see especially sect. 4 there.

28. F. Vissani, J. High Ener. Phys. **9906** (1999) 022

29. H.V. Klapdor-Kleingrothaus, H. Pas, A.Y. Smirnov, Phys.Rev. **D63** (2001) 73005

30. Although the existence of additional (Majorana) phases was perhaps known even before, they were not discussed until the first of ref.s [31], and soon after in J. Schechter, J.W. Valle, Phys.Rev. **D22** (1980) 2227. Their observability in $0\nu2\beta$ decay was first remarked in M. Doi, T. Kotani, H. Nishiura, K. Okuda, E. Takasugi, Phys.Lett. **B102** (1981) 323. See also [32]

31. S.M. Bilenkiĭ, J. Hosek, S.T. Petcov, Phys.Lett. **B94** (1980) 495. P. Langacker, S.T. Petcov, G. Steigman, S. Toshev, Nucl.Phys. **B282** (1987) 589

32. For review works, B. Kayser, Phys.Rev. **D30** (1984) 1023; M. Doi, T. Kotani, E. Takasugi, Prog. Theor. Phys. Suppl. 83 (1985) 1; J.D. Vergados, Phys. Rept.133 (1986) 1

33. S.S.Gershtein and Y.B.Zeldovich, JETP Lett. 4 (1966) 120 [Pisma Zh.Eksp.Teor.Fiz. 4 (1966) 174]

34. S. Pascoli, S. T. Petcov and W. Rodejohann, "On the neutrino mass spectrum and neutrinoless double-beta decay," Phys. Lett. B **558** (2003) 141

35. F. Vissani, Frascati Phys. Ser. **16** (1999) 337.

36. V. Barger, S. L. Glashow, P. Langacker and D. Marfatia, "No-go for detecting CP violation via neutrinoless double beta decay," Phys. Lett. B **540**, 247 (2002)

37. S.W. Allen, R.W. Schmidt and S.L. Bridle, "A preference for a non-zero neutrino mass from cosmological data", astro-ph/0306386. In this analysis, the data of X-ray galaxy cluster were included, but those of Lynman-α forest were not.

38. J.R. Primack, J. Holtzman, A. Klypin and D.O. Caldwell, "Cold + hot dark matter cosmology with $m(\nu_\mu) \sim m(\nu_\tau) \sim 2.4$ eV," Phys. Rev. Lett. **74** (1995) 2160

39. D.N. Spergel *et al.*, astro-ph/0302209. Among other relevant data and analyses, see Ø. Elgaroy *et al.*, Phys. Rev. Lett. **89** (2002) 061301 and A. Lewis and S. Bridle, Phys. Rev. D **66** (2002) 103511

40. Ø. Elgaroy and O. Lahav, JCAP **04** (2003) 004; S.L. Bridle, O. Lahav, J.P. Ostriker and P.J. Steinhardt, "Precision Cosmology? Not Just Yet," Science **299** (2003) 153

41. A.S. Dighe and A.Yu. Smirnov, Phys. Rev. D **62** (2000) 033007 C. Lunardini and A.Yu. Smirnov, Nucl. Phys. B **616** (2001) 307 and hep-ph/0302033; M. Kachelrieß, A. Strumia, R. Tomas and J.W.F. Valle, Phys. Rev. D **65** (2002) 073016

42. T.J. Loredo and D.Q. Lamb, Phys. Rev. D **65** (2002) 063002; see however E. Nardi and J.I. Zuluaga, astro-ph/0306384.

43. P. Desiati, These Proceedings.

44. F. Halzen and D. Hooper, Rept. Prog. Phys. **65** (2002) 1025

45. See for instance the reviews by H.T. Janka and collaborators: "Neutrinos from type II supernovae and the neutrino driven supernova mechanism," Vulcano 1992 Proceedings, page 345-374; "Explosion mechanisms of massive stars," astro-ph/0212314.

46. F.Cavanna *et al*, "Neutrino as astrophysical probes", ICTP Summer School on Astroparticle Physics and Cosmology, Trieste, June 17-July 5, 2002.

47. K. Sato, K. Takahashi and S.I. Ando, Prog. Theor. Phys. Suppl. **146** (2003) 212.

48. M.A. Markov, I.M Zheleznykh, Nucl. Phys. **27** (1961) 385; K. Greisen, Ann. Rev. Nucl. Sci. **10** (1960) 63; J.L. Osborne, S.S. Said, A.W. Wolfendale, Proc. Phys. Soc. **86** (1965), 93; M.R. Krishnaswamy *et al.* [KGF Collaboration], Proc. R. Soc. **A323** (1971), 511; M.F. Crouch *et al.* [CWI Collaboration], Phys. Rev. D **18** (1978) 2239.

49. K. Hirata *et al.* [KAMIOKANDE-II Coll.], Phys. Rev. Lett. **58** (1987) 1490 and Phys. Rev. D **38** (1988) 448; R.M. Bionta *et al.* [IMB Coll.] Phys. Rev. Lett. **58** (1987) 1494; E.N. Alekseev *et al.* [Baksan Coll.] JETP Lett. **45** (1987) 589 and Phys. Lett. B **205** (1988) 209

50. S. Weinberg, Phys. Rev. Lett. **43** (1979) 1566

51. R. Barbieri, J.R. Ellis and M.K. Gaillard, Phys. Lett. B **90** (1980) 249

52. E.K. Akhmedov, Z.G. Berezhiani and G. Senjanovic, Phys. Rev. Lett. **69** (1992) 3013

53. F. Vissani, M. Narayan and V. Berezinsky, hep-ph/0305233.

54. T. Yanagida, proceedings of the *Workshop on Unified Theories and Baryon Number in the Universe*, Tsukuba, 1979, eds. A. Sawada, A. Sugamoto; S. Glashow, in *Cargese 1979, Proceedings, Quarks and Leptons* (1979); M. Gell-Mann, P. Ramond, R. Slansky, proceedings of the *Supergravity Stony Brook Workshop*, New York, 1979, eds. P. Van Niewenhuizen, D. Freeman; R. Mohapatra, G. Senjanović, Phys.Rev.Lett. **44** (1980) 912.

55. M. Magg, C. Wetterich, Phys. Lett. B **94** (1980) 61.

56. R. Mohapatra, G. Senjanović, Phys.Rev.D **23** (1981) 165.

57. M. Fukugita and T. Yanagida, Phys. Lett. B **174** (1986) 45. For an updated review, W. Buchmuller, hep-ph/0306047.

58. R.N. Mohapatra and J.C. Pati, Phys. Rev. D **11** (1975) 566, Phys. Rev. D **11** (1975) 2558. G. Senjanovic and R.N. Mohapatra, Phys. Rev. D **12** (1975) 1502.

59. J.C. Pati and A. Salam, "Lepton Number As The Fourth Color," Phys. Rev. D **10** (1974) 275.

60. H.Georgi, proceedings of Coral Gables 1975, page 329; H. Fritzsch and P. Minkowski, Annals Phys. **93** (1975) 193.

61. A. Melfo and G. Senjanovic, hep-ph/0302216.

62. A.Yu. Smirnov, Nucl. Phys. B **466** (1996) 25

63. B. Bajc, G. Senjanovic and F. Vissani, hep-ph/0110310 and Phys. Rev. Lett. **90** (2003) 051802

64. S. Weinberg, Trans. New York Acad. Sci. **38** (1977) 185, (Also in: C.D. Froggatt, H.B. Nielsen, Origin of symmetries, ibid, 267-283.)

65. C.D. Froggatt and H.B. Nielsen, Hierarchy of Quark Masses, Cabibbo Angles and CP Violation, Nucl. Phys. **B147** (1979) 277.

66. N. Cabibbo, Phys Rev. lett. **10** (1963) 531; M. Kobayashi and T. Maskawa, Prog. Theor. Phys. **49** (1973) 652.

67. L. Wolfenstein, Phys. Rev. Lett. **51** (1983) 1945.

68. Z. Berezhiani, A. Rossi, Phys. Lett. **B 367** (1996) 219

69. J. Sato, T. Yanagida, Phys. Lett. **B430** (1998) 127; Nucl. Phys. Proc. Suppl. **77** (1999) 293; J. Sato, T. Yanagida, Phys. Lett. **493** (2000) 356. N. Irges, S. Lavignac, P. Ramond, Phys. Rev. **D58** (1998) 035003; P. Ramond, Nucl. Phys. Proc. Suppl. **77** (1999) 3.

70. G. Altarelli, F. Feruglio, Phys. Lett. **B439** (1998) 112, J. High Ener. Phys. **9811** (1998)021

71. F. Vissani, J. High Ener. Phys. **9811** (1998) 025; Phys. Lett. **B508** (2001) 79; "A Statistical Approach to Leptonic Mixings and Neutrino Masses", hep-ph/0111373.

72. M. Hirsch, S.F. King, hep-ph/0102103; K. Choi, E.J. Chun, K. Hwang and W.Y. Song, Phys. Rev. D **64** (2001) 113013

73. L.Hall, H. Murayama and N. Weiner, "Neutrino Mass Anarchy", Phys. Rev. Lett. **84** (2000) 2572; A. de Gouvêa and H Murayama, "Statistical tests of Anarchy", hep-ph/0301050

74. G. Altarelli, F. Feruglio and I. Masina, "Models of neutrino masses: Anarchy versus hierarchy", J. High Ener. Phys. **0301** (2003) 035; J.R. Espinosa, "Anarchy in the neutrino sector?", hep-ph/0306019.

75. F.-S. Ling and P. Ramond, "Family Hierarchy and Large Neutrino Mixing", Phys. Lett. **B 29** (2002) 543.

76. Y. Grossman, Y. Nir and Y. Shadmi, "Large Mixing and Large Hierarchy Between Neutrinos with Abelian Flavour Symmetries", J. High Ener. Phys. **10** (1998) 007.

77. F. Feruglio, G. Altarelli, "Phenomenology of Neutrino Masses and Mixings", hep-ph/0306265.

78. Y. Nir and Y. Shadmi, "Testing abelian flavor symmetries with neutrino parameters", J. High Ener. Phys. **05** (1999) 023.

79. Flavor symmetries in different contexts: in SU(5) unification: K. Taichiro, hep-ph/9601243; E. Nardi, D. Aristizabal, hep-ph/0306206; within the MSSM and without GUT: P. Ramond, S. Lavignac, P. Binetruy, hep-ph/9601243; from type-I string: I. Antoniadis, E. Kiritsis, J. Rizos, T.N. Tomaras, hep-th/0210263; from intersecting branes: I. Antoniadis, E. Kiritsis, J. Rizos, T. N. Tomaras, hep-th/0210263.

80. A. Rossi, Z. Berezhiani, Nucl. Phys. (Proc. Suppl.) **101** (2001) 410; R. Barbieri, P. Creminelli and A. Romanino, Nucl. Phys. **B559** (1999) 17; Z. Berezhiani, Phys. Lett. **B417** (1998) 287; Z. Berezhiani, hep-ph/9607363; R. Barbieri, L.J. Hall, A. Romanino, Phys. Lett. **B401** (1997) 47.

81. J.L. Chkareuli, C.D. Froggatt, H.B. Nielsen, Nucl. Phys. **B626** (2002) 307; G.G. Ross, S.F. King, hep-ph/0108112. For an approach similar to that of a 'little higgs' see: S. Bertolini, M. Fabbrichesi, M. Piai, F. Bazzocchi, hep-ph/0306184. For a discrete non-abelian group see: W. Grimus, L. Lavoura, hep-ph/0305046. M. Picariello, R. Ferrari, F. Caravaglios and V. Antonelli, hep-ph/0207347

82. For a review, see M.C. Chen and K.T. Mahanthappa, "Fermion Masses and Mixing and CP-violation in SO(10) Models with Family Symmetries", hep-ph/0305088

83. F. Vissani, "Do experiments suggest a hierarchy problem?," Phys. Rev. D **57** (1998) 7027

84. C.S. Aulakh, B. Bajc, A. Melfo, A. Rasin and G. Senjanovic, Nucl. Phys. B **597** (2001) 89

85. T.E. Clark, T.K. Kuo and N. Nakagawa, Phys. Lett. B **115** (1982) 26

86. D. G. Lee, Phys. Rev. D **49** (1994) 1417.

87. C.S. Aulakh and R.N. Mohapatra, Phys. Rev. D **28** (1983) 217

88. C.S. Aulakh, B. Bajc, A. Melfo, G. Senjanovic and F. Vissani, "The minimal supersymmetric grand unified theory," hep-ph/0306242.

89. H.S. Goh, R.N. Mohapatra, S.P. Ng, hep-ph/0303055

90. H. Georgi and C. Jarlskog, Phys. Lett. B **86** (1979) 297.

91. K.S. Babu and R.N. Mohapatra, Phys. Rev. Lett. **70** (1993) 2845

92. K. Matsuda, Y. Koide, T. Fukuyama, H. Nishiura, Phys. Rev. D **65** (2002) 033008 [E.-ibid. D **65** (2002) 079904]

93. A. Strumia, "Neutrino anomalies," hep-ex/0304039

94. E.K. Akhmedov, G.C. Branco and M.N. Rebelo, Phys. Rev. Lett. 84 (2000) 3535

SESSION III – HEAVY FLAVOUR PHYSICS

Takayuki Kawamura	CHORUS Results on Charm Physics
Wenfeng F. Wang	Recent $\psi(2s)$ Results from BES
Roy A. Briere	CLEO $\|V_{ub}\|$ and $\|V_{cb}\|$ Results and Plans of CLEO-C
Ivan K. Furić	Charm Physics in CDF II
Mikhail Danilov*	Mysteries in Charmonium Production
Matt Herndon	B Physics at CDF
Franco Simonetto	B Meson Decay Properties at BaBar
Nick Hastings	High Precision Measurements of B-Decay Final States with the Belle Detector
Heriberto Castilla*	Recent Results on B physics at D0

* The trasparencies of the missing contributions are available on the web site http://www.pi.infn.it/lathuile/lathuile_2003.html

CHORUS RESULTS ON CHARM PHYSICS

T. Kawamura
for the CHORUS collaboration
CERN, CH-1211 Geneva 23, Switzerland

Abstract

The CHORUS experiment was originally designed to search for $\nu_\mu \rightarrow \nu_\tau$ oscillation by detecting a characteristic decay topology of the τ lepton produced in ν_τ charged current interaction. The hybrid apparatus which consists of active nuclear emulsion targets and electronic detectors was exposed to the CERN-SPS Wide Band Neutrino Beam for the years 1994-1997. The accumulated neutrino interactions in the emulsion are analyzed by full automatic microscope scanning system to detect the signal. Since charmed particles have a life time similar to that of τ lepton, the experiment is also ideal to study charm production. We report here on the analysis of charmed particles performed so far together with some new measurements based on a sub-sample of final statistics of the CHORUS experiment.

1 Introduction

The CHORUS detector [1] is a hybrid setup that combines a nuclear emulsion target with various electronic detectors. The emulsion target of the total mass of 770 kg is segmented into four stacks where each stack consists of eight modules of 36 plates with a size of 36×72 cm^2. Each stack is followed by interface emulsion sheet and by a set of scintillating fiber tracker planes. The nuclear emulsion target allows a three-dimensional reconstruction of short-lived particles such as τ leptons and charmed hadrons.

The emulsion scanning has been performed by fully automatic microscopes equipped with CCD cameras. The track finding-efficiency is higher than 98% for track slopes less than 400 mrad with respect to the direction perpendicular to the emulsion plates. The improvements in the automatic emulsion scanning systems allowed us large-volume data-taking around neutrino interactions located in the emulsion target. Thanks to the sub-micron spatial resolution of the emulsion, production of charmed particles in neutrino interactions followed by their decay can be fully observed. Therefore it is possible to perform a topological identification of charmed hadron decays, which brings very low level background contamination. This technique has been applied in the E531 [2] experiment at FNAL. The CHORUS experiment will collect a sample of ~3,000 neutrino interactions with a charmed particle.

2 Semi-leptonic branching fraction of charm hadrons

The study of dimuon events induced by neutrino interaction provides information on the Cabibbo-Kobayashi-Maskawa (CKM) matrix elements $|V_{cd}|$ and $|V_{cs}|$, the strange quark content of the nucleon and the charm mass. In the experiments by means of electronic detectors, the leading muon is interpreted as originating from the neutrino vertex and the other, of opposite charge, as the product of the charmed particle semi-leptonic decay. In such detectors, the direct detection of the charmed particle is impossible. Using an emulsion target which provides a sub-micron spatial resolution, the type of charmed particle and its decay topology can be identified and therefore a much lower level of background can be achieved.

For the semi-leptonic branching fraction measurement, 1055 events were selected from a sample of 56,172 events analyzed. To evaluate the purity of the selection, a sub-sample of 244 events was visually inspected by eye-scan. Out of the 244 events, 11 do not have a secondary vertex related to the event and 12 were identified as secondary hadronic interactions.

This results in a selection purity of 0.91 ± 0.02 which brings the corrected number of selected charm events to

$$N^{selected} = 956 \pm 35. \quad (1)$$

The efficiency of the charm selection was evaluated with a simulation by merging the emulsion data of the simulated events with real netscan data which do not have a reconstructed vertex, representing the real background. Good agreement is found between data and simulation. The correction factor for the efficiency in the determination of the semi-leptonic branching fraction is defined as

$$R = \frac{\sum_{D_i} \epsilon_{D_i} f_{D_i}}{\sum_{D_i} \epsilon_{D_i^{\mu}} f_{D_i}}, \quad (2)$$

where ϵ_{D_i} is the selection efficiency for charm species D_i, $\epsilon_{D_i^{\mu}}$ the selection efficiency for semi-leptonic decays of D_i, and f_{D_i} the fragmentation fraction. The value of R has been evaluated under all acceptable hypotheses, We use the average value

$$R = 1.01 \pm 0.05, \quad (3)$$

with the systematic error estimated with different hypotheses.

Muons are identified in the calorimeter and the muon spectrometer. For muon momenta above 4 GeV/c, the identification efficiency is of the order of 95%. The secondary muon identification has an average efficiency and average purity of about 55% and 60% respectively. Out of the 956 ± 35 selected charm events, the number of events with a secondary muon is

$$N_{2\mu}^{selected} = 88 \pm 10\,(stat.) \pm 8\,(syst.), \quad (4)$$

corrected for the efficiency and purity of the muon identification.

The average semi-leptonic branching fraction can be written in terms of measurable quantities as:

$$B_{\mu} = \sum_{D_i} f_{D_i} BR(D_i \to \mu X) = \frac{N_{2\mu}^{selected}}{N^{selected}} \times R, \quad (5)$$

where $N^{selected}$ is the number of selected events, corrected for the selection purity, and $N_{2\mu}^{selected}$ is the number of selected events with a secondary muon in the final state, corrected for the selection purity as well as for the muon identification efficiency and purity. We found [3] that

$$B_{\mu} = 0.093 \pm 0.009\,(stat.) \pm 0.009\,(syst.), \quad (6)$$

where the systematic error includes the uncertainty on the Monte Carlo description of the muon identification, as well as the uncertainty on the correction factor related to the fragmentation fractions and selection efficiencies for different species and different topologies.

Dividing the events in three samples on the basis of the visible energy, the energy dependence of B_μ can be determined as shown in Figure 1.

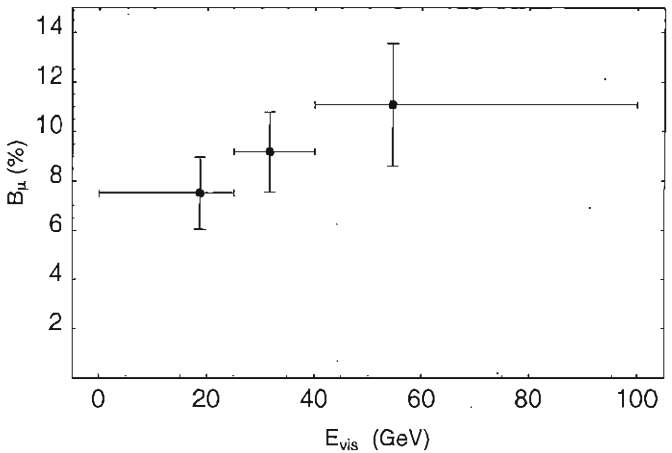

Figure 1: *The average semi-leptonic branching fraction as a function of the visible energy.*

3 Measurement of Λ_c production

The study of Λ_c production has been performed by a statistical approach based on the difference of the lifetimes among charged charm particles, hence the difference of the flight length. Since the lifetime of Λ_c is approximately one fifth of the D^+ lifetime and one third of the D_s lifetime, the charged charm candidates with a short flight decay should form a sample enriched in Λ_c while long flight decay events should be dominated by D^+ and D_s. Therefore, two different sets of selection have been adopted for the analysis.

A : Short flight decay A daughter track must have a minimum distance of 5 μm to 30 μm with respect to a track which is identified as a muon. This selection has been applied to 50,414 ν_μ events.

B : Long flight decay Both of parent track and daughter track are reconstructed. The parent track must have a minimum distance smaller than 5 μm with respect to the reconstructed muon. The daughter track must have a minimum distance of 5 μm to 30 μm with respect to the parent track. This selection has been applied to 56,761 ν_μ events.

The selected candidates, 1614 events for 'A' and 586 events for 'B', were visually inspected to identify their decay topology and to reject background. To ensure a high efficiency of the visual inspection, a cut on the charm flight length has been applied. The results are summarized in Table 1.

Table 1: *Result of visual inspection*

Selection	Cut on flight length of charm	Number of candidates	
		1-prong	3-prong
A	40 μm < F.L. < 400 μm	62	66
B	400 μm < F.L. < 2400 μm	133	195

Combining 'A' and 'B' separating 1-prong from 3-prong decays, and taking into account the detection efficiency and background estimation, the number of Λ_c candidates was found to be $861 \pm 198(stat.) \pm 98(syst.)^{+140}_{-54}(QE)$. At an average neutrino energy of 27 GeV, the Λ_c production cross section in ν_μ charged current interaction was measured [4] to be:

$$\frac{\sigma(\Lambda_c)}{\sigma(CC)} = (1.54 \pm 0.35(stat.) \pm 0.18(syst.)) \times 10^{-2}. \quad (7)$$

4 Measurement of D^0 production

A measurement of the production rate of D^0 mesons was performed based on a sample of 25,693 ν_μ charged-current interaction. The following criteria were applied to select D^0 candidates. A muon track at the primary vertex and at least one daughter track were reconstructed in the emulsion and matched with tracks in the detector. The daughter track was required to

have a significant impact parameter with respect to the primary vertex, which is $3 \sim 30\ \mu\text{m} < \text{I.P.} < 400\ \mu\text{m}$.

These criteria selected 851 events to be visually inspected to confirm the decay topology and we observed 226 events of 2-prong decay (V2) and 57 events of 4-prong decay (V4). The charm-selection efficiency was estimated by simulation. The average efficiency of the D^0 decay search was found to be $(58.6 \pm 0.7)\%$ for V2 and $(70.1 \pm 1.7)\%$ for V4. Based on 282 D^0 decays with an estimated background of 9.2 K^0 and Λ^0 decays, we obtained [5]

$$\frac{\sigma(D^0 \rightarrow \text{V2,V4})}{\sigma(CC)} = (\ 1.99 \pm 0.13(stat.) \pm 0.17(syst.)\ ) \times 10^{-2}. \quad (8)$$

The result represents in good agreement with that of E531 [2] based on a statistically less significant sample as shown in Figure 2. The CHORUS results are shown as solid crosses and compared with those of the E531 experiment as dashed crosses. The curve shows a fit based on the slow rescaling model [6] to NOMAD [7] charm data multiplied by the (D^0/charm) cross section ratio.

5 Measurement of $D^0 \rightarrow$ neutrals

The sum of branching ratios of D^0 decays, V0 + V2 + V4 + V6 + ... , is equal to unity by definition, where V0 denotes D^0 decay into all neutral particles. Since the branching ratio of V6 and greater are expected to be very small, the branching ratio of D^0 decay into all neutrals can be simply expressed as:

$$BR(D^0 \rightarrow \text{V0}) = 1 - \text{V4} \cdot \left(1 + \left(\frac{\text{V4}}{\text{V2}} \right)^{-1} \right). \quad (9)$$

Because the CHORUS experiment detects charm particle by observing its decay topology, it is possible to perform an inclusive measurement of a ratio of $(D^0 \rightarrow \text{V4})/(D^0 \rightarrow \text{V2})$. It was found to be $(23.1 \pm 4.0) \times 10^{-2}$.

Using the $BR(D^0 \rightarrow \text{V4}) = (13.3 \pm 0.7) \times 10^{-2}$ from the PDG [8] tables, which was measured by other experiments for the all decay modes, we obtained a preliminary result of

$$BR(D^0 \rightarrow \text{V0}) = (29.1 \pm 10.4) \times 10^{-2}. \quad (10)$$

The precision of the measurement will be improved with the final statistics.

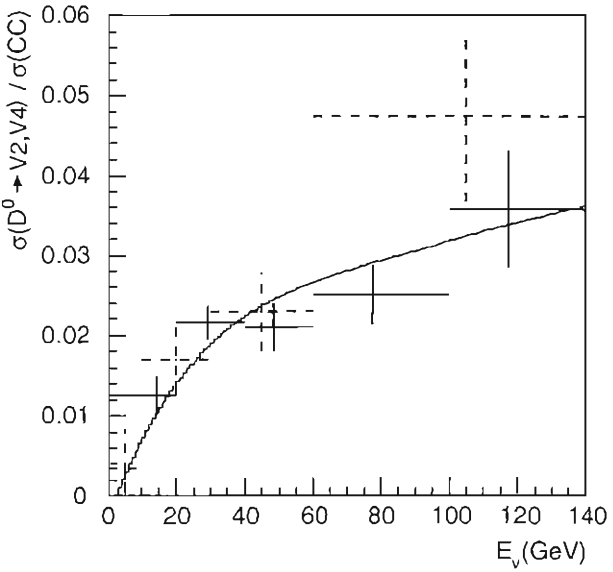

Figure 2: *D^0 production rate as a function of neutrino energy. CHORUS and E531 results are shown as solid and dashed crosses respectively. The curve represents a fit based on the slow rescaling motel to NOMAD charm data multiplied by the (D^0/charm) cross section ratio.*

6 Associated charm production

Associated charm production in neutrino interactions is a very rare process. Therefore it is very difficult to detect. Thanks to the excellent spatial resolution of nuclear emulsion, it is possible to perform a direct observation in the CHORUS experiment.

A search for associated charm production in ν_μ charged-current interactions was performed based on the sample of already located single charm events searching for the charmed partner. One event of double charm decay topology with an estimated background of 0.01 was found [9]. It is considered as evidence of the associated charm production process.

A new search for associated charm production in charged-current and

neutral-current events has been started. Several candidates with the characteristics of associated charm production have been found so far. The analysis will be completed using the final statistics in near future.

References

1. E. Eskut *et al.*, Nucl. Instr. and Meth. **A401** 7 (1997).
2. N. Ushida *et al.*, Phys. Lett. **B206** 375 (1988).
3. A. Kayis-Topaksu *et al.*, Phys. Lett. **B549** 48 (2002).
4. A. Kayis-Topaksu *et al.*, Phys. Lett. **B555** 156 (2003).
5. A. Kayis-Topaksu *et al.*, Phys. Lett. **B527** 173 (2002).
6. R. M. Barnett, *Phys. Rev. Lett.*, **36**, 1163 (1976),
   H. Georgi and H. D. Politzer, *Phys. Rev.* **D14**, 1829 (1976).
7. P. Astier *et al.*, Phys. Lett. **B486** 35 (2000).
8. Particle Data Group, Phys. Rev. **D66** (2002).
9. A. Kayis-Topaksu *et al.*, Phys. Lett. **B539** 188 (2002).

RECENT $\psi(2S)$ RESULTS FROM BES

W. F. Wang (Representing BES Collab.)
IHEP, Beijing 100039, China
E-mail: wangwf@ihep.ac.cn

Abstract

Results on $\psi(2S)$ physics at BES are presented. They are based on 4 million $\psi(2S)$ events collected with the BESI detector, scan data in the vicinity of $\psi(2S)$ resonance and 15 million $\psi(2S)$ events collected with the BESII detector. These results include the $\psi(2S)$ branching fractions of nine exclusive hadronic decays, radiative decays into $\pi\pi$, $K\overline{K}$ and $\eta\eta$ final states, the $\psi(2S)$ decay widths and the first observation of χ_{cJ} (J=0, 1, 2) decays to $\Lambda\overline{\Lambda}$.

1 Introduction

The Beijing Electron Spectrometer, is a conventional cylindrical magnetic detector that is coaxial with the BEPC colliding e^+e^- beams. It is described in detail in reference [1]. Charged particle momenta are determined with a resolution of $\sigma_p/P = 1.7\%\sqrt{1+p^2(\mathrm{GeV})}$ in a 40-layer cylindrical drift chamber. The tracking chamber is surrounded by an array of 48 time of flight (TOF) counters. Radially outside the TOF is a 12-radiation length barrel shower counter (BSC) comprised of gas proportional tubes interleaved with lead sheets. The BSC measures the energies and directions of photon with resolutions of $\sigma_E/E \approx 22\%/\sqrt{E(GeV)}$, $\sigma_\phi = 4.5$ *mrad.* and $\sigma_\theta = 12$ *mrad.* The iron flux return of the magnet is instrumented with three double layers of counters that are used to identify muons.

2 Hadronic and radiative $\psi(2S)$ decays

Perturbative QCD predicts the ratio of J/ψ and $\psi(2S)$ to hadronic final state X branching fractions is [2]:

$$Q_X = \frac{B(\psi(2S) \to X)}{B(J/\psi \to X)} \simeq \frac{B(\psi(2S) \to e^+e^-)}{B(J/\psi \to e^+e^-)} \simeq 12\%. \qquad (1)$$

This relation is known as the "12% rule".

Here, we present first measurements of branching fractions for $\psi(2S)$ decays to $\omega\pi^+\pi^-$, ωK^+K^-, $\omega p\bar{p}$, $\phi\pi^+\pi^-$, $\phi f_0(980)$, ϕK^+K^- and $\phi p\bar{p}$ channels, and supersede previous $b_1\pi$ and $\omega f_2(1270)$ results [3] based on 4 million $\psi(2S)$ data sample collected with the BESI detector. This work further confirmed previous BES finding [4] that the suppression puzzle of the hadronic decays of the $\psi(2S)$ with respect to the J/ψ extends from the VP(Vector-Pseudoscalar) decay to VT(Vector-Tensor) decay, and the $b_1\pi$ (Axial-vector plus Pseudoscalar mode) decay is consistent with pQCD expectation. As to the VS ($\phi f_0(980)$) decay and $Vh\bar{h}$ three-body decays (except for $\phi p\bar{p}$, which needs more statistics), we have provided the first test for the "12% rule", which seems generally valid, although there might be some deviation.

The radiative J/ψ and $\psi(2S)$ decays should be similar to hadronic decays except instead of decaying into three gluons, the radiative mode decays via two gluons and one photon [5]. We report measurements of branching fractions for $\psi(2S) \to \gamma\pi^+\pi^-$, $\gamma\pi^0\pi^0$, γK^+K^-, $\gamma K^0_S K^0_S$, and $\gamma\eta\eta$. The $\pi\pi$ invariant mass distributions for $\psi(2S) \to \gamma\pi\pi$ are shown in Fig. 1, where a clear $f_2(1270)$ is seen. Results are summarized in Tables 2 through 4. First measurements of the $\psi(2S) \to \gamma f_2(1270)$ and $\psi(2S) \to \gamma f_0(1710) \to \gamma K^+K^-$ and $\gamma K^0_S K^0_S$ branching fractions are given. A clear $f_0(1710)$ signal in $\psi(2S)$ radiative decay

Table 1: Branching fractions of $\psi(2S)$ and Q_h values for $\psi(2S)$ and J/ψ hadronic decays.*1

Channel h	$\frac{B_{\psi(2S)\to h}}{B_{\psi(2S)\to\pi^+\pi^- J/\psi}}$ (10^{-4})	$B_{\psi(2S)\to h}$ (10^{-4})	$B_{J/\psi\to h}$ (10^{-4})	$Q_h(\%)$ (%)
$\omega\pi^+\pi^-$	$15.8 \pm 1.9 \pm 2.2$	$4.8 \pm 0.6 \pm 0.7$	72.0 ± 12.0	6.7 ± 1.7
$b_1^\pm\pi^\mp$ *2	$10.6 \pm 1.9 \pm 1.5$	$3.2 \pm 0.6 \pm 0.5$	30.0 ± 5.0	11 ± 3
$\omega f_2(1270)$ *2	$3.4 \pm 1.7 \pm 0.5$	$1.1 \pm 0.5 \pm 0.2$	43.0 ± 6.0	2.4 ± 1.3
		< 1.5		
ωK^+K^-	$4.8 \pm 1.1 \pm 0.7$	$1.5 \pm 0.3 \pm 0.2$	7.4 ± 2.4	20 ± 8
$\omega p\bar{p}$	$2.5 \pm 1.0 \pm 0.4$	$0.8 \pm 0.3 \pm 0.1$	13.0 ± 2.5	6.0 ± 2.8
$\phi\pi^+\pi^-$	$4.8 \pm 0.8 \pm 0.6$	$1.5 \pm 0.2 \pm 0.2$	8.0 ± 1.2	18 ± 5
$\phi f_0(980)(f_0 \to \pi^+\pi^-)$*3	$1.8 \pm 0.6 \pm 0.2$	$0.6 \pm 0.2 \pm 0.1$		
$\phi f_0(980)$*4	$3.4 \pm 1.2 \pm 0.4$	$1.1 \pm 0.4 \pm 0.1$	3.2 ± 0.9	33 ± 15
ϕK^+K^-	$2.0 \pm 0.6 \pm 0.2$	$0.6 \pm 0.2 \pm 0.1$	8.3 ± 1.3	7.3 ± 2.6
$\phi p\bar{p}$	< 0.85	< 0.26	0.45 ± 0.15	< 58

*1 The upper limit is at the 90% confidence level; $B_{J/\psi}$ taken from PDG value.
*2 $b_1^\pm\pi^\mp$ and $\omega f_2(1270)$ events are subsets of $\omega\pi^+\pi^-$ events.
*3 $\phi f_0(980)$ events are subset of $\phi\pi^+\pi^-$ events.
*4 $B_{f_0\to\pi^+\pi^-} = 0.521 \pm 0.016$(PDG'96)

into K^+K^- final states is observed. The results are consistent with the "12%" rule. In addition, first measurements of the branching fractions of χ_{c0} and χ_{c2} decay into $\pi^0\pi^0$, χ_{c0} decay into $\eta\eta$, and an upper limit of the branching fraction of χ_{c2} decay into $\eta\eta$ are reported (see Table 4). For more detail, see reference [6].

Table 2: Values for $B(\psi(2S) \to \gamma f_2(1270))$ and $B(\psi(2S) \to K^+K^-)$ and comparison with the 12% rule.

Final state	$B(\psi(2S)\to)(\times 10^{-4})$	$B(\psi(2S))/B(J/\psi)$
$\gamma f_2(1270)$	$2.12 \pm 0.19 \pm 0.32$	$(15.4 \pm 3.1)\%$
$\gamma f_0(1710) \to \gamma K^+K^-$	$0.302 \pm 0.045 \pm 0.066$	$(7.1^{+2.1}_{-2.0})\%$

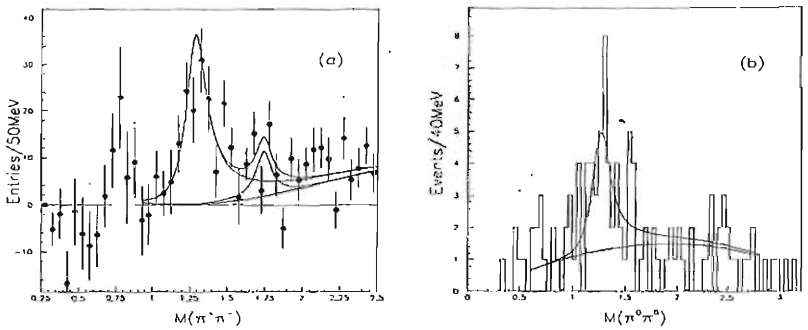

Figure 1: *(a): $M_{\pi^+\pi^-}$ fit result. The four curves presented in the figure are the following: a background curve, a Breit-Wigner function to describe the $f_2(1270)$ on top of the background, a Breit-Wigner function to describe the $f_0(1710)$ on top of the background, and the total of the two Breit-Wigners and the background. The fitting range is 0.9 GeV to 2.5 GeV, since there is some ρ background below 0.9 GeV. The background at higher mass is due to processes such as $\psi(2S) \to$ neutrals J/ψ, $J/\psi \to \pi^+\pi^-\pi^0$. (b): $M_{\pi^0\pi^0}$ fit result. The curves shown are a Breit-Wigner to describe the $f_2(1270)$ and a polynomial to describe the background.*

3 $\psi(2S)$ Resonance Parameters

The $e^+e^- \to$ hadrons, $\pi^+\pi^- J/\psi$, e^+e^-, and $\mu^+\mu^-$ events at 24 energies in the range 3.67–3.71 GeV are selected, and fitted simultaneously to obtain the $\psi(2S)$ resonance parameters based on BESII $\psi(2S)$ scan data [7]. The results are $\Gamma_t = 264 \pm 27$ keV, $\Gamma_h = 258 \pm 26$ keV, $\Gamma_{\pi^+\pi^- J/\psi} = 85.4 \pm 8.7$ keV, $\Gamma_l = 2.44 \pm 0.21$ keV; and $B_h = (97.79 \pm 0.15)\%$, $B_{\pi^+\pi^- J/\psi} = (32.3 \pm 1.4)\%$, $B_l = (0.93 \pm 0.08)\%$. The total width agrees with the BES previous value of 252 ± 37 keV [8] within the error, and the precision of $B_{\pi^+\pi^- J/\psi}$ is better than previous measurements and the current PDG value [9]. The cross sections versus scan point energy and fit curves are shown in Fig. 2, and the fit results are given in Table 5.

4 $\chi_J \to \Lambda\overline{\Lambda}$

It has been shown both in theoretical calculations and experimental measurements that the next higher Fock state (color octet mechanism, COM) plays

Table 3: Branching fractions for $\psi(2S) \to \gamma X \to \gamma P\overline{P}$ modes (P stands for pseudo-scalar).

Mode	$B(\times 10^{-4})$
$\psi(2S) \to \gamma f_2(1270)$ from $\gamma\pi^+\pi^-$	$2.08 \pm 0.19 \pm 0.33$
$\psi(2S) \to \gamma f_2(1270)$ from $\gamma\pi^0\pi^0$	$2.90 \pm 1.08 \pm 1.07$
$\psi(2S) \to \gamma f_2(1270)$ from $\gamma\pi\pi$	$2.12 \pm 0.19 \pm 0.32$
$\psi(2S) \to \gamma f_0(1710) \to \gamma\pi\pi$ from $\gamma\pi^+\pi^-$	$0.301 \pm 0.041 \pm 0.124$
$\psi(2S) \to \gamma f_0(1710) \to \gamma K^+K^-$	$0.302 \pm 0.045 \pm 0.066$
$\psi(2S) \to \gamma f_0(1710) \to \gamma K^0_S K^0_S$	$0.206 \pm 0.094 \pm 0.108$

Table 4: The χ_c decay branching fractions for $\chi_{c0,2} \to \pi^0\pi^0$ or $\eta\eta$.

Mode	$B(\times 10^{-3})$	$B \times B(\psi(2S) \to \gamma\chi_{c0,2})$ $(\times 10^{-4})$
$\chi_{c0} \to \pi^0\pi^0$	$2.79 \pm 0.32 \pm 0.57$	$2.42 \pm 0.28 \pm 0.44$
$\chi_{c2} \to \pi^0\pi^0$	$0.98 \pm 0.27 \pm 0.56$	$0.67 \pm 0.19 \pm 0.38$
$\chi_{c0} \to \eta\eta$	$2.02 \pm 0.84 \pm 0.59$	$1.76 \pm 0.73 \pm 0.49$
$\chi_{c2} \to \eta\eta$	< 1.37	< 0.93

an important role in describing P-wave quarkonium decays [10, 11]. Among these predictions, the partial width of $\chi_{cJ} \to \Lambda\overline{\Lambda}$ is about half of that of $\chi_{cJ} \to p\bar{p}$ (J=1,2) [12].

$\Lambda\overline{\Lambda}$ signals from $\chi_{cJ}(J = 0, 1, 2)$ decays are first observed using 15 million $\psi(2S)$ data collected by BESII [14]. A clear Λ signal can be seen in Fig. 3, and the background below the peak is very small. After requiring that both the $\pi^+\bar{p}$ and the π^-p mass lie within twice the mass resolution around the nominal Λ mass, the $\Lambda\overline{\Lambda}$ invariant mass distribution shown in Fig. 4 is obtained. There are clear χ_{c0}, χ_{c1}, and $\chi_{c2} \to \Lambda\overline{\Lambda}$ signals. The highest peak around the $\psi(2S)$ mass is due to $\psi(2S) \to \Lambda\overline{\Lambda}$ with a fake photon.

Fixing the χ_{c0}, χ_{c1} and χ_{c2} mass resolutions at their Monte Carlo predicted values, and fixing the widths of the three χ_{cJ} states to their world average values [9], the mass spectrum (Fig. 4) was fit with three Breit-Wigner functions folded with Gaussian resolutions and background, including a linear term representing the non $\Lambda\overline{\Lambda}$ background and a component representing the $\Lambda\overline{\Lambda}$ background. Fig. 4 shows the fit result, and the fitted masses are $(3425.6 \pm 6.3)\text{MeV}/c^2$, (3508.5 ± 3.9) MeV/c^2 and (3560.3 ± 4.6) MeV/c^2 for χ_{c0}, χ_{c1} and χ_{c2}, respectively, in agreement with the world average values [9].

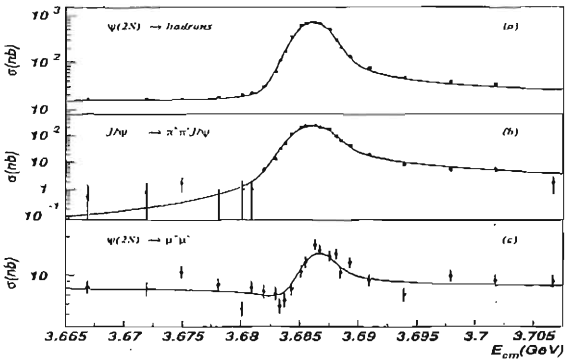

Figure 2: *The cross section for (a) $e^+e^- \to$ hadrons, (b) $e^+e^- \to \pi^+\pi^- J/\psi$, and (c) $e^+e^- \to \mu^+\mu^-$ versus center-of-mass energy. The solid curves represent the results of the fit to the data.*

Table 5: $\psi(2S)$ scan results and comparison with the PDG2002 [9].

Value	BES	PDG2002
Γ_l(keV)	264 ± 27	300 ± 25
Γ_h(keV)	258 ± 26	
$\Gamma_{\pi\pi J/\psi}$(keV)	85.4 ± 8.7	
Γ_l(keV)	2.44 ± 0.21	
$\mathcal{B}_h$(%)	97.79 ± 0.15	98.10 ± 0.30
$\mathcal{B}_{\pi\pi J/\psi}$(%)	32.3 ± 1.4	30.5 ± 1.6
$\mathcal{B}_l$(%)	0.93 ± 0.08	0.7 ± 0.09

The branching ratios of $\chi_{cJ} \to \Lambda\bar{\Lambda}$ obtained are

$$\mathcal{B}(\chi_{c0} \to \Lambda\bar{\Lambda}) = (4.7^{+1.3}_{-1.2} \pm 1.0) \times 10^{-4},$$

$$\mathcal{B}(\chi_{c1} \to \Lambda\bar{\Lambda}) = (2.6^{+1.0}_{-0.9} \pm 0.6) \times 10^{-4},$$

$$\mathcal{B}(\chi_{c2} \to \Lambda\bar{\Lambda}) = (3.3^{+1.5}_{-1.3} \pm 0.7) \times 10^{-4},$$

where the first errors are statistical and the second are systematic.

Compared with the corresponding branching ratios of $\chi_{cJ} \to p\bar{p}$ [9], the branching ratios of χ_{c1} and $\chi_{c2} \to \Lambda\bar{\Lambda}$ agree with the corresponding branching ratios to $p\bar{p}$ within 2-3 sigma. This is somewhat in contradiction with the expectations from reference [12], although the errors are large.

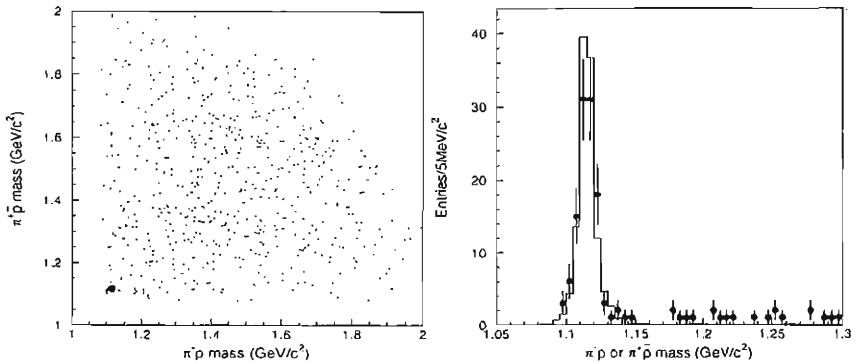

Figure 3: *(a):Scatter plot of $\pi^+\bar{p}$ versus π^-p invariant mass for selected $\gamma\pi^+\pi^-p\bar{p}$ events with the $\pi^+\pi^-p\bar{p}$ mass in the χ_{cJ} mass region. (b): Mass distribution of $\pi^+\bar{p}$ (π^-p) recoiling against a Λ ($\bar{\Lambda}$) (mass $<$ 1.15 GeV) for events in the χ_{cJ} mass region. Dots with error bars are data and the histogram is the Monte Carlo simulation, normalized to the Λ signal region (two entries per event).*

As for $\chi_{c0} \to \Lambda\bar{\Lambda}$, the measured value agrees with the $p\bar{p}$ measurements from BES and E835 [11, 13] within 2 standard deviations. One should also note that there is no prediction for $\mathcal{B}(\chi_{c0} \to \Lambda\bar{\Lambda})$. More detail may be found in reference [14].

5 Summary

Branching fractions are determined, many for the first time, using the 4 million BESI $\psi(2S)$ event sample. They are used to test the "12 %" rule. Results from a fit to a careful scan in the vicinity of the $\psi(2S)$ are presented. Finally, $\Lambda\bar{\Lambda}$ events are observed for the first time in χ_{cJ} decays using the BESII 15 million $\psi(2S)$ event sample, and corresponding branching ratios are determined.

6 acknowledgements

The author would like to thank organizers for their support during the Rencontres. The author also wants to thank Prof. F.A. Harris for his help in preparing the talk and the draft.

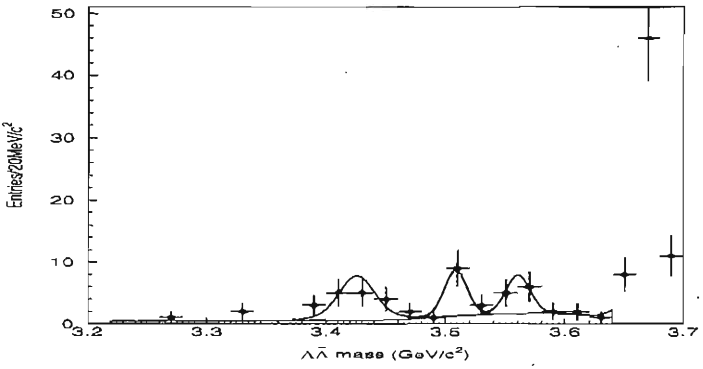

Figure 4: *Mass distribution of $\gamma\Lambda\bar{\Lambda}$ candidates fitted with three resolution smeared Breit-Wigner functions and background, as described in the text.*

References

1. J. Z. Bai *et al.*, (BES Collab.), Nuc. Inst. Meth. **A344**, 319 (1994); J. Z. Bai *et al.*, (BES Collab.), Nuc. Inst. Meth. **A458**, 627 (2001).

2. T. Appelquist and H. D. Politzer, *Phys. Rev. Lett.* **34**, 43 (1975); A. De Rujula and S. L. Glashow, *ibid*, page 46.

3. J.Z. Bai *et al.*, (BES Collab.), Phys. Rev. **D67**, 052002 (2003).

4. Y. S. Zhu, Proceedings of the 28th International Conference on High Energy Physcis, ed. Z. Adjuk and A. K. Wroblewski, World Scientific, 507 (1997); J. Z. Bai *et al.*, (BES Collab.), Phys. Rev. Lett. **81**, 5080 (1998); J.Z. Bai *et al.*, (BES Collab.), Phys. Rev. **D58**, 097101 (1998); J. Z. Bai *et al.*, (BES Collab.), Phys. Rev. Lett. **83**, 1918 (1999); J.Z. Bai *et al.*, (BES Collab.), Phys. Rev. **D63**, 032002 (2001).

5. T. Appelquist, A. De Rújula, H.D. Politzer. S.L. Glashow. Phys. Rev. Lett. **34**, 365 (1975); M. Chanowitz. Phys. Rev. **D 12**, 918 (1975); L. Okun and M. Voloshin, ITEP-95-1976 (unpublished); S.J. Brodsky, T.A. DeGrand, R.R. Horgun, D.G. Coyne, Phys. Lett. **73B**, 203 (1978); K. Koller and T. Walsh. Nucl. Phys. **B140**, 449 (1978).

6. J. Z. Bai *et al.*, (BES Collab.), Phys. Rev. **D67**, 032004 (2003).

7. J. Z. Bai *et al.*, (BES Collab.), Phys. Lett. **B550**, 24 (2002).

8. J. Z. Bai *et al.*, (BES Collab.), Phys. Rev. **D65**, 052004-1 (2002).

9. K. Hagiwara *et al.*, Phys. Rev. **D66**, 010001 (2002).

10. See, for example G.T. Bodwin, E. Braaten and G.P. Lepage, Phys. Rev. **D51**, 1125 (1995); Han-Wen Huang and Kuang-Ta Chao, Phys. Rev. **D54**, 6850 (1996); J. Bolz, P. Kroll and G. A. Schuler, Phys. Lett. **B392**, 198 (1997).

11. J. Z. Bai *et al.* (BES Collab.), Phys. Rev. Lett. **81**, 3091 (1998).

12. S. M. Wong, Eur. Phys. J. **C14**, 643 (2000).

13. S. Bagnasco *et al.* (E835 Collab.), Phys. Lett. **B533**, 237 (2002); M. Ambrogiani *et al.* (E835 Collab.), Phys. Rev. Lett. **83**, 2902 (1999).

14. J.Z. Bai *et al.*, (BES Collab.), accepted by Phys. Rev. **D**, hep-ex/0304012.

CLEO $|V_{ub}|$ AND $|V_{cb}|$ RESULTS AND PLANS FOR CLEO-C

Roy A. Briere
Physics Dept., Carnegie Mellon University,
5000 Forbes Ave., Pittsburgh, PA 15213

Abstract

We begin with a status report on determinations of the CKM matrix elements $|V_{ub}|$ and $|V_{cb}|$ from CLEO. A variety of techniques, some pioneered by CLEO, are employed to measure these parameters. Exclusive decay modes ($B \to D^* \ell\nu$ for $|V_{cb}|$ and $B \to \pi\ell\nu, \rho\ell\nu$ for $|V_{ub}|$) can be used in conjunction with lattice calculations of form-factors. Inclusive determinations of $|V_{cb}|$ are more controlled (but still dependent on quark-hadron duality) due to recent experimental constraints from spectral moments. Similarly, the extraction of $|V_{ub}|$ from the partially inclusive rate of $B \to X\ell\nu$ at the endpoint of lepton momentum now benefits from experimental input from $b \to s\gamma$ decays. However, current precision is still often limited by theoretical issues in interpreting the data. We next give an overview of the upcoming CLEO-c charm-factory running which will also contribute to CKM physics. One of our major goals is to assist in validating the accuracy of modern lattice QCD techniques which can help reduce errors on these CKM matrix elements. Validated lattice results will also improve the extraction of $|V_{td}|$ from current B_d and future B_s mixing results from other experiments.

1 The CLEO II and CLEOII.V Detectors and Datasets

The analyses described here use data taken with two different detector configurations. The CLEOII detector [1] has an excellent CsI calorimeter and large solid angle coverage for both tracks and photons. The CLEOII.V configuration retains these features and adds the first silicon vertex detector [2] used at the $\Upsilon(4S)$; it also represents the first major use of a Helium-based drift gas [3]. Both are very well-understood detectors with high-quality Monte Carlo simulations available.

The $B \to D^* \ell\nu$ analysis and the moment analyses of $B \to X_c \ell\nu$ use only CLEOII data, comprising (3.2 + 1.6) fb^{-1} (on + off resonance) containing 3.4×10^6 $B\bar{B}$ pairs. The $b \to s\gamma, b \to u\ell\nu$ endpoint and $B \to (\pi,\rho)\ell\nu$ analyses use both CLEOII and CLEOII.V; together, these total (9.2 + 4.5) fb^{-1} (on + off resonance) containing 9.7×10^6 $B\bar{B}$ pairs.

2 The Unitarity Triangle

Current knowledge of the $\rho - \eta$ plane is shown in Figure 1.

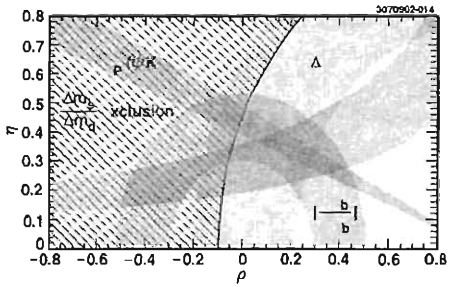

Figure 1: *The $\rho - \eta$ plane with current constraints.*

The goal is not to simply measure ρ, η, but to measure them in many different ways: a lack of consistency would point to new physics. Presently, the best constraints involve one of the angles (β) and two of the sides (proportional to $|V_{ub}|$ and $|V_{td}|$). The quantity $|V_{cb}|$ is also important for normalizing the size of the triangle. The quantity $\sin 2\beta$ is now well-measured and is theoretically clean. However, all of the listed $|V_{ij}|$ would benefit from more precise theoretical calculations. This often may be accomplished by Lattice QCD (LQCD) methods. However, an important part of this would include verification of other precision LQCD results via comparison with high-precision data. This is one thrust of the CLEO-c program discussed later. Use of other related data to aid

theoretical interpretation, exemplified by the moment analyses described later, is also of great interest.

CLEO's approach is thus two-pronged: continuing to supply new experimental data and exploring techniques used to extract $|V_{ub}|$ and $|V_{cb}|$, and also preparing to assist in verifying LQCD-based theoretical improvements.

3 $|V_{cb}|$ from Exclusive Modes: $B \to D^* \ell\nu$

Heavy-Quark Effective Theory (HQET) calculations can cleanly predict the form-factor, $F(1)$, for $B \to D^* \ell\nu$ at zero-recoil (q^2_{max}). CLEO's latest results [4] use both $D^{*+}\ell\nu$ and $D^{*0}\ell\nu$, extracting the intercept at q^2_{max} and the slope (ρ^2) of the form factor. We find $F(1)|V_{cb}| = (4.31 \pm 0.13 \pm 0.18) \times 10^{-2}$ and $\rho^2 = 1.61 \pm 0.09 \pm 0.21$; branching ratios for both $\bar{B} \to D^* \ell\bar{\nu}$ modes are also quoted. Systematic errors include efficiencies (especially slow-pion tracking), charm branching fractions, backgrounds, and form factors (most relevant for ρ^2). We use a recent lattice value [5] of $F(1) = 0.919^{+0.030}_{-0.035}$ to extract

$$|V_{cb}| = (4.69 \pm 0.14 \pm 0.20 \pm 0.18) \times 10^{-2}, \qquad (1)$$

where the uncertainties are statistical, systematic, and theoretical; the total error is 7%.

While our value of $|V_{cb}|$ is somewhat higher than the LEP results, LEP and CLEO are consistent at the 5% level. Differences in the analyses are summarized elsewhere [4].

4 HQET Parameters, Moments, and Inclusive Modes

Use of spectral moments to interpret inclusive semileptonic decays has become popular. Non-perturbative physics may be summarized in a few matrix elements. These include $\bar{\Lambda}$ (the energy of the light degrees of freedom); λ_1 (the b quark Fermi motion energy); and λ_2 (related to the chromo-magnetic interaction and known from $M_{B^*} - M_B$). Both the spectral moments (e.g., means and widths) of E_γ in $b \to s\gamma$, and of E_ℓ and M^2_X in $B \to X\ell\nu$, as well as the inclusive semileptonic rate, depend on $\bar{\Lambda}$ and λ_1 in calculable ways. We can extract these parameters from the moments and then use them in theoretical expressions for the semileptonic rate to solve for $|V_{cb}|$. This does rely on quark-hadron duality; errors on this assumption are unfortunately difficult to quantify.

CLEO first extracted [6] the means and widths of E_γ and M^2_X. Each moment constrains $\bar{\Lambda}$ and λ_1 as shown in the left plot of Figure 2. First moments are used since they yield the most precise constraints; second-moment

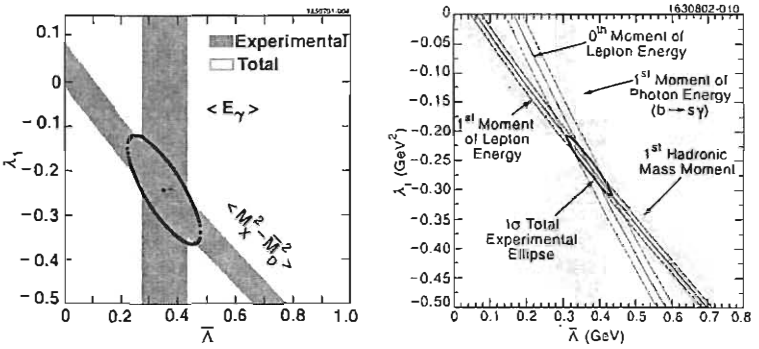

Figure 2: *Left: Measurements of* $\bar{\Lambda}$ *and* λ_1 *using* E_γ *and* M_X^2. *Right: Additional constraints from* E_ℓ. *(Ellipses indicate* $\Delta\chi^2 = 1$.*)*

results are consistent. We extract:

$$\bar{\Lambda} = 0.35 \pm 0.07 \pm 0.10 \text{ GeV}, \quad (2)$$

$$\lambda_1 = -0.236 \pm 0.071 \pm 0.078 \text{ GeV}^2. \quad (3)$$

5 Extracting $|V_{cb}|$ from Inclusive Semileptonic Rate

The HQET expansion for Γ_{sl} is of the form:

$$\Gamma_{sl} \sim |V_{cb}|^2 \, G_F^2 M_B^5 \, (\, \mathcal{G}_0 + \mathcal{G}_1(\bar{\Lambda})/M_B + \mathcal{G}_2(\bar{\Lambda}, \lambda_1, \lambda_2)/M_B^2 + \mathcal{O}(1/M_B^3) \, .) \quad (4)$$

With the three lowest-order HQET parameters in hand and smaller $\mathcal{O}(1/M_B^3)$ terms estimated and included in systematic uncertainties, we can use the inclusive semileptonic rate (from the tagged dilepton method [7]) to measure $|V_{cb}|$. We find:

$$|V_{cb}| = (4.04 \pm 0.09 \pm 0.05 \pm 0.08) \times 10^{-2}. \quad (5)$$

Uncertainties are from 1) CLEO's measurement of Γ_{sl}, 2) HQET parameters $\bar{\Lambda}, \lambda_1$, and 3) the scale for α_s and the coefficients of the $1/M_B^3$ terms. This is a 3.2% determination, but it invokes global quark-hadron duality of unspecified accuracy. It is thus interesting to compare this value with ones from other techniques.

Since our first publication using moments, CLEO has continued to exploit this new technique. Moments of the lepton energy spectrum from $B \to X\ell\nu$ are also useful, our results [8] are shown in the right plot of Figure 2. These

results alone give precise and independent results for the HQET parameters:

$$\bar{\Lambda} = 0.39 \pm 0.03 \pm 0.06 \pm 0.12 \text{ GeV}, \quad (6)$$

$$\lambda_1 = -0.25 \pm 0.02 \pm 0.05 \pm 0.14 \text{ GeV}^2. \quad (7)$$

Using the world-average Γ_{sl}, we obtain a consistent value:

$$|V_{cb}| = (4.08 \pm 0.05 \pm 0.04 \pm 0.09) \times 10^{-2}. \quad (8)$$

This is a 2.7% determination consistent with Eq. (5) but about 2 σ lower than Eq. (1).

6 $|V_{ub}|$ from $B \to X\ell\nu$ at the Lepton Endpoint

Knowledge of the photon spectrum from $b \to s\gamma$ also helps with 'inclusive' $|V_{ub}|$ measurements. The experiments are not fully inclusive, but rather concentrate on extracting $|V_{ub}|$ from the partial decay rate near the endpoint of the lepton momentum spectrum where $b \to c$ backgrounds are reduced. Large continuum data samples are valuable for both $b \to s\gamma$ and the lepton endpoint; continuum backgrounds are not constrained to end near the kinematic limits of B decays.

We can relate the partial leptonic branching fraction to the full momentum spectrum by using our measured photon spectrum from $b \to s\gamma$: the photons and leptons are smeared by a common non-perturbative structure function. This predicts the fraction of the rate, f_u, in the lepton momentum interval (2.2, 2.6) GeV/c as $f_u = 0.130 \pm 0.024 \pm 0.015$ of the total $b \to u\ell\nu$ rate. We finally extract [9]

$$|V_{ub}| = (4.08 \pm 0.34 \pm 0.44 \pm 0.16 \pm 0.24) \times 10^{-3}, \quad (9)$$

where the uncertainties are due to the experimental partial branching fraction, the experimental input used for f_u, the theory relating Γ_{sl} to $|V_{ub}|$, and the theory extracting f_u from $b \to s\gamma$.

7 $|V_{ub}|$ from $B \to \pi\ell\nu, \rho\ell\nu$

Final CLEOII–II.V results [10] for exclusive $b \to u\ell\nu$ modes are now available. These use neutrino reconstruction via missing momentum ($\sigma_{P_{miss}} \sim 110$ MeV). With the $\pi\ell\nu, \rho\ell\nu$ modes already established by CLEO in 1996, we now study the data in three q^2 bins, achieving a significant reduction in model errors as demonstrated in Figure 3. The preferred models are LQCD for $q^2 \geq 16$ GeV^2 and light-cone sum rules (LCSR) for the remainder. From the combined $\pi\ell\nu, \rho\ell\nu$ modes, we extract:

$$|V_{ub}| = (3.17 \pm 0.17 \,^{+0.16}_{-0.17} \,^{+0.53}_{-0.39} \pm 0.03) \times 10^{-3}, \quad (10)$$

where the uncertainties are statistical, experimental systematics, LQCD and LCSR theory, and signal form-factors.

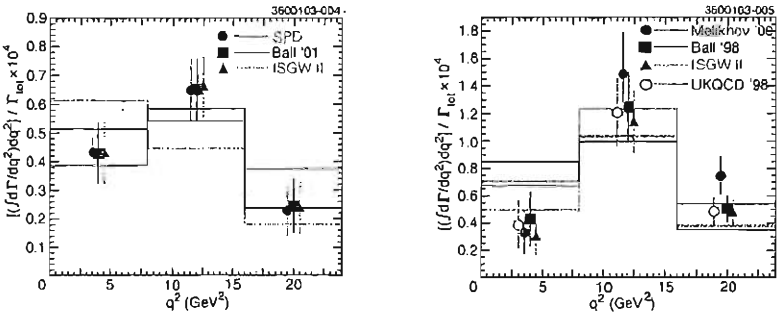

Figure 3: *Predictions (lines) and corresponding experimental partial widths (points) from various models of $B \to \pi \ell \nu$ (left) and $B \to \rho \ell \nu$ (right).*

8 Future of $|V_{cb}|$ and $|V_{ub}|$

Other CLEO analyses are in progress for inclusive semileptonic decays. Work on $|V_{ub}|$ includes an analysis of the full set of kinematic variables for a broad range of lepton momenta (using the hadronic recoil mass measured with neutrino reconstruction). A second analysis of the lepton moments using the dilepton-tagging method (allowing us to cleanly measure leptons down to 600 MeV) will address $|V_{cb}|$ by updating the moments as well as Γ_{sl}.

CLEO and LEP are now joined by BaBar and Belle, where large statistics may allow new methods to be employed. There is also considerable interest in exploring the stability of $B \to X \ell \nu$ moment analyses with varying lepton energy cuts.

We will discuss the future role of CLEO-c below.

9 Transition to CLEO-c: Upsilon Physics

Our just-completed Upsilon resonance running, summarized in Table 1, obtained statistics more than 10 times the best previous datasets (also from CLEO). Studies of spectroscopy will confront LQCD, and gluon-rich Υ decays can be compared to later J/ψ running with CLEO-c. Preliminary results [11] include the first observation of the $\Upsilon(1D)$ states, a study of photon transitions involving the P-wave states, and a search for the $\eta_b(1S)$ in inclusive radiative decays of the $\Upsilon(3S)$.

Table 1: *Upsilon resonance data sets (in pb^{-1}).*

Resonance	Peak	Scan	Below	Total	CLEOII
$\Upsilon(1S)$	1200	110	190	1500	80
$\Upsilon(2S)$	1375	80	465	1900	70
$\Upsilon(3S)$	1450	100	160	1700	130

10 The CLEO-c Run Plan and Anticipated Datasets

CLEO-c is a dedicated program of charm physics near threshold. The project was approved in February, 2003 by the National Science Foundation. The only substantial new construction (wiggler magnets) will be complete by the end of 2003 due to a head start accommodated by R&D funds.

One of the main tasks of CLEO-c is to provide data needed to test modern LQCD calculations. The practitioners claim few percent accuracy; this is crucial for B physics related to the unitarity triangle where we sometimes rely only on LQCD. However, such claims of accuracy are only credible if agreement is demonstrated in other related areas were the LQCD predictions directly confront data. CLEO-c naturally provides this; while B meson decay constants must come from LQCD, D meson decay constants can also be *measured*.

We anticipate about 3 years of running at $\mathcal{L}$ = few $\times 10^{32}$ cm^{-2}s^{-1} for J/ψ and open charm. Even better $\mathcal{L}$ is anticipated at higher energies; e.g., for Λ_c production. Very low background samples of from 130 - 480 times the BES and MARKIII data are expected; an outline of datasets is given in Table 2. Our planned Fall, 2003 run should already provide the world's best $\psi(3770)$ data.

Table 2: *Expected CLEO-c data sets: 2003-2006.*

Energy (GeV)	Event Type	$\int \mathcal{L}\,dt$ (fb^{-1})	# Events
3.77	$D\bar{D}$	3	30×10^6
4.14	$D_s^+ D_s^-$	3	$1\text{–}2 \times 10^6$
3.1	J/ψ	1	1000×10^6
4.6	$\Lambda_c/\bar{\Lambda}_c$	1	0.4×10^6

Much of the power of charm at threshold arises from full-reconstruction of D decays; this 'tagging' is key (see Table 3). The cleanliness of tagged charm is shown in Figure 4. CLEO-c will measure absolute branching fractions for $D^0 \to K^-\pi^+$, $D^+ \to K^-\pi^+\pi^+$, $D_s \to \phi\pi^+$ (and also $\Lambda_c \to pK^-\pi^+$) with the tagged samples; our $1-2\%$ accuracy will help reduce B analyses involving these decays (e.g., $B \to D^*\ell\bar{\nu}$). In semileptonic decays such as $D \to K\ell\nu$ and

Table 3: *Anticipated CLEO-c tagged samples.*

Meson	Single Tags	Double Tags
$D^0\bar{D}^0$	4.80×10^6	180×10^3
D^+D^-	1.90×10^6	70×10^3
$D_s^+D_s^-$	0.27×10^6	6×10^3

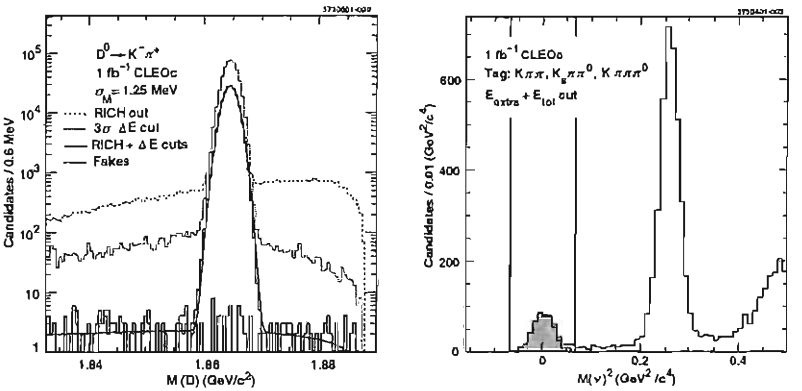

Figure 4: *Left: MC simulation of the tagged D sample; note the log scale! Right: simulation of a measurement of the D decay constant in $D \to \mu\nu$ (the current world sample is one event). Both plots reflect only 1/3 of CLEO-c's anticipated dataset.*

$D \to \pi\ell\nu$, we will determine branching ratios to 2% and extract precision form factors. Few-percent accuracy on form-factor slopes and a 2% accuracy on D decay constants via $D^+ \to \mu\nu$ and $D_s \to \mu\nu, \tau\nu$ will allow the required precise tests of LQCD calculations. There will also be substantial progress possible in low-energy hadronic spectroscopy with $J/\psi \to ggg, \gamma gg$ processes in the expected sample of 10^9 J/ψ decays.

11 CLEO and CESR Upgrades

CLEOIII was designed as a B-factory detector; it is also an excellent detector for charm threshold running. The Ring-Imaging CHerenkov (RICH) detector is an engineering tour-de-force that has delivered solid performance. Combined with dE/dx, we will have excellent particle ID at all momentum. The new low-material CLEOIII drift chamber improves both barrel and endcap calorimeter

performance and features a very thin non-load-bearing inner wall. It made room for the RICH at its outer radius and new superconducting quads at small radius while maintaining excellent resolution. The CLEOIII trigger and DAQ are much improved over CLEOII in terms of bandwidth and flexibility. Finally, our damaged silicon detector has been replaced with a six-layer all-stereo wire drift chamber.

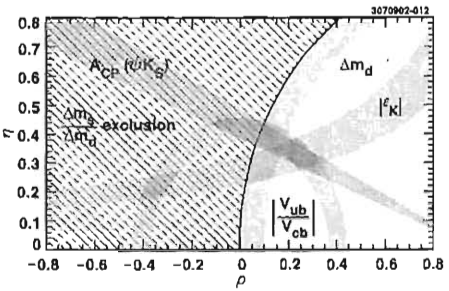

Figure 5: *The $\rho - \eta$ plane as it would appear with current experimental data analyzed with more precise theory.*

The CESR machine is already running with all superconducting RF and superconducting final-focus quadrapoles. The latter are important since the tunable field is necessary to accommodate lower beam energies. The CESR ring is too large for low energy running due to insufficient synchrotron radiation to damp the beams. As a result, we are in the process of installing 14 super-ferric 2.1 Tesla superconducting wiggler magnets. By Fall, 2003 we will be running with about half of this final set of magnets. The future also involves shared machine time: HEP (CLEO) running will get about twice as much beam time as the dedicated light source (CHESS) running with high-energy beams.

Our goals are documented in a 'Yellow Book' Project Description [12]. In particular, the improvement in our knowledge with only theoretical improvements in interpretation is shown in Figure 5. The contrast with the existing situation in Figure 1 is rather striking.

12 Conclusions

The rich output of CLEOII CKM physics measurements has continued with recent inclusive and exclusive measurements of $|V_{ub}|$ and $|V_{cb}|$. We are still a leading force in precision B physics and have pioneered moment analyses to add to our established techniques such as neutrino reconstruction. The CLEO-c program will naturally extend this CKM physics program. In the meantime, new CLEOIII results have included the discovery of the $\Upsilon(1D)$ states and our

final word on rare B Decays. A broad range of other important physics has also been pursued, including FSI phase studies with B decays, D Dalitz plots and D^0 mixing-related analyses, and our usual palette of tau, two-photon and charm baryon physics.

The CLEO-c program benefits B physics and the LQCD community while providing our collaboration with a bright future. Up-to-date information may always be obtained at http://www.lns.cornell.edu/public/CLEO/ .

References to the relevant theoretical work may be found in the cited experimental papers; limited space precluded citing them here. Finally, I must acknowledge the hard work of my CLEO colleagues and the CESR staff as well as our NSF and DOE financial support.

References

1. CLEO Collab., Y. Kubota *et al.*, Nucl. Instr. Meth. **A320**, 66 (1992).
2. T.S. Hill, Nucl. Instr. Meth. **A418**, 32 (1998).
3. R.A. Briere, in "Proceedings of the Seventh International Symposium on Heavy Flavor Physics", ed. C. Campagnari, World Scientific (Singapore, 1999).
4. CLEO Collab., R.A. Briere *et al.*, Phys. Rev. Lett. **89**, 081803 (2002); CLEO Collab., N.E. Adam *et al.*, Phys. Rev. **D67**, 032001 (2003).
5. S. Hashimoto *et al.*, Phys. Rev. **D66**, 014503 (2002).
6. CLEO Collab., S. Chen *et al.*, Phys. Rev. Lett. **87**, 251807 (2001); CLEO Collab., D. Cronin-Hennessy *et al.*, Phys. Rev. Lett. **87**, 251808 (2001).
7. CLEO Collab., B. Barish *et al.*, Phys. Rev. Lett. **76**, 1570 (1996).
8. CLEO Collab., A.H. Mahmood *et al.*, Phys. Rev. **D67**, 072001 (2003).
9. CLEO Collab., A. Bornheim *et al.*, Phys. Rev. Lett. **88**, 231803 (2002).
10. CLEO Collab., S.B. Athar *et al.*, hep-ex/0304019, submitted to PRD.
11. CLEO Collab., S.E. Csorna *et al.*, CLEO CONF 02-06; hep-ex/0207060; CLEO Collab., D. Cinabro *et al.*, CLEO CONF 02-07; hep-ex/0207062; CLEO Collab., A.H. Mahmood *et al.*, CLEO CONF 02-05; hep-ex/0207057.
12. CESR-c Taskforce, CLEO-c Taskforce, and CLEO-c Collab., R.A. Briere *et al.*, CLNS 01/1742 (revised 10/01).

CHARM PHYSICS AT CDF II

Ivan K. Furić
(for the CDF II collaboration)
M.I.T., Fermilab - CDF - MS#318, Batavia, IL 60510-0500

Abstract

The CDF II detector has the capability of triggering on displaced tracks. Because of this ability, CDF II has accrued large samples of charmed meson decays to fully hadronic final states in 64 pb^{-1} of $p\bar{p}$ collision data gathered at $\sqrt{s} = 1.96$ TeV. Using initial Run II data samples, the production cross sections for J/ψ, D^0, D^+, D^{*+} and D_s^+ mesons have been measured. Ratios of branching ratios for Cabibbo suppressed final states and CP asymmetries in D^0 meson decays have been studied. A measurement of the mass difference $m(D_s^+) - m(D^+)$ has been done, and a limit for the branching fraction of the FCNC $D^0 \to \mu^+\mu^-$ decays has been set.

1 Introduction

The CDF II detector [1] is a major upgrade of the original CDF detector which last took data in 1996. In Run I of the Tevatron, CDF made important contributions to B physics, providing some of the best measurements of masses, lifetimes, mixing and branching ratios.

For charm physics results, the most important part of the upgrade are the new integrated tracking system and the new trigger system. The integrated tracking system consists of three silicon systems (L00 [2], SVXII [3], ISL [4]) and a low-material, large-radius drift chamber (COT) [5]. The detector has a brand new three-level trigger system. The new features of the trigger include triggering on muons with lower transverse momenta, and triggering on displaced tracks and vertices [6].

2 J/ψ Production Cross Section

The mechanisms of J/ψ production in $p\bar{p}$ collisions are not well understood. Production cross sections from the assumed two major sources, $b \to J/\psi X$ and direct prompt decays, were measured to be higher than the initial theoretical predictions [7]. Recent theoretical advances in the extraction of the non-perturbative fragmentation functions of the B mesons from LEP data in a way that is consistent with the NLO QCD calculations of the b hadroproduction cross-sections have improved agreement between theoretical predictions and CDF Run I $b \to J/\psi X$ cross section measurements to better than 50 %.

The CDF II detector has an improved dimuon trigger with a lower p_T threshold ($p_T > 1.4$ GeV/c). This has extended the low transverse momentum range of triggered $J/\psi \to \mu^+\mu^-$ down to $p_T(\mu^+\mu^-) \geq 0$ GeV/c. In 39.7 pb of the initial Run-II data, 300 000 $J/\psi \to \mu^+\mu^-$ decays have been reconstructed. As shown in Figure 1, the transverse momentum of the reconstructed J/ψ extends to 0 GeV/c . After correcting for acceptance, trigger and reconstruction efficiencies, an integrated production cross section of $240 \pm 1(stat)^{+35}_{-28}(syst)$ nb has been measured for J/ψ mesons with $p_T(J/\psi) > 0$ GeV/c and $|\eta(J/\psi)| < 0.6$.

3 $D_s^+ - D^+$ Mass Difference

One of the first measurements done with the new sample of charmed meson decays was the measurement of the mass difference $m(D_s^+) - m(D^+)$. In a sample corresponding to 11.6 pb^{-1}, 2 400 $D_s \to \phi\pi$ and 1 400 D^+ decays were reconstructed. The detector invariant mass resolution for these decays is about 8 MeV/c^2 . The momentum scale of the detector was calibrated using 50 000 $J/\psi \to \mu^+\mu^-$ decays. An outline of the procedure is depicted in Figure 2. The

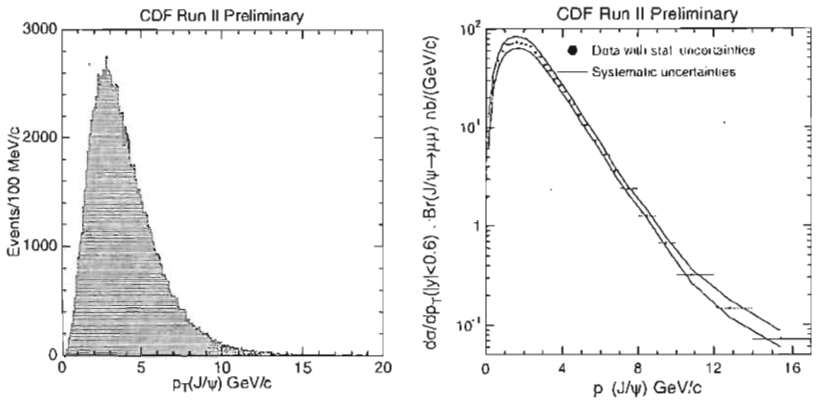

Figure 1: J/ψ cross section measurement: the left plot shows the p_T distribution of the reconstructed J/ψ mesons, and the right shows the differential production cross section ($d\sigma/dp_T$).

invariant mass of the J/ψ decays shows a dependance on the transverse momentum of the reconstructed J/ψ because the energy loss in the tracking system is not accounted for. After accounting for energy loss according to the GEANT material map, a residual p_T dependence can still be seen. Conversion scans of the tracking volume confirm that there is material missing in the GEANT description so material is added by hand to remove the p_T dependence of the J/ψ mass. The magnetic field is scaled so that the J/ψ mass agrees with the world average [8]. The results of the calibration (the amount of missing material and the magnetic field) are cross-checked by reconstructing other charmed and bottom meson decays (D^+, D^0, Υ), and the reconstructed masses are in good agreement with the corresponding world averages. This calibration was then applied to the $D_s^+, D^+ \to \phi\pi$ decays and the mass difference was found to be $m(D_s^+) - m(D^+) = 99.41 \pm 0.38(stat) \pm 0.21(syst)$ MeV/c^2. The result is in good agreement with previous measurements [9], [10]. The systematic error is dominated by signal and background modeling.

4 Charmed Meson Production Cross Sections

In Run I, the B cross section for the $B^+ \to J/\psi K^+$ mode for transverse momentum $p_T(B^+) > 6$ GeV/c and rapidity $|y(B^+)| < 1$ was measured to be

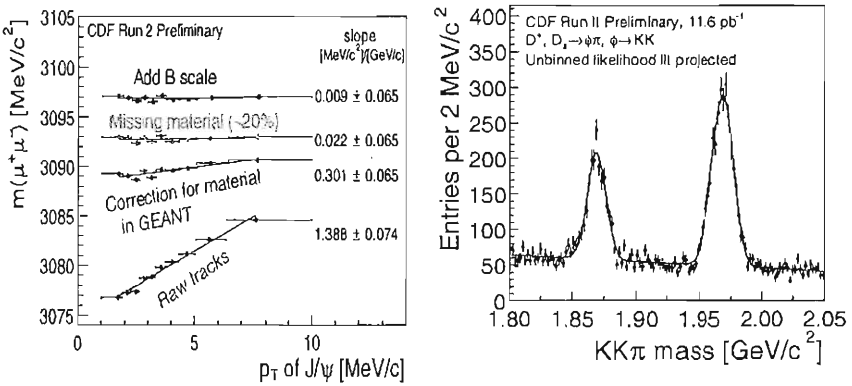

Figure 2: Momentum scale calibration and $m(D_s^+) - m(D^+)$ mass measurement. The left plot depicts the momentum scale calibration procedure, and the right shows the invariant mass distribution for the $D_s^+, D^+ \to \phi\pi$ signals with a superimposed fit.

3.6 ± 0.6 μb [11]. A preliminary measurement of the cross section for D^0, D^+, D^{*+} and D_s^+ mesons was done with 5.7 pb^{-1} of Run II data. The production cross sections were found to be larger than the corresponding bottom meson cross sections: $4.3 \pm 0.1(stat) \pm 0.7(syst)$ μb for D^+, $9.3 \pm 0.1(stat) \pm 1.1(syst)$ μb for D^0 and $5.2 \pm 0.1(stat) \pm 0.8(syst)$ μb for D^{*+} mesons. In the case of the D_s^+ mesons, the integrated production cross section was measured for $p_T(D_s^+) > 8$ GeV/c, $|y(D_s^+)| < 1$ and found to be $0.75 \pm 0.05(stat) \pm 0.22(syst)$ μb. The differential production cross sections $(d\sigma/dp_T)$ for all the mesons are depicted in Figure 3. Theoretical predictions (FONLL [12]) are overlaid in the plots. The error band from the theory curve corresponds to the maximum variation from changing the renormalization scale and the factorization scales between 0.5 and $2.0 \times \sqrt{p_T^2 + m^2}$.

5 Branching Ratios and CP Asymmetry

The study of the precise structure of the CKM matrix has been guided by measurements of mixing and CP violation in the neutral K and B meson sectors. The Standard Model predictions for the rate of mixing and CP violation in the charm sector are small, with the predictions in both cases ranging from 0.1% to 1% [13]. Observation of CP violation above the 1% level would be strong evidence for physics outside the Standard Model. The SU(3) flavor symmetry

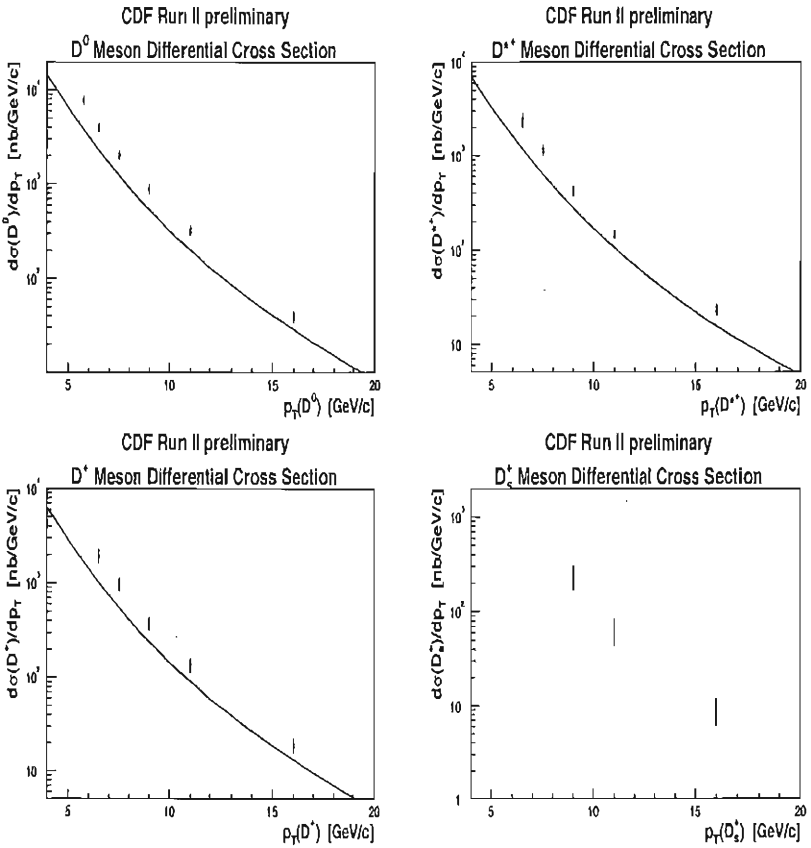

Figure 3: Charm meson differential cross sections for D^0, D^{*+}, D^+ and D_s^+ mesons, respectively. Theoretical predictions are overlaid upon the measurement results.

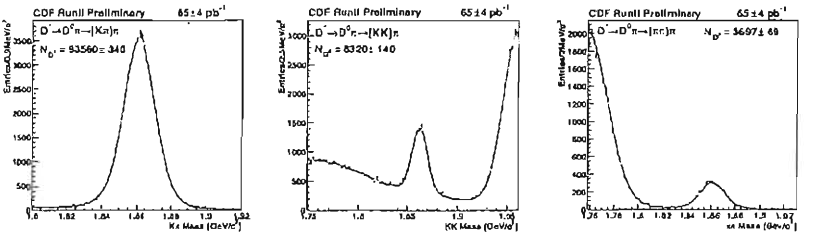

Figure 4: Invariant mass distributions for the three two-body D^0 decays: the dominant $D^0 \to K^-\pi^+$, the Cabibbo suppressed $D^0 \to K^+K^-$ and $D^0 \to \pi^+\pi^-$. All three decay modes are reconstructed by requiring that the D^0 comes from the decay $D^{*+} \to D^0\pi^+$.

predicts $\Gamma(D^0 \to K^+K^-)/\Gamma(D^0 \to \pi^+\pi^-) = 1$ [14], while the world average value is 2.88 ± 0.15 [8]. This deviation is most likely caused by large final state interactions (FSI) [15]. In the initial 65 ± 4 pb^{-1} of Run II data, 93 000 $D^0 \to K^-\pi^+$, 8 300 $D^0 \to K^+K^-$ and 3 700 $D^0 \to \pi^+\pi^-$ decays were reconstructed, as shown in Figure 4. Good signal to background was obtained by requiring that the D^0 always originates from a D^{*+} decay: $D^{*+} \to D^0\pi^+$. Using these samples of D^0 decays, the following measurements of the ratios of branching ratios were obtained by correcting the raw number of reconstructed candidates by the relative trigger and reconstruction efficiencies::

$$\frac{\Gamma(D^0 \to K^+K^-)}{\Gamma(D^0 \to K\pi)} = 9.38 \pm 0.18(stat) \pm 0.10(syst)\ \% \qquad (1)$$

$$\frac{\Gamma(D^0 \to \pi^+\pi^-)}{\Gamma(D^0 \to K\pi)} = 3.686 \pm 0.076(stat) \pm 0.036(syst)\ \% \qquad (2)$$

The direct CP asymmetries for D^0 decays were found to be $2.0 \pm 1.7(stat) \pm 0.6(syst)\%$ for $D^0 \to K^+K^-$ decays and $3.0 \pm 1.9(stat) \pm 0.6(syst)\%$ for $D^0 \to \pi^+\pi^-$ decays.

6 Rare Charm Decays

For the flavor changing neutral current decay $D^0 \to \mu^+\mu^-$, the Standard Model predicts a branching ratio of $Br(D^0 \to \mu^+\mu^-) \sim 10^{-13}$. The present experimental limit is $Br(D^0 \to \mu^+\mu^-) \sim 4.1 \times 10^{-6}$ from BEATRICE [16] (4.2×10^{-6} from E771 [17]), 7 orders of magnitude from the prediction.

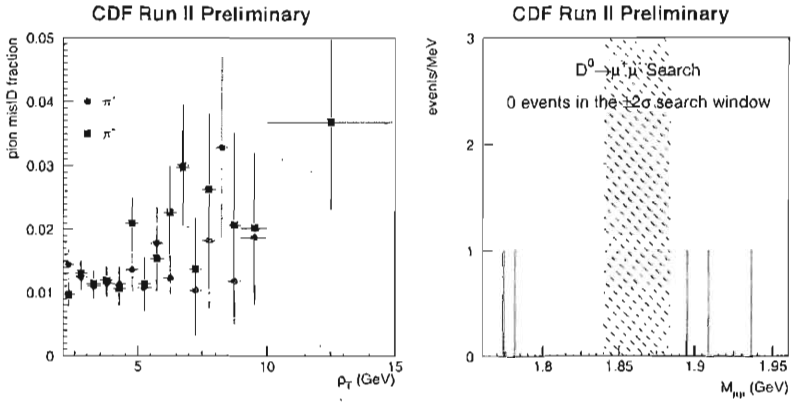

Figure 5: Elements of the $D^0 \to \mu^+\mu^-$ analysis. The left plot depicts the rate at which pions are misidentified as muons, and the right plot shows the absence of events in the search window.

New physics can substantially enhance this mode. In charm meson decays we are constraining couplings to up-type quarks not necessarily constrained by B decays. This makes $D^0 \to \mu^+\mu^-$ an unexplored region to search for new physics.

Using 69 pb^{-1} of Run II data, a search for $D \to \mu^+\mu^-$ decays was performed. As in the CP asymmetry analysis, the D^0 decays were reconstructed in a clean final state by requiring that they originate from $D^{*+} \to D^0\pi^+$ decays. The kinematically similar $D^0 \to \pi^+\pi^-$ decay was used as a normalization mode. The sources of background for this decay are $D^0 \to \pi^+\pi^-$ events in which both pions are misidentified as muons and combinatorial background. Both the pion misidentification rate and the level of the combinatorial background were measured from a kinematically similar but statistically independant set of events. The estimated number of background events in the search window was 1.7 ± 0.7. No events were found in the search window, as seen in Figure 5, and a limit was set on the branching ratio: $Br(D^0 \to \mu^+\mu^-) < 2.4 \times 10^{-6}$ at 90% C.L. This is currently the worlds best limit on the $D^0 \to \mu^+\mu^-$ branching ratio.

7 Summary

The upgraded CDF II detector is back in operation and has gathered around 65 pb^{-1} of data which can be used for charm analyses. Due to its ability to trigger

on displaced tracks and vertices, the spectrum of charm results has extended from $J/\psi \to \mu^+\mu^-$ decays to include hadronic decays of D^0, D^+, D^{*+}, and D_s^+. With the modest amount of data gathered so far, world class results have already been obtained.

References

1. R. Blair *et al.* [CDF II Collaboration], FERMILAB-PUB-96-390-E.
2. T. K. Nelson *et al.* [CDF II Collaboration], FERMILAB-CONF-01/357-E.
3. A. Sill *et al.* [CDF II Collaboration], Nucl. Instrum. Meth., A **447**, 1–8, (2000).
4. T. Affolder *et al.* [CDF II Collaboration], Nucl. Instrum. Meth., A **485**, 6–9, (2002).
5. K. T. Pitts *et al.* [CDF II Collaboration], FERMILAB-CONF-96/443-E.
6. W. Ashmanskas *et al.* [CDF II Collaboration], Nucl. Instrum. Meth., A **447**, 218–222, (2000).
7. F. Abe *et al.*, Phys. Rev. Lett. **79**, 572 (1997).
8. K. Hagiwara *et al.*, Phys. Rev. D **66**, 010001 (2002).
9. D. N. Brown *et al.* [CLEO Collaboration], Phys. Rev. D **50**, 1884 (1994).
10. B. Aubert *et al.* [BaBar Collaboration], Phys. Rev. D - Rapid Comm. **65** 091104 (2002).
11. D. Acosta *et al* [CDF II Collaboration], Phys. Rev. D **65**, 052005 (2002).
12. M. Cacciari, P. Nason, private communication.
13. H. N. Nelson, hep-ex/9908021; A. A. Petrov, hep-ph/0009160; I. I. Bigi, hep-ex/014008; A. F. Falk, Y. Grossman, Z. Ligeti, A. A. Petrov, hep-ph/0110317.
14. M. B. Einhorn and C. Quigg, Phys. Rev. D **12**, 2015 (1975).
15. F. Buccella *et al.*, Phys. Rev. D **51** 3478 (1995).
16. M. Adamovich *et al.* [BEATRICE Collaboration], Phys. Lett. B **408**, 469 (1997).
17. T. Alexopoulos *et al.* [E771 Collaboration], Phys. Rev. Lett. **77**, 2380 (1996).

MYSTERIES IN CHARMONIUM PRODUCTION

Mikhail Danilov
ITEP, Moscow

Written contribution not received

B PHYSICS AT CDF

M. Herndon
The Johns Hopkins University, Baltimore, MD 21218
for the CDF Collaboration

Abstract

The Tevetron Run2a Collider Detector at Fermilab has been taking for over one year. During this time the detector has integrated a physics data sample of approximately $70pb^{-1}$. The size of this sample along with improved detector capabilities, including a displaced track trigger, allow CDF detector to begin to make competitive measurements in various areas of B physics. In this paper we present a selection of the first B physics results from the Run2a physics program.

1 Introduction

The Collider Detector at Fermilab(CDF) for Tevatron Run 2a has been operating for over one year. The Tevatron provides an excellent opportunity to study B physics. The production cross section for B hadrons is very high, approximately $10\mu b$ for hadrons with transverse momentum, $p_T > 6.0$GeV, and rapidity, $|y| < 1$. This represent approximately 1000 b's per second within the sensitive area of CDF at design Tevetron luminosity. In addition the larger center of mass energy, 1.96TeV, allows for the production of all B hadron species including B_s, B_v, Λ_b and χ_b. These heavier B hadrons are the focus of the CDF Run2 B physics program. In this paper we briefly describe the upgraded Tevetron and CDF Run2 detector, outline the Run2 B physics program and present a number of initial physics signatures from the current CDF dataset.

2 Run2a Upgrade

For Run2 the Tevatron and detectors at Fermilab were considerably upgraded. These upgrades include higher energy for the Tevetron and the potential for higher luminosity [1]. The CDF detector upgrades include replacement of the central tracking detectors, extensions and improvements to coverage for the calorimeter and muon system and an improvement in the triggering capabilities [2].

2.1 Tevatron Run2a Upgrade

The collider upgrade consists primarily of a new main injector, a higher center of mass energy for the Tevatron and a recycler for the anti protons. The new main injector replaces the old main ring which was located inside the Tevtron beam line tunnel. The main injector can accelerate and deliver a higher intensity of protons and has more efficient transfer of anti-protons. The recycler which is part of the main injector complex will allow part of the anti-proton beam to be recycled after a Tevatron collider store is done. The current Tevatron configuration collides 36 bunches of of protons and anti protons with each other with a collisions rate of 396ns. The expectation is that the upgraded Tevatron could achieve luminosities of five to ten times those achieved in Run1. As of the January 2003 shutdown, which defines the end of the data taking period from which results are presented here, the Tevatron had achieved a record luminosity of $3.6 \times 10^{31}\text{cm}^{-2}\text{s}^{-1}$.

2.2 CDF Run2a Detector Upgrade

The Run2a CDF detector has been upgraded compared to the Run1 detector configuration to take advantage of the higher luminosity and energy of the up-

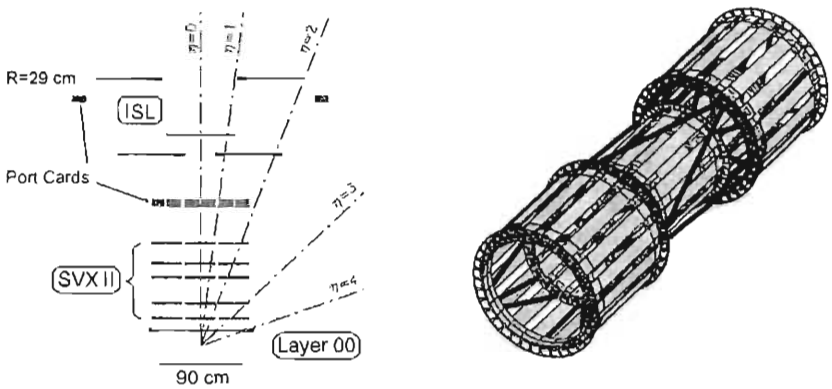

Figure 1: *CDF Run2 silicon detector schematic and outside view of ISL.*

graded Tevetron. The primary focus of the upgrade was the central tracking chambers. The new tracking system consists of a silicon vertex detector(SVXII) and a new open cell drift chamber, the central out tracker(COT). The silicon detector includes a five layers of double sided silicon which provides 3D tracking and vertexing capability within psuedorapidity $|\eta| < 1$. Three of the layers include strips oriented at 90 degrees to the beam line in order to improve 3D vertexing. There are also two extensions to the silicon tracker: The intermediate silicon layers(ISL), which provide additional forward track coverage to $|\eta| < 2$ and an extra measurement point centrally; and an additional single sided layer of silicon mounted on the beampipe at radius of 1.3-1.6cm, which improves $r - \phi$ resolution(L00), see fig. 1. This allows for eight measurement points centrally and seven measurement for forward tracks. The new drift chamber consists of eight super-layers between 44 and 132cm of radius with 12 measurement points per super-layer. Four of the super-layers are axial and four stereo. Tracks with $|\eta| < 1$ are fully contained within the acceptance of the chamber. All wires are instrumented to measure dE/dx. The entire tracker is immersed in a 1.4 Tesla magnetic field to provide bending for measuring the momentum of particles.

The transverse momentum resolution of the drift chamber is $\delta p_T/p_T^2 \sim 0.15\%(GeV/c)^{-1}$ and the impact parameter resolution is $350\mu m$. The silicon detector currently achieves an impact parameter resolution of $\sim 30\mu m$ or $\sim 43\mu m$ including the width of the beam line. This resolution will improve as the understanding of the L00 detector improves.

The capabilities for particle identification were improved as part of the

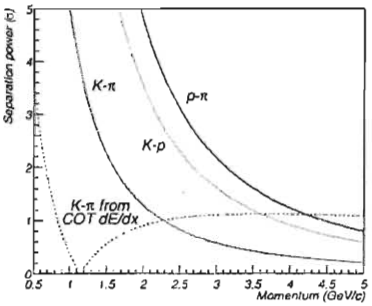

Figure 2: *Performance of the particle identification system*

upgrade. A new time of flight detector(TOF) is installed directly outside of the COT. This detector has a design resolution of 100ps at 1.4m(measured at photo multiplier tube faces). Currently the detector achieves 110ps resolution and 1.25ps resolution over all z. The design resolution should give 2σ resolution for K π separation below 1.6GeV and for proton separation from K and π out to 2.7 and 3.2 GeV respectively. In addition the improved dE/dx resolution of the COT gives separation at higher momentums where the TOF has no sensitivity, see fig.2.

The outer Run2a CDF detector has also been improved. The forward plug calorimeter has been upgraded. The central coverage of the moun chambers has been increased to give near hermetic coverage for muons with $|\eta| < 1$ which corresponds to the area the track trigger functions. Also additional coverage moun has been added to $|\eta| < 1.5$. This is designed to match the cabability of the new track trigger which has a fast turn on just bellow a transverse momentum of 1.5GeV and higher efficiency.

The final component of the upgrade is the trigger upgrade. The new CDF2a trigger has the capability to trigger at 50KHz at the first level of hardware. Tracks found in the first level trigger can be augmented with silicon $r - \phi$ information to find displaced tracks(SVT) in the second level hardware trigger. The third level of the trigger consists of a full event reconstruction including tracking in both the COT and silicon detectors. Fully reconstructed events can be written to tape at 50Hz. The ability to find tracks down to lower momentum and identify them as displaced along with a confirmation of the hardware trigger decision by the full software reconstruction allow for a rich B physics program including dimuon and dielectron triggers, lepton plus SVT triggers and fully hadronic B physics triggers based purely on displaced tracks.

3 CDF Run2a B Physics Program

The Tevaton provides an excellent opportunity to study B physics. The high production cross section and center of mass energy large enough to produce all B species make it possible to perform b physics studies here that can not be equaled at any other facility. In addition, detector improvements so that we can trigger on B hadrons with good efficiency in leptonic, semileptonic and fully hadronic decays modes allow CDF2 to take full advantage of this opportunity. The CDF2 B physics program includes studies of QCD production cross sections, CP violation and mixing properties, all the properties of heavy and excited B states and searches for rare decays.

The low trigger threshold for dimuon events will allows us to study the J/ψ production cross section and the fraction of J/ψs from B hadron decay down to a J/ψ momentum of 0GeV. This will allows to measure the shape and fix the absolute scale of this cross section. I will also be possible to study the total B production cross section down to low momenturns which may resolve long standing questions from Run1 about the B production rates. It is also possible to study quarkonium states such as $\Upsilon(1S)$ and $\chi_b \rightarrow$ Upsilon(1S) feeddown.

For heavy B hadron states such as B_s, B_c, Λ_b and χ_b we will be able to study the Production, mass, lifetime and decay branching ratios. In some cases these will be the first measurements of these properties. For instance, fully hadronic decays modes of the Λ_b.

Rare decays of interest include low rate standard model decays such as $B \rightarrow \mu\mu K^{(*)}$ and decays that would only be visible if there were beyond the standard model contributions such as $B^0, B_s \rightarrow \mu\mu$ and $B_s \rightarrow e\mu$.

The central focus of the CDF2a B physics programs will be the CP violation and mixing studies. CDF has sensitivity to measure a wide array of mixing phenomena, CP triangle angles and weak and strong phases. Among the possible measurements the CDF will excel in are: B_s mixing, x_s in the $B_s^0 \rightarrow D_s\pi$ decay mode, $\sin(2\beta)$ in the $B^0 \rightarrow J/\psi K_s^0$ decay mode, the weak phase of V_{ts} in the $B_s^0 \rightarrow J/\psi\phi$ decays mode, the CP asymmetry of $B^0(B_s^0) \rightarrow hh$ decays and the angle γ in the $B_s^0 \rightarrow D_s^- K^+$ decay mode.

4 Initial Signals for B physics

CDF has detected signals for many of the signals that will be used for the studies outlined above. Already, due to the upgraded capabilities of the CDF detector, we have assembled larger samples of various B decays than in Run1 and observed new decays modes.

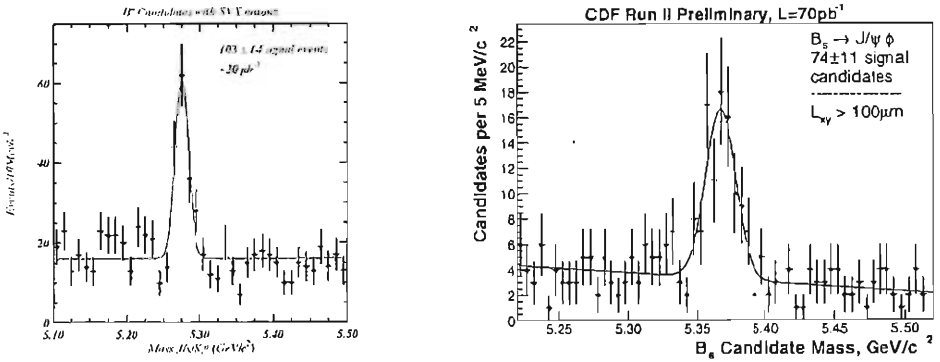

Figure 3: *B mass from* J/ψ *decay mode sof the* B^0 *and* B_s^0

4.1 J/ψ signitures of the B^0 and B_s^0

Using the J/ψ based dimuon trigger we have seen signatures for $B^0 \rightarrow J/\psi K_s^0$, $K_s^0 \rightarrow \pi^+\pi^-$ decays and $B_s^0 \rightarrow J/\psi\phi$, $\phi \rightarrow K^+K^-$. In only $20pb^{-1}$ we already see 103 ± 14 B^0 events compared to 200 event with 5.5 times as much data in Run1. The matches the expectation for the increase in acceptance from the detector upgrade. We also see 74 ± 11 B_s^0 events. These physics samples will be used to perform studies of CP asymmetry in the decay rates of B^0(s) and $\bar{B^0}$(s). In both cases the original flavor of the B will have to be tagged and in the B_s^0 the analysis will be time dependent. Studies of flavor tagging are under-way.

4.2 Λ_b signatures

The Λ_b has been observed in 3 decays modes including a first observation of a fully hadronic decay mode. The decay modes are $\Lambda_b \rightarrow J/\psi\Lambda$, $\Lambda \rightarrow p\pi$, $\Lambda_b \rightarrow \Lambda_c l\nu$, $\Lambda_c \rightarrow pK\pi$ and $\Lambda_b \rightarrow \Lambda_c\pi$, $\Lambda_c \rightarrow pK\pi$. The observation of these three decay modes demonstrates the new capabilities of the CDF2a detector to trigger both on all combinations of leptons and displaced tracks and will allow for a full study of the primary Λ_b decays modes. In addition, particle ID using the TOF and drift chamber dE/dx was used to enhance the purity of the semileptonic Λ_b sample.

4.3 Hadronic Signatures for B_s^0 Physics Studies

Using the fully hadronic two displaced track trigger(TTT) we have observed the signatures $B^0 \rightarrow D^-\pi^+, D^- \rightarrow K^+\pi^-\pi^-$ and $B_s^0 \rightarrow D_s\pi, D_s \rightarrow \phi\pi$ and

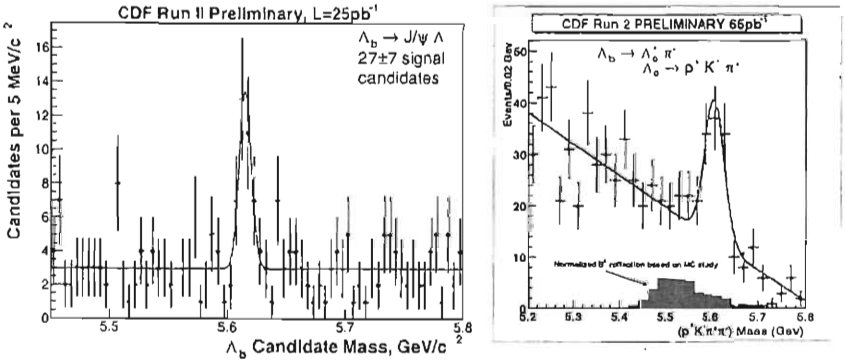

Figure 4: Λ_b *mass from* J/ψ *and fully hadronic decay modes.*

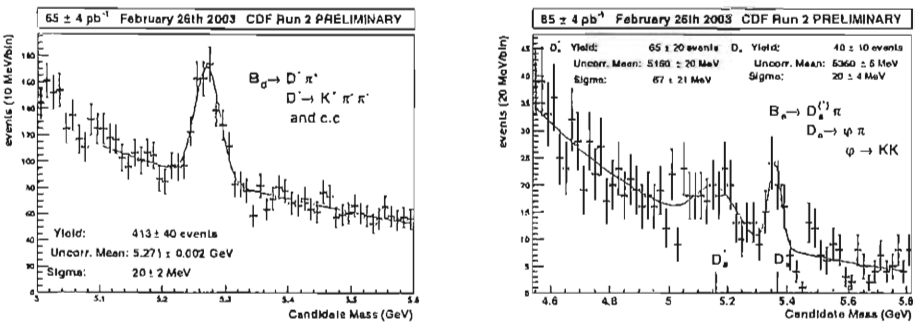

Figure 5: *B mass from hadronic decays to charm of the* B^0 *and* B_s^0.

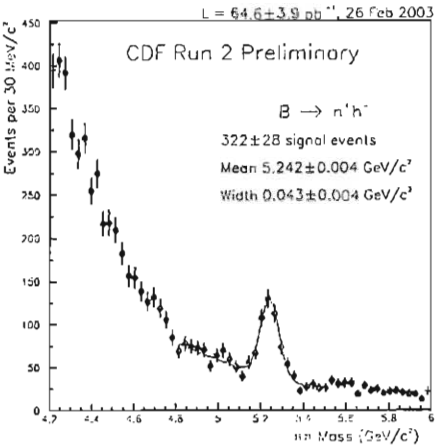

Figure 6: $B \rightarrow hh$ *combined mass.*

$\phi \rightarrow K^+K^-$. These signatures will be used to measure the relative branching ratio of $B_d(s) \rightarrow D(s)\pi$ and to study B_s mixing(x_s).

4.4 $B \rightarrow hh$ Signatures

Also using the TTT we have observed the combined decay modes $B^0 \rightarrow \pi\pi$, $B^0 \rightarrow \pi K$ and $B_s^0 \rightarrow KK$, $B_s^0 \rightarrow K\pi$. These modes will be used to study direct CP violation.

5 Conclusion

The CDF2 detector and the Tevatron have undergone a considerable upgrade for the Tevetron Run2. Increased luminosity and improved detector performance are expected to allow for a diverse B physics program. Already with only small amounts of data the CDF2 experiment sees many of the primary signals for various B physics studies and has made first observation of new decay modes. With continued data taking we expect to make a significant contribution to the body of High Energy Physics knowledge.

References

1. Fermilab Beams Division, "Run II Handbook", Fermilab Report(unpublished) http://www-bd.fnal.gov/runII/index.html.

2. The CDF2 Collaboration, "The CDF II Detector Technical Design Report", 1996, FERMILAB-Pub-96/390-E.

B MESONS DECAY PROPERTIES AT BABAR

Franco Simonetto
INFN and Universita' di Padova

Abstract

Recent measurements of B-mesons decay properties performed by the BABAR experiment are here presented. The implication of these measurements for deeper understanding of some parameters of the Cabibbo Kobaiashi Maskawa mixing matrix is also discussed.

1 Introduction

Within the Standard Model of electro-weak interactions all the flavour-changing processes are described by the Cabibbo-Kobaiashi-Maskawa (CKM) flavour mixing matrix. Transitions between light quarks (u, d, c, s) are described by a unique parameter, the Cabibbo angle, which has been measured with great precision for several years [1]. Only recently, however, some insight has been reached on the parameters which rule transitions and decays of heavy flavours (t, b), thanks to the pioneering studies of ARGUS, CLEO, LEP experiments (plus SLD) and CDF. The high luminosity B-factories (BABAR and BELLE) push these measurement into the precision era.
It is a well known fact that, within the Standard Model, all CP violating processes are described by a unique parameter, the phase of the CKM matrix. All the information related to heavy flavour transitions can be represented in the unitarity triangle, whose area is directly connected to the size of the CP violating phase. Measurements of the semileptonic decay width of the B-mesons to either charmed or charmless final state allow to determine separately the sides of the unitarity triangle corresponding to the parameters V_{cb} and V_{ub}, while V_{td} can be obtained from measurements of $B - \bar{B}$ oscillation. These elements constitute the sides of the unitarity triangle. Its angles can be determined independently by measuring the phases of several CP violating B-decay processes. The simultaneous determination of sides and angles allows to over-constrain the triangle, and, therefore to verify whether or not the CKM matrix gives an overall consistent interpretation of all flavour-changing phenomena. Any hint of inconsistency should be interpreted as a sign of new Physics beyond the Standard Model.
This summarizes the main BABAR Physics programme [2]. A report on up-to-date measurements of CP violating phases can be found elsewhere in these proceedings [3]. The results from a set of measurements of B-flavour oscillation and B meson semi-leptonic decays performed by BABAR, are here presented. The implications for the corresponding parameters of the CKM matrix are also discussed. A similar report from the other B-factory experiment (BELLE) can also be found in these proceedings [4].

2 The BABAR Detector

BABAR is a omni-purpose spectrometer operating at the PEP-II e^+e^- collider in the Stanford Linear Accelerator Center. The detector is designed for precision tracking, vertex reconstruction, particle identification, photon and electron identification. A set of RPC chambers allows for muon identification and coarse measurement of K_L direction. A detailed description of the BABAR detector can be found elsewhere [5]. PEP II operates at a center-of-mass en-

ergy corresponding to the $\Upsilon(4S)$ mass, in the factory regime, i.e. allowing high luminosity and high event yield. The results presented here are based on the data collected during the first three years of full operation (2000-2001-2002) and correspond to about 81 fb^{-1}. About 9 fb^{-1} are also collected at slightly lower energies ("off-peak" events), just below the threshold for the production of $B - \bar{B}$ mesons, for background studies. To allow the measurement of time-dependent quantities (lifetimes, oscillation frequency etc.) the beams are boosted in such a way that the $\Upsilon(4S)$ is not produced at rest, but receives a boost $\beta\gamma \approx 0.55$ along the beam pipe (z axis); this boost is transmitted to the B-mesons. As a consequence, the two particles are on average separated at decay time by about 250 μm, which should be compared to the experimental resolution on vertex reconstruction of about 80 μm. The two particles also move in the transverse (xy) plane, along which they are on average separated by about $30\mu m$.

3 Measurement of the $B - \bar{B}$ mixing frequency Δm_d

The phenomenon of $B_d - \bar{B}_d$ oscillation is mediated by a second order box diagram in the Standard Model, dominated by the exchange of the top quark. Therefore the frequency of the oscillation, corresponding to the mass splitting between the mass eigenstates Δm_d, is proportional to the square of the product of CKM matrix elements $|V_{td}| \cdot |V_{tb}|$. Unitarity bounds impose the constraint $|V_{tb}| \simeq 1$, therefore a measurement of Δm_d can be used to constrain $|V_{td}|$, albeit with some theoretical errors.

When the $\Upsilon(4S)$ decays, it produces in about 50% of the cases a couple of $B_d - \bar{B}_d$ mesons. They then evolve coherently in a $J^{PC} = 1^{--}$ state until the first one decays. The second particle evolves then freely and possibly oscillates. The period of the oscillation equals about nine lifetimes. BABAR has performed several measurements of the B_d lifetime τ_{B_d}, [6, 7, 8] and of the mass splitting Δm_d [10, 9]. The measurement [11] here presented is the most recent and well represent all them. It is also the only case in the world in which τ_{B_d} and Δm_d are determined simultaneously.
The analysis proceeds as follows. B_d mesons are selected from their semileptonic decay $B_d \to D^{*+}\ell^-\nu_\ell$, [1], $D^{*+} \to \pi^+ D^0$, $D^0 \to K^-\pi^+$, $K^-\pi^+\pi^-\pi^+$, $K^-\pi^+\pi^0$, $K^0_S\pi^+\pi^-$. The cut $p_\ell > 1.3$ GeV/c is applied to the lepton momentum[2]. Apart from a small amount of combinatoric events (see figure 1), this sample is produced mostly by B_d decays.The process $B_u \to \pi^- D^{*+}\ell^-\nu_\ell$

[1] Charge conjugated states are always implicitly meant. ℓ stays for either an electron or a muon.

[2] Throughout this article the momentum is always computed in the $\Upsilon(4S)$ rest frame .

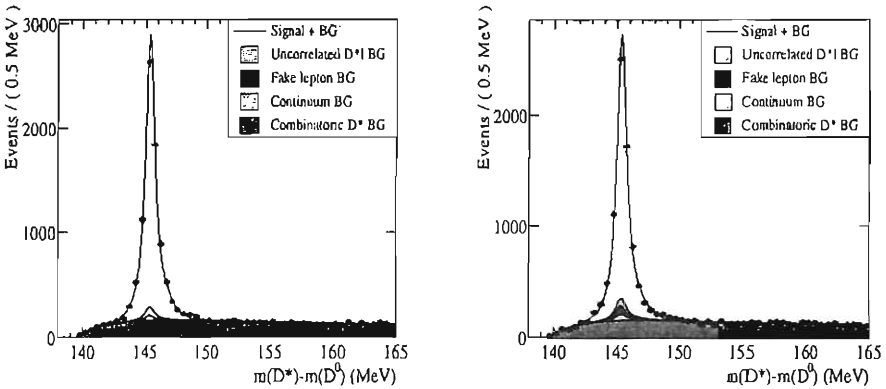

Figure 1: *Mass difference : $M_{D^0\pi^+} - M_{D^0}$ for electron tagged (left) and μ tagged (right) events*

leads to a pollution from charged B mesons, accounting for about 10% of the sample (the exact amount is determined from the data, see below). To save efficiency, the other B meson is not reconstructed, but its decay vertex is reconstructed from the intersection of the tracks from all the other charged particles in the event leaving a sufficient number of hits in the Silicon Vertex Tracker. The proper time difference is then computed in the "boost approximation" as $\Delta t = (Z_1 - Z_2)/(\beta\gamma c)$, where Z_1 and Z_2 are the projection along the beam pipe of the two reconstructed vertices, c the speed of light, and the motion of the two mesons in the transverse direction is neglected. Mixing has taken place if the flavour of this second ("tag") B is equal to the flavour of the reconstructed ("decay") one. The tag flavour is determined by means of an algorithm, which selects several tag methods, in the following hierarchical order:

- if a high momentum lepton is found, a flavour corresponding to the lepton charge is assigned;
- if no lepton is found, the flavour is computed from the algebraic sum of the electrical charge of all the K present in the event;
- if this is zero, a neural network is exploited. The network combines the information from the charges of high-momentum particles (mostly not-properly-identified leptons) and from very low-momentum particles (mostly soft pions from D^{*+} decays). The network answer is organized in

two levels, the former providing a low-efficiency, high-correct-tag-flavour information, and another with higher efficiency, but higher mis-tag rate

- in about 30% of the cases, no tagging is provided. These events are not discarded, because they contribute to the measurement of τ_{B_d}.

Mis-tags (due to leptons from cascade decays $B \to XD, D \to \ell Y$, fake kaons, etc.) lead to a wrong definition of mixed and unmixed event, diluting the sensitivity. The lepton tag has the lowest mis-tag rate but also a low efficiency. The analysis is performed on about 20 fb^{-1} collected during the first year of data taking. About 14000 events are selected. Neglecting resolution effects, but including mis-tags, the fraction of (un)mixed events is:

$$f_{unmixed} \propto e^{(-t/\tau_{B_d})}(1 + (1-2w)cos(\Delta m_d \Delta t)) \quad (1)$$

$$f_{mixed} \propto e^{(-t/\tau_{B_d})}(1 - (1-2w)cos(\Delta m_d \Delta t)) \quad (2)$$

where w is the fraction of wrong tags. Δm_d and τ_{B_d} are computed from an extended maximum likelihood fit to mixed, unmixed and untagged data samples. To reduce the systematic error, at the price of increasing the statistical one, the fit also determines some other relevant parameters, as the fraction of peaking background from B_u (see above), the fraction of wrong tags in each tagging category, most of the parameters of the proper time difference resolution function, etc. The background contribution to the likelihood is computed from data control samples. The following preliminary results are then obtained:

$$\Delta m_d = (0.492 \pm 0.018_{\text{stat.}} \pm 0.013_{\text{syst.}})\ ps^{-1} \quad (3)$$

$$\tau_{B_d} = (1.523 \pm 0.024_{\text{stat.}} \pm 0.022_{\text{syst.}})\ ps \quad (4)$$

The dominant systematic error is due to the limited amount of simulation statistics employed to determine possible biases due to the selection and fit procedure. The correlation between the two parameters is about 20 %. Figure 2 shows the measured asymmetry, $\mathcal{A} = (\mathcal{N}_{unmixed} - \mathcal{N}_{mixed})/(\mathcal{N}_{unmixed} + \mathcal{N}_{mixed})$, as a function of the proper time difference, with overalyed the result of the fit.

This measurement of Δm_d is averaged with the two published values, exploiting largely independent samples, to provide the preliminary BABAR mean value:

$$\Delta m_d = (0.500 \pm 0.008_{\text{stat.}} \pm 0.006_{\text{syst.}})\ ps^{-1} \quad (5)$$

This precise measurement cannot be translated in a precise estimate of V_{td} due to hadronic uncertainties. This are much reduced in the ratio $|\frac{V_{td}}{V_{ts}}|^2 \propto \frac{\Delta m_d}{\Delta m_s}$, which will be determined as soon as Tevatron experiments will observe $B_s\bar{B}_s$ oscillation, measuring therefore Δm_s.

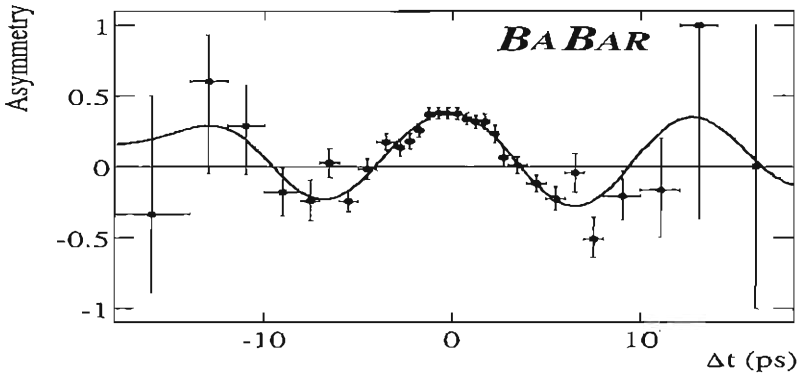

Figure 2: *Asimmetry versus proper time difference. Points with error bars: real data. Continuous line: fit result.*

4 Semileptonic Branching Fraction

BABAR has measured the semileptonic branching fractions for B-decays to charmed and charmless inclusive and exclusive final states. From these measurements values for V_{cb} and V_{ub} are obtained.

4.1 Exclusive Branching Fraction $\mathcal{B}(B_d \to D^{*+}\ell^-\bar{\nu}_\ell)$

The event selection is similar to the one described previously. The background from fake (combinatoric) D^{*+} is computed from a fit to the $\Delta M = M_{D^*} - M_{D^0}$ spectrum. The contributions from continuum events and from B_d decays to a D^{*+} and another heavy particle (D, τ), which then decays to a ℓ^-, is small ($\mathcal{O}(1\%)$) due to the cuts applied and to the modest branching fractions. They are computed from the simulation. Other backgrounds, peaking in ΔM, are computed exploiting kinematics:

- random associations of a ℓ^- from a B meson and a D^{*+} from the other are computed counting the number of "same side" events, for which the angle between the ℓ^- and the D^{*+} is smaller than 90^o, where very few signal events are expected. This number is then propagated to the "opposite side" (angle larger than 90°) using the simulation. Same side events are then removed from the analysis.

- the contribution from $B \to D^{*+}\pi\ell^-\bar{\nu}_\ell$ decays (hereafter referred to as

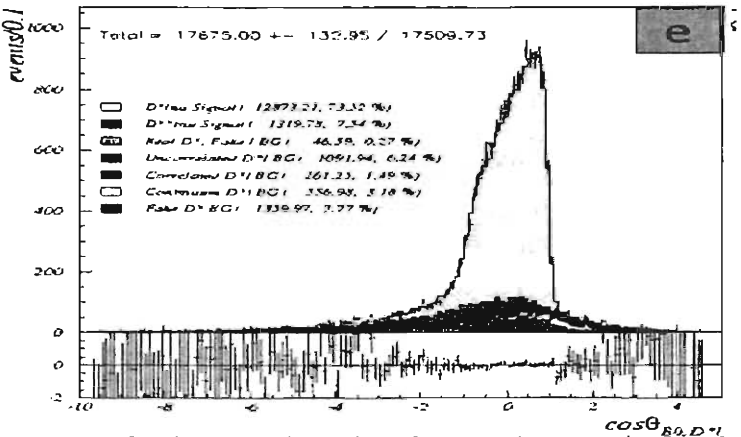

Figure 3: *$cos(\Theta_{BY})$: data (points) vs fit result (histogram). In colour the different contributions from several sources.*

D^{**}) is determined fitting the variable:

$$cos(\Theta_{BY}) = \frac{-(M_B^2 + M_Y^2 - 2E_B E_Y) + M_{miss}^2}{2p_B p_Y} \quad (6)$$

where Y is the pseudo-particle obtained adding the four-momentum of the ℓ^- and of the D^{*+}, and M_{miss}^2 is the square of the invariant mass of the other particles produced from the decay of the B. In the fit, this last quantity is zero, consistently with the hypothesis of pure signal events, for which only a neutrino is missing. Most of the signal events are contained within the physical limit $|cos(\Theta_{BY})| < 1$ (due to resolution effects, some of them leak outside this acceptance), while background events spread to large negative values (see fig 3). The shapes of the distribution for each category are obtained from the simulation. The fractions from signal events and of D^{**} are floated, while all the other components are fixed to the values previously determined.

The measurement exploits all the events collected by BABAR up to now. Events are separated accordingly to the lepton kind (electron or muon) to the D^0 final state (four) and for the year of processing (three). This adds up to twenty-four statistically independent samples. A constraint is applied, requiring that the fraction of D^{**} over the sum of peaking events be the same in all the samples. The singles results are then averaged together, accounting for their mutual correlation. The preliminary BABAR result is

$$\mathcal{B}(B_d \to D^{*+}\ell^-\bar{\nu}_\ell) = (4.92 \pm 0.03 \pm 0.02 \pm 0.24 \pm 0.17)\% \quad (7)$$

where the first (second) error is due to the data (simulation) statistics, the third is due to efficiency computation and background subtraction, including model dependencies of the efficiency, the last is due to the uncertainty in the relevant scale factors (D^0, D^{*+} branching fractions, B_d meson production rates, etc).

4.2 Inclusive Branching Fraction $\mathcal{B}(B \to X_c \ell \bar{\nu}_\ell)$ and $|V_{cb}|$

The measurement is performed from samples of events containing two electrons. The first one is selected for tagging purposes with the tight requirement on its momentum $p_1 > 1.5\ GeV/c$. Then a second electron in the same event is looked for, with electric charge opposite to the first and the looser cut $p_2 > 0.6\ GeV/c$. Charge correlation is imposed to reduce the amount of events from the "cascade" decay $B \to DX$, $D \to \ell Y$. For the same purpose, also a cut on the angle between the two leptons is applied. The value of the cut depends on p_2. The background-subtracted, efficiency-corrected, mixing unfolded p_2 spectrum is fitted with the sum of the spectra from the semileptonic decays to a D, D^*, and $D^*\pi$ final states, as predicted from the simulation (see figure 4). This allows to predict the fraction of events with momentum $p_2 < 0.6\ GeV/c$

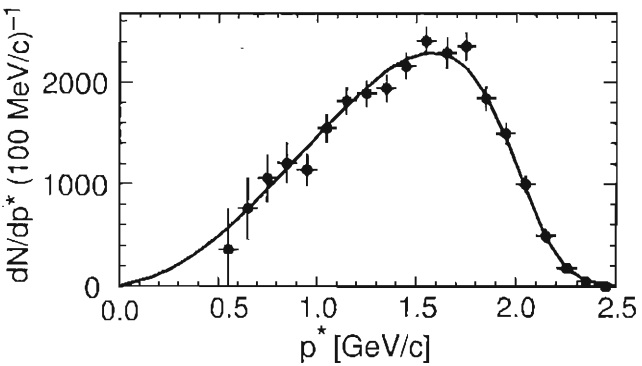

Figure 4: *Electron momentum spectrum, after background subtraction and efficiency correction. The dots show the data, the continuous line represents the fit result.*

as $(6.1 \pm 0.9)\%$. From the measurement of the inclusive branching fraction to charm final states also a value for V_{cb} is obtained. The results are [12]:

$$\mathcal{B}(B \to X_c e \bar{\nu}_e) = (10.87 \pm 0.18 \pm 0.30)\% \quad (8)$$

$$|V_{cb}| = (42.3 \pm 0.7_{\text{exp.}} \pm 2.0_{\text{th.}}) \cdot 10^{-3} \quad (9)$$

The theoretical error on V_{cb} can be reduced by determining some non-perturbative QCD parameters. This will be done measuring the main moments of the lepton and hadron momentum-spectrum in B semileptonic decays.

4.3 Inclusive Branching Fraction $\mathcal{B}(B \to X_u \ell \bar{\nu}_\ell)$ and $|V_{ub}|$

For this measurement, only electrons with momentum $p_e > 2.3$ GeV/c are selected. This cut approximatively corresponds to the upper kinematic limit for electrons produced from semileptonic decays to charm final states and allows to remove this otherwise overwhelming background, while leaving $f_u = (7.4 \pm 1.4 \pm 0.9)\%$ of the original signal sample. This fraction is computed from the spectrum of $B \to s\gamma$ decays, measured originally by CLEO [13], under the hypothesis of a unique function describing transitions of heavy to light quarks. The preliminary result is [14]:

$$\mathcal{B}(B \to X_u e \bar{\nu}_e) = (2.05 \pm 0.27_{\text{exp.}} \pm 0.46_{\text{f}_u}) \cdot 10^{-3} \quad (10)$$

$$|V_{ub}| = (4.43 \pm 0.29_{\text{exp.}} \pm 0.50_{\text{f}_u} \pm 0.35_{b s\gamma} \pm 0.25_{\text{OPE}}) \cdot 10^{-3} \quad (11)$$

where the experimental error, the error obtained propagating the experimental uncertainty on f_u, the one on the hypothesis of a single heavy-to-light function and the residual theoretical errors are shown separately.

4.4 Exclusive Branching Fraction $\mathcal{B}(B \to \rho \ell \bar{\nu}_\ell)$ and $|V_{ub}|$

This measurement allows an independent determination of $|V_{ub}|$ with different theoretical errors. Events are selected by requiring a high-momentum lepton, $p_\ell > 2.0$ GeV/c, and either a charged or a neutral ρ meson, reconstructed from its decay to two pions. The missing neutrino is reconstructed from the missing energy and missing momentum in the event. A correction is applied to account for cracks in the detector which deteriorate hermeticity. The variable $\Delta E = \sqrt{s}/2 - E_{vis}$ is computed by imposing the kinematic constraints from the mass of the neutrino and the mass of the B meson. The data sample is divided in two, depending on the momentum of the lepton ($2.0 < p_\ell < 2.3$ GeV/c and $2.0 < p_\ell < 2.7$ GeV/c respectively). The first region is mostly populated from decays to charm final states, while the second is enriched in signal events. The fraction of charmed and charmless decays in the two momentum regions is determined from a fit to the two dimensional distribution of ΔE and of the ρ mass M_{rho}. The preliminary result is [15] :

$$\mathcal{B}(B \to \rho \ell \bar{\nu}_\ell) = (3.29 \pm 0.42_{\text{stat.}} \pm 0.47_{\text{syst.,exp.}} \pm 0.60_{\text{syst.,th.}}) \cdot 10^{-4} \quad (12)$$

$$|V_{ub}| = (3.64 \pm 0.22_{\text{stat.}} \pm 0.25_{\text{syst.,exp}} {}^{+0.39}_{-0.66} {}_{\text{syst.,th.}}) \cdot 10^{-3} \quad (13)$$

where the theoretical error is guessed from the spread of the results obtained using different models to both compute the (large) fraction of the non-observed

spectrum and to relate then the measured branching fraction to $|V_{ub}|$. Albeit with large uncertainties, it should be noted that this exclusive result is considerably smaller than the inclusive one. This observation applies also to the results from other experiments, [16], and is a hint of some inconsistency between the models which describe the inclusive and the exclusive charmless semileptonic decays of b hadrons.

5 Conclusions

The BABAR collaboration is pursuing successfully its Physics programme, consisting in refined measurements of B meson properties and test of the heavy-flavour sector of the Standard Model. The very precise preliminary measurement of the $B_d - \bar{B}_d$ mixing parameter:

$$\Delta m_d \quad = \quad 0.500 \pm 0.008_{\mathrm{stat.}} \pm 0.006_{\mathrm{syst.}} \tag{14}$$

is obtained by averaging three measurements based on different data samples. An interpretation of this result in terms of the fundamental parameters of the CKM matrix with small model errors requires however the simultaneous measurement of the $B_s - \bar{B}_s$ mixing frequency expected soon from experiments operating at the Tevatron.

Several measurements of inclusive and exclusive semileptonic branching fractions of the B mesons allow to determine $|V_{cb}|$ with $\sim 2\%$ and $|V_{ub}|$ with $\sim 20\%$ precision. Further progress can be obtained by inspection of the lepton and hadron spectra, and from progress in the theory which relate the observed quantities with the fundamental CKM parameters.

References

1. K.Hagiwara *et al*, "The Review of Particle Physics", Physical Rev. **D66**, 010001 (2002).
2. P.F. Harrison and H.R. Quinn,Editors, "The BABAR Physics Book", SLAC-R-504 (1998).
3. R. Faccini , these proceedings.
4. N. Hastings, these proceedings.
5. B. Aubert *et al*, *BABAR collaboration*, Nucl. Inst. and Methods **A479**, 1 (2002).
6. B. Aubert *et al*, *BABAR collaboration*, Phys. Rev. Lett. **87**, 201803 (2002).
7. B. Aubert *et al*, *BABAR collaboration*, Phys. Rev. Lett. **89**, 011802 (2002).

8. B. Aubert *et al*, *BABAR collaboration*, SLAC-PUB-9602, submitted to Physical Rev. D-Rapid Communications.

9. B. Aubert *et al*, *BABAR collaboration* Phys. Rev. Lett. **88**, 2515 (2002).

10. B. Aubert *et al*, *BABAR collaboration* Phys. Rev. Lett. **88**, 221803 (2002).

11. B. Aubert *et al*, *BABAR collaboration*, SLAC-PUB-9579, submitted to Physical Rev. D-Rapid Communications.

12. B. Aubert *et al*, *BABAR collaboration*, Physical Rev. D-Rapid Communications **67**.

13. A.Bornheim *et al*, *CLEO collaboration*, Phys. Rev. Lett. **88**, 231803 (2002).

14. B. Aubert *et al*, *BABAR collaboration*, SLAC-PUB-9282, hep-ex/0207081.

15. B. Aubert *et al*, *BABAR collaboration*, SLAC-PUB-9618, hep-ex/0301001, submitted to Phys. Rev. Lett.

16. M. Battaglia, invited talk at First International Conference on Frontiere Science, Frascati 10/07-11/2002

HIGH PRECISION MEASUREMENTS OF B DECAY FINAL STATES WITH THE BELLE DETECTOR

N. C. Hastings for the Belle collaboration
IPNS, KEK, 1-1 Oho Tsukuba-shi, Ibaraki-ken, 305-0801, Japan

Abstract

A number of high precision measurements have been made using the data collected by the Belle detector at the KEKB collider. Three different mixing analyses, a charged and neutral B meson lifetime analysis and an inclusive semileptonic branching fraction analysis have all yielded high precision results. These analyses are presented in this article.

1 Introduction

The excellent performance of the KEKB collider and Belle detector at KEK, Japan have made high precision measurements using B meson decays possible. These measurements are presented here.

2 KEKB and Belle

The KEKB accelerator is a high luminosity asymmetric energy electron ($E_{e^-} = 8.0$ GeV) and positron ($E_{e^+} = 3.5$ GeV) collider operating at the $\Upsilon(4S)$ resonance. Between turn on in December 1999 to March 2003 it has produced over 100 fb^{-1} of data corresponding to more than one hundred million $B\overline{B}$ pairs. The mixing and lifetime analyses presented in this paper use 29.1 fb^{-1} and the inclusive lepton analysis uses 5.1 fb^{-1} of this data.

The Belle detector is a large solid angle, multi-component magnetic spectrometer. The detector comprises of a three layer Silicon Vertex Detector (SVD) for precise vertex position determination, a 50 layer Central Drift Chamber (CDC) for charged particle tracking and dE/dx measurement. An Aerogel Čerenkov Counter (ACC) array provides kaon and pion separation in the high momentum region and a system of Time Of Flight (TOF) counters provided low momentum particle identifiaction (PID) and trigger information. The instrumented flux return of the 1.5 T superconducting solenoid forms the K–Long and Muon Detector (KLM) which provides K_L and muon identification. Details of the Belle detector can ber found elsewhere [1].

The asymmetric energies of the KEKB beams boost ($\beta\gamma = 0.425$) the $\Upsilon(4S)$ and its daughter $B\overline{B}$ mesons in the laboratory frame, allowing them to travel a measurable distance within the detector so that time dependent measurements can be made.

3 Time dependent B analyses at Belle

Since the B meson mass is only slightly less than half the $\Upsilon(4S)$ mass, the B mesons produced at KEKB are almost at rest in the center of mass system (CMS) frame. However, since the accelerator beam energies are asymmetric the B mesons travel a measurable distance within the Belle detector before they decay. Additionally, since the beam energy asymmetry and therefore the boost is known, the proper-time difference between the B meson decays, Δt is known by measuring the decay vertex separation. Furthermore, the flavour of a decaying B tags the flavour of the other B at that time. These concepts are illustrated in figure 1 on the following page.

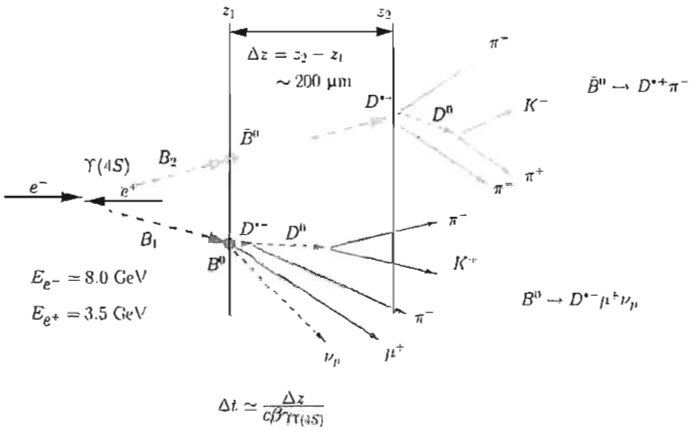

Figure 1: *The principle of time dependent measurements at Belle.*

4 B meson lifetime and Neutral B meson mixing

The mass difference of the neutral B meson mass eigen states, Δm_d is a fundamental parameter in the B meson system. The techniques that have been employed to measure it in $\Upsilon(4S) \to B^0\bar{B}^0$ decays fall into two categories, namely inclusive and exclusive. Both analysis types have been performed at Belle and have yielded high precision results. In the former category dilepton events have been used [2] and in the latter, analyses using decays to semileptonic states [3] and flavour specific hadronic modes [4].

The hadronic modes have also been used to obtain precise lifetime measurements for both neutral and charged B mesons [5].

4.1 Mixing with dilepton events

The fully inclusive dilepton method provides a very large data set and hence small statistical errors, with systematic uncertainties at a manageable level.

The charge of a primary lepton from a B meson decay tags the flavour of the parent B meson. As such, if two primary leptons are found in an event then the flavours of both B mesons are known. If the charges of the leptons are of the same sign then the B mesons must have been of the same–flavour (SF) and therefore mixing has occurred. Unmixed or opposite–flavour (OF) events are indicated by leptons with the same charge. By measuring the distance between the intersection of each lepton track and the beam profile the proper

time difference between the two B meson decays is known.

Events are selected which contain two leptons satisfying $1.1\ \mathrm{GeV}/c < p^* < 2.3\ \mathrm{GeV}/c$, whose opening angle satisfies $-0.8 < \cos\theta_{\ell\ell} < 0.95$. By calculating the invariant mass of all leptons (electrons) and oppositely charged tracks, events (electrons) are reject which are consistent with J/ψ decay (pair production). Details of these cuts and others can be found elsewhere [2]. After all cuts 230881 OF and 49838 SF events are found, with signal components estimated to be 67.1% and 33.8% respectively.

A binned maximum likelihood fit is performed on the SF and OF Δz distributions. The root functions of signal components for neutral and charged B mesons are given by:

$$P_{\mathrm{unmixed/mixed}} \propto e^{-\frac{\Delta z}{\tau_{B^0}\beta\gamma c}}\left(1 \pm \cos\left(\Delta m_d \frac{\Delta z}{\beta\gamma c}\right)\right), \qquad P_{\mathrm{charged}} \propto e^{-\frac{\Delta z}{\tau_{B^+}\beta\gamma c}}. \tag{1}$$

These root functions are convolved with a detector resolution function extracted from the Δz distribution of lepton pairs from J/ψ decays. The shapes of the background components are based on heavily corrected Δm_d dependent Monte Carlo (MC) Δz distributions.

The mixing parameter Δm_d and the fraction of charged to neutral B meson production; f_+/f_0 at the $\Upsilon(4S)$ are determined in the fit:

$$\Delta m_d = [0.503 \pm 0.08(\mathrm{stat}) \pm 0.010(\mathrm{syst})]\ \mathrm{ps}^{-1}, \tag{2}$$

$$f_+/f_0 = 1.01 \pm 0.03(\mathrm{stat}) \pm 0.09(\mathrm{syst}). \tag{3}$$

The largest systematics in the mixing result arise from the knowledge of the lifetime ratio $\tau_{B^\pm}/\tau_{B^0}$ ($0.005\ \mathrm{ps}^{-1}$) and the resolution function ($0.005\ \mathrm{ps}^{-1}$). The systematic error of f_+/f_0 is dominated by the lifetime ratio.

The mixing asymmetry function and fit result are shown in figure 2 on the next page.

4.2 Fully reconstructed B decays

Fully reconstructing a B meson from all of its daughter particles provides excellent signal to background separation, well reconstructed B decay vertices and the ability to use the remaining tracks and clusters in the event to determine the flavour of the other B.

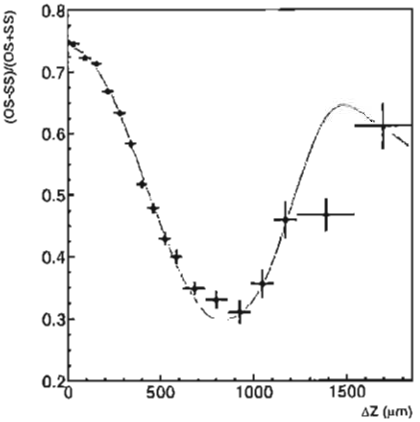

Figure 2: *The dilepton OF−SF asymmetry. The points with error bars show the data and the curve shows the fit result.*

4.2.1 *Mixing with semileptonic decays*

The decay $B^0 \to D^{*-}\ell\nu$ [1] is reconstructed using an electron or muon and the D^{*-} from the following secondary decays $D^{*-} \to \bar{D}^0\pi^-$, $\bar{D}^0 \to K^+\pi^-$, $K^+\pi^-\pi^0$, $K^+\pi^-\pi^-\pi^+$ and $\pi^0 \to \gamma\gamma$. Cuts are placed on the momenta of the lepton and the D^{*-}; $1.4 < p_\ell/\mathrm{GeV}/c < 2.4$, $p_{D^{*-}} < 2.6$ GeV/c and $\theta_{D^{*-},\ell} > 90°$.

An additional kinematic constraint is applied on the angle between the B^0 flight direction and the direction of the $D^{*-}\ell$ system. The cosine of this angle is determined from the energy and the magnitudes of the momenta of the B^0 and $D^{*-}\ell$ system.

$$m_\nu^2 = \overbrace{(E_B - E_{D^*\ell})^2 - |\vec{p}_B|^2 - |\vec{p}_{D^*\ell}|^2}^{MM^2} - \overbrace{2|\vec{p}_B||\vec{p}_{D^*\ell}|}^{C}\cos\theta_{B,D^*\ell} \qquad (4)$$

The neutrino mass is assumed to be zero, leaving:

$$\cos\theta_{B,D^*\ell} = -\frac{MM^2}{C} \qquad (5)$$

The angle is then required to be in the physical region (with allowances for detector smearing); $|\cos\theta_{B,D^*\ell}| < 1.1$. The $\cos\theta_{B,D^*\ell}$ distribution is shown

[1] Charge conjugates are implied unless stated otherwise throughout this article.

in figure 3. After all selection criteria have been made 16397 events are found

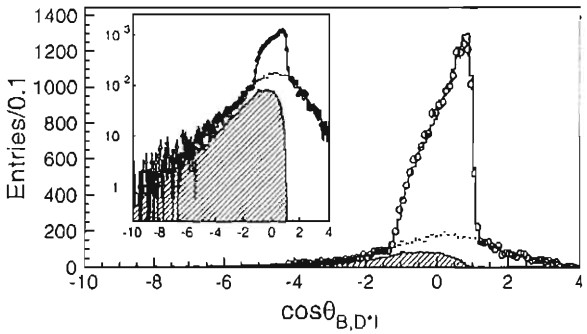

Figure 3: *The $\cos\theta_{B,D^*\ell}$ distribution. The points show the data, the solid line is a result of a fit to MC. The total background is show by the dashed line and the hatched histogram represents the $D^{**}\ell\nu$ background contribution. The inset shows the same plot with a logarithmic vertical scale.*

in the signal region and the signal fraction is estimated to be 80.4%. Backgrounds are estimated to be 7.8% for fake D^{*-} (from m_{D^0} an pion charge sidebands), 7.2% from $B^+ \to D^{**}\ell\nu$ ($\cos\theta_{B,D^*\ell}$ fit), random $D^{*-}\ell$ combinations ($\cos\theta_{B,D^*\ell}$ with $\vec{p}_\ell \to -\vec{p}_\ell$) and 1.8% from non $b\bar{b}$ continuum which is estimated using off-resonance data.

4.2.2 *Hadronic decays*

In the mixing analysis hadronic B decays are reconstructed via $B^0 \to D^-\pi^+$, $D^{*-}\pi^+$, $D^{*-}\rho^+$. The secondary ρ mesons are reconstructed from pairs of neutral and charged pions. The other secondary mesons are reconstructed via the same modes as in the semileptonic analysis in section 4.2.1.

For lifetime determination the above modes and $B^0 \to J/\psi K_S$, $J/\psi K^{*0}$ and $B^+ \to \bar{D}^0\pi^+$, $J/\psi K^+$ are used. Secondaries are reconstructed in the following modes: $J/\psi \to \ell^+\ell^-$, $K_S \to \pi^+\pi^-$ and $K^{*0} \to K^+\pi^-$.

The B mesons are selected using the beam energy difference $\Delta E = E_B - E_{\rm beam}$ and the beam constrained mass $M_B = \sqrt{E^2_{\rm beam} - |\vec{p}_B|^2}$, where $E_{\rm beam}$ is the energy of one beam in the CMS, E_B and $\vec{p}_B$ are the reconstructed energy and momentum of the B meson in the CMS. A two dimensional fit is performed on the M_B-ΔE distribution to obtain signal and background probabilities. A projection of the fit is shown in figure 4 on the next page. After all selection criteria have be made 2269 $D^-\pi^+$, 2490 $D^{*-}\pi^+$ and 1901 $D^{*-}\rho^+$ candidates

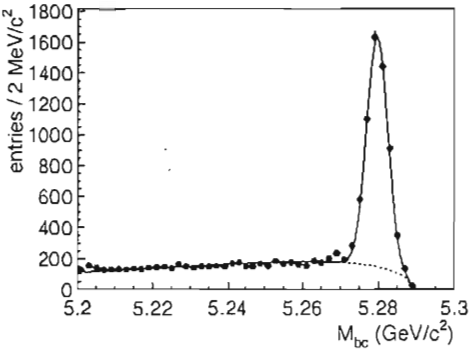

Figure 4: *Beam constrained mass for candidates in the hadronic mixing analysis. The points show the data, the dashed curve shows the background component and the solid curve represents the total fit result.*

are found for the mixing analysis. The sample for the lifetime consists of 7863 neutral and 12043 charged B mesons.

4.2.3 Flavour tagging and vertexing

The semileptonic and hadronic mixing analyses both use the same flavour tagging method as the Belle $\sin 2\phi_1$ analysis [6]. This method uses information from all the remaining clusters and tracks in the event in a likelihood to determine the flavour of the other B; $q(= \pm 1)$ and the quality of the tag $r(= 0.0 - 1.0)$. An r value of zero implies no tagging information and a value of one implies an unambiguous tag.

The event by event interaction point and tracks with associated SVD hits are used to determine B decay vertices.

The reconstructed B meson vertex position is found by fitting the pseudo $D^{+/0}$ track with the primary pion or lepton (or ρ daughter charged pion) track. If the event contains a D^{*-}, the daughter slow pion track is refitted and constrained to pass through the reconstructed vertex position.

The associated or tag B meson vertex is found by using the remain tracks with SVD hits in the event after rejecting those tracks which are consistent with K_S decays. In the semileptonic analysis additional cuts are made to suppress charm daughters. In the hadronic analysis a more sophisticated resolution function is used to accommodate these finite lifetime particles.

The Δt resolution is found to be about 1.4 ps and is dominated the by the associated B vertex resolution.

4.2.4 *Fitting*

Unbinned maximum likelihood fits to the Δt distributions are performed to extract Δm_d and lifetimes. The mixing analyses simultaneously fit to SF and OF distributions, while in the lifetime analysis a simultaneous fit to the charged and neutral B events is used.

Signal components of a Δt fit function contain a B meson exponential lifetime term, and in the case of mixing fits a cosine $\cos(\Delta m_d \Delta t)$ and wrong tag term $(1-2w)$. These parts are then convolved with a resolution function. For example the mixing analyses have signal Probablity Density Functions (PDFs) like:

$$P_{\text{unmixed/mixed}} \propto \int^{\Delta t'} e^{-\Delta t'/\tau}[1 \pm (1-2\omega)\cos(\Delta m_d \Delta t')]R(\Delta t - \Delta t')d\Delta t'. \quad (6)$$

In the semileptonic analysis the response function is an event-by-event double Gaussian;

$$R = f_1 G(\Delta t; \mu_1, \sigma_1) + (1 - f_1) G(\Delta t; \mu_2, \sigma_2), \quad (7)$$

where the widths σ_1 and σ_2 are functions of the vertex fit errors σ_{rec} and σ_{tag}; $\sigma_{1(2)} = S_{1(2)}\sqrt{\sigma_{\text{rec}}^2 + \sigma_{\text{tag}}^2}$ and $S_{1(2)}, \mu_{1(2)}$ and f_1 are obtained from a Δt fit with no tagging and a fixed τ_{B^0}.

In the hadronic analyses a more sophisticated response function is used. This response function is also used in the Belle $\sin 2\phi_1$ analysis [6] and is described in detail elsewhere [5]. Briefly, it is an event-by-event function with three components representing; (i) detector resolution, (ii) non-primary tracks and (iii) the kinematic approximation ($\Delta t \simeq \Delta z/\beta\gamma c$). The first two components have simplified forms for single track vertices.

The background components typically are made up of one or more terms with a non-zero lifetime, a zero lifetime component (continuum) and an outlier term. The shapes and fractions of these components are taken from data sidebands when possible and MC when not.

4.2.5 *Results*

The mixing results are;

$$\text{Semileptonic: } \Delta m_d = [0.494 \pm 0.012(\text{stat}) \pm 0.015(\text{syst})]\ \text{ps}^{-1}, \quad (8)$$

$$\text{Hadronic: } \Delta m_d = [0.528 \pm 0.017(\text{stat}) \pm 0.011(\text{syst})]\ \text{ps}^{-1}. \quad (9)$$

The main sources of systematic error in the semileptonic analysis are the D^{**} component (0.007 ps^{-1}), fit range (0.007 ps^{-1}), resolution function (0.006 ps^{-1}) and the shape of the background (0.006 ps^{-1}). The fit results for the semileptonic analysis is shown in figure 5. The main sources of systematic error in the hadronic analysis are from the parameters used in the resolution function (0.008 ps^{-1}) and the fitting method (0.005 ps^{-1}).

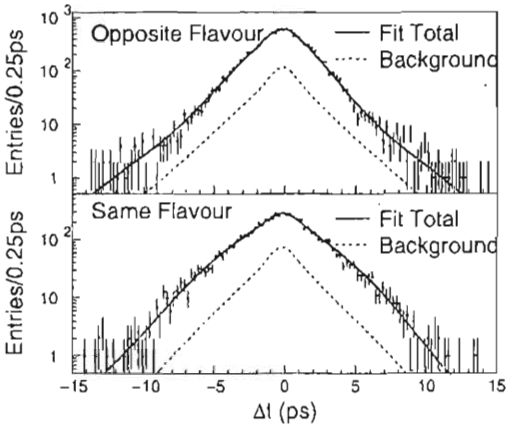

Figure 5: *The Δt distributions and fit results for the semileptonic mixing analysis.*

The results of the lifetime analysis are:

$$\tau_{B^0} = [1.554 \pm 0.030(\text{stat}) \pm 0.019(\text{syst})] \text{ ps}, \quad (10)$$

$$\tau_{B^+} = [1.695 \pm 0.026(\text{stat}) \pm 0.015(\text{syst})] \text{ ps}, \quad (11)$$

$$\tau_{B^+}/\tau_{B^0} = 1.091 \pm 0.023(\text{stat}) \pm 0.014(\text{syst}). \quad (12)$$

The major contributions to the systematic errors for τ_{B^0}, τ_{B^+} and τ_{B^+}/τ_{B^0} respectively are the background shape 0.12 ps, 0.007 ps, 0.011, the resolution function 0.010 ps, 0.009 ps, 0.006 and the fitting procedure 0.006 ps, 0.007 ps and 0.005. The fit results for both mixing and lifetime are shown in figure 6 on the next page.

5 Inclusive semileptonic branching fractions

Most measurements of the inclusive semileptonic branching fraction from B mesons are smaller than 11%. Conversely most theoretical predictions are

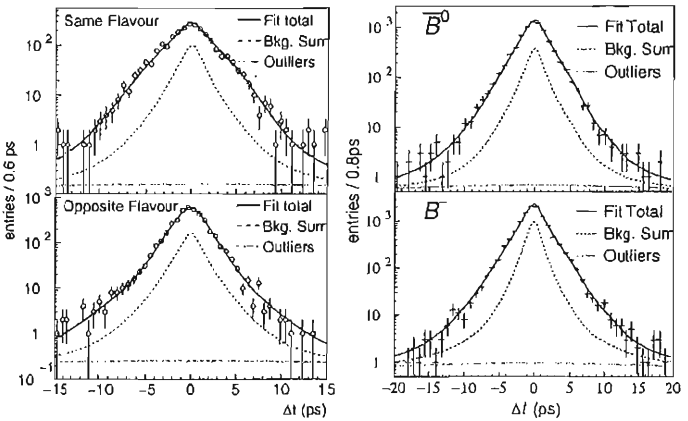

Figure 6: *The Δt distributions and fit results for the hadronic events. The plots on the left show the mixing analysis on the right the lifetime analysis.*

larger than 12%, however NLO corrections can accommodate a smaller branching fraction although this would require an enhanced $b \to c\bar{c}s$, which is not observed. Precision measurements are useful to confirm this anomaly.

An inclusive lepton branching fraction can also be used to extract the magnitude of the Cabbibo, Kobayashi and Maskawa (CKM) matrix element V_{cb}.

In this analysis events with two leptons are selected. The first or "tag lepton" reduces non $B\overline{B}$ backgrounds and normalises the event sample to reduce systematic errors associated with the knowing how many $B\overline{B}$ events are in the sample. The second lepton is the "Spectrum electron". Muons are not used since their purity is an order of magnitude worse. The ratio of electron energy to momentum normally utilised in electron identification is not used to select electrons in this analysis. Instead this distribution is fitted to obtain the true electron yield.

Both tag lepton and spectrum electron must pass J/ψ and gamma conversion vetos and the total longitudinal momentum of the event must be less than $0.2E_{CM}/c$. The tag lepton is required to satisfy $1.4 < p^*_\ell/\mathrm{GeV}/c < 2.2$, $45° < \theta_{\mathrm{lab}} < 125°$ and the spectrum electron must satisfy $p_{\mathrm{lab}} > 0.5$ GeV/c and $46° < \theta_{\mathrm{lab}} < 125°$. To reduce continuum events and events where both tracks originate from the same B the opening angle of the tracks must satisfy $-0.8 < \cos\theta_{\ell e} < 0.998$. Additionally the event must satisfy $p_e/\mathrm{GeV}/c + \cos\theta_{\ell e} > 1.2$

or $\cos\theta_{\ell e} > 0.3$.

The candidate events are separated into 46 p_e and 4 θ_e bins and the E/p distribution in each bin is fit to obtain the true electron yield. The signal PDFs are obtained from $\gamma \rightarrow e^+e^-$ events and the background PDFs are obtained from tracks failing the electron identification requirements using no E/p information. The electron yields in OF and SF events are 19722 ± 147 and 11224 ± 117 respectively.

Non $b \rightarrow qe\nu$ and non $b \rightarrow c \rightarrow q'e\nu$ contributions are subtracted from the spectrum electron CMS momentum distributions for SF and OF. A $B^0\bar{B}^0$ or B^+B^- will result in a SF(OF) pair for a $b \rightarrow c \rightarrow q'e\nu$ ($b \rightarrow qe\nu$) transition, while a $B^0\,B^0$ or $\bar{B}^0\,\bar{B}^0$ will result in SF(OF) pair for a $b \rightarrow qe\nu$ ($b \rightarrow c \rightarrow q'e\nu$) transition. The spectrums are thus described by:

$$\frac{dN_{\rm OF}}{dp_0} \propto \frac{dB(b \rightarrow qe\nu)}{dp}(1-\chi) + \frac{dB(b \rightarrow c \rightarrow q'e\nu)}{dp}\ \chi, \qquad (13)$$

$$\frac{dN_{\rm SF}}{dp_0} \propto \frac{dB(b \rightarrow qe\nu)}{dp}\ \chi\ + \frac{dB(b \rightarrow c \rightarrow q'e\nu)}{dp}(1-\chi), \qquad (14)$$

where $\chi = \chi_d f_0$. After efficiency corrections equations 13 and 14 are solved simultaneously to extract the $b \rightarrow qe\nu$ and $b \rightarrow c \rightarrow q'e\nu$ distributions. The

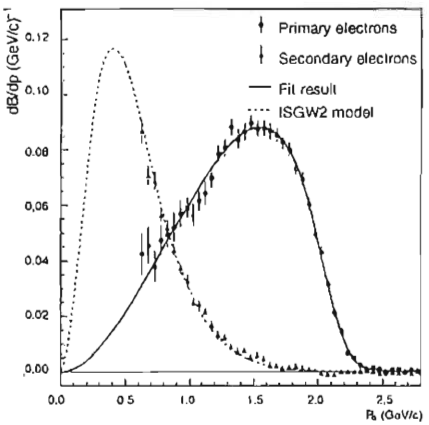

Figure 7: *Electron spectra for primary ($b \rightarrow qe\nu$) and secondary ($b \rightarrow c \rightarrow q'e\nu$) semileptonic decays. The fits are described in the text.*

$b \rightarrow qe\nu$ spectrum is fitted with a semi-empirical shape and the $b \rightarrow c \rightarrow q'e\nu$ spectrum with the ISGW2 model [7]. The branching fraction $\mathcal{B}(B \rightarrow Xe^+\nu_e) =$

$(10.90 \pm 0.12 \pm 0.49)\%$ where the first error is statistical and the second systematic, was obtained. The dominant sources of systematic uncertainties are the tracking efficiency (2.9%), electron identification (2.0%) and background subtraction (1.8%).

The contribution from charmless decays was subtracted and heavy quark effective theory was used to determine

$$|V_{cb}| = 0.0408 \pm 0.0010(\text{exp}) \pm 0.0025(\text{theo}), \tag{15}$$

where the first error is the statistical and systematic errors combined and the second error is from theoretical uncertainties.

6 Conclusions

The excellent performance of the KEKB accelerator and Belle detector have made it possible to perform high precession B meson mixing, lifetime and branching fraction measurements.

7 Acknowledgements

The author thanks the organisers for an informative and enjoyable conference and acknowledges the support of the Japanese Society for the Promotion of Science.

References

1. S. Mori *et al*, Nucl. Instrum. Meth. **A479**, 117–232 (2002).

2. N. C. Hastings *et al*, Phys. Rev. **D67**, 052004 (2003).

3. K. Hara *et al*, Phys. Rev. Lett. **89**, 251803 (2002).

4. T. Tomura *et al*, Phys. Lett. **B542**, 207–215 (2002).

5. K. Abe *et al*, Phys. Rev. Lett. **88**, 171801 (2002).

6. K. Abe *et al*, Phys. Rev. **D66**, 032007 (2002).

7. K. Abe *et al*, Phys. Lett. **B547**, 181–192 (2002).

RECENT RESULTS ON B PHYSICS AT D0

Heriberto Castilla
CINVESTAV-IPN, Mexico City Mexico

Written contribution not received

SESSION IV – HEAVY IONS PHYSICS

Sebastian White	Recent Results from the Heavy Ion Collider Program at RHIC
Vladimir R. Zoller	Decorrelation of Forward Dijets in DIS off Nuclei

Hard Scattering in RHIC Heavy Ion Collisions

Sebastian N. White
Brookhaven National Laboratory, Upton, NY 11973 USA

Abstract

The RHIC collider recently completed its third data taking run. The data on high p_t particle production in central Au-Au collisions exhibit striking differences from those of pp collisions. The measurment of inclusive spectra, particle correlations and their dependence on centrality(number of nucleon collisions) strongly favor a picture in which hard scattered partons re-interact with a medium of very high gluon density. Creating these conditions and measuring its properties is a primary goal of RHIC.

1 Introduction

Hadron production at high transverse momentum (p_t) has become an important tool for the study of Heavy Ion collisions. Since hard scattering processes occur early in the collision they are most likely to probe the initial partonic phase. High p_t particle production is calculable and well tested in pp collisions so it is a well understood probe. Finally, it is relatively straightforward to scale from a system approximating elementary pp interactions to one in which a large number of binary collisions occur. Both types of collisions are sampled in Heavy Ion data with a well defined relative frequency given by geometry (ie probability growing with impact parameter). The experimental tools for characterizing impact parameter are described in some detail below. The number of binary collisions is related to the nuclear overlap function by the Glauber model.

The four RHIC experiments (Brahms, Phenix, Phobos and Star) have measured high p_t spectra of identified hadrons out to x_t of 0.1 for central Au-Au collisions (with beam energies up to 100GeV/n) as well as for peripheral ones. The dramatic change in behavior with centrality is further confirmed by comparison data taken with pp and d-Au colliding beams. These are perhaps the most interesting results to come from RHIC to date.

A departure from binary scaling has been anticipated by theoretical calculations which predict a suppression of high p_t hadrons due to induced radiative energy loss in the dense field of partons also produced in the collision [3]. But a similar suppression has also been predicted based on saturation of gluon flux in the initial state of the colliding nuclei [4]. Suppression of high p_t hadrons would be also be seen in d-Au collisions according to the latter picture.

Qualitatively, the same suppression observed for mesons should also be seen for hadrons if in both cases the dominant source is hard scattering followed by fragmentation into hadrons.

2 Centrality Classification

The RHIC experiments [1] primarily measure particle spectra near 90^o in the lab. For example, the PHENIX experiment features both a magnetic spectrometer and an electromagnetic calorimeter (to measure charged particles and π^o, respectively) which subtend ± 0.35 in η. Two key parameters which characterize Heavy Ion collisions are depicted in Fig.1- the nuclear overlap and the orientation of the reaction plane. To varying degrees, these are measured with detectors in the forward direction.

The nuclear overlap (centrality) is related through the Glauber model to parameters which are expected to characterize the scaling of nuclear collisions with respect to more elementary NN interactions. These are- the number of participants (N_{part}) which approximately characterizes soft interactions and

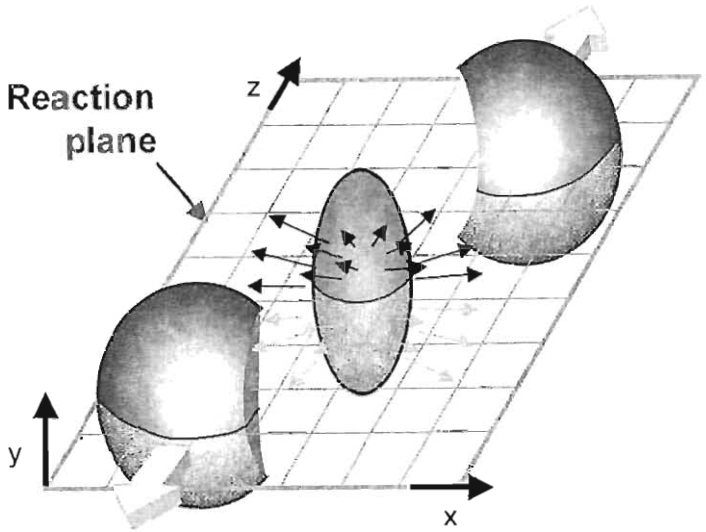

Figure 1: *Heavy Ion collision geometry.*

the number of binary collisions (N_{bin}) which is relevant for hard processes. Since both of these parameters increase monotonically with Nuclear overlap there tend to be equivalent methods to sort the data into centrality classes- for example, based on particle multiplicity in an independent region of phase space. Ideally the forward, "non-participant" remnants of the beam would give the least biased determination of overlap and reaction plane (and this method was used in fixed target experiments). However at a collider practical considerations allow only measurement of neutron remnant multiplicity and angle in Zero Degree Calorimeters (ZDC). Nevertheless the neutron multiplicity tag extends the sensitivity of the experiments to very peripheral collisions where particle multiplicities are low and efficiency corrections would otherwise dominate the centrality error.

The PHENIX experiment uses a combination of forward detectors- the Beam-Beam Counters and ZDC's -to measure reaction plane and overlap.

The reaction plane measurement is needed because the coordinate space anisotropy of the overlap region is reflected in the spectra of produced particles as a function of azimuthal angle relative to the plane,Φ. The "elliptic flow" parameter v_2 which measures the second harmonic of the flux vs. Φ increases steadily from AGS up to RHIC energies [7]. The dependence of elliptic flow on momentum and particle type is interesting in itself but also needs to be taknb into acoount when studying particle correlations in jets.

3 Global Event Characteristics

Early Measurements from RHIC included those of global event properties such as particle multiplicities and transverse energy. These can be used to calculate the initial energy density within 1 fm/c after the collision yielding $\sim$ 5

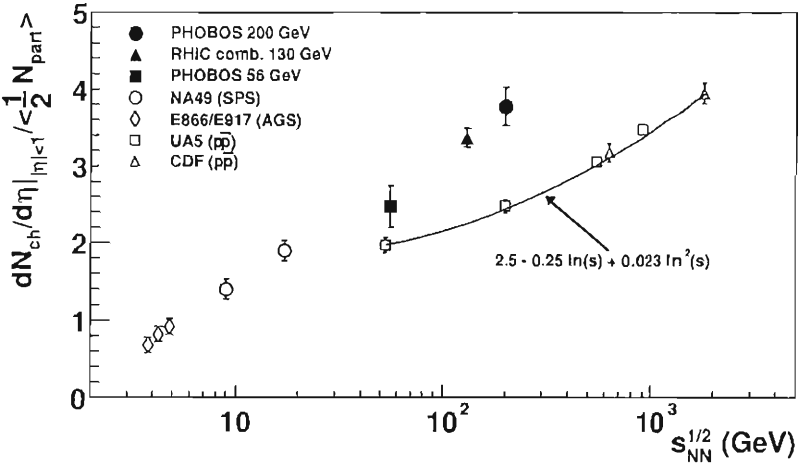

Figure 2: *Energy dependence of Charged Multiplicity.*

$25\mathrm{GeV}/fm^3$.

Fig.2 shows the dependence of the charged particle multiplicity (at mid-rapidity) on beam energy. The charged particle multiplicity grows approximately as log(s) and reaches a maximum of $\frac{dN^{ch}}{d\eta} \simeq 600$ in Au-Au collisions at RHIC. Extrapolating these data (as log(s)) to LHC energies gives about a factor of 2 higher multiplicity than RHIC.

PHENIX has also measured transverse energy density at mid-rapidity from which one can calculate that the average E_t per particle is about 800 MeV, essentially identical to what is found in SPS fixed target measurements.

4 Hadron Yields at High p_t

Hard scattering processes are expected to scale relative to pp collisions according to the number of binary collisions.To test this hypothesis we divide the Heavy ion yields by the corresponding inclusive spectra seen in pp data scaled by the average number binary collisions calculated for the same centrality class. This ratio, $R_{AA}(p_t)$, is called the nuclear modification factor. If Ion collisions were really just like multiple pp collisions then R=1 independent of p_t. Similarly the ratio of central to peripheral yields ($R_{CP}(p_t)$) scaled by their corresponding N_{bin} is sometimes reported. In this case the systematic uncertainties are dominated by errors in centrality class determination .

There is by now a significant amount of high ($p_t > 2\mathrm{GeV/c}$) data from all 4 RHIC experiments on inclusive charged particles as well as neutral pion and other identified hadrons. Fig. 3 shows the inclusive π^0 yield for central collisions in PHENIX. Also shown is the scaled yield in pp collisions. The

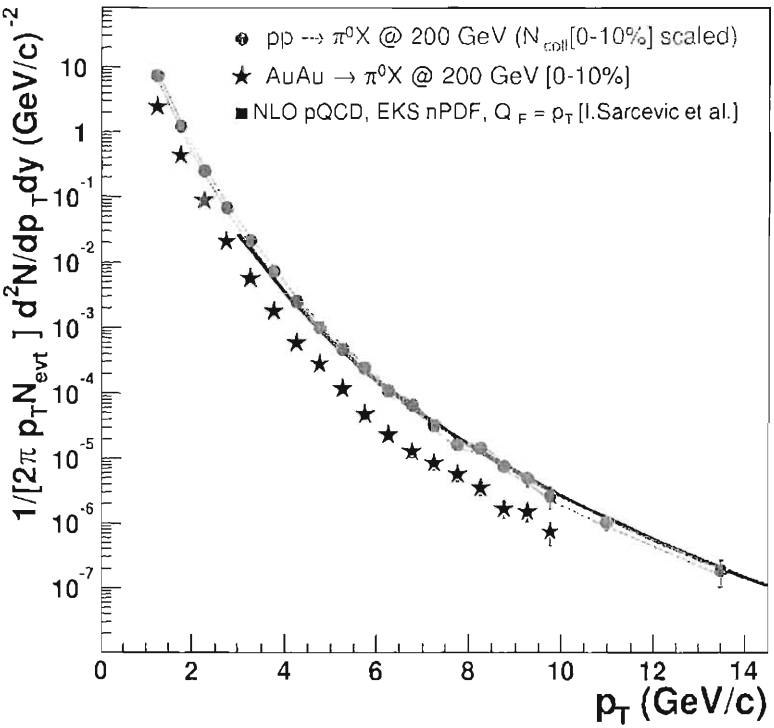

Figure 3: *PHENIX measurement of the π^0 yield in 10% highest centrality events compared to the scaled pp distribution.*

spectra from Central Au-Au collsions are suppressed by a factor of 4-5 relative to the expectations from binary collision scaling. No corresponding suppression is observed in more peripheral collisions.

The clear observation of modification in the inclusive hadron spectra is now complemented with new data from RHIC on other aspects of the particle spectra- their correlations and their dependence on particle species.

If the suppression of high pt hadrons results from parton energy loss in the dense medium related modification of associated hadrons forming back-to-back jets should yield further details of the jet modification mechanisms. Most of the time jet energies are too low at RHIC to reconstruct them above the underlying event energy. Nevertheless, the jet features can be reconstructed statistically from the correlations between high p_t hadrons and these are used to characterize the features of jet suppression vs. centrality [6]. This is illustrated in Fig. 4 which shows that the correlations due to particles in the same jet as the "trigger" hadron and the opposite side jet can be extracted in peripheral collisions and reproduce the features of pp jets. In central collisions, on the other hand, the opposite side correlations change dramatically and the far side jet is no longer visible above background.

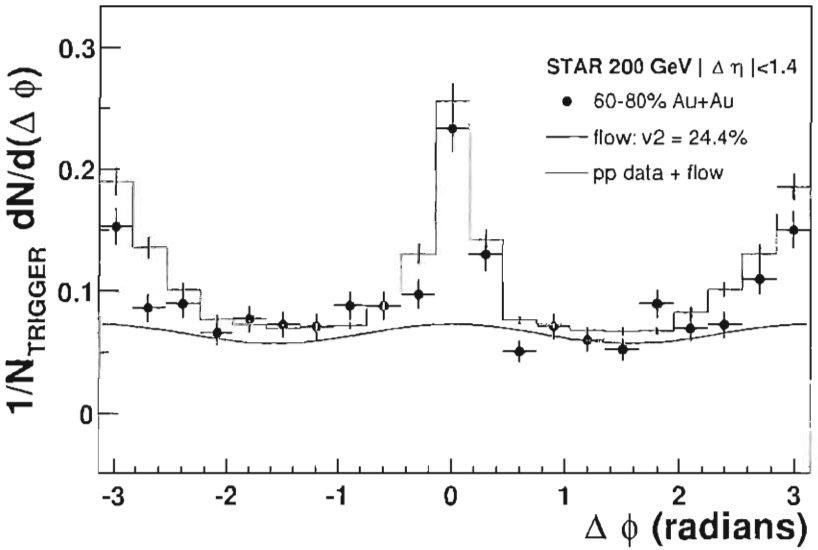

Figure 4: *Angular correlation of high p_t tracks with a 4-6 GeV/c "trigger" particle.*

The suppression at high p_t is strongly dependent on the hadron species. For example, there is no proton suppression in the 2-4 GeV/c p_t range. This would be surprising if hadrons are predominantly described by jet fragmentation. However there is growing evidence that hadron production in the momentum range studied in the present data is better described in terms of recombination of lower pt partons [8]. This is perhaps most clearly seen in the flow of identified hadrons vs p_t. Figure 5 illustrates this in the comparison of meson and baryon v2 parameters. If flow is characterizing the collective motion of partons before hadronization then the recombination mechanism for hadron production would predict a simple relation among hadrons depending on the number of valence quarks and this is very clearly seen in the data.

5 Conclusion

The first two runs of RHIC have brought an order of magnitude increase in cms energy over previous Heavy Ion data. Compared to previously available data their global properties follow a trend of continuous evolution in particle and energy density. However, the realm of hard scattering has changed dramatically with the increase in energy allowing for detailed studies of matter produced in this new energy regime. Subsequent runs will continue these studies with greater detail and new probes.

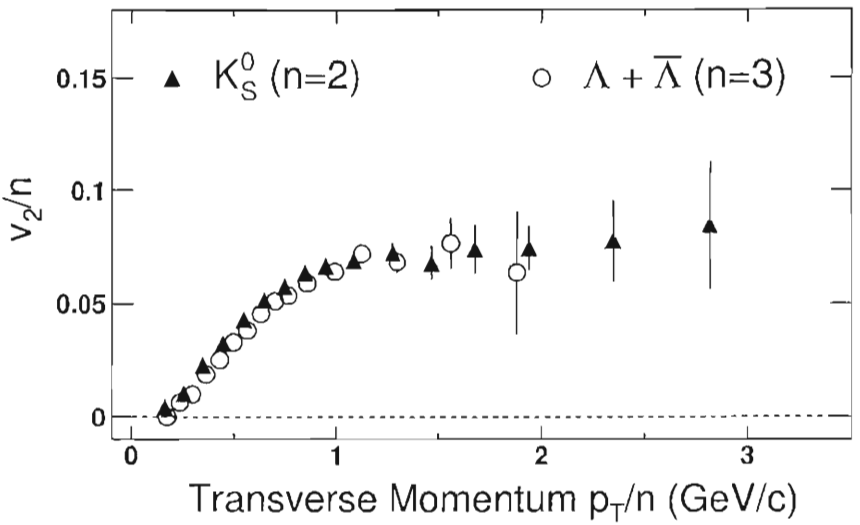

Figure 5: *Flow parameter dependence on particle type* .

6 Acknowledgements

I would like to thank the organizers for the opportunity to participate in a very stimulating and enjoyable meeting. This work was supported by the US Dept. of Energy.

References

1. A collection of articles on RHIC detectors may be found in Nucl. Instr. and Methods **A499**, pp.235-880 (2003).
2. B. Back *et al*, Phys. Rev. Lett. **85**, 3100 (2000).
3. X.N.Wang and M.Gyulassy, Phys. Rev. Lett. **68** 1480 (1992).
4. D. Kharzeev, E. Levin and L. McLerran, Phys. Lett. **B 561** 93(2003).
5. K. Adcox *et al*, Phys. Rev. Lett. **86**, 3500 (2001).
6. C. Adler *et al*, Phys. Rev. Lett. **90** 082302 (2003).
7. C. Alt *et al* nucl-ex/0303001.
8. D. Molnar and S.A. Voloshin, Phys.Rev.Lett.**91** 092301 (2003).

DECORRELATION OF FORWARD DIJETS IN DIS OFF NUCLEI

V.R. Zoller
ITEP, Moscow, Russia

Abstract

Based on the color dipole QCD approach we discuss the multiple scattering mechanism (MSM) of suppression of back-to-back azimuthal correlations of high p_T forward dijets in DIS off nuclei. We quantify the effect in terms of acoplanarity/decorrelation momentum of jets. For hard dijets the decorrelation momentum is found to be of the order of the nuclear saturation momentum Q_A. Minijets with the transverse momentum below the saturation scale are proved to be completely decorrelated. The analysis of DIS indicates that in heavy ion collisions the contribution of MSM to the reactions dynamics can be of the order of magnitude of the decorrelation effect observed at RHIC.

1 Introduction

Recent observation of gradual disappearance of azimuthal back-to-back correlations of high p_T particles with centrality of $AuAu$ collisions at RHIC [1] is presently viewed as a consequence of the jet energy loss in hot quark-gluon plasma produced in central collisions. Another possible explanation is that initial and final state interactions associated with multiple parton scatterings on hard stage of the process produce uncorrelated monojets.

To get an idea of the size of the multiple scatterings (MS) effect at RHIC we start with the QCD description of the breakup of photons into forward dijets in small-x deep inelastic scattering (DIS) off nuclei in the saturation regime [2]. In [2] we reported a derivation of the general formula for the two-body transverse momentum distribution. Our formalism, based on the technique [3, 4, 5], includes consistently the diffractive attenuation of color dipoles and effects of transitions between different color states of the $q\bar{q}$-pair propagating through the nucleus. Opacity of nuclei brings in a new scale Q_A which separates the regimes of opaque nuclei and weak attenuation [6, 7, 8, 9]. For hard dijets the decorrelation momentum is found to be of the order of the nuclear saturation momentum Q_A [2]. For parton momenta below the saturation scale Q_A the evolution of sea from gluons was shown to be dominated by the anti-collinear, anti-DGLAP splitting [9]. As a result, minijets with the transverse momentum below the saturation scale are proved to be completely decorrelated [2].

Turning back to the RHIC observation we argue that MS mechanism may contribute substantially to the effect of vanishing of back-to-back azimuthal correlations of high p_T hadrons in central nucleus-nucleus collisions.

2 Breakup of photons into hard dijets on nuclear targets

We consider DIS at $x \lesssim x_A = 1/R_A m_N \ll 1$ which is dominated by interactions of $q\bar{q}$ Fock states of the photon and make use of the conventional approximation of two t-channel gluons in DIS off free nucleons [10]. The two-gluon exchange approximation amounts to neglecting diffractive DIS off free nucleons which is justified by a small fraction of diffractive DIS, $\eta_D \ll 1$ [11]. We sum unitarity cuts of the forward Compton scattering amplitude which describe the transition from the color-neutral $q\bar{q}$ dipole to the color-octet $q\bar{q}$ pair. It should be emphasized that we are interested in the unitarity cuts which correspond to the genuine inelastic DIS with color excitation of the target nucleus.

For $x \lesssim x_A$ the propagation of the $q\bar{q}$ pair inside nucleus can be treated in the straight-path approximation. Let $\mathbf{b}_+$ and $\mathbf{b}_-$ be the impact parameters of the quark and antiquark, respectively, and $S_A(\mathbf{b}_+, \mathbf{b}_-)$ be the S-matrix for

interaction of the $q\bar{q}$ pair with the nucleus. Regarding the color states $|c\rangle = |1\rangle, |8\rangle$ of the $q\bar{q}$ pair, we sum over all octet and singlet states. Then the 2-jet inclusive spectrum is calculated in terms of the 2-body density matrix as

$$\frac{d\sigma_{in}}{dzd^2\mathbf{p}_+d^2\mathbf{p}_-} = \frac{1}{(2\pi)^4}\int d^2\mathbf{b}'_+d^2\mathbf{b}'_-d^2\mathbf{b}_+d^2\mathbf{b}_-$$
$$\times \exp[-i\mathbf{p}_+(\mathbf{b}_+ - \mathbf{b}'_+) - i\mathbf{p}_-(\mathbf{b}_- - \mathbf{b}'_-)]\Psi^*\Psi$$
$$\times\Big\{\sum_{A^*}\sum_c\langle 1;A|S^*_A|A^*;c\rangle\langle c;A^*|S_A|A;1\rangle$$
$$-\langle 1;A|S^*_A|A;1\rangle\langle 1;A|S_A|A;1\rangle\Big\}. \qquad (1)$$

In (1) $\Psi = \Psi(Q^2,z,\mathbf{b}_+ - \mathbf{b}_-)$ stands for the wave function of the $q\bar{q}$ Fock state of the photon with virtuality Q^2 and the photon light-cone momentum fraction z carried by the quark. Notice, that the calculation of the 2-body density matrix enter four straight-path trajectories $\delta^{(2)}(\mathbf{b}_\pm), \delta^{(2)}(\mathbf{b}'_\pm)$ and S_A and S^*_A describe the propagation of two quark-antiquarks pairs, $q\bar{q}$ and $q'\bar{q}'$, inside a nucleus. In the integrand of (1) we subtracted the coherent diffractive component of the final state.

Upon the application of closure to sum over nuclear final states A^* the integrand of (1) can be considered as an intranuclear evolution operator for the 2-body density matrix (for the related discussion see refs. [12], [13])

$$\sum_{A^*}\sum_c\langle A|\Big\{\langle 1|S^*_A|c\rangle\Big\}|A^*\rangle\langle A^*|\Big\{\langle c|S_A|1\rangle\Big\}|A\rangle =$$
$$= \langle A|\left\{\sum_c\langle 1|S^*_A|c\rangle\langle c|S_A|1\rangle\right\}|A\rangle. \qquad (2)$$

Let the eikonal for the quark-nucleon and antiquark-nucleon QCD gluon exchange interaction be $T^a_+\chi(\mathbf{b})$ and $T^a_-\chi(\mathbf{b})$, where T^a_+ and T^a_- are the $SU(N_c)$ generators for the quark and antiquarks states, respectively. The vertex V_a for excitation of the nucleon $g^aN \to N^*_a$ into color octet state is so normalized that after application of closure the vertex g^ag^bNN is δ_{ab}. Then, to the two-gluon exchange approximation, the S-matrix of the $(q\bar{q})$-nucleon interaction equals

$$S_N(\mathbf{b}_+,\mathbf{b}_-) = 1 + i[T^a_+\chi(\mathbf{b}_+) + T^a_-\chi(\mathbf{b}_-)]V_a - \frac{1}{2}[T^a_+\chi(\mathbf{b}_+) + T^a_-\chi(\mathbf{b}_-)]^2. \quad (3)$$

The profile function for interaction of the $q\bar{q}$ dipole with a nucleon is $\Gamma(\mathbf{b}_+,\mathbf{b}_-) = 1 - S_N(\mathbf{b}_+,\mathbf{b}_-)$. For a color-singlet dipole $(T^a_+ + T^a_-)^2 = 0$ and the dipole cross section for interaction of the color-singlet $q\bar{q}$ dipole with the nucleon equals

$$\sigma(\mathbf{b}_+ - \mathbf{b}_-) = 2\int d^2\mathbf{b}_+\langle N|\Gamma(\mathbf{b}_+,\mathbf{b}_-)|N\rangle$$

$$= \frac{N_c^2 - 1}{2N_c} \int d^2\mathbf{b}_+ [\chi(\mathbf{b}_+) - \chi(\mathbf{b}_-)]^2 \,. \tag{4}$$

The nuclear S-matrix of the straight-path approximation is

$$S_A(\mathbf{b}_+, \mathbf{b}_-) = \prod_{j=1}^{A} S_N(\mathbf{b}_+ - \mathbf{b}_j, \mathbf{b}_- - \mathbf{b}_j) \,,$$

where the ordering along the longitudinal path is understood. We evaluate the nuclear expectation value in (2) in the standard dilute gas approximation. To the two-gluon exchange approximation, per each and every nucleon N_j only the terms quadratic in $\chi(\mathbf{b}_j)$ must be kept in the evaluation of the single-nucleon matrix element $\langle N_j | S_N^* S_N | N_j \rangle$ which enters the calculation of $S_A^* S_A$. Following the technique developed in [4, 5] we can reduce the calculation of the evolution operator for the 2-body density matrix (2) to the evaluation of the S-matrix $S_{4A}(\mathbf{b}_+, \mathbf{b}_-, \mathbf{b}'_+, \mathbf{b}'_-)$ for the scattering of a fictitious 4-parton state composed of the two quark-antiquark pairs in the overall color-singlet state. Because $(T_+^a)^* = -T_-^a$, within the two-gluon exchange approximation the quarks entering the complex-conjugate S_A^* in (2) can be viewed as antiquarks, so that

$$\sum_c \langle 1 | S_A^* | c \rangle \langle c | S_A | 1 \rangle = \sum_{c'c} \delta_{c'c} \langle c'c | S_{4A} | 11 \rangle \,, \tag{5}$$

where $S_{4A}(\mathbf{b}'_+, \mathbf{b}'_-, \mathbf{b}_+, \mathbf{b}_-)$ is an S-matrix for the propagation of the two quark-antiquark pairs in the overall singlet state. While the first $q\bar{q}$ pair is formed by the initial quark q and antiquark $\bar{q}$ at impact parameters $\mathbf{b}_+$ and $\mathbf{b}_-$, respectively, in the second $q'\bar{q}'$ pair the quark q' propagates at an impact parameter $\mathbf{b}'_-$ and the antiquark $\bar{q}'$ at an impact parameter $\mathbf{b}'_+$.

If $\sigma_4(\mathbf{b}'_+, \mathbf{b}'_-, \mathbf{b}_+, \mathbf{b}_-)$ is the color-dipole cross section operator for the 4-body state, then the evaluation of the nuclear expectation value for a dilute gas nucleus in the standard approximation of neglecting the size of color dipoles compared to a radius of heavy nucleus gives [14]

$$S_{4A}(\mathbf{b}'_+, \mathbf{b}'_-, \mathbf{b}_+, \mathbf{b}_-) = \exp\{-\frac{1}{2}\sigma_4(\mathbf{b}'_+, \mathbf{b}'_-, \mathbf{b}_+, \mathbf{b}_-) T(\mathbf{b})\} \,, \tag{6}$$

where $T(\mathbf{b}) = \int db_z n_A(b_z, \mathbf{b})$ is the optical thickness of a nucleus at an impact parameter $\mathbf{b} = \frac{1}{4}(\mathbf{b}_+ + \mathbf{b}'_+ + \mathbf{b}_- + \mathbf{b}'_-)$, and $n_A(b_z, \mathbf{b})$ is nuclear matter density with the normalization $\int d^2\mathbf{b} T(\mathbf{b}) = A$. The single-nucleon S-matrix (3) contains transitions from the color-singlet to the both color-singlet and color-octet $q\bar{q}$ pairs. However, only color-singlet operators contribute to $\langle N_j | S_N^* S_N | N_j \rangle$, and hence the matrix σ_4 only includes transitions between the $|11\rangle$ and $|88\rangle$ color-singlet 4-parton states, the $|18\rangle$ states are not allowed.

After some color algebra, we find matrix elements $\sigma_{11} = \langle 11|\sigma_4|11\rangle$, $\sigma_{18} = \sigma_{81} = \langle 11|\sigma_4|88\rangle$ and $\sigma_{88} = \langle 88|\sigma_4|88\rangle$ (details of the derivation are presented in [2]). For forward hard jets with the momenta $\mathbf{p}_\pm^2 \gg Q_A^2$, which are produced from interactions with the target nucleus of small color dipoles in the incident photon the two eigenvalues of the operator σ_4 are

$$\Sigma_2 \approx \sigma_{11}$$

and

$$\Sigma_1 \approx \sigma_{88}.$$

For small color-singlet dipoles $\Sigma_2 \approx \sigma_{11} \approx 0$ and the nuclear distortion factor takes on a simple form

$$\sum_{A^*}\sum_{c}\langle A|\langle 1|S_A^*|c\rangle\langle c|S_A|1\rangle|A\rangle - \langle 1;A|S_A^*|A;1\rangle\langle 1;A|S_A|A;1\rangle$$

$$= (\langle 11| + \sqrt{N_c^2-1}\langle 88|)\exp\left\{-\frac{1}{2}\sigma_4 T(\mathbf{b})\right\}\cdot|11\rangle - \exp\left\{-\frac{1}{2}\sigma_{11}T(\mathbf{b})\right\}$$

$$\approx \sqrt{N_c^2-1}\,\frac{\sigma_{18}}{\sigma_{88}}\left\{1-\exp\left[-\frac{1}{2}\sigma_{88}T(\mathbf{b})\right]\right\}. \qquad (7)$$

The introduction of this nuclear distortion factor into (1) gives the hard dijet inclusive cross section:

$$\frac{d\sigma_{in}}{d^2\mathbf{b}dzd^2\mathbf{p}_+d^2\mathbf{\Delta}} = T(\mathbf{b})\sum_{j=0}^{\infty} w_A(\mathbf{b},j)\int d^2\boldsymbol{\kappa} f^{(j)}(\mathbf{\Delta}-\boldsymbol{\kappa})\frac{d\sigma_N}{dzd^2\mathbf{p}_+d^2\boldsymbol{\kappa}}. \qquad (8)$$

where the acoplanarity/decorrelation momentum $\mathbf{\Delta}$ is

$$\mathbf{\Delta} = \mathbf{p}_+ + \mathbf{p}_-,$$

the probability of finding j spatially overlapping nucleus in a Lorentz-contracted nucleus is

$$w_A(\mathbf{b},j) = \frac{1}{j!}\frac{\gamma(j+1,2\lambda_c\nu_A(\mathbf{b}))}{2\lambda_c\nu_A(\mathbf{b})},$$

$$\nu_A(\mathbf{b}) = \frac{1}{2}\alpha_S\sigma_0 T(\mathbf{b}),$$

$$\lambda_c = N_c^2/(N_c^2-1)$$

and $\gamma(j,x) = \int_0^x dy y^{j-1}\exp(-y)$ is an incomplete gamma-function. The function

$$f^{(j)}(\boldsymbol{\kappa}) = \int\prod_{i=1}^{j} d^2\boldsymbol{\kappa}_i f(\boldsymbol{\kappa}_i)\delta(\boldsymbol{\kappa}-\sum_{i=1}^{j}\boldsymbol{\kappa}_i), \quad f^{(0)}(\boldsymbol{\kappa}) = \delta(\boldsymbol{\kappa}) \qquad (9)$$

in eq.(8) is a collective gluon field of j overlapping nucleons introduced in [15].

The probabilistic form of a convolution of the differential cross section on a free nucleon target with the manifestly positive defined distribution $f^{(j)}(\kappa)$ in (8) can be understood as follows. Hard jets originate from small color dipoles. It is the quantum mechanical interference that suppresses interaction with soft gluons of the small-sized color-singlet $q\bar{q}$ state. However, the first inelastic interaction inside a nucleus converts the $q\bar{q}$ pair into the color-octet state, in which color charges of the quark and antiquark do not neutralize each other, rescatterings of the quark and antiquark in the collective color field of intranuclear nucleons become uncorrelated, and the broadening of the momentum distribution with nuclear thickness follows a probabilistic picture.

3 Decorrelation of dijets in DIS off nuclei: numerical estimates

To quantify the azimuthal decorrelation of two forward jets we find it convenient to introduce the mean transverse acoplanarity momentum squared $\langle \mathbf{\Delta}_T^2(\mathbf{b}) \rangle$, where $\mathbf{\Delta}_T$ is transverse to an axis of the jet with higher momentum. It is assumed that jets are hard, $|\mathbf{p}_+| \gg Q_A$. The convolution property of the hard dijet cross section (8) suggests

$$\langle \mathbf{\Delta}_T^2(\mathbf{b}) \rangle_A \approx \langle \boldsymbol{\kappa}_T^2(\mathbf{b}) \rangle_A + \langle \mathbf{\Delta}_T^2 \rangle_N \,, \tag{10}$$

where $\langle \mathbf{\Delta}_T^2 \rangle_N$ refers to DIS on a free nucleon, and $\langle \boldsymbol{\kappa}_T^2(\mathbf{b}) \rangle_A$ is the nuclear broadening term The sign $\approx$ in (10) reflects the kinematical limitations on $\mathbf{p}_-$ and $\boldsymbol{\kappa}$ in the practical evaluation of the acoplanarity distribution. In a typical final state it is the harder jet with larger transverse momentum which defines the jet axis and the acoplanarity momentum $\mathbf{\Delta}$ will be defined in terms of components of the momentum of softer jet with respect to that axis, for instance, see [16]. For the sake of definiteness, we present numerical estimates for the Gedanken experiment in which we classify the event as a dijet if the quark and antiquark are produced in different hemispheres, i.e., if the azimuthal angle ϕ between two jets exceeds $\pi/2$, the quark jet has fixed $|\mathbf{p}_+|$ and the antiquark jet has higher transverse momentum $|\mathbf{p}_+| \lesssim |\mathbf{p}_-| \lesssim 10|\mathbf{p}_+|$ (in the discussion of the experimental data one often refers to the higher momentum jet as the trigger jet and the softer jet as the away jet [16]). The free-nucleon quantity $\langle \mathbf{\Delta}_T^2 \rangle_N$ can be estimated starting with the small-$\mathbf{\Delta}$ expansion for excitation of hard, $\mathbf{p}_+^2 \gg \varepsilon^2 = z(1-z)Q^2$, light flavor dijets from transverse photons

$$\begin{aligned} \frac{d\sigma_N}{dz d^2\mathbf{p}_+ d^2\mathbf{\Delta}} &\approx \frac{1}{\pi} e_f^2 \alpha_{em} \alpha_S(\mathbf{p}_+^2) \left[z^2 + (1-z)^2 \right] \\ &\times \frac{1}{\Delta^4} \cdot \frac{\partial G(x, \Delta^2)}{\partial \log \Delta^2} \cdot \frac{\Delta^2}{(\varepsilon^2 + \mathbf{p}_+^2)(\varepsilon^2 + \mathbf{p}_+^2 + \mathbf{\Delta}^2)} \,, \end{aligned} \tag{11}$$

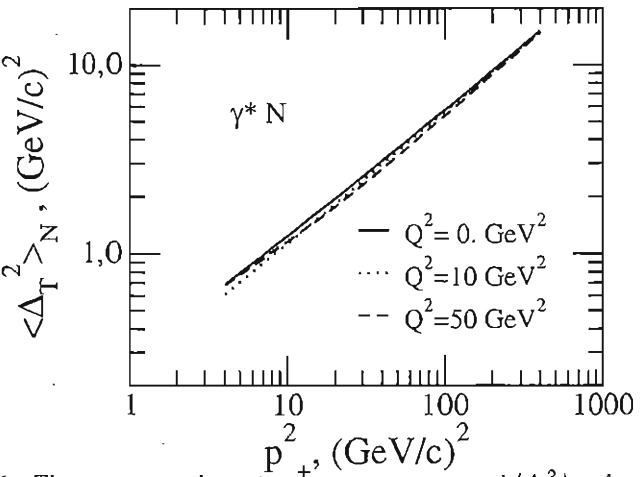

Figure 1: *The mean acoplanarity momentum squared* $\langle \mathbf{\Delta}_T^2 \rangle_N$ *for DIS on a free nucleon target with production of trigger jets with the transverse momentum higher than* $\mathbf{p}_+$ *for several values of* Q^2. *The numerical results are for* $x = 0.01$ *and the input unintegrated gluon SF of the proton is taken from ref.* [17].

where $\partial G(x, \mathbf{\Delta}^2)/\partial \log \mathbf{\Delta}^2 = \mathcal{F}(x, \mathbf{\Delta}^2)$ is the unintegrated gluon structure function (SF) of the free nucleon [17]. Then a quick estimate

$$\langle \mathbf{\Delta}_T^2 \rangle_N \approx \mathbf{p}_+^2 \frac{\mathcal{F}(x, \mathbf{p}_+^2)}{2G(x, \mathbf{p}_+^2)}, \tag{12}$$

correctly describes the numerical results shown in fig. 1. As far as the dijets are hard, $\mathbf{p}_+^2 \gtrsim z(1-z)Q^2 \sim \frac{1}{4}Q^2$, the acoplanarity momentum distribution would not depend on Q^2, which holds still better if one considers $\sigma_T + \sigma_L$. This point is illustrated in fig. 1, where we show $\langle \mathbf{\Delta}_T^2 \rangle_N$ at $z = 1/2$ for several values of Q^2. Because of this weak dependence on Q^2 here-below we make no distinction between DIS and real photoproduction, $Q^2 = 0$. In the practical evaluations of the nuclear contribution $\langle \kappa_T^2(\mathbf{b}) \rangle_A$ one can use the eq.(8) which gives the result

$$\langle \kappa_T^2(\mathbf{b}) \rangle_A \approx \frac{1}{2} \lambda_c Q_A^2(\mathbf{b}) \left[\log \frac{2p_+}{\sqrt{\lambda_c} Q_A(\mathbf{b})} - 1 \right], \tag{13}$$

where

$$Q_A^2(\mathbf{b}) \approx \frac{4\pi^2}{N_c} \alpha_S(Q^2) G(x, Q^2) T(\mathbf{b}). \tag{14}$$

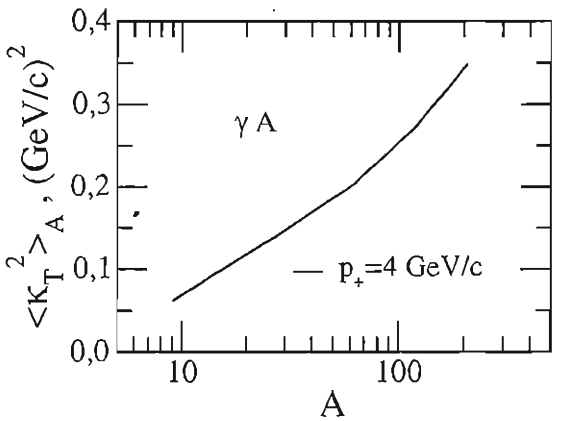

Figure 2: *The atomic mass number dependence of nuclear broadening contribution, $\langle \kappa_T^2(\mathbf{b}) \rangle_A$, to the mean acoplanarity momentum squared for real photoproduction off nuclei at $x = 0.01$. The input unintegrated gluon SF of the proton is taken from ref.* [17].

For average DIS on heavy nuclei the reference value is $\langle Q^2_{Au}(\mathbf{b}) \rangle = 0.9$ $(GeV/c)^2$, see [2]. The atomic mass number dependence of nuclear broadening $\langle \kappa_T^2 \rangle_A$ for jets with $p_+ = 4$ GeV/c in average DIS off nucleus is shown in fig. 2. The principal reason why $\langle \kappa_T^2 \rangle_A$ is numerically small compared to $\langle Q^2_{Au}(\mathbf{b}) \rangle$ is that even for such a heavy nucleus as ^{197}Au the no-broadening probability in average DIS is large, $\langle w_{Au}(\mathbf{b}, 0) \rangle \approx 0.5$. A comparison of the free nucleon broadening $\langle \Delta_T^2 \rangle_N$ from fig. 1 with the nuclear contribution $\langle \kappa_T^2(\mathbf{b}) \rangle_A$ from fig. 2 shows that the nuclear mass number dependence of azimuthal decorrelation of dijets in average DIS off nuclei will be relatively weak.

However, nuclear broadening will be substantially stronger for a subsample of central DIS events at $\mathbf{b} \sim 0$. In fig. 3 we show for the gold, ^{197}Au, target a dependence of the averaged nuclear broadening $\langle \kappa_T^2(\mathbf{b}) \rangle_A$ on the impact parameter at several values of p_+.

One can enhance Q_A^2 and nuclear contribution $\langle \kappa_T^2(\mathbf{b}) \rangle_A$ still further selecting DIS events when the photon breaks up into the $q\bar{q}$ pair on the front face of a nucleus. Experimentally, precisely such events are isolated by selecting very large multiplicity or very high transverse energy of produced secondary particles ([16] and references therein).

Now we comment on the recent finding by the STAR collaboration of a disappearance of back-to-back high p_T hadron correlation when going from peripheral to central gold-gold collisions at RHIC [16]. The application of

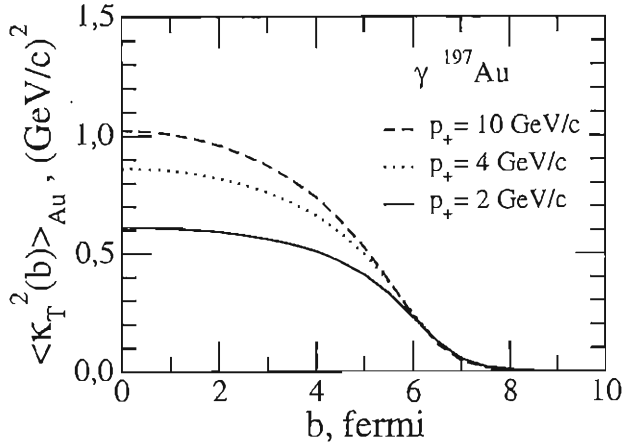

Figure 3: *The impact parameter dependence of the nuclear broadening contribution,* $\langle\kappa_T^2(\mathbf{b})\rangle_A$, *to the mean acoplanarity momentum squared from peripheral DIS at large impact parameter to central DIS at* $\mathbf{b}=0$ *for several values of the away jet momentum* p_+. *The numerical results are for* $x=0.01$ *and the input unintegrated gluon SF of the proton is taken from ref.* [17].

color dipole formalism to hard hadron-nucleus interactions [4] suggests that our analysis of acoplanarity of forward hard jets can be readily generalized to mid-rapidity jets. One only has to choose an appropriate system of dipoles, for instance, the open heavy flavor production can be treated in terms of the intranuclear propagation of the gluon-quark-antiquark system in the overall color-singlet state. At RHIC energies jets with moderately large p_T are for the most part due to gluon-gluon collisions. In our language that can be treated as a breakup of gluons into dijets and azimuthal decorrelation of hard jets must be discussed in terms of intranuclear propagation of color-octet gluon-gluon dipoles. For such gluon-gluon dipoles the relevant saturation scale Q_{8A}^2 is larger [18] than that for the quark-antiquark dipoles by the factor $2\lambda_c = C_A/C_F = 9/4$. Arguably, in central nucleus-nucleus collisions distortions in the target and projectile nuclei add up and the effective thickness of nuclear matter is about twice of that in DIS. Then, the results shown in fig. 2 suggest that for central gold-gold collisions the nuclear broadening of gluon-gluon dijets could be quite substantial, $\langle\kappa_T^2(\mathbf{b}=0)\rangle_{AuAu}$ ~(3-4) $(GeV/c)^2$ for average central $AuAu$ collisions and even twice larger if collisions take place at front surface of colliding nuclei.

The principal effect of nuclear broadening is a reduction of the probability

of observing the back-to-back jets

$$P(b) \approx \frac{\langle \Delta_T^2 \rangle_N}{\langle \kappa_T^2(\mathbf{b}) \rangle_A + \langle \Delta_T^2 \rangle_N} \tag{15}$$

and one needs to compare $\langle \Delta_T^2 \rangle_N$ to $\langle \kappa_T^2(\mathbf{b}) \rangle_A$. Our eq. (12) for the free nucleon case holds as well for the gluon-gluon collisions. Then the results shown in fig. 1 entail $\langle \Delta_T^2 \rangle_N \approx \langle \kappa_T^2(0) \rangle_{AuAu}$ ~(3-4) $(GeV/c)^2$ at the jet momentum $p_+ = p_J$ = (6-8) GeV/c and our nuclear broadening would become substantial for all jets with p_+ below the decorrelation threshold momentum p_J. In practice, the STAR collaboration studied the azimuthal correlation of two high-p_T hadrons and for the quantitative correspondence between the STAR observable and azimuthal decorrelation in the parent dijet one needs to model fragmentation of jets into hadrons (for the modern fragmentation schemes see [19]), here we notice that the cutoff p_+ in our Gedanken experiment is related to the momentum cutoff $p_{T,min}$ of associated tracks from the away jet, whereas our jet of momentum $\mathbf{p}_-$ can be regarded as a counterpart of the trigger jet of STAR. The STAR cutoff p_T = 2GeV/c corresponds to the parents jets with the transverse momentum $p_+ \sim (2-3)p_T$ =(4-6) GeV which is comparable to, or even smaller than, the decorrelation threshold momentum p_J = (6-8) GeV/c. Then eq. (15) suggests that in the kinematics of STAR the probability to observe the back-to-back away and trigger jets decreases approximately twofold from peripheral to central $AuAu$ collisions,

$$P(0) \approx 0.5\,,$$

and perhaps even stronger, so that our azimuthal decorrelation may contribute substantially to the STAR effect.

4 Remark on breakup of photons into semihard dijets

In our previous analysis [9] of the single particle spectrum it has been discovered that the transverse momentum distribution of sea quarks is dominated by the anticollinear, anti-DGLAP splitting of gluons into sea, when the transverse momentum of the parent gluons is larger than the momentum of the sea quarks. That suggests strongly a complete azimuthal decorrelation of forward minijets with the transverse momenta below the saturation scale, $p_\pm \lesssim Q_A$. In [2] this limiting case has been considered in detail. The principal point is that the minijet-minijet inclusive cross section depends on neither the minijet nor decorrelation momentum. This observation proves a disappearance of the azimuthal correlation of minijets with the transverse momentum below the saturation scale.

5 Acknowledgments

It is a pleasure to thank Mario Greco for inviting me to talk. Special thanks to all organizers for making the Conference run so smoothly.

References

1. S. White, these proceedings.
2. N.N. Nikolaev,W. Schäfer, B.G. Zakharov, V.R. Zoller, Nonlinear k_T-factorization for Forward Dijets in DIS off Nuclei in the Saturation Regime, e-Print Archive: hep-ph/0303024
3. N.N. Nikolaev and B.G. Zakharov, Z. Phys. **C49**, 607 (1991).
4. N.N. Nikolaev, G. Piller and B.G. Zakharov, J. Exp. Theor. Phys. **81**, 851 (1995); Z. Phys. **A354**, 99 (1996). 115
5. B.G. Zakharov, JETP Lett. **63**, 952 (1996); JETP Lett. **65**, 615 (1997); Phys. Atom. Nucl. **61**, 838 (1998).
6. A.H. Mueller, Nucl. Phys. 285 **B558** (1999) 285; Lectures at the Cargèse Summer School, August 6-18, 2001, `arXiv:hep-ph/0111244`.
7. A.H. Mueller, Nucl. Phys. **B335** 115 (1990).
8. L. McLerran and R. Venugopalan, Phys. Rev. **D49**, 2233 (1994); **D55**, 5414 (1997); E. Iancu, A. Leonidov and L. McLerran, Lectures at the Cargèse Summer School, August 6-18, 2001, `arXiv:hep-ph/0202270`.
9. N.N. Nikolaev, W. Schäfer, B.G. Zakharov, V.R. Zoller, JETP Lett. **76**, 195 (2002).
10. J.F. Gunion and D.E. Soper, Phys.Rev. **D15**, 2617 (1977).
11. M. Genovese, N.N. Nikolaev and B.G. Zakharov, J. Exp. Theor. Phys. **81**, 633 (1995); Zh. Eksp. Teor. Fiz. **108**, 1155 (1995).
12. B.G. Zakharov, Sov. J. Nucl. Phys. **46**, 92 (1987); Yad. Fiz. **46**, 148 (1987).
13. N.N. Nikolaev, J. Speth, B.G. Zakharov, J. Exp. Theor. Phys. **82** 1046 (1996); Zh. Eksp. Teor. Fiz. **109**, 1948 (1996).
14. R. J. Glauber, Lectures in Theoretical Physics,**1**, 315 (ed. W. E. Brittin et al. (Interscience Publishers, Inc., New York, 1959).

15. N.N. Nikolaev, W. Schäfer and G. Schwiete, JETP Lett. **72**, 583 (2000); Pisma Zh. Eksp. Teor. Fiz. **72**, 583 (2000); Phys. Rev. **D63**, 014020 (2001).

16. C. Adler, *et al.* (STAR Collaboration), Phys. Rev. Lett. **90**, 082302 (2003).

17. I.P.Ivanov and N.N.Nikolaev, Phys. Atom. Nucl. **64**, 753 (2001); Yad. Fiz. **64**, 813 (2001); Phys. Rev. **D65**, 054004 (2002).

18. N.N.Nikolaev and B.G.Zakharov, J. Exp. Theor. Phys. **78**, 806 (1994); Z. Phys. **C64**, 631 (1994).

19. T.Sjöstrand *et al.*, Comp. Phys. Commun. **135**, 238 (2001).

SESSION V – ELECTROWEAK AND TOP QUARK PHYSICS

Andrea Venturi	W Mass at LEP and Electronweak Fit Results
Thomas Schöner-Sadenius	LEP1 Heavy Flavour Electroweak Physics and 2–Fermion Process at LEP2
Bob Kehoe	Recent Run II Electroweak and Physics QCD Results from and DØ
Anyes Taffard	Electroweak and Top Physics at CDF in Run II
Marumi Kado	Recent Top Quark Physics Results from DØ
Boris I. Ermolaev	Forward-Backward Charge Asymmetry at Very High Energies
Charles A. Nelson	Consequences of a Large Top-quark Chiral Weak–Moment

W MASS AT LEP AND ELECTROWEAK FIT RESULTS

Andrea Venturi
Isitituto Nazionale di Fisica Nucleare, Sezione di Pisa
On behalf of the LEP Collaborations: ALEPH, DELPHI, L3 and OPAL

Abstract

One of the main physics goals of the second phase of the LEP collider program (LEP2) is the precise determination of the mass of the W boson. In this paper the measurements from the direct reconstruction of the invariant mass of the W^+W^- decay products, performed by the four Collaborations (ALEPH, DELPHI, L3 and OPAL) with the data collected at centre of mass energies from 172 to 209 GeV, are described. New updated preliminary results are presented and the evaluation of the systematic uncertainties is described. Finally the impact of this measurement on the global electroweak fit is discussed.

1 Introduction

The standard model of the electroweak interactions (SM), at the tree level, requires the knowledge of only three parameters (plus the fermions masses) to predict the masses of all the gauge bosons and their couplings to the fermions. Usually, Fermi's coupling G_F, Z mass M_Z and the fine structure constant α_{QED} are regarded as the input parameters because of their very precise determination. When higher order radiative corrections are introduced more parameters contributes to the model predictivity and the most important are: the top mass m_{top}, the QCD coupling constant α_s and the Higgs boson mass M_H. In this framework the relevance of the direct determination of the W boson mass M_W, together with m_{top}, is crucial and twofold. The direct measurement of M_W can be compared with the indirect determination obtained from the electroweak measurements at the Z resonance and from the neutrino scattering experiments, to test the SM, and it can be used to improve the indirect determination of M_H, the only parameter which has not been determined directly, yet.

The present indirect determination of M_W from the electroweak fit is: ${M_W}^{ind} = 80.373 \pm 0.032\,\text{GeV}$ [1] while the result of the direct measurement from Tevatron (and UA2) is: ${M_W}^{pp} = 80.454 \pm 0.059\,\text{GeV}$ [2].

In 1996 the LEP2 phase started and until 2000 the LEP e^+e^- collider was operated at centre of mass energies from 161 to 209 GeV, which exceeded the W pair production threshold. About $700\,\text{pb}^{-1}$ where collected by each experiment (90% at centre of mass energies close to or larger than 189 GeV) which correpond to a yield of slightly less than ten thousands identified WW events by each LEP experiment.

The precise measurement of the W mass has been one of the main physics goals of LEP2 project. An early determination was perfomed by measuring the WW production cross section at the threshold ($\sqrt{s} = 161, 172\,\text{GeV}$): ${M_W}^{thr} = 80.400 \pm 0.220 \pm 0.025_{LEP}\,\text{GeV}$. Then, from $\sqrt{s} = 172\,\text{GeV}$, the W mass has been measured from the direct reconstruction of the invariant mass of the W^+W^- decay products in fully hadronic (qqqq) and semileptonic ($\ell\nu$qq) final states, which correspond to 46% and 44% of the WW events, respectively. This method is by far the most precise at LEP and it will be described in more details in the following of this paper. Another determination of M_W, using the fully leptonic final states ($\ell\nu\ell\nu$) (10% of the WW pairs), was performed by ALEPH and OPAL but it has, practically, no impact on the combined result due to the poor statistical accuracy.

2 Analysis Technique

2.1 Event Selection

The direct W mass reconstruction is performed with fully hadronic and semileptonic events. The fully hadronic events are selected as high multiplicity events with small missing energy. All the four experiments use multivariate techniques to separate the signal from the dominant background which consists in 4 jets-like QCD events. The efficiencies range between 83% and 89% and the purities between 85% and 88%. The semileptonic events are selected by looking for an isolated electron or muon, with loose identification cuts, or for low multiplicity jets from τ decays. Multivariate techniques are used for these channels, as well, achieving purities of about 90-99%. About 4500 $W^+W^- \rightarrow qqqq$ events and 4000 $W^+W^- \rightarrow qq\ell\nu$ events have been collected and used for the W mass measurement by each experiment.

2.2 Event Reconstruction and Kinematic Fit

The direct reconstruction of the W mass requires: a good reconstructed invariant mass resolution, the knowledge of the neutrino momentum in the semileptonic events to reconstruct both W's masses and a highly efficient procedure to assign the final state particles to one of the two W's, particularly in the fully hadronic events.
At an e^+e^- collider like LEP, where the produced events are almost monoenergetic and with null total momentum, the first two requirements are fulfilled by perfoming a kinematic fit with the constraints of the total energy equal to the LEP beams energy and null total momentum. Firstly the isolated lepton, in semileptonic events, and the hadronic jets from W's decays (4 or 2 jets in fully hadronic or semileptonic events, respectively), are reconstructed using the charged tracks and the calorimeter deposits. Subsequently their 4-momenta are changed within the expected resolutions to fulfill the four constraints (4C). For semileptonic events with e or μ the null total momentum constraint is used to determine the neutrino momentum and therefore only one constraint is left for the fit (1C). The resolution can be further improved by requiring in the fit that the two W masses are equal (5C or 2C). In addition OPAL and DELPHI allows the jet clusterization in 5 or 3 jets to improve the reconstruction of events with a hard radiated gluon. In the $\tau\nu qq$ events the energy of the τ is badly reconstructed because of the additional escaping neutrinos, therefore only the mass of the hadronically decaying W is measured by performing a fit requiring the W energy to be equal to the beam energy. The resolution of the reconstructed mass is improved by a factor 3-4 by the kinematic fit, depending on the event final state and on the use of the equal mass constraint, and it ranges between 2 and 3 GeV, typically.

After the clustering in four (five) jets the fully hadronic events have a six-(ten-)fold ambiguity in the jet pairing. ALEPH chooses the combination with the largest WW production matrix element or the second largest if it has a smaller sum of the di-jet opening angles, OPAL selects the combination with the largest value of a relative likelihood built, for the 4 jets case, with the two masses difference and the sum of the di-jet opening angles, L3 retains the two combinations with the largest 5C fit likelihood while DELPHI builds, for each event, the likelihood of the kinematic fit as a function of the two W masses combining all the jet pairings weighted using the jet charge and the production angle information. The purity of these pairing algorithms range between 80 and 90% of correct pairings.

2.3 Mass Extraction

Once the events are reconstructed and the kinematic fit has been performed estimators are determined and used to measure M_W. Typical estimators are the two reconstructed di-jet, or lepton-neutrino, invariant masses (or the combined one if the equal mass constraint is applied), and their estimated statistical uncertainties, as obtained from the kinematic fit. To exploit the full statistical power, in the fully hadronic channel, DELPHI combine the full kinematic fit likelihood, as a function of the masses, of each event.
Because of effects like initial state radiation (ISR), which affects the kinematic fit constraints, detector resolutions and thresholds and particle losses in the beam hole, these mass estimators have a bias which, on average, is about 200-300 MeV. Therefore simulated events are used to correct for it. ALEPH, L3 and OPAL adopt a Monte Carlo re-weighting technique: the estimator distributions, for example the reconstructed mass spectra, in the data are compared to the same distributions in simulated weighted events whose weights depend on the W mass, according to the matrix element calculation of a four-fermion generator. DELPHI extracts the W mass value by maximizing the combination of the event likelihood functions (from the kinematic fit for the hadronic channel and from the convolution of the Breit-Wigner and a Gaussian for the semileptonic channels) and then correcting for the bias with calibration curves estimated from simulated events.
To measure the width of the W boson Γ_W the same procedures described above are followed but instead of constraining the W width to the W mass according to the SM, a two parameter fit is performed.

3 New Results and LEP Combination Procedure

For the winter conferences 2003 a new set of preliminary results, using the data collected between 183 and 207 GeV, has been presented by the ALEPH

collaboration [3]. These new results are due to a change in the reconstruction of the neutral deposits in the electromagnetic calorimeter (ECAL). Deposits confined in a single ECAL stack, out of the three stacks ECAL is segment into in depth, are removed from the event reconstruction and, in $e\nu qq$ and $\mu\nu qq$ events, the opening angle of the cone around the lepton, which contains the deposits which are not used for the hadronic jets, has been increased from 2 to 8 degrees. On average about 2% of the total energy is affected. This event "cleaning" has been motivated by the poor simulation of the multiplicity of these deposits both the in the standard ALEPH ECAL simulation, based on a parametrized version of the EGS simulation of the e.m. showers, and in a test simulation based on the complete EGS simulation. After the "cleaning" the agreement is improved, in particular with the full EGS simulation, which has been used for the systematic uncertainty estimation. With respect to the previous results, the new ALEPH results are lower by about 50 MeV in the fully hadronic channel, 85 MeV in the semileptonic channels and up to 150 MeV in the $e\nu qq$ channel. The systematic uncertainties due to calorimeter simulation have been increased by about 5-10 MeV with respect to the previous results.

For the determination of the LEP-wide result [4], each experiments provided a set of measurements of M_W obtained with the qqqq and $\ell\nu qq$, separately, for each centre of mass energy point, together with the corresponding statistical and systematic uncertainties and correlations. The LEP result is obtained by combining those results to minimize the combined uncertainty. Therefore the combined result is dominated by the systematic uncertainties which are correlated among the experiments and among the energy points. Presently, being all the data, but OPAL's 205-207 GeV data, analyzed, the statistical and systematic uncertainties of the combined preliminary result are 29 MeV and 31 MeV, respectively. In the following section a detailed description of the main systematic uncertainties is presented.

4 Systematic uncertainties

4.1 LEP beam energy

The powerful tool of the total energy constraint used by the kinamatic fit, introduces a dependence of the measured M_W upon the knowledge of the LEP beam energy E_b. The uncertainty on the determination of E_b translates into an uncertainty on M_W approximately as follows: $\Delta M_W/M_W \simeq \Delta E_b/E_b$. At LEP2 the beam energy is measured using the resonant depolarization technique to calibrate accurately the magnetic field measurement obtained with NMR probes up to 60 GeV and then extrapolating this calibration up to the physics energies using the NMR magnetic field measurement. This exatrapolation is checked with dedicated flux-loop measurements. The present uncertainty, dominated

by the spread between the two determinations, is ΔE_b = 20-25 MeV [5] which translates into an uncertainty of about 17 MeV on the W mass. Work is in progress to cross-check the final results and, possibly, reduce the uncertainty, with a beam spectrometer and with the measurement of the sychrotron tune which allow a determination of the beam energy from the beam deflection and the beam energy losses, respectively.

4.2 Fragmentation and Hadronization

The simulation of the fragmentation and hadronization of the partons produces by the event generators is performed using phenomenological models. This step of the event generation affects particle spectra, angular distributions and baryon/meson rate. The interplay of these quantities with the detector finite resolutions and thresholds introduce an uncertainty on M_W due to the uncertainty on the fragmentation models.
All the LEP collaborations rely upon the JETSET string model for their simulation and upon their own tuning of this model obtained by comparing the huge amount of LEP1 data at the Z resonance with the MC simulations.
The systematic uncertainty on M_W due to the fragmentation and hadronization simulation is estimated by comparing the M_W results obtained with different MC models, like Herwig and Ariadne, or by varying the internal JETSET parameters within their tuning uncertainties and, partially, by comparing real data with MC events and reweighting MC events to improve the agreement of event shape variables or particle production rates. The present range of uncertainties is ΔM_W = 10-30 MeV, depending on the channel and on the experiment and the average contribution to the LEP combined result is ΔM_W = 18 MeV, since this uncertainty is treated as correlated among the channels and the experiments.

4.3 Final State Interactions

The uncertainty due to the so called final state interactions (FSI) affects only the M_W measurements from the qqqq channel and can be considered as an additional uncertainty due to fragmentation and hadronization. W bosons are so short living ($\sim$ 0.1 fm) compared to the hadronization scale ($\sim$ 1 fm) that the hadronic decay products of the two W's can interact among each other. Roughly speaking we cannot ask ourselves which W a particle comes from and practically this affects the reconstructed W mass ditributions. Since these effects are not included in the usual MC fragmentation models, they are a possible source of bias for the M_W measurement.
The processes which are considered as sources of FSI are the colour reconnection (CR) [6], which is due to the interference between QCD amplitudes where colour

singlets are produced across decay products of different W's, and the Bose-Einstein correlation (BEC) [7], which enhance the production of identical pions close in the phase space and could be effective also for pions from different W's. Both CR and BEC are important only at the end of the hadronic shower or after the hadronization, therefore a full MC simulation is impossible and the prediction of their effects relies on phenomenological MC models.
Since this additional uncertainty affects only the M_W determination with the qqqq channel, its weight in the combined result is reduced and it depends strongly on the size of this uncertainty.

4.3.1 *Colour Reconnection*

The prediction about the M_W bias due to CR effects have been studied using several MC models which have not been rejected by a comparison with LEP1 data, when possible: SK models (I,II,II') [8], implemented in JETSET, Herwig [9], Ariadne 2 [10] and GAL [11]. When possible they have been tuned using Z resonance data and this is not the case for the SK models. The predicted M_W biases range from 30 to 80 MeV for Herwig, the lowest one, GAL and Ariadne II, the largest one, while SKI model has a free parameter k_i which allows to vary the fraction of "colour reconnected" events and, consequently, the M_W bias which can be up to 300 MeV for 100% reconnected events and about 40 MeV for 30% of reconnected events, a value suggested by the authors of SKI.
Since Summer 2002 a different procedure has been followed to estimate the CR uncertainty of the LEP combined M_W result. Instead of using the theorists' driven approach and quote the bias predicted by SKI with 30% of reconnected events, it was decided to use a data-driven approach where the decision about the models and the model parameter values to be used is based on analyses, sensitive to CR effects, which compare the real data to the CR MC models. Presently the analysis used by the LEP collaborations is the measurement of the particle flow in the inter-jet regions in fully hadronic W^+W^- events [12]. The density of particle, projected in the inter-jet plane and normalized to the di-jet opening angle, is compared between the inter-W and the intra-W regions and compared to the predictions of the MC models with and without CR. The present results show no sensitivity to observe or exclude CR effects for Herwig and Ariadne models while for the SKI model the one-sigma upper limit is $k_i = 2.13$ which corresponds to a bias of 74 MeV at $\sqrt{s} = 172$ GeV and 105 MeV at $\sqrt{s} = 207$ GeV. These values are the uncertainties used for the determination of the LEP combined M_W result and are treated as correlated among the experiments. Due to this new procedure the present weight of the qqqq channel in the M_W measurement is only 9% while it was 27% before Summer 2002.

Possible improvement on the CR uncertainty should come from alternative M_W measurements, less sensitive to CR effects. Colour reconnection is expected to affect mainly low momentum particles and particles far away from the jet cores and indeed it has been observed by the LEP collaborations that W mass measurements performed by removing low momentum particles (P_{cut} analyses) or particles far away from the jet axis (cone analyses) are less sensitive to CR effects [13]. Therefore these analyses allow both a M_W measurement which is less sensitive to FSI uncertainties and to set tighter constraint, than the particle flow analysis, on the CR MC models by comparing the predicted shifts between the standard and the less sensitive analyses and the real measured shift.

4.3.2 *Bose-Einstein Correlation*

The present estimation of the M_W uncertainty due to BEC has been obtained by using the LUBOEI model [14] implemented JETSET, which introduces a correlation between pions from different W's. The value of the parameters which control the correlation strenght and the source scale are obtained by the measurement of the BEC in Z decay events at LEP1. The average, among the experiments, bias is $\Delta M_W{}^{BE} = 35\,\mathrm{MeV}$.
Each LEP collaboration has been performing analyses which aim to determine the presence and the strenght of this correlation between pions from different W's. The correlations between identical pions measured in fully hadronic events are compared to the same correlations measured in fake fully hadronic WW events created by mixing to real semileptonic WW events where no correlation exist between the different W's. Presently L3 [15] and ALEPH [16] have no hint of correlation while DELPHI [17] observes a correlation with a significance of more than two sigmas. The (in)consistency of these results is under investigation and, possibly, a less conservative estimate of the BEC uncertainty on M_W will be available in the future.

4.4 Detector simulation

The finite resolutions and thresholds of real detectors introduce biases and resolution effect on the M_W estimator. Therefore an appropriate simulation of the detector effects is needed both for the jets and the leptons recontruction. When possible the MC simulation is corrected using the large amount of data collected at the Z resonance during LEP1 and the dedicated calibration runs at the Z pole during LEP2. An example is the jet energy and the lepton momentum which are "re-calibrated" using the real data.
The systematic uncertainties are estimated from the statistical accuracy of these corrections and by comparing the results obtained with modified versions of the detector simulations, driven by real and MC data comparisons. The

present uncertainties are ΔM_W = 5-35 MeV for the semileptonic channel and ΔM_W = 5-25 MeV for the fully hadronic channel, depending on the experiment. Since they are not considered as correlated among the experiments, the uncertainties on the combined results are 14 MeV and 10 MeV for the semileptonic and fully hadronic channel, respectively.

4.5 QED radiative corrections

Higher order QED corrections affect the measurement of M_W through the initial state photon radiation, because the photons escape undetected in the beam pipe and introduce biases due to the kinematic fit constraints, the Coulomb interaction between the W's and their decay products, which affects the invariant mass distribution, and, to less extent, the photon emission by the lepton in semileptonic events.
The ISR modeling has been investigated by comparing results obtained with computations at different orders of α and, on average, the uncertainty on M_W is about 10 MeV. More recently full $\mathcal{O}(\alpha)$ corrections became available [18] and they will be used for the final results even if preliminary studies show that they should not contribute a significant additional uncertainty on M_W, while they have a sizeable effect on the triple gauge couplings determination [19].

5 LEP Combined Results

Following the procedure described in the previous sections, the M_W measurements obtained by the four collaborations with the direct reconstruction are combined, together with the measurements from the WW cross section at the threshold. The LEP combined preliminary result is [4]:

$$M_W = 80.412 \pm 0.029(\text{stat}) \pm 0.031(\text{syst})\ \text{GeV} \quad (1)$$

and the combined Γ_W preliminary result is:

$$\Gamma_W = 2.150 \pm 0.068(\text{stat}) \pm 0.060(\text{syst})\ \text{GeV}. \quad (2)$$

As a consistency check, and to investigate possible effects due to FSI, the combination procedure is modified to obtain the W mass from the fully hadronic or the semileptonic channel only and their difference. The results obtained from the individual channels are:

$$M_W(\text{qqqq}) = 80.420 \pm 0.035(\text{stat}) \pm 0.101(\text{syst})\ \text{GeV} \quad (3)$$

$$M_W(\ell\nu\text{qq}) = 80.411 \pm 0.032(\text{stat}) \pm 0.030(\text{syst})\ \text{GeV} \quad (4)$$

with a correlation of 18%, and the difference is:

$$\Delta M_W(\text{qqqq} - \text{qq}\ell\nu) = +22 \pm 43\ \text{MeV} \quad (5)$$

which has been determined by setting to zero the FSI uncertainties, since it is a check of the possible effects of FSI.

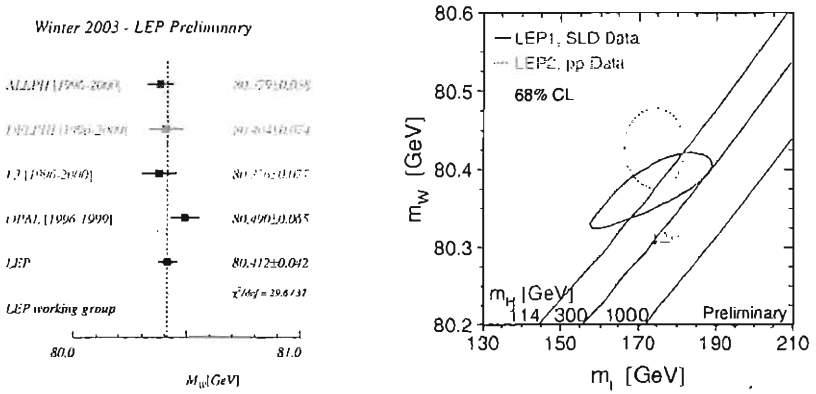

Figure 1: *Measurements of* M_W *by the LEP experiments and combined result (left). Direct and indirect determination of W boson and top quark masses compared with the SM prediction (right).*

6 Electroweak Fit

The direct determinations of M_W and Γ_W from LEP are combined with the Tevatron results and the world average results are [1]:

$$M_W = 80.426 \pm 0.034\,\text{GeV} \quad (6)$$

$$\Gamma_W = 2.139 \pm 0.069\,\text{GeV}. \quad (7)$$

The direct measurement of M_W is in agreement with the indirect determination from the electroweak fit, as described in the introduction, and, together with the Z-pole results, the direct m_{top} measurement, the neutrino scattering and the atomic parity violation results, it is included in the global EW fit, whose $\chi^2/\text{dof} = 25.5/15$ (4.4%) where the largest constribution comes from the NuTeV neutrino scattering experiment [20]. Without NuTeV result it becomes $\chi^2/\text{dof} = 26.7/14$ (27.3%). Finally the EW fit allows an indirect determination of the Higgs mass

$$M_H = 91^{+58}_{-37}\,\text{GeV} \quad (8)$$

from which a 95% C.L. upper limit is obtained:

$$M_H < 211\,\text{GeV}. \tag{9}$$

These results are stable with or without the NuTeV result in the fit.

References

1. The LEP Electroweak Working Group, LEPEWWG/2003-01 ; The LEP Electroweak Working Group, CERN-EP/2002-091.
2. Tevatron Electroweak Working Group, *Combination of CDF and D0 Results on W Boson Mass and Width*, FERMILAB-FN-0716.
3. ALEPH Collaboration, *Measurement of the W mass in e^+e^- Collisions at $\sqrt{s}$ between 183 and 209 GeV*, ALEPH 2003-005 CONF 2003-003.
4. LEP W Working Group, *Combined Preliminary results on the Mass and Width of the W Boson Measured by the LEP Experiments*, LEPEWWG/MASS/2003-01 and references therein.
5. LEP Energy Working group, Eur. Phys. J. **C11**, 573 (1999); LEP Energy Working Group, *Evaluation of the LEP centre-of-mass energy for data taken in 2000*, LEPEWG 01/01 and references therein.
6. T. Sjostrand and V.A. Khoze, Phys. Rev. Lett. **72**, 28 (1994).
7. L. Lonnblad and T. Sjostrand, Phys. Lett. **B351**, 293 (1995).
8. T. Sjostrand and V.A. Khoze, Z. Phys. **C62**, 281 (1994).
9. G. Corcella *et al.*, JHEP **0101**, 010 (2001), hep-ph/0011363.
10. L. Lonnblad, Z. Phys. **C70**, 107 (1996).
11. J. Rathsman, Phys. Lett. **452**, 364 (1999).
12. LEP W Working Group, *Combined Preliminary results on Colour Reconnection Using Particle Flow in* $e^+e^- \to W^+W^-$, LEPEWWG/FSI/2002-01 and references therein.
13. DELPHI Collaboration, *Updated measurement of Colour Reconnection model parameters using m_W analyses*, DELPHI 2003-003 CONF 626.
14. L. Lonnblad and T. Sjostrand, Eur. Phys. J. **C2**, 165 (1998).
15. L3 Collaboration, Phys. Lett. **B547**, 139 (2002).

16. ALEPH Collaboration, *Further studies on Bose-Einstein Correlations in W-pair decays*, ALEPH 2001-064 CONF 2001-044.

17. DELPHI Collaboration, *Bose-Einstein Correlations in* $e^+e^- \to W^+W^-$ *Events*, DELPHI 2002-032 CONF 566.

18. A. Denner *et al.*, Phys. Lett. **B475**, 127 (2000); S. Jadach *et al.*, Phys. Rev. **D61**, 113010/1-9 (2000).

19. R. Bruneliere *et al.*, Phys. Lett. **B533**, 75 (2002).

20. NuTeV Collaboration, G.P. Zeller *et al.*, Phys. Rev. Lett. **88** 091802 (2002).

LEP1 HEAVY FLAVOUR ELECTROWEAK PHYSICS AND 2-FERMION PROCESSES AT LEP2

Thomas Schörner-Sadenius
CERN, Division EP, 1211 Geneva 23, Switzerland and
Hamburg University, Luruper Chaussee 149, 22761 Hamburg, Germany

Abstract

Results from heavy flavour electroweak physics at LEP1 are reviewed together with measurements of 2-fermion processes at LEP2. For the former measurements the emphasis is on analyses of heavy quark forward-backward asymmetries, $A_{FB}^{b,c}$, and on the partial decay widths of the Z^0 to heavy quarks, $R_{b,c}$. The measurements of the heavy quark asymmetries are used to extract the effective electroweak mixing angle for leptons, $\sin^2\theta_{eff}^{lept}$. A 2.9σ discrepancy between measurements of this quantity from $\mathcal{A}_l(SLD)$ and from A_{FB}^b is observed. The 2-fermion processes at LEP2 are used to place stringent limits on physics processes beyond the Standard Model. However, all measured quantities are in reasonable agreement with the Standard Model expectations, and all calculated limits are well above the highest LEP2 center-of-mass energies.

1 Overview

Although the LEP experiments finished data taking in 2000, the analysis efforts are still strong in all four collaborations. In this article I will give an overview of the status of two rather distinct experimental areas, namely the heavy flavour electroweak measurements at LEP1 and 2-fermion processes at LEP2. Whereas the former class of analyses basically serve as a test of the electroweak Standard Model, with the main interest on the extraction of the weak mixing angle $\sin^2\theta_{eff}$, the LEP2 2-fermion measurements can be used for generating limits on models for new physics beyond the Standard Model.

This article is structured as follows: Section 2 is devoted to the LEP1 heavy flavour measurements. After a short overview of general issues and experimental techniques the results of the partial decay width and forward-backward asymmetry measurements for heavy quarks are shown. At the end of the section, an interpretation of these results in terms of the Standard Model, namely the electroweak mixing angle $\sin^2\theta_{eff}$, is given. Section 3 reviews measurements of 2-fermion processes at LEP2. A large part of the section is devoted to the interpretation of the measurements in terms of new physics models, such as contact interactions, Z' bosons or low scale gravity in large extra dimensions. Section 4 concludes the paper and gives an outlook.

2 LEP1 Heavy Flavour Electroweak Physics

2.1 Introduction

Measurements of b and c quark final states at LEP allow detailed insights into the properties of the electroweak Standard Model. The measurements considered here are a) the heavy flavour partial decay widths of the Z^0, R_b and R_c, and b) the heavy quark forward-backward asymmetries, A_{FB}^b and A_{FB}^c.

R_q is defined as the decay width of the Z^0 to quarks of flavour q, normalized to the total hadronic decay width, and is proportional to the sum of the squared vector and axial vector couplings of the Z^0:

$$R_q := \frac{\Gamma^q}{\Gamma^{had}} \propto g_{Vq}^2 + g_{Aq}^2, \tag{1}$$

R_q is therefore sensitive to vertex corrections to the $q\bar{q}Z^0$ vertex and might thus serve to detect signs of new physics modifying these vertices. Conceptually the measurement of $R_{b,c}$ is simple: One has to count the number of events with $b\bar{b}$ or $c\bar{c}$ final states and normalize to the number of all hadronic final state events. So the largest challenge, besides understanding the rather involved systematic uncertainties, is providing an efficient, clean and well-understood b or c flavour tag.

The forward-backward asymmetry measurements are more complicated. The asymmetry for flavour q is defined as

$$A_{FB}^{q} := \frac{N_F^q - N_B^q}{N_F^q + N_B^q} \tag{2}$$

where N_F^q (N_B^q) is the number of events of flavour q in which the initial quark goes into the forward (backward) hemisphere. The forward hemisphere is defined by the electron beam direction. Since at the Z^0 pole

$$A_{FB}^{q,0} = \frac{3}{4}\mathcal{A}_e\mathcal{A}_b \tag{3}$$

with

$$\mathcal{A}_f = 2\frac{g_{Vf} \cdot g_{Af}}{g_{Vf}^2 + g_{Af}^2} \tag{4}$$

the asymmetries provide direct access to the electroweak mixing angle $\sin^2\theta_{eff}$ via the relation $g_V/g_A = 1 - 4Q \cdot \sin^2\theta_{eff}$. Due to the charge factor Q in the former relation, the sensitivity of the asymmetries to the heavy quark couplings $\mathcal{A}_q$ is much reduced with respect to the electron coupling $\mathcal{A}_e$ (even more for b than for c quarks). So the measurements serve in fact as a determination of the mixing angle for electrons (or leptons, assuming lepton universality), $\sin^2\theta_{eff}^{lept}$.

The SLD e^+e^- collider, in contrast to LEP, has the possibility to polarize the electron beam so that additional measurements become available. One can for example, from a measurement of the left-right forward-backward asymmetry, A_{LRFB}, directly extract the heavy flavour couplings $\mathcal{A}_{b,c}$ which are not accessible at LEP. SLD measurements are also used in the heavy flavour fits that will be covered in the next sections.

The measurements of the partial decay widths [1] are final. The latest contributions to the forward-backward asymmetry measurements were presented at the 2002 summer conferences: OPAL prepared a new measurement of the b quark asymmetry using an inclusive charge tag [2] which superseeded their old result and substantially reduced the statistical and systematic uncertainties. DELPHI presented new preliminary measurements of the lepton-tagged b and c asymmetries [3] which included new systematic studies. It is therefore fair to say that the LEP1 heavy flavour electroweak measurements are slowly coming to an end. The only missing pieces are a lepton-tag asymmetry measurement from OPAL and the inclusive b asymmetry measurement from DELPHI. In addition, some SLD measurements are also only preliminary (A_{LRFB}, R_c).

2.2 Tools: Flavour and Charge Tags

As became apparent in the previous section, the heavy flavour measurements rely on flavour tagging, and, in case of the asymmetry measurements, also

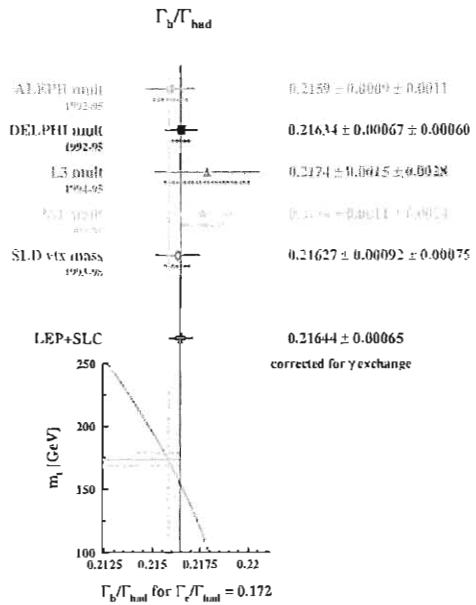

Figure 1: *A compilation of measurements of R_b from LEP and SLD. Also the Standard Model expectation, which depends on the mass of the top quark m_t, is shown.*

on tagging the charges of the outgoing quarks. The determination of these quantities is facilitated by the usually clear 2-jet structure of hadronic events at or around the Z^0 which allows the events to be divided in two hemispheres along the plane perpendicular to the thrust axis. The flavour and charge tagging tools can then be applied in the two hemispheres independently. Due to this basic structure nearly all information needed for the extraction of the partial decay widths and asymmetry values can be taken from the data without relying too much on Monte Carlo input.

Heavy flavour events can be tagged using heavy quark secondary decay vertices or high p_T leptons from semileptonic decays $b, c \to l$. The variables describing the decay vertices or the decay leptons are usually combined using likelihoods or artificial neural networks to result in one flavour tagging variable with high separation power between b or c quark hemispheres and the light flavour background, respectively. Purities of 95 % with efficiencies of 20 to 30 % can be reached. Another possibility is to tag c hemispheres using D^*

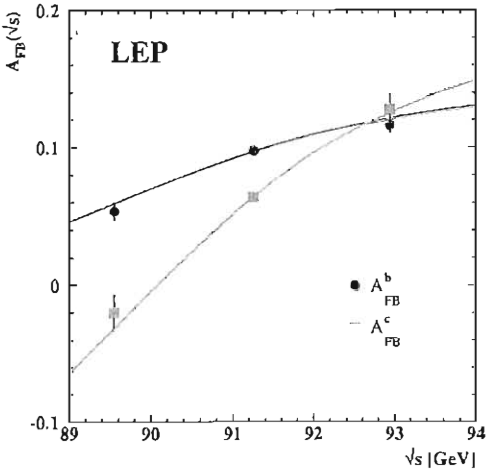

Figure 2: *The* b *and* c *quark asymmetries as a function of the center-of-mass energy, compared to the ZFITTER Standard Model prediction.*

mesons.

The charge of hemispheres which is needed for the forward-backward asymmetry analyses can be determined from a variety of observables. The OPAL analysis mentioned above uses the jet charge of the highest energy jet in the hemisphere, the weighted charge sum of all tracks connected to the secondary vertex in the hemisphere and, in addition, the charge of kaons originating from cascade decays $b \rightarrow c \rightarrow s$ measured using the dE/dx information from the OPAL central jet chamber. These variables are again combined in an artificial neural network. Charge tags like the one just described are self-calibrating in the sense that their efficiency and purity can be determined from the data themselves, thus reducing the dependence on external inputs from Monte Carlo simulations. It turns out that the correlation between the charge tags in the two event hemispheres is one of the dominant sources of systematic uncertainty.

In case of lepton-tagged asymmetry measurements, basically the same variables as for the flavour tag can be used: lepton momentum and transverse momentum, vertex fit probability, to mention a few, together with some charge information from the hemisphere opposite to the one with the identified lepton.

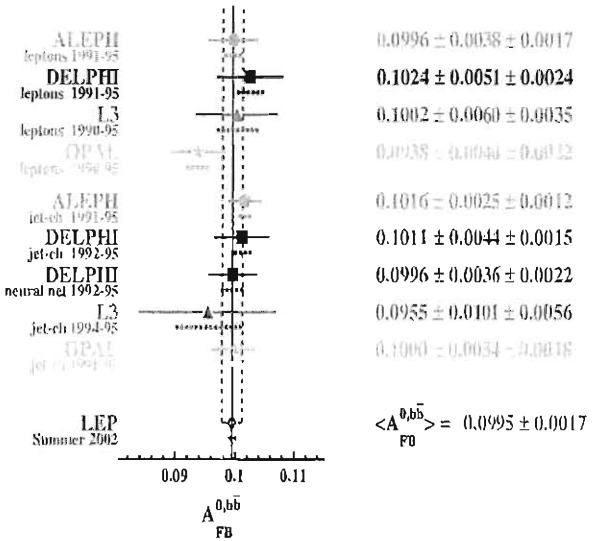

Figure 3: *A compilation of A_{FB}^{b} measurements from LEP and SLD.*

2.3 Results on Heavy Quark Decay Widths and Asymmetries

In order to get a more precise picture of heavy flavour electroweak physics, the various measurements of the partial decay widths and asymmetries are combined in a χ^2 minimisation procedure. In this fit, the correlations between various measurements due to mutual dependencies and to common external inputs are taken into account. Together with the LEP measurements of $R_{b,c}$ and $A_{FB}^{b,c}$ the SLD measurements of $\mathcal{A}_b$ and $\mathcal{A}_c$ are used in this fit. Some additional auxiliary parameters (charm hadron production fractions, b semileptonic branching ratios) are also determined.

Figure 1 shows a compilation of measurements of R_b together with the R_b result of the heavy flavour fit [1]. The measurements of the four LEP experiments and of SLD are in good overall agreement. The fit results in a value $R_b = 0.21644 \pm 0.00065$. This value, indicated by the solid vertical line, is well compatible with the Standard Model prediction based on the best electroweak knowledge and the Tevatron top mass measurement (left vertical line). The various measurements of R_c are also averaged and result in a value of $R_c = 0.1717 \pm 0.0031$, again in good agreement with the theoretical expectation.

Turning to the asymmetry measurements, first all asymmetry measure-

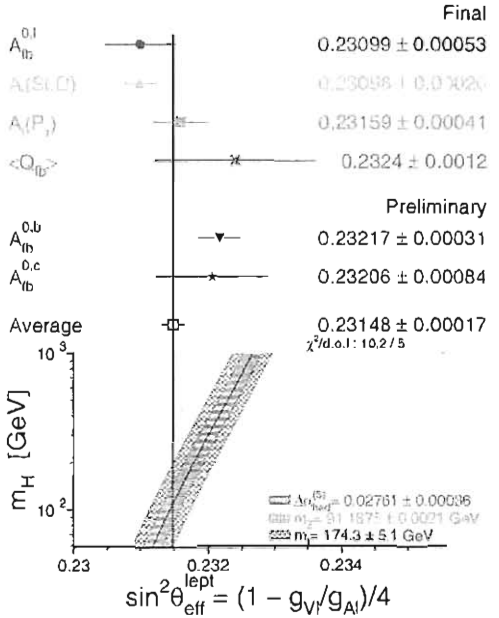

Figure 4: *A compilation of measurements of the effective electroweak mixing angle for leptons, together with the LEP+SLD average.*

ments are corrected to three distinct energies (the Z^0 pole and ±2 GeV away from it), and the averaged asymmetry is extracted for these three energies separately. The result is shown in figure 2. Since the variation of the asymmetry with the center-of-mass energy is consistent with the Standard Model expectation, all asymmetry measurements are corrected to the Z^0 pole, corrected for photon radiation and quark mass effects, and combined. The contributing A_{FB}^b measurements [2, 3, 4, 5] and the derived global value of $A_{FB}^{b,0} = 0.0995 \pm 0.0015 \pm 0.0007$ are shown in figure 3. The average is dominated by the inclusive jet charge analyses from ALEPH, DELPHI and OPAL. For the c asymmetry [3, 5, 6] we find $A_{FB}^{c,0} = 0.0713 \pm 0.0031 \pm 0.0018$. In both cases the first error is statistical, and the second systematic. The common systematic uncertainty is 0.0004 (0.0009) for the b (c) asymmetry, resulting mainly from corrections due to gluon radiation.

2.4 Standard Model Interpretation

One can go one step further using some results of the heavy flavour electroweak fit described above (A_{FB}^{b} and A_{FB}^{c}), LEP combined measurements of the leptonic forward-backward asymmetry (A_{FB}^{l} and $\mathcal{A}_l(P_\tau)$) and the SLD $\mathcal{A}_l$. Expressing all these quantities in terms of the vector and axial vector couplings of the Z^0, g_V and g_A, one can extract the effective electroweak mixing angle for leptons, $\sin^2\theta_{eff}^{lept}$.

As can be seen from figure 4, the resulting single values for this quantity fall roughly in two classes: the leptonic measurements (A_{FB}^{l}, $\mathcal{A}_l(P_\tau)$, $\mathcal{A}_l(SLD)$), which are dominated by the SLD number, tend to be slightly low, whereas the hadronic or inclusive results, in particular for A_{FB}^{b}, are rather high. The observed discrepancy of 2.9σ results in a χ^2 of 10.2/5, corresponding to a 7 % probability.

The final $\sin^2\theta_{eff}^{lept}$ value is 0.23148±0.00017, where the uncertainty is dominated by statistics. This combined value of the mixing angle, interpreted in the framework of the Standard Model, prefers a Higgs mass slightly above 100 GeV, whilst the A_{FB}^{b} measurements alone suggest a heavier Higgs of about 400 GeV.

3 2-Fermion Processes at LEP2

3.1 Introduction

The emphasis in measurements of 2-fermion processes at LEP2 is on searching for signs of new physics in the interference of new processes with the off-resonance Z^0/γ exchange. There are, however, a few general issues that have to be considered before deriving general results for 2-fermion processes. The most prominent problem is initial state radiation. Electron-positron annihilation events at center-of-mass energies above the Z^0 pole tend to radiate an energetic photon in the initial state, forcing the propagator back to the Z^0 mass. There is therefore a large contribution to the overall event sample at an effective center-of-mass energy corresponding to the Z^0. These events, which do not contain any information not known from LEP1 physics, are rejected using a cut on the effective center-of-mass energy $\sqrt{s'}$ of the order of $0.85\text{-}0.9\sqrt{s}$. In addition to this complication, corrections have to be applied in order to compensate for different signal definitions and different treatments of ISR-FSR interference before the data of different experiments can be combined.

3.2 Measurements

The conceptually simplest measurement of 2-fermion processes is clearly that of the total cross-section as a function of the center-of-mass energy $\sqrt{s}$. After the

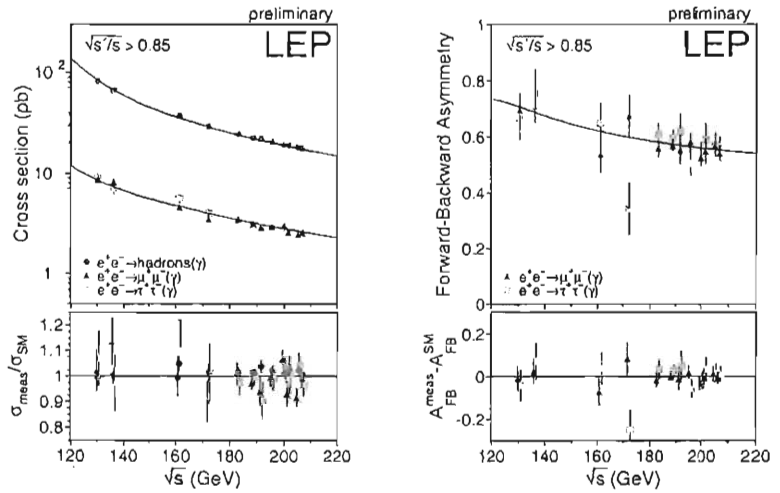

Figure 5: *The total cross-section and the forward-backward asymmetry for hadronic, μ and τ final states as a function of the center-of-mass energy, $\sqrt{s}$.*

above mentioned corrections have been applied, all measurements for quark, μ and τ final states from the four LEP collaborations are combined in a single χ^2 fit to give the average cross-sections (see [7]) and the LEP EW 2f subgroup web page [8]) for an overview on all measurements used). The results are shown as a function of $\sqrt{s}$ in the left part of figure 5. The bottom part of the figure also shows the ratio of the data to the Standard Model expectation, indicating an overall good agreement for the leptonic channels. The hadronic measurements are slightly low (1.7σ). The overall χ^2 is 160/180. The same data are also used for the extraction of the forward-backward asymmetry; the result, again as a function of $\sqrt{s}$, is shown in the right half of figure 5. Here, the overall description of all data is satisfactory.

In a next step, differential cross-sections as a function of the scattering angle $\cos\theta$ are extracted for all three lepton generations in seven regions of the center-of-mass energy between 189 and 207 GeV. For the e^+e^- final states, the additional t channel contribution which is not present for the other lepton generations leads to a divergence of the cross-section towards $\cos\theta = 1$. The description of the data is satisfactory, except for the lowest bins for $\mu^+\mu^-$ and $\tau^+\tau^-$ final states at $\sqrt{s} = 202$ GeV. However, in these bins there are only low statistics, and for all other (lower and higher) energies this feature is not

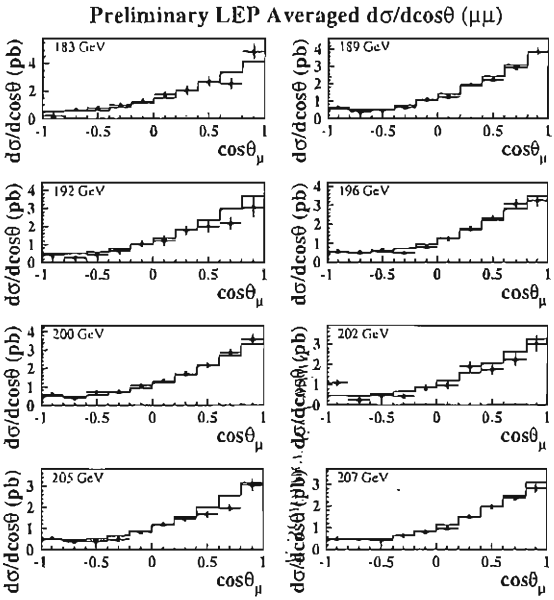

Figure 6: *Differential cross-section as a function of* $\cos\theta$ *for* $e^+e^- \rightarrow \mu^+\mu^-$ *for different center-of-mass energies. The data excess in the leftmost bin at 202 GeV is also present in the* τ *channel.*

present, see figure 6.

For heavy flavour quarks, the partial decays widths $R_q = \sigma_{q\bar{q}}/\sigma_{hadrons}$ and the forward-backward asymmetries are measured separately. For R_c, the only measurement is provided by ALEPH. The agreement between data and the ZFITTER Standard Model expectation is acceptable, except perhaps for R_b which tends to be low by about 2σ over all energies.

3.3 Interpretation in Non-standard Models

The data described above are interpreted in several physics models: electron-lepton and lepton-quark contact interactions, Z′ bosons, and low scale gravity in large extra dimensions.

In the framework of contact interactions it is assumed that LEP2 has sensitivity to additional contributions to the Langragian which are parametrized

in the form

$$\mathcal{L}_{eff} = \frac{g^2}{(1+\delta)\Lambda^2} \sum_{i,j=L,R} \eta_{ij} \bar{e}_i \gamma_\mu e_i \bar{f}_j \gamma^\mu f_j \qquad (5)$$

with a coupling strength g for which usually $g^2/4\pi = 1$ is assumed, with Λ as the mass scale of the interaction, and with $\delta = 1$ (0) for $f = e$ ($f \neq e$). Also contained in the formula are the possibilities to define the helicity of the currents (L, R) and the sign of the interference of the new physics contributions with the Standard Model processes, $\eta_{ij} = \pm 1$. For the various models that can be built from this Langrangian, the predictions are fitted to the measured total and/or differential cross-sections and asymmmetries; the fitting parameter is defined as $\epsilon := 1/\Lambda^2$. The fitted ϵ values are converted into 95% confidence level limits on Λ which for all models are larger than 2.1 to 21.7 TeV, depending on the model. It is therefore fair to say that no signs for contact interactions have been found at LEP2. The left part of figure 7 shows an example for the limits in the μ plus τ channel for various models.

Z′ bosons are an ingredient of several new physics models: In the E6 Grand Unified Theory, the group structure breaks down to the known Standard Model $SU(3)_c \times SU(2)_L \times U(1)_Y$, but additional U(1) subgroups are also present which lead to Z′ bosons. The Sequential Standard Model postulates the existence of a Z′ boson with the same couplings as the standard Z boson[1]. And in the so-called Left-Right Model, the existence of an additional $SU(2)_R$ subgroup would lead to Z′ and W′$^{\pm}$ bosons. The effect of the Z′ can be parametrised as a contact term in the cross-section, so that the modified cross-section prediction can be fitted to the data, aiming for the extraction of the mass $M_{Z'}$ of the new boson. Depending on the model considered the derived limit for Z′ bosons is found to be between 431 and 1787 GeV and therefore beyond the reach of LEP2.

Quantum gravity is a candidate for solving the hierarchy problem, i.e. for providing the missing link between the electroweak scale of order $\mathcal{O}$(1 TeV) and the Planck scale $M_{Pl} = 10^{16}$ TeV. Assuming that quantum gravity lives in 4+n dimensions, whereas our Standard Model phenomenology is confined to the usual 3+1 dimensions, it is possible that the 4+n quantum gravity pendant to the Planck scale is of the order of the electroweak scale. This new 'Planck scale' M_D would be related to the usual Planck scale M_{Pl} via

$$M_{Pl}^2 = M_D^{2+n} \cdot R^n \qquad (6)$$

with R the size of the new additional dimensions. The effect of quantum gravity would be the exchange of virtual gravitons, a process which would interfere with

[1]The mixing between the Z and the Z′ is found to be consistent with 0, as is expected from LEP1 where no sign of Z′ was found in the precision measurements of the Z.

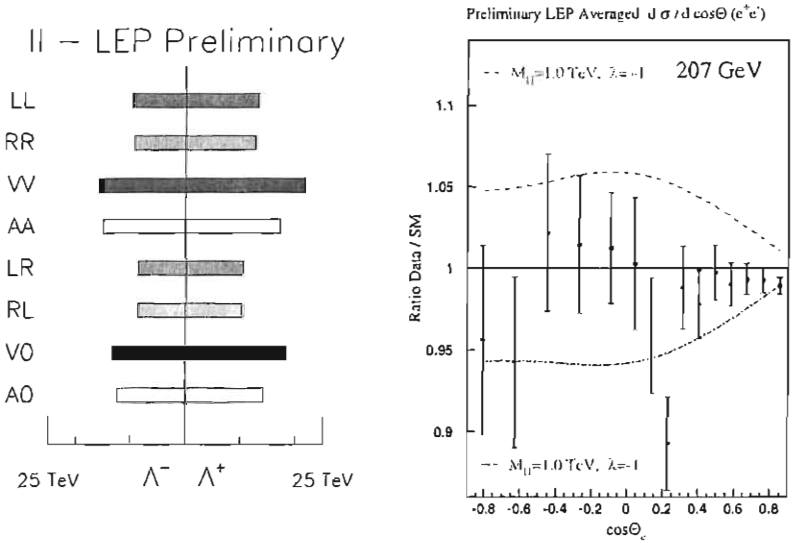

Figure 7: *Left: Examples for limits on contact interactions for μ plus τ final states. Right: Comparison of the e^+e^- final state differential cross-section with the Standard Model expectation and with predictions including virtual graviton exchanges at a mass scale of 1 TeV.*

the Standard Model Z^0 exchange and would thus modify the cross-sections measured at LEP2. The cross-section including the effect of graviton exchange is of the form

$$\frac{d\sigma}{d\cos\theta} = SM + A \cdot \frac{\lambda}{M_H^4} + B \cdot (\frac{\lambda}{M_H^4})^2 \qquad (7)$$

with a Standard Model term, an interference term and a pure new physics term with an amplitude proportional to λ/M_H^4 (for contact interactions the new physics amplitude is proportional to the inverse of the mass scale squared). The parameter λ, which cannot be known without the knowledge of the full quantum gravity theory, is usually set to ± 1. Then a fit depending on the parameter $\epsilon = \lambda/M_H^4$ is performed, and a limit on the mass scale M_H, which is related to the new Planck scale M_D, can be derived. At the 95% confidence level, $M_H > 1.20$ TeV (1.09 TeV) for $\lambda = +1$ (-1). So also signs of quantum gravity cannot be seen at LEP2. Figure 7, right, shows the ratio of the measured

differential $e^+e^- \to e^+e^-$ cross-section at 207 GeV together with the Standard Model expectation. The data are well compatible with 1. The two model predictions for the virtual graviton exchange with a graviton mass of 1 TeV and $\lambda = \pm 1$, however, clearly fail to describe the data.

4 Conclusions and Outlook

The LEP and SLD heavy flavour electroweak measurements have become very stable over the past few years and are almost all finalized. The interpretation in the electroweak Standard Model leads to an interesting discrepancy of 2.9σ between hadronic and leptonic measurements of the effective electroweak mixing angle for leptons, $\sin^2\theta^{lept}_{eff}$, which is basically due to a discrepancy between the SLD $\mathcal{A}_l$ and the LEP A^b_{FB} contributions to the average. To discover the origin of this discrepancy will be a task for future colliders.

The measurements of 2-fermion processes at LEP2 energies are in a good overall agreement with the Standard Model expectation. The cross-sections and asymmetries measured by the LEP collaborations are nevertheless used to extract limits on new physics beyond the Standard Model. Models considered include contact interactions, Z′ bosons, and low scale gravity. No signs of new physics at LEP are observed. The limits for new physics are mostly well above 1 TeV.

5 Acknowledgements

I would like to thank the LEP/SLD heavy flavour and 2-fermion electroweak working groups for the results presented in this review. In addition, I would like to thank P. Wells, K. Sachs, R. Hawkings and M. Elsing for their critical reading of this text, and the La Thuile conference organizers for their hospitality.

References

1. M. Acciarri *et al.*, Eur. Phys. J. **C13** 47 (2000); G. Abbiendi *et al.*, Eur. Phys. J. **C8** 217 (1999); K. Abe *et al.*, Phys. Rev. Lett. **80** 660 (1998); R. Barate *et al.*, Eur. Phys. J. **C4** 557 (1998); R. Barate *et al.*, Eur. Phys. J. **C16** 597 (2000); P. Abreu *et al.*, Eur. Phys. J. **C12** 209 (2000); P. Abreu *et al.*, Eur. Phys. J. **C12** 225 (2000); K. Ackerstaff *et al.*, Eur. Phys. J. **C1** 439 (1998); G. Alexander *et al.*, Z. Phys. **C72** 1 (1996); SLD Collaboration, paper 174 contributed to ICHEP98 Vancouver, Canada.

2. G. Abbiendi *et al.*, Phys. Lett. **B546** 29 (2002).

3. DELPHI Collaboration, DELPHI-2002-028 CONF 562.

4. M. Acciarri *et al.*, Phys. Lett. **B439** 225 (1998); M. Acciarri *et al.*, Phys. Lett. **B448** 152 (1999); DELPHI Collaboration, DELPHI-2001-048 CONF 476; A. Heister *et al.*, Eur. Phys. J **C22** 201 (2001).

5. P. Abreu *et al.*, Eur. Phys. J. **C10** 219 (1999); G. Alexander *et al.*, Z. Phys. **C73** 379 (1996); A. Heister *et al.*, Eur. Phys. J **C24** 177 (2002); OPAL Collaboration, OPAL Physics Note 226.

6. R. Barate *et al.*, Phys. Lett. B434 (1998) 415.

7. LEP Electroweak Working Group $f\bar{f}$ Subgroup, LEP2FF/02-03.

8. http://www.cern.ch/LEPEWWG/lep2/

RECENT RUN II ELECTROWEAK AND QCD RESULTS FROM DØ

Robert Kehoe (*for the DØ Collaboration*)
Michigan State U., Dept. Physics and Astronomy, East Lansing, MI 48824

Abstract

The DØ Detector is a hermetic, multipurpose detector residing at one interaction region designated for $p\bar{p}$ collisions at 2 TeV at the Fermilab Tevatron. Both the detector and accelerator have undergone major upgrades to increase the luminosity and handle higher interaction rates. This paper presents recent results from Run II data which explore QCD and electroweak physics at the energy frontier. The dijet mass cross section and a search for Z' in dielectron decays are presented, and these are already approaching sensitivities seen in Run I. Additionally, the first measurement of the $\sigma_Z * BR(Z \rightarrow \mu\mu)$ is given for the new collision energy.

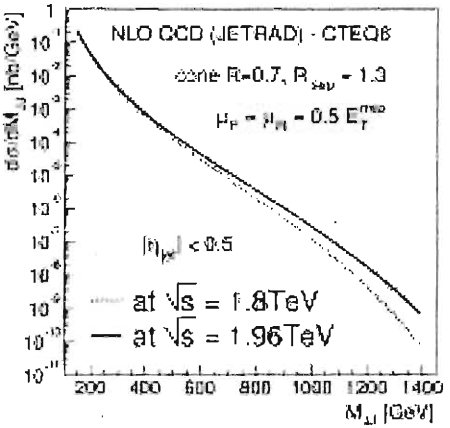

Figure 1: *The calculated NLO cross-section vs dijet invariant mass is shown. The increase in cross section for large masses is indicated.*

1 DØ at the Tevatron

As a multipurpose collider detector, DØ has the typical three main divisions of the type: innermost tracking, calorimetry, and outermost muon tracking. The tracking detectors are completely new for Run II of the Tevatron and consist of a compact silicon vertex detector surrounded by a scintillating fiber tracker. These are, in turn, surrounded by a 2T solenoid permitting momentum measurement of individual tracks. Both the silicon and fiber trackers provide full coverage for particles more central than $|\eta| = 2.0$, and moderate coverage in the forward region. Covering the full region to $|\eta| = 5$, the calorimetry is primarily comprised of the central and endcap cryostats utilizing depleted uranium absorber and liquid argon as the sampling medium. Much of the electronics for the calorimeter have been replaced to handle the higher collision rates in Run II. The central muon system consists of one layer of proportional drift tubes before and two layers after a 1.4 T toroid and covers the region $|\eta| < 1.0$. The new forward system covers to $|\eta| = 2.0$ and is composed of mini-drift tubes.

The trigger is three-tiered consisting of one hardware followed by two consecutive software levels. This system is currently reading out to tape at the 50 Hz design goal. Data-taking efficiency is currently approximately 85% and improving.

2 Dijet Mass Cross Section

QCD next-to-leading order (NLO) calculations can be probed via measurement of the cross section of dijets vs. the dijet invariant mass. For instance, QCD

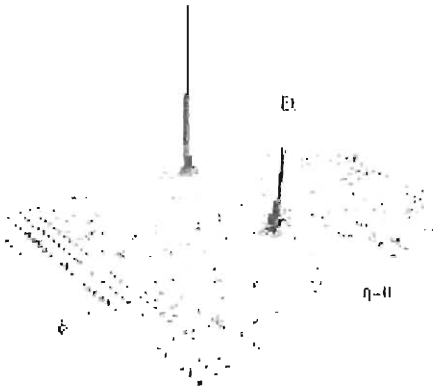

Figure 2: *Highest mass event with two leading jets in central ($|\eta| \leq 0.5$) region. The mass is 838 GeV.*

predicts a factor of two increase in cross section at high mass when comparing $\sqrt{s} = 1.8$ and 2 TeV (see Figure 1). On an absolute scale, we really test QCD folded with parton distribution functions (PDFs) and a measure of the high mass cross section provides a handle on the proton structure at large values of x. The identification of a resonance at high mass would indicate new physics. Quark compositeness would show up as an increased cross section at very high mass scales.

The data sample used for this analysis is 34.1 pb^{-1}. For event quality, we require that the missing transverse energy, $\not\!\!E_T$, satisfy the relation $\frac{\not\!\!E_T}{P_T^{jet}} < 0.7$. This removes rare instrumental backgrounds to high E_T jet events. We also require that the primary vertex be reconstructed with at least 4 tracks, and that $|z| < 50$ cm. Jets are reconstructed using the Run II cone algorithm as defined in [1]. The jets are required to satisfy $|\eta| \leq 0.5$ and at least two jets are required. The invariant mass is calculated from the leading two jets. Under these conditions the highest mass observed with two central leading jets is 838 GeV, shown in Figure 2.

2.1 Jet Energy Scale

The measured raw momentum of jets is ideally the vector sum of the momenta of the constituent particles. However, even aside from the inherent energy resolution of the calorimeter, a number of effects degrade the one-to-one correspondence between input particle momenta and observed jet energy.

First, there is an *offset* coming mainly from physical underlying event and net energy from asymetric noise after pedestal suppression. This can be measured at low luminosity by taking the typical E_T density in minimum bias

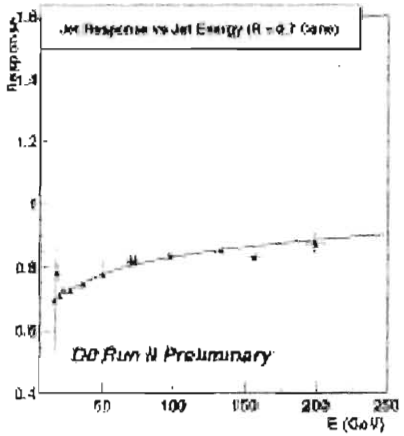

Figure 3: *Jet response vs. jet energy for* $\Delta R = 0.7$ *cone jets. The logarithmic fit vs. energy is indicated.*

events. Second, the detector itself has an energy *response* different from 1.0 due to small but non-negligible nonlinearities and dead regions. We currently utilize the method of measuring this developed in Run I [2] which employs total event E_T imbalance (i.e. $\not\!\!E_T$) in direct photon plus jet candidate events. The response as a function of jet energy is shown in Figure 3. Third, particles shower transversely in the detector sometimes causing them to spill energy outside of their jet cone. We determine this from jet transverse shapes as measured in data.

Errors for the jet energy scale are currently largely statistical, particularly in the central region. However, as the jet energy increases past 200 GeV, the systematic error also increases because we are extrapolating from small photon statistics.

2.2 Trigger Selection

We utilize four triggers for this analysis with Level 3 E_T jet thresholds of: 25 GeV, 45 GeV, 65 GeV and 95 GeV. An offline invariant mass cut is also applied for events from each trigger to ensure full efficiency. These thresholds are: 150 GeV, 180 GeV, 300 GeV and 390 GeV. The mass spectrum and approximate prescales for these triggers are shown in Figure 4. The overlap of the distributions for adjacent triggers indicates the validity for the offline mass cuts.

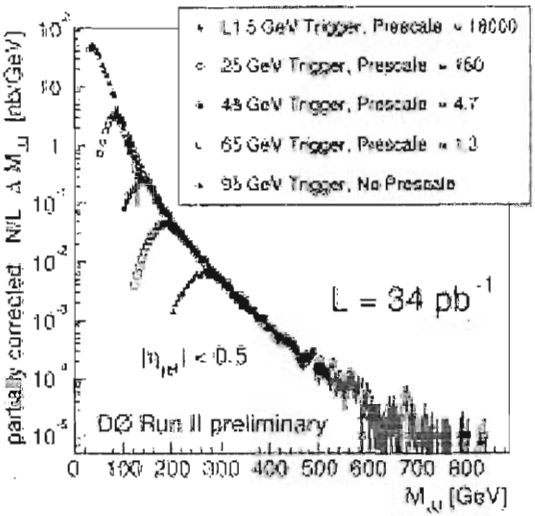

Figure 4: *Invariant mass spectra passing four high E_T inclusive jet triggers plus a low E_T trigger for comparison. Effective prescales and Level 3 E_T thresholds are indicated.*

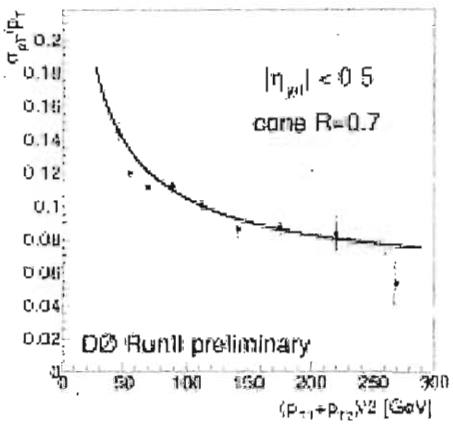

Figure 5: *Fractional E_T resolutions as a function of typical E_T for central jets with a cone of $\Delta R = 0.7$. Uncertainties are statistical only.*

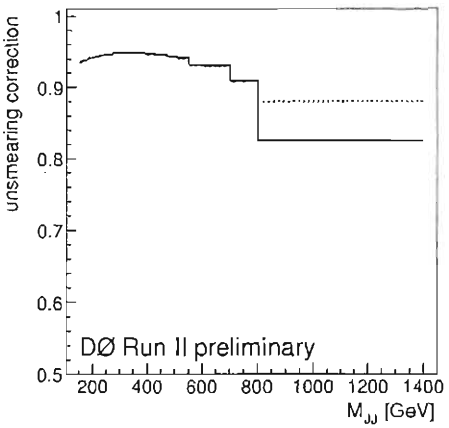

Figure 6: *Bin-by-bin unsmearing correction vs. dijet mass. Both ansatz functions shown are in agreement.*

2.3 Energy Resolution

Given a fundamentally falling cross section with increasing mass, the jet resolutions modify the observed histogram of events vs. mass. This effect must be unfolded in order to quantify the underlying cross section behavior. The first step of this correction involves the determination of the jet energy resolution itself. We use essentially the same sample of dijet events as the invariant mass cross section analysis. We calculate in each event an asymmetry parameter,

$$A = \frac{P_T^{jet1} - P_T^{jet2}}{P_T^{jet1} + P_T^{jet2}} \tag{1}$$

which is related to the fractional energy resolution by $\frac{\sigma_{P_T}}{P_T} = \sqrt{2}\sigma_A$. This resolution can then be plotted vs. the average jet energy in the event as shown in Figure 5. We further correct this value for unfound third jets and for the effect of particle jet resolution which should not be included in the unsmearing.

We consider two different ansatz functions which describe the functional form of the fundamental 'true' cross section with mass. These functions are then smeared and a χ^2 is calculated with respect to the data. The function parameters are tuned by minimizing this χ^2. The ratio of the final ansatz function to the final smeared distribution provides the unsmearing correction. Figure 6 shows the result of this fit in each mass bin. The correction is essentially flat as a function of mass, and the two ansatz functions give essentially the same unsmearing correction.

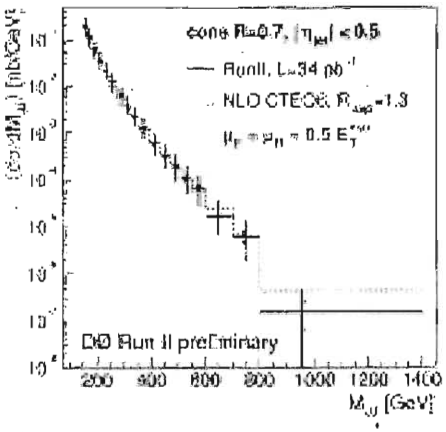

Figure 7: *Cross section vs. M_{jj}. NLO QCD (dotted histogram) agrees with observation within uncertainties.*

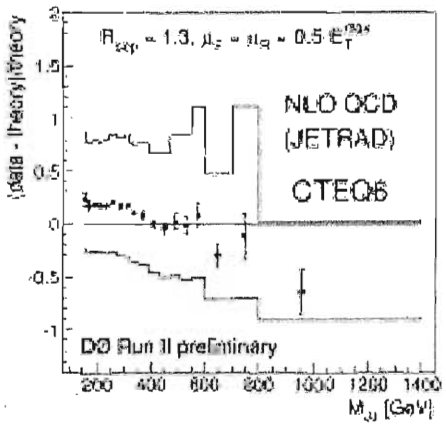

Figure 8: *(data-theory)/theory using CTEQ6 pdf. Total uncertainty indicated (solid band).*

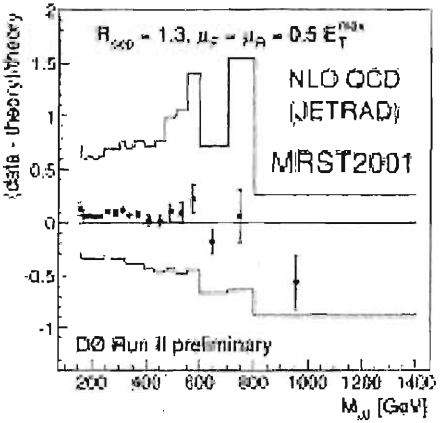

Figure 9: *(data-theory)/theory using MRST2001 pdf. Total uncertainty indicated (solid band).*

2.4 Observed Cross Section

The observed cross section can be calculated by

$$\left\langle \frac{d\sigma}{dM_{jj}} \right\rangle = \frac{N_{evt}}{L\epsilon_{eff}} \frac{C_{unsmear}}{\Delta M_{jj}} \tag{2}$$

where ϵ_{eff} quantifies cut efficiences and $C_{unsmear}$ is the unsmearing correction per mass bin. Cut efficiencies are estimated from data to be 78% for vertex quality, and 97% for jet quality. The cross section vs. invariant mass is indicated in Figure 7 with the total error. The 10% luminosity error, which is fully correlated bin-to-bin, is not shown. Within errors, there is agreement with the NLO theory using the CTEQ6 pdf.

In order to see the level of agreement, we plot (data-theory)/theory using CTEQ6 (Figure 8) and MRST2001 (Figure 9). There is agreement within the rather large uncertainties. The E_T resolution and jet quality uncertainties are sizable, but the overall uncertainty is dominated by the jet energy scale uncertainty. The jet energy scale uncertainty is $\pm^{52\%}_{38\%}$ for the 150 GeV to 160 GeV bin, and $\pm^{190\%}_{73\%}$ for the 800 to 1400 GeV bin.

3 Measurement of $\sigma_Z * BR(Z \to \mu\mu)$

One of the key measurements of DØ's electroweak physics program concerns the measurement of the production cross sections of the W and Z vector bosons. We have previously presented preliminary measurements of $\sigma * BR$ for the electron decays of these states; here we present the first $Z \to \mu\mu$ measurement from Run II.

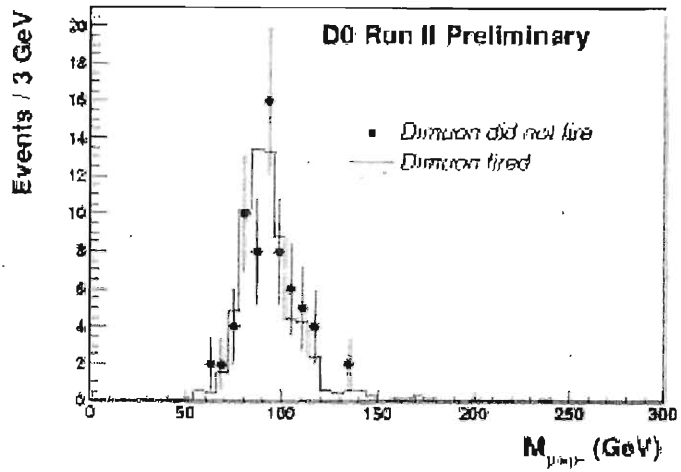

Figure 10: *$M_{\mu\mu}$ for dimuon events when probe muon fired Level 1 (histogram) and did not fire Level 1 (points). Similar shpoes indicate low background in efficiency determination.*

We employ a trigger which requires two muons at Level 1, and one muon at Level 2. For this analysis, we gathered 31.8 pb^{-1} of the data taken with this trigger. The trigger efficiency is measured from data. For instance, the Level 1 single muon efficiency is obtained by considering a *tag* muon from the Z and matching it to a fired Level 1 muon in a single muon trigger. The low background under the Z means that we can estimate the Level 1 muon efficiency for the other *probe* muon by counting the rate at which the dimuon trigger fires in this sample (see Figure 10). The Level 1 efficiency is 91%. A similar approach is taken for Level 2 and gives a single muon efficiency of 86%. These efficiencies have since been improved.

Our offline event selection requires two muons, each within $|\eta| < 1.8$, and each matching a track in the fiber and silicon trackers. The tracking efficiency is estimated using the same tag/probe approach as described above, where here the probe muon may lack a track match. The calculated tracking efficiency is currently 82%. This inefficiency is considerably reduced in more recent versions of the reconstruction as the tracking algorithms are optimized. Each muon must have $P_T > 15$ GeV and must be isolated in both the calorimeter and the tracker. Timing cuts are employed to remove the low cosmic ray background. The muons must be oppositely charged and have a separation in $\eta - \phi$ of $\Delta R_{\mu\mu} > 2.0$. 1585 events pass these cuts.

3.1 Dimuon Backgrounds

The Z dimuon background consists of three components: heavy flavor (i.e. $b\bar{b}$), $Z \to \tau\tau$, and Drell-Yan. Heavy flavor production can result in occasional

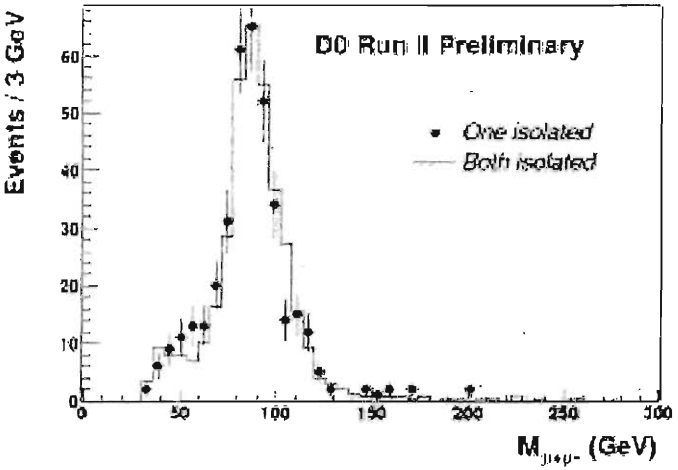

Figure 11: *$M_{\mu\mu}$ for dimuon events when probe muon is isolated (histogram) and not isolated (points). Similarity indicates heavy flavor (i.e. non-isolated) muon background is small and estimated to be 1% ± 1% of sample with only one isolated muon.*

events where two muons from b or c decay appear isolated. We consider the high P_T dimuon sample and observe the change in shape of the invariant mass distribution when we remove the isolation requirement on one of the muons. The heavy flavor contribution would preferentially congregate at low masses (i.e. just above the kinematically required 30 GeV). As shown in Figure 11, we observe no difference between the sample with one isolated muon and two isolated muons. Given the statistics, this background is less than 1%. Therefore, we assume this background is 1% of the total dimuon sample and consider this estimate as having a 1% systematic uncertainty.

In order to understand the $Z \to \tau\tau \to \mu\mu$ and the Drell-Yan background, we utilize PYTHIA and a fast detector simulation. The muon resolution has been tuned to that measured in data. The $Z \to \tau\tau$ background is shown in Figure 12 and is $< 1\%$ of the high P_T dimuon sample. The Drell-Yan background is estimated by comparing a sample of Z dimuon events with a sample of $Z + \gamma^*$ dimuon events. A correction factor is derived ($= N_Z/N_{Z+\gamma^*}$) which allows us to account for the number of γ^* events we should observe.

3.2 Measured $\sigma * BR$

The efficiency calculation for this analysis can be factored as

$$\epsilon_Z = \epsilon_{MC}^{eff} \times \epsilon_{fz} \times (2\epsilon_{L2} - \epsilon_{L2}^2) \times \epsilon_q \times \epsilon_{isol} \times \epsilon_{cosmic} \qquad (3)$$

where the last three terms concern opposite charge, isolation and cosmic veto requirements for muons. The first term, ϵ_{MC}^{eff}, contains several components

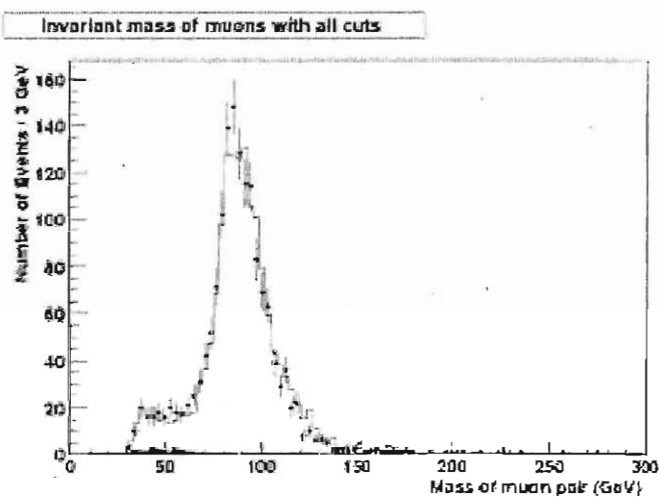

Figure 12: *$M_{\mu\mu}$ for dimuon events for Z+Drell-Yan Monte Carlo (histogram), $Z \to \tau\tau$ (solid, near 50 GeV masses) and data (points). The Z+Drell-Yan provides a good description of the observed distribution.*

containing the main inefficiency and uncertainty contributions for the cross section determination. The components of this term are the raw acceptance from Monte Carlo (0.403 ± 0.012), Level 1 muon (0.912 ± 0.017), loose muon identification (0.909 ± 0.01) and track efficiency (0.822 ± 0.014). Our determination is

$$\sigma * BR = 263.8 \pm 6.6(stat) \pm 17.3(sys) \pm 26.4(lum)\, pb.$$

Figure 13 indicates this measurement in addition to other measurements of the W and Z cross sections at hadron colliders.

4 $Z' \to ee$ Search

The existence of a neutral vector boson similar to the Z but heavier is expected in many models which describe new physics. One popular variation on these consists of the so called left-right symmetric models which postulate a right-handed gauge group $SU(2)_R$ to restore parity symmetry. Such a theory has the added feature that small masses for left-handed neutrinos are naturally accounted for.

In general, a search for a Z' as predicted by the various models and decaying to dielectrons naturally shares a lot with analyses studying dielectron decays of the Z boson. Our search pursues this path with an emphasis on maximizing efficiency. The data sample used for this analysis consists of 50 pb^{-1} of collider data. A single electron trigger is used which requires one Level 1 electromagnetic tower and a Level 3 electron with shower shape cut.

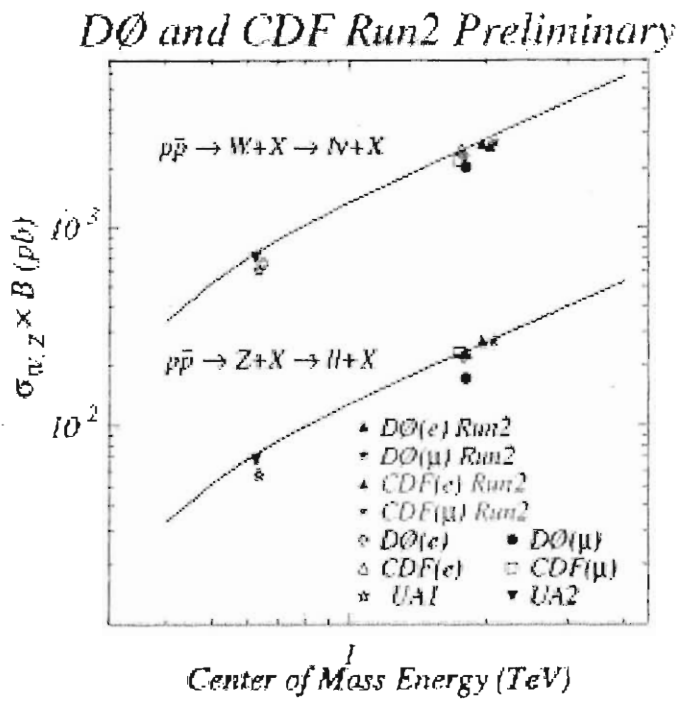

Figure 13: $\sigma_{Z,W}$ *vs. center of mass energy.*

The kinematic selection requires two electron candidates with $|\eta| < 2.5$ and $E_T > 25$ GeV. Electron identification utilizes only calorimeter-based quantities including isolation and energy fraction in electromagnetic layers. We also use an H-matrix shower shape cut. This presents a special challenge because the Z' search probes much higher electron energies than are observed in typical Z decays. Because the shower shape will alter as the electron energy increases, and because the normal shower shape efficiencies are measured from the Z sample, we determined how to effectively use this parameter to select high mass Z's. We generate Z's with PYTHIA in mass bins from 300 GeV thru 800 GeV and process all events with a full plate level GEANT simulation. The efficiency of a fixed cut is observed to fall with energy, so we adopt a E_T-dependent H-matrix cut for this analysis.

4.1 Backgrounds

The background for high mass dielectron events comes from Z+Drell-Yan production and the QCD fake background. To study the former, we generate PYTHIA events using the CTEQ4L pdf in conjunction with the fast detector simulation described earlier. We correct the leading order cross section calculated by PYTHIA with a mass-dependent factor derived from [3].

The QCD instrumental background arises predominantly from dijet events

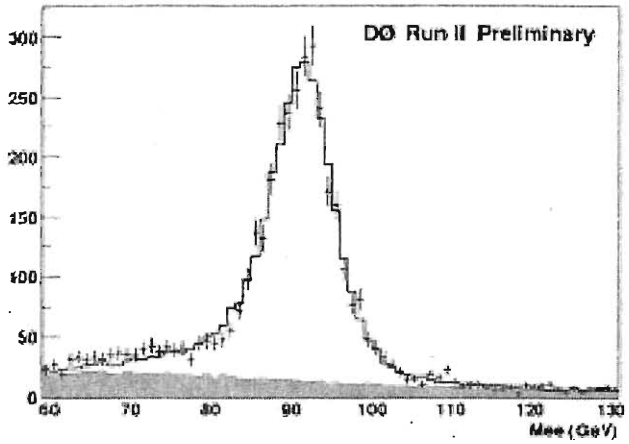

Figure 14: *QCD (green) and Z+Drell-Yan (solid histogram) contributions in the Z mass region.*

where one jet fragments to a leading π^0. This background dominates at high mass where the Drell-Yan cross section falls off rapidly. We obtain the M_{ee} distribution for this background from the data.

Once we have the shapes of the Drell-Yan and QCD backgrounds, we determine the normalization for each by allowing each to float in a fit to the dielectron data in the mass window 65 GeV $< M_{ee} <$ 115 GeV. The result is indicated in Figure 14.

4.2 Results

Figure 15 shows the full M_{ee} spectrum. The highest mass event with two central electrons has $M_{ee} = 386$ GeV and is shown in Figure 16. The data points are consistent with the sum of Drell-Yan and QCD for all masses. Figure 15 also indicates an example of a Z' with 600 GeV mass.

The lack of an excess translates into a limit on the cross section for Z' production. In order to relate this cross section limit to a limit on the mass, we consider a reference model with the following properties. We assume the coupling to quarks and leptons is the same as the standard model Z, and that top decays are available when $M_{Z'}$ permits. We also assume that the Z' width scales with mass like the Z, and that decays to Zs are suppressed. For this kind of Z', we can determine, as a function of $M_{Z'}$, the dependence of the acceptance to find two electrons satisfying our selection. We utilize our Z' events calculated with PYTHIA and the fast detector simulation, and calculate the acceptance relative to that of a Z as a function of Z' mass. The increased acceptance with $M_{Z'}$ is plotted in Figure 17.

Given this acceptance and the couplings to quarks, we can determine a

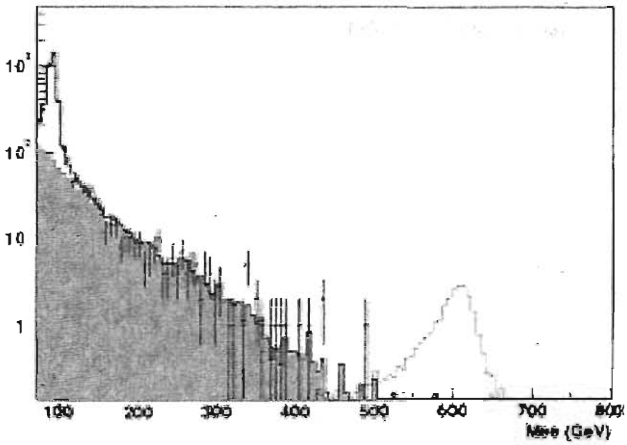

Figure 15: *QCD (green) and Z+Drell-Yan (solid histogram) contributions at all reconstructed masses. The data agree well with the background expected. An example Z' peak at 10x the expected statistics is shown for comparison.*

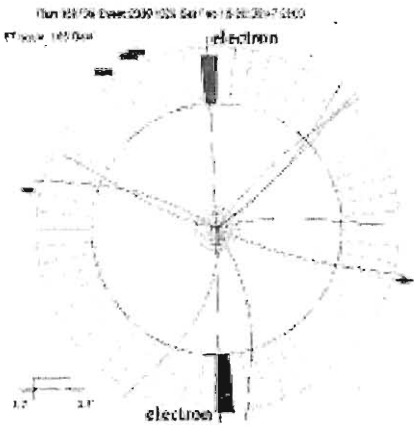

Figure 16: *Highest mass event with two electrons in central region. M_{ee} = 386 GeV. Two electrons in the calorimeter are indicated top and bottom, along with matching central tracks.*

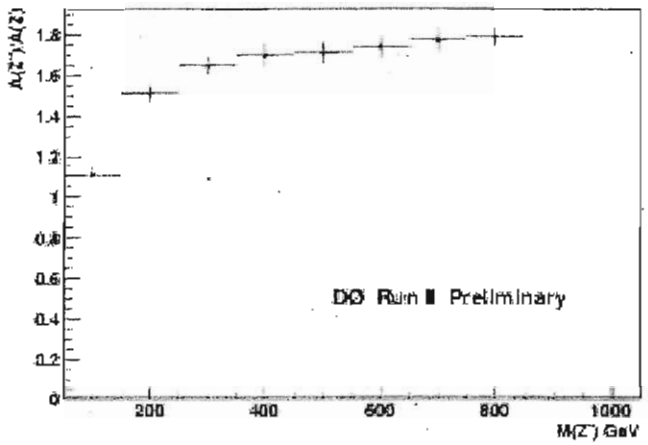

Figure 17: *Variation in acceptance as a function of the dielectron reconstructed mass.*

limit on the mass as shown in Figure 18. We obtain $M_{Z'} > 620$ GeV @ 95% c.l.

5 Summary and Conclusions

Studies at the highest mass scales in both the QCD and electroweak sectors have gotten off to a strong start at DØ in Run II. For QCD, we have observed that the dijet mass cross section agrees at all masses with NLO theory within the current errors. The inclusive jet cross section will be ready for presentation at the Summer conferences. The near-term plan involves substantially reducing the jet energy scale errors and expanding the use of the forward pseudorapidity coverage. Ultimately, we will substantially improve errors and energy resolutions through the use of tracking.

We have also augmented our existing W and Z cross section measurements in electron channels [4] with the first Z dimuon cross section times branching ratio in Run II,

$$263.8 \pm 6.6(stat) \pm 17.3(sys) \pm 26.4(lum)\, pb.$$

The $W \to \mu\nu$ cross section, as well as updated electron analyses, will be ready for the summer conferences. A search for Z' in the dielectron channel was presented yielding a mass limit of 620 GeV at the 95% c.l.

While these results begin to approach the sensitivities of Run I, the data samples presented are just the beginning of what is expected in the coming months and years from the Tevatron. The understanding of the detector is improving rapidly, and we expect rapid progress to cutting edge science in the near future.

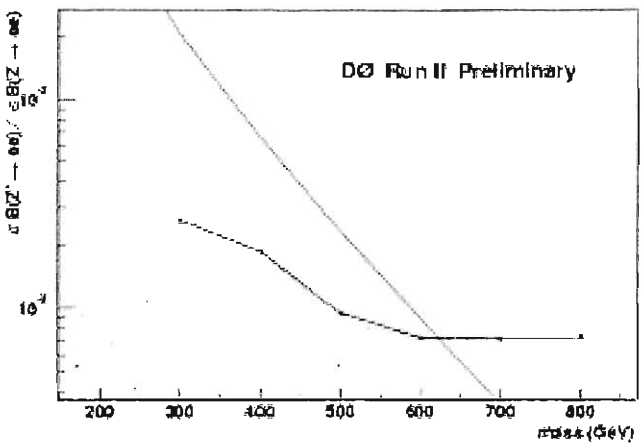

Figure 18: *Limit on cross section as a function of Z' mass (connected dots). Theoretical $\sigma * BR$ is also indicated (solid line).*

References

1. G. Blazey, et al., Proc. of Physics at Run II: QCD and Weak Boson Physics Workshop, Batavia, IL (Nov. 4-6, 1999), FERMILAB-CONF-00-092-E.

2. B. Abbott, et al., Nucl. Instr. and Meth. **A424**, 352 (1999).

3. Hamburg, van Neerven and Matsura, Nucl. Phys. **B359**, 343 (1991).

4. A. Alton (for the DØ Collab.), Proc. of 14th Topical Conf. on Hadron Collider Physics, Karlsruhe, Germany (Sep. 29-Oct. 4, 2002).

ELECTROWEAK AND TOP PHYSICS AT CDF IN RUN II

Anyes Taffard
Liverpool University, Liverpool, L69 7ZD, U.K.
For the CDF collaboration

Abstract

The CDF experiment at the Tevatron has used $p\bar{p}$ collisions at $\sqrt{s} = 1.96$ TeV to measure the production cross sections of W and Z bosons using several leptonic final states. An indirect measurement of the W width and the ratio of tau and electron electroweak couplings have been extracted. The forward-backward charge asymmetry, A_{FB}, in Drell-Yan dilectron production has been measured up to an invariant mass of 600 GeV/c^2. CDF has also started looking for WW production in the dilepton channel, $WW' \rightarrow ll'\nu\nu$, with the aim of measuring its cross section and derive limits on on the anomalous WWZ and WWγ couplings.. The presence of a top quark signal in the Tevatron data has been reestablished by measuring the top quark pair production cross section in the *dilepton* channel, $t\bar{t} \rightarrow WbW\bar{b} \rightarrow l\nu_l bl'\overline{\nu}_{l'}\bar{b}$ and in the *lepton plus jets* channel, $t\bar{t} \rightarrow WbW\bar{b} \rightarrow q\bar{q}'bl\overline{\nu}_l\bar{b} + l\nu_l bq\bar{q}'\bar{b}$. A pre-tagged *lepton plus jets* sample has also been used to reconstruct the top quark mass.

1 Introduction

The Collider Detector at Fermilab (CDF) has started recording $p\bar{p}$ interactions with its full functionality during 2002. CDF has used the physics-quality data collected until January 2003, corresponding to an integrated luminosity of 72 pb^{-1}, to re-established W, Z and top signals. With those first Run II signals, CDF has measured their production rate in different decay channels, and has extracted measurement of the W width, forward-backward asymmetry, ratio of tau and electron electroweak couplings, and has made a first attempt in reconstructing the top quark mass.

2 W and Z Cross Sections

W and Z bosons are produced at the Tevatron through $q\bar{q}$ annihilation. W boson appears in the detector as a high-momentum lepton and large missing energy due to the undetected neutrino. As the z component of p^{ν} is not measured, all quantities are measured in the transverse plane. A Z boson appears as two high-momentum opposite-signed leptons with an invariant mass around 90 GeV/c^2.

The cross section can be expressed as:

$$\sigma \cdot B = \frac{N_{obs} - N_{bkg}}{A\varepsilon \int \mathcal{L}dt} \quad (1)$$

where N_{obs} is the number of observed candidates, N_{bkg} is the estimated number of background events, A is the kinematic and geometrical acceptance, ε is the total efficiency and $\int \mathcal{L}dt$ is the integrated luminosity.

2.1 W Cross Section Measurements

At CDF, $W \rightarrow e\bar{\nu}_e$ candidates are collected with a trigger selecting high-E_T central electron candidates; after requiring one tight electron candidate with $E_T > 25$ GeV matched to a track of $p_T > 10$ GeV/c and missing transverse energy $\not\!\!E_T > 25$ GeV, 38628 events remain in the data. The main background source comes from QCD dijet events, where a jet mimics the electron signal and large $\not\!\!E_T$ is due to a poorly measured jet. This background is evaluated by assuming that its distribution is flat in the electron isolation plane versus $\not\!\!E_T$. By extrapolating from the low isolation and small $\not\!\!E_T$ region (non-W) to the high isolation and large $\not\!\!E_T$ region (W dominated), $1344 \pm 82 \pm 672$ events are estimated from that process. Additional backgrounds from $W \rightarrow \tau\bar{\nu}_\tau$ decays (768 ± 22 events) or misidentified $Z^0/\gamma^* \rightarrow e^+e^-$ decays (344 ± 17 events) are estimated from Monte Carlo simulations. The transverse mass spectrum of the candidate events and the estimated background is shown in fig.1 (left).

The total acceptance is $A_{e\nu} = 23.4 \pm 0.05$ (stat.) ± 0.70 (sys.)%, where the systematic error is dominated by the uncertainty on the parton distribution function (PDF) and the knowledge of the material in the tracking volume. The result is:

$$\sigma_W \cdot B(\mathrm{W} \to \mathrm{e}\overline{\nu}_\mathrm{e}) = 2.64 \pm 0.01 \text{ (stat.)} \pm 0.09 \text{ (sys.)} \pm 0.16 \text{ (lum.) } nb \quad (2)$$

in good agreement with the NNLO calculations [1], 2.731 ± 0.002 nb.

$\mathrm{W} \to \mu\overline{\nu}_\mu$ candidates are collected from high-p_T muon triggers. After requiring an isolated muon with $p_T > 20$ GeV/c and $\not\!\!E_T > 20$ GeV, 21599 W candidates remain. Backgrounds in this channel include misidentified boson decays ($Z^0/\gamma^* \to \mu^+\mu^-$, $\mathrm{W} \to \tau\overline{\nu}_\tau$), cosmic rays and QCD processes; their sum is estimated to 10.82 ± 0.18 (stat.) ± 0.96 (sys.)%. The total acceptance is $A_{\mu\nu} = 14.8 \pm 0.5$ (stat.)%, where the systematic error is dominated by the uncertainty on the PDF and the measurement of the W recoil. The result is:

$$\sigma_W \cdot B(\mathrm{W} \to \mu\overline{\nu}_\mu) = 2.64 \pm 0.02 \text{ (stat.)} \pm 0.12 \text{ (sys.)} \pm 0.16 \text{ (lum.) } nb \quad (3)$$

again in good agreement with the NNLO calculations.

$\mathrm{W} \to \tau\overline{\nu}_\tau$ candidates can also be selected at CDF by collecting events with a $\not\!\!E_T > 25$ GeV at the level 1 hardware trigger complemented by a subsequent τ identification at the level 3 software trigger. Monojet candidates are kept if they have a single jet with $E_T > 25$ GeV containing one charge leading track with $p_T > 4.5$ GeV in a 10^o cone and no other track in a $10^o - 30^o$ cone around the leading track. Tight electron events from $\mathrm{W} \to \mathrm{e}\overline{\nu}_\mathrm{e}$ decay are explicitly removed. 2345 events pass the selection, with an estimated background of 612 ± 61 events mainly due to QCD processes. The cross section times branching ratio is measured to be:

$$\sigma_W \cdot B(\mathrm{W} \to \tau\overline{\nu}_\tau) = 2.62 \pm 0.07 \text{ (stat.)} \pm 0.21 \text{ (sys.)} \pm 0.16 \text{ (lum.) } nb \quad (4)$$

Additionally, by using the previously excluded $\mathrm{W} \to \mathrm{e}\overline{\nu}_\mathrm{e}$ candidates in the same data sample, the ratio of the electroweak coupling constants is extracted to be:

$$\frac{g_\tau}{g_e} = 0.99 \pm 0.04 \text{ (stat.)} \pm 0.07 \text{ (sys.)} \quad (5)$$

2.2 Z Cross Section Measurements

The selection of $Z^0/\gamma^* \to \mathrm{e}^+\mathrm{e}^-$ candidates is done by requiring two central electrons with opposite charge, $E_T > 25$ GeV and $p_T > 10$ GeV/c with and invariant mass between 66 and 116 GeV/c^2. 1830 candidate events are obtained with an estimated background of 10 ± 5 events. The total acceptance is $A_{ee} = 11.49 \pm 0.07$ (stat.) ± 0.64 (sys.)%, where the systematic error is dominated by

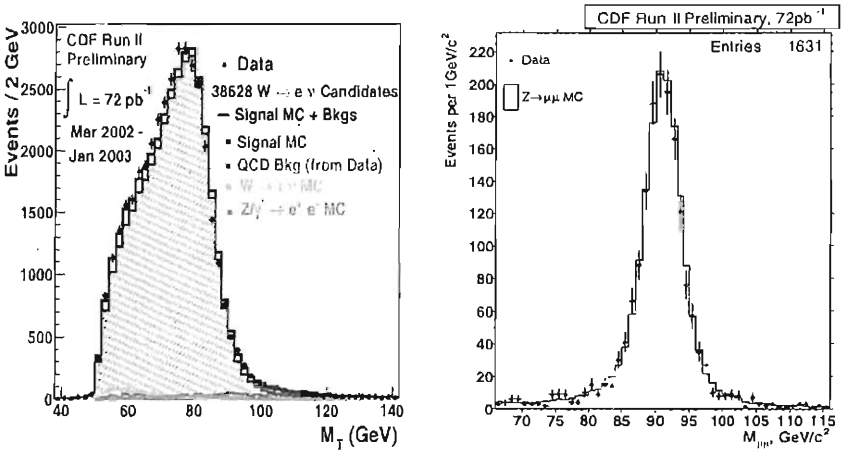

Figure 1: *Transverse mass distribution of* $W \to e\bar{\nu}_e$ *candidates (left) and invariant mass of* $Z^0/\gamma^* \to \mu^+\mu^-$ *candidates (right) collected by the CDF experiment in 72* pb^{-1}.

the uncertainty on the PDF and the modeling of the material budget in the tracking volume. The cross section times branching ratio is measured to be:

$$\sigma_Z \cdot B(Z^0 \to e^+e^-) = 267.0 \pm 6.3\ (\text{stat.}) \pm 15.2\ (\text{sys.}) \pm 16.0\ (\text{lum.})\ pb \quad (6)$$

higher but consistent that the NNLO calculation [1] of 250.5 ± 3.8pb.

$Z^0/\gamma^* \to \mu^+\mu^-$ candidates are selected by requiring one isolated central muon with $p_T > 20$ GeV/c and an second isolated high-p_T track passing minimum ionizing energy requirements. The same invariant mass window as in the electron channel is considered. From the 1631 candidates (see fig.1, right), CDF measures:

$$\sigma_Z \cdot B(Z^0 \to \mu^+\mu^-) = 246 \pm 6\ (\text{stat.}) \pm 15\ (\text{sys.}) \pm 15\ (\text{lum.})\ pb \quad (7)$$

in good agreement with the NNLO calculations.

3 W/Z ratio and W width

Using the cross section measurements in the electron channel presented in sections 2.1 and 2.2, the ratio of the cross sections times branching ratios is computed to be:

$$R_e = \frac{\sigma_W \cdot B(W \to e\bar{\nu}_e)}{\sigma_Z \cdot B(Z^0 \to e^+e^-)} = 9.88 \pm 0.24\ (\text{stat.}) \pm 0.47\ (\text{sys.}) \quad (8)$$

and is found lower but consistent with the NNLO prediction ($R = 10.66 \pm 0.05$ [1]). Similarly, using the muon results, CDF computes:

$$R_\mu = 10.69 \pm 0.27 \text{ (stat.)} \pm 0.33 \text{ (sys.)} \tag{9}$$

The indirect measurement of $\Gamma(W)$ can be extracted using equation 10, where $\sigma(p\bar{p} \to W)/\sigma(p\bar{p} \to Z)$ is taken from theoretical predictions [1], $\Gamma(W \to l\nu)$ is taken from the P.D.G. [2] and $\Gamma(Z \to ee)/\Gamma(Z)$ from the LEP measurements [2].

$$\Gamma(W) = \frac{\sigma(p\bar{p} \to W)}{\sigma(p\bar{p} \to Z)} \frac{\Gamma(W \to e\nu)}{\Gamma(Z \to ee)} \frac{\Gamma(Z)}{R} \tag{10}$$

Using R_e, CDF extractes:

$$\Gamma(W) = 2.29 \pm 0.06 \text{ (stat.)} \pm 0.10 \text{ (sys.) GeV} \tag{11}$$

while using R_μ, CDF obtains:

$$\Gamma(W) = 2.11 \pm 0.05 \text{ (stat.)} \pm 0.07 \text{ (sys.) GeV} \tag{12}$$

Both results are found in relatively good agreement with the most recent average of 2.118 ± 0.042 GeV [3] and the theoretical prediction of 2.067 ± 0.021 GeV. Fig.2 (right) shows those results with previous measurements of the W boson width.

4 Forward-Backward Dilectron Asymmetry

The reaction $p\bar{p} \to ll'$, where l stands for and isolated high-p_T electron or muon, is mediated by virtual photon at low invariant mass ($M_{l^+l^-}$) values, by the Z^0 for $M_{l^+l^-}$ around the Z pole and by photon-Z interference everywhere else. The presence of both vector and axial-vector couplings of electroweak bosons to fermions in the process $q\bar{q} \to Z^0/\gamma^* \to l^+l^-$ gives rise to an asymmetry in the polar angle (θ) of the electron momentum in the center of mass frame of the lepton pair. The forward-backward asymmetry is defined as:

$$A_{FB} = \frac{N_F - N_B}{N_F + N_B} \tag{13}$$

where N_F is the number of forward events with positive $\cos\theta$ and N_B is the number of backward events with negative $\cos\theta$.

A_{FB} is a direct probe of the relative strength of the vector and axial-vector couplings over the Q^2 range considered. Additionally, A_{FB} allows to constrains the properties of any additional heavy neutral gauge boson not included in the

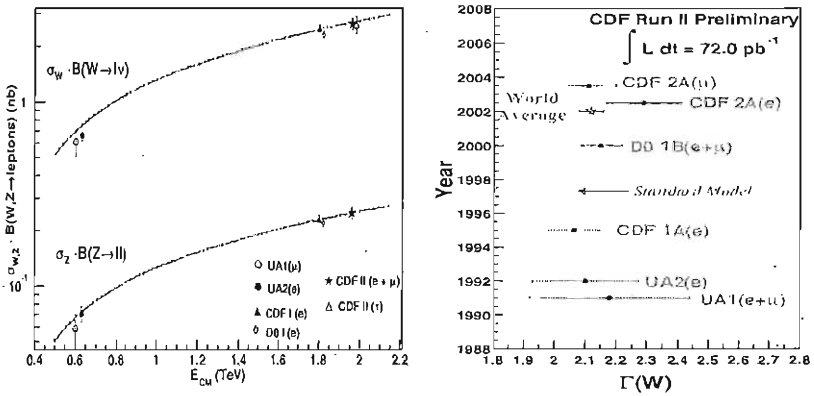

Figure 2: *Left: Comparison of the cross section measurements for W and Z boson with NNLO calculations (line). Right: Comparison of CDF Run II results on the W boson width with the previous measurements and SM predictions.*

Standard Model, and is complementary to a direct search for them via excesses in the total cross section.

CDF uses 5438 events with $40 < M_{e^+e^-} < 600$ GeV/c^2 from $p\bar{p} \to Z^0/\gamma^* + X \to e^+e^- + X$ process to measure the forward-backward asymmetry over a wide Q^2 range. The results are showed in fig.3 and agree well with the theoretical predictions.

5 WW production in dilepton channel

The study of WW production in the dilepton channel, $WW' \to ll'\nu\nu$ (l = e *or* μ) with Run II data will improve the measurement of the WW cross section and the limits on the anomalous WWZ and WWγ couplings. CDF has started looking for WW decay to dilepton in the 72 pb^{-1} of data collected so far, by selecting two high-p_T isolated electron(s) or muon(s) with opposite charge and $\not\!\!E_T > 25$ GeV. Vetos to reject $t\bar{t}$ and Z events are applied. Table 1 summaries the number of data candidates, estimated background events and expected signal. The results are found consistent with the SM WW production and background, but a cross section measurement has not been derived at this time due to the lack of statistics.

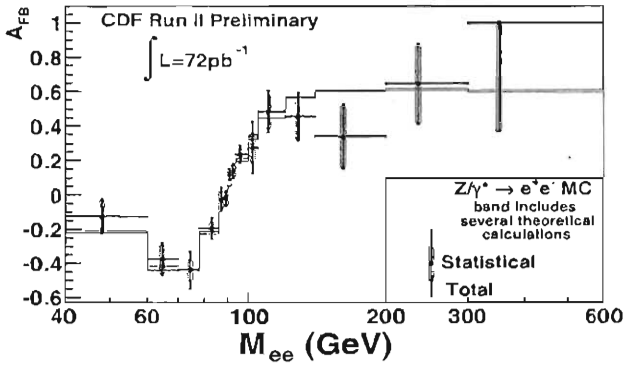

Figure 3: *CDF measurement of the forward-backward asymmetry, A_{FB}, of electron-positron pairs compared with theoretical predictions.*

Table 1: *WW to dilepton results in 72 pb^{-1}.*

Source	ee	$\mu\mu$	eμ	ll
Backgrounds	0.29 ± 0.13	0.46 ± 0.18	0.77 ± 0.60	1.52 ± 0.64
$WW \to ll\nu\nu$	0.54 ± 0.12	0.65 ± 0.14	1.55 ± 0.34	2.74 ± 0.59
Data	1	0	1	2

6 Top Quark Production Cross Section

To this date, all direct measurements of top quark have been performed at the Tevatron, where top quarks are pair produced via $q\bar{q}$ annihilation (90%) and gg fusion (10%). Within the SM, top quark decay almost exclusively to Wb. The $t\bar{t}$ *dilepton* channel, where both W's decay leptonically, to e or μ ($t\bar{t} \to WbW\bar{b} \to l\nu_l bl'\nu_{l'}\bar{b}$), has the smallest branching ratio of 5%. In the so-called *lepton plus jets* channel, where one W decays leptonically and the other hadronically ($t\bar{t} \to WbW\bar{b} \to q\bar{q}'bl\overline{\nu}_l\bar{b} + \bar{l}\nu_l bq\bar{q}'\bar{b}$), the branching ratio is in the order of 30%. Due to the increase in the center of mass energy to from 1.8 TeV in Run I to 1.96 TeV in Run II, the $t\bar{t}$ cross section will increase by about 30%.

6.1 $\sigma_{t\bar{t}}$ in the *dilepton* channel

Dilepton $t\bar{t}$ events are selected by requiring two central isolated high-p_T electron or muon of opposite charge, $\not\!\!E_T > 25$ GeV and at least 2 jets within $|\eta| < 2.0$

Table 2: $t\bar{t}$ *dilepton results for 72* pb^{-1}.

Source	ee	$\mu\mu$	eμ	ll
All Backgrounds	0.103 ± 0.056	0.093 ± 0.054	0.100 ± 0.037	0.30 ± 0.12
SM $t\bar{t} \to l\nu_l bl'\overline{\nu}_{l'}\bar{b}$	0.47 ± 0.05	0.059 ± 0.07	1.44 ± 0.16	2.5 ± 0.3
Data	1	1	3	5

and $E_T > 10$ GeV. Drell-Yan ($Z^0/\gamma^* \to e^+e^-, \mu^+\mu^-$), are rejected by requiring that the the dilepton invariant mass, M_{ee} or $M_{\mu\mu}$ to be outside the range of 76 to 106 GeV/c^2. In order to eliminate instrumental contributions to the $\not\!\!E_T$ due to mismeasured energies of lepton or jets, CDF requires $\not\!\!E_T > 50$ GeV if $\Delta\phi(\not\!\!E_T, l \text{ or } j) < 20^o$ [1]. Finally, to enhance the signal to background ratio, $H_T > 200$ GeV[2] is required. The main background processes that remain after this selection are dibosons (WW, WZ), Drell-Yan ($Z^0/\gamma^* \to e^+e^-, \mu^+\mu^-$), $Z^0/\gamma^* \to \tau^+\tau^-$ and *fake lepton*. Table 2 summaries the total background estimate, the expected $t\bar{t}$ *dilepton* signal and the number of data candidates. Figure 4 (left) shows the dilepton candidates and the expected $t\bar{t}$ MC with $M_{top} = 175$ GeV/c^2. The cross section is measured to be:

$$\sigma_{t\bar{t}} = 13.2 \pm 5.9 \text{ (stat.)} \pm 1.5 \text{ (sys.)} \pm 0.8 \text{ (lum.) pb} \qquad (14)$$

and is found to be higher but consistent with the NLO prediction of $6.70^{+0.71}_{-0.88}$pb [4].

6.2 $\sigma_{t\bar{t}}$ in the *lepton+jets* channel

The *letpton plus jets* event selection consists of requiring one central isolated high-p_T electron or muon, $\not\!\!E_T > 20$ GeV, at least 1 jet within $|\eta| < 2.0$ and $E_T > 15$ GeV and Z boson veto. The 1 and 2 jets bins are used as a control sample and only ≥ 3 jets are used to compute $\sigma_{t\bar{t}}$. To increase the signal to background ratio, the Silicon Vertex Detector is used to identify the b-quark displaced vertices. A jet is b-tagged if it contains a secondary vertex with at least two charged tracks and $L_{xy}/\sigma_{xy} > 3$ [3]. The efficiency for identifying at least one b quarks in $t\bar{t}$ decays is about 45% and is measured from $t\bar{t}$ MC and corrected with a data to MC scale factor. The mistags from

[1] $\Delta\phi(\not\!\!E_T, l \text{ or } j)$ is the azimutal separation between the vector $\not\!\!E_T$ and the nearest lepton or jet.

[2] H_T is the scalar sum of the transverse energy of the leptons, jets and neutrino in the event.

[3] L_{xy} is the distance in the transverse plane to the beam direction between the secondary and primary vertices. σ_{xy} is the error on L_{xy}.

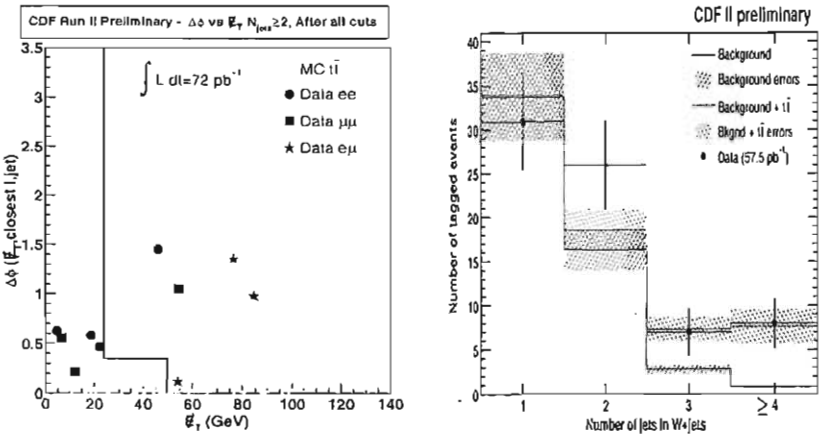

Figure 4: *Left: $t\bar{t}$ dilepton candidates found in 72 pb^{-1} in the plane $\Delta\phi(\not\!\!E_T, l$ or $j)$ versus $\not\!\!E_T$. The yellow dotes are MC Herwig $t\bar{t}$. Right: Number of events in the W+jets sample with at least one b-tag. The 3^{rd} and 4^{th} bins are used to extract $\sigma_{t\bar{t}}$.*

light quarks and gluon jets are evaluated using the negative tag rate of L_{xy} extracted from inclusive jet samples and applied to the W+jets data. $Wb\bar{b}$ and $Wc\bar{c}$ backgrounds are estimated from W+jets data using the Run I heavy flavor composition in W+jets and the b-tagging efficiency. The non-W background is estimated from W+jets data using the isolation versus $\not\!\!E_T$ method used in the W cross section analyses (see sec.2.1). Other small contribution from WW/WZ, Drell-Yan and single top production are evaluated from the MC. Table 3 summarizes the background estimate, with and without $t\bar{t}$ contribution, and the number of data candidates before and after requiring at least 1 jet with a b-tag. From the 15 candidates in ≥ 3 jets events (see fig.4 right), the cross section is measured to be:

$$\sigma_{t\bar{t}} = 5.3 \pm 1.9 \text{ (stat.)} \pm 0.8 \text{ (sys.)} \pm 0.3 \text{ (lum.) } pb \qquad (15)$$

lower but consistent with the NLO prediction [4].

7 Top Quark Mass Measurement

The most precise determination of the top mass can be obtained by using the *lepton plus jets* sample. The 24 combinations, 12 corresponding to the jet-parton match where every combination has two solutions for the neutrino

Table 3: $t\bar{t}$ *lepton+jets results for* 57.5 pb^{-1}.

Source	W+1jet	W+2jets	W+3jets	W≥4jets
SM Backgrounds	33.8 ± 5.0	16.4 ± 2.4	2.88 ± 0.05	0.87 ± 0.2
SM backgrounds + $t\bar{t}$	34.0 ± 5.0	18.65 ± 2.4	7.35 ± 1.4	7.62 ± 2.0
Events before b-tagging	4913	768	99	26
Events (≥1 b-tag)	31	26	7	8

p_z, can be reduce down to 12 by requiring 1 b-tagged jet and to 4 with 2 b-tagged jets. The method used to reconstruct the top mass consists of using a constraint-fitting technique ($M_{l\nu} = M_W; M_{jj} = M_W; M_t = M_{\bar{t}}$) and choosing the combination with the lowest χ^2. The reconstructed top mass distribution from the data is then compared to the parametrized templates of top plus background Monte Carlo. The top mass is then extracted by fitting the observed and expected distributions using a maximum likelihood method.

CDF first attempt in reconstructing the top mass with Run II data, has used events with one lepton and 4 jets, but without any b-tagging requirement. The top mass obtained (see fig. 5) is:

$$171^{+14.4}_{-12.5}\ (\text{stat.}) \pm 9.9\ (\text{sys.})\ \text{GeV}/c^2 \tag{16}$$

The systematic error is dominated by the uncertainty on the jet energy measurement, which is currently of 9.3 GeV/c^2 compared to 4.4 GeV/c^2 achieved in Run I. CDF aims to reduce this error to ≈ 2 GeV/c^2.

8 Summary

The W, Z and $t\bar{t}$ production cross sections have been measured in several decay channels by CDF using the first Run II physics quality data. All measurements obtained are in agreement with the theoretical predicition at 1.96 TeV. CDF has calculated the ratio of the W and Z cross section, R, and used it to extract an indirect measurement of the W width. $Z^0/\gamma^* \rightarrow e^+e^-$ events have been use to measure the forward-backward asymmetry up to 600 GeV/c^2. CDF has also started selecting $WW' \rightarrow ll'\nu\nu$, in order to measure the WW cross section and derive limits on the anomalous WWZ and WWγ couplings. Finally, the first attempt in measuring the top quark mass using Run II data has been made.

9 Acknowledgments

Thanks to all the participants of the Electroweak and Top groups for their efforts in making those Winter 2003 measurements a reality.

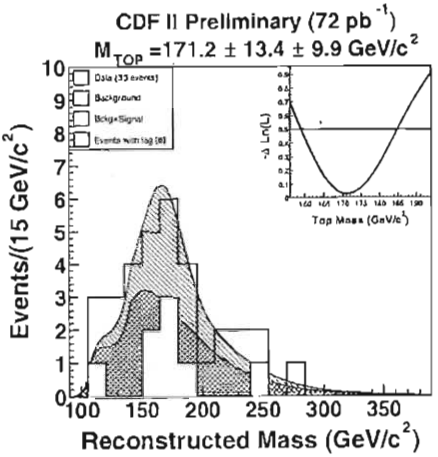

Figure 5: *Reconstructed top mass distribution of pre-tagged l+4jets events. The yellow histogram represents events with a b-tag jet, but the information is not used in the top mass reconstruction.*

References

1. R.Hamberg, W.L.Van Neerven and T.Matsuura, Nucl. Phys. **B359**,343 (1991).
   R.V. Harlander and W.B.Kilgore, Phys. Rev. Lett. **88**, 201801 (2002)
   W.J.Stirling, Private Communication.

2. 2002 Particle Data Group review

3. K.Hagiwara et al., Phys.Rev.**D66** (2002)

4. M.Cacciari, S.Frixione, M.L.Mangano, P.Nason and G.Ridolfi, hep-ph/0303085.

RECENT TOP QUARK PHYSICS RESULTS FROM DØ

Marumi Kado
Lawrence Berkeley National Laboratory
1 Cyclotron Road, Berkeley, CA 94720, USA

Abstract

A first measurement by DØ of the $t\bar{t}$ cross section at $\sqrt{s} = 1.96$ TeV with $\approx$50 pb^{-1} of data in the dilepton, topological lepton+jets and soft-lepton-tag lepton+jets channels is presented. Overall, 17 events are observed with an expected background of 6.5 ± 0.6. This excess corresponds to an observation probability of three standard deviations and the measured $t\bar{t}$ cross section is:

$$\sigma_{p\bar{p}\to t\bar{t}} = 8.5^{+4.5}_{-3.6}\ (\text{stat})\ ^{+6.3}_{-3.5}\ (\text{sys})\ \pm 0.8\ (\text{lumi})\ \text{pb}.$$

An improved measurement of the top quark mass in the lepton+jets channels with Run I data is also reported.

1 INTRODUCTION

The top quark was discovered by the CDF and DØ collaborations almost a decade ago at the Tevatron in its first phase of operation at a center-of-mass energy of 1.8 TeV [1] (Run I). In spring 2001 its new phase at 2 TeV (Run II) began. In this new phase, a data sample at least twenty times larger is expected to be collected. In a yet-to-be-approved third phase another factor of approximately five is foreseen. When these goals are reached more about the top quark properties will be known, in particular its mass.

At Run II the DØ detector has undergone numerous upgrades[1] and has now passed its commissioning phase, as illustrated by the measurements of jets and high transverse momentum leptons cross sections presented at this conference [2]. The amount of data collected is approximately 50 pb^{-1}, which corresponds roughly to the integrated luminosity used for the first observation of the top quark published at Run I [1]. The questions of the observation of the top quark at Run II and the measurement of its production cross section are thus addressed. Moreover, the measurement of this rare process can further substantiate the evaluation of the new DØ detector performances.

2 MEASUREMENT OF THE $t\bar{t}$ CROSS SECTION AT RUN II

The most recent calculations of the $t\bar{t}$ cross section at Tevatron provide predictions for $\sigma_{p\bar{p}\to t\bar{t}}$ ranging from 5.4 to 7.4 pb [3]. In the Standard Model, the top quark is expected to decay predominantly into a W boson and a b quark. The channels in which the top quark is sought are determined therefore by the decay modes of the W boson pair. The channels can be classified as follows: the dilepton channel, where both W bosons decay leptonically into an electron or a muon (ee, $\mu\mu$, $e\mu$), the lepton + jets channel where one of the W bosons decays leptonically and the other hadronically (e+jets, μ+jets), and the all-jets channel where both W bosons decay hadronically. This note will focus entirely on the dilepton and lepton + jets channels. For the lepton+jets channels two approaches are used: a topological analysis, using only kinematic

[1] The calorimeter readout electronics were rebuilt to cope with the faster bunch-crossing rate at Run II. The inner volume of the detector has been magnetized with a 1.2 m diameter solenoid producing a 2T field. The tracker consists of a scintillating fiber detector and of a silicon detector. The Run I muon PDT system in the central region has been complemented with a Mini Drift Tube (MDT) system in the forward region and a new scintillator pixel system. An improved shielding to reduce the effects of beam related backgrounds has been installed.

selection criteria, and a soft-muon tag, for which at least one jet is tagged as a b-jet from the presence of a non-isolated soft-muon.

2.1 Data Sets

From August 2002, until January 2003, about 96.8pb^{-1} were delivered to the experiment, 68.2 pb^{-1} were recorded and 66.5 pb^{-1} were reconstructed. To cope with the high luminosity and to efficiently select $t\bar{t}$ events, for each analyzed channel, specific triggers were designed and specific data quality criteria were designed. The amounts of data analyzed in each channel are thus different.

All signal and background Monte Carlo events are generated at $\sqrt{s}$ = 1.96 TeV with the leading order CTEQ4L [8] parton distribution functions. $t\bar{t}$ events are simulated using PYTHIA 6.203 [9] at a top quark mass of 175 GeV. Background W+jets events are simulated using the leading-order VECBOS [10] matrix elements, coupled to HERWIG [11] to simulate the underlying event, initial state radiation, parton hadronization, and the decay of the W boson. All other backgrounds are generated using PYTHIA. After hadronization, all signal and background events have additional minimum bias proton-antiproton events superimposed. The number of added events is taken from a Poisson distribution with a mean of 0.5. The events are then processed through full GEANT simulation of the DØ detector.

2.2 Dilepton Analyses

The ee or a $\mu\mu$ channels represent the smallest fraction of $t\bar{t}$ events ($\approx$ 1/81 each). The signature of these two channels is two flavor-like high-p_T isolated leptons, two b-quark jets, and a significant transverse missing energy ($\not\!\!E_T$) from the two neutrinos. The largest background contributions are of instrumental nature, mostly from the mismeasurement of the $\not\!\!E_T$ and the misidentification of jets. These include: $Z \to \ell^+\ell^-$, heavy-flavor quark production, and W+jets. Physically irreducible backgrounds, such as, $Z \to \tau\tau$ and $WW \to \ell^+\ell^-$, have very low rates. Altogether, 0.6 ± 0.3 ee (resp. 1.0 ± 0.5 $\mu\mu$) background events are expected with $\approx$97% (resp. $\approx$98%) being due to instrumental backgrounds. Assuming a production cross section of 7 pb, 0.3 events are expected in each channel. Two events are observed in $\mu\mu$ data, and four events are collected in ee data. The results for the ee and $\mu\mu$ channels are summarized in Table 1.

The $e\mu$ decay channel represents a slightly larger fraction of $t\bar{t}$ events ($\approx$ 2$\times$1/81) and is cleaner, since it has no background from Z production. For this channel backgrounds also fall into the instrumental and irreducible categories. Their relative contributions are more balanced. The instrumental backgrounds are mainly from heavy flavor multijet and W+jets events. The irreducible backgrounds are of similar nature as those in the like-flavor dilepton

Table 1: Summary of individual analysis channel, where N^{obs} is the number of observed candidate events, $\mathcal{B}$ is the channel branching fraction, and ε the overall signal efficiency.

	Dilepton Channels					
	N^{obs}	$\mathcal{B}$	Bkg.	$\int \mathcal{L}dt$	ε	σ (pb)
ee	4	0.012	1.00	48.2 pb^{-1}	5.9%	$105.9^{+82.1\ +96.2}_{-59.6\ -39.7}$
$\mu\mu$	2	0.012	0.59	42.6 pb^{-1}	7.7%	$35.8^{+42.9\ +24.4}_{-28.0\ -11.5}$
$e\mu$	1	0.025	0.07	33 pb^{-1}	8.9%	$13.2^{+19.3\ +1.7}_{-10.1\ -0.8}$
	Lepton-plus-jets Channels (topological)					
	N^{obs}	$\mathcal{B}$	Bkg.	$\int \mathcal{L}dt$	ε	σ (pb)
e+jets	4	0.147	2.7	49.5 pb^{-1}	3.5%	$5.2^{+9.4\ +9.1}_{-6.7\ -3.1}$
μ+jets	4	0.147	2.7	40.0 pb^{-1}	5.8%	$3.8^{+6.9\ +3.9}_{-4.9\ -5.4}$
	Lepton-plus-jets Channels (Soft Muon b Tag)					
	N^{obs}	$\mathcal{B}$	Bkg.	$\int \mathcal{L}dt$	ε	σ (pb)
e+jets	2	0.147	0.16	40.0 pb^{-1}	1.3%	$24.1^{+23.0\ +7.0}_{-14.3\ -4.6}$
μ+jets	0	0.147	0.74	40.0 pb^{-1}	2.0%	< 8.5

channels, *i.e.*, $Z \to \tau\tau$ and $WW \to e\mu$. Altogether, 0.1 ± 0.1 background events are expected (≈70% from instrumental sources). Assuming a production cross section of 7 pb, 0.50 events are expected, and one event is observed. The results for the $e\mu$ channel are summarized in Table 1.

2.3 Leptons+Jets Analyses

The lepton+jets channels represent a significantly larger fraction of $t\bar{t}$ events ($\approx 2\times 6/81$). The signature of the lepton+jets events is one isolated high-E_T electron or muon, a large $\not\!\!E_T$ and four or more high-E_T jets. The two main backgrounds are from W+jets production and multijet events. Two complementary approaches are used in the analysis of these channels, the first using only topological selection cuts, and the second using the presence of a non isolated muon in at least one jet to tag b-quark jets. The first approach is efficient but not very pure, the second is pure but not very efficient due to the rather low fraction of b-quark jets decaying semi-leptonically to muons.

2.3.1 Topological Approach

The general philosophy of this analysis is to evaluate as much as possible background contributions from the data, it is carried out essentially in four steps:

(i) a preselection is applied to enrich our sample in W+jets and top production events;

(ii) the W+jets (and $t\bar{t}$) contribution is isolated from the multijet background;

(iii) the W+jets background normalization at high jet multiplicity is derived

(iv) a topological selection is applied in order to further discriminate $t\bar{t}$ events from backgrounds.

The preselection used to obtain a data sample enriched in W+jets events is similar to that used in the measurement of the W production cross section [2], with a soft-muon veto applied in order to eliminate overlaps with the soft-muon tagging approach described in Sec. 2.3.2. The contamination from multijet background events at the preselection level is obtained using two samples, one with loose restrictions (N^{ℓ}) and the other with tighter restrictions further enriched in W+jets and $t\bar{t}$ "signal" events (N^{t}). For the e+jets and μ+jets channels, the discrimination criteria are respectively the match of the EM cluster to a central track and the muon isolation. The rates at which "signal" and multijet background events filter from one set to the other (ε_{sig} and ε_{MJT}), are estimated respectively using control samples of Z and low $\not\!\!E_T$ multijet data events. The numbers of "signal" W+jets and $t\bar{t}$ events ($N^{\mathrm{W+t\bar{t}}}$) and background (N^{MJT}) are then obtained by solving:

$$N^{\ell} = N^{\mathrm{W+t\bar{t}}} + N^{\mathrm{MJT}} \quad (1)$$

$$N^{t} = \varepsilon_{sig} N^{\mathrm{W+t\bar{t}}} + \varepsilon_{MJT} N^{\mathrm{MJT}} \quad (2)$$

i.e.:

$$N^{\mathrm{W+t\bar{t}}} = \frac{N^{t} - \varepsilon_{MJT} N^{\ell}}{\varepsilon_{sig} - \varepsilon_{MJT}} \quad \text{and} \quad N^{\mathrm{MJT}} = \frac{\varepsilon_{sig} N^{\ell} - N^{t}}{\varepsilon_{sig} - \varepsilon_{MJT}} \quad (3)$$

The transverse W mass distributions in each multiplicity bin are shown in Figs. 1 and 2. This background evaluation method will be referred to as the matrix method.

To discriminate the $t\bar{t}$ signal from the W+jets background, at least four jets are required to be reconstructed. The $t\bar{t}$ contribution is evaluated assuming

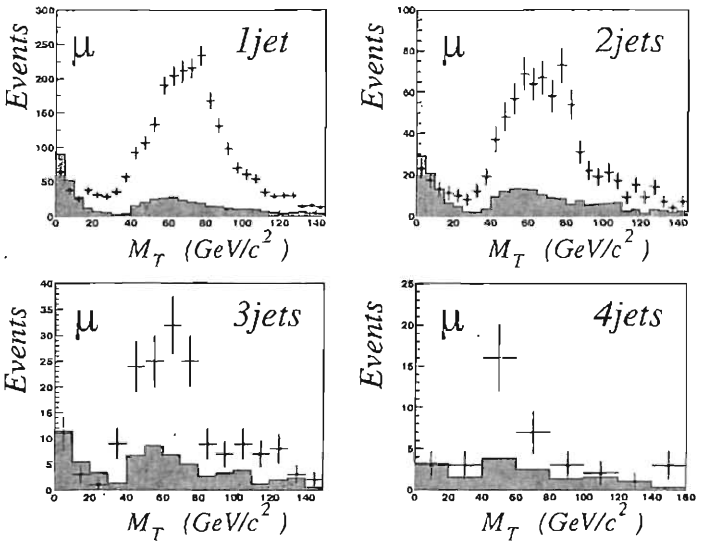

Figure 1: Transverse mass distribution in the ≥ 1, ≥ 2, ≥ 3, and ≥ 4-jet multiplicity bins for the μ+jets channel. Dots are the observed numbers of events after selections, histograms represent the multijet background contribution. The two-peak structure observed in the "background" distribution results from kinematic requirements and two distinct topological configurations: the lepton is pointing in the direction of the missing transverse energy and it is pointing opposite of the missing transverse energy.

Berends' empirical scaling law [12], which relates cross sections for the n^{th} and the $(n+1)^{th}$ jet multiplicities by:

$$\frac{\sigma[W + (n+1)\ jets]}{\sigma[W + n\ jets]} = \alpha$$

where α depends on jet selection criteria (such as transverse energy and acceptance). As a function of jet multiplicity $\geq i$ the number of W+jets events is:

$$N_{\geq i}^{W+t\bar{t}} = N_1^W \times \alpha^{i-1} + f_{\geq i}^{t\bar{t}} N^{t\bar{t}}$$

where $N_{\geq i}^{W+t\bar{t}}$ is the number of events after background subtraction using the matrix method, N_1^W is the number of W events with at least one jet in the final

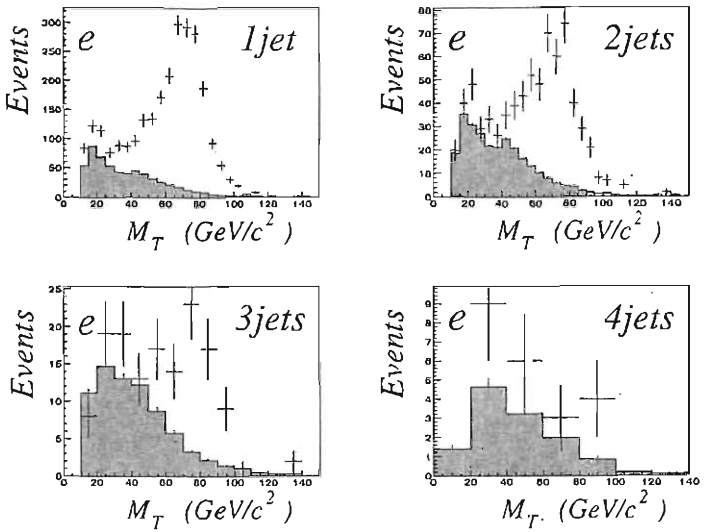

Figure 2: Transverse mass distribution in the ≥ 1, ≥ 2, ≥ 3, and ≥ 4-jet multiplicity bins for the e+jets channel. Dots are the observed numbers of events after selections, histograms represent the multijet background contribution. The two-peak structure observed in the "background" distribution results from kinematic requirements and two distinct topological configurations: (1) the lepton is pointing in the direction of the missing transverse energy and (2) it is pointing opposite of the missing transverse energy.

state, $f_{\geq i}^{t\bar{t}}$ is the fraction of $t\bar{t}$ events and i the inclusive jet multiplicity. The fractions $f_{\geq i}^{t\bar{t}}$ are computed from a Monte Carlo simulation. The values of α, N_1^W, and $N_{\geq i}^{t\bar{t}}$ are obtained from a fit to the $N^{\mathrm{W}+\mathrm{t}\bar{\mathrm{t}}}$ distribution. The number of W events in the ≥ 4 jets topology is thus given by:

$$N_4^W = N_1^W \times \alpha^3$$

The values of $N_{\geq i}^{\mathrm{W}+\mathrm{t}\bar{\mathrm{t}}}$ are shown in Fig. 3.

Finally $t\bar{t}$ signal events are further separated from background events using further topological selection cuts which were used at Run I [13]. In particular the two most discriminating variables were the scalar sum of all jet transverse energies $H_T = \Sigma_{jets} E_T$ and the aplanarity $\mathcal{A}$. After all cuts

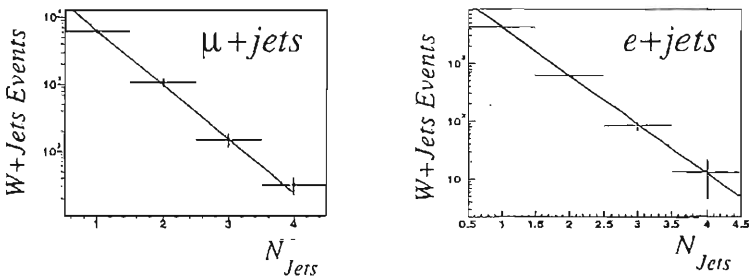

Figure 3: Yield of inclusive W+N_{jets} as a function of N_{jets}, for the μ+jets and e+jets analyses.

are applied four events remain in both the e+jets and μ+jets channels, while 2.7 ± 0.6 and 2.7 ± 1.1 were expected from background processes, respectively. For a $t\bar{t}$ cross section of 7 pb, 1.8 ± 0.4 and 2.4 ± 0.4 signal events were expected. The results for these channels are summarized in Table 1.

2.3.2 *Soft Muon b Jet Tagging*

In the analyses with soft-muon tag, the same preselections as in the topological approach are applied with a mild topological selection and requiring at least three jets.

The soft muon tag consists in the requirement that a muon with $p_T > 4\,\mathrm{GeV}/c$ is found within $\Delta R = 0.5$ of the jet axis. When this requirement is applied, two events are selected in the e+jets channel and none in the μ+jets channel. The multijet background is estimated using the matrix method. The background from W+jets is obtained by applying a tagging probability to the samples of events before soft-muon tagging is required and to which multijet background is subtracted using the matrix method. The average event tag rate for W+jets events is respectively 0.0156 and 0.0163 in the e+jets and μ+jets channels. The total backgrounds in the e+jets and μ+jets channels are 0.16 ± 0.10 and 0.74 ± 0.38, respectively. In total, assuming a $t\bar{t}$ cross section of 7 pb, 1.4 e+jets and μ+jets events are expected. The results for these two channels are also summarized in Table 1.

2.4 Combination

Taking the systematic uncertainties on the background estimate into account, the significance of the observation corresponds to a three-standard-deviations

effect. Combining all channels yields a measured cross section of:

$$\sigma_{p\bar{p}\to t\bar{t}} = 8.5^{+4.5}_{-3.6}\ (\text{stat})\ ^{+6.3}_{-3.5}\ (\text{sys})\ \pm 0.8\ (\text{lumi})\ \text{pb}.$$

3 Improved Measurement of the Top Quark Mass in the Lepton+Jets Channels

At Run I, in the lepton+jets channel the top quark mass was measured until recently using a 2C kinematic fit where the lepton and the neutrino on the one hand and two jets on the other hand were constrained to originate from a W boson. In this approach the full top event information was not taken into account. To optimally take advantage of all available event characteristics in discriminating signal from backgrounds, the likelihood method proposed by Kondo et al. [15] based on the production matrix element is applied.

In this approach the first order $t\bar{t}$ production in the s-channel matrix element is used to model the signal probability P_t. The background probability P_{bkg} is modeled using the W+4jets matrix element as estimated by VECBOS [10]. Out of the 91 events selected in the 125 pb^{-1} of data collected in Run I, only those 77 with exactly 4 jets are kept. A further purity requirement using P_{bkg} is used, further restricting the selected sample to 22 events. It is with this data sample that an unbinned global likelihood fit is applied yielding:

$$M_t = 179.9 \pm 3.6 \pm 5.4\ \text{GeV}$$

as illustrated in Fig. 5a and b. The reduction in the statistical uncertainty compared to the Run I result (5.6 GeV) corresponds to an increase by a factor of 2.4 in luminosity. Such an increase is largely due to the increased ability of this method to select good jet assignments to enter the fit.

The large systematic uncertainty on this measurement is dominated by the 4.9 GeV systematic uncertainty due to the jet energy scale. As shown in Fig. 5c and d the W mass can be measured in those events used for the top mass fit. The redundancy of the W mass measurement could be used to further constrain the jet energy scale uncertainty specifically for those events entering the top mass fit, and hopefully reduce the jet energy scale relate systematic uncertainty.

4 Conclusion

A first measurement of the $t\bar{t}$ cross section at the new Tevatron center-of-mass energy of 1.96 GeV was performed in two dilepton channels (ee, $e\mu$ and $\mu\mu$) and four lepton+jets channels (e+jets, μ+jets, e+jets/μ and μ+jets/μ). The individual results of each analysis are summarized in Table 1 and in Figure 4.

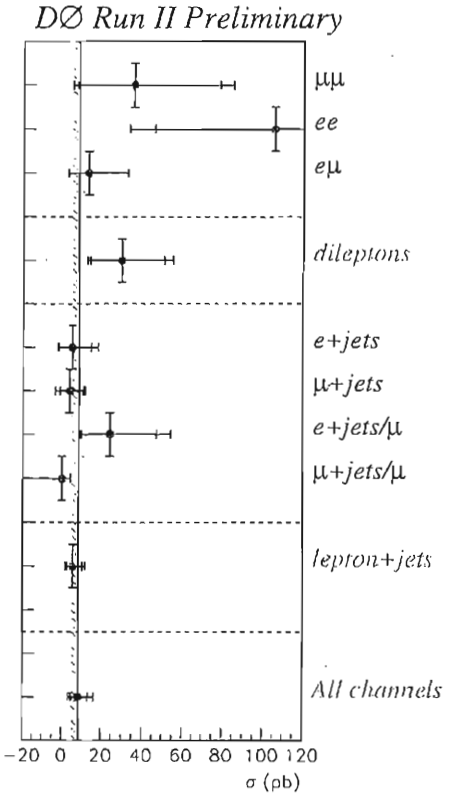

Figure 4: Summary of individual cross sections, dilepton and lepton+jets subcombinations, and the full combination of measurements. The theoretical prediction is indicated by the slanted band.

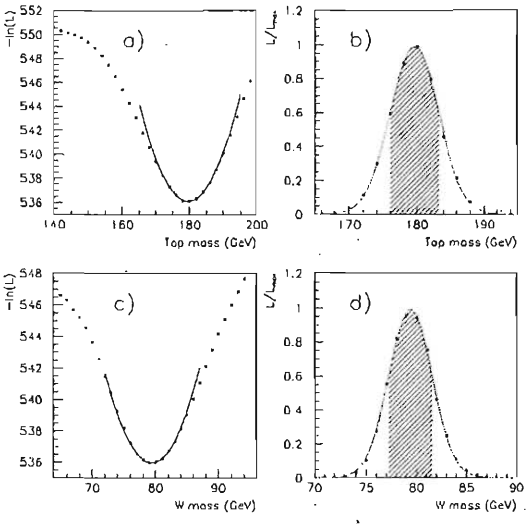

Figure 5: The logarithm of the likelihood (a) and the normalized likelihood (b) as a function of the top mass illustrating the fit of the top mass. The logarithm of the likelihood (c) and the normalized likelihood (d) as a function of the W mass illustrating the fit of the W mass when the top mass is fixed to its fitted value. The uncertainties of the fits are illustrated by the slanted area in (b) and (d).

The combined result yields a measured cross section of:

$$\sigma_{p\bar{p}\to t\bar{t}} = 8.5^{+4.5}_{-3.6}\ \text{(stat)}\ ^{+6.3}_{-3.5}\ \text{(sys)}\ \pm 0.8\ \text{(lumi)}\ \text{pb}.$$

Taking the systematic uncertainties on the background estimate into account, the significance of the observation corresponds to a three-standard-deviations effect.

An improved measurement of the top mass using Run I data was performed yielding:

$$M_t = 179.9 \pm 3.6 \pm 5.4\ \text{GeV}$$

5 Acknowledgments

I would like to thank the organizers of Les Rencontres de Physique de la Vallée d'Aoste for their wonderful hospitality and Robert Zitoun for his careful reading of these proceedings. This work was supported by the Director, Office of

Science, Office of High Energy and Nuclear Physics, of the U.S. Department of Energy under contract no. DE-AC03-76SF00098.

References

1. S. Abachi *et al.* [D0 Collaboration], Phys. Rev. Lett. **74**, 2632 (1995). F. Abe*et al.* [CDF Collaboration], Phys. Rev. Lett. **74**, 2626 (1995).

2. R. Kehoe, *these proceedings.*

3. M. Cacciari, S. Frixione, M. L. Mangano, P. Nason and G. Ridolfi, HEP-PH/0303085.

4. A. Bross *et al.*, "The D0 scintillating fiber tracker," *Prepared for SCIFI97: Conference on Scintillating and Fiber Detectors, South Bend, Indiana, 2-6 Nov 1997.*

5. B. Quinn [D0 Collaboration], "The D0 Silicon Microstrip Tracker," Nucl. Instrum. Meth. A **501** (2003) 7.

6. C. C. Miao [D0 Collaboration], "The D0 Run II luminosity monitor," Nucl. Phys. Proc. Suppl. **78** (1999) 342.

7. B. Abbott *et al.* [D0 Collaboration], "Determination of the absolute jet energy scale in the D0 calorimeters," Nucl. Instrum. Meth. A **424**, 352 (1999)

8. H. L. Lai *et al.*, "Global QCD analysis and the CTEQ parton distributions," Phys. Rev. D **51**, 4763 (1995)

9. T. Sjostrand, L. Lonnblad and S. Mrenna, "PYTHIA 6.2: Physics and manual," hep-ph/0108264.
T. Sjostrand, "High-energy physics event generation with PYTHIA 5.7 and JETSET 7.4," Comput. Phys. Commun. **82**, 74 (1994).

10. F. A. Berends, H. Kuijf, B. Tausk and W. T. Giele, "On The Production Of A W And Jets At Hadron Colliders," Nucl. Phys. B **357**, 32 (1991).

11. G. Marchesini, B. R. Webber, G. Abbiendi, I. G. Knowles, M. H. Seymour and L. Stanco, "HERWIG: A Monte Carlo event generator for simulating hadron emission reactions with interfering gluons. Version 5.1 - April 1991," Comput. Phys. Commun. **67**, 465 (1992).
G. Corcella *et al.*, "HERWIG 6: An event generator for hadron emission reactions with interfering gluons (including supersymmetric processes)," JHEP 0101, 010 (2001)

12. F. A. Berends, J. B. Tausk and W. T. Giele, "Top search in multi - jet signals," Phys. Rev. D **47**, 2746 (1993).

13. V. M. Abazov *et al.* [D0 Collaboration], Phys. Rev. D **67**, 012004 (2003)

14. M. L. Mangano, M. Moretti, F. Piccinini, R. Pittau and A. D. Polosa, "ALPGEN, a generator for hard multiparton processes in hadronic collisions," hep-ph/0206293.

15. R. H. Dalitz and G. R. Goldstein, Proc. R. Soc. Lond. **A 445**, 2803 (1999); K. Kondo *et al.*, J. Phys. Soc. Jap. **62**, 1177 (1993).

FORWARD-BACKWARD CHARGE ASYMMETRY AT VERY HIGH ENERGIES

B.I. Ermolaev
CFTC, University of Lisbon Av. Prof. Gama Pinto 2,
P-1649-003 Lisbon, Portugal and
Ioffe Physico-Technical Institute, 194021 St.Petersburg, Russia
M. Greco
Dipartamento di Fisica and INFN, University of Rome III, Italy
S.M. Oliveira
CFTC, University of Lisbon Av. Prof. Gama Pinto 2,
P-1649-003 Lisbon, Portugal
S.I. Troyan
St.Petersburg Institute of Nuclear Physics, 188300 Gatchina, Russia

Abstract

The impact of the electroweak radiative corrections on the value of the forward-backward asymmetry in e^+e^- annihilation into a quark-antiquark pair is considered in the double-logarithmic approximation at energies much higher than the masses of the weak bosons.

1 Introduction

The forward-bacward asymmetry for the charged hadrons produced in e^+e^- annihilation at high energies in vicinity of the Z -boson mass has been the object of intensive theoretical and experimental investigation. It is interesting to make a theoretical analysis of this phenomenon for much higher enegies where the leading, double-logarithmic (DL) contributions come not only from integrating over virtual photon momenta but also from virtual W and Z bosons. Indeed, at the annihilation energies much higher than 100 Gev, when masses of virtual electroweak bosons are small compared to their momenta, the initial $SU(2)xU(1)$ symmetry is restored in a certain sense and accounting for higher loop DL contributions involving the W, Z bosons is nonless imporatnt than the standard accounting for the photon DL contributions. The value of the asymmetry at such energies would be expressed rather through the Cazimir operators of the electroweak gauge group than through electric charges. In a sense, studing the forward-backward asymmetry at such enegries is one of the simplest ways to see the total effects of contributions of the electroweak radiative corrections of higher orders. Our theoretical study can be useful in future when Next linear colliders will explore e^+e^- annihilation at very high energies, probing further the Standard Model and eventually looking for New Physics.

In accordance with the present theoretical conceptions, we divide investigation of the annihilation into two stages: first we calculate the sub-process: e^+e^- -annihilation into a quark-antiquark pair (which is studied with perturbative methods) and then, numerically, account for hadronization effects which are quite different for converting the quarks into mesons and barions. We consider e^+e^- annihilate into two hadronic jets in the kinematics when the leading particles of every jet goes in cmf close to the beam axis, so they are within the cones with opening angles $\theta \ll 1$ and the axes around the e^- and e^+ directions. We obtain that the forward-backward asymmetry manifests itself as follows: the number of the hadrons with the positive electric charges, N_+ in the cone around the e^+ -direction exeeds the number of the negatively charged hadrons, N_- (see Ref. [1]). It is depicted in Fig. 1. The opposite effect is true for the other cone, around the e^- direction. The space outside of the cones is neutral. The numerical evaluations of the asymmetry are plotted in Fig. 2 separately for the produced mesons and barions. In particular, Fig.2 shows that the value of the asymmetry is high enouph to be measured at energies ≈ 1 TeV and grows steeply with energy.

In order to arrive at this result, let us consider first the basic sub-process of the annihilation: $e^+(p_2)e^-(p_1)$ annihilation into a quark $q(p_3)$ and its antiparticle $\bar{q}$. All these particles can belong either to the $SU(2)$ doublets or to the singlets. Our first goal is to calculate the scattering amplitudes of the

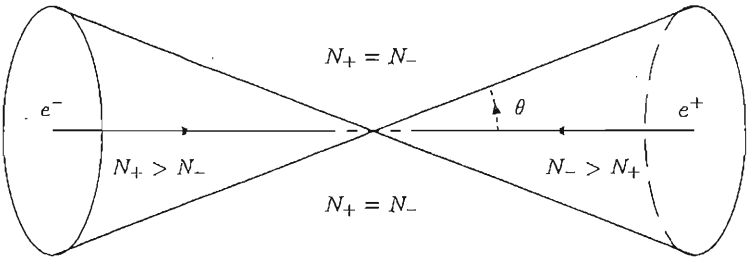

Figure 1: *Relations between charged hadrons in diferent angular regions.*

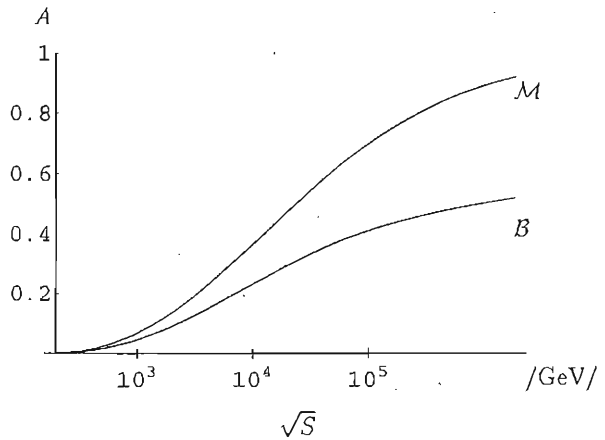

Figure 2: *Estimation of charge asymmetry A of leading charged hadrons in e^+e^- annihilation: The curve $\mathcal{M}$ is for the meson asymmetry and the curve $\mathcal{B}$ is for the asymmetry of barions.*

annihilation in the t- kinematics where

$$s = (p_1 + p_2)^2 \gg t = (p_3 - p_1)^2 \tag{1}$$

and in the u- kinematics:

$$s = (p_1 + p_2)^2 \gg u = (p_4 - p_1)^2 \ . \tag{2}$$

In order to account for DL contributions to all orders in the electroweak couplings, we use the evolution equations with respect to the infrared cut-off. This cut-off M is chosen in the transverse momentum space so that momenta of all virtual particles obey

$$k_{i\perp} > M \ . \tag{3}$$

Although only the Feynman graphs vith virtual photons can have the infrared divergencies, it is convenient to keep the restriction (3) for momenta of all virtual particles, assuming that

$$M \geq M_Z \approx M_W \ . \tag{4}$$

With assumptions of Eqs. (34), one can neglect all masses and be safe of the infrared singularities at the same moment. On the other hand, the scattering amplitudes now depend on M. It makes possible to evolute them in M and to put $M = M_Z \approx M_W$ in the final expressions. As DL contributions appear in the regions where $k_{i\perp}$ obey the strong inequalities of the kind $k_{i\perp} \gg k_{j\perp}$, it is always possible to find the virtual particle with minimal ($\equiv k_\perp$) transverse momentum in every such a region. Obviously, only integration over $k_\perp$ involves M as the lowest limit. Integrations over other transverse momenta are M-independent. DL contributions of the softest particles can be factorized. It allows to compose infrared evolution equations (IREE) for the scattering amplitudes. The most difficult is the case when both the initial electron and the final quark belong to the $SU(2)$ doublets. In order to simplify the IREE, one can use the $SU(2)$ simmetry restored at such high energies and consider annihilation of lepton-antilepton pair into a quark-antiquark pair. After that, it is convenient to exapand the scattering amplitude into the sum of the irreducible $SU(2)$ representations, using the standard projection operators multiplied by the invariant amplitudes $A_j, (j = 1, 2, 3, 4)$. At last, in order to calculate the invariant amplitudes in kinematics (1, 2), it is convenient to use the Mellin transform

$$A_j = \int_{-i\infty}^{i\infty} \frac{d\omega}{2\pi i} \left(\frac{s}{\kappa}\right)^\omega F_j(\omega) \tag{5}$$

where $\kappa = t, j = 1, 2$ for A_j in kinematics (1) and $\kappa = u, j = 3, 4$ when the kinematics is the u -inematics of Eq. (1). In the case of the collinear kinematics

where $\kappa = M^2$, amplitudes F_j obey (we consider amplitudes with the positive signatures only):

$$\omega F_j(\omega) = a_j + \frac{b_j}{8\pi^2}\frac{dF_j^{(+)}(\omega)}{d\omega} + \frac{c_j}{8\pi^2}\left[F_j^{(+)}(\omega)\right]^2 , \tag{6}$$

with a_j, b_j, c_j being numerical factors:

$$a_1 = \frac{3g^2 + g'^2 Y_1 Y_2}{4}, \quad a_2 = \frac{-g^2 + g'^2 Y_1 Y_2}{4}, \tag{7}$$
$$a_3 = \frac{-3g^2 + g'^2 Y_1 Y_2}{4}, \quad a_4 = \frac{g^2 + g'^2 Y_1 Y_2}{4} ,$$

$$b_1 = \frac{g'^2 (Y_1 - Y_2)^2}{4}, \quad b_2 = \frac{8g^2 + g'^2 (Y_1 - Y_2)^2}{4}, \tag{8}$$
$$b_3 = \frac{g'^2 (Y_1 - Y_2)^2}{4}, \quad b_4 = \frac{8g^2 + g'^2 (Y_1 + Y_2)^2}{4} ,$$

$$c_1 = c_2 = 1, \quad c_3 = c_4 = -1 . \tag{9}$$

Solutions to Eq. (6) can be expressed in terms of the Parabolic cylinder functions D_p:

$$F_j(\omega) = \frac{a_j}{\lambda_j}\frac{D_{p_j - 1}(\omega/\lambda_j)}{D_{p_j}(\omega/\lambda_j)} \tag{10}$$

where $p_j = a_j c_j / b_j$ and $\lambda_j = \sqrt{b_j/(8\pi^2)}$.

When the scattering angles are becoming larger so that

$$s \gg -\kappa \gg \mu^2 , \tag{11}$$

the invariant amplitudes A_j are expressed in terms of F_j in the following way:

$$A_j(\rho, \kappa) = a_j S_j \int_{-i\infty}^{i\infty} \frac{dl}{2\pi i} e^{\lambda_j l(\rho - \eta)} \frac{D_{p_j - 1}(l + \lambda_j \eta)}{D_{p_j}(l + \lambda_j \eta)} \tag{12}$$

where $\eta = \ln(\kappa/\mu^2)$ and factors h_j can be taken from Ref. [1]:

$$h_1 = \frac{3g^2 + g'^2 Y_l Y_q}{2}, \qquad h_2 = \frac{-g^2 + g'^2 Y_l Y_q}{2}, \tag{13}$$
$$h_3 = \frac{3g^2 - g'^2 Y_l Y_q}{2}, \qquad h_4 = \frac{-g^2 - g'^2 Y_l Y_q}{2}.$$

The factor S_j in Eq. (12) is the Sudakov form factor. Actually it is a product of the Sudakov form factors of the leptons and of the quarks. As follows from Eqs. (8,13), Due to the gauge invariance, it does not depend on j, i.e. is same for all invariant amplitudes. It can be seen also explicitly from Eqs. (8,13),

$$S = \exp\left[-\frac{1}{8\pi^2}\left(\frac{3}{2}g^2 + \frac{Y_l^2 + Y_q^2}{4}g'^2\right)\frac{\eta'^2}{2}\right] \quad (14)$$

This form factor accumulates DL contributions of soft virtual EW bosons and vanishes in the final expressions for the cross sections when bremsstrahlung of soft EW bosons with the cmf energies ϵ_k, $\mu < \epsilon_k < \sqrt{\kappa}$, is taken into account.

According to the results of Ref. [1], the amplitude for the forward $e^+e^- \to u\bar{u}$ -annihilation, M_u^F is expressed in terms of amplitudes A_3, A_4 of Eq. (12):

$$M_u^F = \frac{A_3 + A_4}{2}\,, \quad (15)$$

whereas the backward amplitude M_u^B for the same quarks is equal to the amplitude A_4 of Eq. (12):

$$M_u^B = A_4\,. \quad (16)$$

Similarly, the forward amplitude M_d^F for $e^+e^- \to d\bar{d}$ is

$$M_d^F = \frac{A_1 + A_2}{2}\,, \quad (17)$$

while the backward amplitude for this process is

$$M_d^B = A_2\,. \quad (18)$$

We use the folloing terminology: by the forward kinematics for $e^+e^- \to q\bar{q}$ -annihilation we mean that quarks with positive electric charges, u and $\bar{d}$, are produced around the initial e^+ - beam, in the cmf, within a cone with a small opening angle θ,

$$1 \gg \theta \geq \theta_0 = \frac{2M}{\sqrt{s}} \quad (19)$$

By backward kinematics we means just the opposite – the electric charge scatters backwards in a cone with the same opening angles.

The differential cross section $d\sigma_F$ for the forward annihilation is

$$d\sigma_F = d\sigma^{(0)}\left[|M_u^F|^2 + |M_d^F|^2\right] \equiv d\sigma^{(0)}\left[F_u + F_d\right]\,, \quad (20)$$

and similarly, the differential cross section $d\sigma_B$ for the backward annihilation is

$$d\sigma_B = d\sigma^{(0)} \left[|M_u^B|^2 + |M_d^B|^2\right] \equiv d\sigma^{(0)} \left[B_u + B_d\right], \tag{21}$$

where $d\sigma^{(0)}$ stands for the Born cross section, though without couplings. We define the forward-backward asymmetry as:

$$A \equiv \frac{d\sigma_F - d\sigma_B}{d\sigma_F + d\sigma_B} = \frac{F - B}{F + B} \tag{22}$$

where

$$F = F_u + F_d, \qquad B = B_u + B_d \,. \tag{23}$$

Contributions to the asymmetry from right leptons and quarks can be ealily obtained in a similar way. Then, using the standard programmes for hadronisation [3] and doing numerical calculations, we obtain the forward-backward asymmetry for e^+e^- annihilation into charged mesons and barions. The results are plotted in Fig. 2.

Finally, we would like to note that when the annihilation energy is high enouph to produce, in addition to the two quark jets, W or Z bosons with energies $\gg$ 100 GeV, it turnes out that the cross section $\sigma^{(n\gamma)}$ of n hard photon production, the cross section $\sigma^{(nZ)}$ of nZ boson production and the cross section $\sigma^{(nW)}$ of nW boson production obey very simple asymptotical relations (see Ref. [2]):

$$\frac{\sigma^{(nZ)}}{\sigma^{(n\gamma)}} \approx \tan^{2n}\theta_W \,, \tag{24}$$

$$\frac{\sigma^{(n\gamma)}}{\sigma^{(nW)}} \sim s^{-0.36}. \tag{25}$$

The ratios of these cross sections as functions of the annihilation energy are plotted in Figs. 3,4.

2 Acknowledgement

The work is supported by grants POCTI/FNU/49523/2002, SFRH/BD/6455/2001 and RSGSS-1124.2003.2 .

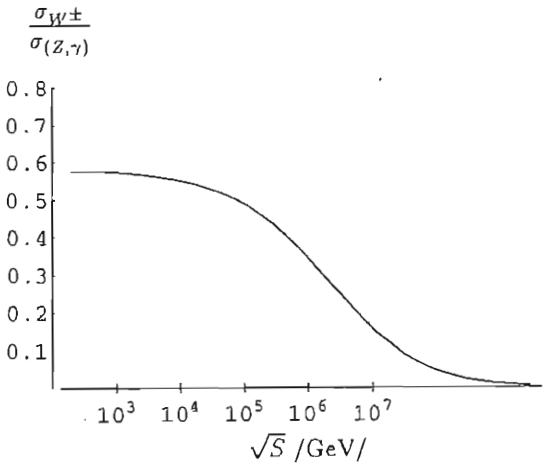

Figure 3: *Total energy dependence of $W^\pm$ to (Z,γ) rate in e^+e^- annihilation.*

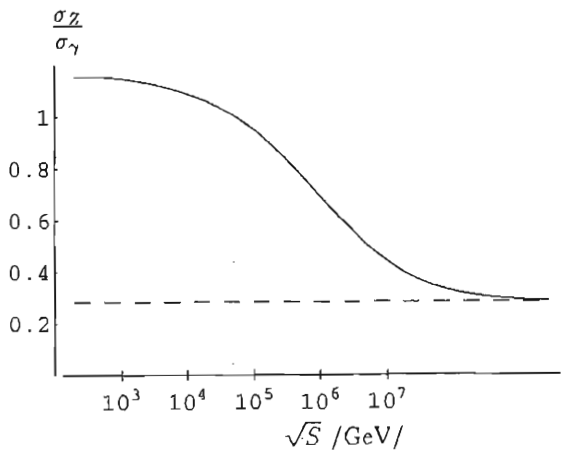

Figure 4: *Total energy dependence of Z to γ rate in e^+e^- annihilation. The dashed line shows the asymptotical value of the ratio:* $\tan^2\theta_W \approx 0.28$.

References

1. B.I. Ermolaev *et al*, Phys.Rev. **D67**, 014017, (2003).

2. B.I. Ermolaev *et al*, Phys.Rev. **D66**, 114018, (2002).

3. T.Sjöstrand. Computer Physics Commun. **82**, 74, (1994).

CONSEQUENCES OF A LARGE TOP-QUARK CHIRAL WEAK-MOMENT

Charles A. Nelson
Department of Physics, State University of New York at Binghamton
Binghamton, N.Y. 13902, USA

Abstract

This talk concerns some theoretical patterns of the helicity amplitudes for $t \to W^+b$ decay. The patterns involve both the standard model's decay helicity amplitudes, $A_{SM}(\lambda_{W^+}, \lambda_b)$, and the amplitudes $A_+(\lambda_{W^+}, \lambda_b)$ in the case of an additional $t_R \to b_L$ tensorial coupling of relative strength $\Lambda_+ = E_W/2 \sim 53GeV$. Such an additional electroweak coupling would arise if the observed top-quark has a large chiral weak-transition-moment. The A_+ amplitudes are interpreted as corresponding to the observed top-quark decays. Three tWb-transformations $A_+ = M\ A_{SM}, ...,$ are used in simple characterization of the values of Λ_+, m_W/m_t, and m_b/m_t. Measurement of the sign of the $\eta_L = \pm 0.46(SM/+)$ helicity parameter, due to the large interference between the W longitudinal and transverse amplitudes, could exclude such a chiral weak-transition-moment in favor of the SM prediction.

1 Introduction

While the theoretical analysis discussed in this talk does involve the observed mass values of the top-quark, W boson, and the b-quark, it is not a matter of any presently available empirical data disagreeing with a standard model (SM) prediction. Instead, the interest is because of some theoretical patterns of the helicity amplitudes for $t \to W^+b$ decay. The theoretical patterns involve both the standard model's decay helicity amplitudes, $A_{SM}(\lambda_{W^+}, \lambda_b)$, and the amplitudes $A_+(\lambda_{W^+}, \lambda_b)$ in the case of an additional $t_R \to b_L$ tensorial coupling of relative strength $\Lambda_+ = E_W/2 \sim 53GeV$. To focus the discussion, in this talk the A_+ amplitudes are interpreted as corresponding to the observed top-quark decays $t \to W^+b$ [1]. This identification hypothesis might be excluded by future theoretical analysis and/or empirical data; in (I), alternatives to this identification were considered [2]. Experimental tests and measurements in ongoing and forthcoming [1,3,4] top-quark decay experiments at hadron and l^-l^+ colliders should be able to significantly clarify matters. The explicit expressions for these amplitudes, and other details, are given in (I) and in a "hep-ph" preprint (II) [2].

Measurement of the sign of the $\eta_L \equiv \frac{1}{\Gamma}|A(-1,-\frac{1}{2})||A(0,-\frac{1}{2})|\cos\beta_L = \pm 0.46(SM/+)$ helicity parameter[5], due to the large interference between the $W_{Longitudinal}$ and $W_{Transverse}$ amplitudes, could exclude such a large chiral weak-transition-moment in $t \to W^+b$ decay in favor of the SM prediction. On the other hand, measurement of the SM predicted fraction of final $W_{Longitudinal}$ versus final $W_{Transverse}$ bosons for this decay mode would not distinguish between the two cases. The definitive empirical test must establish the sign of $cos(\beta_L)$ where β_L is the relative phase of the two $\lambda_b = -1/2$ amplitudes, $A(0,-1/2)$ and $A(-1,-1/2)$, c.f. Table 1 below.

In the t-quark rest frame, the matrix element for $t \to W^+b$ is

$$\langle \theta_1^t, \phi_1^t, \lambda_{W^+}, \lambda_b | \frac{1}{2}, \lambda_1 \rangle = D^{(1/2)*}_{\lambda_1,\mu}(\phi_1^t, \theta_1^t, 0) A_i(\lambda_{W^+}, \lambda_b) \qquad (1)$$

where $\mu = \lambda_{W^+} - \lambda_b$ in terms of the W^+ and b-quark helicities. Due to rotational invariance, there are four independent $A_i(\lambda_{W^+}, \lambda_b)$ amplitudes for the most general Lorentz coupling. We use the Jacob-Wick phase-convention for the amplitudes and use the subscript "i" to identify the amplitude's associated coupling; in this paper i = SM, $(f_M + f_E)$ for only the additional $t_R \to b_L$ tensorial coupling, and (+) for $A_+(\lambda_W, \lambda_b) = A_{SM}(\lambda_W, \lambda_b) + A_{f_M+f_E}(\lambda_W, \lambda_b)$ when $\Lambda_+ = E_W/2$. With respect to the latter case, the Lorentz coupling involving both the SM's $(V-A)$ coupling and an additional $t_R \to b_L$ tensorial coupling of arbitrary relative strength Λ_+ is $W_\mu^* J_{bt}^\mu = W_\mu^* \bar{u}_b(p) \Gamma^\mu u_t(k)$ where $k_t = q_W + p_b$, and

$$\frac{1}{2}\Gamma^\mu = g_L \gamma^\mu P_L + \frac{g_{f_M+f_E}}{2\Lambda_+} \iota \sigma^{\mu\nu}(k-p)_\nu P_R \qquad (2)$$

Table 1: Amplitudes in Standard Model and at Ambiguous Moduli Points

	$A(0,-\frac{1}{2})$	$A(-1,-\frac{1}{2})$	$A(0,\frac{1}{2})$	$A(1,\frac{1}{2})$
$A_{g_L=1}$ in $g_L=1$ units				
$V-A$	338	220	-2.33	-7.16
$S+P$	-338	220	-24.4	-7.16
f_M+f_E	220	-143	1.52	-4.67
$A_{New}=A_{g_L=1}/\sqrt{\Gamma}$				
$V-A$	0.84	0.54	-0.0058	-0.018
$S+P$	-0.84	0.54	-0.060	-0.018
f_M+f_E	0.84	-0.54	0.0058	-0.018

Thus, for $\Lambda_+ = E_W/2$ in $g_L = g_{f_M+f_E} = 1$ units, which corresponds to the (+) amplitudes, the Lorentz structure of the effective coupling is very simple

$$\gamma^\mu P_L + \imath\sigma^{\mu\nu} v_\nu P_R \tag{3}$$

$$= P_R\,(\gamma^\mu + \imath\sigma^{\mu\nu} v_\nu) \tag{4}$$

where $P_{L,R} = \frac{1}{2}(1 \mp \gamma_5)$ and v_ν is the W-boson's relativistic four-velocity.

The interest in these particular couplings arose as a by-product of a consideration [6] of future measurements of competing observables in $t \to W^+ b$ decay. In particular, we considered the SM's the g_{V-A} coupling values of helicity decay parameters versus those for " $(V - A)$ + single additional Lorentz structures." It was found that versus the SM's dominant L-handed b-quark amplitudes, there are two "dynamical phase-type ambiguities" produced respectively by an additional $(S + P)$ coupling and by an additional $t_R \to b_L$ tensorial coupling, see the $A\left(0, -\frac{1}{2}\right)$ and $A\left(-1, -\frac{1}{2}\right)$ columns of Table 1. Such a dynamical-ambiguity produced physically by the additional Lorentz structure is to be contrasted to the mathematical forcing of a "phase-ambiguity" by simply changing by-hand the sign of one, or more, of the four helicity amplitudes $A(\lambda_W, \lambda_b)$. By tuning the effective-mass-scale associated with the additional coupling constant, the additional $(S + P)$ coupling, $(f_M + f_E)$ coupling, has respectively changed the sign of the $A\left(0, -\frac{1}{2}\right)$, $A\left(-1, -\frac{1}{2}\right)$ amplitude. In $g_L = g_{S+P} = g_+ = 1$ units, the corresponding effective-mass scales are $\Lambda_{S+P} \sim -35GeV$, $\Lambda_+ \sim 53GeV$. The numerical patterns shown in the table in the case of the additional Λ_{S+P} coupling are not surprising for the $(S + P)$ coupling because it only contributes to the $W_{Longitudinal}$ amplitudes. However, associated with the additional $t_R \to b_L$ tensorial coupling, labeled $(f_M + f_E)$ in this table, three interesting numerical puzzles arise at the 0.1% level in the (+) amplitudes versus the SM's pure $(V - A)$ amplitudes.

The 1st puzzle is that the $A_+(0, -1/2)$ amplitude has the same value as the $A_{SM}(-1, -1/2)$ amplitude in the SM; see the corresponding two "220" entries in the top of Table 1. From the empirical t-quark and W-boson mass values, the mass ratio $y = \frac{m_W}{m_t} = 0.461 \pm 0.014$. This can be compared with the puzzle's associated mass relation

$$1 - \sqrt{2}y - y^2 - \sqrt{2}y^3 = x^2\left(\frac{2}{1-y^2} - \sqrt{2}y\right) - x^4\left(\frac{1-3y^2}{(1-y^2)^3}\right) + \ldots \tag{5}$$

$$= 1.89x^2 - 0.748x^4 + \ldots$$

which follows by setting $A_+(0, -1/2) = A_{SM}(-1, -1/2)$ and then expanding in $x^2 = (m_b/m_t)^2$ the $A_+(0, -1/2)$ amplitude, with $\Lambda_+ = E_W/2 = \frac{m_t}{4}[1 + y^2 - x^2]$ in $g_L = g_+ = 1$ units. Since empirically $x^2 \simeq 7 \cdot 10^{-4}$, there is only a

4th significant-figure correction from the finite b-quark mass to the only real-valued solution $y = 0.46006$ ($m_b = 0$) of this mass relation. The 0.1% level of agreement of the two "220" entries of Table 1 is due to the present central value of m_t, and to the central value and 0.05% precision of m_W. The error in the empirical value of the mass ratio y is dominated by the current 3% precision of m_t.

The 2nd and 3rd numerical puzzles are the occurrence of the same magnitudes of the two R-handed b-quark amplitudes $A_{New} = A_{g_L=1}/\sqrt{\Gamma}$ for the SM and for the additional $t_R \to b_L$ tensorial coupling. This is shown in the $A\left(0, \frac{1}{2}\right)$ and $A\left(1, \frac{1}{2}\right)$ columns in the bottom half of Table 1. As explained below, for $\Lambda_+ = E_W/2$ the magnitudes of these two R-handed moduli are actually exactly equal and not merely numerically equal to the 0.1% level.

We will next discuss different types of helicity amplitude relations involving both the standard model's decay helicity amplitudes, $A_{SM}(\lambda_{W^+}, \lambda_b)$, and the amplitudes $A_+(\lambda_{W^+}, \lambda_b)$ in the case of an additional $t_R \to b_L$ tensorial coupling of relative strength Λ_+. These relations in some cases "explain" and in other cases analytically realize as theoretical patterns, these and other numerical puzzles of Table 1.

Helicity amplitude relations of types (i) and (ii) are exact ratio-relations holding for all $y = \frac{m_W}{m_t}, x = \frac{m_b}{m_t}$, and Λ_+ values,. By the type (iii) ratio-relations holding for all $y = \frac{m_W}{m_t}$ and $x = \frac{m_b}{m_t}$ values, the tWb-transformation $A_+ = M\ A_{SM}$ where $M = v\ diag(1, -1, -1, 1)$ characterizes the mass scale $\Lambda_+ = E_W/2$. The parameter v is the velocity of the W-boson in the t-quark rest frame. Somewhat similarly, the amplitude condition (iv), $A_+(0, -1/2) = aA_{SM}(-1, -1/2)$ with $a = 1 + O(v \neq y\sqrt{2}, x)$, and the amplitude condition (v), $A_+(0, -1/2) = -bA_{SM}(1, 1/2)$ with $b = v^{-8}$, determine respectively the scale of two additional 4x4 tWb-transformation matrices P and B. Thereby, (iv) and (v) characterize the values of the mass ratios $y = m_W/m_t$ and $x = m_b/m_t$. $O(v \neq y\sqrt{2}, x)$ denotes small corrections. It is not understood why the values are simple for the parameters a and b.

2 Helicity amplitude relations

The first type of ratio-relations holds separately for $i = (SM), (+)$: (i):

$$\frac{A_i(0, 1/2)}{A_i(-1, -1/2)} = \frac{1}{2}\frac{A_i(1, 1/2)}{A_i(0, -1/2)} \tag{6}$$

The second type of ratio-relations relates the amplitudes in the two cases (ii): Two sign-flip relations, note sign changes of amplitudes in Table 1,

$$\frac{A_+(0, 1/2)}{A_+(-1, -1/2)} = \frac{A_{SM}(0, 1/2)}{A_{SM}(-1, -1/2)} \tag{7}$$

$$\frac{A_+(0,1/2)}{A_+(-1,-1/2)} = \frac{1}{2}\frac{A_{SM}(1,1/2)}{A_{SM}(0,-1/2)} \tag{8}$$

and two non-sign-flip relations

$$\frac{A_+(1,1/2)}{A_+(0,-1/2)} = \frac{A_{SM}(1,1/2)}{A_{SM}(0,-1/2)} \tag{9}$$

$$\frac{A_+(1,1/2)}{A_+(0,-1/2)} = 2\frac{A_{SM}(0,1/2)}{A_{SM}(-1,-1/2)} \tag{10}$$

The third type of ratio-relations, follows by determining the effective mass scale, Λ_+, so that there is an exact equality for the ratio of left-handed amplitudes (iii):

$$\frac{A_+(0,-1/2)}{A_+(-1,-1/2)} = -\frac{A_{SM}(0,-1/2)}{A_{SM}(-1,-1/2)}, \tag{11}$$

This was the tuning condition used to produce the dynamical phase-ambiguities of Table 1 [6]. Equivalently, $\Lambda_+ = E_W/2$ follows from each of:

$$\frac{A_+(0,-1/2)}{A_+(-1,-1/2)} = -\frac{1}{2}\frac{A_{SM}(1,1/2)}{A_{SM}(0,1/2)}, \tag{12}$$

$$\frac{A_+(0,1/2)}{A_+(1,1/2)} = -\frac{A_{SM}(0,1/2)}{A_{SM}(1,1/2)}, \tag{13}$$

$$\frac{A_+(0,1/2)}{A_+(1,1/2)} = -\frac{1}{2}\frac{A_{SM}(-1,-1/2)}{A_{SM}(0,-1/2)}, \tag{14}$$

Alternatively, the value of Λ_+ can be characterized by postulating the existence of a tWb-transformation $A_+ = M\ A_{SM}$ where $M = v\ diag(1,-1,-1,1)$, with $A_{SM} = [A_{SM}(0,-1/2), A_{SM}(-1,-1/2), A_{SM}(0,1/2), A_{SM}(1,1/2)]$ and analogously for A_+.

Assuming (iii), the fourth type of relation is the equality (iv):

$$A_+(0,-1/2) = aA_{SM}(-1,-1/2), \tag{15}$$

where $a = 1 + O(v \neq y\sqrt{2}, x)$. This is equivalent to the velocity formula $v = ay\sqrt{2}\left(\frac{1}{1-(E_b-q)/m_t}\right) \simeq ay\sqrt{2}$, for $m_b = 0$. For $a = 1$, (iv) leads to the mass relation discussed above, Eq.(5). However, for $a = 1$, (iv) also leads to $\sqrt{2} = v\gamma(1+v) = v\sqrt{\frac{1+v}{1-v}}$ so $v = 0.6506\ldots$ without input of a specific value for m_b. But by Lorentz invariance v must depend on m_b. Accepting (iii) as exact, we interpret this to mean that $a \neq 1$. As shown in (II), the $O(v \neq y\sqrt{2}, x)$ corrections in a, required by Lorentz invariance, arise from $v \neq y\sqrt{2}$ and $x \neq 0$.

Equivalently, for a arbitrary, (15) can be expressed postulating the existence of a second tWb-transformation $A_+ = P\ A_{SM}$ where

$$P \equiv v \begin{bmatrix} 0 & a/v & 0 & 0 \\ -v/a & 0 & 0 & 0 \\ 0 & 0 & 0 & -v/2a \\ 0 & 0 & 2a/v & 0 \end{bmatrix} \tag{16}$$

The above two tWb-transformations do not relate the $\lambda_b = -\frac{1}{2}$ amplitudes with the $\lambda_b = \frac{1}{2}$ amplitudes. From (i) thru (iv), in terms of a parameter b, the equality (v):

$$A_+(0,-1/2) = -bA_{SM}(1,1/2), \tag{17}$$

is equivalent to $A_+ = B\ A_{SM}$

$$B \equiv \begin{bmatrix} 0 & 0 & 0 & -b \\ 0 & 0 & 2b & 0 \\ 0 & v^2/2b & 0 & 0 \\ -v^2/b & 0 & 0 & 0 \end{bmatrix} \tag{18}$$

The choice of $b = v^{-8} = 31.152$, gives

$$B \equiv v \begin{bmatrix} 0 & 0 & 0 & -v^{-9} \\ 0 & 0 & 2v^{-9} & 0 \\ 0 & v^9/2 & 0 & 0 \\ -v^9 & 0 & 0 & 0 \end{bmatrix} \tag{19}$$

and corresponds to the mass relation $m_b = \frac{m_t}{b}\left[1 - \frac{vy}{\sqrt{2}}\right] = 4.407...GeV$ for $m_t = 174.3GeV$.

If one does not distinguish the (+) versus SM indices, respectively of the rows and columns, these three tWb-transformation matrices have some simple properties, for details see (Π): The anticommuting 4x4 matrices M, P with a arbitrary, and Q satisfy the closed algebra $[\overline{M},\overline{P}] = 2\overline{Q}, [\overline{M},\overline{Q}] = 2\overline{P}, [\overline{P},\overline{Q}] = 2\overline{M}$. The bar denotes removal of the overall "v" factor, $M = v\overline{M}, ...$ Note that Q is not a tWb-transformation; Q is obtained from the first listed commutator.

Including the B matrix with both a and b arbitrary, the "commutator + anticommutator" algebra closes with 3 additional matrices C, H, G obtained by $\{\overline{M},\overline{B}\} = -2\overline{C}; [\overline{P},\overline{B}] = 2\overline{H}$; and $\{\overline{P},\overline{C}\} = -2\overline{G}$. This has generated an additional tWb transformation $G \equiv v\overline{G}$; but $C \equiv v\overline{C}$ and $H \equiv v\overline{H}$ are not tWb transformations.

3 Discussion

The elements of the three logically-successive tWb transformations are constrained by the exact helicity amplitude ratio-relations (i) and (ii). Thereby,

the type (iii) ratio-relation fixes $\Lambda_+ = E_W/2$ and the overall scale of the tWb-transformation matrix M. Somewhat similarly, the amplitude condition (iv) with $a = 1 + O(v \neq y\sqrt{2}, x)$ and the amplitude condition (v) with $b = v^{-8}$ determine respectively the scale of the tWb-transformation matrices P and B and characterize the values of m_W/m_t and m_b/m_t. The overall scale can be set here by m_t or m_W. From the perspective of further "unification", m_W is more appropriate since its value is fixed in the SM.

The additional $t_R \to b_L$ tensorial coupling violates the conventional gauge invariance transformations of the SM and traditionally in electroweak studies such anomalous couplings have been best considered as "induced" or "effective". The f_E component corresponds to a "second class current" [7]. f_E has a distinctively different reality structure, and time-reversal invariance property versus the first class V, A, f_M [8].

In the present context, supersymmetry could provide a more general and useful off-shell theoretical framework in which to consider these theoretical patterns of the helicity amplitudes for $t \to W^+b$ decay. Form factor effects would naturally occur. In the extant MSSM literature, see more complete references in (II), sizable "one-loop-level" reductions in the $t \to W^+b$ partial decay width have been reported: From SM Higgs and additional MSSM's Higg's there is a small $\leq 2\%$ correction. However, from SUSY electroweak corrections, there is in [9] an up to 10% reduction, depending on $tan(\beta)$. From QCD including some two-loop-level corrections and SUSY QCD corrections in the summary of [10] a 25% reduction is reported. It is to be emphasized that, firstly, the (+) partial width considered in the present paper constitutes a very large, net 56% reduction versus the Born-level SM value and that, secondly, these cited SUSY calculations have been for the partial width, so other couplings instead of an additional effective $t_R \to b_L$ tensorial coupling, might be predominantly responsible for these reported reductions.

4 Experimental Tests/Measurements

Empirically, important tests of the physical relevance of the theoretical patterns to the observed top-quark decays are:
(a) Measurement of the sign of the $\eta_L \equiv \frac{1}{\Gamma}|A(-1,-\frac{1}{2})||A(0,-\frac{1}{2})|\cos\beta_L = \pm 0.46(SM/+)$ helicity parameter via determination of stage-two spin-correlation observables [5] for the $t\bar{t} \longrightarrow l\bar{l} + jets$ channel. These values for η_L are essentially the maximal possible deviations since $|\eta_L| = 0.5$ is the kinematic limit. The differences from $|\eta_L| = 0.5$ are due to $m_b \neq 0$.
(b) Measurement of the closely associated $\eta_L{}' \equiv \frac{1}{\Gamma}|A(-1,-\frac{1}{2})||A(0,-\frac{1}{2})|\sin\beta_L$ helicity parameter. This would provide useful complementary information, since in the absence of T_{FS}-violation, $\eta_L{}' = 0$ [6]. T_{FS}-violation can occur due to intrinsic time-reversal violation and/or large W^+b final-state interactions.

It is very important to exclude sizable T_{FS}-violation and/or CP-violation in top-quark decays.
(c) Measurement of the partial width for $t \to W^+ b$, e.g. by single top-quark production at a hadron collider [11]. The v^2 factor which differs their associated partial widths corresponds to the SM's $\Gamma_{SM} = 1.55 GeV$, versus $\Gamma_+ = 0.66 GeV$ and a longer-lived (+) top-quark if this mode is dominant.

5 Acknowledgments

We thank experimental and theoretical physicists for discussions, and the Fermilab Theory Group for a visit during the summer of 2002. This work was partially supported by U.S. Dept. of Energy Contract No. DE-FG 02-86ER40291.

References

1. CDF collaboration, T. Affolder, et.al., Phys.Rev.Lett. **84**, 216(2000); DØ collaboration, B. Abbott, et.al., Phys.Rev.Lett. **85**, 256(2000).

2. C.A. Nelson, Phys. Rev. **D65**, 074033 (2002); hep-ph/0304198.

3. ATLAS Technical Proposal, CERN/LHCC/94-43, LHCC/P2 (1994); CMS Technical Design Report, CERN-LHCC- 97-32; CMS-TDR-3 (1997).

4. Pro. of APS/DPF/DPB Summer Study, Snowmass-2001-E3020, eConf C010630; Tesla Tech. Design Report, DESY 2001-011, http://tesla.desy.de/ ; Japanese Linear Collider Group, JLC-I, KEK-Report 92-16(1992); Linear Collider Physics Resource Book, American Linear Collider Working Group, SLAC-R-570, http://www.slac.stanford.edu/grp/th/LCBook/.

5. C.A. Nelson, B.T. Kress, M. Lopes, and T.P. McCauley, Phys. Rev. **D56**, 5928(1997).

6. C.A. Nelson, p. 369 in "Physics at Extreme Energies," eds. Nguyen van Hieu and Jean Tran Thanh Van, The Gioi Publishers, Vietnam 2001; C.A. Nelson and L.J. Adler, Jr., Eur. Phys. J. **C17**, 399(2000); and C.A. Nelson and A.M. Cohen, Eur. Phys. J. **C8**, 393(1999).

7. S. Weinberg, Phys. Rev. **112**,1375(1958).

8. N. Cabbibo, Phys. Rev. Lett. **12**, 137(1964); c.f. C.A. Nelson, Phys. Lett. **B355**, 561(1995).

9. D. Garcia, W. Hollik, R.A: Jimenez, J. Sola, Nucl. Phys. **427**, 53(1994).

10. A. Dabelstein, W. Hollik, C. Junger, R.A. Jimenez, J. Sola, Nucl. Phys., **B454**, 75(1995).

11. S. Willenbrock and D. A. Dicus, Phys. Rev. **D34**, 155(1986); C.-P. Yuan, *ibid.***D41**, 42 (1990); R.K. Ellis and S. Parke, *ibid.***D46**, 3785(1992); G. Bordes and B. van Eijk, Z. Phys. **C57**, 81(1993); and T. Stelzer, Z. Sullivan, and S. Willenbrock, Phys. Rev. **D56**, 5919(1997).

SESSION VI – CP VIOLATION AND RARE DECAYS

Takeo Higuchi	Measurements of the Unitarity Triangle by Belle
Sandrine Laplace	Rare B decays and Direct CP Violation at BaBar
Riccardo Faccini	Measurements of CP Violation in Mixing with the BaBar Experiment at PEP-II
Alexei Drutskoy	Direct CP Violation Searches at Belle
Gino Isidori	New Physics in $B_d - \bar{B}_d$ Mixing and CKM Fits
Ivan Mikulec	CP Violation and Rare Decays in the K Sector at NA48
Eugeny Shabalin	Semi-Phenomenological Approach to the Estimate of CP–Effects in $K\pm \to 3\pi$ Decays
Giancarlo D'Ambrosio	Theory of Rare Kaon Decays

MEASUREMENT OF THE UNITARITY TRIANGLE BY BELLE

T. Higuchi for the Belle collaboration
High Energy Accelerator Research Organization

Abstract

We present measurements of the Cabbibo-Kobayashi-Maskawa matrix elements from CP-violating parameters observed in $b \to c\bar{c}s$, $b \to s\bar{q}q$, and $b \to u\bar{u}d$ transitions; and the $B^0 \to D_s^+\pi^-$ decay that is dominated by the $b \to u$ tree transition. The analyses presented here are based on a sample of 85×10^6 $B\overline{B}$ pairs collected at the $\Upsilon(4S)$ resonance with the Belle detector at the KEKB asymmetric-energy e^+e^- collider. We determine the interior angles of the unitarity triangle as $\sin 2\phi_1 = 0.719 \pm 0.074(\text{stat}) \pm 0.035(\text{syst})$ and $78^\circ \leq \phi_2 \leq 152^\circ$ (at 95.5% C.L.). We find consistent $\sin 2\phi_1$ to above number in the $B^0 \to \eta' K_S^0$ and $K^+K^-K_S^0$ decays, and a deviated number by 2.1σ in the $B^0 \to \phi K_S^0$ decay. The side of the unitarity triangle is determined to be $|V_{ub}| = (3.5^{+1.0}_{-0.9}) \times 10^{-3}$.

1 Introduction

In 1973, Kobayashi and Maskawa (KM) proposed a model, where the CP violation is accommodated as an irreducible complex phase in the weak-interaction quark mixing matrix [1], which is defined as

$$\begin{pmatrix} V_{ud} & V_{us} & V_{ub} \\ V_{cd} & V_{cs} & V_{cb} \\ V_{td} & V_{ts} & V_{tb} \end{pmatrix}, \tag{1}$$

where the nontrivial complex phases are conventionally assigned to the furthest off-diagonal elements, V_{ub} and V_{td}. Unitarity of this Cabbibo-Kobayashi-Maskawa matrix (CKM matrix) implies that $\sum_i V_{ij}V_{ik}^* = \delta_{jk}$, which gives the following relation involving V_{ub} and V_{td}:

$$V_{ud}V_{ub}^* + V_{cd}V_{cb}^* + V_{td}V_{tb}^* = 0. \tag{2}$$

This expression can be visualized as a closed triangle, known as a unitarity triangle, in the complex plane as shown in Fig. 1. The three interior angles of

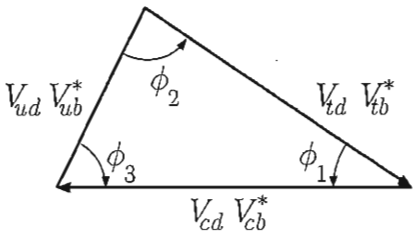

Figure 1: *The unitarity triangle relevant to B decays.*

the unitarity triangle originate from the irreducible complex phase are defined as [2]:

$$\begin{aligned} \phi_1 &\equiv \pi - \arg(-V_{td}V_{tb}^*/-V_{cd}V_{cb}^*), \\ \phi_2 &\equiv \arg(V_{td}V_{tb}^*/-V_{ud}V_{ub}^*), \\ \phi_3 &\equiv \arg(V_{ud}V_{ub}^*/-V_{cd}V_{cb}^*). \end{aligned} \tag{3}$$

Recent measurements of the mixing-induced CP-violating asymmetry parameter $\sin 2\phi_1$ [3] strongly support the Kobayashi-Maskawa mechanism. However, a full test of the KM mechanism requires additional measurements for the sides and other angles of the unitarity triangle.

In this paper, we report the recent results from the Belle with 78 fb^{-1} data sample on the $\Upsilon(4S)$ resonance, which corresponds to 85×10^6 $B\overline{B}$ pairs, collected before July 2002, concentrating on (1) an improved measurement of $\sin 2\phi_1$ using $b \to c\bar{c}s$ transition, (2) first study of CP violation in $b \to s\bar{q}q$ transition that is equivalent to $\sin 2\phi_1$ within the standard model prediction, and (3) an evidence for CP violation in $B^0 \to \pi^+\pi^-$ and constraint on ϕ_2. We also present (4) a determination of $|V_{ub}|$ at Belle using $B^0 \to D_s^+\pi^-$ decay [4].

2 KEKB and Belle

The data are collected with the Belle detector [5] at the KEKB energy asymmetric collider [6], which collides 8.0 GeV electron on 3.5 GeV position operating at the $\Upsilon(4S)$ resonance. At KEKB, the $\Upsilon(4S)$ is produced with a Lorentz boost of $\beta\gamma = 0.425$ nearly along the electron beamline (z-direction). The produced $\Upsilon(4S)$ immediately decays to a coherent P-wave $B\overline{B}$ pair. The recorded maximum luminosity by the accelerator is $> 1.05 \times 10^{34}$ cm^{-2}s^{-1}, and we have accumulated 149 fb^{-1} data, where approximately 90% of them are on $\Upsilon(4S)$ resonance.

The Belle detector is a large-solid-angle spectrometer that includes a silicon vertex detector (SVD), a central drift chamber (CDC), an array of aerogel threshold Cherenkov counters (ACC), time-of-flight (TOF) scintillation counters, and an electromagnetic calorimeter comprised of CsI(Tl) crystals (ECL) located inside a superconducting solenoid coil that provides a 1.5 T magnetic field. An iron flux-return located outside of the coil is instrumented to detect K_L^0 mesons and to identify muons (KLM).

3 Measurements of $\sin 2\phi_1$

The KM-schemed Standard Model (SM) predicts a CP-violating asymmetry in the time-dependent decay rates for B^0 and $\overline{B}^0$ to a common CP eigenstate, f_{CP}:

$$\Gamma(B^0 \to f_{CP}) = \frac{e^{-|\Delta t|/\tau_{B^0}}}{4\tau_{B^0}}\left[1 - \mathcal{S}\sin(\Delta m_d \Delta t) - \mathcal{A}\cos(\Delta m_d \Delta t)\right], \quad (4)$$

$$\Gamma(\overline{B}^0 \to f_{CP}) = \frac{e^{-|\Delta t|/\tau_{B^0}}}{4\tau_{B^0}}\left[1 + \mathcal{S}\sin(\Delta m_d \Delta t) + \mathcal{A}\cos(\Delta m_d \Delta t)\right], \quad (5)$$

$$\begin{aligned} A_{CP}(\Delta t) &\equiv \frac{\Gamma(\overline{B}^0 \to f_{CP}) - \Gamma(B^0 \to f_{CP})}{\Gamma(\overline{B}^0 \to f_{CP}) + \Gamma(B^0 \to f_{CP})} \\ &= \mathcal{S}\sin(\Delta m_d \Delta t) + \mathcal{A}\cos(\Delta m_d \Delta t), \end{aligned} \quad (6)$$

where $\Gamma(B^0, \overline{B}^0 \to f_{CP})$ is the decay rate for a B^0 or $\overline{B}^0$ to a CP eigenstate f_{CP}, Δm_d is the mass difference between the two B^0 mass eigenstates. The

Table 1: *The SM-predicted values for $\mathcal{S}$ and $\mathcal{A}$ in relation with the ϕ_1 and ϕ_2. The ξ_f is the CP eigenvalue of the decay final state. The assumed approximation in this table is written in the text.*

Transition	$b \to c\bar{c}s$	$b \to s\bar{q}q$	$b \to u\bar{u}d$
$\mathcal{S}$	$-\xi_f \sin 2\phi_1$	$-\xi_f \sin 2\phi_1$	$+\xi_f \sin 2\phi_2$ (?)
$\mathcal{A}$	0	0	(?)

$\Delta t \equiv t_{CP} - t_{\rm tag}$ is defined as a time interval from the time $t = t_{\rm tag}$ of B meson decay to flavor specific final state $f_{\rm tag}$ to the time $t = t_{CP}$ of $B \to f_{CP}$ decay. The CP-violating parameters $\mathcal{S}$ and $\mathcal{A}$ in Eq. (6) are expressed as

$$\mathcal{S} = \frac{|\lambda|^2 - 1}{|\lambda|^2 + 1}, \qquad \mathcal{A} = \frac{2\mathcal{I}m(\lambda)}{|\lambda|^2 + 1}, \tag{7}$$

where λ is a complex parameter that depends on both the B^0-$\overline{B}^0$ mixing and the amplitudes for B^0 and $\overline{B}^0$ decay to f_{CP}. In the SM, to a good approximation, $|\lambda|$ is equal to the absolute value of the ratio of $\overline{B}^0$ to B^0 decay amplitudes.

At the KEKB, two B mesons are produced by $\Upsilon(4S)$ decay in the coherent P-wave state. In this case, when one of the B mesons decay into $f_{\rm tag}$ at the time $t = t_{\rm tag}$, the flavor of the other B at $t = t_{\rm tag}$ is projected onto the one with the opposite bottom quantum number. The procedure to determine the B flavor of $B \to f_{CP}$ decay from the B flavor of $B \to f_{\rm tag}$ decay is called "flavor tagging".

Two B mesons originating from the $\Upsilon(4S)$ are almost at rest in the center-of-mass system (cms) of the $\Upsilon(4S)$. Since the $\Upsilon(4S)$ is produced with a Lorentz boost factor of $\beta\gamma = 0.425$ along the z-axis at the KEKB, the Δt can be determined from the displacement in z between the f_{CP} and $f_{\rm tag}$ decay vertices: $\Delta t \simeq (z_{CP} - z_{\rm tag})/\beta\gamma c \equiv \Delta z/\beta\gamma c$.

The SM-predicted values for $\mathcal{S}$ and $\mathcal{A}$ are listed in Table 1 in relation with the interior angles of the unitarity triangle, where the ξ_f is the CP eigenvalue of the decay final state. The SM predicts no direct CP violation, $\mathcal{A} = 0$, for $b \to c\bar{c}s$ ($b \to s\bar{q}q$) transition with negligible contribution from a penguin diagram (tree diagram). As for the $b \to u\bar{u}d$ transition, the tree and penguin diagram contribute in same order and consequently the direct CP violation can be expected. It is also expected that $\mathcal{S}$ is deviated from $+\xi_f \sin 2\phi_2$.

In this section, we describe the measurement of $\sin 2\phi_1$ using $b \to c\bar{c}s$ transition, together with the flavor tagging and vertex reconstruction. Sections 4 and 5 are involved in the study of CP violation in $b \to s\bar{q}q$ and $b \to u\bar{u}d$ ($B^0 \to \pi^+\pi^-$) transitions, respectively.

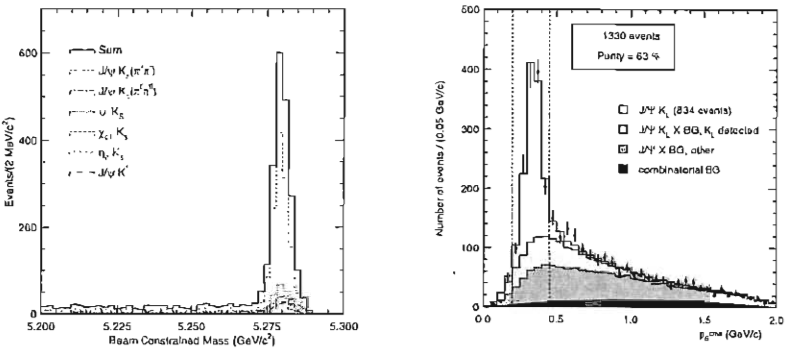

Figure 2: *The beam-energy constrained mass distribution for all decay modes other than $J/\psi K_L^0$ (left) The $p_B^{\rm cms}$ distribution for $B^0 \to J/\psi K_L^0$ candidates with the results of the fit (right).*

3.1 Reconstruction of CP eigenstate

We reconstruct B^0 decays to the following CP eigenstates: $J/\psi K_S^0$, $\psi(2S)K_S^0$, $\xi_{c1}K_S^0$, and $\eta_c K_S^0$ having $\xi_f = -1$; and $J/\psi K_L^0$ having $\xi_f = +1$. We also use the decay $B^0 \to J/\psi K^{*0}$, $K^{*0} \to K_S^0\pi^0$, which is a mixture of even and odd CP, depending on the relative orbital angular momentum of the J/ψ and K^{*0}. We find that the final state is primarily $\xi_f = +1$; the $\xi_f = -1$ fraction is $0.19 \pm 0.02(\text{stat}) \pm 0.03(\text{syst})$ [7].

The J/ψ and $\psi(2S)$ are reconstructed via their decays to $\ell^+\,\ell^-$ ($\ell = e, \mu$). The $\psi(2S)$ is also reconstructed from $J/\psi\pi^+\pi^-$, and ξ_{c1} via $J/\psi\gamma$. The η_c is detected in the $K_S^0K^-\pi^+$, $K^+K^-\pi^0$, and $p\bar{p}$ modes. For the $J/\psi K_S^0$ mode, we use $K_S^0 \to \pi^+\pi^-$ and $\pi^0\pi^0$ decays; for other decays we only use $K_S^0 \to \pi^+\pi^-$.

For reconstructed $B \to f_{CP}$ candidates other than $J/\psi K_L^0$, we identify B decays using the energy difference $\Delta E \equiv E_B^{\rm cms} - E_{\rm beam}^{\rm cms}$ and the beam-energy constrained mass $M_{\rm bc} \equiv \sqrt{(E_{\rm beam}^{\rm cms})^2 - (p_B^{\rm cms})^2}$, where $E_{\rm beam}^{\rm cms}$ is the beam-energy in the cms of the $\Upsilon(4S)$ resonance, and $E_B^{\rm cms}$ and $p_B^{\rm cms}$ are the cms energy and momentum of the reconstructed B candidate, respectively. Figure 2 (left) shows the $M_{\rm bc}$ distributions for all B^0 candidates except for $B^0 \to J/\psi K_L^0$ that have ΔE values within the signal region. Table 2 lists the numbers of observed candidates.

Candidate $B^0 \to J/\psi K_L^0$ are selected by requiring ECL and/or KLM hit patterns that are consistent with the presence of a shower induced by a K_L^0 meson. Figure 2 (right) shows the $p_B^{\rm cms}$ distribution, calculated with the

Table 2: *The numbers of reconstructed $B \to f_{CP}$ candidates before flavor tagging and vertex reconstruction, $N_{\rm rec}$; the numbers of events used for the* $\sin 2\phi_1$ *determination, $N_{\rm ev}$; and the estimated signal purity in the signal region for each f_{CP} mode.*

Mode	ξ_f	$N_{\rm rec}$	$N_{\rm ev}$	Purity
$J/\psi(\ell^+\ell^-)K^0_S(\pi^+\pi^-)$	-1	1285	1116	0.976 ± 0.001
$J/\psi(\ell^+\ell^-)K^0_S(\pi^0\pi^0)$	1	188	162	0.82 ± 0.02
$\psi(2S)(\ell^+\ell^-)K^0_S(\pi^+\pi^-)$	-1	91	76	0.96 ± 0.01
$\psi(2S)(J/\psi\pi^+\pi^-)K^0_S(\pi^+\pi^-)$	-1	112	96	0.91 ± 0.01
$\chi_{c1}(J/\psi\gamma)K^0_S(\pi^+\pi^-)$	-1	77	67	0.96 ± 0.01
$\eta_c(K^0_S\pi^+)K^0_S(\pi^+\pi^-)$	-1	72	63	0.65 ± 0.04
$\eta_c(K^+K^-\pi^0)K^0_S(\pi^+\pi^-)$	-1	49	44	0.72 ± 0.04
$\eta_c(p\bar{p})K^0_S(\pi^+\pi^-)$	-1	21	15	0.94 ± 0.02
All with $\xi_f = -1$	-1	1895	1639	0.936 ± 0.003
$J/\psi(\ell^+\ell^-)K^{*0}(K^0_S\pi^0)$	$-1(19\%)/$ $+1(81\%)$	101	89	0.92 ± 0.01
$J/\psi(\ell^+\ell^-)K^0_L$	$+1$	1330	1230	0.63 ± 0.04
All		3326	2958	0.81 ± 0.01

$B^0 \to J/\psi K^0_L$ two-body decay hypothesis. The histograms are the results of a fit to the signal and background distributions. There are 1330 entries in total in the $0.20 \le p_B^{\rm cms} \le 0.45$ GeV/c signal region; the fit indicates a signal purity of 63%.

The reconstruction and selection criteria for all f_{CP} channels used in the measurement are described in more detail elsewhere [8].

3.2 Flavor tagging

Charged leptons, pions, kaons, and Λ baryons that are not associated with the reconstructed CP eigenstate decay are used to identify the b-flavor of the accompanying B meson, which decays into flavor specific mode.

Based on the measured properties of these tracks, two parameters, q and r, are assigned to an event. The first, q, has the discrete value $+1$ (-1) when the tag-side B meson is more likely to be a B^0 ($\overline{B}^0$). The parameter r is an event-by-event flavor-tagging dilution factor that ranges from $r = 0$ for no flavor discrimination to $r = 1$ for an unambiguous flavor assignment. It is used only to sort data into six intervals of r, according to the estimated flavor purity.

The wrong-tag probabilities for each of these intervals, w_l $(l = 1, 6)$, which are used in the final fit, are determined directly from the data. Samples of B^0

Table 3: *The event fractions ϵ_l and wrong-tag probabilities w_l for each r interval. The errors include both statistical and systematic uncertainties. The event fractions are obtained from the $J/\psi K^0_S$ simulation.*

l	r interval	ϵ_l	w_l
1	0.000 – 0.250	0.398	0.458 ± 0.006
2	0.250 – 0.500	0.146	0.336 ± 0.009
3	0.500 – 0.625	0.104	0.228 ± 0.010
4	0.625 – 0.750	0.122	$0.160\ ^{+0.009}_{-0.008}$
5	0.750 – 0.875	0.094	0.112 ± 0.009
6	0.875 – 1.000	0.136	0.020 ± 0.006

decays to exclusively reconstructed self-tagging channels are utilized to obtain w_l using time-dependent B^0-$\overline{B}^0$ mixing: $(N_{\rm OF} - N_{\rm SF})/(N_{\rm OF} + N_{\rm SF}) = (1 - 2w_l)\cos(\Delta m_d \Delta t)$, where $N_{\rm OF}$ and $N_{\rm SF}$ are the numbers of opposite ($B^0\overline{B}^0 \to B^0\overline{B}^0$) and same ($B^0\overline{B}^0 \to B^0B^0, \overline{B}^0\overline{B}^0$) flavor events. The event fraction and wrong-tag probability for each r interval are summarized in Table 3. The total effective tagging efficiency is $\sum_{l=1}^{6} \epsilon_l(1-2w_l)^2 = 0.288 \pm 0.006$, where ϵ_l is the event fraction for each r interval.

3.3 Vertex reconstruction

The decay vertices of B^0 mesons are reconstructed using tracks that have enough SVD hits; i.e. both z and r-ϕ hits in at least one SVD layer and at least one additional layer with a z hit, where the r-ϕ plane is perpendicular to the z axis. Each vertex position is required to be consistent with the interaction-point (IP) profile, which is determined run-by-run and smeared in the r-ϕ plane by 21 μm to account for the B meson decay length.

The vertex position for the f_{CP} decay is reconstructed using leptons from J/ψ decays or charged hadrons from η_c decays.

The algorithm for the $f_{\rm tag}$ vertex reconstruction is chosen to minimize the effect of long-lived particles, secondary vertices from charmed hadrons, and a small fraction of poorly reconstructed tracks [9]. From all the charged tracks with associated SVD hits except those used for f_{CP}, we select tracks with a position error in the z direction of less than 500 μm, and with an impact parameter with respect to the f_{CP} vertex of less than 500 μm. Track pairs with opposite charges are removed if they form a K^0_S candidate satisfying an invariant mass within 15 MeV/c^2 of the nominal K^0_S mass. If the reduced χ^2 associated with the $f_{\rm tag}$ vertex exceeds 20, the track making the largest χ^2 contribution is removed and the vertex is refitted. This procedure is repeated

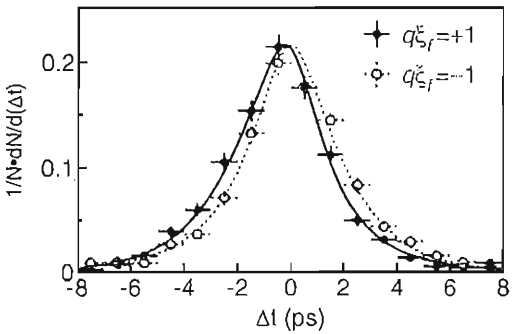

Figure 3: *The Δt distributions for the events with $q\xi_f = +1$ (solid points) and $q\xi_f = -1$ (open points). The results of the global fit with $\sin 2\phi_1 = 0.719$ are shown as solid and dashed curves, respectively.*

until an acceptable reduced χ^2 is obtained.

The proper-time interval resolution function $R_{\rm sig}(\Delta t)$ is formed by convolving four components: the detector resolutions for z_{CP} and $z_{\rm tag}$, the shift in the $z_{\rm tag}$ vertex position due to secondary tracks originating from charmed particle decays, and the kinematic approximation that the B mesons are at rest in the cms [9]. A small component of broad outliers in the Δz distribution, caused by mis-reconstruction, is represented by a Gaussian function. We determine twelve resolution parameters and the neutral- and charged-B lifetimes simultaneously from fits to the Δt distributions of hadronic B decays: $B^0 \to J/\psi K^0_S$, $J/\psi K^{*0}(K^+\pi^-)$, $D^-\pi^+$, $D^{*-}\rho^+$, and $B^+ \to J/\psi K^+$, $\overline{D}^0\pi^+$. We obtain an average Δt resolution of ~ 1.43 ps (rms).

3.4 Determination of $\sin 2\phi_1$

After flavor tagging and vertex reconstruction, we obtain the numbers of $B^0 \to f_{CP}$ candidates and purities listed in Table 2.

Figure 3 shows the observed Δt distributions for the $q\xi_f = +1$ (solid points) and $q\xi_f = -1$ (open points) event samples. The asymmetry between two distributions demonstrates the violation of CP symmetry.

We determine $\sin 2\phi_1$ by performing an unbinned maximum-likelihood fit to the observed Δt distribution. The probability density function (PDF) expected for the signal distribution is given by letting $\mathcal{S} = \sin 2\phi_1$ and $\mathcal{A} = 0$ in Eq. (4, 5) as

$$\mathcal{P}_{\rm sig}(\Delta t, q, w_l, \xi_f) = \frac{e^{-|\Delta t|/\tau_{B^0}}}{4\tau_{B^0}}\left[1 - q\xi_f(1-2w_l)\sin 2\phi_1 \sin(\Delta m_d \Delta t)\right], \quad (8)$$

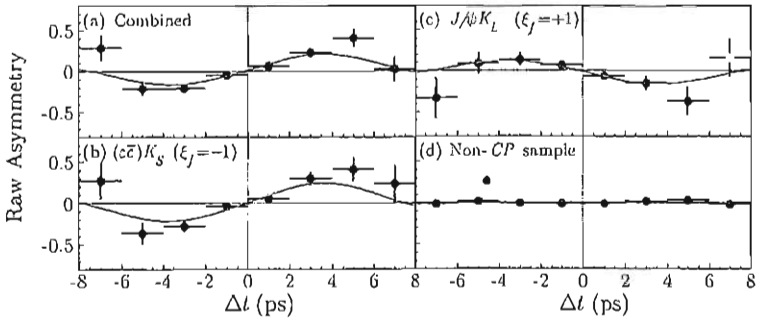

Figure 4:- *(a) The raw asymmetry for all modes combined. The asymmetry for $J/\psi K_L^0$ and $J/\psi K^{*0}$ is converted to account for the opposite CP eigenvalue. The corresponding plots for (b) $(c\bar{c})K_S^0$, (c) $J/\psi K_L^0$, and (d) non-CP control samples are also shown. The curves are the results of the unbinned maximum-likelihood fit applied separately to the individual data samples.*

where we fix the B^0 lifetime τ_{B^0} and mass difference at their world average values [10]. The $(1-2w_l)$ accounts for the effect of incorrect flavor assignment. The PDF is convolved with the proper-time interval resolution function $R_{\rm sig}(\Delta t)$. The PDF for combinatorial background event is modeled by a sum of exponential and prompt components convolved with a sum of two Gaussians, which is regarded as a resolution function for the background. Event-by-event signal fraction is calculated as a function of $p_B^{\rm cms}$ for $J/\psi K_L^0$ and ΔE and $M_{\rm bc}$ for other decay modes.

The only free parameter in the final fit is $\sin 2\phi_1$. The result of the fit is

$$\sin 2\phi_1 = 0.719 \pm 0.074(\text{stat}) \pm 0.035(\text{syst}). \qquad (9)$$

Figures 4 (a)– 4 (c) show the raw asymmetries and the fit results for all modes combined, $(c\bar{c})K_S^0$, and $J/\psi K_L^0$, respectively.

The systematic error is dominated by uncertainties in the vertex reconstruction (0.022). Other significant contributions come from uncertainties in w_l (0.015), the resolution function parameters (0.014), a possible bias in the $\sin 2\phi_1$ fit (0.011), and the $J/\psi K_L^0$ background fraction (0.010). The errors introduced by uncertainties in τ_{B^0} and Δm_d are less than 0.010.

A fit to the non-CP eigenstate modes $B^0 \to D^{(*)-}\pi^+$, $D^{*-}\rho^+$, $J/\psi K^{*0}$ $(K^+\pi^-)$, and $D^{*-}\ell^+\nu$, where no asymmetry is expected, yields 0.005 ± 0.015 (stat). Figure 4 (d) shows the raw asymmetry for these non-CP control samples.

Figure 5 shows the constrained apex of the unitarity triangle on the $\bar{\rho}$-$\bar{\eta}$

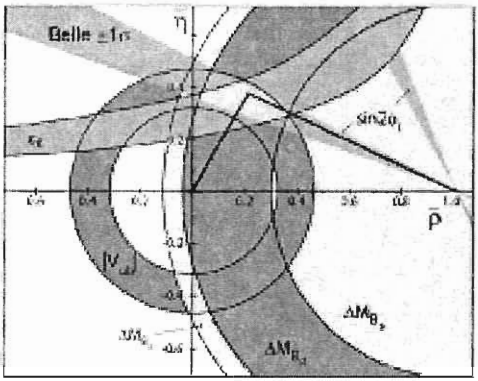

Figure 5: *The constraint on the apex of the unitarity triangle by the fitted* $\sin 2\phi_1$ *result and results from other experiments.*

plane, on which the triangle is normalized by the length of the bottom side, by the fitted $\sin 2\phi_1$ result and results from other experiments.

4 CP Violation in $b \to s\bar{q}q$ Transition

Despite the success to measure the CP-violating parameter $\sin 2\phi_1$ by the Belle and BaBar [11] collaborations, many tests remain before one can conclude that the KM model provides a complete description. For example, the charmless decays $B^0 \to \phi K^0_S$, $B^0 \to K^+K^-K^0_S$, and $B^0 \to \eta' K^0_S$, which are mediated by the $b \to s\bar{s}s$ transition ($B^0 \to \eta' K^0_S$ also receives $b \to s\bar{d}d$ and $b \to s\bar{u}u$ penguin contributions) are potentially sensitive to new CP-violating phases from physics beyond the SM [12]. SM contributions from the $b \to u\bar{u}s$ tree diagram are expected to be highly suppressed [13, 14]. Thus, the SM predicts that CP violation measurements in these charmless modes should yield $\sin 2\phi_1$ to a good approximation. Consequently, a significant deviation in the time-dependent CP asymmetry in these modes from that is observed in the $b \to c\bar{c}s$ transition would be an evidence of a CP-violating phase not expected in the KM model.

In this section, we report the first measurement of CP asymmetries in the $B^0 \to \phi K^0_S$ and $K^+K^-K^0_S$ decays, and an improved measurement for the $B^0 \to \eta' K^0_S$ decay [15] based on the 78 fb^{-1} data sample.

4.1 Reconstruction of CP eigenstate

We reconstruct B^0 decays to ϕK^0_S and $\eta' K^0_S$ final states for $\xi_f = -1$, and $B^0 \to K^+K^-K^0_S$ decays that are a mixture of $\xi_f = +1$ and -1. K^+K^- pairs that are consistent with $\phi \to K^+K^-$ decay are excluded from the $B^0 \to K^+K^-K^0_S$ sample. We find that the $K^+K^-K^0_S$ state is primarily $\xi_f = +1$; the $\xi_f = +1$ fraction is $1.04 \pm 0.19(\mathrm{stat}) \pm 0.06(\mathrm{syst})$ [14]. In the following determination of $\mathcal{S}$ and $\mathcal{A}$, we fix $\xi_f = +1$.

The intermediate meson states are reconstructed from the following decay chains: $\eta' \to \rho^0(\to \pi^+\pi^-)\gamma$ or $\eta' \to \pi^+\pi^-\eta(\to \gamma\gamma)$, $K^0_S \to \pi^+\pi^-$, and $\phi \to K^+K^-$. Candidate $K^0_S \to \pi^+\pi^-$ decays are oppositely charged track pairs that have an invariant mass within 15 (12, 16) MeV/c^2 of the nominal K^0_S mass for the $B^0 \to \phi K^0_S$ ($B^0 \to K^+K^-K^0_S$, $B^0 \to \eta' K^0_S$) mode. We select candidate $\phi \to K^+K^-$ decays requiring that the K^+K^- invariant mass is within 10 MeV/c^2 of the nominal ϕ meson mass, the ϕ meson momentum in the cms exceeds 2.0 GeV/c, and the K^+K^- vertex is consistent with the IP. For selection of non-resonant $K^+K^-K^0_S$ candidates, more stringent kaon-identification than ϕ meson is required, and $D^0 \to K^+K^-$ or $\chi_{c0} \to K^+K^-$ decay are explicitly eliminated. Two decay channels are used for η' reconstruction: $\eta' \to \eta\pi^+\pi^-$ with $\eta \to \gamma\gamma$, and $\eta' \to \rho^0\gamma$ with $\rho^0 \to \pi^+\pi^-$.

For reconstructed $B \to f_{CP}$ candidates, we identify B meson decays using the ΔE and the M_{bc}.

In order to suppress background from the $e^+e^- \to q\bar{q}$ ($q = u,\ d,\ s$) and $c\bar{c}$ continuum, we form signal and background likelihood functions, $\mathcal{L}_{\mathrm{S}}$ and $\mathcal{L}_{\mathrm{BG}}$, from a set of variables that characterize the event topology [14, 15]. We determine $\mathcal{L}_{\mathrm{S}}$ from Monte Carlo (MC) and $\mathcal{L}_{\mathrm{BG}}$ from data, and impose mode-dependent thresholds on the likelihood ratio $LR \equiv \mathcal{L}_{\mathrm{S}}/(\mathcal{L}_{\mathrm{S}} + \mathcal{L}_{\mathrm{BG}})$.

4.2 Vertex reconstruction

The decay vertices of B^0 mesons are reconstructed with the same algorithm as that for $b \to c\bar{c}s$ transition. We select tracks for vertex reconstruction using the same selection criteria as $b \to c\bar{c}s$ transition. We also require the vertex to be consistent with IP profile. The only difference from the $b \to c\bar{c}s$ analysis is the tracks used for z_{CP} reconstruction. The z_{CP} vertex is reconstructed with charged kaons for the $B^0 \to \phi K^0_S$ and $B^0 \to K^+K^-K^0_S$ decays and with charged pions from ρ^0 or η' decays for the $B^0 \to \eta' K^0_S$ decay.

Table 4 lists the number of observed $B^0 \to f_{CP}$ candidates after flavor tagging and vertex reconstruction. Figure 6 shows the M_{bc} distributions for the reconstructed B candidates that have ΔE values within the signal region.

Table 4: *The numbers of reconstructed $B^0 \to f_{CP}$ candidates used for $\mathcal{S}$ and $\mathcal{A}$ determination, $N_{\rm ev}$, and the estimated signal purity in the ΔE-$M_{\rm bc}$ signal region for each f_{CP} mode.*

Mode	ξ_f	$N_{\rm ev}$	Purity
ϕK^0_S	-1	53	$0.67^{+0.07}_{-0.05}$
$K^+K^-K^0_S$	$+1(100\%)$	191	$0.50^{+0.04}_{-0.03}$
$\eta' K^0_S$	-1	299	0.49 ± 0.05

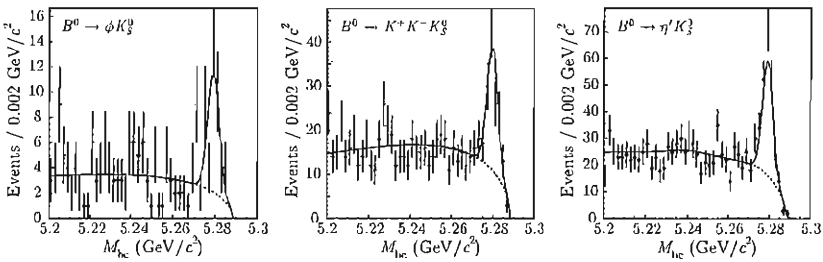

Figure 6: *The beam-energy constrained mass distributions for $B^0 \to \phi K^0_S$ (left), $B^0 \to K^+K^-K^0_S$ (center), and $B^0 \to \eta' K^0_S$ (right) within the ΔE signal region. Solid curves show the fit to signal plus background distributions, and dotted curves show the background contributions. The background for $B^0 \to \eta' K^0_S$ decay includes an MC-estimated $B\overline{B}$ background component.*

Table 5: *Results of the fits to the Δt distributions. The first errors are statistical and the second errors are systematic. The third error for the $K^+K^-K^0_S$ mode arise from the uncertainty in the fraction of the CP-odd component.*

Mode	$-\xi_f \mathcal{S}$ ($= \sin 2\phi_1$ in the SM)	$\mathcal{A}$ ($= 0$ in the SM)
ϕK^0_S	$-0.73 \pm 0.64 \pm 0.22$	$-0.56 \pm 0.41 \pm 0.16$
$K^+K^-K^0_S$	$+0.49 \pm 0.43 \pm 0.11^{+0.33}_{-0.00}$	$-0.40 \pm 0.33 \pm 0.10^{+0.00}_{-0.26}$
$\eta' K^0_S$	$+0.71 \pm 0.37^{+0.05}_{-0.06}$	$+0.26 \pm 0.22 \pm 0.03$

4.3 Determination of $\mathcal{S}$ and $\mathcal{A}$

We determine $\mathcal{S}$ and $\mathcal{A}$ in Eq. (4, 5) for each mode by performing an unbinned maximum-likelihood fit to the observed Δt distribution. The PDF expected for the signal distribution is given with accounting for the effect of incorrect flavor assignment by

$$\mathcal{P}_{\rm sig}(\Delta t, q, w_l, \xi_f) = \frac{e^{-|\Delta t|/\tau_{B^0}}}{4\tau_{B^0}} \Big\{ 1 - q\xi_f (1 - 2w_l) \big[\mathcal{S} \sin(\Delta m_d \Delta t) + \mathcal{A} \cos(\Delta m_d \Delta t) \big] \Big\} \quad (10)$$

The only free parameters in the final fit are $\mathcal{S}$ and $\mathcal{A}$.

Table 5 summarizes the results of the fits. The table shows the values of $\mathcal{A}$ and $-\xi_f \mathcal{S}$, which, in the SM, is equal to $\sin 2\phi_1$. The first errors are statistical and the second errors are systematic. The third error for the $K^+K^-K^0_S$ mode arises from the uncertainty in the fraction of the CP-odd component [14].

Figure 7 (upper row) shows the observed Δt distributions for $q\xi_f = -1$ (upper figure) and $q\xi_f = +1$ (lower figure) event samples for each f_{CP} mode. Figure 7 (lower row) shows the raw asymmetries in each Δt bin without background subtraction, which is defined by

$$A \equiv \frac{N_{q\xi_f=-1} - N_{q\xi_f=+1}}{N_{q\xi_f=-1} + N_{q\xi_f=+1}}, \quad (11)$$

where $N_{q\xi_f=+1(-1)}$ is the number of observed candidates with $q\xi_f = +1(-1)$. The curves show the results of the unbinned maximum-likelihood fit to the asymmetry distribution, $-\xi_f \mathcal{S} \sin(\Delta m_d \Delta t) - \xi_f \mathcal{A} \cos(\Delta m_d \Delta t)$. These are the first measurements of the CP-violating parameters for the $B^0 \to \phi K^0_S$ and $B^0 \to K^+K^-K^0_S$ decays. The result for the $\eta' K^0_S$ supersedes the previous result [15]. We obtain values consistent with the present world average of $\sin 2\phi_1 = +0.734 \pm 0.054$ [16] in the $B^0 \to K^+K^-K^0_S$ and $\eta' K^0_S$ decays, while a 2.1σ deviation is observed in the $B^0 \to \phi K^0_S$ decay.

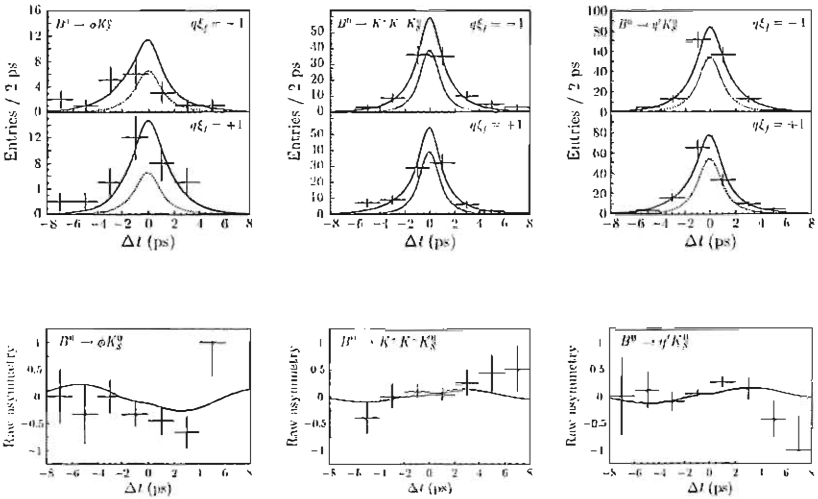

Figure 7: *The upper row shows the Δt distributions for the $B^0 \to \phi K^0_S$ (left), $B^0 \to K^+K^-K^0_S$ (center), and $B^0 \to \eta' K^0_S$ (right) decays. The upper and lower plots are for $q\xi_f = -1$ and $q\xi_f = +1$ candidates, respectively. The solid curves show the results of the global fits, and dashed curves show the background distributions. The lower row shows the Δt asymmetries, A, in each bin for the $B^0 \to \phi K^0_S$ (left), $B^0 \to K^+K^-K^0_S$ (center), and $B^0 \to \eta' K^0_S$ (right), respectively. The curves show the results of the unbinned maximum-likelihood fit.*

The largest source of systematic error for the $B^0 \to \phi K^0_S$ mode is the uncertainty in the signal fraction and the background Δt shape (± 0.17 for $\mathcal{S}$ and ± 0.14 for $\mathcal{A}$ in total) determined from the events in the sideband regions in the ΔE vs. $M_{\rm bc}$ plane. Other significant contributions come from uncertainties in the vertex reconstruction, the resolution function parameters, wrong-tag probability, τ_{B^0}, and Δm_d. Systematic uncertainties from these sources are also examined for the other modes. We find that the largest uncertainties arise from the vertex reconstruction (± 0.09 for $\mathcal{S}$ and ± 0.08 for $\mathcal{A}$) for the $B^0 \to K^+K^-K^0_S$ mode, and from the resolution function parameters ($^{+0.03}_{-0.04}$ for $\mathcal{S}$) and the signal fraction (± 0.02 for $\mathcal{A}$) for the $B^0 \to \eta' K^0_S$ mode.

Fits to the same samples with the direct CP violation parameter $\mathcal{A}$ fixed at zero yield $-\xi_f \mathcal{S} = -0.83 \pm 0.72$(stat) for $B^0 \to \phi K^0_S$, $-\xi_f \mathcal{S} = +0.59 \pm 0.47$(stat) for $B^0 \to K^+K^-K^0_S$, and $-\xi_f \mathcal{S} = +0.77 \pm 0.38$(stat) for $B^0 \to \eta' K^0_S$. As a consistency check for the $\mathcal{S}$ term, we select the charged B meson decays $B^+ \to \phi K^+$ and $B^+ \to \eta' K^+$ and apply the same fit procedure. We obtain $\mathcal{S} = 0.05 \pm 0.32$(stat), $\mathcal{A} = 0.29 \pm 0.21$(stat) for the $B^+ \to \phi K^+$ decay and $\mathcal{S} = -0.03 \pm 0.20$(stat), $\mathcal{A} = 0.05 \pm 0.13$(stat) for the $B^+ \to \eta' K^+$ decay. Both results on the $\mathcal{S}$ term are consistent with no CP asymmetry, as expected.

5 CP Violation in $B^0 \to \pi^+\pi^-$ Decay

A measurement of time-dependent CP asymmetry in $B^0 \to \pi^+\pi^-$ decay is sensitive to direct CP violation and the ϕ_2, one of the interior angles of the unitarity triangle. If the decay proceeded only via $b \to u$ tree amplitude, we would have $\mathcal{S} = \sin 2\phi_2$ and $\mathcal{A} = 0$, or equivalently $|\lambda| = 0$. The situation is complicated by the possibility of the significant contributions from gluonic $b \to d$ penguin amplitudes that have a different weak phase and additional strong phases. As a result, $\mathcal{S}$ may not be equal to $\sin 2\phi_2$ and direct CP violation, $\mathcal{A} \neq 0$, occur.

In this section, we present a measurement of direct and mixing-induced CP violation in the $B^0 \to \pi^+\pi^-$ decay and constraints on the ϕ_2, based on the 78 fb^{-1} data sample.

5.1 Reconstruction of $B^0 \to \pi^+\pi^-$ decays

We use oppositely charged track pairs that are positively identified as pions according to the likelihood ratio for a particle to be a $K^\pm$ meson, KID $\equiv \mathcal{L}_K/[\mathcal{L}_K + \mathcal{L}_\pi]$, which is based on the combined information from the ACC and the CDC dE/dx measurements. Here we use KID<0.4 as the default requirement for the selection of pions. For tracks in the momentum range that covers the $B^0 \to \pi^+\pi^-$ signal, this requirement has a pion efficiency of 91% and 10.3% of kaons are misidentified as pions (10.0$\pm$0.2% from K^- and 10.6$\pm$0.2% from K^+).

We also select $B^0 \to K^+\pi^-$ candidates, which have the same track topology as $B^0 \to \pi^+\pi^-$ candidates, by positively identifying one charged track as a kaon and the other as a pion. We use KID>0.6 for the selection of kaons. This requirement has a kaon efficiency of 84% and a misidentification rate from pions of 5%.

Candidate B mesons are identified using the ΔE and the $M_{\rm bc}$. The signal region is defined as 5.271 GeV/c^2 < $M_{\rm bc}$ < 5.287 GeV/c^2 and $|\Delta E|$ < 0.057 GeV, corresponding to $\pm 3\sigma$ from the central values.

To suppress background from the $e^+e^- \to q\bar{q}$ continuum ($q = u,\ d,\ s,\ c$ in this section), we form signal and background likelihood ratio, from two variables, as well as $b \to s\bar{q}q$ transition. One variable is a Fisher discriminant determined from six modified Fox-Wolfram moments [17]; the other is the cms B flight direction with respect to the z axis. In the $M_{\rm bc}$ and ΔE signal region, we find major contributions from signal events, misidentified $B^0 \to K^+\pi^-$ events, three-body B-decays, and continuum background. Figure 8 shows the ΔE distributions for the $B^0 \to \pi^+\pi^-$ candidates that are in the $M_{\rm bc}$ signal region with $LR > 0.825$ (left) and with $LR \leq 0.825$ (right), respectively,

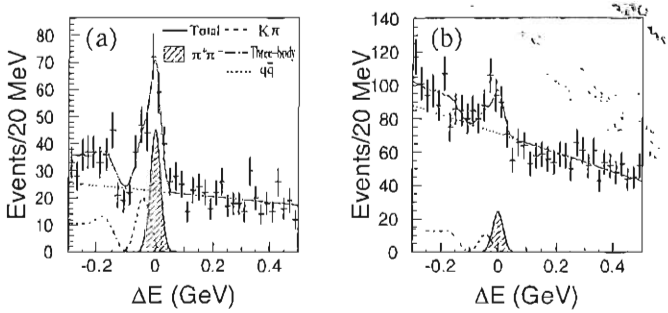

Figure 8: *The ΔE distributions of $B^0 \to \pi^+\pi^-$ candidates in the $M_{\rm bc}$ signal region for (a) $LR > 0.825$, and (b) $LR \leq 0.825$. The sum of the signal and the background function is shows as a solid curve. The solid curve with hatched area represents $\pi^+\pi^-$ component, the dashed curve represents $K^+\pi^-$ component, the dotted curve represents the continuum background, and the dot-dashed curve represents the charmless three-body B decay background component.*

5.2 Vertex reconstruction

The decay vertices of B^0 mesons are reconstructed with the same algorithm as that for $b \to c\bar{c}s$ transition. The vertex position of $B^0 \to \pi^+\pi^-$ decay is

reconstructed from two charged pion tracks with requiring the consistency to the IP profile.

5.3 Determination of $\mathcal{S}$ and $\mathcal{A}$

We determine $\mathcal{S}$ and $\mathcal{A}$ in Eq. (4, 5) by performing an unbinned maximum-likelihood fit to the observed Δt distribution as well as other decay modes. The only free parameters in the final fit are $\mathcal{S}$ and $\mathcal{A}$. The result of the fit to the 760 $B^0 \to \pi^+\pi^-$ candidates (391 B^0- and 369 $\overline{B}^0$-tags) that remain after flavor tagging and vertexing is

$$\begin{aligned} \mathcal{S} &= -1.23 \pm 0.27(\text{stat}) \pm 0.08(\text{syst}) \\ \mathcal{A} &= +0.77 \pm 0,41(\text{stat})^{+0.08}_{-0.07}(\text{syst}). \end{aligned}$$

Here we quote the rms values from the MC distribution with parameterized $\mathcal{S}$ and $\mathcal{A}$ as the statistical uncertainties of the result, because the log-likelihood ratio curves from our data deviate from parabola and the estimation of the uncertainties using log-likelihood ratio, $-2\ln(L/L_{\max})$, is not appropriate.

In Figs. 9 (a) and (b), we show the raw, unweighted Δt distributions for the 148 B^0- and 127 $\overline{B}^0$-tagged events with $LR > 0.825$. The fit curves use $\mathcal{S}$ and $\mathcal{A}$ values that are obtained from all of the LR-r regions. The background-subtracted Δt distributions are shown in Fig. 9 (c). Figure 9 (d) shows the background-subtracted CP asymmetry between the B^0- and $\overline{B}^0$-tagged events as a function of Δt. The result of the fit is superimposed and is shown by the solid curve.

The most dominant source of systematic error comes from background fraction determination ($^{+0.06}_{-0.05}$ for $\mathcal{S}$ and $^{+0.06}_{-0.06}$ for $\mathcal{A}$). Other significant sources of the systematic uncertainty are vertex reconstruction, fit bias, wrong-tag probability, τ_{B^0}, Δm_d, direct CP violation in the $B^0 \to K^+\pi^-$ decay, resolution function parameters, and background shape.

We use the Feldman-Cousins frequentist approach [18] to determine the statistical significance of our measurement. In order to form confidence intervals, we use the $\mathcal{S}$ and $\mathcal{A}$ distributions of the results of fits to MC pseudo-experiments for various input values of $\mathcal{S}$ and $\mathcal{A}$. The distributions incorporate possible biases at the boundary of the physical region as well as a correlation between $\mathcal{S}$ and $\mathcal{A}$; these effects are taken into account by this method. The distributions are also smeared with Gaussian functions that account for systematic errors. Figure 10 shows the resulting two-dimensional confidence regions in the $\mathcal{S}$ vs. $\mathcal{A}$ plane. The case that CP symmetry is conserved, $\mathcal{S} = \mathcal{A} = 0$, is ruled out at the 99.93% confidence level (C.L.), equivalent to 3.4σ significance for Gaussian errors. The minimum C.L. for $\mathcal{A} = 0$, the case of no direct CP violation, occurs at $(\mathcal{S}, \mathcal{A}) = (-1.0, 0.0)$ and is 97.3%, which corresponds to 2.2σ significance.

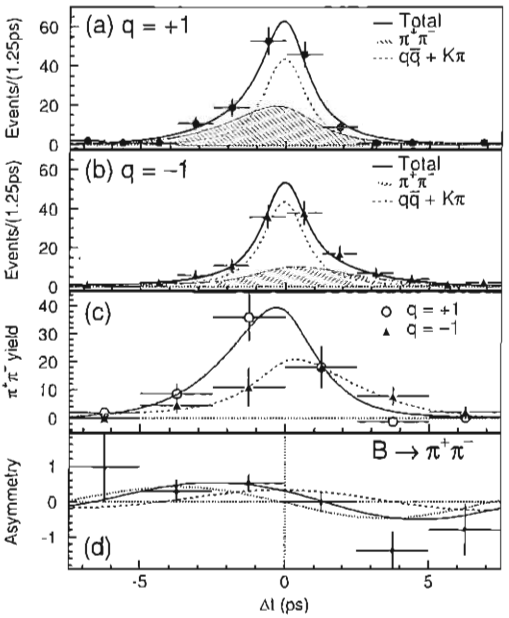

Figure 9: *The raw, unweighted Δt distributions for the 275 $B^0 \to \pi^+\pi^-$ candidates with LR > 0.825 in the signal region: (a) 148 candidates with $q = +1$, i.e. the tag side is identified as B^0; (b) 127 candidates with $q = -1$; (c) $B^0 \to \pi^+\pi^-$ yields after background subtraction. The errors are statistical only and do not include the error on the background subtraction; (d) the CP asymmetry for $B^0 \to \pi^+\pi^-$ after background subtraction. In Figs. (a) through (c), the curves show the results of the unbinned maximum-likelihood fit to the Δt distributions of the 760 $B^0 \to \pi^+\pi^-$ candidates. In Fig. (d), the solid curve shows the resultant CP asymmetry, while the dashed (dotted) curve is the contribution from the cosine (sine) term.*

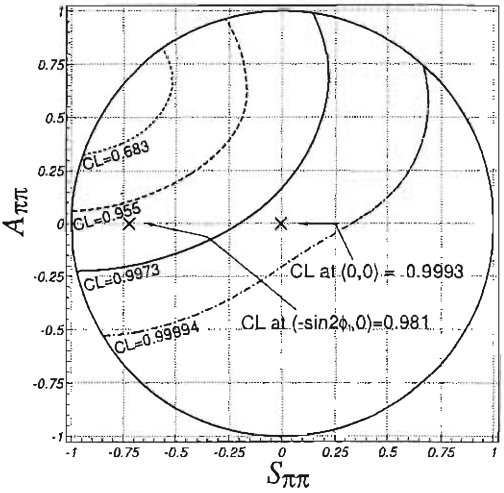

Figure 10: *Confidence regions for S and A.*

5.4 Constraints on ϕ_2

Using the definitions of Eq. (3), the decay amplitudes for B^0 and $\overline{B}^0$ to $\pi^+\pi^-$ are

$$\begin{aligned} A(B^0 \to \pi^+\pi^-) &= -(|T|e^{i\delta_T}e^{i\phi_3} + |P|e^{i\delta_P}), \\ A(\overline{B}^0 \to \pi^+\pi^-) &= -(|T|e^{i\delta_T}e^{-i\phi_3} + |P|e^{i\delta_P}), \end{aligned} \tag{12}$$

where T and P are the amplitudes for the tree and penguin graphs, respectively, and δ_T and δ_P are their strong phases. Here we adopt the notation of Ref. [19] and use the convention in which the top-quark contributions are integrated out in the short-distance effective Hamiltonian. In addition, the unitarity relation $V_{ub}^*V_{ud} + V_{cb}^*V_{cd} = -V_{tb}^*V_{td}$ is applied. Explicit expressions for $\mathcal{S}$ and $\mathcal{A}$ are

$$\begin{aligned} \mathcal{S} &= \left[\sin 2\phi_2 + 2|P/T|\sin(\phi_1 - \phi_2)\cos\delta - |P/T|^2\sin 2\phi_1\right]/\mathcal{R}, \\ \mathcal{A} &= -\left[2|P/T|\sin(\phi_2 + \phi_1)\sin\delta\right]/\mathcal{R}, \\ \mathcal{R} &= 1 - 2|P/T|\cos\delta\cos(\phi_2 + \phi_1) + |P/T|^2, \end{aligned} \tag{13}$$

where $\delta \equiv \delta_P - \delta_T$. We take $-180° \le \delta \le 180°$. When $\mathcal{A}$ is positive and $0° < \phi_1 + \phi_2 < 180°$, δ is negative.

Recent theoretical estimations prefer $|P/T| \sim 0.3$ with large uncertainties [20, 21, 22, 23]. Figures 11 (a)-(e) show the regions for ϕ_2 and δ corresponding to the 68.3% C.L., 95.5% C.L. and 99.73% C.L. region of $\mathcal{A}$ and $\mathcal{S}$

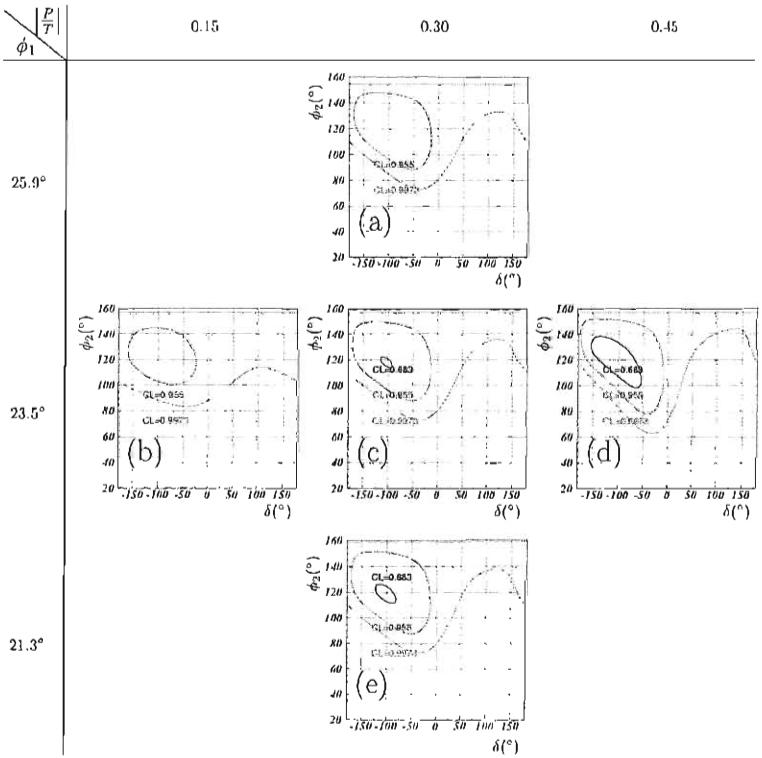

Figure 11: *The regions for ϕ_2 and δ corresponding to the 68.3%, 95.5%, and 99.73% C.L. regions of $\mathcal{A}$ and $\mathcal{S}$ in Fig. 10 for (a) $\phi_1 = 25.9°$, $|P/T|$=0.3, (b) $\phi_1 = 23.5°$, $|P/T|$=0.15, (c) $\phi_1 = 23.5°$, $|P/T|$=0.3, (d) $\phi_1 = 23.5°$, $|P/T|$=0.45, and (e) $\phi_1 = 21.3°$, $|P/T|$=0.3. The horizontal dashed lines correspond to $\phi_2 = 180° - \phi_1$.*

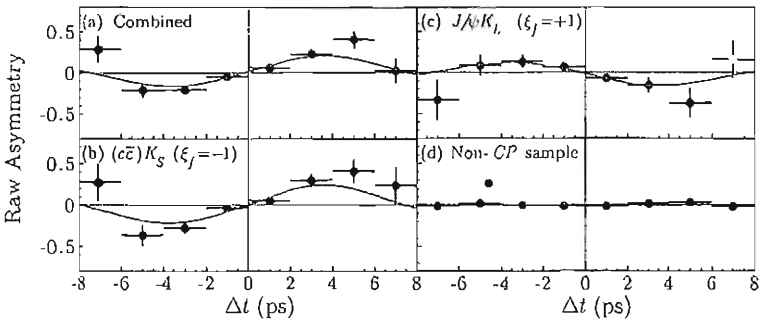

Figure 4:- *(a) The raw asymmetry for all modes combined. The asymmetry for $J/\psi K_L^0$ and $J/\psi K^{*0}$ is converted to account for the opposite CP eigenvalue. The corresponding plots for (b) $(c\bar{c})K_S^0$, (c) $J/\psi K_L^0$, and (d) non-CP control samples are also shown. The curves are the results of the unbinned maximum-likelihood fit applied separately to the individual data samples.*

where we fix the B^0 lifetime τ_{B^0} and mass difference at their world average values [10]. The $(1-2w_l)$ accounts for the effect of incorrect flavor assignment. The PDF is convolved with the proper-time interval resolution function $R_{\rm sig}(\Delta t)$. The PDF for combinatorial background event is modeled by a sum of exponential and prompt components convolved with a sum of two Gaussians, which is regarded as a resolution function for the background. Event-by-event signal fraction is calculated as a function of $p_B^{\rm cms}$ for $J/\psi K_L^0$ and ΔE and $M_{\rm bc}$ for other decay modes.

The only free parameter in the final fit is $\sin 2\phi_1$. The result of the fit is

$$\sin 2\phi_1 = 0.719 \pm 0.074({\rm stat}) \pm 0.035({\rm syst}). \qquad (9)$$

Figures 4 (a)– 4 (c) show the raw asymmetries and the fit results for all modes combined, $(c\bar{c})K_S^0$, and $J/\psi K_L^0$, respectively.

The systematic error is dominated by uncertainties in the vertex reconstruction (0.022). Other significant contributions come from uncertainties in w_l (0.015), the resolution function parameters (0.014), a possible bias in the $\sin 2\phi_1$ fit (0.011), and the $J/\psi K_L^0$ background fraction (0.010). The errors introduced by uncertainties in τ_{B^0} and Δm_d are less than 0.010.

A fit to the non-CP eigenstate modes $B^0 \to D^{(*)-}\pi^+$, $D^{*-}\rho^+$, $J/\psi K^{*0}$ $(K^+\pi^-)$, and $D^{*-}\ell^+\nu$, where no asymmetry is expected, yields 0.005 ± 0.015 (stat). Figure 4 (d) shows the raw asymmetry for these non-CP control samples.

Figure 5 shows the constrained apex of the unitarity triangle on the $\bar{\rho}$-$\bar{\eta}$

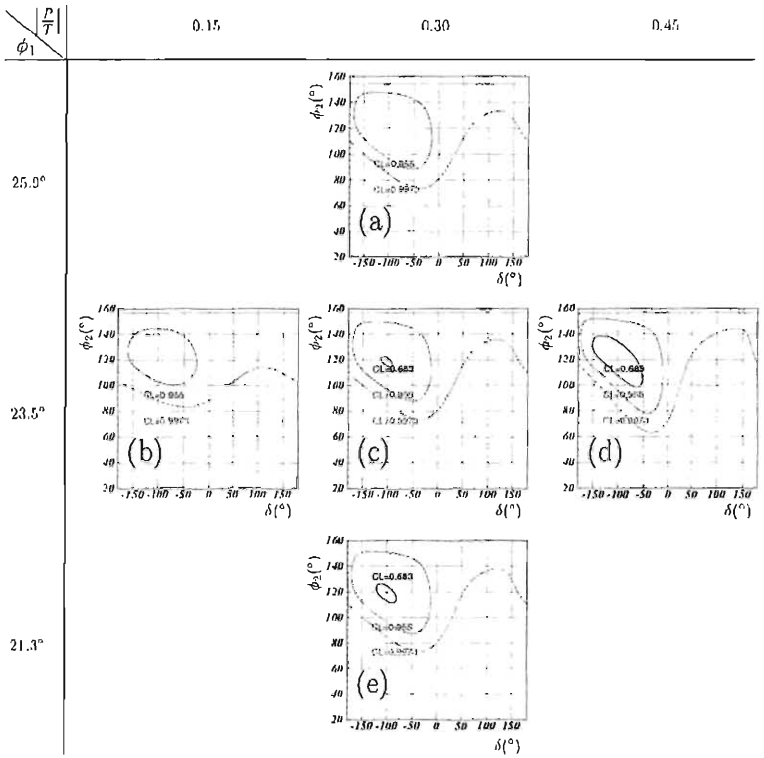

Figure 11: *The regions for ϕ_2 and δ corresponding to the 68.3%, 95.5%, and 99.73% C.L. regions of $\mathcal{A}$ and $\mathcal{S}$ in Fig. 10 for (a) $\phi_1 = 25.9°$, $|P/T|$=0.3, (b) $\phi_1 = 23.5°$, $|P/T|$=0.15, (c) $\phi_1 = 23.5°$, $|P/T|$=0.3, (d) $\phi_1 = 23.5°$, $|P/T|$=0.45, and (e) $\phi_1 = 21.3°$, $|P/T|$=0.3. The horizontal dashed lines correspond to $\phi_2 = 180° - \phi_1$.*

(shown in Fig. 10) for representative values of $|P/T|$ and ϕ_1. Note that a value of ($\mathcal{S}$,$\mathcal{A}$) inside the 68.3% C.L. contour requires a value of $|P/T|$ greater than $\sim$0.3.

The allowed region is not very sensitive to variations of ϕ_1 within the errors of the measurements, as can be seen by comparing Figs. 11 (a), (c) and (e). The range of ϕ_2 that corresponds to the 95.5% C.L. region of $\mathcal{A}$ and $\mathcal{S}$ in Fig. 10 is

$$78^\circ \leq \phi_2 \leq 152^\circ,$$

for $\phi_1 = 23.5^\circ$ and $0.15 \leq |P/T| \leq 0.45$. The result is in agreement with constraints on the unitarity triangle from other measurements [16].

6 Measurement of $|V_{ub}|$

The precise measurement of $|V_{ub}|$ is one of the potential measurements to show the first discrepancy of the SM. This section describes the measurement of branching fraction of the $B^0 \to D_s^+\pi^-$ decay first, and then describes the $|V_{ub}|$ determination based on the 78 fb^{-1} data sample using the $B^0 \to D_s^+\pi^-$ decay, which is dominated by $b \to u$ transition without penguin contribution.

6.1 Reconstruction of $B^0 \to D_s^+\pi^-$ decay

We reconstruct D_s^+ mesons in the channels $D_s^+ \to \phi\pi^+$, $\overline{K}^{*0}K^+$, and $K_S^0K^+$. The ϕ (K^{*0}) mesons are formed from the K^+K^- ($K^+\pi^-$) pairs with invariant mass within 10 (50) MeV/c^2 of the nominal ϕ (K^{*0}) mass. The K_S^0 mesons are reconstructed from two pions that have an invariant mass within 6 MeV/c^2 of the nominal K_S^0 mass. The signal region of the D_s^+ candidates is defined to be within 12 MeV/c^2 of the nominal D_s^+ mass. The reconstructed D_s^+ candidates are combined with a charged pion to form a B meson candidates. We identify a candidate event using ΔE and $M_{\rm bc}$, where the signal region is defined to be $5.272 < M_{\rm bc} < 5.288$ GeV/c^2 and $|\Delta E| < 0.03$ GeV/c^2. The scatter plot in ΔE and $M_{\rm bc}$ for the signal candidates within the $M(D_s)$ signal region is shown in Fig. 12; a significant enhancement in the B signal region is observed.

To suppress the large combinatorial background that is dominated by the $e^+e^- \to q\bar{q}$ continuum process, we use variables that characterize the event topology: one is a Fisher discriminant, the other is a thrust angle between the thrust axis of the B candidate and that of the rest of the event.

Possible backgrounds from $q\bar{q}$ with real D_s^+ mesons are also considered. These events peak in the mass spectrum of D_s but not in ΔE and $M_{\rm bc}$ distributions. Background events in the $M_{\rm bc}$ sideband region indicate that the background contamination to the signal region is less than 0.5 events.

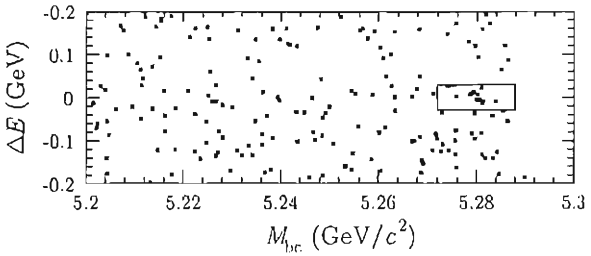

Figure 12: *The ΔE-$M_{\rm bc}$ scatter plot for the signal candidates within the $M(D_s)$ signal region. The points represent the experimental data, and the box shows the meson signal region.*

The B decays, such as $B^0 \to D^+(\to K^-\pi^+\pi^+)\pi^-$, with one pion misidentified as kaon, have large branching fractions and can peak in the $M_{\rm bc}$ signal region. To eliminate the background from these decays, we exclude event candidates that are consistent with the $D^+ \to K^-\pi^+\pi^+$ mass hypothesis within 15 MeV/c^2 when the two same-sign particles are considered to be pions independently of their particle identification. For the $D_s^+ \to K_S^0 K^+$ mode, there is a similar background from $B^0 \to D^+\pi^-$, $D^+ \to K_S^0\pi^+$. This background is suppressed by excluding candidates consistent within 20 MeV/c^2 with the $D^+ \to K_S^0\pi^+$ hypothesis.

Possible backgrounds from B decays via $b \to c$ transitions ($B \to D_s DX$) are considered. The D_s^+ from these decays have a lower momentum and are kinetically separated from the signal. We analyzed a MC sample of $B\overline{B}$ generic decay and found no peaking background.

We have found that the background may peak in the signal region of $M(D_s)$ or ΔE but not in both simultaneously. To extract the signal we perform a binned maximum-likelihood fit to the two-dimensional distribution of data in $M(D_s)$-ΔE plane. In the fit, we allow three background components (combinatorial, $q\bar{q}$ events, and B decays) to vary independently. We find $10.1^{+4.4}_{-3.7}$(stat) signal yield in the signal region. Figures 13 and 14 show the $M(D_s)$ and ΔE spectra, respectively, for the selected candidates in the B signal region together with the fitted curves. The statistical significance of the fit result is 3.6σ, which is defined by $\sqrt{-2\ln(L_0/L_{\rm max})}$, where $L_{\rm max}$ and L_0 denote the maximum likelihood with the fitted signal yield and with the signal yield fixed to zero, respectively. This indicates an evidence for the $B^0 \to D_s^+\pi^-$ decay.

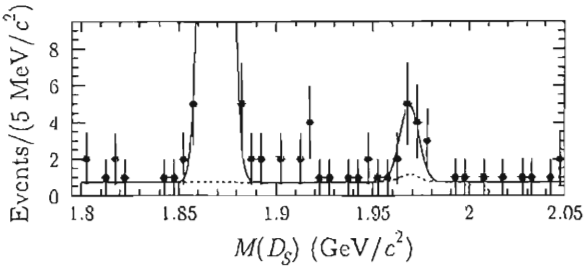

Figure 13: *The $M(D_s)$ spectrum for the signal candidates in the B signal region. The solid and dashed curves show the fitted signal plus background combined shape and background only shape, respectively. A clear peak in the lower mass region corresponds to the D^+ mass.*

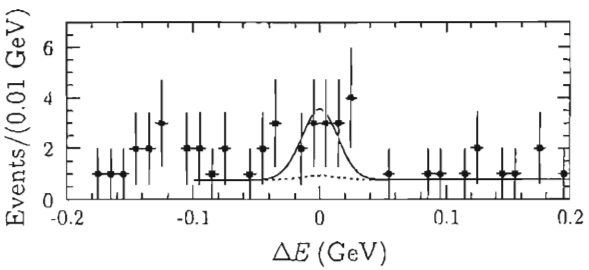

Figure 14: *The ΔE spectrum for the signal candidates in the B signal region. The solid and dashed curves show the fitted signal plus background combined shape and background only shape, respectively.*

6.2 Branching fraction measurement

The observed yield corresponds to the branching fraction of $\mathcal{B}(B^0 \to D_s^+\pi^-) = (2.4^{+1.0}_{-0.8}(\text{stat}) \pm 0.7(\text{syst})) \times 10^{-5}$.

The $B^0 \to D_s^{*+}\pi^-$ final states, where the low energy photon from the $D_s^* \to D_s\gamma$ decay is missed, can populate the $B^0 \to D_s^+\pi^-$ signal region. They would produce a long tail on the negative side of the ΔE distribution. We estimate 2% contamination to the signal region, which is included as a systematic uncertainty of the branching fraction.

The $\overline{B}^0 \to D_s^+K^-$ decay with misidentified kaon as pion possibly contaminates the $B^0 \to D_s^+\pi^-$ signal region; the uncertainty due to this effect is found to be negligible ($< 1\%$).

Following sources of systematic error are found to be dominant: K_S^0 reconstruction efficiency (6%), signal shape parameterization (5%), MC statistic (3%), track finding efficiency (2% per track), and charged hadron identification efficiency (2% per particle). The uncertainty in the D_s^+ meson branching fractions, which is dominated by 25% error in $\mathcal{B}(D_s^+ \to \phi\pi^+)$, is also taken into account. The overall systematic uncertainty is 28%.

6.3 $|V_{ub}|$ determination

Since the dominant systematic uncertainty on the branching fraction measurement comes from the branching fraction of $D_s^+ \to \phi\pi^+$, $\mathcal{B}_{\phi\pi}$, we also report $\mathcal{B}(B^0 \to D_s^+\pi^-) \times \mathcal{B}_{\phi\pi} = (16.4^{+4.5}_{-3.8}(\text{stat}) \pm 2.1(\text{syst})) \times 10^{-5}$. Using $\mathcal{B}(B^0 \to D_s^+\pi^-)/\mathcal{B}(B^0 \to D_s^+D^-) = (0.424 \pm 0.041) \times |V_{ub}/V_{cb}|^2$, and $\mathcal{B}(B^0 \to D_s^+D^-) \times \mathcal{B}_{\phi\pi} = (3.0 \pm 1.1) \times 10^{-4}$ calculated from a CLEO's result [25], we can extract a model-dependent value $|V_{ub}/V_{cb}| = (8.2^{+3.5}_{-2.9}(\text{stat}) \pm 3.4(\text{syst}))$, where no error on the factorization assumption or other sources of model dependence are included. We obtain $|V_{ub}| = (3.5^{+1.0}_{-0.9}) \times 10^{-3}$ according to $|V_{cb}| = (41.2 \pm 2.0) \times 10^{-3}$ [10].

7 Summary

We have presented the measurements of the Cabbibo-Kobayashi-Maskawa matrix components in B^0 decays to the following CP eigenstates: $(c\bar{c})K_S^0$, $J/\psi K_L^0$, $J/\psi K^{*0}$, ϕK_S^0, $\eta' K_S^0$, $K^+K^-K_S^0$, and $\pi^+\pi^-$ using data collected at the $\Upsilon(4S)$ resonance with the Belle detector at the KEKB asymmetric-energy e^+e^- collider.

One of the angles of the unitarity triangle, ϕ_1, has been determined as:

$$\sin 2\phi_1 = 0.719 \pm 0.074(\text{stat}) \pm 0.035(\text{syst}). \qquad (14)$$

The decays, $B^0 \to \phi K^0_S$, $\eta' K^0_S$, and $K^+K^-K^0_S$ are dominated by the $b \to s\bar{s}s$ transition and are sensitive to a new CP-violating phase. Our results for the $\eta' K^0_S$ and $K^+K^-K^0_S$ modes are consistent with those obtained for the $B^0 \to J/\psi K^0_S$ and other decays governed by the $b \to c\bar{c}s$ transition, while 2.1σ deviation is found in the ϕK^0_S mode.

We have found the the CP violation in the $B^0 \to \pi^+\pi^-$ decay. The determined CP-violating parameters give the favored ϕ_2 region at 95.5% confidence level as $78^\circ \leq \phi_2 \leq 152^\circ$.

We have also presented the measurement of $|V_{ub}|$ using the $B^0 \to D_s^+\pi^-$ decay: $|V_{ub}| = (3.5^{+1.0}_{-0.9}) \times 10^{-3}$.

Acknowledgments

We are deeply indebted to the organizers of the conference for inviting us to present our results. We also would like to express our acknowledgment to the KEKB accelerator group for their excellent machine operation.

References

1. M. Kobayashi and T.Maskawa, Prog. Theor. Phys. **49**, 652 (1973).
2. H. Quinn and A. I. Sanda, Eur. Phys. J. C **15**, 626 (2000). Another naming convention, $\beta = \phi_1$, $\alpha = \phi_2$, and $\gamma = \phi_3$, is also used in the literature.
3. K. Abe *et al.* [Belle Collaboration], Phys. Rev. D **66**, 071102(R) (2002); B. Aubert *et al.* [BaBar Collaboration], Phys. Rev. Lett. **89**, 201802 (2002);
4. Throughout this paper, the inclusion of the charge conjugate mode decay is implied unless otherwise stated.
5. Belle Collaboration, S. Mori *et al.*, Nucl. Instrum. Meth. A **479**, 117 (2002).
6. B. Kikutani ed., KEK Preprint 2001-157 (2001), to appear in Nucl. Instrum. Meth. A.
7. K. Abe *et al.* [Belle Collaboration], Phys. Lett. B **538**, 11 (2002).
8. K. Abe *et al.* [Belle Collaboration], Phys. Rev. Lett. **87**, 091802 (2001); K. Abe *et al.* [Belle Collaboration], Phys. Rev. D **66**, 032007 (2002).
9. K. Abe *et al.* [Belle Collaboration], Phys. Rev. Lett. **88**, 171801 (2002).
10. K. Hagiwara *et al.* [Particle Data Group], Phys. Rev. D **66**, 010001 (2002).

11. BaBar Collaboration, B. Aubert *et al.*, Phys. Rev. Lett. **87**, 091801 (2001); BaBar Collaboration, B. Aubert *et al.*, Phys. Rev. D **66**, 032003 (2002); BaBar Collaboration, B. Aubert *et al.*, Phys. Rev. Lett. **89**, 201802 (2002).

12. Y. Grossman and M. P. Worah, Phys. Lett. B **395**, 241 (1997); T. Moroi, Phys. Lett. B **493**, 366 (2000); M. Raidal, Phys. Rev. Lett. **89**, 231803 (2002); M. Ciuchini and L. Silvestrini, Phys. Rev. Lett. **89**, 231802 (2002); D. Chang, A. Masiero and H. Murayama, hep-ph/0205111 (2002).

13. D. London and A. Soni, Phys. Lett. B **407**, 61 (1997); Y. Grossman, G. Isidori and M. P. Worah, Phys. Rev. D **58**, 057504 (1998).

14. Belle Collaboration, A. Garmash *et al.*, hep-ex/0208030, BELLE-CONF-0225, contributed paper for the 31st International Conference on High Energy Physics (2002).

15. Belle Collaboration, K.-F. Chen and K. Hara *et al.*, Phys. Lett. B **546**, 196 (2002).

16. Y. Nir, hep-ph/0208080, to appear in the Proceedings of the 31st International Conference on High Energy Physics (2002).

17. The Fox-Wolfram moments were introduced in G. C. Fox and S. Wolfram, Phys. Rev. Lett. **41**, 1581 (1978). The Fisher discriminant used by Belle is described in B.C.K Casey *et al.* [Belle Collaboration], Phys. Rev. D **66**, 092002 (2002); and K. Abe *et al.* [Belle Collaboration], Phys. Lett. B **511**, 151 (2001).

18. G. J. Feldman and R. D. Cousins, Phys. Rev. D **57**, 3873 (1998).

19. M. Gronau and J.L. Rosner, Phys. Rev. D **65**, 093012 (2002).

20. M. Gronau and J.L. Rosner, Phys. Rev. D **65**, 013004 (2002).

21. Z. Luo and J.L. Rosner, Phys. Rev. D **65**, 054027 (2002).

22. M. Beneke, G. Buchalla, M. Neubert, and C. T. Sachrajda, Nucl. Phys. B **606**, 245 (2001).

23. The authors of Ref. [20] use SU(3) flavor symmetry to estimate $|P|$ from the measured $B \to K^0\pi^+$ decay rate, and factorization [21] to estimate $|T|$ from the decay rate for $B \to \pi\ell\nu$.

24. R. A. Briere *et al.* [CLEO Collaboration], Phys. Rev. Lett. **86**, 3718 (2001); T. J. Gersion *et al.* [Belle Collaboration], hep-ex/0205033 (2002); H. C. Huang *et al.* [Belle Collaboration], hep-ex/0205062 (2002).

25. D. Gibaut *et al.* [CLEO Collaboration], Phys. Rev. D **53**, 4734 (1996).

RARE B DECAYS AND DIRECT CP VIOLATION AT *BABAR*

Sandrine Laplace
Laboratoire de l'Accélérateur Linéaire, IN2P3-CNRS et Université Paris-Sud
BP 34, F-91898 Orsay Cedex, France

on behalf of the *BABAR* collaboration

Abstract

The search for rare B decays and direct CP violation at *BABAR* is described. The following measurements (based on integrated luminosities ranging from 56.4 to 81.9 fb^{-1}) are summarized: the inclusive branching fractions and direct CP asymmetries of $B^+ \to h^+h^-h^+$ ($h = \pi, K$), the exclusive branching fractions of $B^+ \to K^+\pi^-\pi^+$ (where significant signals are observed in the $B^+ \to K^{*0}(892)\pi^+$, $B^+ \to f_0(980)K^+$, $B^+ \to \chi_{c0}K^+$, $B^+ \to \overline{D}^0\pi^+$ and $B^+ \to$ higher $K^{*0}\pi^+$ channels), the branching fractions of $B^+ \to \rho^0\rho^+$ and $B^0 \to \rho^0K^{*+}$, and finally, the branching fractions, the longitudinal components, and the direct CP asymmetries in $B \to \phi K^*$.

1 Introduction

Measurements of the branching fractions and direct CP asymmetries of rare B decays using the *BABAR* detector [1] are presented. Rare B decays can be classified according to their suppression factor:

- **a small CKM matrix element**, as for charmless B decays which amplitudes are suppressed by a factor $|V_{ub}|/|V_{cb}| \simeq \lambda$ compared to charm B decay amplitudes. Measurements related to the decays $B \to hhh (h = \pi, K)$, $B \to \rho\rho$ and $B \to K^*\rho$ are presented.
- **a dominant diagram involving a loop**, which amplitudes are suppressed by either
  - $\alpha_S/4\pi$ for gluonic penguin ($b \to s$ gluon) as in the exclusive decays $B \to \eta' K^*$ and $B \to \phi K^*$.
  - $\alpha_{QED}/4\pi$ for radiative penguins ($b \to s\gamma/d\gamma$), as in the exclusive decays $B \to K^*\gamma$ and $B \to \rho\gamma$ or the inclusive decay $b \to s\gamma$, and for electroweak penguins ($b \to sZ(l\bar{l})/s\gamma(l\bar{l})$), as in the exclusive decay $B \to K\nu\bar{\nu}$.

All the measurements mentioned above were presented in my talk, but only the results newly released during the winter conferences are detailed in these proceedings, *i.e.*, $B \to hhh (h = \pi, K)$, $B \to \rho\rho$, $B \to K^*\rho$ and $B \to \phi K^*$.

The motivation for such measurements is twofold: first, they could allow to see indirect effects of new physics particles virtually created in loop. Such effects may show up in different branching fractions and CP asymmetries than those predicted by the Standard Model. One concentrates here on time-integrated direct CP asymmetries. Time-dependent asymmetries are described elsewhere [2].

Time-integrated direct CP asymmetries require at least two (Standard Model or New Physics) amplitudes contributing to a process with different weak and strong phases: calling A the total amplitude of the process B^0 (B^+) $\to f$ and $\bar{A}$ the one of the CP conjugated process $\overline{B}^0$ (B^-) $\to f$, one can split the amplitudes A and $\bar{A}$ into a sum of real amplitudes A_k, CP-odd weak phases ϕ_k and CP-even strong phases δ_k:

$$A = \sum_k A_k e^{i\phi_k} e^{i\delta_k}, \quad \bar{A} = \sum_k A_k e^{-i\phi_k} e^{i\delta_k}. \tag{1}$$

The asymmetry between A and $\bar{A}$ can then be written in terms of differences of weak and strong phases (the expression below is given in the case where two

amplitudes contribute to the process):

$$|A|^2 - |\bar{A}|^2 = -4A_1A_2\sin(\phi_1 - \phi_2)\sin(\delta_1 - \delta_2). \quad (2)$$

Beyond the search for hints of new physics, measurements of rare B decays can help constraining the Standard Model unknown parameters. For example, time-dependent CP asymmetries in $B \to \pi\pi$ and $B \to \eta' K^*$, $B \to \phi K^*$ allow to measure $\sin 2\alpha$ and $\sin 2\beta$ where α and β are two angles of the Unitarity Triangle; the ratio of the $B \to \rho\gamma$ and $B \to K^*\gamma$ rates constrains the ratio of CKM matrix elements $|V_{td}|/|V_{ts}|$; finally, the $b \to s\gamma$ spectrum helps to measure V_{ub} and to constrain Heavy Quark Effective Theory parameters.

2 The *BABAR* detector and dataset

The *BABAR* detector is described elsewhere [1] in detail. It consists of a tracking system composed from a 5-layer double sided silicon micro strip vertex tracker (SVT) and from a 40-layer drift chamber (DCH), both operating in a 1.5 T solenoidal magnetic field. Charged particle identification is mainly performed using a ring imaging Cherenkov detector (DIRC): the separation between kaons and pions ranges between 8σ for a momentum of 2 GeV/c^2 and 4σ for a momentum of 4 GeV/c^2. Photons and neutral hadrons are detected in a CsI(Tl) electromagnetic calorimeter. The identification of muons and neutral hadrons is done in the flux return instrumented with many layers of resistive plate chambers (IFR).

The data used in the analyses presented here were collected between 1999 and 2002. The total luminosity integrated at the $\Upsilon(4S)$ resonance (on-resonance data) is 81.9 fb^{-1}, and the one integrated 40 MeV below the $\Upsilon(4S)$ resonance (off-resonance data, used for continuum background studies) is 9.6 fb^{-1}. Some of the analyses are performed on a fraction of the total integrated luminosity only.

3 Kinematics and event topology at a B factory: background fighting

At the PEP-II B factory, B mesons are produced by colliding electrons and positrons at a center of mass energy equal to the $\Upsilon(4S)$ mass. At this energy, the $b\bar{b}$ cross-section corresponds to about 25% of the total cross-section (including as well lighter quark production, called thereafter continuum). Continuum is a first source of background. Cross-talk from other B decays is a second source of background referred to as B background in the following.

The kinematic and topological variables described in this section are used to distinguish signal B events from continuum and B backgrounds.

3.1 Kinematic variables

The conservation of energy and momentum allows us to build the following two (nearly uncorrelated) kinematic variables:

- The variable ΔE is defined as:

$$\Delta E = E_B^* - \sqrt{s}/2, \tag{3}$$

  where E_B^* is the B candidate energy and $\sqrt{s}$ is the beam energy, both calculated in the $\Upsilon(4S)$ center of mass. When the B candidate corresponds to a real B decay, ΔE is close from zero, up to the resolution which is dominated by the reconstruction of the B energy (a few tens of MeV, depending on the nature of the daughters of the B).

- the energy-substituted mass, $m_{\rm ES}$, is defined by:

$$m_{\rm ES} = \sqrt{(s/2 + \vec{p}_i.\vec{p}_B)^2/E_i^2 - \vec{p}_B^2}, \tag{4}$$

  where E_i and $\vec{p}_i$ are respectively the total energy and the momentum of the e^+e^- pair in the laboratory frame, and $\vec{p}_B$ is the momentum of the reconstructed B candidate. For a real B decay, $m_{\rm ES}$ peaks around the B mass, up to the resolution of 2.6 MeV/c^2 dominated by the beam energy dispersion.

Kinematic variables are used both for continuum and B background rejection. Because they are mostly uncorrelated, these two variables are often combined into a likelihood function.

3.2 Topological variables

At the $\Upsilon(4S)$ energy, $B^0\overline{B}^0$ pairs are produced almost at rest in the $\Upsilon(4S)$ center of mass. Therefore, in this frame, the B daughters are isotropically distributed. Oppositely, for the lighter quarks (mainly for the u, d, s quarks, to a lesser extend for the c quark) extra energy is available to boost the produced particles, leading to a back-to-back jet structure.

Moreover, in the process $e^+e^- \to \Upsilon(4S) \to B\overline{B}$ where the spin-1 $\Upsilon(4S)$ decays into two spin-0 B mesons, the angular distribution of the B in the center of mass follows a $\sin^2\theta_B$ distribution where θ_B is the angle between the B direction and the beam axis. Contrarily, in the process $e^+e^- \to f\bar{f}$ (where f is a fermion), the distribution follows $1+\cos^2\theta_T$ where θ_T is the angle between the "jet direction" and the beam axis.

Topological variables can be built to take advantage of these shape properties. Amongst them, one can retain:

- $\cos\theta(T_B, z)$: the cosine of the angle between the B candidate thrust direction and the beam axis. True B decays lead to a flat distribution, while one retrieve the $1 + \cos^2\theta$ distribution mentioned earlier for continuum background.

- L_0 and L_2: momentum weighted monomials defined as:

$$L_n = \sum_{i=\mathrm{ROE}} p_i |\cos(\theta_{T_B,i})|^n \ , \tag{5}$$

  where $\cos(\theta_{T_B,i})$ is the cosine between the thrust direction of the B candidate and the i-th track of the Rest Of the Event, ROE, (corresponding to what remains in the event once the B candidate tracks are removed).

Because topological variables are related to B decays and continuum production properties, they are mostly used for continuum background rejection, while being inefficient for B background rejection.

Often highly correlated amongst each others, they are combined using Fisher [3] or neural network discriminants. Figure 1 shows the Fisher discriminant outputs using the variables L_0 and L_2 for $B^0 \to \pi^+\pi^-$ Monte Carlo and continuum background. One obtains a good separation between these two categories of events.

4 Charmless B decays

4.1 Inclusive rates and direct CP violation in $B^+ \to h^+h^-h^+$ ($h = \pi, K$)

Measurements of the $B^+ \to h^+h^-h^+$ ($h = \pi, K$) decays can be used to determine the Unitarity Triangle angle γ and to help reducing uncertainties on the measurement of the angle α [4]. Amongst the six final states considered here, two of them do not occur in first or second order in the weak interaction coupling, and are therefore highly suppressed in the Standard Model: $B^+ \to K^-\pi^+\pi^+$ and $B^+ \to K^+K^+\pi^-$.

$B^+ \to h^+h^-h^+$ decays have been studied using an integrated luminosity of $81.9 fb^{-1}$. B candidates consist of combinations of three charged tracks having at least 12 hits in the DCH, a minimal transverse momentum of 100 MeV/c and originating from the beam spot. The ΔE and m_{ES} variables are computed assuming the three tracks to be pions. For modes containing kaons, the resulting ΔE distributions are shifted by roughly -45 MeV per kaon. Charged pions and kaons are identified using dE/dx information from the SVT and the DCH, and for tracks with momentum above 700 MeV/c, using the Cherenkov angle and number of photons measured by the DIRC. Kaon selection efficiency is on average 80% and mis-identification of pions as kaons is below 5% up to a momentum of 4 GeV/c. Pions are required to fail both the kaon and electron

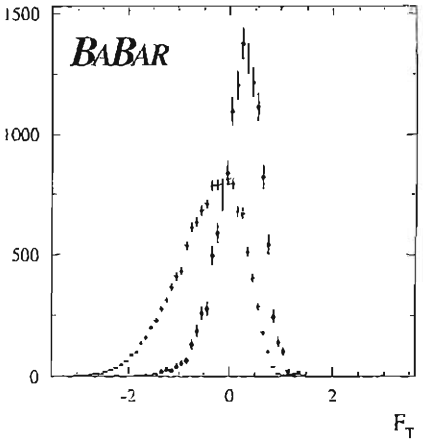

Figure 1: *Fisher discriminant output using the variables L_0 and L_2 (cf. Eq. 5) for Monte Carlo $B^0 \to \pi^+\pi^-$ signal (dots) and continuum background (crosses).*

selection algorithms. The latter is based on dE/dx, EMC shower shapes, and E/p ratio. The mis-identification of electrons as pions is 5%, and of kaons as pions is 20%.

Candidates with an intermediate neutral resonance mass compatible with any of the charm meson D^0, J/ψ, $\psi(2S)$ and χ_{c0} masses are vetoed. Continuum background is suppressed cutting on $\cos\theta(T_B, z)$ and a Fisher discriminant formed from the summed scalar momenta of all charged and neutral particles from the rest of the event within the nine nested cones coaxial with the thrust axis of the B candidate [5] (we will refer to this Fisher discriminant as the CLEO Fisher in the following). The cuts on these topological variables are optimized for each signal mode to achieve maximum sensitivity for the branching fraction, and lead to a rejection of around 90% of the continuum background. The residual background level is extrapolated from the sideband region in the $m_{ES} - \Delta E$ plane into the signal region (defined as $|m_{ES} - m_B| < 8$ MeV/c^2 and $|\Delta E - \langle \Delta E \rangle| < 60$ MeV where $\langle \Delta E \rangle|$ is the mean value of ΔE measured in the control sample $B^- \to D^0\pi^-$ and $B^- \to D^0K^-$).

Several effects are taken care of when computing the branching fraction of each signal mode:

- The dependence of the efficiency of the signal selection described above on the position of the event in the Dalitz plot.

- The Dalitz plot dependent cross-feed between modes with N kaons towards modes with $N-1$ kaons due to mis-identification of kaons as pions.
- The Dalitz plot independent cross-feed due to double mis-identification of kaons as pions, or mis-identification of pions as kaons.
- The Dalitz plot independent remaining charm and charmless B background cross-feed coming from D^0 and $\overline{D}^0$ for the $B^+ \to \pi^+\pi^-\pi^+$ and $B^+ \to K^+\pi^-\pi^+$ channels, and from $B^+ \to \eta'(\to \rho^0\gamma)K^+$ for the $B^+ \to K^+\pi^-\pi^+$ channel.

Results are summarized in Table 2. Signals are observed with around 6σ of significance for the modes $B^0 \to \pi^+\pi^-\pi^+$, $B^0 \to K^+\pi^-\pi^+$ and $B^0 \to K^+K^-K^+$. For these modes, both the branching ratio and the direct CP asymmetry are quoted. All CP asymmetries are compatible with zero. The significance of the $B^0 \to K^+K^-\pi^+$ signal is weak, therefore only a 90% CL upper limit is quoted. Finally, no events are observed for the two Standard-Model highly suppressed decays $B^+ \to K^-\pi^+\pi^+$ and $B^+ \to K^+K^+\pi^-$.

Systematic uncertainties on the branching fractions arise from background and cross-feed estimations, and from the signal efficiencies (charged particle tracking, topological variables cuts, particle identification, ΔE and $m_{\rm ES}$ variables). Systematic uncertainties on the CP asymmetries arise from tracking charge bias and particle identification.

4.2 Exclusive branching fractions of $B^+ \to K^+\pi^-\pi^+$

The study of the $B^+ \to K^+\pi^-\pi^+$ decay aims at various goals:

- search for direct CP violation,
- constrain the angle γ using interferences between $B^+ \to \chi_{c0}K^+$ and other $B^+ \to K^+\pi^-\pi^+$ decays [6, 7],
- determine the contributions from resonances involved.

In the analysis presented here, the branching ratios of both resonant and non-resonant $B^+ \to K^+\pi^-\pi^+$ decays are measured in two steps:

- in a first step, the $B^+ \to K^+\pi^-\pi^+$ Dalitz plot is split into eight regions which are expected to be dominated by a particular resonance. The yield in each region is measured using a maximum likelihood fit, with no assumption on the intermediate resonance.
- in a second step, these yields are interpreted as branching fractions assuming a model for the contributions to the Dalitz plot. The uncertainties on this model and the effects of overlap and interferences between the various contributions are considered in the systematic studies.

4.2.1 Yield measurement in each Dalitz regions

The Dalitz regions are described in Table 1. Regions I, II and III (resp. IV, V and VI) are narrow bands in the invariant mass $m_{K\pi}$(resp. $m_{\pi\pi}$). The resonances contributing to the regions II and VI "higher" modes are unknown at this stage. The "high mass" region VII could contain higher charmless and charmonium resonances as well as a non-resonant contribution.

The areas where the $m_{K\pi}$narrow bands cross the $\pi\pi$ resonances are excluded to avoid interferences, and similarly where the $\pi\pi$ resonances cross the $\overline{D}^0$ band. The other crossing regions are not excluded as the integrated interferences vanish (as long as the $m_{K\pi}$ cuts are symmetric).

Finally, the charm mode region III is used as a control sample for systematic studies.

Table 1: *Regions in the $B^+ \to K^+\pi^-\pi^+$ Dalitz plot. The symbols "$!\chi_{c0}$" and "$!\overline{D}^0$" imply the exclusion of the χ_{c0} resonance ($3.355 < m_{\pi\pi} < 3.475$ GeV/c^2), and the $\overline{D}^0$ ($1.8 < m_{K\pi} < 1.9$ GeV/c^2).*

Regions	Dominant contribution	Selection criteria $m_{K\pi}$(GeV/c^2)	$m_{\pi\pi}$(GeV/c^2)
I	$K^{*0}(892)\pi^+$	$0.816 < m_{K\pi} < 0.976$	$m_{\pi\pi} > 1.5$ and $!\chi_{c0}$
II	higher $K^{*0}\pi^+$	$0.976 < m_{K\pi} < 1.8$	$m_{\pi\pi} > 1.5$ and $!\chi_{c0}$
III	$\overline{D}^0\pi^+$	$1.835 < m_{K\pi} < 1.895$	$!\chi_{c0}$
IV	$\rho^0(770)K^+$	$!\overline{D}^0$	$0.6 < m_{\pi\pi} < 0.9$
V	$f_0(980)K^+$	$!\overline{D}^0$	$0.9 < m_{\pi\pi} < 1.1$
VI	higher fK^+	$!\overline{D}^0$	$1.1 < m_{\pi\pi} < 1.5$
VII	higher mass	$m_{K\pi} > 1.9$	$m_{\pi\pi} > 1.5$ and $!\chi_{c0}$
VIII	$\chi_{c0}K^+$	$m_{K\pi} > 1.9$	$3.37 < m_{\pi\pi} < 3.46$

Signal events are selected by forming three charged track combinations where two tracks are identified as pions, and one as kaon using the methods described in section 4.1.

Continuum background is suppressed by requiring $|\cos\theta(T_B, z)| < 0.9$ and by using the CLEO Fisher in the maximum likelihood fit.

B backgrounds arise from the following sources: combinatorial background from unrelated tracks; specific three- and four-body $B \to D$ decays; charmless three- and four-body decays (mainly $B^+ \to \eta'(\rho^0(770)\gamma)K^+$). The backgrounds which significantly contribute to the signal yields are parameterized in the final fit; otherwise, they are subtracted from the signal yield. The modes $B^+ \to J/\psi K^{(*)+}$ and $B^+ \to \psi(2S)K^{(*)+}$ are vetoed.

A maximum likelihood fit is performed to extract the yield in each Dalitz

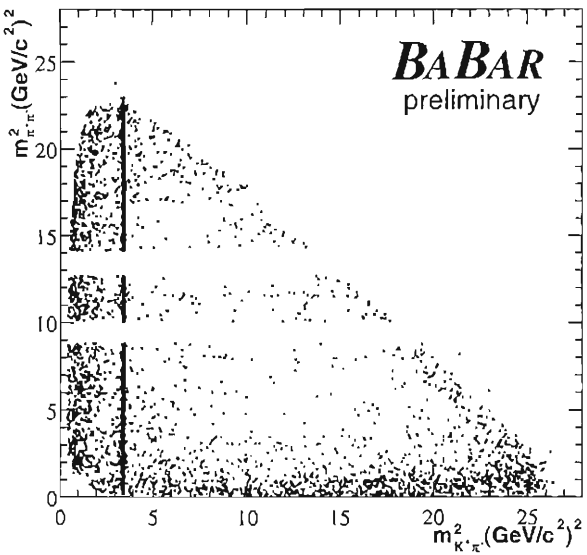

Figure 2: *Dalitz plot for on-resonance data within the signal region* $5.2715 < m_{\rm ES} < 5.2865$ GeV/c^2 *after cutting on a likelihood ratio formed from the* ΔE *and* $\mathcal{F}$ *PDFs to enhance the signal over background ratio*

region. Probability Density Functions (PDFs) are formed for the variables $m_{\rm ES}$, ΔE and Fisher $\mathcal{F}$. The likelihood in each Dalitz region is given by:

$$\mathcal{L} = \exp\left(-\sum_{i=1}^{M} n_i\right) \prod_{j=1}^{N} \left(\sum_{l=1}^{M} n_l \mathcal{P}_l(\vec{\alpha}, \vec{x_j})\right), \qquad (6)$$

where $\mathcal{P}_l$ are the PDFs of the variables $\vec{x}_j = \{\Delta E, m_{\rm ES}, \mathcal{F}\}$, parameterized by the parameters $\vec{\alpha}$ (determined before the final multivariate fit), for the event number j and the hypothesis l = {signal, continuum background, B background}.

Figure 2 shows the Dalitz plot for on-resonance data within the signal region $5.2715 < m_{\rm ES} < 5.2865$ GeV/c^2 after cutting on a likelihood ratio formed from the ΔE and $\mathcal{F}$ PDFs to enhance the signal over background ratio.

4.2.2 Branching fraction measurement

One distinguishes two categories of modes:

- modes which do not suffer from cross-feed with other modes, like in regions III ($\overline{D}^0\pi^+$) and VIII ($\chi_{c0}K^+$). In this case, their branching ratios are simply obtained by:

$$\mathcal{B} = \frac{Y}{N_{B\bar{B}}\epsilon}, \tag{7}$$

  where Y is the signal yield measured in the previous stage, $N_{B\bar{B}} = (61.6 \pm 6.8) \times 10^6$ is the number of $B\bar{B}$ pairs, and ϵ is the reconstruction efficiency calculated using signal Monte Carlo events and corrected to account for data/Monte Carlo discrepancies in tracking and particle identification.

- for the other modes suffering from cross-talk, one uses:

$$\mathcal{B} = M^{-1}Y/N_{B\bar{B}}, \tag{8}$$

  where $\mathcal{B}$ and Y are now branching ratio and yield vectors, and M is a matrix representing the probability of an event of a particular mode to be found in a given region. The branching fractions depend on the resonance model assumed in calculating the matrix M, which is split into two component matrices, P and ϵ, such that $M_{ij} = P_{ij}\epsilon_{ij}$. The P matrix accounts for the event distribution within the Dalitz plot, and ϵ for the reconstruction efficiencies. One assumes one dominant resonance per region, as indicated in the second column of table 1. For regions II, VI and VII, many contributions are possible: the model chosen here respectively includes $K_0^{*0}(1430)$, $f_2(1270)$ and a flat non-resonant $K^+\pi^-\pi^+$. The masses and widths are taken from the PDG [8], and resonances are modelled by a Breit-Wigner, except for the $\rho(770)$ where the Blatt-Weisskopf parametrization is used [9]. This model suffers from large uncertainties: the dominant resonance is unknown is some regions, there are uncertainties on the masses and widths of the resonances and on the choice of lineshapes. Alternative resonances and lineshapes are used for systematic studies. Possible interferences between resonances are also considered for systematics.

The obtained branching fractions are given in table 2. The systematic errors include components from the measurement itself (tracking efficiencies, particle identification, Fisher PDF, number of $B\bar{B}$ pairs), from the model (resonances contributions, masses, widths and lineshapes) and from the possible interferences (computed by allowing each contribution to have a random phase). These two last sources of systematics are dominant over the first one except for the $B^+ \to \overline{D}^0\pi^+$ mode where only the first source is present. Significant signals are observed in the $B^+ \to K^{*0}(892)\pi^+$, $B^+ \to f_0(980)K^+$, $B^+ \to \chi_{c0}K^+$, $B^+ \to \overline{D}^0\pi^+$ and $B^+ \to$ higher $K^{*0}\pi^+$ channels

Table 2: *Results for the measurements summarized in this proceeding. The first error quoted is statistical and the second error corresponds to systematics. Upper limits are quoted at 90% CL.*

Mode	BF (10^{-6})	A_{CP}	$\mathcal{L}$ (fb^{-1})
	Charmless B decays		
	Inclusive $B^+ \to h^+h^-h^+$ $(h = \pi, K)$ (sec. 4.1)		
$B^+ \to \pi^+\pi^-\pi^+$	$10.9 \pm 3.3 \pm 1.6$	$-0.39 \pm 0.33 \pm 0.12$	81.9
$B^+ \to K^+\pi^-\pi^+$	$59.1 \pm 3.8 \pm 3.2$	$0.01 \pm 0.07 \pm 0.03$	81.9
$B^+ \to K^+K^-K^+$	$29.6 \pm 2.1 \pm 1.6$	$0.02 \pm 0.07 \pm 0.03$	81.9
$B^+ \to K^+K^-\pi^+$	< 6.3	-	81.9
$B^+ \to K^-\pi^+\pi^+$	< 1.8	-	81.9
$B^+ \to K^+K^+\pi^-$	< 1.3	-	81.9
	Exclusive $B^+ \to K^+\pi^-\pi^+$ (sec. 4.2)		
$B^+ \to K^{*0}(892)\pi^+$	$10.3 \pm 1.2\ ^{+1.0}_{-2.7}$	-	56.4
$B^+ \to f_0(980)K^+$	$9.2 \pm 1.2\ ^{+2.1}_{-2.6}$	-	56.4
$B^+ \to \chi_{c0}K^+$	$1.46 \pm 0.35 \pm 0.12$	-	56.4
$B^+ \to \overline{D}^0\pi^+$	$184.6 \pm 3.2 \pm 9.7$	-	56.4
$B^+ \to$ higher $K^{*0}\pi^+$	$25.1 \pm 2.0\ ^{+11.0}_{-5.7}$	-	56.4
$B^+ \to \rho^0(770)K^+$	< 6.2	-	56.4
$B^+ \to K^+\pi^-\pi^+$	< 17.0	-	56.4
$B^+ \to$ higher fK^+	< 12.0	-	56.4
	$B^+ \to \rho^0\rho^+$ and $B^+ \to \rho^0K^{*+}$ (sec. 4.3)		
$B^+ \to \rho^0\rho^+$	$9.9^{+2.6}_{-2.5} \pm 1.1$	-	81.9
$B^+ \to \rho^0K^{*+}$	$7.7^{+2.1}_{-2.0} \pm 1.4$	-	81.9
	Gluonic penguins		
	$B \to \phi K^*$ (sec. 5.1)		
$B^0 \to \phi K^{*0}$	$11.1^{+1.3}_{-1.2} \pm 1.1$	$+0.04 \pm 0.12 \pm 0.02$	81.9
	$\Gamma_L/\Gamma = 0.65 \pm 0.07 \pm 0.04$		
$B^+ \to \phi K^{*+}$	$12.1^{+2.1}_{-1.9} \pm 1.5$	$+0.16 \pm 0.17 \pm 0.04$	81.9
	$\Gamma_L/\Gamma = 0.46 \pm 0.12 \pm 0.05$		

4.3 Branching ratios of $B^+ \to \rho^0\rho^+$ and $B^+ \to \rho^0 K^{*+}$

The first decay described here, $B^+ \to \rho^0\rho^+$, enters the isospin analysis of the $B \to \rho\rho$ modes which aims at measuring the angle α of the unitarity triangle. The second decay, $B^+ \to \rho^0 K^{*+}$, is expected to be dominated by $b \to s$ loops where physics beyond the Standard Model could enter.

These two decays are reconstructed in the following sub-decays: $K^{*+} \to K^+\pi^0$, $K^0(\to K^0_S(\to \pi^+\pi^-))\pi^+$, $\rho^+ \to \pi^+\pi^0$ and $\rho^0 \to \pi^+\pi^-$. Charged tracks are reconstructed using the same criteria than in section 4.1, except for the K^0_S candidates to allow for a displaced vertex. The K^0_S candidates must satisfy $|m(\pi^+\pi^-) - m(K^0)| < 12$ MeV/c^2, with the cosine of the angle between their reconstructed flight and momentum directions greater than 0.995, and the measured proper decay time greater than five times its uncertainty. Photons with a minimum energy of 30 MeV are paired to form π^0's, with a typical invariant mass resolution of 7 MeV/c^2. One therefore selects π^0 by applying a ± 15 MeV/c^2 interval around the nominal π^0 mass. The K^* and ρ resonances are formed by pairing two particles which invariant masses are within the following intervals: $0.75 < m(K\pi) < 1.05$ GeV/c^2 for the K^* and $0.52 < m(\pi\pi) < 1.00$ GeV/c^2 for the ρ. To suppress combinatorial background, one cuts at -0.5 on the helicity angle, defined as the angle between the direction of one of the two daughters (K for K^* and π^+ for ρ) and the parent B direction in the resonance rest frame.

B mesons are kinematically isolated by requiring $m_{ES} > 5.2$ GeV/c^2 and $|\Delta E| < 0.2$ GeV. The continuum background is rejected by cutting on $|\cos\theta(T_B, z)| < 0.8$. A Fisher discriminant is also constructed (and used in the final likelihood fit) based on the nine cones of the CLEO Fisher, and the additional variables $\cos\theta(T_B, z)$ and the cosine of the polar angle between the B momentum and the beam axis.

Charmed B background coming from $D \to K\pi, K\pi\pi$ is vetoed. The remaining small B background is accounted for in the fit.

The final result is extracted using a maximum likelihood fit. The selection efficiencies for transverse and longitudinal angular polarization are averaged and are assigned a systematic error defined by the RMS of a uniform efficiency between the extreme cases (9% for $\rho^0 K^{*+}_{K^0\pi^+}$, 19% for $\rho^0 K^{*+}_{K^+\pi^0}$, 18% for $\rho^0\rho^+$). The branching fractions are given in table 2. Significant signals (above 4σ) are observed in both channels.

Projections plots of the invariant masses of $K\pi$ for the $B^+ \to \rho^0 K^{*+}$ decay, and $\pi^+\pi^-$ for the $B^+ \to \rho^0\rho^+$ decay, are shown in Figure 3.

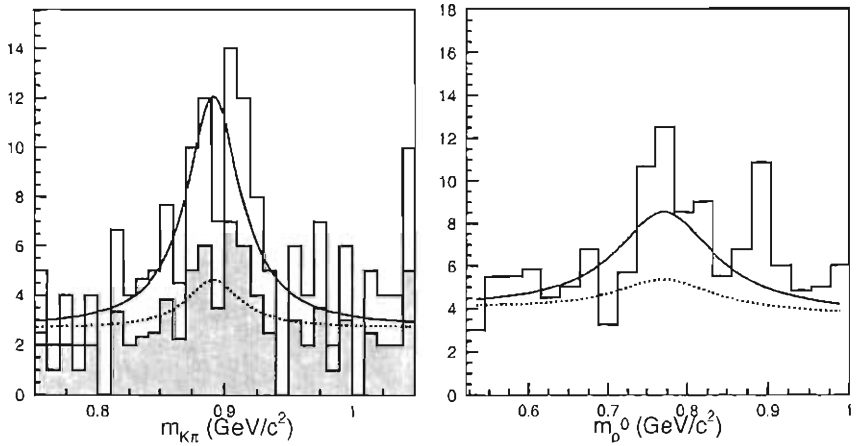

Figure 3: *Projections onto the invariant masses of $K\pi$ (left plot) for the $B^+ \to \rho^0 K^{*+}$ decay, and of $\pi^+\pi^-$ (right plot) for the $B^+ \to \rho^0\rho^+$ decay. The histograms show the data (for the K^* projection, the shaded area shows the $K^+\pi^0$ final state only), and the solid (resp. dashed) line shows the signal-plus-background (resp. background only) PDF projections.*

5 Gluonic penguins

5.1 Branching fractions, longitudinal components, and direct CP asymmetries in $B \to \phi K^*$

The decays $B \to \phi K^*$ are expected to proceed through pure $b \to s$ loops, where new physics could enter. Therefore, the measurement of direct CP violation, as well as the measurement of $\sin 2\beta$ via the time-dependent analysis of $B^0 \to \phi K^{*0}$ [2], can probe physics beyond the Standard Model. The analysis of angular distributions in these vector-vector final states is also of interest since information about the decay dynamics can be obtained [10].

The analysis proceeds in a very similar way than what is described in section 4.3, with the additional feature that longitudinal components and direct CP asymmetries are measured in the final likelihood fit. Due to limited statistics, the angular analysis is simplified, and only the longitudinal components $f_L = \Gamma_L/\Gamma$ are obtained using two-helicity angle distributions:

$$\frac{1}{\Gamma}\frac{d^2\Gamma}{d\cos\theta_1 d\cos\theta_2} = \frac{9}{4}\left(\frac{1}{4}(1-f_L)\sin^2\theta_1\sin^2\theta_2 + f_L\cos^2\theta_1\cos^2\theta_2\right), \quad (9)$$

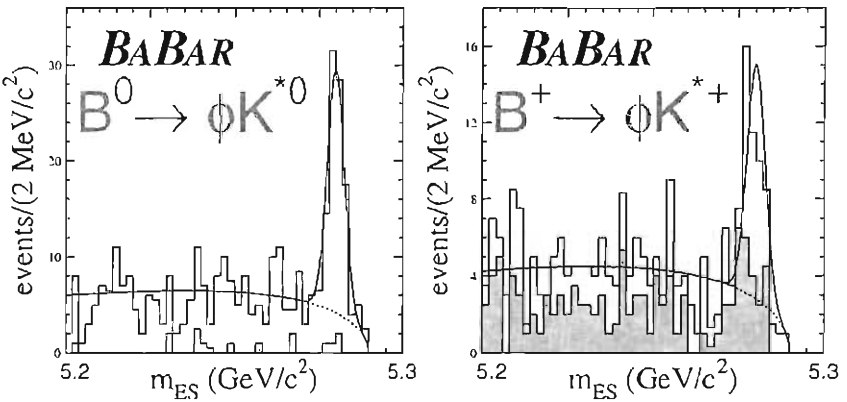

Figure 4: *Projections onto m_{ES} for $B^0 \to \phi K^{*0}$ (left plot) and $B^+ \to \phi K^{*+}$ (right plot). The histograms show the data (the shaded area shows the $K^+\pi^0$ final state only), and the solid (resp. dashed) line shows the signal-plus-background (resp. background only) PDF projections.*

where θ_1 and θ_2 are respectively the helicity angles of the K^* and the ϕ.

The results are summarized in table 2. Significant signals ($> 10\sigma$) are observed in both channels. Both direct CP asymmetries are compatible with zero.

Projections onto m_{ES} of both signals are shown in figure 4.

6 Conclusions

All results presented in these proceedings are summarized in table 2. Many new channels are observed with a large statistical significance. Measurements of direct CP violation do not indicate any significant deviation from zero. A first angular analysis is performed on the vector vector final states $B \to \phi K^*$: one measures a large longitudinal component, which should simplify the time dependent analysis allowing to measure $\sin 2\beta$ in $B^0 \to \phi K^{*0}$. These results, and many others, should become extremely precise as the integrated luminosity will reach $500 fb^{-1}$ in the year 2005, and more than 1 ab^{-1} at the end of the decade.

References

1. B. Aubert *et al.*, *BABAR* Collaboration, *Nucl. Instrum. Methods* A **479**, 1 (2002)
2. R. Faccini, these proceedings.
3. R.A. Fisher, Annals of Eugenics, **179** (1936)
4. A. Snyder and H. Quinn, *Phys. Rev.* D **48**, 2139 (1993)
5. D.M. Asner *et al.*, CLEO Collaboration, *Phys. Rev.* D **53**, 1039 (1996)
6. N.G. Deshpande, G. Eilam, X.G. He, J. Trampetic, *Phys. Rev.* D **52**, 5354 (1995)
7. S. Fajfer, R.J. Oakes, T.N.Pham, *Phys. Lett.* B **539**, 67 (2002)
8. Particle Data Group, *Phys. Rev.* D **66**, 01001 (2002)
9. J.M. Blatt and V.F. Weisskopf, *Theoretical Nuclear Physics* (Wiley, New York, 1952) 361
10. G. Kramer, W.F Palmer, *Phys. Rev.* D **45**, 193 (1992); C.H. Chen, Y.Y. Keum, H.N. Li, *Phys. Rev.* D **66**, 054013 (2002)

MEASUREMENTS OF CP VIOLATION IN MIXING WITH THE BABAR EXPERIMENT AT PEP-II

Riccardo Faccini
Università degli Studi "La Sapienza " e I.N.F.N. Roma

Abstract

With the advent of the asymmetric B-Factories, measurements of CP violation in the interference between mixing and decay are extensively used to probe the Standard Model. This note will discuss the existing methods for the measurements of the angles of the unitary triangle and comment on the present results obtained by the *BABAR* experiment at PEP-II.

1 CP violation in the interference between mixing and decay.

CP violation in the Standard Model results into a non-trivial complex phase in the Cabibbo-Kobayashi-Maskawa (CKM) weak-interaction quark mixing matrix [1]. With an appropriate choice of phases the nontrivial complex phases are assigned to the furthest off-diagonal elements V_{ub} and V_{td} of the CKM matrix. The unitarity of this CKM matrix can be visualized with a triangle in the $(\overline{\rho}, \overline{\eta})$ plane (see contribution from T. Higuchi in this volume), also reported in figure 1.

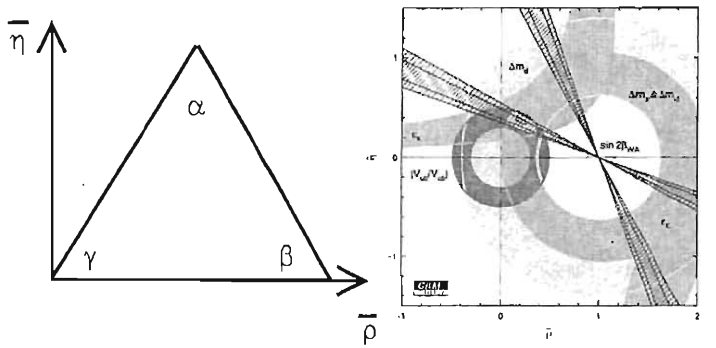

Figure 1: Left: The unitarity triangle relevant to B decays. The angles α, β and γ are also known as ϕ_1, ϕ_2, and ϕ_3 respectively. Right: Constraints on the position of the apex of the Unitarity Triangle in the $(\overline{\rho}, \overline{\eta})$ plane, including the direct measurement of $\sin(2\beta)$.

Asymmetric B factories allow direct measurements of the interior angles of the unitary triangle in B decays [2]. If a neutral B meson can decay into a given final state f either directly or by first oscillating into its anti-particle, the decay probability at a time Δt after production is

$$f_{\pm}(\Delta t) = \frac{e^{-|\Delta t|/\tau_{B^0}}}{2\tau_{B^0}(1+|\lambda|^2)}\{\frac{1+|\lambda|^2}{2} \pm [Im\lambda \sin(\Delta m_d \Delta t) - \frac{1-|\lambda|^2}{2}\cos(\Delta m_d \Delta t)]\} \quad (1)$$

where the $+$ $(-)$ sign refers to B^0 $(\overline{B}^0)$ mesons, Δm_d is the neutral B mesons' mixing frequency and τ_{B^0} is the lifetime. The complex parameter $\lambda = e^{-2i\beta}\frac{\bar{A}}{A} = |\lambda| e^{-i(2\beta+\phi_f)}$ depends on the amplitudes for B^0 (A) and $\overline{B}^0$ $(\overline{A})$ decay to the state f.

The angle which is measured depends on the ratio of amplitudes $\frac{\bar{A}}{A}$ and therefore on the final state. In particular if both amplitudes have the same

phase (such as in the case of $b\to c\bar{c}s$ decays, e.g. $f = J/\psi K^0_S$), $\phi_f = 0, \pi$ and $\sin 2\beta$ is measured; if both amplitudes are proportional to V_{ub} (such as in charmless B decays, e.g. $f = \pi^+\pi^-$), $\phi_f = \gamma$ and $\sin 2\alpha$ is measured and if only one amplitude is proportional to V_{ub} (such as in $B^0\to D\pi$) $\sin(2\beta+\gamma)$ is measured.

The situation becomes more complicated when more than one amplitude contributes to the decay. This mostly happens when a scalar decays in two vectors (e.g. $B\to J/\psi K^{*0}$ or $B^0\to D^* D^*$) or if gluonic $b\to d$ or $b\to s$ penguins are comparable in size with the tree diagrams (e.g. $B^0\to\pi\pi$ or $B^0\to D^{(*)}D^{(*)}$).

Finally, if the final state f is not a CP eigenstate the four possible decay paths $B^0(\bar{B}^0)\to f(\bar{f})$ need to be considered and equation 1 holds separately for the state f and $\bar{f}$. Results are then reported parameterizing the Δt distributions as

$$f_{\pm,\eta}(\Delta t) \propto 1 \pm [(S+\eta\Delta S)\sin(\Delta m_d \Delta t) - (C+\eta\Delta C)\cos(\Delta m_d \Delta t))\} \quad (2)$$

where $\eta = \pm 1$ depending on whether the final state is f or $\bar{f}$, C and S are sensitive to direct CP and CP violation in mixing respectively and ΔC and ΔS are dilutions which are insensitive to CP violation.

Experimentally the measurement of time-dependent CP asymmetry requires:

- a large sample of $\Upsilon(4S)$ decays into $B^0\overline{B}^0$ pairs. The $\Upsilon(4S)$ decay frame needs to be boosted in order to dilate the B mesons' flight length so that it can be measured. The PEP-II accelerator [3] is well suited for this because of its extremely high luminosity (as high as $3\times 10^{33}/\mathrm{cm}^2/\mathrm{sec}$ during the years 1999-2002 data taking) and because of the center-of-mass boost ($\beta\gamma = 0.56$).

- an efficient full reconstruction of B decays. This implies an accurate measurement of momenta and energies as well as efficient identification of leptons, photons, K^0_S and K^0_L mesons.

- a measurement of Δt. This is related to the measurement of Δz, the spatial distance between the decay vertexes.

- a determination of the flavor of the accompanying B ("tagging"); this is based on the identification of electrons, muons and charged kaons and the measurement of their charge.

The *BABAR* experiment is described in [4] and details of these experimental issues are out of the scope of this note and can be found in [5]. The effective tagging efficiency is $(28.1\pm 0.7)\%$ and the resolution on Δt is approximately 1.1ps.

2 Measurements of β

The measurements of β can be catalogued into three categories depending on the Feynman diagrams involved. They are all characterized by a ratio of amplitudes λ which is real (i.e. $\phi_f = 0$).

2.1 $b \to c\bar{c}s$ transitions.

In this type of decays both the tree, which are dominant, and the penguin diagrams have the same phase and therefore $Im\lambda = -\eta_f \sin 2\beta$ where $\eta_f = \pm 1$ is the CP eigenvalue. These are therefore extremely clean measurements from the theoretical point of view. This category includes $X_{cc}K^0_S$ ($\eta_f = -1$), $J/\psi K^0_L$ ($\eta_f = -1$) and $J/\psi K^{*0}$ ($K^{*0} \to K^0_S\pi^0$) modes. The latter mode is a decay of a scalar into two vector mesons and therefore an angular analysis is required to extract the fraction of CP odd and CP even components [6]. The measurements of $\sin 2\beta$ in this modes [7] have achieved an extremely good precision:

$$\sin 2\beta = 0.741 \pm 0.067\,(\text{stat}) \pm 0.034\,(\text{syst}) \tag{3}$$

The breakdown of the several B decay modes is reported in Table 1 and Figure 1 shows the comparison of the indirect constraints in the $(\bar{\rho}, \bar{\eta})$ plane with this direct determination of β.

Table 1: Number of events N_{tag} in the signal region after tagging and vertexing requirements, signal purity P, and results of fitting for CP asymmetries in the B_{CP} sample and in various subsamples. Errors are statistical only.

Sample	N_{tag}	$P(\%)$	$\sin 2\beta$
$J/\psi K^0_S$,$\psi(2S)K^0_S$,$\chi_{c1}K^0_S$,$\eta_c K^0_S$	1506	94	0.76, 0.07
$J/\psi K^0_L$ ($\eta_f = +1$)	988	55	0.72, 0.16
$J/\psi K^{*0}(K^{*0} \to K^0_S\pi^0)$	147	81	0.22, 0.52
Full CP sample	2641	78	0.74,0.07
$J/\psi K^0_S$, $\psi(2S)K^0_S$, $\chi_{c1}K^0_S$, $\eta_c K^0_S$ only ($\eta_f = -1$)			
$J/\psi K^0_S$ ($K^0_S \to \pi^+\pi^-$)	974	97	0.82, 0.08
$J/\psi K^0_S$ ($K^0_S \to \pi^0\pi^0$)	170	89	0.39, 0.24
$\psi(2S)K^0_S$ ($K^0_S \to \pi^+\pi^-$)	150	97	0.69, 0.24
$\chi_{c1}K^0_S$	80	95	1.01, 0.40
$\eta_c K^0_S$	132	73	0.59, 0.32

2.2 $b \to c\bar{c}d$ transitions.

The modes in this category are characterized by Cabibbo suppressed tree and penguin amplitudes with different phases. There is no reliable prediction on the relative amplitude of the two contributions. This category comprises both colour allowed modes ($B \to D^{(*)}D^{(*)}$) and colour suppressed ones ($B \to J/\psi\pi^0$):

- The $B \to D^+D^-$ decay is experimentally extremely challenging because of large irreducible background and it has not been observed yet.
- The $B \to D^{*\pm}D^{\mp}$ decays are instead cleaner and a signal of 113 events has been observed (Figure 2). They are not CP eigenstates and therefore the S and C parameters have to be extracted [8]:

$$C + \Delta C = -0.22 \pm 0.37 \pm 0.10 \quad (4)$$
$$C - \Delta C = -0.47 \pm 0.40 \pm 0.12 \quad (5)$$
$$S + \Delta S = -0.24 \pm 0.69 \pm 0.12 \quad (6)$$
$$S - \Delta S = -0.82 \pm 75 \pm 14 \quad (7)$$

where the first error is statistical and the second systematic.

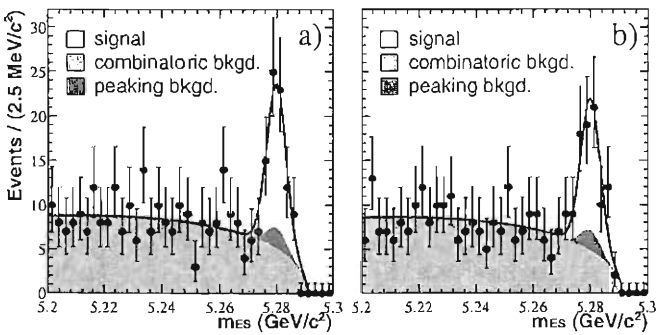

Figure 2: Fit to the B mass estimator m_{ES} with a gaussian signal component, combinatorial, and a peaking background. Left: $B \to D^{*+}D^-$; Right: $B \to D^{*-}D^+$

The prediction in absence of penguin is $S = -\sin 2\beta$ and $C = \Delta C = \Delta S = 0$, and the results agree with it, albeit with very large errors.

- The $B \to D^{*+}D^{*-}$ decay is a decay into two vector mesons and requires therefore angular analysis to determine the CP content. The measurement of the fraction of the $\eta_f = -1$ decays [9] $R_T = 0.07 \pm 0.06\,(\text{stat}) \pm$

0.03 (syst) shows that this is mostly a $\eta_f = +1$ decay. This simplifies the study of the CP violation in mixing because allows to neglect to first approximation the fact that the tree and the penguins could have different CP compositions. We therefore perform the time-dependent analysis assuming that the $\eta_f = -1$ component has the same value of $\lambda = e^{2i\beta}$ as the $b \to c\bar{c}s$ modes, and fitting only the $\eta_f = +1$ component, λ_+. In absence of penguins the predictions are $Im\lambda_+ = -\sin 2\beta$ and $|\lambda_+| = 1$, while we measure:

$$Im\lambda_+ = 0.31 \pm 0.43\,(\text{stat}) \pm 0.13\,(\text{syst}) \quad (8)$$

$$|\lambda_+| = 0.98 \pm 0.25\,(\text{stat}) \pm 0.09\,(\text{syst}) \quad (9)$$

The difference between measured and expected values of $Im\lambda_+$ seems to indicate that the penguin contribution might not be small. Figure 3 shows the result of the fit to the Δt distribution.

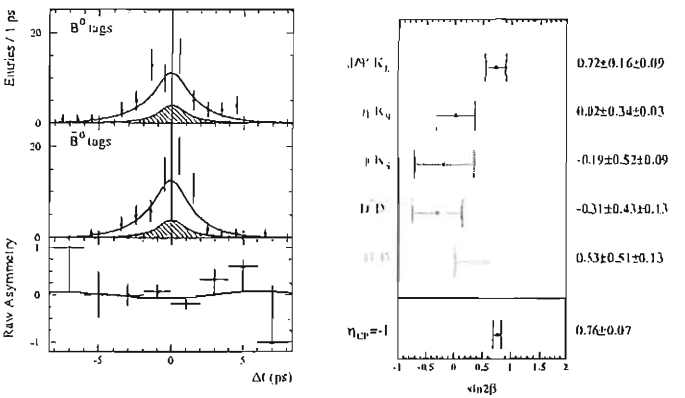

Figure 3: Left: Distributions of Δt for events enhanced in signal $D^{*+}D^{*-}$ decays, with the B recoiling the fully reconstructed one tagged as (a) B^0 (N_{B^0}) or (b) $\bar{B}^0$ ($N_{\bar{B}^0}$), and (c) the asymmetry $\left[N_{B^0} - N_{\bar{B}^0}\right] / \left[N_{B^0} + N_{\bar{B}^0}\right]$ as a function of Δt. Right: compilation of measurements of $\sin 2\beta$.

- Also the $B \to J/\psi\pi^0$ decays have been observed [10] and the S and C parameters have been measured in order to verify the presence of penguin pollution ($C \neq 0$) and the presence of CP violation ($S \neq 0$, $S = -\sin 2\beta$ in absence of penguins):

$$S = 0.05 \pm 0.49\,(\text{stat}) \pm 0.16\,(\text{syst}) \quad (10)$$

$$C = 0.38 \pm 0.41\,(\text{stat}) \pm 0.09\,(\text{syst}) \quad (11)$$

Also here there is an hint of effect of the penguin pollution.

2.3 $b \to s\bar{s}s$

These decays are characterized by the absence of the tree contribution. The penguin diagram is real and therefore $\phi_f = 0, \pi$ and the measured angle is β. This predition is exact in the Standard Model and can be modified only by the existence of additional diagrams from new physics, in particular from new particles in the penguin loop.

The only mode investigated so far with these characteristics is $B \to \phi K^0_S$. A signal of about 70 events has been observed and an S coefficient, expected to be equal to $\sin 2\beta$ is measured to be [11]:

$$S = -0.18 \pm 0.51\,(\text{stat}) \pm 0.06\,(\text{syst}) \tag{12}$$

lower than the expectation.

The $B \to \eta' K^0_S$ decay mode is also a good candidate for $b \to s\bar{s}s$ transitions, but the quark content of the η' meson is unknown and there are probably $b \to u\bar{u}s$ and $b \to d\bar{d}s$ tree contributions with a different phase ($\phi_f = 2\gamma$). A signal of about 200 events has been observed and an S coefficient, is measured to be [12]:

$$S = 0.02 \pm 0.34\,(\text{stat}) \pm 0.03\,(\text{syst}) \tag{13}$$

once more a bit lower than the expectation.

Figure 3 shows a summary of the measurements presented so far, translated in terms of $\sin 2\beta$ in absence of penguins or new physics contributions. The comparison of the $b \to c\bar{c}d$ and $b \to s\bar{s}s$ modes with the theoretically clean $b \to c\bar{c}s$ modes shows that these measurements are systematically lower. This is an interesting hint that requires more data to become significant.

3 Measurements of α

When the underlying process is $b \to u\bar{u}d$ $\phi_f = 2\gamma$ and $\sin 2\alpha$ is measured. This is the case of B decays to multipions, which suffer from the presence of $b \to d$ gluonic penguins with a different phase ($\phi_f = 2\beta$). As a consequence $C \neq 0$ and $S = \sqrt{1 - C^2} \sin 2\alpha_{\text{eff}}$, where α_{eff} depends on the magnitudes and relative strong and weak phases of the tree and penguin amplitudes. In the case of $B \to \pi^+\pi^-$ ($B \to \rho^+\pi -$), measurements of the branching fractions for the decays $B \to \pi^+\pi^0$ ($B \to \rho^+\pi^0$) and $B \to \pi^0\pi^0$ ($B \to \rho^0\pi^0$) can be used to extract α from a measurement of α_{eff} [13].

With respect to the measurements of $\sin 2\beta$ these modes have larger backgrounds and therefore likelihood analyses need to be applied to fight them. The $B \to \rho\pi$ sample is larger but is more difficult to investigate since it is not a CP

eigenstate and therefore four parameters need to be fitted (see equation 2) and since the ρ has a finite width ($\Gamma = 150\,\mathrm{MeV}/c^2$). This implies larger combinatorial backgrounds ($\rho^+ \to \pi^+\pi^0$) and the need for a full Dalitz analysis of the $B \to \pi^+\pi^-\pi^0$ system. Since there is not enough statistics to perform the Dalitz analysis, regions of the phase space of the three-pion system enriched in $B \to \rho^+\pi^-$ events are considered.

The Δt distribution in the $B \to \pi^+\pi^-$ decays is shown in Figure 4, together with the measured asymmetry. The corresponding fit results are [14]

$$S = 0.02 \pm 0.34\,(\mathrm{stat}) \pm 0.05\,(\mathrm{syst}) \quad (14)$$

$$C = -0.30 \pm 0.25\,(\mathrm{stat}) \pm 0.04\,(\mathrm{syst}), \quad (15)$$

In order to determine α given a measurement of α_{eff} the isospin relationships between the final states $\pi^+\pi^-$, $\pi^+\pi^0$, and $\pi^0\pi^0$ are studied. Assuming isospin invariance, the shift in α is bound by the relation $\sin^2(\alpha_{\mathrm{eff}} - \alpha) < \mathcal{B}(B^0 \to \pi^0\pi^0)/\mathcal{B}(B^+ \to \pi^+\pi^0)$ [13], where the branching fractions are averaged over $B^0/\overline{B}^0$ and B^+/B^-. Details of the branching fraction measurements are reported elsewhere [15], and summarized in Table 2. Including correlations and systematic errors, we find $\mathcal{B}(B^0 \to \pi^0\pi^0)/\mathcal{B}(B^+ \to \pi^+\pi^0) < 0.61$ at 90% C.L., which corresponds to $|\alpha_{\mathrm{eff}} - \alpha| < 51°$.

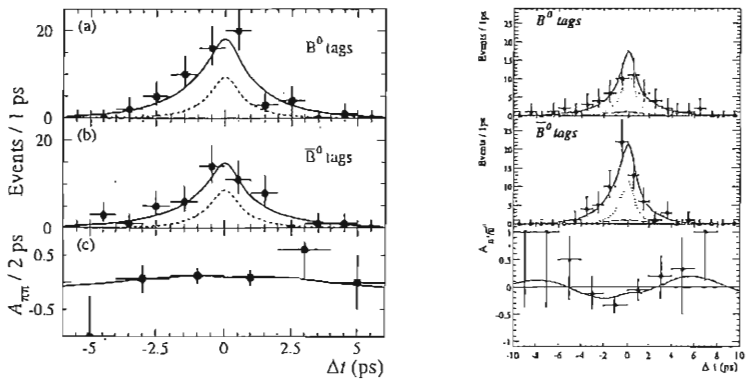

Figure 4: Distributions of Δt for events enhanced in signal $\pi\pi$ decays (Left) or $\rho\pi$ decays (Right), with the B recoiling the fully reconstructed one tagged as (a) B^0 (N_{B^0}) or (b) $\overline{B}^0$ ($N_{\overline{B}^0}$), and (c) the asymmetry $\left[N_{B^0} - N_{\overline{B}^0}\right] / \left[N_{B^0} + N_{\overline{B}^0}\right]$ as a function of Δt. Solid curves represent projections of the maximum likelihood fit, dashed curves represent the background events.

The Δt distribution in the $B \to \rho^+\pi-$ decays is shown in Figure 4, together

Table 2: Summary of results for total detection efficiencies, fitted signal yields N_S, charge-averaged branching fractions B for the two-pion B decays. Branching fractions are calculated assuming equal rates for $\Upsilon(4S) \to B^0\overline{B}^0$ and B^+B^-. The upper limit yields and branching fractions for $\pi^+\pi^0$ correspond to the 90% C.L.

Mode	Efficiency (%)	N_S	B(10^{-6})
$\pi^+\pi^-$	38.0 ± 0.8	$157 \pm 19 \pm 7$	$4.7 \pm 0.6 \pm 0.2$
$\pi^+\pi^0$	26.1 ± 1.7	$125^{+23}_{-21} \pm 10$	$5.5^{+1.0}_{-0.9} \pm 0.6$
$\pi^0\pi^0$	16.5 ± 1.7	23^{+10}_{-9} (< 46)	< 3.6

with the measured asymmetry. The corresponding fit results are [16]:

$$S = 0.16 \pm 0.25\,(\text{stat}) \pm 0.07\,(\text{syst}), \quad (16)$$

$$C = 0.45^{+0.18}_{-0.19}\,(\text{stat}) \pm 0.09\,(\text{syst}), \quad (17)$$

$$\Delta S = 0.15 \pm 0.26\,(\text{stat}) \pm 0.05\,(\text{syst}), \quad (18)$$

$$\Delta C = 0.38^{+0.19}_{-0.20}\,(\text{stat}) \pm 0.11\,(\text{syst}). \quad (19)$$

There is some hint of direct CP violation that will require more data to be confirmed. The measurements needed to perform the isospin analysis in these modes are expected to be ready by 2003 summer conferences.

A theoretically cleaner way to perform the analysis would be to do the time dependent Dalitz analysis of the $B \to \pi^+\pi^-\pi^0$ decay since this would allow to account both for the penguin pollution and for the resonant structure [17]. Although this is a good candidate to be the ultimate way to measure α, the available statistics is not yet sufficient.

4 Measurements of γ

Modes where the amplitude A is proportional to the Cabibbo-Kobayaski-Maskawa matrix element V_{cb} while $\bar{A}$ is proportional to V_{ub} are sensitive to $\sin 2\beta + \gamma$ since the relative phase between the two matrix elements is $\phi_f = \gamma$. The most reknown of such modes is $B \to D^{(*)}\pi$ [18]. It is not a CP eigenstate and in addition the ratio of the amplitudes is expected to be small $|\lambda| \sim |\frac{V_{ub}}{V_{cb}}| \sim 0.02$. This implies that the expected CP asymmetry is extremely small and that $|\lambda|$ cannot be measured on the $B \to D^{(*)}\pi$ sample itself. It could infact be measured from the cosine coefficient in equation 1, but distinguishing $1 - \lambda^2$ from 1 when $\lambda \sim 0.02$ requires much more data than available. However it has been

suggested [18] that $|\lambda|$ can be inferred from measurements of the ratios of the branching fractions $\mathcal{B}(B^0 \to D_s^{(*)+}\pi^-)/\mathcal{B}(B^0 \to D^{(*)-}\pi^+)$ using SU(3) symmetry relation:

$$|\lambda^{(*)}|^2 = |f_D^{(*)}/f_{D_s}^{(*)}|^2 \tan^2\theta_C \mathcal{B}(B^0 \to D_s^{(*)+}\pi^-)/\mathcal{B}(B^0 \to D^{(*)-}\pi^+). \quad (20)$$

From the available measurements of the Cabibbo angle, $\tan^2\theta_C = 0.2250 \pm 0.0027$, $\mathcal{B}(B^0 \to D^-\pi^+ = (0.30 \pm 0.04)\%$, $\mathcal{B}(B^0 \to D^{*-}\pi^+ = (0.276 \pm 0.021)\%$ [20], the form factors $f_{D_s}/f_D = 1.11 \pm 0.02$ and $f_{D_s^*}/f_D^* = 1.10 \pm 0.01$ [19], and with the *BABAR* results for $\mathcal{B}(B^0 \to D_s^+\pi^-) = (3.2 \pm 0.9 \pm 1.0)10^{-5}$ and $\mathcal{B}(B^0 \to D_s^{*+}\pi^-) = (1.9^+_{-1.2}1.3 \pm 0.5)10^{-5}$ [21] we obtain

$$|\lambda| = 0.021^{+0.004}_{-0.005}; \qquad |\lambda^*| = 0.017^{+0.005}_{-0.007}. \quad (21)$$

Preliminary results on $\sin 2\beta + \gamma$ are expected by 2003 summer conferences.

References

1. N. Cabibbo *Phys. Rev. Lett.* 10:531 (1963). M. Kobayashi and T. Maskawa progtp 49 652 1973.
2. For more complete pedagogical discussions of theoretical aspects of CP violation in B decays, see: Y. Nir and H. Quinn Ann. Rev. Nucl. and Part. Sci. 42:211 (1992); G.C. Branco, L. Lavoura, and J.P. Silva *International Series of Monographs on Physics*, Oxford University Press (1999); I.I. Bigi and A. I. Sanda *Cambridge Monographs on Particle Physics, Nuclear Physics and Cosmology*, 9:1 (2000).
3. *PEP-II: An asymmetric B Factory, Conceptual Design Report*, SLAC-418, LBL-5379 (1993).
4. B. Aubert, et al. (*BABAR* Collaboration)
5. *BABAR* Collaboration, B. Aubert *et al.*, *Phys. Rev.* D 65:, (0)91104 (2002)
6. *BABAR* Collaboration, B. Aubert *et al.*, *Phys. Rev. Lett.* 8:7 (2)41801 2001
7. B. Aubert *et al.* (BABAR Collaboration), Phys. Rev. Lett. 89, 201802 (2002).
8. B. Aubert *et al.* (BABAR Collaboration), hep-ex/0303004, submitted to Phys. Rev. Lett.

9. B. Aubert *et al.* (BABAR Collaboration),hep-ex/0207072

10. B. Aubert *et al.* (BABAR Collaboration), hep-ex/0303018, submitted to Phys. Rev. Lett.

11. B. Aubert *et al.* (BABAR Collaboration),hep-ex/0207070

12. B. Aubert *et al.* (BABAR Collaboration),hep-ex/0303046

13. M. Gronau and D. London, *Phys. Rev. Lett.* 65:3 (3)81 1990 , Y. Grossman and H.R. Quinn, *Phys. Rev.* D 5:8 (0)17504 1998 .

14. B. Aubert *et al.* (BABAR Collaboration), *Phys. Rev.* D 6:5 (0)51502 2002 .

15. *BABAR* Collaboration, B. Aubert *et al.*,hep-ex/0303028, submitted to Phys. Rev. Lett.

16. *BABAR* Collaboration, B. Aubert *et al.*, hep-ex/0207068.

17. A. E. Snyder and H. R. Quinn, *Phys. Rev.* D 4:8 (2)139 1993 .

18. I. Dunietz, *Phys. Lett.* B 427:1 (7)9 1998 .

19. D. Becirevic,Nucl.Phys.Proc.Suppl. 94 (2001) 337-341.

20. Particle Data Group, K. Hagiwara *et al.*, *Phys. Rev.* **60**, 0 (1)0001 2002 .

21. *BABAR* Collaboration, B. Aubert *et al.*, *Phys. Rev. Lett.* 0:0 (2)003 .

DIRECT CP VIOLATION SEARCHES AT BELLE

A. Drutskoi,
Institute for Theoretical and Experimental Physics,
B. Cheremushkinskaja, 25, Moscow, 117218, Russia
E-mail:drutskoi@iris1.itep.ru

Abstract

Recent Belle collaboration searches for direct CP-violation are discussed. Branching fraction flavor asymmetries have been measured for decay modes: $B \to K\pi$, $B \to \pi\pi$, $B \to \omega K$, $B \to \eta' K$ and $B \to D^0 K$. The asymmetries are consistent with zero within statistical and systematic errors. The decay channel $B^+ \to \phi\phi K^+$ is observed for the first time.

1 Introduction

Recent time-dependent measurements of the CP-violating parameter $\sin 2\phi_1$ by the Belle [1] and BaBar [2] collaborations established CP violation in the neutral B meson system that is consistent with Standard Model (SM) expectations. Time-integrated direct CP violation in the B decays is not yet observed and this fundamental task still has to be done by the B factories.

Direct CP violation is manifested by the non-zero branching fraction flavor asymmetry:

$$A_{CP}(f) = \frac{N(\bar{B} \to \bar{f}) - N(B \to f)}{N(\bar{B} \to \bar{f}) + N(B \to f)} \tag{1}$$

To obtain a non-zero asymmetry two interfering decay channels with different weak and strong phases are required. Within the SM frame the weak phases difference is provided by weak phases between the Cabibbo-Kobayashi-Maskawa matrix elements. An example of two interfering channels is shown in Fig.1, where the tree and penguin diagrams for the decay channel $B^0 \to K^+\pi^-$ are drawn.

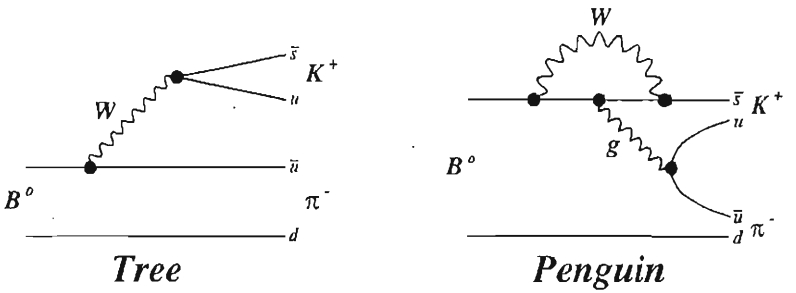

Figure 1: *The tree and penguin diagrams for the decay channel* $B^0 \to K^+\pi^-$.

The amplitudes of the $B \to f$ and $\bar{B} \to \bar{f}$ transitions have a form:

$$A(B \to f) = |T|e^{i\phi_t + i\delta_t} + |P|e^{i\phi_p + i\delta_p} \tag{2}$$

$$A(\bar{B} \to \bar{f}) = |T|e^{-i\phi_t + i\delta_t} + |P|e^{-i\phi_p + i\delta_p}\,, \tag{3}$$

where ϕ_t and ϕ_p are weak phases from the Cabibbo-Kobayashi-Maskawa matrix and δ_t and δ_p are strong phases. Penguin and tree amplitudes are labeled by P and T.

The asymmetry can be calculated from eq.2 and eq.3 as:

$$A_{CP} = \frac{2R\sin(\phi_t - \phi_p)\sin(\delta_t - \delta_p)}{1 + R^2 + 2R\cos(\phi_t - \phi_p)\cos(\delta_t - \delta_p)}\,, \tag{4}$$

where $R = |T|/|P|$.

Assuming only SM contributions and the weak phases from the Cabibbo-Kobayashi-Maskawa matrix, the conditions required to obtain large asymmetries, can be established from eq.4. The ratio of the interfering amplitudes should be close to unity and the weak phase and strong phase differences have to be large.

Large asymmetries could also be induced by new particles, such as charged Higgs bosons or supersymmetric particles, contributing to the penguin loop amplitude.

The data samples used in the analyses were collected with the Belle detector [3] at KEKB, an asymmetric energy double storage ring collider with 8 GeV electrons and 3.5 GeV positrons. Belle is a general-purpose large-solid-angle detector that consists of a three-layer Silicon Vertex Detector (SVD), a 50-layer Central Drift Chamber (CDC), a mosaic of Aerogel Čerenkov Counters (ACC), a Time of Flight Counter system (TOF), and a CsI(Tl) Electromagnetic Calorimeter (ECL) located inside a superconducting solenoid coil with a 1.5 T magnetic field. An iron flux-return located outside the coil is instrumented to identify K_L^0 and muons (KLM).

2 Results

2.1 Charmless $B \to K\pi$ decays

2.1.1 *Decay* $B^+ \to K^0\pi^+$

The decay $B^+ \to K^0\pi^+$ [1] is expected to be an almost pure $b \to s$ penguin process and, thus, no sizable asymmetry is predicted in the context of the SM. However, the previously published result, based on an analysis of a 29 fb^{-1} data sample, was $A_{CP}(K^0\pi^+) = 0.46 \pm 0.15 \pm 0.02$ [4]. An asymmetry of this magnitude cannot be explained in the SM, even with the inclusion of interference of the basic penguin amplitude with a large $B^+ \to (K^+\pi^0)_{tree} \to K^0\pi^+$ re-scattering process, and would be an indication of a new physics contribution in the penguin loop.

In the new measurement with a luminosity of 78 fb^{-1} (see Fig.2), the asymmetry $A_{CP}(K^0\pi^+) = 0.07^{+0.09+0.01}_{-0.08-0.03}$ is obtained and a 90% confidence level interval -0.10< $A_{CP}(K^0\pi^+)$ <0.22, is set, where Gaussian statistics are assumed and the systematic error is added linearly. Possible asymmetries in the detector response and reconstruction for the B signal events and the $q\bar{q}$ background events are checked using decay mode $B^+ \to D^0(\to K^+\pi^-)\pi^+$ and B meson mass sideband events.

[1] the charge conjugate modes are implicitly included here and throughout.

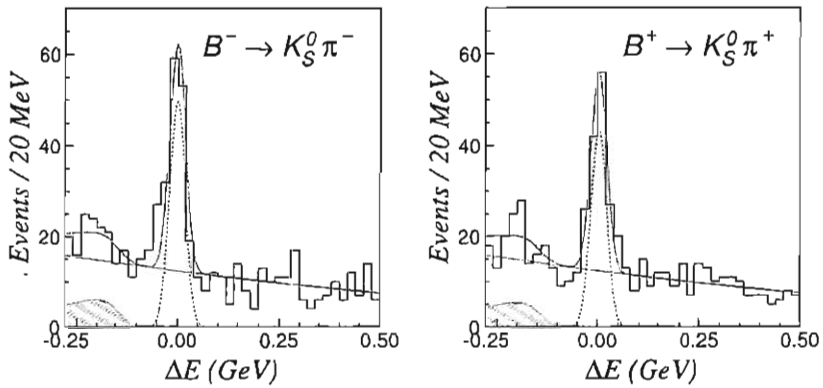

Figure 2: *The ΔE distribution for the $B^+ \to K^0\pi^+$ candidates divided into B^- (left) and B^+ (right) samples. The fit results are shown as the solid, dashed and dotted curves for the total, signal and $q\bar{q}$ background, respectively; the hatched area indicates the contribution from other charmless B decays.*

2.1.2 *Decay $B^0 \to K^+\pi^-$*

The decay channel $B^0 \to K^+\pi^-$ is described by the tree and penguin diagrams (Fig.1), which interfere. Therefore the asymmetry for this decay channel is sensitive to the angle ϕ_3, if we assume the unitarity triangle of the Cabibbo-Kobayashi-Maskawa matrix. In paper [5] an asymmetry is predicted to reach up to 10% for this decay. Preliminary Belle results are obtained with a luminosity of 78 fb^{-1}. The asymmetry is found to be $A_{CP}(K^+\pi^-) = -0.07 \pm 0.06 \pm 0.01$ and a 90% confidence level interval -0.18< $A_{CP}(K^+\pi^-)$ <0.04, is set.

2.1.3 *Decay $B^+ \to K^+\pi^0, B^+ \to \pi^+\pi^0$*

Both decay modes $B^+ \to K^+\pi^0$ and $B^+ \to \pi^+\pi^0$ are measured simultaneously. To separate these modes, opposite requirements are applied on π^+/K^+ likelihood particle identification. Both channels have cross reflections slightly shifted in the ΔE distribution, which are respectively treated in the fit. Similar to the previous decay mode, the $B^+ \to K^+\pi^0$ mode has the contribution from both the tree and penguin diagrams. The decay mode $B^+ \to \pi^+\pi^0$ has a weak phase from the vertex V_{td} within the penguin diagram. Preliminary Belle results obtained with a luminosity of 78 fb^{-1} are: $A_{CP}(K^+\pi^0) = 0.23 \pm 0.11^{+0.01}_{-0.04}$ with a 90% confidence level interval -0.01< $A_{CP}(K^+\pi^0)$ <0.42 and $A_{CP}(\pi^+\pi^0) = -0.14 \pm 0.24^{+0.05}_{-0.04}$ with a 90% confidence level interval -0.57< $A_{CP}(\pi^+\pi^0)$ <0.30. The systematic uncertainty of the detector response was studied by testing the asymmetry of the B meson mass sideband events.

2.2 Charmless $B^+ \to \omega K^+$ and $B^+ \to \eta' K^+$ decays

The $B^+ \to \omega K^+$ and $B^+ \to \eta' K^+$ modes are expected to have contributions from both tree and penguin diagrams. Additionally the $B^+ \to \eta' K^+$ mode is expected to have a contribution from the penguin diagram with $s\bar{s}$ creation. The amplitude of the color-suppressed tree diagram is expected to be only a few percent of that for the penguin one, therefore the asymmetry has to be small within the SM. However the branching fraction of $B^+ \to \eta' K^+$ decay appears to be anomalously large [6], this mode is especially interesting to search for effects of direct CP violation, due to possible sensitivity to physics beyond the SM. The obtained values of asymmetries for $B^+ \to \eta' K^+$ (Fig.2) and $B^+ \to \omega K^+$ decay modes are in agreement with zero (Table 1).

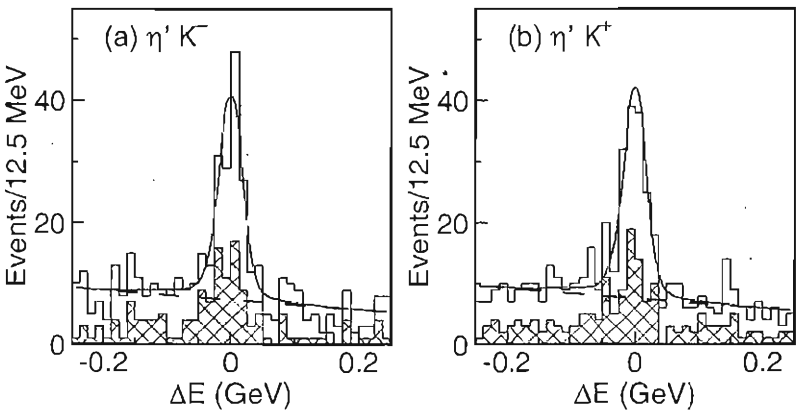

Figure 3: *The ΔE distribution for the $B^\pm \to \eta' K^\pm$ candidates: (a) for $\eta' K^-$, (b) for $\eta' K^+$. The cross hatched histograms indicate the $\eta\pi\pi$ channel; the solid histograms are the sum of both η' decay channels ($\eta\pi\pi$ and $\rho\gamma$). The curves are the fitted backgrounds (dashed) and the sum of signal and background (solid).*

2.3 Charmed $B^+ \to D^0 K^+$ decay

Theoretical studies on B meson dynamics have demonstrated the direct accessibility of the angle ϕ_3 using the process $B^+ \to D^0 K^+$ [7]. If the D^0 is reconstructed as a CP eigenstate, the $b \to c$ and $b \to u$ processes interfere and this interference can lead to direct CP violation. However the branching fractions for D meson decay modes to CP eigenstates are only of order 1 %. Since CP violation is expected to be small.

The D^0 mesons were reconstructed in the following decay channels. For $CP = +1$ modes, decay channels $D_1 \to K^-K^+$ and $D_1 \to \pi^-\pi^+$ are used, while for $CP = -1$ modes, decay modes $D_2 \to K^0_S\pi^0, K^0_S\phi, K^0_S\omega, K^0_S\eta, K^0_S\eta'$ are used. With a luminosity of 78 fb^{-1}, the Belle collaboration obtained $A_{CP}(D_1K^+) = 0.06 \pm 0.19 \pm 0.04$ and $A_{CP}(D_2K^+) = -0.19 \pm 0.17 \pm 0.05$ asymmetries, which agree well with zero within errors.

2.4 First observation of $B^+ \to \phi\phi K^+$ decays

The decay mode $B^+ \to \phi\phi K^+$ is the first observation of a $b \to s\bar{s}s\bar{s}s$ transition. The decay $B \to \phi\phi K$ can also probe a new CP-violating phase in the $b \to s$ transition [8]. Direct CP violation could be enhanced to the level of 40% if there is sizable interference between transitions due to physics beyond the SM and $B \to \eta_c K$ decay with $\eta_c \to \phi\phi$.

Fig. 4 shows signals in $M(\phi\phi) < 2.85$ GeV/c^2 and $2.94 < M(\phi\phi) < 3.02$ GeV/c^2 regions, having significances 5.1σ and 8.8σ respectively. The branching fractions obtained are: $Bf(B^+ \to \phi\phi K^+) = (2.6^{+1.1}_{-0.9} \pm 0.3) \times 10^{-6}$ and $Bf(B^+ \to \eta_c K^+) \times Bf(\eta_c \to \phi\phi) = (2.2^{+1.0}_{-0.7} \pm 0.3) \times 10^{-6}$. With increased statistics the measurement of asymmetry in this mode can provide an important test of beyond SM contributions.

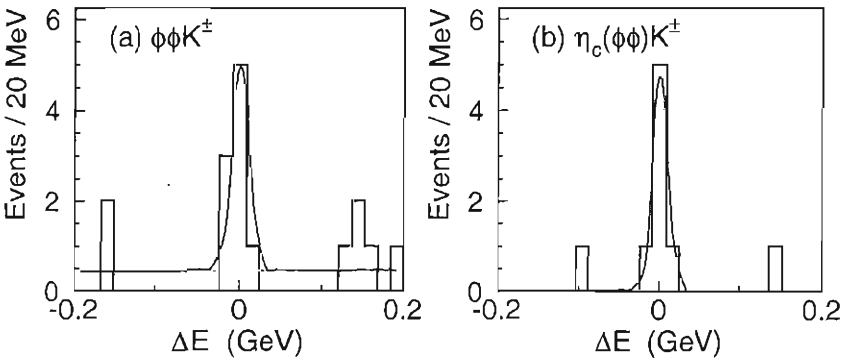

Figure 4: *The ΔE distributions overlaid with the fitted curves for a) the $B^+ \to \phi\phi K^+$ candidates with $M_{\phi\phi} < 2.85$ GeV/c^2 and b) the $B^+ \to \eta_c K^+$ candidates with $\eta_c \to \phi\phi$.*

3 Conclusions

Asymmetries have been measured in many B decay modes (Table 1). All the asymmetries obtained are consistent with zero. Statistical precision has reached

10% level, which is close to the maximum values predicted within the SM. The branching fractions of the order of 10^{-6} have been measured for the decay mode $B^+ \to \phi\phi K^+$ for the first time.

Table 1: *Asymmetries, 90% confidence level intervals and luminosities for the studied B decay channels.*

Mode	A_{CP}	90% C.L.	Luminosity
$B^+ \to K^0_S\pi^+$	$0.07^{+0.09+0.01}_{-0.08-0.03}$	$-0.10 < A_{CP} < 0.22$	78 fb$^-$1
$B^0 \to K^+\pi^-$	$-0.07 \pm 0.06 \pm 0.01$	$-0.18 < A_{CP} < 0.04$	78 fb$^-$1, prel.
$B^+ \to K^+\pi^0$	$0.23 \pm 0.11^{+0.01}_{-0.04}$	$-0.01 < A_{CP} < 0.42$	78 fb$^-$1, prel.
$B^+ \to \pi^+\pi^0$	$-0.14 \pm 0.24^{+0.05}_{-0.04}$	$-0.57 < A_{CP} < 0.30$	78 fb$^-$1, prel.
$B^+ \to \eta' K^+$	$-0.015 \pm 0.070 \pm 0.009$	$-0.13 < A_{CP} < 0.10$	41.8 fb$^-$1
$B^+ \to \omega K^+$	$-0.21 \pm 0.28 \pm 0.03$	$-0.70 < A_{CP} < 0.28$	29.4 fb$^-$1
$B^+ \to D_1 K^+$	$0.06 \pm 0.19 \pm 0.04$	$-0.26 < A_{CP} < 0.38$	78 fb$^-$1
$B^+ \to D_2 K^+$	$-0.19 \pm 0.17 \pm 0.05$	$-0.47 < A_{CP} < 0.11$	78 fb$^-$1

References

1. Belle collaboration, K. Abe *et.al.*, Phys. Rev. **D66**, 071102 (2002).
2. BaBar collaboration, B. Aubert *et.al.*, Phys. Rev. Lett. **89**, 201802 (2002).
3. Belle Collaboration, A. Abashian *et al.*, Nucl. Instr. Meth. **A479**, 117 (2002).
4. Belle collaboration, B.C.K. Casey *et.al.*, Phys. Rev. **D66**, 092002 (2002).
5. M. Beneke *et.al.*, Nucl. Phys. **B606**, 245 (2001).
6. Belle collaboration, K. Abe *et.al.*, Phys. Lett. **B517**, 309 (2001).
7. M. Gronau and D. Wyler, Phys. Lett. **B265**, 172 (1991).
8. M. Hazumi, hep-ph/0303089.

NEW PHYSICS IN B_d-$\bar{B}_d$ MIXING AND CKM FITS

Gino Isidori
INFN, Laboratori Nazionali di Frascati, I-00044 Frascati, Italy

Abstract

In a wide class of new-physics models large deviations form the SM are expected mainly in $\Delta B = 2$ observables. As we shall show, despite the recent precise data from B factories, this scenario is still far from being excluded: present data show a perfectly consistent picture not only for the "standard" solution $\phi_d = \arg[\mathcal{M}(B_d^0 - \overline{B}_d^0)] \sim 47°$, but also for $\phi_d \sim 133°$. The present role of $\mathcal{A}_{CP}(B_d \to \pi^+\pi^-)$ and $\mathrm{BR}(K^+ \to \pi^+\nu\bar{\nu})$, and the possible future role of additional measurements in shedding light on this scenario are discussed.

1 Introduction

Thanks to the efforts at B factories, the exploration of CP violation is now entering another exciting stage, allowing us to confront the Cabibbo–Kobayashi–Maskawa (CKM) mechanism with data. After the discovery of mixing-induced CP violation in the "gold-plated" mode $B_d \to J/\psi K_S$, as well as important other measurements, one of the most interesting questions is now to what extent the possible space for new physics (NP) has already been reduced. From this perspective, the present consistency of CKM fits should not be over emphasized: in order to constraint the parameter space of possible NP models, we cannot simply test the consistency of the SM hypothesis. In principle, all observables potentially sensitive to NP, namely all short-distance dominated flavour-changing neutral current (FCNC) amplitudes, should be left as free parameters. A completely model-independent approach of this kind is very difficult, because of the larger number of couplings involved. However, we may still perform useful predictive analyses within certain general classes of new-physics scenarios. In the present paper we analyse one of such classes, namely a scenario with large generic NP contributions to B_d^0–$\overline{B_d^0}$ mixing ($\Delta B = 2$), eventually also to ϵ_K ($\Delta S = 2$), but *not* to the $\Delta B = 1$ and $\Delta S = 1$ decay amplitudes. As we shall discuss, this scenario is well motivated by simple dimensional arguments in a wide class of models, including supersymmetric frameworks. [1, 2] Within this scenario a crucial role to determine the structure of the unitarity triangle is played by CP asymmetries in $B_d \to \pi^+\pi^-$ and by rare decays, such as $K^+ \to \pi^+\nu\bar{\nu}$ and $B_d \to \mu^+\mu^-$. As we shall show, present data are perfectly consistent with a non-standard CKM fit where the preferred $\bar{\rho}$–$\bar{\eta}$ region is the upper-left quadrant and the B_d^0–$\overline{B_d^0}$ mixing amplitude receives $\mathcal{O}(1)$ NP contributions.

2 CKM fits with NP in B_d^0–$\overline{B_d^0}$ mixing

In presence of NP in B_d^0–$\overline{B_d^0}$ mixing, the weak phase ϕ_d, determined by the $B_d \to J/\psi K_S$ CP-violating asymmetry,

$$\mathcal{A}_{CP}^{mix}(B_d \to J/\psi K_S) = -\sin\phi_d = 0.734 \pm 0.054 \,, \quad (1)$$

$$\phi_d = \left(47^{+5}_{-4}\right)^\circ \vee \left(133^{+4}_{-5}\right)^\circ \,, \quad (2)$$

cannot be trivially identified with the CKM phase 2β:

$$\phi_d = \phi_d^{SM} + \phi_d^{NP} = 2\beta + \phi_d^{NP} \,. \quad (3)$$

In other words, we may not convert the experimental information on ϕ_d into a direct constraint in the $\bar{\rho}$–$\bar{\eta}$ plane. Similarly, we may not use the SM interpre

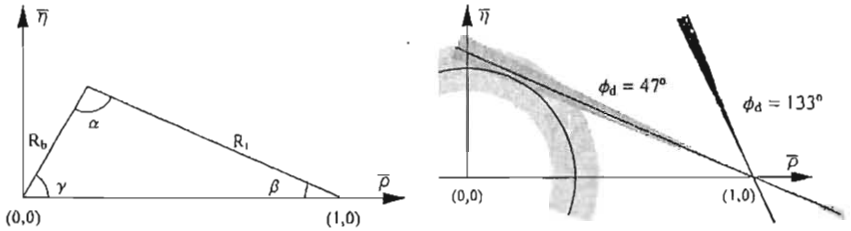

Figure 1: Left: Definition of the CKM unitarity triangle. Right: Standard procedure adopted in the literature to represent the two solutions for ϕ_d in (2).

tation of the $B_{d,s}$ mass differences $\Delta M_{d,s}$ to determine the unitarity-triangle side $R_t \equiv |V_{td}V_{tb}^*/V_{cd}V_{cb}^*|$, as discussed recently by several authors [3, 4].

On general grounds, the only constraint on the unitarity triangle which is expected to be very robust as far as the impact of NP is concerned, is the so-called $|V_{ub}|$ circle (see Fig. 1), or the side

$$R_b \equiv \left|\frac{V_{ud}V_{ub}^*}{V_{cd}V_{cb}^*}\right| = \left(1-\frac{\lambda^2}{2}\right)\frac{1}{\lambda}\left|\frac{V_{ub}}{V_{cb}}\right| = \sqrt{\overline{\rho}^2+\overline{\eta}^2}\,. \tag{4}$$

Indeed, the value of R_b is determined by means of exclusive and inclusive transitions of the type $b \to u\ell\overline{\nu}_\ell$ and $b \to c\ell\overline{\nu}_\ell$, which are dominated by SM tree-level amplitudes. The value of R_b allows us to obtain the following bounds for the "true" angle β of the unitarity triangle (see Fig. 1):

$$(\sin\beta)_{\max} = R_b^{\max}, \quad (\sin 2\beta)_{\max} = 2R_b^{\max}\sqrt{1-(R_b^{\max})^2}. \tag{5}$$

Using the rather conservative experimental range $R_b = 0.38 \pm 0.08$, which corresponds to $R_b^{\max} = 0.46$, we obtain

$$|\beta|_{\max} = 27.4°. \tag{6}$$

Whereas the former solution $\phi_d \sim 47°$ in (2) satisfies this bound nicely, this is definitely not the case for $\phi_d \sim 133°$. The latter solution cannot be accommodated in the SM and requires NP contributions to B_d^0–$\overline{B_d^0}$ mixing, i.e. we now need $\phi_d^{\rm NP} \neq 0$ in (3). At this point, one may rise the question of how we may represent this second solution in the $\overline{\rho}$–$\overline{\eta}$ plane. In the literature, this is usually simply done through a second branch, corresponding to

$$\beta \sim 133°/2 = 66.5° \quad \text{and} \quad \beta \sim -(180° - 66.5°) = -113.5°, \tag{7}$$

as we have shown in Fig. 1. Since in this case we know that $\phi_d^{\rm NP} \neq 0$, it is clear that this procedure –valid to test the SM consistency– cannot be applied: if

we allow sizable NP effects in loop-induced FCNC amplitudes, any $\bar{\rho}$–$\bar{\eta}$ point compatible with the R_b circle is allowed and both solutions for ϕ_d in (2) are possible.

If we wish to determine more precisely the structure of the unitarity triangle, some additional experimental or theoretical input is required. In principle, the best solution would be to constrain γ by means of processes dominated by tree-level SM amplitudes, such as $B_d \to DK$ modes: [5] this would avoid making any assumption about loop-mediated amplitudes, potentially sensitive to NP. Unfortunately, we cannot yet confront these methods with data.

Given the present situation, $B_d \to \pi^+\pi^-$ modes offers a very interesting alternative: if we use ϕ_d as an input, and employ the CP-averaged $B_d \to \pi^\mp K^\pm$ branching ratio to control the penguin effects, we may determine γ from the CP-violating $B_d \to \pi^+\pi^-$ observables. [6] This procedure requires some dynamical assumption about SM penguin amplitudes, that in the future can be tested and minimized with the help of $B_s \to K^+K^-$ modes. [7] The most delicate point of this procedure is that $B_d \to \pi^+\pi^-$ decays are not mediated by pure tree-level amplitudes and, on general grounds, may well be affected by NP. As we shall discuss in the next section, there is a interesting and rather general class of SM extensions where NP yields sizable contributions to B_d^0–$\overline{B_d^0}$ mixing only, leaving the decay amplitudes – including the loop-induced ones – almost unaffected. The use of CP asymmetries in $B_d \to \pi^+\pi^-$ to fix γ, which we shall employ in Section 4, is therefore very well suited for this type of scenarios. [1]

3 New Physics in B_d^0–$\overline{B_d^0}$ Mixing

As far as flavour physics is concerned, extensions of the SM can be classified into two wide categories: models with minimal flavour violation (MFV) and models with new sources of flavour mixing. Within the highly-constrained class of MFV models, the only source of flavour-symmetry breaking terms is given by the SM Yukawa couplings. As a consequence, all flavour-changing transitions are still ruled by the CKM matrix. For this reason, many of the standard CKM constraints hold also in MFV models: the determination of R_t in terms of $\Delta M_s/\Delta M_d$ is still valid, and the relation between $\sin\phi_d$ and $\sin 2\beta$ can differ at most by an overall sign, i.e. $\phi_d^{\rm NP} = 0°$ or $\phi_d^{\rm NP} = 180°$. It is then easy to realize that within MFV models the structure of the unitarity triangle is fixed – up to a twofold ambiguity – even without $B_d \to \pi^+\pi^-$ data, and that there is no room for the non-standard solution $\phi_d \sim 133°$.

In the wide class of models with new sources of flavour mixing, it is rather natural to expect extra $\mathcal{O}(1)$ contributions to the B_d^0–$\overline{B_d^0}$ amplitude, with arbitrary phases, so that we may accommodate any value of $\phi_d^{\rm NP}$. It is also very natural to assume that these NP effects have a negligible impact on $\Delta B = 1$

amplitudes dominated by tree-level SM contributions; this happens essentially in all realistic models. On the other hand, it is less obvious why these new sources of flavour-symmetry breaking – being able to induce $\mathcal{O}(1)$ corrections to B_d^0–$\overline{B_d^0}$ mixing – should have a small impact on $\Delta B = 1$ amplitudes arising only at the loop level within the SM. This hypothesis certainly does not represent the most general NP scenario; however, it can be realized under rather general conditions.

The generic NP scenario we shall advocate is a model where non-standard effects are negligible in all amplitudes that receive tree-level SM contributions (independently of possible CKM suppressions). Moreover, in order to protect the effects on $\Delta B = 1$ FCNC amplitudes, we shall add the following two general requirements:

i) the effective scale of NP is substantially higher than the electroweak scale;

ii) the adimensional effective couplings ruling $\Delta B = 2$ transitions can always be expressed as the square of two $\Delta B = 1$ effective couplings.

Employing an effective-theory language, what we mean under these two hypotheses is that the generic dimension-six operators encoding NP contributions to B_d^0–$\overline{B_d^0}$ and $\Delta B = 1$ transitions can be written as

$$Q^{\rm NP}_{\Delta B=2} = \frac{\delta^2_{bd}}{\Lambda^2_{\rm eff}}(\bar{b}\Gamma d)(\bar{b}\Gamma d), \qquad Q^{\rm NP}_{\Delta B=1} = \frac{\delta_{bd}}{\Lambda^2_{\rm eff}}(\bar{b}\Gamma d)(\bar{q}\Gamma q), \tag{8}$$

where δ_{bd} denotes the new $\Delta B = 1$ effective flavour-changing coupling, Γ indicates generic Dirac and/or colour structures, and possible coefficient functions of $\mathcal{O}(1)$ have been ignored. Coherently with the requirement ii), we shall also assume that $(\mathrm{SU}(2)_L \times \mathrm{U}(1)_Y)$-breaking operators of dimension less than six, such as the chromomagnetic operator, play a negligible role. The overall normalization of the two operators in (8), or the definition of the effective scale $\Lambda_{\rm eff}$, has been chosen such that the corresponding SM $\Delta B = 2$ term is

$$Q^{\rm SM}_{\Delta B=2} = \frac{(V^*_{tb}V_{td})^2}{M^2_W}(\bar{b}\Gamma d)(\bar{b}\Gamma d). \tag{9}$$

Choosing this normalization, we have implicitly factorized out an overall coefficient of $\mathcal{O}[(g/\sqrt{2})^4/(16\pi^2)]$ in the effective Hamiltonian, both in the $\Delta B = 2$ and in the $\Delta B = 1$ cases. As a result, within the SM, the loop-induced $\Delta B = 1$ operators can be written as

$$Q^{\rm SM}_{\Delta B=1} = C\frac{V^*_{tb}V_{td}}{M^2_W}(\bar{b}\Gamma d)(\bar{q}\Gamma q), \tag{10}$$

where the coefficient function C is of $\mathcal{O}(1)$ in the case of pure short-distance-dominated electroweak operators (such as those generated by Z-penguin and

W-box diagrams) and substantially larger than unity for those that receive large logarithmic corrections via RGE.

Since the measurement of the B_d^0–$\overline{B_d^0}$ mass difference falls in the ballpark of the SM expectations, the new flavour-changing coupling δ_{bd} cannot be arbitrarily large: barring fine-tuned scenarios with severe cancellations among different terms, we can allow at most $\mathcal{O}(1)$ corrections to the SM amplitude. This implies

$$\frac{\langle Q^{\rm NP}_{\Delta B=2}\rangle}{\langle Q^{\rm SM}_{\Delta B=2}\rangle} \lesssim 1 \qquad \rightarrow \qquad \frac{\delta_{bd}}{\Lambda_{\rm eff}} \lesssim \frac{V_{tb}^* V_{td}}{M_W}, \tag{11}$$

where possible $\mathcal{O}(1)$ factors associated with the matrix elements of the operators have been neglected.

Owing to the different parametric dependence from scale factor and flavour-changing coupling of $\Delta B = 2$ and $\Delta B = 1$ operators in (8), if the condition (11) is fulfilled the corresponding non-standard effects induced in $\Delta B = 1$ flavour-changing neutral-current transitions turn out to be suppressed at least by a factor $\mathcal{O}(M_W/\Lambda_{\rm eff})$ relative to the SM level:

$$\frac{\langle Q^{\rm NP}_{\Delta B=2}\rangle}{\langle Q^{\rm SM}_{\Delta B=2}\rangle} \lesssim 1 \qquad \rightarrow \qquad \frac{\langle Q^{\rm NP}_{\Delta B=1}\rangle}{\langle Q^{\rm SM}_{\Delta B=1}\rangle} \leq \frac{1}{C}\frac{M_W}{\Lambda_{\rm eff}}. \tag{12}$$

Since the coefficient C is substantially larger than 1 for QCD-penguin amplitudes, the suppression is even more severe in this case. We have thus obtained a natural justification for the smallness of non-standard effects in $\Delta B = 1$ loop-induced amplitudes in the well-motivated scenario of a heavy NP scale ($\Lambda_{\rm eff} \gg M_W$).

Although rather qualitative, the above argument has the great advantage of being almost independent of the details of the NP model. Indeed, it can be realized in very different frameworks, from low-energy supersymmetry to models with large extra dimensions. As can be easily understood, this argument does not apply only to B_d^0–$\overline{B_d^0}$ mixing: it is characteristic of any type of $\Delta F = 2$ meson–antimeson mixing versus the corresponding $\Delta F = 1$ loop-induced amplitudes, provided the corresponding assumption ii) is fulfilled. For this reason, in the phenomenological determination of the CKM matrix of Section 4, we shall try to avoid the use of observables such as ε_K or ΔM_s, which are sensitive to the K^0–$\overline{K^0}$ and B_s^0–$\overline{B_s^0}$ mixing amplitudes, respectively.

In principle, the case of $b \to s$ transitions is somehow different from the $b \to d$ and $s \to d$ ones, since the B_s^0–$\overline{B_s^0}$ mass difference has not yet been measured. This is indeed one of the reasons why speculations about possible large NP effects in penguin-mediated $b \to s$ transitions, such as $B \to \pi K$ and – especially $B \to \phi K$ – are still very popular. However, we recall that the available data on ΔM_s already show a preference for this observable to be close

to its SM expectation. If we assume that NP effects in ΔM_s can be at most of $\mathcal{O}(1)$, we can accommodate large NP effects in $b \to s$ transitions only by means of violations of the conditions i) and ii), or by fine-tuning. Therefore, in order to understand the consistency of our scenario, it will be very interesting to follow the evolution of future measurements of $B \to \pi K$ and $B \to \phi K$ decays, together with the constraints on ΔM_s.

4 Impact of $B_d \to \pi^+\pi^-$ in the Unitarity Triangle

The decay $B_d^0 \to \pi^+\pi^-$ originates from $\bar{b} \to \bar{u}u\bar{d}$ quark-level transitions. Within the SM and the scenario for NP discussed before, we may write the corresponding decay amplitude as follows:

$$A(B_d^0 \to \pi^+\pi^-) \propto \left[e^{i\gamma} - de^{i\theta}\right], \tag{13}$$

where the CP-conserving strong parameter $de^{i\theta}$ measures – sloppily speaking – the ratio of penguin to tree contributions in $B_d \to \pi^+\pi^-$. If we had negligible penguin contributions, i.e. $d = 0$, the corresponding CP-violating observables were simply given by

$$\begin{aligned} \mathcal{A}_{CP}^{dir}(B_d \to \pi^+\pi^-) &= 0, \\ \mathcal{A}_{CP}^{mix}(B_d \to \pi^+\pi^-) &= \sin(\phi_d + 2\gamma) \stackrel{SM}{=} -\sin 2\alpha, \end{aligned} \tag{14}$$

where we have, in the last identity, also used the SM relation $\phi_d = 2\beta$ and the unitarity relation $2\beta + 2\gamma = 2\pi - 2\alpha$. Note that the phases ϕ_d and γ enter directly in the $B_d \to \pi^+\pi^-$ observables, and not α. Consequently, since ϕ_d can be fixed straightforwardly through $B_d \to J/\psi K_S$, we may use $B_d \to \pi^+\pi^-$ to probe γ, which has important advantages when dealing with penguin and NP effects. [6, 7]

Measurements of the CP-violating $B_d \to \pi^+\pi^-$ observables are already available:

$$\mathcal{A}_{CP}^{dir}(B_d \to \pi^+\pi^-) = \begin{cases} -0.30 \pm 0.25 \pm 0.04 & \text{(BaBar [8])} \\ -0.77 \pm 0.27 \pm 0.08 & \text{(Belle [9])} \end{cases} \tag{15}$$

$$\mathcal{A}_{CP}^{mix}(B_d \to \pi^+\pi^-) = \begin{cases} -0.02 \pm 0.34 \pm 0.05 & \text{(BaBar [8])} \\ +1.23 \pm 0.41^{+0.07}_{-0.08} & \text{(Belle [9])}. \end{cases} \tag{16}$$

The BaBar and Belle results are unfortunately not fully consistent with each other. Hopefully, the experimental picture will be clarified soon. If we nevertheless form the weighted averages of (15) and (16), using the rules of the Particle Data Group (PDG), we obtain

$$\mathcal{A}_{CP}^{dir}(B_d \to \pi^+\pi^-) = -0.51 \pm 0.19\ (0.23) \tag{17}$$

$$\mathcal{A}_{CP}^{mix}(B_d \to \pi^+\pi^-) = +0.49 \pm 0.27\ (0.61), \tag{18}$$

where the errors in brackets are the ones increased by the PDG scaling-factor procedure. Direct CP violation at this level would require large penguin contributions with large CP-conserving strong phases. Interestingly, a significant impact of penguins on $B_d \to \pi^+\pi^-$ is also indicated by data on the $B \to \pi K, \pi\pi$ branching ratios, as well as by theoretical considerations. Consequently, it is already evident that the penguin contributions to $B_d \to \pi^+\pi^-$ *cannot* be neglected.

Over the recent years, many approaches to control the impact of the penguin contributions on the extraction of weak phases from the CP-violating $B_d \to \pi^+\pi^-$ observables have been proposed. [10, 11] In the following we shall adopt the method by proposed by R. Fleischer and J. Matias, referring to their original work for more details. [6] The two CP-violating asymmetries are written as

$$\mathcal{A}_{\rm CP}^{\rm dir}(B_d \to \pi^+\pi^-) = f_1(d,\theta,\gamma), \quad \mathcal{A}_{\rm CP}^{\rm mix}(B_d \to \pi^+\pi^-) = f_2(d,\theta,\gamma,\phi_d), \quad (19)$$

which are *exact* parameterizations within the SM, and hold also within our general NP scenario. If we fix ϕ_d through (2), these two equations depend on three unknown parameters, d, θ and γ. In order to extract these quantities we then need an extra constraint. In principle, the best additional constraint is given by one of the following observables:

$$\mathcal{A}_{\rm CP}^{\rm dir}(B_s \to K^+K^-) = g_1(d',\theta',\gamma), \quad \mathcal{A}_{\rm CP}^{\rm mix}(B_s \to K^+K^-) = g_2(d',\theta',\gamma,\phi_s)\,, \quad (20)$$

where $d' = d$ and $\theta' = \theta$ in the limit of exact U-spin symmetry and ϕ_s can be assumed to be negligible (or can be fixed through CP-violating effects in $B_s \to J/\psi\phi$). Unfortunately, the $B_s \to K^+K^-$ mode is not accessible yet. However, since $B_s \to K^+K^-$ is related to $B_d \to \pi^\mp K^\pm$ through an interchange of spectator quarks, we may connect these two channels under very reasonable dynamical assumptions and then use the $B_d \to \pi^\mp K^\pm$ modes, which have already been observed at the B factories, [12] to control the penguin effects in $B_d \to \pi^+\pi^-$. The key quantity is then the following ratio of the CP-averaged $B_d \to \pi^+\pi^-$ and $B_d \to \pi^\mp K^\pm$ branching ratios:

$$H \equiv \frac{1}{\epsilon}\left(\frac{f_K}{f_\pi}\right)^2 \left[\frac{\mathrm{BR}(B_d \to \pi^+\pi^-)}{\mathrm{BR}(B_d \to \pi^\mp K^\pm)}\right] = 7.5 \pm 0.9\,, \quad (21)$$

where the factor f_K/f_π involving the kaon and pion decay constants takes into account factorizable U-spin-breaking corrections, and $\epsilon \equiv \lambda^2/(1-\lambda^2)$. If, in addition to U-spin symmetry, we make plausible dynamical assumptions to replace the $B_s \to K^+K^-$ channel with the $B_d \to \pi^\mp K^\pm$ ones, we may write H as a function of $\{\gamma,\ d,\ \theta\}$ and, using also (19), we finally determine the three parameters.

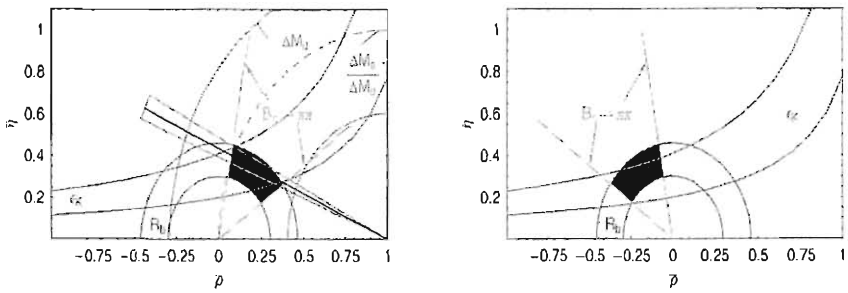

Figure 2: Allowed regions for the apex of the unitarity triangle determined from the combination of R_b and the CP-violating $B_d \to \pi^+\pi^-$ observables, as described in the text, using the standard B_d^0–$\overline{B_d^0}$ mixing phase $\phi_d \sim 47°$ (left) or the non-standard solution $\phi_d \sim 133°$ (right).

Following this procedure (we refer to the original works [6] for more detail), leads to

$$35° \lesssim \gamma \lesssim 79° \,(\phi_d = 47°), \quad 101° \lesssim \gamma \lesssim 145° \,(\phi_d = 133°). \tag{22}$$

These two solutions are related to each other through

$$\phi_d \to 180° - \phi_d, \quad \gamma \to 180° - \gamma. \tag{23}$$

Because of the unsatisfactory experimental situation concerning the CP asymmetries of $B_d \to \pi^+\pi^-$, the ranges in (22) should mainly be considered as an illustration of how this strategy is working. Indeed, in order to obtain (22), we have just used the "ordinary" errors in (17) and (18), and not the enlarged ones given there in brackets.

It should be noted that we have assumed in (22) – as is usually done – that $\gamma \in [0°, 180°]$. This range is implied by the interpretation of ε_K, provided that: i) NP does not change the sign of the $\Delta S = 2$ amplitude with respect to the SM; ii) the "bag" parameter B_K is positive (as indicated by all existing non-perturbative calculations). If we relaxed these assumptions about NP and/or "bag" parameters, we would need to double the solutions and consider the specular case $\gamma \in [180°, 360°]$.

Using (22), we may now fix the apex of the unitarity triangle. To this end, we combine the constraint on R_b with the ranges of γ. The results of this exercise are shown in Fig. 2 for $\phi_d = 47°$ (left) and $\phi_d = 133°$ (right). In order to guide the eye, we have also included in Fig. 2 the well-known SM ε_K hyperbola. In the left plot we show also the $\beta = 23.5°$ branch, which corresponds to the SM interpretation of $\phi_d = 47°$, as well as the circle with radius R_t around $(1, 0)$ that is fixed through ΔM_d, and the constraint arising

from the lower bound on $\Delta M_s/\Delta M_d$. It is remarkable that we obtain a perfect agreement of our $B_d \to \pi^+\pi^-$ range, which does *not* rely on ε_K or B^0_d–$\overline{B^0_d}$ mixing, with *all* these constraints. On the other hand, the case of $\phi_d = 133^\circ$ shown in the right plot of Fig. 2 requires large NP contributions to B^0_d–$\overline{B^0_d}$ mixing, so that we may there *no longer* use ΔM_d or $\Delta M_s/\Delta M_d$ to determine the side R_t of the unitarity triangle (this is why these constraints are not shown on the right plot).

As can be seen in Fig. 2, both the $\phi_d = 47^\circ$ and the $\phi_d = 133^\circ$ regions are consistent with the ε_K hyperbola. On the other hand, the two solutions leads to very different predictions for the rate of rare $(b,s) \to d$ transitions, such as $K^+ \to \pi^+\nu\overline{\nu}$ and $B_d \to \mu^+\mu^-$, which are proportional to $|V_{td}|^2$. In particular, the rate expected in the non-standard case are about twice as large as the SM ones. Interestingly, the experimental result of the E787 Collaboration, [13] $\mathrm{BR}(K^+ \to \pi^+\nu\overline{\nu}) = (1.57^{+\,1.75}_{-\,0.82}) \times 10^{-10}$, has a central value which perfectly fit with this non-standard prediction. [3]

5 Outlook

A fit to the CKM unitarity triangle in presence of NP is clearly more complicated by the presence of a large number of new free parameters. Nonetheless, as we have seen, we can already start to analyze in a model-independent way the wide class of NP scenarios where large modifications of the SM occur only in $\Delta F = 2$ amplitudes.

This analysis, which is still not very precise because of the large experimental uncertainties on $\mathcal{A}_{CP}(B_d \to \pi^+\pi^-)$, shows that a large NP contribution to B^0_d–$\overline{B^0_d}$ mixing cannot be excluded yet. In particular, present data are perfectly consistent with a non-standard CKM fit where the preferred $\bar{\rho}$–$\bar{\eta}$ region is the upper-left quadrant. This solution is associated to the non-standard B^0_d–$\overline{B^0_d}$ mixing phase $\phi_d \sim 133^\circ$ and, interestingly, leads to a prediction for $\mathrm{BR}(K^+ \to \pi^+\nu\overline{\nu})$ in better agreement with experiments.

This non-standard solution certainly requires some amount of fine-tuning to mimic the SM case and the statistical significance of the $\mathrm{BR}(K^+ \to \pi^+\nu\overline{\nu})$ measurement should not be over emphasized. Nonetheless, we believe this is an interesting scenario that should not be disregarded. Future precise measurements on rare FCNC decays, or new information on CKM phases by means of tree-level dominated transitions, would help to exclude or confirm this fascinating hypothesis.

This work is partially supported by IHP-RTN, EC contract No. HPRN-CT-2002-00311 (EURIDICE).

References

1. Y. Grossman, Y. Nir and M.P. Worah, *Phys. Lett.* **B407** (1997) 307.
2. R. Fleischer, G. Isidori and J. Matias, *JHEP* **0305**, 053 (2003).
3. G. D'Ambrosio and G. Isidori, *Phys. Lett.* **B530** (2002) 108.
4. D. Becirevic *et al.*, *Nucl. Phys.* **B634** (2002) 105; R. Fleischer, *Phys. Rep.* **370** (2002) 537.
5. M. Gronau and D. Wyler, *Phys. Lett.* **B265** (1991) 172; D. Atwood, I. Dunietz and A. Soni, *Phys. Rev. Lett.* **78** (1997) 3257; R. Fleischer and D. Wyler, *Phys. Rev.* **D62** (2000) 057503. Y. Grossman, Z. Ligeti and A. Soffer, LBNL-51630 [hep-ph/0210433]; M. Gronau, CERN-TH/2002-331 [hep-ph/0211282].
6. R. Fleischer, *Eur. Phys. J.* **C16** (2000) 87; R. Fleischer and J. Matias, *Phys. Rev.* **D66** (2002) 054009.
7. R. Fleischer, *Phys. Lett.* **B459** (1999) 306.
8. B. Aubert *et al.* (BaBar Collaboration), *Phys. Rev. Lett.* **89** (2002) 281802.
9. K. Abe *et al.* (Belle Collaboration), Belle preprint 2003-1 [hep-ex/0301032].
10. See e.g.: M. Gronau and D. London, *Phys. Rev. Lett.* **65** (1990) 3381; R. Fleischer and T. Mannel, *Phys. Lett.* **B397** (1997) 269; Y. Grossman and H.R. Quinn, *Phys. Rev.* **D58** (1998) 017504; J. Charles, *Phys. Rev.* **59** (1999) 054007; D. London, N. Sinha and R. Sinha, *Phys. Rev.* **D63** (2001) 054015; M. Gronau and J.L. Rosner, *Phys. Rev.* **D66** (2002) 053003.
11. M. Beneke *et al.*, *Nucl. Phys.* **B606** (2001) 245; M. Ciuchini *et al.*, *Phys. Lett.* B **515**, 33 (2001) A.I. Sanda and K. Ukai, *Prog. Theor. Phys.* **107** (2002) 421; Y.-Y. Keum, DPNU-02-30 [hep-ph/0209208].
12. CLEO Collaboration (A. Bornheim *et al.*), CLEO 03-03 [hep-ex/0302026]; BaBar Collaboration (B. Aubert *et al.*), hep-ex/0207065; hep-ex/0206053; Belle Collaboration (B.C. Casey *et al.*), *Phys. Rev.* **D66** (2002) 092002.
13. E787 Collaboration (S. Adler *et al.*), *Phys. Rev. Lett.* **88** (2002) 041803.

CP violation and rare decays in kaons at NA48

Ivan Mikulec
Institut für Hochenergiephysik, Nikolsdorfergasse 18, A-1050 Wien, Austria

Abstract

NA48 has finished the measurement of direct CP violation in neutral kaon decays to $\pi\pi$ with a combined result $Re(\varepsilon'/\varepsilon) = (14.7 \pm 2.2) \times 10^{-4}$. A new preliminary measurement of charged asymmetry $\delta_L(e) = (3.317 \pm 0.100) \times 10^{-3}$ has been obtained from data taken in the year 2001. From a special near target run in the year 2000, two new preliminary results are presented: $Im(\eta_{000}) = (-1.2 \pm 1.3) \times 10^{-2}$ and $BR(K_S \to \pi^0\gamma\gamma)_{z>0.2} = (4.9 \pm 1.7) \times 10^{-8}$. The decay $K_S \to \pi^0\gamma\gamma$ has been observed for the first time.

1 Introduction

The NA48 detector has been designed to measure direct CP violation in the decays of K_L and K_S into $\pi\pi$, described by the parameter $Re(\varepsilon'/\varepsilon)$, by using simultaneous far- and near-target beams [1]. In the year 2001 the beams were created by 400 GeV protons hitting the far target with an intensity of $\sim 2.4 \times 10^{12}$ protons during the 5.2 s long SPS pulse (ppp). The protons which do not interact in the far target are attenuated and directed to the near target with an intensity of $\sim 5 \times 10^7$ ppp.

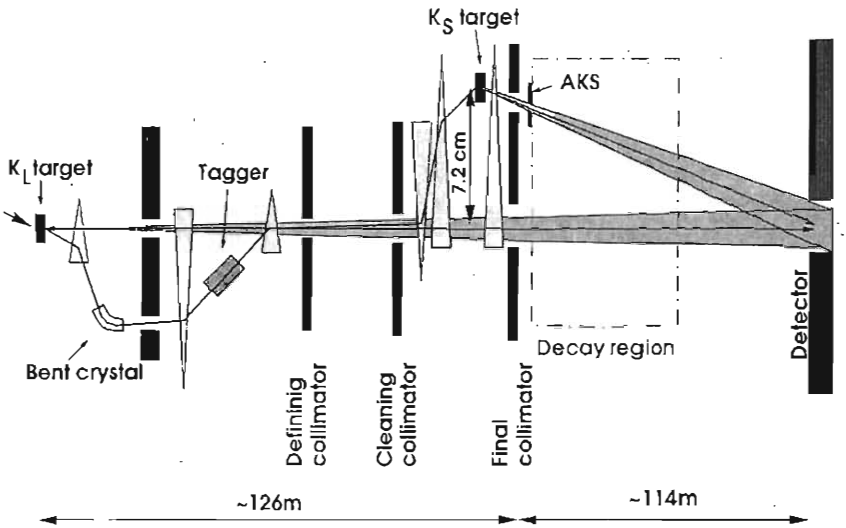

Figure 1: *Example of figure caption.*

The main device for charged particle detection is the magnetic spectrometer [2]. It consists of a dipole magnet and four drift chambers, two before and two after the magnet. The spatial resolution of $\sim$100 μm per plane results in a momentum resolution of

$$\frac{\sigma_P}{P} = [0.48 \oplus 0.009 P(GeV/c)]\%. \quad (1)$$

The whole spectrometer is placed in a helium tank separated from the vacuum decay region by a thin KEVLAR window. A time resolution of $\sim$150 ps for a $\pi^+\pi^-$ event is given by a scintillator hodoscope placed between the spectrometer and the calorimeter.

A liquid krypton calorimeter (LKr) [3], placed behind the hodoscope, is used to measure the energy, position and time of electro-magnetic showers initiated by photons. The energy resolution is

$$\sigma(E)/E \simeq 0.090/E \oplus 0.032/\sqrt{E} \oplus 0.0042 \qquad (2)$$

where E is in GeV. The position and time resolutions for a single photon with energy larger than 20 GeV are better than 1.3 mm and 300 ps, respectively.

The LKr calorimeter is followed by a sampling hadron calorimeter composed of 48 steel plates, interleaved with scintillator planes with a readout in horizontal and vertical projections and by a muon anti-counter system.

In order to determine from which beam the decay originated a tagging station composed of thin scintillator strips is located on the path of the proton beam between far and near targets. The time resolution of this device is ~140 ps and double-pulse resolution is 4-5 ns.

The beginning of the K_S decay region is sharply defined by an anti-counter (AKS), located at the exit of the near-target collimator.

Photons escaping the outside limits of the calorimeter acceptance are detected by seven ring shaped scintillator counters equipped with iron converters (AKL).

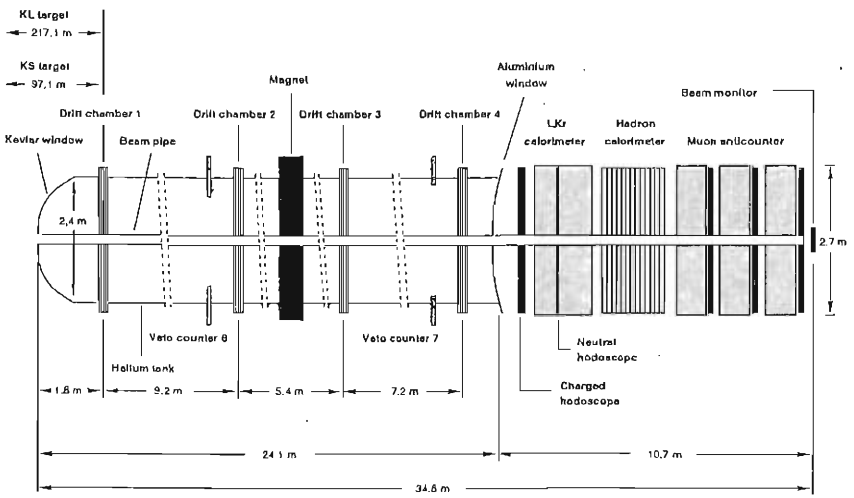

Figure 2: *Example of figure caption.*

More about the detector and the experimental configuration can be found in [4].

In the year 2000, the drift chambers of the spectrometer were in repair after an accident after the end of 1999 run. The KEVLAR window was removed and the helium tank evacuated. The last part of this special run was devoted to neutral K_S rare decays using only near-target beam with an intensity of $\sim 10^{10}$ ppp.

2 The measurement of $Re(\varepsilon'/\varepsilon)$

The main aim of the 2001 run was not only to add more statistics to the already published $Re(\varepsilon'/\varepsilon)$ result [4] but also to perform additional systematic checks. This was possible due to several changes in the experimental conditions (Table 1). Besides rebuilt drift chambers and a change in the beam energy, a significant increase of the duty cycle allowed to collect 29% of the total statistics with reduced instantaneous beam intensity. The fact that the result is fully compatible with the one obtained from 1997–1999 period confirms the robustness of the $Re(\varepsilon'/\varepsilon)$ measurement with respect to the accidental beam activity [5].

Table 1: *Change in conditions of the $Re(\varepsilon'/\varepsilon)$ run in 2001.*

	98-99	2001
proton energy	450 GeV/c	400 GeV/c
SPS cycle time	14.4 s	16.8 s
spill length (effective)	2.4 s (1.7 s)	5.2 s (3.6 s)
duty cycle	0.17	0.31
K_L beam intensity	$\sim 1.5 \times 10^{12}$ ppp	$\sim 2.4 \times 10^{12}$ ppp
K_S beam intensity	$\sim 3 \times 10^{7}$ ppp	$\sim 5 \times 10^{7}$ ppp
		+ rebuilt spectrometer

The result from 2001 data only is [5]

$$Re(\varepsilon'/\varepsilon) = (13.7 \pm 3.1) \times 10^{-4} \tag{3}$$

and the combined result together with other NA48 published data is

$$Re(\varepsilon'/\varepsilon) = (14.7 \pm 2.2) \times 10^{-4} \tag{4}$$

This final result reaches the design accuracy and leads to a world average of $(16.6 \pm 1.6) \times 10^{-4}$.

3 Measurement of the K_{e3} charge asymmetry

The charge asymmetry in K_{e3} decays is defined as

$$\delta_L(e) \equiv \frac{BR(K_L \to \pi^- e^+ \nu_e) - BR(K_L \to \pi^+ e^- \overline{\nu_e})}{BR(K_L \to \pi^- e^+ \nu_e) + BR(K_L \to \pi^+ e^- \overline{\nu_e})} \tag{5}$$

If CPT symmetry holds, this observable is equal to $2Re(\epsilon)$.

During the 2001 run along with $\pi\pi$ samples for $Re(\varepsilon'/\varepsilon)$ measurement about 2×10^8 K_{e3} decays have been collected. The systematic effects due to detector asymmetry is reduced by regular changes of the spectrometer magnet polarity. The backgrounds could be reduced to a negligible level by selection cuts. The main source of systematic uncertainties arises from charge dependent interactions of $\pi^\pm$ in the electro-magnetic calorimeter which are reflected in asymmetric trigger and particle identification efficiencies (Table 2). The corrections are calculated using various control samples involving charged pions like $K_S \to \pi^+\pi^-$ and $K_L \to \pi^+\pi^-\pi^0$. In spite of the significant momentum dependence of the corrections the result does not depend on the pion momentum (Fig: 3).

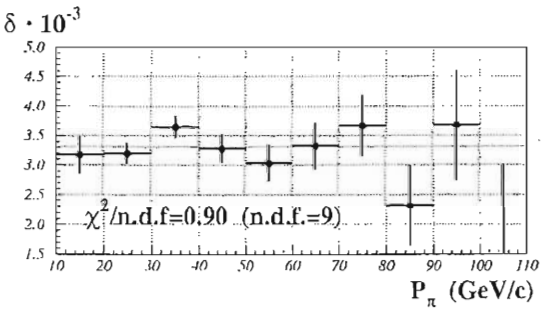

Figure 3: $\delta_L(e)$ *as a function of pion momentum.*

The preliminary result

$$\delta_L(e) = (3.317 \pm 0.070_{stat} \pm 0.072_{syst}) \times 10^{-3} \tag{6}$$

is in a good agreement with previous measurements notably with recently published result of KTeV collaboration [6].

Table 2: *Summary of systematic effects in the $\delta_L(e)$ analysis*

	in 10^{-5}		
Trigger	+26.2	$\pm$	6.0
Punch trough	-1.4	$\pm$	3.5
Pion ID	-17.1	$\pm$	2.4
Acceptance		$\pm$	0.5
Background		$\pm$	0.5

4 Measurement of η_{000}

The CP violating parameter η_{000} is defined as

$$\eta_{000} \equiv \frac{A(K_S \rightarrow \pi^0\pi^0\pi^0)}{A(K_L \rightarrow \pi^0\pi^0\pi^0)} \tag{7}$$

If CPT symmetry is conserved, the real part of η_{000} is given by CP violation in mixing and is equal to $Re(\epsilon)$, while the imaginary part can be sensitive to direct CP violation.

The data for this measurement has been collected during the last period of 2000 data taking in special conditions with a high intensity near-target beam and without spectrometer. Almost 6×10^6 $K^0 \rightarrow \pi^0\pi^0\pi^0$ events have been collected. This data is normalised to pure $K_L \rightarrow \pi^0\pi^0\pi^0$ sample from far-target beam run immediately preceding the near-target run in practically same detector conditions which leads to cancellation of the acceptance in the first order. The result is obtained from a fit to a function

$$f(E,t) = \frac{I^{near}_{3\pi^0}}{I^{far}_{3\pi^0}} = A(E)\big[1 + |\eta_{000}|^2 e^{t/\tau_L - t/\tau_S} + 2D(E)e^{t/2\tau_L - t/2\tau_S}(Re(\eta_{000})cos(\Delta mt) - Im(\eta_{000})sin(\Delta mt))\big] \tag{8}$$

in kaon energy E and proper time t bins. The $D(E)$ denotes $K^0 - \overline{K^0}$ production dilution at the target and is fixed to the values measured by NA31 [7]. The fit results shown in Fig. 4 are

$$Re(\eta_{000}) = (-2.6 \pm 1.0_{stat} \pm 0.5_{syst}) \times 10^{-2} \tag{9}$$

$$Im(\eta_{000}) = (-3.4 \pm 1.0_{stat} \pm 1.1_{syst}) \times 10^{-2} \tag{10}$$

with systematic uncertainties summarised in the Table 3. The uncertainty of this preliminary measurement is ten times smaller than the best previously published result by CPLEAR [8]. This allows to improve the CPT conservation test based on Bell-Steinberger unitarity relation which relates the CPT

violating phase δ to CP violating amplitudes in neutral kaon decays. This test was previously limited by the precision of η_{000} and using this new measurement it can be improved by 40% to $Im(\delta) = (-1.2 \pm 3.0) \times 10^{-5}$. This can be converted to $m_{K^0} - m_{\overline{K^0}} = (-1.7 \pm 4.2) \times 10^{-19}$ GeV/c^2 assuming CPT violation only in the $K^0 - \overline{K^0}$ mixing.

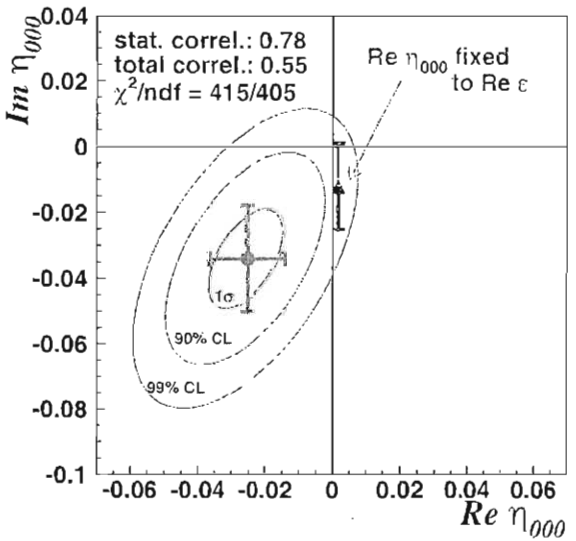

Figure 4: *Preliminary results of the η_{000} fit.*

Assuming CPT conservation and fixing the real part of η_{000} to $Re(\epsilon) = 1.6 \times 10^{-3}$ the imaginary part of η_{000} can be constrained with better precision to

$$Im(\eta_{000}) = (-1.2 \pm 1.3) \times 10^{-2} \tag{11}$$

This corresponds to a limit on $K_S \to \pi^0\pi^0\pi^0$ branching ratio of $BR(K_S \to \pi^0\pi^0\pi^0) < 3.0 \times 10^{-7}$ at 90% CL. This result improves almost by two orders of magnitude the best limit obtained by the SND collaboration [9].

Table 3: *Summary of systematic effects in the η_{000} analysis*

	in 10^{-2}	
	$Re(\eta_{000})$	$Im(\eta_{000})$
Accidentals	± 0.1	$\pm$ 0.6
Energy scale	± 0.1	$\pm$ 0.1
$K^0 - \overline{K^0}$ dilution	± 0.3	$\pm$ 0.4
Acceptance	± 0.3	$\pm$ 0.8
Binning	± 0.1	$\pm$ 0.2
Total	± 0.5	$\pm$ 1.1

5 Precise measurement of the decay $K_S \to \gamma\gamma$

The decay $K_S \to \gamma\gamma$ is particular due to a clean and unambiguous calculation of the leading $O(p^4)$ term in the Chiral Perturbation theory χPT [10] which predicts $BR(K_S \to \gamma\gamma) = 2.1 \times 10^{-6}$.

Using data from high intensity near-target run in the year 2000 the branching ratio was determined to [11]

$$BR(K_S \to \gamma\gamma) = (2.78 \pm 0.06_{stat} \pm 0.03_{syst} \pm 0.02_{ext}) \times 10^{-6} \qquad (12)$$

where most of the systematic uncertainties come from background subtraction. The background from $K_S \to \pi^0\pi^0$ decays has been strongly reduced by choosing very short decay region only few meters downstream of the collimator exit. The irreducible background from $K_L \to \gamma\gamma$ decays has been calculated by estimating the K_L flux using $K_L \to \pi^0\pi^0\pi^0$ decays and by measuring

$$\frac{\Gamma(K_L \to \gamma\gamma)}{\Gamma(K_L \to \pi^0\pi^0\pi^0)} = (2.81 \pm 0.01_{stat} \pm 0.02_{syst}) \times 10^{-3} \qquad (13)$$

from far-target beam data taken also in the year 2000.

The measured $K_S \to \gamma\gamma$ branching ratio exceeds by 30% the χPT prediction and indicates a significant higher loop correction to the leading term.

6 First observation of the $K_S \to \pi^0\gamma\gamma$

The decay $K_S \to \pi^0\gamma\gamma$ proceeds through pseudo-scalar meson pole and has been studied in the framework of χPT [12]. These calculations predict $BR(K_S \to \pi^0\gamma\gamma)_{z>0.2} = 3.8 \times 10^{-8}$ with a cut off of $z \equiv m^2_{\gamma\gamma}/m^2_K > 0.2$. In addition, χPT predicts a momentum dependence of the weak $K\pi^0\pi^0$ vertex reflected in the shape of the z spectrum. The best experimental limit was recently given by NA48 [13] with a $BR(K_S \to \pi^0\gamma\gamma)_{z>0.2} < 3.3 \times 10^{-7}$.

From high intensity near-target data taken in the year 2000, 31 $K_S \to \pi^0\gamma\gamma$ candidate events have been extracted. Background from the beam pile-up has been reduced by using veto counters surrounding the detector and by imposing tight time constraints on the showers detected in the electro-magnetic calorimeter. The remaining pile-up background was estimated using out-of-time events. The background from $K_S \to \pi^0\pi^0$ decays including those with $\pi^0 \to ee\gamma$ decay have been suppressed using kinematic cuts. The background from $\Xi^0 \to \Lambda\pi^0 \to n\pi^0\pi^0$ decay was suppressed by rejecting events with large energy asymmetries. The small irreducible $K_L \to \pi^0\gamma\gamma$ background was estimated using Monte Carlo and assuming equal K_S and K_L production at the target. The summary of remaining backgrounds and systematic uncertainties is given in Table 4. Fig. 5 shows the distribution of the invariant mass m_{12} reconstructed from the $\gamma\gamma$ pair associated with the π^0 compared to the expected background contributions.

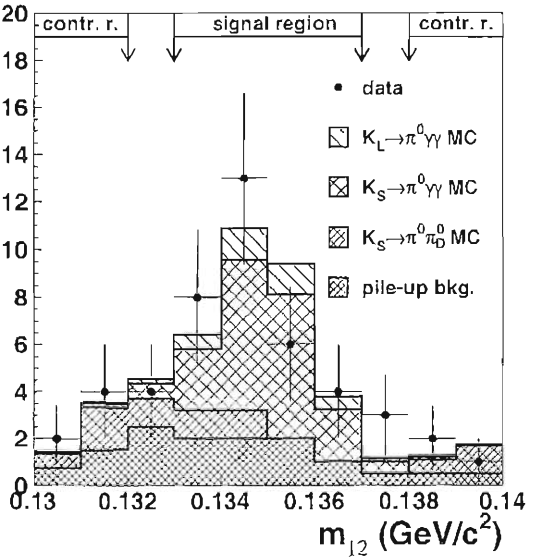

Figure 5: *The distribution of invariant mass of the photon pair assigned to the π^0. The data in the control region is compatible with background while the signal region contains conspicuous excess compatible with the $K_S \to \pi^0\gamma\gamma$ signal.*

After background subtraction 17.4 ± 6.2 events remain in the sample. This

Table 4: *Summary of systematic effects in the* $K_S \to \pi^0\gamma\gamma$ *analysis*

	events		
Number of events in sig. region	31.0	±	5.6
Beam activity	-7.4	±	2.4
$K_S \to \pi^0\pi^0_D$ background	-2.4	±	1.2
$K_L \to \pi^0\gamma\gamma$	-3.8	±	0.0
Acceptance		±	0.7
Remaining	17.4	±	6.2

leads to a preliminary measurement of the branching ratio

$$BR(K_S \to \pi^0\gamma\gamma)_{z>0.2} = (4.9 \pm 1.6_{stat} \pm 0.8_{syst}) \times 10^{-8} \qquad (14)$$

which is in a good agreement with the theoretical prediction.

References

1. N. Doble *et al.*, Nucl. Instr. Meth. B **119** (1996) 181.
2. D. Bedèrède *et al.*, Nucl. Instr. Meth. A **367** (1995) 88.
3. G. Unal for NA48 collaboration, 9th International Conference on Calorimetry in HEP, in: Frascati Physics Series, Vol. **21** (2001) 361.
4. A. Lai et al., Eur. Phys. J. C **22** (2001) 231.
5. R. Batley et al., Phys. Lett. B **544** (2002) 97.
6. A. Alavi-Harati et al., Phys. Rev. Lett. **88** (2002) 181601.
7. G. Barr et al., Phys. Lett. B **317** (1993) 233.
8. A. Angelopoulos et al., Phys. Lett. B **425** (1998) 391.
9. M.N. Achasov et al., Phys. Lett. B **459** (1999) 674.

10. G. D'Ambrosio and D. Espriu, Phys. Lett. B **175** (1986) 237.
J.L. Goity, Z. Phys. C **34** (1987) 341.

11. A. Lai et al., Phys. Lett. B **551** (2003) 7.

12. G. Ecker, A. Pich and E. de Rafael, Phys. Lett. B **189** (1987) 363.

13. R. Batley et al., Phys. Lett. B **556** (2003) 105.

SMI - PHENOMENOLOGICAL APPROACH TO THE ESTIMATE OF CP–EFFECTS IN K± → 3π DECAYS

Evgeny Shabalin [1]
Institute for Theoretical and Experimental Physics, Moscow, Russia

Abstract

The amplitudes of the $K^{\pm} \to 3\pi$ and $K \to 2\pi$ decays are expressed in terms of different combinations of one and the same set of CP-conserving and CP-odd parameters. Extracting the magnitudes of these parameters from the data on $K \to 2\pi$ dacays, we estimate an expected CP-odd difference between the values of the slope parameters g^+ and g^- of the energy distributions of "odd" pions in $K^+ \to \pi^+\pi^+\pi^-$ and $K^- \to \pi^-\pi^-\pi^+$ decays.

1 Introduction

The observation of CP effects in $K^{\pm} \to 3\pi$ decays would allow to understand better how the mechanisms of CP violation work.

Now the Collaboration NA48/2 is ready to begin a search for such effect with accuracy $\delta(\frac{g^+ - g^-}{g^+ + g^-}) \leq 2 \cdot 10^{-4}$.

Contrary to the case of $K_L \to 2\pi$ decay where CP violates both in $\Delta S = 2$ and $\Delta S = 1$ transitions, in the $K^{\pm} \to 3\pi$ decays, only the last (so-called "direct") CP violation takes place. Experimentally, an existance of the direct CP violation in $K_L \to 2\pi$ decays, predicted by Standard Model (SM) and characterised by the parameter ε' is establised: $\varepsilon'/\varepsilon = (1.65 \pm 0.16)10^{-3}$. But the large uncertainties in the theoretical predictions

$$\frac{\varepsilon'}{\varepsilon} = (17^{+14}_{-10})10^{-4} \quad [1], \qquad \frac{\varepsilon'}{\varepsilon} = (1.5 - 31.6)10^{-4} \quad [2]$$

do not allow to affirm that the contributions from the sources of CP violation beyond the Kobayashi-Maskawa phase are excluded.

To avoid the uncertainties in the theoretical calculation of the ingredients of the theory, we use the following procedure. We express the amplitudes of $K_L \to 2\pi$ and $K^{\pm} \to 3\pi$ in terms of one and the same set of parameters, and calculating $g^+ - g^-$ we use the magnitudes of these parameters extracted from data on $K \to 2\pi$ decays.

2 The scheme of calculation

A theory of $\Delta S = 1$ non-leptonic decays is based on the effective lagrangian [3]

$$L(\Delta S = 1) = \sqrt{2} G_F \sin\theta_C \cos\theta_C \sum c_i O_i \tag{1}$$

where

$$O_1 = \bar{s}_L \gamma_\mu d_L \cdot \bar{u}_L \gamma_\mu u_L - \bar{s}_L \gamma_\mu u_L \cdot \bar{u}_L \gamma_\mu d_L \qquad (\{8_f\}, \Delta I = 1/2) \tag{2}$$

$$O_2 = \bar{s}_L \gamma_\mu d_L \cdot \bar{u}_L \gamma_\mu u_L + \bar{s}_L \gamma_\mu u_L \cdot \bar{u}_L \gamma_\mu d_L + 2\bar{s}_L \gamma_\mu d_L \cdot \bar{d}_L \gamma_\mu d_L + 2\bar{s}_L \gamma_\mu d_L \cdot \bar{s}_L \gamma_\mu s_L \qquad (\{8_d\}, \Delta I = 1/2) \tag{3}$$

$$O_3 = \bar{s}_L \gamma_\mu d_L \cdot \bar{u} \gamma_\mu u_L + \bar{s} \gamma_\mu u_L \cdot \bar{u} \gamma_\mu d_L + 2\bar{s}_L \gamma \mu d_L \cdot \bar{d}_L \gamma_\mu d_L - 3\bar{s}_L \gamma_\mu d_L \cdot \bar{s}_L \gamma_\mu s_L \qquad (\{27\}, \Delta I = 1/2) \tag{4}$$

$$O_4 = \bar{s}_L\gamma_\mu d_L \cdot \bar{u}\gamma_\mu u_L + \bar{s}_L\gamma_\mu u_L \cdot \bar{u}_L\gamma_\mu d_L - \\ - \bar{s}_L\gamma_\mu d_L \cdot \bar{d}_L\gamma_\mu d_L \qquad (\{27\}, \Delta I = 3/2) \tag{5}$$

$$O_5 = \bar{s}_L\gamma_\mu\lambda^a d_L(\sum_{q=u,d,s}\bar{q}_R\gamma_\mu\lambda^a q_R) \qquad (\{8\}, \Delta I = 1/2) \tag{6}$$

$$O_6 = \bar{s}_L\gamma_\mu d_L(\sum_{q=u,d,s}\bar{q}_R\gamma_\mu q_R) \qquad (\{8\}, \Delta I = 1/2) \tag{7}$$

This set is sufficient for calculation of the CP-even parts of the amplitudes under consideration. To calculate the CP-odd parts , it is necessary to add the so-called electroweak contributions originated by the operators O_7, O_8:

$$O_7 = \frac{3}{2}\bar{s}\gamma_\mu(1+\gamma_5)d \cdot (\sum_{q=u,d,s}e_q\bar{q}\gamma_\mu(1-\gamma_5)q) \qquad (\Delta I = 1/2, 3/2) \tag{8}$$

$$O_8 = -12\sum_{q=u,d,s}e_q(\bar{s}_L q_R)(\bar{q}_R d_L), \quad e_q = (\frac{2}{3}, -\frac{1}{3}, -\frac{1}{3}), \quad (\Delta I = 1/2, 3/2) \tag{9}$$

The coefficients c_{5-8} have the imaginary parts necessary for CP violation.

The bosonization of these operators can be done using the relations [4]

$$\bar{q}_j(1+\gamma_5)q_k = -\frac{1}{\sqrt{2}}F_\pi r\left(U - \frac{1}{\Lambda^2}\partial^2 U\right)_{kj} \tag{10}$$

$$\bar{q}_j\gamma_\mu(1+\gamma_5)q_k = i[(\partial_\mu U)U^\dagger - U\left(\partial_\mu U^\dagger\right) - \frac{rF_\pi}{\sqrt{2}\Lambda^2}\left(m(\partial_\mu U^\dagger) - (\partial_\mu U)m\right)_{kj} \tag{11}$$

if the non-linear realization of chiral symmetry is used:

$$U = \frac{F_\pi}{\sqrt{2}}\left(1 + \frac{i\sqrt{2}\hat{\pi}}{F_\pi} - \frac{\hat{\pi}^2}{F_\pi^2} + a_3\left(\frac{i\hat{\pi}}{\sqrt{2}F_\pi}\right)^3 + 2(a_3-1)\left(\frac{i\hat{\pi}}{\sqrt{2}F_\pi}\right)^4 + ...\right) \tag{12}$$

where

$$\hat{\pi} = \begin{pmatrix} \frac{\pi_0}{\sqrt{3}} + \frac{\pi_8}{\sqrt{6}} + \frac{\pi_3}{\sqrt{2}} & \pi^+ & K^+ \\ \pi^- & \frac{\pi_0}{\sqrt{3}} + \frac{\pi_8}{\sqrt{6}} - \frac{\pi_3}{\sqrt{2}} & K^0 \\ K^- & \bar{K}^0 & \frac{\pi_0}{\sqrt{3}} - \frac{2\pi_8}{\sqrt{6}} \end{pmatrix} \tag{13}$$

The PCAC condition demands $a_3 = 0$ [5] and we adopt this condition, bearing in mind that, on mass shell, the values of the mesonic amplitudes are independent of a_3.

Using also the relations between matrices in the colour space

$$\delta^\alpha_\beta \delta^\gamma_\delta = \tfrac{1}{3}\delta^\alpha_\delta \delta^\gamma_\beta + \tfrac{1}{2}\lambda^\alpha_\delta \lambda^\gamma_\beta$$
$$\lambda^\alpha_\beta \lambda^\gamma_\delta = \tfrac{16}{9}\delta^\alpha_\beta \delta^\gamma_\beta - \tfrac{1}{3}\lambda^\alpha_\delta \lambda^\gamma_\beta$$

and the Fierz transformation relation

$$\bar{s}\gamma_\mu(1+\gamma_5)d \cdot \bar{q}\gamma_\mu(1-\gamma_5)q = -2\bar{s}(1-\gamma_5)q \cdot \bar{q}(1+\gamma_5)d$$

and representing $M(K \to 2\pi)$ in the form

$$M(K_1^0 \to \pi^+\pi^-) = A_0 e^{i\delta_0} - A_2 e^{i\delta_2} \tag{14}$$
$$M(K_1^0 \to \pi^0\pi^0) = A_0 e^{i\delta_0} + 2A_2 e^{i\delta_2} \tag{15}$$
$$M(K^+ \to \pi^+\pi^0) = -\frac{3}{2} A_2 e^{i\delta_2} \tag{16}$$

we obtain

$$A_0 = G_F F_\pi \sin\theta_C \cos\theta_C \frac{m_K^2 - m_\pi^2}{\sqrt{2}} \cdot [c_1 - c_2 - c_3 + \frac{32}{9}\beta(Re\tilde{c}_5 + iIm\tilde{c}_5)] \tag{17}$$

$$A_2 = G_F F_\pi \sin\theta_C \cos\theta_C \frac{m_K^2 - m_\pi^2}{\sqrt{2}} \cdot [c_4 + i\frac{2}{3}\beta\Lambda^2 Im\tilde{c}_7 (m_K^2 - m_\pi^2)^{-1}] \tag{18}$$

where

$$\tilde{c}_5 = c_5 + \frac{3}{16}c_6; \quad \tilde{c}_7 = c_7 + 3c_8; \quad \beta = \frac{2m_\pi^4}{\Lambda^2(m_u + m_d)^2}.$$

The contributions from $\tilde{c}_7 O_7$ into $Re A_0$ and $Im A_0$ are small because $\tilde{c}_7/\tilde{c}_5 \sim \alpha_{em}$ and we neglected these corrections. From data on widths of $K \to 2\pi$ decays we obtain

$$c_4 = 0.328; \quad c_1 - c_2 - c_3 + \frac{32}{9}\beta Re\tilde{c}_5 = -10.13. \tag{19}$$

At $c_1 - c_2 - c_3 = -2.89$ [3], [6] and $\beta = 6.68$ we obtain

$$\tilde{c}_5 = -0.305. \tag{20}$$

From the expression for A_2, it is seen that the contribution of the operators $O_{7,8}$ is enlarged by the factor Λ^2/m_K^2 in comparison with the rest operators contribution.

Using the general relation

$$\varepsilon' = ie^{i(\delta_2-\delta_0)}\left[-\frac{ImA_0}{ReA_0}+\frac{ImA_2}{ReA_2}\right]\cdot|\frac{A_2}{A_0}| \tag{21}$$

and the experimental value $\varepsilon' = (3.4 \pm 0.45)10^{-6}$ we come to the relation

$$-\frac{Im\tilde{c}_5}{Re\tilde{c}_5}\left(1-\Omega_{\eta,\eta'}+20.66\frac{Im\tilde{c}_7}{Im\tilde{c}_5}\right) = 1.48\cdot 10^{-4}. \tag{22}$$

where $\Omega_{\eta,\eta'}$ takes into account the effects of $K^0 \to \pi^0\eta(\eta') \to \pi^0\pi^0$ transitions.

The naive estimate gives

$$-\frac{Im\tilde{c}_5}{Re\tilde{c}_5} \approx 1.7 s_2 s_3 \sin\delta \tag{23}$$

where s_2, s_3 and δ are the parameters of CKM matrix. At

$$4.6\cdot 10^{-4} \le s_2 s_3 \le 6.7\cdot 10^{-4} \qquad \text{(Landsberg'2002)}$$

$$\frac{Im\tilde{c}_5}{Re\tilde{c}_5} = (-9.6 \div -1.8)10^{-4}\sin\delta \tag{24}$$

and

$$\frac{Im\tilde{c}_7}{Im\tilde{c}_5} = \begin{cases} -0.026 & \text{for} \quad \Omega_{\eta,\eta'} = 0.3 \\ -0.041 & \text{for} \quad \Omega_{\eta,\eta'} = 0 \end{cases} \tag{25}$$

3 Decay $K^\pm \to \pi^\pm\pi^\pm\pi^\mp$

In the leading p^2 approximation

$$M(K^+ \to \pi^+(p_1)\pi^+(p_2)\pi^-(p_3)) = k[1+ia_{KM}+\frac{1}{2}gY(1+ib_{KM})+....], \tag{26}$$

where

$$k = G_F \sin\theta_C \cos\theta_C m_K^2 c_0 (3\sqrt{2})^{-1} \tag{27}$$

$$a_{KM} = \left[\frac{32}{9}\beta Im\tilde{c}_5 + 4\beta Im\tilde{c}_7\left(\frac{3\Lambda^2}{2m_K^2}+2\right)\right]/c_0 \tag{28}$$

$$b_{KM} = \left[\frac{32}{9}\beta Im\tilde{c}_5 + 8\beta Im\tilde{c}_7\right]/(c_0+9c_4) \tag{29}$$

$$g = -\frac{3m_\pi^2}{2m_K^2}(1 + 9c_4/c_0); \qquad Y = (s_3 - s_0)/m_\pi^2 \tag{30}$$

$$c_0 = c_1 - c_2 - c_3 - c_4 + \frac{32}{9}\beta Re\tilde{c}_5 = -10.46 \tag{31}$$

As the field K^+ is the complex one and its phase is arbitrary, we can replace K^+ by $K^+(1 + ia_{KM})(\sqrt{1 + a_{KM}^2})^{-1}$. Then

$$M(K^+ \to \pi^+\pi^+\pi^-(p_3)) = k[1 + \frac{1}{2}gY(1 + i(b_{KM} - a_{KM})) + ...] \tag{32}$$

Though this expression contains the imaginary CP-odd part, it does not lead to observable CP effects. Such effects arise due to interference between CP-odd imaginary part with the CP-even imaginary part produced by rescattering of the final pions. Then

$$M(K^+ \to \pi^+\pi^+\pi^-) = k[1 + ia + \frac{1}{2}gY(1 + ib + i(b_{KM} - a_{KM}) + ...] \tag{33}$$

where a and b are corresponding CP-even imaginary parts of the amplitude. These parts can be estimated (in p^2) approximation calculating the imaginary part of the two-pion loop diagrams with

$$M(\pi^+(r_2)\pi^-(r_3) \to \pi^+(p_2)\pi^-(p_3)) = F_\pi^{-2}[(p_2 + p_3)^2 + (r_2 - p_2)^2 - 2m_\pi^2]$$
$$M(\pi^0(r_2)\pi^0(r_3) \to \pi^+(p_2)\pi^-(p_3)) = F_\pi^{-2}[(p_2 + p_3)^2 - m_\pi^2]$$
$$M(\pi^+(r_1)\pi^+(r_2) \to \pi^+(p_1)\pi^+(p_2)) = F_\pi^{-2}[(r_1 - p_1)^2 + (r_1 - p_2)^2 - 2m_\pi^2]$$

Then we find:

$$a = 0.12065; \qquad b = 0.714 \tag{34}$$

Using the definition of the slope paramater

$$|M(K^\pm \to \pi^\pm\pi^\pm\pi^\mp(p_3))|^2 \sim 1 + \frac{g}{1 + a^2}Y\,(1 + ab \pm a(b_{KM} - a_{KM})) + ... \tag{35}$$

we find

$$R_g \equiv \frac{g^+ - g^-}{g^+ + g^-} = \frac{a(b_{KM} - a_{KM})}{1 + ab} \tag{36}$$

At the fixed above numerical values of the parameters we obtain

$$(R_g)_{p^2} = 0.030\frac{Im\tilde{c}_5}{Re\tilde{c}_5}(1 - 14.9\frac{Im\tilde{c}_7}{Im\tilde{c}_5}) = -(4 \pm 0.75) \cdot 10^{-5}\sin\delta \tag{37}$$

This numerical result is obtained for $\Omega_{\eta,\eta'} = 0.3$. For zero magnitude of this parameter, a value would be $(-4.6 \pm 0.86)10^{-5}$.

4 The role of p^4 and other corrections

The corrections to the result obtained in the conventional chiral theory up to leading p^2 approximation are of two kinds. The first kind corrections are connected with a necessity to take into account the observed enlargement of S-wave $I = 0$ $\pi\pi$ amplitude having no explanation in conventional chiral theory. The corrections of the second kind are the p^4 corrections. As it was argued in [7], [8] both kinds corrections can be properly estimated in the framework of special linear $U(3)_L \otimes U(3)_R$ σ model with broken chiral symmetry. The above mentioned enlargement of S wave in this model is originated by mixing between the $\bar{q}q$ and $(G^a_{\mu\nu})^2$ states. In such a model

$$U = \hat{\sigma} + i\hat{\pi}$$

where $\hat{\sigma}$ is 3×3 matrix of scalar partners of the mesons of pseudoscalar nonet. The relations between diquark combinations and spinless fields are as given by eqs.(10) ,(11), but without the terms proportional to Λ^{-2}. Such contributions in σ model appear from an expansion of the intermediate scalar mesons propagators. The parameter Λ^2 acquires a sence of difference $m^2_{a_0(980)} - m^2_\pi$. The strength of mixing between the isosinglet σ meson and corresponding gluonic state is characterised by the parameter ξ.

If the p^2 approximation gives

$$(k)_{p^2} = 1.495 \cdot 10^{-4}, \qquad (g)_{p^2} = -0.172 \tag{38}$$

instead of

$$(k)_{exp} = 1.72 \cdot 10^{-4}, \qquad (g)_{exp} = -0.2154 \pm 0.0035, \tag{39}$$

the corrected values of these CP-even parameters of $K^+ \to \pi^+\pi^+\pi-$ amplitude practically coincide with the experimental ones [7]:

$$(k)_{(p^2+p^4;\ \xi=-0.225)} = 1.72 \cdot 10^{-4}, \qquad (g)_{(p^2+p^4;\ \xi=-0.225)} = -0.21. \tag{40}$$

The meaning of the parameter ξ is explained in [7],[8]. The expressions for the corrected $\pi\pi \to \pi\pi$ amplitudes are presented in [8].

Calculating the CP-even imaginary part of the $K^\pm \to \pi^\pm\pi^\pm\pi^\mp$ amplitude originated by two-pion intermediate states, we obtain

$$a(p^2 + p^4;\ \xi = -0.225) = 0.16265 \tag{41}$$

$$b(p^2+p^4;\ \xi=-0.225)=0.762 \tag{42}$$

An estimate of the parameter a can be obtained also without any calculations using the circumstance that at $\sqrt{s}=\sqrt{s_0}$, the only significant phase shift is δ_0^0. The rest phase shifts are very small: $|\delta_0^2(s_0)|<1.8^\circ$ and $\delta_1^1(s_0)<0.3^\circ$ [9]. Then, according to eq.(33), $a\approx\tan\delta_0^0(s_0)$, or $a=0.13\pm0.05$, if $\delta_0^0(s_0)=(7.50\pm2.85)^\circ$ [10] and $a=0.148\pm0.018$, if $\delta_0^0(s_0)=(8.4\pm1.0)^\circ$ [11]. These results coincide inside the error bars with the result (41). The corrected magnitude of R_g is

$$(R_g)_{(p^2+p^4;\ \xi=-0.225)}=0.039\frac{Im\tilde{c}_5}{Re\tilde{c}_5}\left(1-11.95\frac{Im\tilde{c}_7}{Im\tilde{c}_5}\right)\sin\delta=-(4.9\pm0.9)10^{-5}\sin\delta. \tag{43}$$

This result is by 22% larger in absolute magnitude than that calculated in the leading approximation. Therefore, we come to conclusion that the corrections to the result obtained in the framework of conventional chiral theory to the leading approximation are not negligible (20-30 %), but not so large, as it was declared in [12].

5 Conclusion

If the arguments against the correctness of eq.(23) will not be found, an expected value of R_g in the Standard Model is not larger in absolute magnitude than $6\cdot10^{-5}\sin\delta$.

References

[1] Bertolini S et al., *Nucl.Phys.B* **514** 93 (1998)

[2] Hambye T et al., *Nucl.Phys.B* **564** 391 (2000)

[3] Shifman M A, Vainshtein A I, Zakharov V I, *Zh.Eksp.i Teor.Fiz. (JETP)* **72** 1277 (1977)

[4] Bardeen W A, Buras A J, Gerard J-M, *Nucl.Phys.B* **293** 787 (1987)

[5] Cronin J, *Phys.Rev.* **161** 1483 (1967)

[6] Okun L B, *Leptons and Quarks* (North-Holland Publ.Co. 1982) pp.315,323

[7] Shabalin E P, *Nucl. Phys. B* **409** 87 (1993)

[8] Shabalin E P, *Physics of Atomic Nuclei* **61** 1372 (1998)

[9] Shabalin E P, *Physics of Atomic Nuclei* **63** 594 (2000)

[10] Rosselet L et al., *Phys. Rev. D* **15** 574 (1977)

[11] Pislak S et al., *Phys. Rev. Lett.* **87** 221801 (2001)

[12] Bel'kov A A et al., *Phys. Lett. B* **283** (1993)

THEORY OF RARE KAON DECAYS

Giancarlo D'Ambrosio
INFN-Sezione di Napoli
I-80126 Napoli, Italy
E-mail: giancarlo.dambrosio@na.infn.it

Abstract

We discuss theoretical issues in rare and radiative kaon decays. We show that $K \to \pi\nu\bar{\nu}$ and $K \to \pi e\bar{e}$ are very useful to extract short-distance information: both to test the Standard Model or to determine accurately the CKM matrix. We emphasize also channels where we can understand non-perturbative aspects of QCD.

1 Introduction

Though the Standard Model (SM) is in very good shape, LHC is getting close and we might have surprises. In fact questions, like a satisfactory solution of the hierarchy, do not have yet a satisfactory answer. Also some very decisive tests of the SM, like the $g-2$ or the amount of direct CP violation in $K_L \to \pi\pi$ are plagued by uncertainties related to our ignorance on hadronic matrix elements. Thus our goal is to show that in rare kaon decays [1, 2, 3, 4] there are: i) *Golden modes*, like $K \to \pi\nu\bar{\nu}$ [5], completely dominated by short distance, where the SM is challenged to a very meaningful level and ii) channels, like $K_L \to \pi^0 e\bar{e}$ where our good knowledge of long distance dynamics allows us to single out quite accurately the interesting short distance dependence [6]. We will study the auxiliary (to $K_L \to \pi^0 e\bar{e}$) channels $K_S \to \gamma\gamma$ and $K_S \to \pi^0 e\bar{e}$. $K_S \to \gamma\gamma$ is completely dominated by long distance [7, 8] but accurately predicted by chiral perturbation theory (ChPT) and thus it is an important test of the theory. $K_S \to \pi^0 e\bar{e}$, as we shall see, is important to extract useful information from $K_L \to \pi^0 e\bar{e}$ and also an important chiral dynamics test .

B-physics will test SM measuring the CKM triangle [1] with sizes $V_{qb}^* V_{qd}$; the area of this triangle, $J_{CP}/2$, is invariant for all CKM triangles and non-zero if CP is violated; in the Wolfenstein parametrization:

$$|J_{CP}| \overset{Wolfenstein}{\simeq} A^2\lambda^6\eta \tag{1}$$

with $V_{us} = \lambda$, $V_{cb} = A\lambda^2$, $\Im m(V_{td}) = -A\lambda^3\eta$. As we shall see, as a consequence of our improved understanding of low energy physics we can test precisely (1) in rare kaon channels [1]. This is particularly exciting since there are several experiments aiming the required accuracy [3].

2 $K \to \pi\nu\bar{\nu}$

The SM predicts the $V-A \otimes V-A$ effective hamiltonian

$$\mathcal{H} = \frac{G_F}{\sqrt{2}} \frac{\alpha}{2\pi \sin^2\theta_W} \Big(\underbrace{V_{cs}^* V_{cd}}_{\lambda} X_{NL} + \underbrace{V_{ts}^* V_{td}}_{A^2\lambda^5\,(1-\rho-i\eta)} X(x_t) \Big) \bar{s}_L \gamma_\mu d_L \; \bar{\nu}_L \gamma^\mu \nu_L$$

$x_q = m_q^2/M_W^2$, θ_W the Weinberg angle and X's are the Inami-Lin functions with Wilson coefficients known at next-to-leading order [5]. $SU(2)$ isospin symmetry relates hadronic matrix elements for $K \to \pi\nu\bar{\nu}$ to $K \to \pi l\bar{\nu}$ to

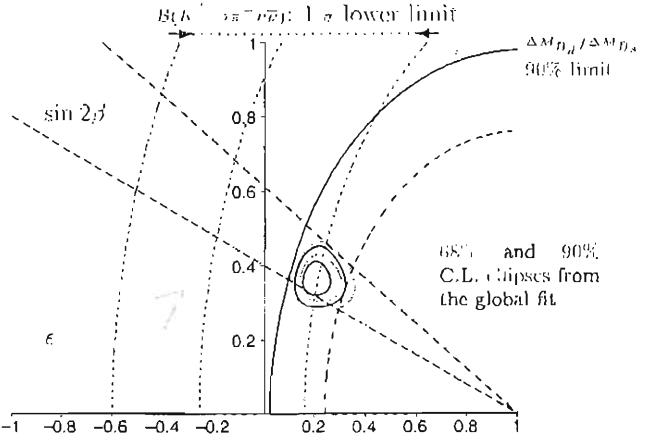

Figure 1: We show in the two ellipses the allowed region in the $\bar{\rho} - \bar{\eta}$ plane by the global fit without imposing the $\mathcal{B}(K^+ \to \pi^+\nu\bar{\nu})$; the dotted curves on the left define the $\mathcal{B}(K^+ \to \pi^+\nu\bar{\nu})$: 1 σ lower bound [16]: the mismatch between the central value implied by $\mathcal{B}(K^+ \to \pi^+\nu\bar{\nu})$ and the ellipses of the global fit can be also interpreted in terms of NP in $\Delta B = 2$ transitions than the effective supersymmetry scenario [20] may be appealing [16], $\tilde{Q}^i$ are the $SU(2)_L$ quark doublets

a very good precision [9]. QCD corrections have been evaluated at next-to-leading order [1] and the main uncertainties is due the strong corrections to the charm loop contribution.

The structure in (2) leads to a pure CP violating contribution to $K_L \to \pi^0\nu\bar{\nu}$, induced only from the top loop contribution and thus proportional to $\Im m(\lambda_t)$ ($\lambda_t = V_{ts}^* V_{td}$) and free of hadronic uncertainties. This leads to the prediction [5]

$$\mathcal{B}B(K_L \to \pi^0\nu\bar{\nu})_{SM} = 4.25 \times 10^{-10} \left[\frac{\bar{m}_t(m_t)}{170GeV}\right]^{2.3} \left[\frac{\Im m(\lambda_t)}{\lambda^5}\right]^2 . \qquad (3)$$

$K^\pm \to \pi^\pm\nu\bar{\nu}$ receives CP conserving and violating contributions proportional to $\Re e(\lambda_c)$, $\Re e(\lambda_t)$ and $\Im m(\lambda_t)$. Theoretical uncertainty from the charm loop induces 5% error on the width. If one takes into account the various indirect limits, i.e. V_{ub} and ε, on CKM elements one obtains the SM values [1, 5, 12]:

$$\mathcal{B}(K_L \to \pi^0\nu\bar{\nu}) = (2.8 \pm 1.0)\times 10^{-11} \quad \mathcal{B}(K^\pm \to \pi^\pm\nu\bar{\nu}) = (0.72 \pm 0.21)\times 10^{-10} \qquad (4)$$

Two events have been observed by E787 [13] leading to

$$\mathcal{B}(K^\pm \to \pi^\pm\nu\bar{\nu}) = \left(1.57^{+1.75}_{-0.82}\right) \times 10^{-10} \qquad \text{E787} \qquad (5)$$

The existing upper bound exists for the neutral decay: $B(K_L \to \pi^0\nu\bar{\nu}) \leq 5.9 \times 10^{-7}$ [14], can be improved: the isospin structure of any $\bar{s}d$ operator (bilinear in the quark fields) leads to the model independent relation [15] and to an interesting bound with E787 [13]

$$\mathcal{B}(K_L \to \pi^0\nu\bar{\nu}) < \frac{\tau_{K_L}}{\tau_{K^+}} B(K^+ \to \pi^+\nu\bar{\nu}) \underset{E787}{<} 1.7 \cdot 10^{-9} \quad \text{at} \quad 90\% C.L.$$

Future measurements: i) K^+, BNL (E787 and E949) should improve the present result, while CKM at Fermilab should measure the branching with a 10% accuracy, ii) K_L, KOPIO at BNL and KEK are aiming to measure this channel [3].

One can speculate that the central value in (5) is overshooting the SM prediction in (4) [16] and NP is required. Referring to the original reference (and [17]) for a detailed discussion, we show in Fig.(1) the $K^+ \to \pi^+\nu\bar{\nu}$ preferred values $\bar{\rho}-\bar{\eta}$ versus the values allowed by $\sin(2\beta)$, ϵ and $\Delta M_{B_d}/\Delta M_{B_s}$. The relevance of $K \to \pi\nu\bar{\nu}$ is shown by this consideration: we can reconciliate the central value $\mathcal{B}(K^+ \to \pi^+\nu\bar{\nu})$ (see Fig. 1) with the SM prediction in (4) adding NP in $\Delta B = 2$. This possibility seems also motivated by other B-observables, like $B \to \pi K$ [18]. However it is not harmless to add FCNC. Let's look the SM Yukawa structure

$$\mathcal{L}^Y_{SM} = \bar{Q}Y_D DH + \bar{Q}Y_U UH_c + \bar{L}Y_E EH + \text{h.c.} \tag{6}$$

where Q, U, D (L, E) are respectively the quark (lepton) doublets and singlets. Diagonalization of the quark matrices lead to the CKM unitary matrix, V_{ij} and GIM mechanism for FCNC writing. Approximately (neglecting strong correction)

$$\mathcal{H}^{SM}_{\Delta F=2} \sim \frac{G_F^2 M_W^2}{16\pi^2}\left[\frac{(V^*_{ld}m_l^2 V_{lb})^2}{v^4}(\bar{d}_L\gamma^\mu b_L)^2 + \frac{(V^*_{ld}m_l^2 V_{ls})^2}{v^4}(\bar{d}_L\gamma^\mu s_L)^2\right] + \text{c, u} \tag{7}$$

In supersymmetry new flavour structures are generated by the soft mass terms:

$$\mathcal{L}_{soft} = \tilde{Q}^\dagger m_Q^2 \tilde{Q} + \tilde{L}^\dagger m_L^2 \tilde{L} + \tilde{\bar{U}} a_u \tilde{Q} H_u + \cdots \tag{8}$$

The diagonalization of these contributions add new flavour matrices to the CKM V in (7). For instance assuming the dominance of the LL gluino-sdown box diagrams [19]

$$\mathcal{H}^{\tilde{g}}_{\Delta F=2} \sim \frac{\alpha_s^2}{9M^2_{\tilde{Q}}}\left[(\delta^{LL}_{12})^2\ (\bar{s}_L\gamma_\mu d_L)^2 + \cdots\right] \qquad K-\bar{K} \Longrightarrow \quad \frac{(\delta^{LL}_{12})^2}{M^2_{\tilde{Q}}} \leq \frac{1}{(100\text{TeV})^2} \tag{9}$$

where δ_{12}^{LL} measures the departure from the identity matrix of m_Q^2 in (8) and M_Q is an average value for m_Q^2 [19]. This shows the *supersymmetric flavour problem*, i.e. the difficulties to solve *simultaneously* the hierarchy problem ($m_{soft} \leq 1$ TeV) and NO FCNC.

There are two scenarios that can justify the lack of FCNC in eq. (9): *effective supersymmetry* [20] and *Minimal Flavour violation* (MFV) [21]. *Effective supersymmetry* still keep naturalness by allowing only the third family of squarks to be below 1 TeV, then NP is expected in $\Delta B = 2$-transitions (due to δ_{13}^{LL}), while the first two families of squarks are decoupled, i.e. heavier than 5 TeV and $\delta_{12}^{LL} \sim 0$. This would be very exciting and a lot of phenomenolgy could be accessible in the near future [16, 18].

However there is no obvious reason why the three families are so much different so that and we have pursued also a a different strategy to have New Physics at the TeV scale but no FCNC: NP must obey some flavour symmetry (MFV) so that GIM mechanism it is still at work for the the three families. In supersymmetry, for instance, this global symmetry would strongly constrain the flavor matrices in (8), so that (9) turns in [22, 21]:

$$\mathcal{L}_{\Delta F=2} = \frac{C}{\Lambda^2_{MFV}}\left[\frac{(V_{id}^* m_i^2 V_{ib})^2}{v^4}(\bar{d}_L\gamma^\mu b_L)^2 + \frac{(V_{id}^* m_i^2 V_{is})^2}{v^4}(\bar{d}_L\gamma^\mu s_L)^2\right] \qquad (10)$$

Fixing $C \sim 1 \Longrightarrow$ a very strong bound on Λ^2_{MFV}. The flavour symmetry can be invoked in several contests. In fact it was originally introduced in Technicolour [23] to be protected from FCNC: the underlying preonic dynamics, generating the vev's for the gauge and fermionic masses should preserve the global symmetry G_F broken only by some spurions

$$G_F = \overbrace{\mathrm{U}(3)_Q \otimes \mathrm{U}(3)_U \otimes \mathrm{U}(3)_D \otimes \mathrm{U}(3)_L \otimes \mathrm{U}(3)_E}^{\text{global symmetry}} + \overbrace{Y_{U,D,E}}^{\text{spurions}} \qquad (11)$$

and spurion quantum numbers determined by (6). This symmetry generates the $\mathcal{L}_{\Delta F=2}$ in (10). In order to solve the flavour problem this symmetry has been invoked also in supersymmetry, gauge mediation [24] and large extra dimensions [25]. We have determined the general dim-6 lagrangian consistent with the symmetry in (11) in terms of some unknown coefficients c_n

$$\mathcal{L}_{MFV}(Q,U,D,L,E,H) = \mathcal{L}_{\Delta F=2} + \mathcal{L}_{\Delta F=1} = \frac{1}{\Lambda^2}\sum_n c_n \mathcal{O}_n \; + \; \text{h.c.} \qquad (12)$$

Several results have been obtained from this analysis: i) putting $c_n \sim 1$ we can obtain strong constraints on Λ from different processes, i.e. ϵ_K, $\Delta m_{B_d} \Longrightarrow$

$\Lambda > 5\text{TeV}$ [26, 21] and $B \to X_s\gamma \Longrightarrow \Lambda > 8\text{TeV}$ [26, 21], ii) interesting new correlations among B and K-physics, for instance $\mathcal{B}(K_L \to \mu\bar{\mu}) \Longleftrightarrow \mathcal{B}(B \to Kl^+l^-)$, etc. to be tested in the very near future with the B- and K-factories and iii) if the CKM matrix elements are known with 5% accuracy, a measurement at some percent level of $\mathcal{B}(K_L \to \pi^0\nu\bar{\nu})$ has the chance to be the deepest probe of the SM; in fact Λ_{MFV} can be pushed to 12TeV [21]. Still in the MFV framework but with two Higgses, i.e. in the case in which both Higgses are pretty light, we have obtained all $\tan\beta$-enhanced Higgs-mediated FCNC contributions. Particularly relevant are their effects in $B \to \ell^+\ell^-$, ΔM_B and $B \to X_s\gamma$ [21].

3 Chiral Perturbation Theory and $K_S \to \gamma\gamma$

QCD is non-perturbative at energy scales below 1 GeV and thus symmetry arguments must be invoked in order to be predictive. QCD for massless quarks exhibits the global symmetry $SU(3)_L \otimes SU(3)_R$ and there are strong phenomenological arguments (Goldberger-Treiman relation, ...) that the pion is the Goldstone boson of the broken symmetry $SU(3)_L \otimes SU(3)_R \to SU(3)_V$. Thus χPT [27, 4, 2, 28] is an effective field theory based on the following two assumptions: i) the pseudoscalar mesons are the Goldstone bosons (G.B.) of the symmetry above, ii) there is a *(chiral) power counting* , i.e. the theory has a small expansion parameter: $p^2/\Lambda^2_{\chi SB}$ and/or $m^2/\Lambda^2_{\chi SB}$, where p is the external momenta, m the masses of the G.B.'s and $\Lambda_{\chi SB}$ is the chiral symmetry breaking scale: $\Lambda_{\chi SB} \sim 4\pi F_\pi \sim 1.2$ GeV. Being an effective field theory, loops and counterterms are required by unitarity and have to be evaluated order by order [27, 2, 28]. It turns out more practical to descibe the chiral fields through a non-linear realization, $U = e^{i\sqrt{2}\Phi/F}$ and $\Phi = \sum_i \lambda_i\phi^i$, λ_i are the Gell-Mann matrices, $F \sim F_\pi$. We can split the lagrangian in a strong ($\Delta S = 0$) and in a weak non-leptonic piece ($\Delta S = 1$): $\mathcal{L} = \mathcal{L}_{\Delta S=0} + \mathcal{L}_{\Delta S=1}$, and then consider the chiral expansion

$$\mathcal{L}_{\Delta S=0} = \mathcal{L}^2_{\Delta S=0} + \mathcal{L}^4_{\Delta S=0} + \cdots = \frac{F^2}{4}\underbrace{\langle D_\mu U D^\mu U^\dagger + \chi U^\dagger + U\chi^\dagger\rangle}_{\pi\to l\nu,\ \pi\pi\to\pi\pi} + \sum_i L_i O_i + \cdots \tag{13}$$

$$\mathcal{L}_{\Delta S=1} = \mathcal{L}^2_{\Delta S=1} + \mathcal{L}^4_{\Delta S=1} + \cdots = G_8 F^4 \underbrace{\langle \lambda_6 D_\mu U^\dagger D^\mu U\rangle}_{K\to 2\pi/3\pi} + \underbrace{G_8 F^2 \sum_i N_i W_i}_{K^+\to\pi^+\gamma\gamma,\ K\to\pi\pi\gamma} + \cdots, \tag{14}$$

where χ is the appropriate $SU(3)$-spurion that generate the G.B. masses and the second terms in (13) and (14) represent respectively the strong $\mathcal{O}(p^4)$

(Gasser-Leutwyler [27]) and the weak $\mathcal{O}(p^4)$ [29] lagrangian. One of the most fantastic χPT predictions is the $\pi\pi$-scattering lenghts [27, 4, 28] in terms only of the pion decay constant, F_π: the $\mathcal{O}(p^2)$ result is phenomenologically correct up to 30% corrections [31].

$K_S \to \gamma\gamma$ has vanishing short-distance contributions and thus it is a pure long-distance phenomenon; since the external particles are neutral there is no $\mathcal{O}(p^2)$ amplitude. For the same reason, if we write down the $\mathcal{O}(p^4)$ counterterm structure, $F_{\mu\nu}F^{\mu\nu}\langle\lambda_6 QU^+QU\rangle$, this gives a vanishing contribution. This implies that at $\mathcal{O}(p^4)$: i) we have only a loop contribution in Fig. 2 and ii) this contribution is scale-independent [7]:

$$A(K_S \to \gamma\gamma) = \frac{2\alpha F}{\pi M_K^2}(G_8 + \frac{2}{3}G_{27})\,(M_K^2 - M_\pi^2)\cdot\left(1 + \frac{M_K^2}{M_\pi^2}\ln^2\frac{\beta-1}{1+\beta}\right)\cdot$$
$$\left[(q_1\epsilon_2)(q_2\epsilon_1) - (\epsilon_1\epsilon_2)(q_1q_2)\right], \qquad \beta = \sqrt{1 - 4M_\pi^2/M_K^2} \qquad (15)$$

where G_8, defined in (14) and G_{27}, the coefficient of $\Delta I = 3/2$-transitions are completely predicted by the $K \to \pi\pi$ amplitudes. This is the *ideal* test of χPT (and in general of effective field theories) at the *quantum level*. At higher order, $\mathcal{O}(p^6)$, π-loop corrections are small [32], while contributions to $A^{(6)}$ from $\mathcal{L}^6_{\Delta S=1}$, are chirally suppressed:

$$\mathcal{L}^6_{\Delta S=1} \supset \frac{c}{(4\pi F_\pi)^2}F^{\mu\nu}F_{\mu\nu}\langle\lambda_6 Q^2\chi U^+\rangle \qquad \Rightarrow \frac{A^{(6)}}{A^{(4)}} \sim \frac{m_K^2}{(4\pi F_\pi)^2} \sim 0.2, \quad (16)$$

where $c \sim \mathcal{O}(1)$ has to be determined phenomenologically but has no vector Meson (VMD) contributions and so it is not enhanced by the factor $(4\pi F_\pi)^2/m_V^2 \sim (1200/770)^2$. So we can compare the $\mathcal{O}(p^4)$ prediction in (15) with the recent NA48 result [8]:

$$\mathcal{B}(K_S \to \gamma\gamma) = \begin{cases} \text{TH} \quad (p^4) \quad 2.1 \times 10^{-6} \\ \\ \text{NA48} \quad (2.78 \pm 0.072) \times 10^{-6} \end{cases} \qquad \Rightarrow \frac{A^{(6)}}{A^{(4)}} \sim 15\% \qquad (17)$$

The error in the amplitude, is smaller than the naive expectation in (16), 20-30% and fixes c in Eq.(16), which actually, as we shall see, it is useful to determine completely $K_L \to \pi^0\gamma\gamma$ [33].

4 $K \to \pi\gamma\gamma$ decays and the CP-conserving $K_L \to \pi^0\ell^+\ell^-$

$K_L \to \pi^0\ell^+\ell^-$ is a classical example of how our control on low energy theory may help to disentangle short-distance physics. In fact the effective current⊗current structure of weak interactions obliges short-distance contributions to $K_L \to$

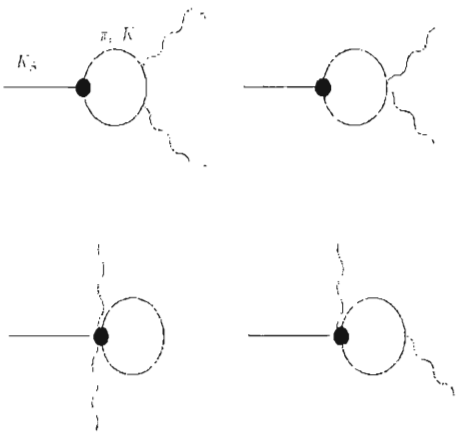

Figure 2: $K_S \to \gamma\gamma$: the • represents the $\mathcal{O}(p^2)$ weak vertex, proportional to G_8, defined in (14), [7]

$\pi^0\ell^+\ell^-$, analogously to $K_L \to \pi^0\nu\bar{\nu}$, discussed in the previous section to be direct CP-violating [1, 28]. However, differently from the neutrino case, $K_L \to \pi^0\ell^+\ell^-$ receives also non-negligible long-distance contributions: i) indirect CP-violating from one-photon exchange, discussed in the next section, and ii) CP-conserving from two-photon exchange, where the photons can be on-shell (two-photon discontinuity) and thus directely related to the observable $K_L \to \pi^0\gamma\gamma$ decay, or off-shell and then a form factor should be used [34, 33]. It is possible [35] to avoid the potential large background contribution from $K_L \to e^+e^-\gamma\gamma$ [36]. The present bounds from KTeV [3, 37] are

$$B(K_L \to \pi^0 e^+ e^-) < 5.1 \times 10^{-10} \quad \text{and} \quad B(K_L \to \pi^0 \mu^+ \mu^-) < 3.8 \times 10^{-10}. \tag{18}$$

The general amplitude for $K_L(p) \to \pi^0(q_1)\gamma(q_2)\gamma(q_2)$ can be written in terms of two Lorentz and gauge invariant amplitudes $A(z,y)$ and $B(z,y)$:

$$\mathcal{A}(K_L \to \pi^0\gamma\gamma) = \frac{G_8\alpha}{4\pi}\epsilon_{1\mu}\epsilon_{2\nu}\Big[A(z,y)(q_2^\mu q_1^\nu - q_1\cdot q_2\ g^{\mu\nu}) + \\ + \frac{2B(z,y)}{m_K^2}(p\cdot q_1\ q_2^\mu p^\nu + p\cdot q_2\ p^\mu q_1^\nu - p\cdot q_1\ p\cdot q_2\ g^{\mu\nu} - q_1\cdot q_2\ p^\mu p^\nu)\Big] \tag{19}$$

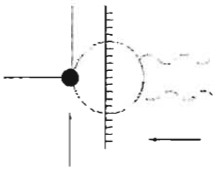

Figure 3: $K_L \to \pi^0\gamma\gamma$: unitarity contributions from $K \to 3\pi$: X, Y Dalitz var. 41, 42)

where $y = p(q_1 - q_2)/m_K^2$ and $z = (q_1+q_2)^2/m_K^2$. Then the double differential rate is given by

$$\frac{\partial^2\Gamma}{\partial y\,\partial z} \sim [\,z^2\,|\,A + B\,|^2 + \left(y^2 - \frac{\lambda(1,r_\pi^2,z)}{4}\right)^2 |\,B\,|^2\,], \qquad (20)$$

where $\lambda(a,b,c)$ is the usual kinematical function and $r_\pi = m_\pi/m_K$. Thus in the region of small z (collinear photons) the B amplitude is dominant and can be determined separately from the A amplitude. This feature is crucial in order to disentangle the CP-conserving contribution $K_L \to \pi^0 e^+e^-$. In fact the lepton pair produced by photons in S-wave, like an $A(z)$-amplitude, are suppressed by the lepton mass while the photons in $B(z,y)$ are also in D-wave and so the resulting $K_L \to \pi^0 e^+e^-$ amplitude, $A(K_L \to \pi^0 e^+e^-)_{CPC}$, does not suffer from the electron mass suppression [38, 39].

The leading $\mathcal{O}(p^4)$ $K_L \to \pi^0\gamma\gamma$ amplitude [40] is affected by two large $\mathcal{O}(p^6)$ contributions: i) the full unitarity corrections from $K \to 3\pi$ [41, 42] in Fig. 3 and ii) local contributions. Fig. 3 enhances the $\mathcal{O}(p^4)$ branching ratio by 40% and generates a B-type amplitude. Local contributions are generated by three independent counterterms, as the one in Eq. (16), with the unknown coefficients α_1, α_2 and β leading to contributions to A and B in Eq. (19) [42]:

$$A_{CT} = \alpha_1(z - r_\pi^2) + \alpha_2, \quad B_{CT} = \beta. \qquad (21)$$

If we assume VMD [43, 44], these couplings are related in terms of one constant, a_V:

$$\alpha_1 = \frac{\beta}{2} = -\frac{\alpha_2}{3} = -4a_V. \qquad (22)$$

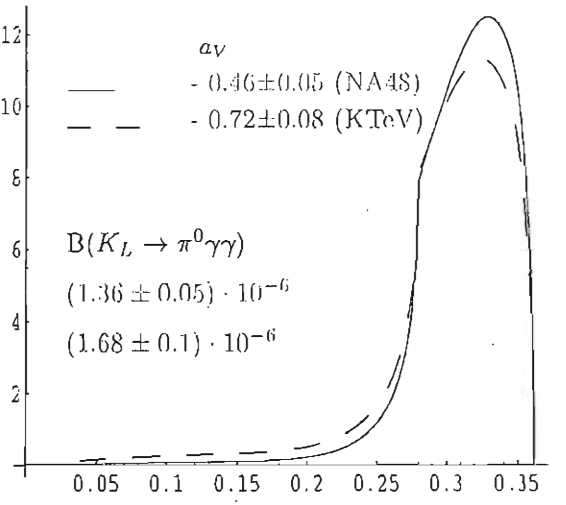

Figure 4: $K_L \to \pi^0\gamma\gamma$ diphoton-invariant mass spectrum for two values of a_V:−0.46 (full curve), −0.7 (dashed curve), corresponding respectively to the NA48 and KTeV measured value.

Though chiral counting suggests $\alpha_i, \beta \sim 0.2$, VMD enhances this typical size. Actually a model, FMV, describing weak interactions of pseudoscalars (ϕ's) with vectors, $\mathcal{L}_W^{FMV}(\phi, V^\mu)$, based on factorization and couplings fixed by the Wilson coefficient of the Q_- operator, predicts:

$$\mathcal{L}_W^{FMV}(\phi, V^\mu) \quad \Longrightarrow \quad a_V = -0.6. \tag{23}$$

Two experiments have measured these decays in terms of one parameter, a_V: KTeV [46] and NA48 [47]. Their results and spectrum are shown in from Fig. 4 As we can see from Fig. 4 the spectrum at low z is very sensitive to the value of a_V, or more generally to the size of the amplitude B in Eq. (19).
Recentely Gabbiani and Valencia [48] suggested to fit the experimental z-spectrum (and the rate) with all three parameters in Eq. (21). In fact, VMD even in the best case is known to be only a good approximation and thus we think this is a non-trivial VMD test. In fact we have shown in Ref. [33] that a complete analysis of the $\mathcal{O}(p^6)$ CT 's, which takes into account also the decay $K_S \to \gamma\gamma$ allows to exclude several of the three parameters fit and actually VMD is in good shape, particularly if events at low $m_{\gamma\gamma}$ spectrum are just below the exclusion plot of NA48 (see figure (5)).

An important issue is that while the size of $B(K_L \to \pi^0 e^+ e^-)^{\gamma\gamma\ \text{on-shell}}_{CPC}$ is an issue that can be established firmly from the $K_L \to \pi^0\gamma\gamma$ spectrum, the contribution when the two intermediate photons are off-shell is model dependent and a form factor is needed [34]. Howewer very recentely, we have studied

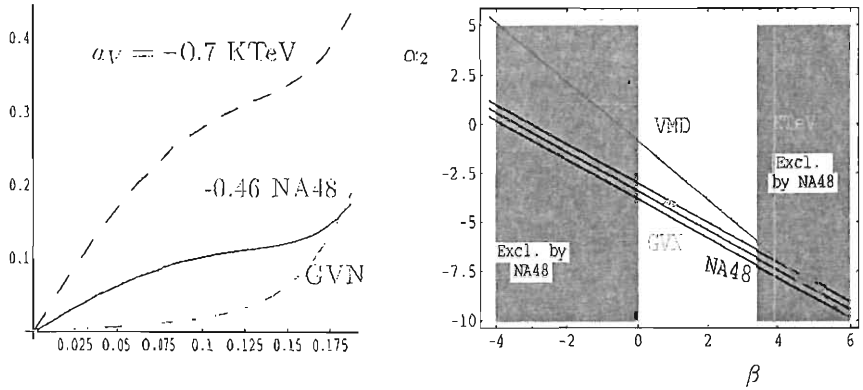

Figure 5: $K_L \to \pi^0\gamma\gamma$: on the left side zoomed diphoton invariant mass distribution, the green curve is one suggested by Ref. [48] in the 3-parameter fit and still allowed. On the right side the $\beta - \alpha_2$ plot [33]; again the possibility of Ref. [48] and the VMD line (each point is associated to a different value of a_V). VMD likes events just near the exclusion region of NA48.

this problem [33] with a general form factor, motivated by VMD:

$$f(q_1^2, q_2^2) = 1 + a\left(\frac{q_1^2}{q_1^2 - m_V^2} + \frac{q_2^2}{q_2^2 - m_V^2}\right) + b\frac{q_1^2 q_2^2}{(q_1^2 - m_V^2)(q_2^2 - m_V^2)}\ , \qquad (24)$$

where a, b are low energy parameters, which however must obey the sum rule $1 + 2a + b = 0$ in order to go to zero for $q_1^2, q_2^2 \to \infty$. as required by short distance. Thus we can eliminate b. Also for $a = -1$ we obtain the form factor in ref. [34]. This form factor has been used also in $K_L \to \mu\bar{\mu}$ [49]. So we can parametrize

$$\begin{aligned} B(K_L \to \pi^0 e^+ e^-)_{\rm CPC} &= 7.0 \times 10^{-14} \times |B(0)|^2 \\ &\times \left\{1 + \left[1.4 + 1.4(1+a) + 0.4(1+a)^2\right]\right\}\ , \qquad (25) \end{aligned}$$

where we can see that $B(K_L \to \pi^0 e^+ e^-)_{\rm CPC}$ is negligible for reasonable values of a [33].

5 $K^\pm \to \pi^\pm \ell^+ \ell^-$ and $K_S \to \pi^0 \ell^+ \ell^-$

The CP-conserving decays $K^\pm(K_S) \to \pi^\pm(\pi^0)\ell^+\ell^-$ are dominated by the long-distance process $K \to \pi\gamma \to \pi\ell^+\ell^-$ [50]. The decay amplitudes can in general

be written in terms of one form factor $W_i(z)$ $(i = \pm, S)$:

$$A\left(K_i \to \pi^i \ell^+ \ell^-\right) = -\frac{e^2}{M_K^2 (4\pi)^2} W_i(z)(k+p)^\mu \bar{u}_\ell(p_-)\gamma_\mu v_\ell(p_+) \ , \qquad (26)$$

$z = q^2/M_K^2$; $W_i(z)$ can be decomposed as the sum of a polynomial piece plus a non-analytic term, $W_i^{\pi\pi}(z)$, generated by the $\pi\pi$ loop, analogously to the one in Fig. 3 for $K_L \to \pi^0\gamma\gamma$, completely determined in terms of the physical $K \to 3\pi$ amplitude [51]. Keeping the polynomial terms up to $\mathcal{O}(p^6)$ we can write

$$W_i(z) = G_F M_K^2 \left(a_i + b_i z\right) + W_i^{\pi\pi}(z) \ , \qquad (27)$$

where the parameters a_i and b_i parametrize local contributions starting respectively at $\mathcal{O}(p^4)$ and $\mathcal{O}(p^6)$. Recent data on $K^+ \to \pi^+ e^+ e^-$ and $K^+ \to \pi^+ \mu^+ \mu^-$ by BNL-E865 [52] have been successfully fitted using Eq. (27) and lead to

$$a_+ = -0.587 \pm 0.010, \qquad b_+ = -0.655 \pm 0.044 \ . \qquad (28)$$

Recentely HyperCP [53] has attempted to measure the CP-violating width charge asymmetry in $K^\pm \to \pi^\pm \mu^+ \mu^-$ and it has found that it is consistent with 0 at 10% level. Though the CKM prediction with accurate cuts is $\sim 10^{-4}$ [51], we are beginning to test new physics affecting the operator $\bar{s}d\bar{\mu}\mu$ [54]. The experimental size of the ratio b_+/a_+ exceeds the naive dimensional analysis estimate $b_+/a_+ \sim \mathcal{O}[M_K^2/(4\pi F_\pi)^2] \sim 0.2$, but can be explained by a large VMD contribution. Chiral symmetry alone does not allow us to determine the unknown couplings a_S and b_S in terms of a_+ and b_+ [50, 51]. Neglecting the $\Delta I = 3/2$ suppressed non-analytic term $W_S^{\pi\pi}(z)$, we obtain [51]

$$B(K_S \to \pi^0 e^+ e^-) = \left[46.5 a_S^2 + 12.9 a_S b_S + 1.44 b_S^2\right] \times 10^{-10} \approx 5 \times 10^{-9} \times a_S^2 \ , \qquad (29)$$

Very recently NA48/1 Collaboration at CERN has been announced the first experimental evidence of the $K_S \to \pi^0 e^+ e^-$ transition. The observation of 7 events in a clean signal region (with 0.15 expected background events) leads to the preliminary result [55]:

$$B(K_S \to \pi^0 e^+ e^-)_{m_{ee} > 165 \text{ MeV}} = \left(3.0^{+1.5}_{-1.2} \pm 0.2\right) \times 10^{-9} \ , \qquad (30)$$

which implies

$$|a_S| = 1.08^{+0.26}_{-0.21} \ , \qquad (31)$$

in good agreement with the naive chiral counting expectation $a_S = \mathcal{O}(1)$ [51] and also with the phennomenological model of ref. [56]. This leads to the very

interesting interference:

$$B(K_L \to \pi^0 e^+ e^-)_{CPV} = \left[15.3\, a_S^2 - 6.8 \frac{\Im\lambda_t}{10^{-4}}\, a_S + 2.8 \left(\frac{\Im\lambda_t}{10^{-4}} \right)^2 \right] \times 10^{-12} , \tag{32}$$

where $\lambda_t = V_{td}V_{ts}$. The sign of the interference term is model-dependent. However assuming i) VMD and ii) a short distance relation among a_+ and a_S we make a good prediction of a_S, this allows us to trust the short distance positive sign for the interference [33]. This is very encouraging for future searches in $K_L \to \pi^0 e^+ e^-$.

6 Conclusions

The measurements by E787 [13] in $K^+ \to \pi^+ \nu\bar{\nu}$ in (5) and by KTeV [37] $K_L \to \pi^0 e^+ e^-$ in (18) furnish the best limits in rare kaon decays. There are theoretical motivations to believe that it is important to push more these researches. The measurement by NA48/1 of $K_S \to \pi^0 e^+ e^-$ [55] and its theoretical implications [33] lead us to believe that now $K_L \to \pi^0 e^+ e^-$ must be pushed even more. In fact to this goal also the auxilary channells $K_L \to \pi^0\gamma\gamma$ and $K_S \to \gamma\gamma$ have been important [33]. Other channells, like $K_L \to \mu\bar{\nu}u$ [49, 57], may bring additional Flavour infos. Here the needed additional info comes from $K_L \to l^+l^-\gamma$ and $K_L \to e^+e^-\mu^+\mu^-$.

7 Acknowledgements

I wish to thank G. Buchalla, A. Ceccucci, G. Gindice, G. Isidori, A Strumia, M. Martini, I. Mikulec for nice discussion and/or collaboration. This work is supported in part by TMR, EC–Contract No. ERBFMRX–CT980169 (EURODAΦNE).

References

1. G. Buchalla, [hep-ph/9912369], Y. Nir, *Nucl. Phys. Proc. Suppl.* **117** (2003) 111 [hep-ph/0208080]; A.J. Buras, [hep-ph/9905437]; L. Littenberg and G. Valencia, *Ann. Rev. Nucl. Part. Sci.* **43** (1993) 729; A.R.. Barker and S.H. Kettell, Ann. Rev. Nucl. Part. Sci. **50** (2000) 249 [hep-ex/0009024]; and references therein.

2. J.F. Donoghue, E. Golowich and B.R. Holstein, *Dynamics of the Standard Model* (Cambridge Univ. Press, 1992).

3. L. Littenberg, [hep-ex/0212005].

4. G. D'Ambrosio and G. Isidori, *Int. J. Mod. Phys.* **A 13** (1998) 1 [hep-ph/9611284].

5. L. Littenberg, *Phys. Rev.* **D 39** 3322 (1989); J. Ellis and J.S. Hagelin *Nucl. Phys.* **B 217** (1983); G. Buchalla and A.J. Buras, *Phys. Rev.* **D 54** (1996) 6782.

6. G. D'Ambrosio, plenary talk at KAON 2001, Pisa, June 2001, [hep-ph/0110354].

7. G. D'Ambrosio and D. Espriu, *Phys. Lett.* **B 175** 237 (1986); J.L. Goity, *Z. Phys.* **C 34**, (1987) 341; F. Buccella, G. D'Ambrosio and M. Miragliuolo, *Il Nuovo Cimento* **104 A** (1991) 777.

8. A. Lai *et al.*, *Phys. Lett.* **B 551** (2003) 7 [hep-ex/0210053].

9. W.Marciano and Z. Parsa, *Phys. Rev.* **53**, R1 (1996).

10. G. Buchalla and G. Isidori, *Phys. Lett.* **B 440** (1998) 170, and references therein.

11. G. Buchalla and A.J. Buras, *Nucl. Phys.* **B 548** (1999) 309.

12. For a recent discussion see e.g.: M. Ciuchini *et al.*, *JHEP* **0107** (2001) 013 [hep-ph/0012308]; A. Hocker, H. Lacker, S. Laplace and F. Le Diberder, *Eur. Phys. J.* **C 21** (2001) 225 [hep-ph/0104062]; A. J. Buras, [hep-ph/0109197].

13. S. Adler *et al.* [E787 Collab.], *Phys. Rev. Lett.* **84** (2000) 3768 [hep-ex/0002015]; S. Adler *et al.* [E787 Collab.], [hep-ex/0111091].

14. A.Alavi-Harati et al., KTeV collaboration, *Phys. Rev.* **D 61** (2000) 072006 [hep-ex/9907014].

15. Y. Grossman and Y. Nir, *Phys. Lett.* **B 398**, 163 (1997).

16. G. D'Ambrosio and G. Isidori, *Phys. Lett.* **B 530** (2002) 108 [hep-ph/0112135].

17. G. Isidori, [hep-ph/0301159].

18. R. Fleischer, G. Isidori and J. Matias, [hep-ph/0302229].

19. J.S. Hagelin, S. Kelley and T. Tanaka, *Nucl. Phys.* **B 415** (1994) 293; F. Gabbiani, E. Gabrielli, A. Masiero and L.Silvestrini *Nucl. Phys.* **B 477** (1996) 321 [hep-ph/9604387].

20. S. Dimopoulos and G. F. Giudice, *Phys. Lett.* **B 357** (1995) 573 [hep-ph/9507282]; A. Cohen, D.B. Kaplan and A. E. Nelson, *Phys. Lett.* **B 388** (1996) 588 [hep-ph/9607394]; A. Cohen, D.B. Kaplan, F. Lepeintre and A. E. Nelson, *Phys. Rev. Lett.* **78** (1997) 2300 [hep-ph/9610252].

21. G. D'Ambrosio, G. F. Giudice, G. Isidori and A. Strumia, *Nucl.Phys.* **B 645** (2002) 155, [hep-ph/0207036].

22. A. Ali and D. London, *Eur. Phys. J.* **C 9** (1999) 687 [hep-ph/9903535].

23. R. S. Chivukula and H. Georgi, *Phys. Lett.* **B 188** (1987) 99.

24. M. Dine and A. E. Nelson, *Phys. Rev.* **D 48** (1993) 1277 [hep-ph/9303230]; M. Dine, A. E. Nelson and Y. Shirman, *Phys. Rev.* **D 51** (1995) 1362 [hep-ph/9408384]; G. F. Giudice and R. Rattazzi, *Phys. Rep.* **322** (1999) 419 [hep-ph/9801271].

25. T. Banks, M. Dine and A. E. Nelson, *JHEP* **9906** (1999) 014 [hep-th/9903019]; N. Arkani-Hamed, L. J. Hall, D. R. Smith and N. Weiner, *Phys. Rev.* **D 61** (2000) 116003 [hep-ph/9909326]; R. Rattazzi and A. Zaffaroni, *JHEP* **0104** (2001) 021 [hep-th/0012248].

26. A. J. Buras *et al.*, *Phys. Lett.* **B 500** (2001) 161 [hep-ph/0007085]; A. J. Buras and R. Fleischer, *Phys. Rev.* **D 64** (2001) 115010 [hep-ph/0104238]; S. Laplace, Z. Ligeti, Y. Nir and G. Perez, *Phys. Rev.* **D 65** (2002) 094040 [hep-ph/0202010].

27. S. Weinberg, *Physica* **A 96** (1979) 327; J. Gasser and H. Leutwyler, *Ann. Phys.* (N.Y.) **158** (1984) 142; A.V. Manohar and H. Georgi, *Nucl. Phys.* **B 234** (1984) 189.

28. E. de Rafael, in *CP Violation and the limits of the Standard Model*, TASI 1994 proceedings, ed. J.F. Donoghue (World Scientific, 1995), [hep-ph/9502254]; A. Pich, *Rept. Prog. Phys.* **58** (1995) 563, [hep-ph/9502336]; G. Ecker, *Prog. Part. Nucl. Phys.* **35** (1995) 1, [hep-ph/9501357]; G. Colangelo and G. Isidori, [hep-ph/0101264].

29. G. Ecker, J. Kambor and D. Wyler, *Nucl. Phys.* **B 394** (1993) 101.

30. G. D'Ambrosio and J. Portoles, *Nucl. Phys.* **B 533** (1998) 494 [hep-ph/9711211].

31. J. Bijnens, G. Colangelo and G. Ecker, *JHEP* **9902** (1999) 020 [hep-ph/9902437]; G. Colangelo, J. Gasser, H. Leutwyler, *Nucl. Phys* **B 603** (2001) 125 [hep-ph/0103088].

32. J. Kambor and B.R. Holstein, *Phys. Rev.* **D 49** (1994) 2346.

33. G. Buchalla, G. D'Ambrosio and G. Isidori, arXiv:hep-ph/0308008.

34. J.F. Donoghue and F. Gabbiani, *Phys. Rev.* **D 51** (1995) 2187.

35. A. Belyaev *et al.*, [hep-ph/0107046].

36. H.B. Greenlee,*Phys. Rev.* D 42 (1990) 3724.

37. A. Alavi-Harati *et al.*, KTeV Collaboration, *Phys. Rev. Lett.* **84** 5279 (2000); A. Alavi-Harati *et al.*,*Phys. Rev. Lett.* **86** (2001) 397 [hep-ex/0009030]; http://kpasa.fnal.gov:8080/public/ktev_results.html.

38. J.F. Donoghue, B. Holstein and G. Valencia,*Phys. Rev.* **D 35** (1986) 2769; T. Morozumi and H. Iwasaki, *Prog. Theor. Phys.* **82** (1989) 371; J. Flynn and L. Randall, *Phys. Lett.* **B 216** (1989) 221.

39. G. Ecker, A. Pich and E. de Rafael, *Nucl. Phys.* **B 303** (1988) 665.

40. G. Ecker, A. Pich and E. de Rafael, *Phys. Lett.* **B 189**, (1987) 363; L. Cappiellc and G. D'Ambrosio, *Nuovo Cim.* **A 99** (1988) 155.

41. L. Cappiello, G. D'Ambrosio and M. Miragliuolo, *Phys. Lett.* **B 298** (1993) 423.

42. A. G. Cohen, G. Ecker and A. Pich, *Phys. Lett.* **B 304** (1993) 347.

43. L.M. Sehgal, *Phys. Rev.* **D 38** (1988) 808; P. Heiliger and L.M. Sehgal, *Phys. Rev.* **D 47** (1993) 4920.

44. G. Ecker, A. Pich and E. de Rafael,*Phys. Lett.* **B 237** (1990) 481.

45. G. D'Ambrosio and J. Portolés, *Nucl. Phys.* **B 492** (1997) 417 [hep-ph/9610244].

46. A.Alavi-Harati *et al.*, KTeV collaboration, *Phys.Rev.Lett.* **83** (1999) 917 [hep-ex/9902029].

47. A. Lai *et al.* [NA48 Collaboration], *Phys. Lett.* **B 536** (2002) 229 [hep-ex/0205010].

48. F. Gabbiani and G. Valencia, *Phys. Rev.* **D 64** (2001) 094008 [hep-ph/0105006]; F. Gabbiani and G. Valencia, *Phys. Rev.* **D 66** (2002) 074006 [hep-ph/0207189].

49. G. D'Ambrosio, G. Isidori and J. Portolés, *Phys. Lett.* **B 423** (1998) 385 [hep-ph/9708326].

50. G. Ecker, A. Pich and E. de Rafael, *Nucl. Phys.* **B 291** (1987) 692.

51. G. D'Ambrosio, G. Ecker, G. Isidori and J. Portolés, *JHEP* **08** (1998) 004 [hep-ph/9808289].

52. R.Appel *et al.*, E865 collaboration, *Phys. Rev. Lett.* **83** (1999) 4482; H.Ma *et al.*, E865 collaboration, *Phys. Rev. Lett.* **84** (2000) 2580 [hep-ex/9910047].

53. H. K. Park *et al.* HyperCP Collaboration, *Phys. Rev. Lett.* **88** (2002) 111801 [hep-ex/0110033].

54. G. D'Ambrosio and D. N. Gao, *JHEP* **0207** (2002) 068 [hep-ph/0203087]; A. Messina, *Phys. Lett.* **B 538** (2002) 130 [hep-ph/0202228].

55. A. Lai *et al.*, NA48 Collaboration, *Phys. Lett.* **B 514** (2001) 253; M. Patel [NA48/1 Collaboration], talk presented at CERN (10 June 2003), availble at http://na48.web.cern.ch/NA48/

56. L.M. Sehgal, *Nucl. Phys.* **B 19** (1970) 445.

57. D. Greynat and E. de Rafael, [hep-ph/0303096].

SESSION VII – QCD

Marco Contalbrigo	A First Measurement of the Tensor Structure Function b_1^d
Luca Passalacqua	Recent Results from the KLOE Experiment
Jörg Pretz	COMPASS – Status and Perspective
Robert Snihur*	Jet studies at CDF in Run 2
Igor Dremin	Jet physics at LEP and QCD
Harald Fritzsch	A Time Variation of the QCD Coupling Constant

* The trasparencies of the missing contributions are available on the web site http://www.pi.infn.it/lathuile/lathuile_2003.html

A FIRST MEASUREMENT OF THE TENSOR STRUCTURE FUNCTION b_1^d

Marco Contalbrigo
INFN e Università di Ferrara - Via del Paradiso 12, 44100 Ferrara, ITALIA
(on behalf of the HERMES Collaboration)

Abstract

The HERMES experiment studies the spin structure of the nucleon using the 27.6 GeV longitudinally polarized positron beam of HERA and an internal target of pure gases. In addition to the well-known spin structure function g_1, measured precisely with longitudinally polarized proton and deuteron targets, the use of a tensor-polarized deuteron target provides access to the tensor structure function b_1^d. The latter, measured with an unpolarized beam, quantifies the dependence of the parton momentum distribution on the nucleon spin. HERMES had a 1-month dedicated run with a tensor polarized deuterium target during the 2000 data taking period. Here preliminary results on the tensor structure function b_1^d are presented for the kinematic range $0.002 < x < 0.85$ and $0.1\ \mathrm{GeV}^2 < Q^2 < 20\ \mathrm{GeV}^2$.

1 Introduction

The HERMES experiment [1] has been designed to measure the nucleon spin structure functions from deep inelastic scattering (DIS) of polarized positrons and electrons from polarized gaseous targets (H, D, ^{3}He). Three of the main leading-twist structure functions are listed in the table below, along with their interpretation in the Quark-Parton Model. The sums are over quark and anti-quark flavours q and the dependences on Q^2 and Bjorken x are omitted for simplicity:

	Proton	Deuteron
F_1	$\frac{1}{2}\sum_q e_q^2 [q^+ + q^-]$	$\frac{1}{3}\sum_q e_q^2 [q^+ + q^- + q^0]$
g_1	$\frac{1}{2}\sum_q e_q^2 [q^+ - q^-]$	$\frac{1}{2}\sum_q e_q^2 [q^+ - q^-]$
b_1	$--$	$\frac{1}{2}\sum_q e_q^2 [2q^0 - (q^- + q^+)]$

The unpolarized structure function F_1 measures the quark momentum distribution summed over all the possible helicity states. The spin-dependent structure function g_1 is sensitive to the spin structure of the nucleon, measuring the imbalance of quarks with the same (q^+) or opposite (q^-) helicity with respect to the nucleon they belong to. For targets of spin 1 such as the deuteron, the tensor structure function b_1 compares the quark momentum distribution between the zero-helicity state of the hadron (q^0) and the average of the helicity-1 states ($q^+ + q^-$). As the deuteron is a weakly-bound state of spin-half nucleons, b_1^d was initially predicted to be small [2]. More recently, coherent double scattering models have predicted a sizable b_1^d at low x [3, 4, 5, 6], violating the sum rule which suggests a vanishing first moment of b_1^d [7]. Although b_1^d describes basic properties of the spin-1 deuterium nucleus, and may affect the experimental determination of g_1^d, it has not yet been measured. In 2000, HERMES collected a dedicated data set with a tensor polarized deuterium target for the purpose of making a first measurement of b_1^d. Preliminary results from these data are presented in this paper.

2 Hermes setup

The HERMES experiment is installed in the HERA ring where the beam positrons become transversely polarized by emission of synchrotron radiation (Sokolov-Ternov effect). Longitudinal beam polarization, needed for the g_1^d measurement, is obtained with two spin rotators placed upstream and downstream of the HERMES apparatus. As b_1^d appears in the symmetric part of the hadronic tensor [2], its measurement is independent from the beam polarization.

A feature of the HERMES experiment unique to DIS experiments is its tensor-polarizable gaseous target [8]. An atomic beam source (ABS) generates a Deuterium atomic beam and selects the two hyperfine states (out of the existing six) with the desired nuclear polarization. An elliptical 40 cm long, 75 μm thick Al tube (target cell) confines the polarized gas along the positron beam line. A longitudinal magnetic field provides the quantization axis for the nuclear spin inside the cell. Every 90 seconds, the polarization of the injected gas is changed. A diagnostic system continuously measures the atomic and molecular abundances and the nuclear polarization of the atoms inside the target cell. The vector V and tensor T atomic polarizations of the target are defined as

$$V = \frac{n^+ - n^-}{n^+ + n^- + n^0} \qquad T = \frac{n^+ + n^- - 2n^0}{n^+ + n^- + n^0}, \tag{1}$$

where n^+, n^-, n^0 are the atomic populations inside the cell with positive, negative and zero spin projection onto the beam axis. For the b_1^d measurement, an average tensor polarization greater than 80 % was obtained, at the same time keeping the residual vector polarization at the level of only 1 %.

The HERMES detector is a forward spectrometer with a dipole magnet providing a field integral of 1.3 Tm. A horizontal iron plate shields the HERA beam lines from the field, thus dividing the spectrometer into two identical halves with a minimum vertical acceptance of ± 40 mrad. The acceptance extends to ± 140 mrad vertically and to ± 170 mrad horizontally. In this analysis 36 drift chamber planes in each detector-half were used for tracking. Positron identification is accomplished using a probability method based on signals of three subsystems: a lead-glass block calorimeter, a transition-radiation detector, and a preshower hodoscope. For positrons in the momentum range of 2.5 to 27 GeV, the identification efficiency exceeds 98 % with a less than 0.5 % hadron contamination. The average polar angle resolution is 0.6 mrad, and the average momentum resolution is 1 – 2 %.

3 Measurement

Depending on the beam (P_B) and target (V and T) polarizations, the lepton-nucleon DIS cross section measured by the experiment is sensitive to the vector A_1 (A_2 is here neglected) and tensor A_{zz} asymmetries of the virtual photon nucleon cross section

$$\sigma_{\rm meas} = \sigma_U \left[1 + P_B D_\gamma V A_1 + \frac{1}{2} T A_{zz} \right] \tag{2}$$

	P_B	V	T
σ^+	1	1	1
σ^-	1	−1	1
σ^0	0	0	−2

where σ is an abbreviation for $d\sigma/dxdy$. $\sigma_U = (\sigma^+ + \sigma^- + \sigma^0)/3$ is the unpolarized cross section and D_γ accounts for the polarization transfer from the lepton to the virtual photon. Here and in the following no higher-twist contribution (g_2, b_3, b_4) is considered. No contributions from the unmeasured double spin-flip structure function Δ [9] is considered, too. The vector asymmetry A_1 is related to g_1^d; it can be measured with a polarized beam (e.g. $D_\gamma P_B = 1$)

$$A_1 = \frac{\sigma^+ - \sigma^-}{2\sigma_U V} = \frac{g_1}{F_1} = A_1^{meas}\left[1 + \frac{1}{2}T A_{zz}\right]. \qquad (3)$$

Here A_1^{meas} is the asymmetry typically measured by experiments, where $(\sigma^+ + \sigma^-)$ is used rather than $2\sigma_U$. The tensor term, until now neglected in g_1^d measurements, is needed to ensure that the denominator is proportional to σ_U and so to F_1. The tensor asymmetry A_{zz}, and the related b_1^d, provide the missing information on the difference between the cross section for the 0-helicity target state and the spin-averaged ± 1-helicity states:

$$A_{zz} = \frac{(\sigma^+ + \sigma^-) - 2\sigma^0}{3\sigma_U T} = -\frac{2}{3}\frac{b_1}{F_1}. \qquad (4)$$

The A_{zz} measurement is not biased by the vector asymmetry A_1 only if either the vector polarization is negligible or the beam polarization is zero. At Hermes, the target residual vector polarization in the σ^0 case and in the case of the sum $\sigma^+ + \sigma^-$ is of the order of 1 % and has a negligible effect on the A_{zz} measurement. The vector contribution is further reduced by grouping together data with opposite beam helicities thus achieving an effectively unpolarized beam. Inclusive deep-inelastic events are selected in the same way as for the HERMES g_1^d analysis by requiring $Q^2 > 0.1$ GeV^2 and $W^2 > 3.24$ GeV^2. The kinematic range for the b_1^d measurement covers the intervals $0.002 < x < 0.85$ and $0.1 < y < 0.91$. For this analysis, the x-range is divided into 6 bins. For each x-bin the following asymmetry between yields is calculated:

$$A_{zz} = \frac{1}{T} \cdot \left[\frac{(N/L)^+ + (N/L)^- - 2 \cdot (N/L)^0}{(N/L)^+ + (N/L)^- + (N/L)^0}\right]. \qquad (5)$$

where the superscripts refer to the target spin orientations. The numbers of events selected per spin state (N) are corrected for the background arising from charge symmetric processes. The corresponding luminosities (L) used for normalization are measured from Bhabha scattering from the target gas electrons. The radiative corrections on A_{zz} are calculated using POLRAD [10]. For this preliminary result the inelastic radiative tail is neglected due to the small size of A_{zz} and the elastic radiative tail is estimated from a not fully

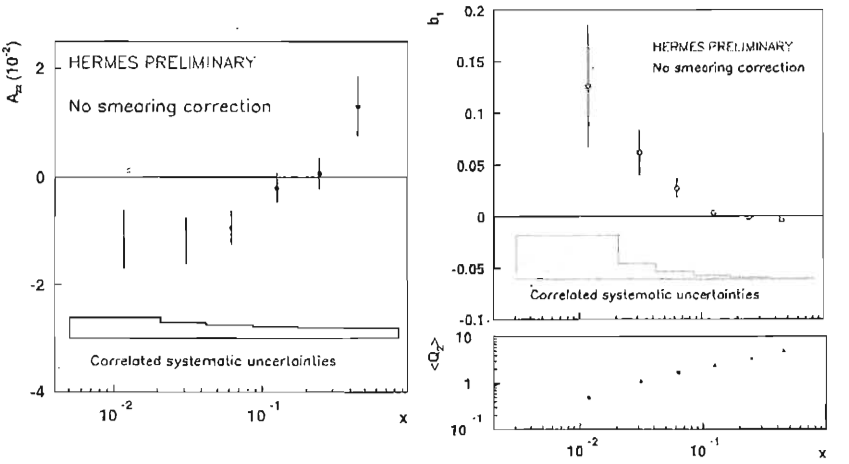

Figure 1: *The tensor asymmetry A_{zz} (left) and the tensor structure function b_1^d (right) as measured by* HERMES . *The error bars are statistical only and the shaded band shows the estimated systematic uncertainty. The bottom panel on the right plot shows the average Q^2 of the measurements.*

updated parameterization of the deuteron quadrupole form factor [11]. The subtraction of the radiative background increases the size of the statistical and systematic uncertainties by almost a factor of 2 at low x.

The measured A_{zz} is presented in Fig. 1. The systematic uncertainties are correlated over the kinematical bins, being dominated by the target density normalization between different injection modes of the ABS. The target polarization measurement, the uncertainty on the alignment of the spectrometer, and the hadron contamination give negligible systematic effects. Data with opposite beam polarizations were independently analyzed and give compatible A_{zz} results. No systematic error has been estimated from the still incomplete radiative correction. A_{zz} is found to be less than 2 %. From this result, the bias of the tensor asymmetry on the HERMES g_1^d measurement is estimated to be less than 1 %.

The structure function b_1^d is extracted from the tensor asymmetry via the relation $b_1^d = -\frac{3}{2} A_{zz} \frac{(1+\gamma^2)F_2^d}{2x(1+R)}$, where the structure function F_1^d has been expressed in terms of the ratio $R = \sigma_L/\sigma_T$ [12] and the structure function F_2^d (γ is a kinematic factor). $F_2^d = F_2^p(1 + F_2^n/F_2^p)$ is calculated using parameterizations for F_2^p [13] and F_2^n/F_2^p [14]. Fig. 1 displays the result for b_1^d,

which is small but different from zero. The structure function b_2^d has also been extracted, using the Callan-Gross relation $b_2^d = \frac{2x(1+R)}{(1+\gamma^2)} b_1^d$. The data indicate a rise at low x as predicted by the most recent theoretical models [3, 4, 5, 6]. A comparison of the measured b_2^d with the prediction of one of the models [6] is given in Fig. 2. In conclusion HERMES has provided the first direct measure-

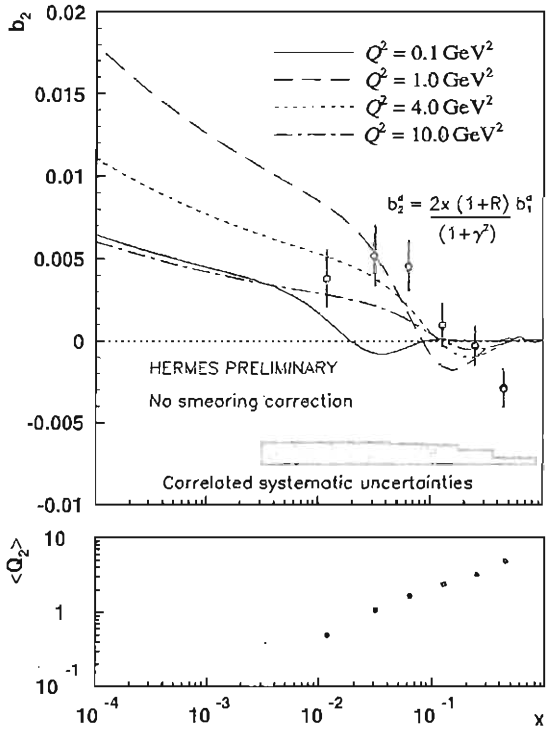

Figure 2: *The tensor-polarized structure function b_2^d. The error bars are statistical only and the shaded band shows the estimated systematic uncertainty. The bottom panel shows the average Q^2 of the measurements. The curves are from calculations within the re-scattering model of Ref.* [6] *for Q^2 values in the range of the* HERMES *measurement.*

ment of the structure function b_1^d in the kinematic range $0.002 < x < 0.85$ and $0.1\ \mathrm{GeV}^2 < Q^2 < 20\ \mathrm{GeV}^2$. The preliminary result for the tensor asymmetry is sufficiently small to produce an effect of less than 1 % on the measurement

of g_1^d. The dependence of b_1^d on Bjorken x is in qualitative agreement with expectations based on coherent double scattering models [3, 4, 5, 6] and favors a sizeable b_1^d at low-x. This may suggest a significant tensor polarization of the sea-quarks, violating the Close-Kumano sum rule [7]. This observation is analogous to the well-established $\overline{u} - \overline{d}$ asymmetry of the sea and the consequent violation of the Gottfried sum rule [15].

References

1. HERMES Coll., K. Ackerstaff *et al*, Nucl. Instrum. Methods A **417**, 230 (1998)
2. P. Hoodbhoy *et al*, Nucl. Phys. B **312**, 571 (1989), H. Khan *et al*, Phys. Rev. C **44**, 1219 (1991)
3. M. Strikman, Probing polarized nucleon structure in semi-inclusive deep inelastic processes, in: Proc. Symposium on Spin Structure of the Nucleon (ed. V.H. Hughes and C. Cavata) 153 (World Scientific, Singapore, 1995)
4. N. N. Nikolaev *et al*, Phys. Lett. B **398**, 245 (1997)
5. J. Edelmann *et al*, Phys. Rev. C **57**, 3392 (1998)
6. K. Bora *et al*, Phys. Rev. D **57**, 6906 (1998)
7. F. E. Close *et al*, Phys. Rev. D **42**, 2377 (1990)
8. C. Baumgarten *et al*, Nucl. Instrum. Methods A **482**, 606 (2002)
9. E. Sather *et al*, Phys. Rev. D **42**, 1424 (1990)
10. I. V. Akushevich *et al*, J. Phys. G **20**, 513 (1994)
11. Kobushkin *et al*, Phys. At. Nucl. G **58**, 1477 (1995)
12. L. W. Whitlow *et al*, Phys. Lett. B **250**, 193 (1990)
13. ALLM97 parameterization: H. Abramowicz *et al*, hep-ph 9712415
14. NMC Coll., P. Amaudruz *et al*, Nucl. Phys. B **371**, 3 (1992)
15. S. Kumano, Phys. Rept. **303**, 183 (1998)

RECENT RESULTS FROM THE KLOE EXPERIMENT

THE KLOE COLLABORATION*

Presented by Luca Passalacqua

Abstract

Thanks to the continuously improving performances of the DAΦNE e^+e^- collider the KLOE experiment has collected by 2003 an amount of data well sufficient to address many relevant measurements, although still insufficient to measure the CP violation parameters at the desired level of accuracy.

The preliminary results reported here were obtained using wide samples of the full 500 pb^{-1} data set and include: the BR of the K_{e3} decay of the K_S with the first ever done measurement of its charge asymmetry, the ratio of BRs $(K_S \to \pi^+\pi^-(\gamma))/(K_S \to \pi^0\pi^0)$, the ratio of BRs $(K_L \to \gamma\gamma)/(K_L \to 3\pi^0)$, a detailed study of the decay $\phi \to \pi^+\pi^-\pi^0$, the ratio of BRs $(\phi \to \eta'\gamma)/(\phi \to \eta\gamma)$ with the determination of the pseudoscalar mixing angle φ_P, the BRs of the two radiative decay modes $\phi \to f_0\gamma$ and $\phi \to a_0\gamma$.

Prospects for the measurement of the $e^+e^+ \to \pi^+\pi^-$ cross section via radiative return are also presented.

1 Introduction

DAΦNE [1] is an e^+e^- collider working at the ϕ resonance peak, and located in the Frascati INFN laboratories. The design luminosity of DAΦNE is about $4.2 \cdot 10^{32} cm^{-2} s^{-1}$, with 120 bunches beams of equal energy circulating in two different rings and colliding with a small angle to avoid parasitic crossings. The ϕ meson is produced with a transverse momentum of about 12 MeV and decays abundantly ($\sim 49\%$) to K^+K^- and ($\sim 34\%$) to $K_S K_L$, the latter being a pure $J^{PC} = 1^{--}$ quantum state. Thus DAΦNE provides two highly pure, almost monochromatic, back-to-back Kaon beams.

The KLOE experiment [2] is located in one of the two interaction points of DAΦNE. The detector has been primarly designed for the measurement of CP and CPT violation in the $K^0 - \bar{K}^0$ system, and more generally for the study of kaons' decays and the investigation of the properties of light scalars such as the $a_0(980)$ and $f_0(980)$. A unique feature of KLOE is the possibility of tagging the presence of a K_S (K_L) by detecting a K_L (K_S) flying in the opposite direction. K_S and K_L are easily distinguishable on the basis of their mean decay path: $\lambda_S \sim 6\, mm$ and $\lambda_L \sim 340\, cm$.

The DAΦNE collider has been commissioned in 1999, when it delivered its first 2 pb^{-1} of data. Since then it has been operated with continously improving luminosity reaching a maximum peak luminosity of $7.8 \cdot 10^{31} cm^{-2} s^{-1}$ at the end of 2002. The total integrated luminosity collected by KLOE amounts to about 500 pb^{-1}. Several results obtained with the 25 pb^{-1} data sample collected during the year 2000 have been recently published [6, 7, 8, 9, 10]. The data sample of year 2001 (190 pb^{-1}) and that of the year 2002 (300 pb^{-1}) are still being analyzed. Some preliminary results are presented here.

2 The KLOE detector

A schematic view of the KLOE detector is shown in fig.1. It looks like a typical e^+e^- detector, although the topology of most decays is very different to that encountered at higher energies. The detector consists mainly in a large volume drift chamber surrounded by an electromagnetic calorimeter. A superconductiong coil provides a 0.52 T solenoidal magnetic field.

The drift chamber [3] is a 3 m long and 4 m in diameter cylinder closed by spherical endplates, with about 52000 wires disposed on 58 concentrical

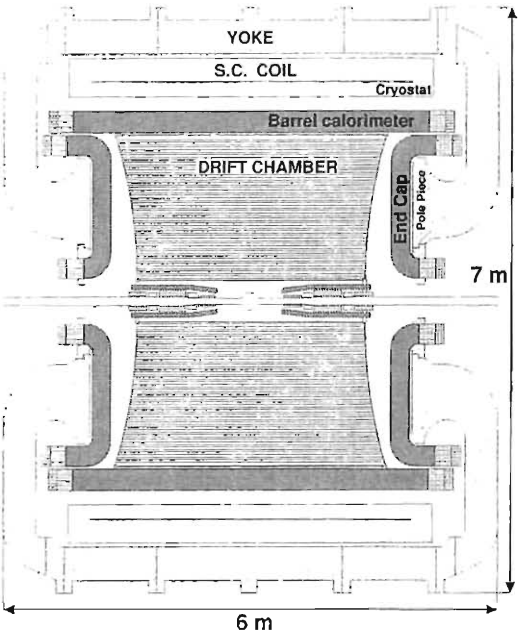

Figure 1: *Schematic view of the KLOE detector.*

layers and strung with a stero angle in an *all stereo* configuration. In order to minimize multiple scattering and K_L regeneration and to maximize detection efficiency of low energy photons, the chamber is operated with a 90% helium - 10% isobutane gas mixture, while its walls are made of light materials (mostly carbon fiber composites). The momentum resolution for tracks at large polar angle is $\sigma_p/p \leq 0.4\%$, the spatial resolutions are $\sigma_{r,\phi} \approx 150\mu m$ and $\sigma_z \approx 2mm$.

The calorimeter [4] is a fine sampling lead-scintillating fiber one, composed by 24 barrel modules and 2x32 end modules, with photomultiplier readout at both sides. Module thickness is 23 cm ($\sim 15X_0$) and the total solid angle coverage is 98% . The energy resolution, as measured using $e^+e^- \rightarrow e^+e^-\gamma$ events, is $\sigma_E/E = 5.7\%/\sqrt{E(GeV)}$. The intrinsic time resolution, as measured using $e^+e^- \rightarrow e^+e^-\gamma$ and $e^+e^- \rightarrow 2\gamma$ events, is $\sigma_t = 54\,ps/\sqrt{E(GeV)} \oplus 50\,ps$. Two smaller calorimeters, QCAL [5], made with lead and scintillating tiles are wrapped around the low beta quadrupoles to maximize the hermeticity.

3 K_S decays

The presence of a K_S is tagged by identifying the interactions of the companion K_L in the calorimeter. Approximately 30% of the K_L's produced in $\phi \to K_S K_L$ events reaches the calorimeter before decaying and interacts therein. Such an interaction, referred to as K_L *crash*, has a very clear signature consisting of a high energy ($E > 200\,MeV$) cluster in the calorimeter, not associable to any charged particle detected in the event, which is delayed by about $30\,ns$ wrt all other clusters, due to K_L small velocity ($\beta \sim 0.22$). The cluster position, exploiting the ϕ decay kinematics, allows to infer the momentum of the K_S. Moreover about 40% of the K_L crashes independently satisfy trigger requirements, thus facilitating trigger efficiency studies.

3.1 $\mathrm{BR}(K_S \to \pi^+\pi^-(\gamma))/\mathrm{BR}(K_S \to \pi^0\pi^0)$

This ratio is the first part of the famous double ratio used to measure $\Re(\epsilon'/\epsilon)$.

$K_S \to \pi^+\pi^-$ decays are identified, in the sample tagged by K_L crash, by requiring the presence of two oppositely charged tracks, originating from the interaction region and satisfying loose cuts in momentum p and polar angle θ. Such cuts define the acceptance for the decay, which is evaluated using Monte Carlo simulation (MC), while the single track reconstruction efficiency is evaluated directly from subsamples of $K_S \to \pi^+\pi^-$ events, in (p, θ) bins. The ratio of data and MC efficiency is found to be constant over all the acceptance region, and MC efficiency is scaled accordingly. The previous selection includes also $K_S \to \pi^+\pi^-\gamma$ events, with an efficiency decreasing with increasing E_γ (or with increasing $\pi^+\pi^-$ invariant mass). Such efficiency is obtained from simulation down to $20\,MeV$ photons, extrapolated to $E_\gamma = 0$ and folded with the theoretical photon spectrum [11] to obtain the overall efficiency. No threshold is applied to E_γ.

$K_S \to \pi^0\pi^0$ decays are selected (in the same K_L tagged sample) by requiring the presence of at least 3 prompt neutral clusters in the calorimeter. A cluster is defined to be prompt when $|T_{cl} - R/c| < 5\sigma_t$, where T_{cl} is the cluster time of flight, R is the calorimeter radius and σ_t is the measured time resolution. Loose cuts in energy and polar angle are applied to each cluster, thus defining the acceptance for the decay, which is then obtained from simulation. The photon detection efficiency is evaluated using $\phi \to \pi^+\pi^-\pi^0$ events, in which

one photon and the two pions tracks are used to determine the kinematics of the remaining photon, which is then searched for.

The trigger efficiency is evaluated as the combined probability of the K_S decay and of the K_L-crash to satisfy the trigger condition. Events in which the K_L-crash alone is enough to satisfy the trigger are used to estimate the trigger probability of the K_S decay, and vice versa. Using the 17 pb^{-1} sample of data collected in year 2000, the following result is obtained [7]

$$\frac{\Gamma(K_S \to \pi^+\pi^-(\gamma))}{\Gamma(K_S \to \pi^0\pi^0)} = 2.239 \pm 0.003_{stat} \pm 0.015_{syst}. \qquad (1)$$

This measurement has the best statistical significance [12] ever reached. It is also the first that takes fully into account the emission of a photon. The ratio in (1) can be expressed in terms of the transition amplitudes between states of $\Delta I = 0$ (A_0) and $\Delta I = 2$ (A_2), and of the difference between their phase shifts $\delta_2 - \delta_0$. Predictions form chiral perturbation theory [13] give $\delta_2 - \delta_0 = (45 \pm 6)°$, while $\pi\pi$ scattering [14] provides an estimate of $(47.7 \pm 1.5)°$. If it is assumed $(A_0/A_2)^2 = (3\tau_S/4\tau)BR(K^\pm \to \pi^\pm\pi^0)^{-1} - 1 = (22.2 \pm 0.07)^2$, the PDG value for $\Gamma(K_S \to \pi^+\pi^-)/\Gamma(K_S \to \pi^0\pi^0)$ yields $\delta_2 - \delta_0 = (56.7 \pm 3.8)°$, while using the present KLOE measurement we obtain $\delta_2 - \delta_0 = (48 \pm 3)°$.

3.2 BR($K_S \to \pi^\pm e^\mp \bar{\nu}(\nu)$)

Assuming CPT conservation and the $\Delta S = \Delta Q$ rule, the K_S and K_L partial widths for the K_{e3} decay must be equal [15], and the corresponding K_S branching ratio can be easily obtained from that of the K_L. KLOE has performed a direct measurement of this K_S branching ratio [6] using the year 2000 data sample. The update of such measurement with 2001 data is presented here.

$K_S \to \pi e \nu$ events are selected, in the K_L-crash tagged sample, by requiring the presence of two oppositely charged tracks which form a vertex in the interaction region. Loose momentum and angular cuts are applied, and the vertex invariant mass, evaluated in the hypothesis that both tracks belong to pions, is required to be smaller than 490 MeV, thus rejecting 95% of the $K_S \to \pi^+\pi^-$ decays. Vertex reconstruction and preselection efficiencies are evaluated by MC.

The $K_S \to \pi e \nu$ decays are identified and the π/e assignement is made by means of the time of flight of the two tracks, which are then both required to

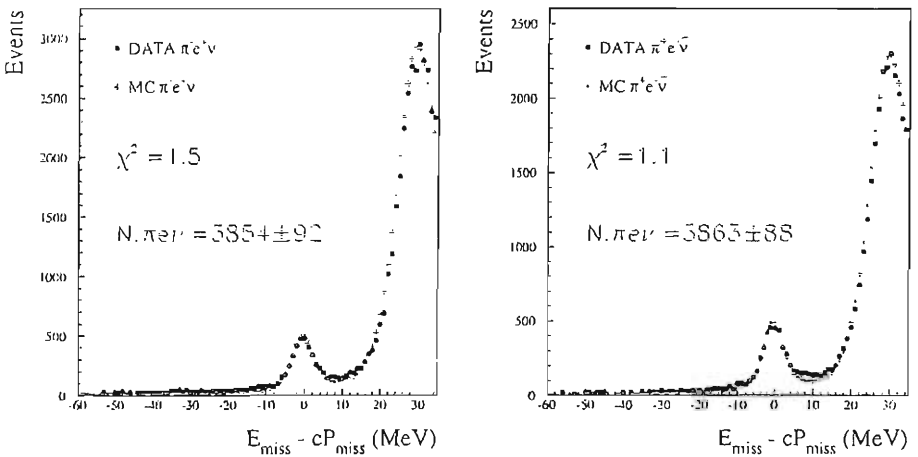

Figure 2: $E_{miss} - P_{miss}$ distribution for $K_S \to \pi e \nu$ candidates. Solid markers represent data, crosses are the MC based fit.

be associated to a calorimeter cluster. For each track the difference $\delta_t(m) = t_{cl} - L/\beta(m)$ is computed, where t_{cl} is the time of the associated cluster, L is the measured track length and $\beta(m)$ is the particle velocity obtained from the measured momentum with a mass hypotesis $m = m_e$ or $m = m_\pi$. In order to avoid any systematics related to the determination af the absolute timing of the event T_0, the selection is made on the difference $\delta_{t,ab} = \delta_t(m_a)_1 - \delta_t(m_b)_2$, where mass hypothesis a (b) is used for track 1 (2). For the correct mass assignement we expect $\delta_{t,ab} \sim 0$, therefore a cut is applied at $\delta t, ab < 1\,ns$. The π/e identification efficiency is measured in a sample of $K_L \to \pi e \nu$ in which the K_L decays near the interaction region. Such a sample can be selected with high purity (99.7%) just by means of kinematics, without using calorimeter times. The track-to-cluster association efficiency is measured both in the K_L-tagged

$K_S \to \pi^+\pi^-$ sample and in a $\phi \to \pi^+\pi^-\pi^0$ sample. In all such topologies the events are reconstructed independently on the presence or absence of a calorimeter cluster from one of the tracks. The overall efficiency to detect a $K_S \to \pi e\nu$ decays is 0.208 ± 0.004.

In fig.2 it is shown the distribution of the selected events in $E_{miss} - P_{miss}$ (the neutrino energy and momentum, if the mass assignement is correct) for the two possible charge states, obtained using 170 pb^{-1} collected in 2001 (solid markers). Signal events are included in the peak around zero, while the residual $K_S \to \pi^+\pi^-$ background shows up in the positive region. The number of signal events in the distribution is obtained from a fit, shown in the figure with crosses, which uses the MC distributions for signal and background having as a free parameter their independent normalizations. The fit yelds $N_{\pi^+e^-\bar{\nu}} = 3863 \pm 88$, $N_{\pi^-e^+\nu} = 3854 \pm 92$, and $N_{\pi^\pm e^\mp \nu(\bar{\nu})} = 7732 \pm 127$ for the sum of the two distributions. By normalizing these numbers to the number of $K_S \to \pi^+\pi^-$ in the same data sets we get the preliminary KLOE results:

$$\begin{array}{ll} BR(K_S \to \pi^+e^-\bar{\nu}) & = (3.44 \pm 0.09 \pm 0.06) \cdot 10^{-4} \\ BR(K_S \to \pi^-e^+\nu) & = (3.31 \pm 0.08 \pm 0.05) \cdot 10^{-4} \\ BR(K_S \to \pi^\pm e^\mp \nu(\bar{\nu})) & = (6.76 \pm 0.12 \pm 0.10) \cdot 10^{-4} \end{array} \qquad (2)$$

On the basis of such results it is possible to build the K_S semileptonic charge asimmetry $A_S = (\Gamma_S^+ - \Gamma_S^-)/(\Gamma_S^+ + \Gamma_S^-)$, where $\Gamma_S^{+(-)}$ are the partial decay widths of the K_S into $\pi^{+(-)}e^{-(+)}\nu$. When CPT invariance holds, A_S is equal to the corresponding K_L asimmetry A_L [15]. KLOE has performed the first measurement of A_S ever done, obtaining the following preliminary result

$$A_S = (1.9 \pm 1.7_{stat} \pm 0.6_{syst}) \cdot 10^{-2} \qquad (3)$$

which compares well with the present (much more precise) A_L measurement [16]. It is also possible to test the $\Delta S = \Delta Q$ rule, assuming the validity of CPT invariance. The relevant parameter for such test is $\Re(x^+) \approx \langle \pi^- e^+ \nu | H_{weak} | \bar{K}^0 \rangle / \langle \pi^- e^+ \nu | H_{weak} | K^0 \rangle$ [15], which can be extracted from the K_S and K_L semileptonic decay partial amplitudes: $\Gamma_S^{semil}/\Gamma_L^{semil} = 1 + 4\Re(x^+)$. The present KLOE measurement of $BR(K_S \to \pi e\nu)$ yields:

$$\Re(x^+) = (2.2 \pm 5.3_{stat} \pm 3.5_{syst}) \cdot 10^{-3} \qquad (4)$$

in good agrement with the previous measurement performed by CPLEAR [17].

4 K_L decays

The presence of a K_L is tagged by identifying the decay $K_S \to \pi^+\pi^-$. Such events are easily selected by requiring two oppositely charged tracks which form a vertex laying in cylindrical fiducial volume centered in the interaction region, having radius of $4\,cm$ and length of $16\,cm$. No other tracks must be connected to the vertex, and loose cuts are applied to its total momentum and invariant mass. The measured K_S momentum provides a very good estimate of the K_L one, with an angular resolution of $\sim 1°$ and a momentum resolution of $\sim 2\,MeV$. The overall tag efficiency is about 85%.

4.1 $\mathrm{BR}(K_L \to \gamma\gamma)/\mathrm{BR}(K_L \to 3\pi^0)$

A measurement of the $K_L \to \gamma\gamma$ decay rate provides interesting tests of chiral perturbation theory and can be used as a constraint for the calculation of the $K_L \to \mu^+\mu^-$ decay rate. KLOE has performed this measurement using a sample of $362\,\mathrm{pb}^{-1}$ collected during 2001 and 2002 [18]. K_L decays are searched for in a fiducial volume defined by $30\,cm < r_t < 170\,cm$ and $|z| < 140\,cm$ (r_t being the transverse decay coordinate and z the longitudinal one). About 31.5% of the K_L decay in such a volume. The position of the K_L neutral decay vertex can be determined by each of the photons emitted in the decay, using the flight direction of the K_L (provided by the K_S) and the position and time of the photon cluster on the calorimeter. The final value of the K_L decay length L_K is obtained from an energy weighted average of the $L_{K,i}$ determined by each individual photon. The accuracy of this method is tested in $K_L \to \pi^+\pi^-\pi^0$ events by comparing neutral and charged vertex positions, and its resolution is evaluated, using the neutral decay events themselves, to be $\sim 2\,cm$ with a sligth dependence on the K_L decay length. In this analysis it is crucial to identify correctly the bunch crossing that originated the event. This is done by identifying one of the two pions produced by the K_S decay and by measuring its track length l_π, momentum and time of flight of the associated calorimeter cluster t_{cl}. By requiring $|l_\pi/\beta_\pi - t_{cl}| < 2\,ns$ for at least one of the K_S pions, the probability of correct bunch crossing identification becomes $(99.4 \pm 0.1)\%$, as measured by comparing charged and neutral vertex positions in a $K_L \to \pi^+\pi^-\pi^0$ sample.

$K_L \to \pi^0\pi^0\pi^0$ decays are selected by requiring the presence of at least

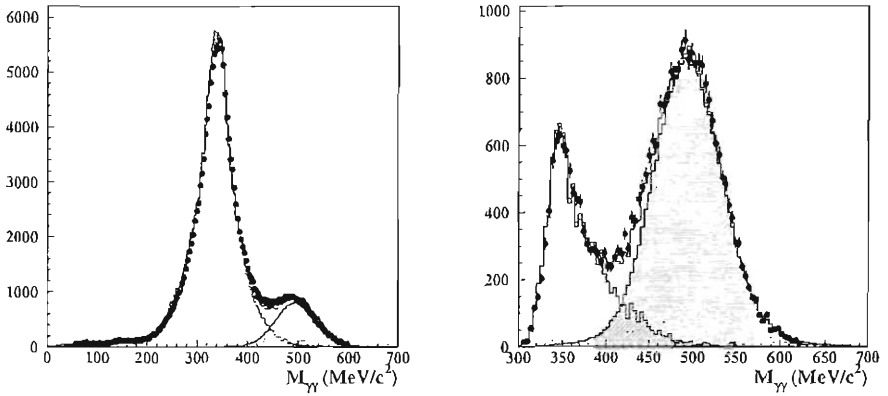

Figure 3: $M_{\gamma\gamma}$ distribution before (left) and after (right) the $K_L \to \gamma\gamma$ final selection (E' and α cuts). Dots are data, histograms are MC (full, signal and background).

3 calorimeter clusters not associated to any track, with energy larger than $20\,MeV$, distance from any other cluster larger than $40\,cm$, and yielding L_K in the fiducial volume, with $|L_{K,i} - L_K| < 4\sigma_{L_K}$. The MC estimated selection efficiency is (99.80± 0.01)% . Only events with 3 and 4 clusters are contaminated by background, as indicated by a data-MC comparison of the total energy distributions. The background originates from $K_L \to \pi^+\pi^-$ events and by misreconstructed $K_L \to \pi^+\pi^-\pi^0$ decays. In order to reject it, tighter selections are applied on energy and position of the clusters in the 3 and 4 clusters sample, and events with tracks not associated to the K_S decay and with first hit in the drift chamber nearer than $30\,cm$ to the K_L vertex are vetoed. After all cuts the 3 and 4 clusters samples contribute only to less than 8% of the total statistics, with a residual background contamination, evaluated by MC, of (18.6±1.0)%

in the 3 clusters sample, and (7.0±0.2)% in the 4 clusters sample. The trigger efficiency, measured in data, is (99.88±0.04)%. After background subtraction and efficiency correction, the measured number of $K_L \to \pi^0\pi^0\pi^0$ decays in the data sample is $N_{3\pi^0} = 9,802,200 \cdot (1 \pm 0.0010 \pm 0.0016)$.

$K_L \to \gamma\gamma$ are first preselected by requiring the presence of at least 2 calorimeter clusters not associated to tracks, with energy $E > 100\,MeV$. For the two most energetic such clusters, loose requirements are made on total energy, relative angle, time difference and compatibility of L_K determination. The preselection efficiency is 89.5% for signal events, evaluated by MC. In the left part of fig.3 the distribution of the invariant mass of the couples of clusters surviving the preselection is shown, together with the MC expectations for signal and background. At this stage a peak around M_K is already present, but not yet resolved from background. To enhance it, the photon energies are computed with better accuracy assuming $E_\gamma = M_K/2$ in the K_L center of mass and boosting them to the laboratory. The boost is obtained from $p\tilde{K}_L = \tilde{p_\phi} - p\tilde{K}_S$ and from clusters and K_L decay vertex coordinates. The so computed total energy in the laboratory, E', is required to be $|E' - 510| < 5\sigma'$, where $\sigma' = 1.8\,MeV$ was evaluated from a fit to the experimental E' distribution. Moreover the angle α between $p\tilde{K}_L$ and the laboratory total $\gamma\gamma$ momentum (obtained from the recomputed photon energies and their clusters positions) is required to be smaller than 15°. The final $M_{\gamma\gamma}$ distribution is shown in the right part of fig.3. The selection efficiency was evaluated using a sample of $K_L \to \gamma\gamma$ with high purity (S/B$\sim 10^3$) selected by applying hard, uncorrelated cuts on other kinematic variables [18], and was found to be $(81.0 \pm 0.3_{stat} \pm 0.5_{syst})\%$. The trigger efficiency was evaluated from data as for $K_L \to 3\pi^0$ decays. The number of $K_L \to \gamma\gamma$ decays was then obtained from a fit to the $M_{\gamma\gamma}$ distribution using MC shapes for signal and background. After correcting for the efficiencies we get $N_{2\gamma} = 27,375 \cdot (1 \pm 0.0076 \pm 0.0081)$, which yields

$$\frac{\Gamma(K_L \to \gamma\gamma)}{\Gamma(K_L \to \pi^0\pi^0\pi^0)} = (2.793 \pm 0.022_{stat} \pm 0.024_{syst}) \cdot 10^{-3} \qquad (5)$$

in good agreement with the recent NA48 measurement [20]. Using the known value of $\mathrm{BR}(K_L \to \pi^0\pi^0\pi^0)$ and τ_L we get $\Gamma(K_L \to \gamma\gamma) = (7.5 \pm 0.1) \cdot 10^{-12} eV$, which is in agreement with the $\mathcal{O}(p^6)$ predisctions of ChPT provided the value of the pseudoscalar mixing angle is close to our recent measurement [8].

5 Study of the decay $\phi \to \pi^+\pi^-\pi^0$

The decay of the ϕ meson to $\pi^+\pi^-\pi^0$ is dominated by the $\rho\pi$ intermediate states $\rho^+\pi^-$, $\rho^-\pi^+$, $\rho^0\pi^0$ with equal amplitudes. Additional contributions to $e^+e^- \to \pi^+\pi^-\pi^0$ are the so called "direct term" and $e^+e^- \to \omega\pi$ ($\omega \to \pi^+\pi^-$). Taking into account all contributions, a fit to the Dalitz plot of the process allows to determine masses and widths of the three ρ charge states [19]. CPT invariance requires equality of masses and widths of ρ^+ and ρ^-, while isospin-violating electromagnetic effects may originate possible differences in mass or width between ρ^0 and $\rho^\pm$. Starting from a 16 pb^{-1} data sample collected in year 2000, events are selected by requiring the presence of two non collinear tracks, with opposite sign curvature and polar angle $\theta > 40°$. The acollinearity cut is $\Delta\theta < 175°$, and rejects $e^+e^-\gamma$ events without affecting the signal. Then imposing the conservation of the ϕ meson energy and momentum, the missing mass M_{miss} is computed, and required to be within $20\,MeV$ of the π^0 mass. This corresponds to an effective cut of $< 20\,MeV$ on the total ISR radiated energy. Finally two neutral clusters in the calorimeter are required, with $E > 10\,MeV$ and arrival time compatible with that of a photon emitted in the interaction point. The two photon opening angle in the π^0 rest frame must have $cos\theta_{\gamma\gamma} < -0.98$. After such selection the residual background contrinution is less tham 10^{-5}, while the efficiency for the signal varies between 20% and 30% over the kinematic range of the process.

Table 1: Fitted results for ρ masses and widths (in MeV). See text for details.

parameter	fit(a)	fit(b)	fit(c)
M_{ρ^0}	$775.5 \pm 0.5 \pm 0.3$	$775.9 \pm 0.5 \pm 0.5$	$775.9 \pm 0.6 \pm 0.5$
M_{ρ^+}		$775.5 \pm 0.5 \pm 0.4$	$776.3 \pm 0.6 \pm 0.7$
M_{ρ^-}			$774.8 \pm 0.6 \pm 0.4$
Γ_{ρ^0}	$143.9 \pm 1.3 \pm 1.1$	$147.3 \pm 1.5 \pm 0.7$	$147.4 \pm 1.5 \pm 0.7$
Γ_{ρ^+}		$143.7 \pm 1.3 \pm 1.2$	$144.7 \pm 1.4 \pm 1.2$
Γ_{ρ^-}			$142.9 \pm 1.3 \pm 1.4$

The Dalitz plot is built up as a function of the two variables $x = T^+ - T^-$ and $y = T^0$, where T^{+-0} are the kinetic energies of π^{+-0} in the center

of mass system. The resolution on x and y is about $1\,MeV$ over the full kinematic range. The Dalitz plot is divided in $8.75 \times 8.75\,MeV^2$ bins, for a total of 1874 bins within the kinematic boundary. The trigger and selection efficiency have been evaluated as a function of x and y using MC simulation with corrections based on data control samples. In particular the the low energy photon detection efficiency has been obtained from $e^+e^-\gamma$ events. The calibration of the momentum scale is checked across the entire kinematic range by comparing the measured M_{miss} with the π^0 mass. Three fits have been performed to the Dalitz plot density distribution: a) a fit assuming CPT and isospin invariance, *i.e.* $M_{\rho^0} = M_{\rho^+} = M_{\rho^-}$ and $\Gamma_{\rho^0} = \Gamma_{\rho^+} = \Gamma_{\rho^-}$; b) a fit assuming only CPT invariance, *i.e.* $M_{\rho^+} = M_{\rho^-}$ and $\Gamma_{\rho^+} = \Gamma_{\rho^-}$; c) a fit without limitations on masses and widths. The fit results are shown in table 1. Systematic uncertainties come mainly from the fit stability with respect to the selection cuts and from the absolute momentum calibration. The ρ masses are significantly larger and the widths smaller than the PDG averages [12], but are close to the most recent measurements. The direct term and $\omega\pi$ contributions were also included in the fits, and found to be significantly different from zero. In particular the visible cross section for the process $e^+e^- \to \omega\pi^0 \to \pi^+\pi^-\pi^0$ at $\sqrt{s} = 1019.4\,MeV$ was found to be $92 \pm 15\,pb$.

6 ϕ radiative decays

The study of ϕ meson radiative decays is one of the design goals of KLOE. Three main measurements have been performed with the year 2000 data sample: the BR($\phi \to \eta'\gamma$) [8], the BR($\phi \to f_0\gamma$) [9] and the BR($\phi \to a_0\gamma$) [10]. All such measurements are being updated with larger data sets.

The $\phi \to \eta'\gamma$ decay is identified in the channel in which $\eta' \to \eta\pi^+\pi^-$ and $\eta \to \gamma\gamma$. The $\phi \to \eta\gamma$ decay is identified in the channel in which $\eta \to \pi^+\pi^-\pi^0$. In both cases the final state is $\pi^+\pi^-\gamma\gamma\gamma$, so that many systematics effects cancel out in the ratio $BR(\phi \to \eta'\gamma)/BR(\phi \to \eta\gamma)$. Events with two oppositely charged tracks and three prompt clusters are selected. Background from $\phi \to K_S K_L$ and $\phi \to \pi^+\pi^-\pi^0$ are rejected by simple cuts on particles' energy and momentum. $\eta'\gamma$ and $\eta\gamma$ decays are disentangled by a cut on the E_1, E_2 plane, the energies of the two most energetic photons. The number of $\eta'\gamma$ events is then obtained from a fit to the reconstructed η' invariant mass: in the year 2000 sample we have $124 \pm 12 \pm 5$ events in the peak, and in the 2001 sample

we have already more than 700 events in the peak. The published [8] result $BR(\phi \to \eta'\gamma)/BR(\phi \to \eta\gamma) = (4.70 \pm 0.47 \pm 0.31) \cdot 10^{-3}$ allows to infer the vaue of the pseudoscalar mixing angle: in the flavour basis $\varphi_P = (41.8^{+1.9}_{-1.6})^\circ$, and in the singlet-octet basis $\vartheta_P = (12.9^{+1.9}_{-1.6})^\circ$. Using the PDG value for $BR(\phi \to \eta\gamma)$ we get $BR(\phi \to \eta'\gamma = (6.10 \pm 0.61 \pm 0.43) \cdot 10^{-5}$, which is compatible with zero gluonium contribution to the η' state.

The $\phi \to f_0\gamma$ and $\phi \to a_0\gamma$ are identified in KLOE by their five photons final states ($f_0 \to \pi^0\pi^0$ and $a_0 \to \eta\pi^0$, $\eta \to \gamma\gamma$). Various backgrounds are present, the main ones coming from $\phi \to \rho^0\pi^0$ and from $e^+e^- \to \omega\pi^0$, which are rejected by means of kinematic fits asumin various event topologies. Cuts are applied to the reconstructed masses of the intermediate particles and on the χ^2 probability of the fits. Published KLOE measurements are $BR(\phi \to \pi^0\pi^0\gamma) = (1.09 \pm 0.03 \pm 0.05) \cdot 10^{-4}$ and $BR(\phi \to \eta\pi^0\gamma) = (1.08 \pm 0.05 \pm 0.06) \cdot 10^{-4}$. The analyses of larger data samples are being performed and are in agreement with the present results. Finally, the mass spectra of the two processes are sensitive to the nature of f_0 and a_0: the spectra measured by KLOE are compatible with a $qq\bar{q}\bar{q}$ nature for the f_0, while for the a_0 conclusions cannot be drawn up to now.

7 Hadronic cross section

The recent measurements of a_μ by the E821 collaboration [21] has stimulated new interest in the measurement of the cross section of $e^+e^- \to hadrons$ at low energy. In fact, the hadronic contribution to a_μ at low energy cannot be computed, but is related to $\sigma(e^+e^- \to hadrons)$ via a dispersion integral. The process $e^+e^- \to \pi^+\pi^-$, with $M_{\pi\pi} < 1\,GeV$ accounts for about 70% of δa_μ^{had} and for 12% of the hadronic corrections to $\alpha(M_Z)$. KLOE can measure $d\sigma(e^+e^- \to \pi^+\pi^-/dM^2_{\pi\pi}$ by studying $e^+e^- \to \pi^+\pi^-\gamma$ events in which the photon is radiated in the initial state. This has the advantage that sistematic erors due to luminosity and beam energy enter into the measurement only once, and not for each point as in an energy scan, but on the other hand it requires theoretic understanding of ISR to better than 1% . Events are selected requiring two oppositely charged tracks, with polar angle $\theta < 40^\circ$ and forming a vertex near the interaction region. To enhance ISR, with respect to FSR and $\phi \to \pi^+\pi^-\pi^0$ background, only small angle photons are accepted. As the forward and backward angles within a cone of 15° are obscured by

the QCALs, photons are not required to be detected, but the $\pi^+\pi^-$ missing momentum is required to have polar angle smaller than 15°. Moreover at least one of the two tracks has to be identified as a pion, on the basis of time of flight and shower shape in the calorimeter. Selection efficiency is better than 96%. Using a 73 pb^{-1} data sample, collected in year 2001, KLOE has now a $d\sigma(e^+e^- \to \pi^+\pi^-)/dM^2_{\pi\pi}$ distribution, for $M^2_{\pi\pi}$ ranging from 0.2 to 1 GeV^2, with statistical error $\sim$ 1% in each bin. In the coming months KLOE will perform the analysis on a sample twice as large and reduce the systematic errors to below the 1% level.

8 Acknowledgements

It is a pleasure to acknowledge the precious help of A. Passeri in the preparation of this presentation and the warm hospitality of the 2003 edition of the La Thuile conference.

*The KLOE Collaboration: A. Aloisio, F. Ambrosino, A. Antonelli, M. Antonelli, C. Bacci, G. Bencivenni, S. Bertolucci, C. Bini, C. Bloise, V. Bocci, F. Bossi, P. Branchini, S. A. Bulychjov, R. Caloi, P. Campana, G. Capon, T. Capussela, G. Carboni, G. Cataldi, F. Ceradini, F. Cervelli, F. Cevenini, G. Chiefari, P. Ciambrone, S. Conetti, E. De Lucia, P. De Simone, G. De Zorzi, S. Dell'Agnello, A. Denig, A. Di Domenico, C. Di Donato, S. Di Falco, B. Di Micco, A. Doria, M. Dreucci, O. Erriquez, A. Farilla, G. Felici, A. Ferrari, M. L. Ferrer, G. Finocchiaro, C. Forti, A. Franceschi, P. Franzini, C. Gatti, P. Gauzzi, S. Giovannella, E. Gorini, E. Graziani, M. Incagli, W. Kluge, V. Kulikov, F. Lacava, G. Lanfranchi, J. Lee-Franzini, D. Leone, F. Lu, M. Martemianov, M. Matsyuk, W. Mei, L. Merola, R. Messi, S. Miscetti, M. Moulson, S. Müller, F. Murtas, M. Napolitano, A. Nedosekin, F. Nguyen, M. Palutan, E. Pasqualucci, L. Passalacqua, A. Passeri, V. Patera, F. Perfetto, E. Petrolo, L. Pontecorvo, M. Primavera, F. Ruggieri, P. Santangelo, E. Santovetti, G. Saracino, R. D. Schamberger, B. Sciascia, A. Sciubba, F. Scuri, I. Sfiligoi, A. Sibidanov, T. Spadaro, E. Spiriti, M. Testa, L. Tortora, P. Valente, B. Valeriani, G. Venanzoni, S. Veneziano, A. Ventura, S. Ventura, R. Versaci, I. Villella, G. Xu.

9 Note added in proof

At the summer 2003 Lepton-Photon Symposium KLOE presented [22] the measurement of the hadronic cross section $\sigma(e^+e^- \to \pi^+\pi^-)$ using radiative returns. From the data the contribution to the muon anomaly a_μ was inferred, which was found to be (in 10^{-10} units):

$$\delta a_\mu^{had} = 374.1 \pm 1.1_{stat} \pm 5.2_{syst} \pm 2.6_{theo} \, {}^{+7.5}_{-0.0}|_{FSR} \qquad (6)$$

in agreement with the (updated) determination from the CMD-2 Collaboration.

References

1. S.Guiducci et al., Proceedings of PAC'99, New York, March 1999.
2. The KLOE Collaboration, KLOE: a general purpose detector for DAΦNE, LNF-92/019 (IR) (1992).
3. M.Adinolfi *et al.*, Nucl.Instr.Meth. **A488** 1-23 (2002)
4. M.Adinolfi *et al.*, Nucl.Instr.Meth. **A482** 363-385 (2002)
5. M.Adinolfi *et al.*, Nucl.Instr.Meth. **A483** 649 (2002)
6. The KLOE Collaboration, Phys.Lett. **B535** 37 (2002)
7. The KLOE Collaboration, Phys.Lett. **B538** 21-26 (2002)
8. The KLOE Collaboration, Phys.Lett. **B541** 45-51 (2002)
9. The KLOE Collaboration, Phys.Lett. **B537** 21 (2002)
10. The KLOE Collaboration, Phys.Lett. **B536** 209 (2002)
11. V.Cirigliano *et al.*, Eur.Phys.J. **C18** (2000) 83
12. Particle Data Group, Phyical Review **D66** (2002) 1.
13. J.Gasser, U.G.Meissner, Proceeding of the Lepton Photon Symposium, Geneva 1991, vol.1, 202-204.
14. G.Colangelo, J.Gasser, H.Leutwyler, Nucl.Phys. **B603** (2001) 125-179
15. L.Maiani, The second DAΦNE physics handbook (Frascati 1992), vol.1, 21
16. A.Alavi-Harati *et al.*, Phys.Rev.Lett. **88** (2002) 181601
17. A.Angelopoulos *et al.*, Eur.Phys.J. **C22** (2001) 55-79
18. The KLOE Collaboration, hep-ex/0305035, KLOE note n.186, 4/03
19. The KLOE Collaboration, Phys.Lett. **B561** (2003) 55
20. A.Lai *et al.*, Phys.Lett.**B551** (2003) 7
21. H.N.Brown *et al.*, Phys.Rev.Lett. **86** (2001) 2227
22. The KLOE Collaboration, hep-ex/0307051, KLOE note n.189, 7/03

COMPASS – STATUS AND PERSPECTIVE

Jörg Pretz
Physikalisches Institut, Universität Bonn
on behalf of the COMPASS collaboration

Abstract

COMPASS (**CO**mmon **M**uon and **P**roton **A**pparatus for **S**tructure and **S**pectroscopy) is a fixed target experiment at CERN studying nucleon spin structure in polarised deep inelastic muon nucleon scattering and hadron spectroscopy using hadron beams [1]. This talk discusses the physics objectives of the muon beam program and gives a status report of the experiment.

1 Introduction: The Nucleon Spin Puzzle

In an intuitive picture the spin of the nucleon is completely carried by its valence quarks. The analysis of axial matrix elements of weak baryon decays shows that this contribution is reduced to about 60%, if the sea quarks are assumed to be unpolarised. It came as a big surprise when deep inelastic scattering (DIS) experiments revealed that the contribution of the quarks to the nucleon spin is even smaller and only 20-30% with a negative strange quark contribution of about -10%. However the interpretation of DIS results is not without ambiguity if the helicity contribution of the gluons to the nucleon spin is large. One of the most interesting open questions in understanding the spin structure of the nucleon is therefore the size of the helicity contribution of gluons, ΔG.

2 The Spin Physics Program

The main goal of the COMPASS experiment is the measurement of the helicity contribution of gluons in the nucleon spin, ΔG. Other measurements discussed in this paper are:

- A flavor decomposition of the quark helicity contributions, $\Delta u_V(x), \Delta d_V(x), \Delta s(x), \ldots$,
- the transverse spin distribution functions $\Delta_T g(x)$.

Up to now most of the experiments focused on inclusive deep inelastic scattering where only the scattered lepton is observed in the final state ($l+N \rightarrow l'+X$). Common to all measurements mentioned above is the observation of part of the hadronic final state:

$$l + N \rightarrow l' + \mathbf{hadrons} + X$$

This so called semi-inclusive process allows a deeper insight in the structure of the nucleon, since it allows us to tag the parton participating in a deep inelastic process. The observation of a π^+ for instance indicates that a u or a $\bar{d}$-quark was struck in the nucleon. The observation of a strange particle indicates that an s-quark participated in the scattering process.

In the following the variables Q^2, x and y have their usual meaning: four momentum transfer, Bjorken variable and the fraction of the beam energy carried by the virtual photon in the target rest frame. z denotes the fraction of the virtual photon energy carried by a hadron in the target rest frame.

2.1 The measurement of ΔG

Tagging of a gluon is more complicated since the photon doesn't couple directly to the gluon. The gluon can participate in a deep inelastic process via the

photon-gluon fusion process ($\gamma^* + g \rightarrow c + \bar{c}$). In the hadronic final state the process manifests itself by the observation of charmed hadrons. This is illustrated in Fig. 1. Since there is no intrinsic charm quark in the proton and

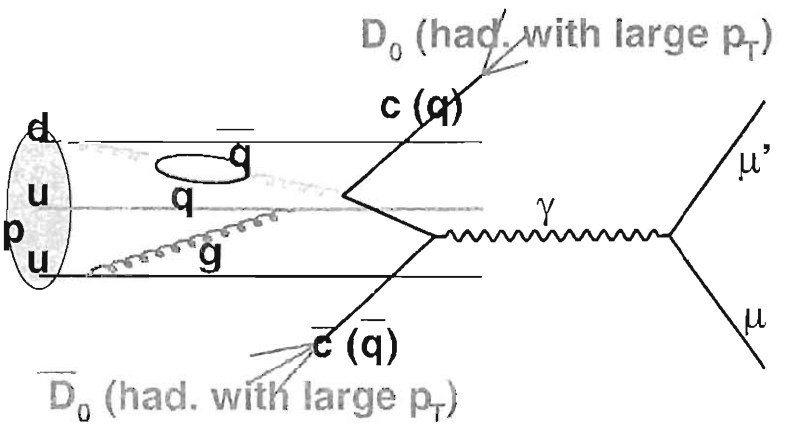

Figure 1: Deep inelastic scattering with a photon gluon fusion process as partonic subprocess.

the production of charm quarks in the fragmentation process is suppressed, the observation of a charmed hadron clearly tags the gluon. On average 1.1 D^0 or $\bar{D}^0$ are produced in the fragmentation of the partonic process $\gamma^* + g \rightarrow c + \bar{c}$. The D^0's can be detected via several decay channels. The most promising one is $D^0 \rightarrow K^- + \pi^+$.

In a leading order process where the photon is directly absorbed by a quark ($\gamma^* + q \rightarrow q$), hadrons are mainly produced along the axis of the virtual photon. In a photon gluon fusion process where light quarks are produced ($\gamma^* + q \rightarrow q + \bar{q}$) the observation of a hadron pair with large transverse momentum, p_T, with respect to the virtual photon tags a gluon as well. This tagging is less clean due to concurrent background processes like the QCD compton ($\gamma^* + q \rightarrow q + g$) which also leads to the creation of hadrons with large transverse momenta.

To allow an interpretation of the data in perturbative QCD the scale in the partonic process has to be larger than ≈ 1 GeV^2. For inclusive processes this scale is simply given by the virtuality of the photon, Q^2. Therefore inclusive experiments focused mainly on the kinematic region $Q^2 > 1$GeV^2. In the two processes to measure ΔG the scale is given by $4m_c^2$ and p_T^2, respectively. Therefore one can exploit the full statistics down to $Q^2 \approx 0$. Since low Q^2 correlates with small scattering angles this is an experimentally challenging

task.

Up to now only the tagging of the gluon was discussed. To measure its helicity distribution one has to measure the double spin asymmetry

$$A^{exp} = \frac{N^{\uparrow\downarrow} - N^{\uparrow\uparrow}}{N^{\uparrow\downarrow} + N^{\uparrow\uparrow}} = P_t P_b f D \frac{\int_{4m_c^2}^{2MEy} \Delta\sigma(s)^{\gamma g \to c\bar{c}} \Delta G(\eta, s) ds}{\int_{4m_c^2}^{2MEy} \sigma(s)^{\gamma g \to c\bar{c}} G(\eta, s) ds} . \quad (1)$$

In this equation $N^{\uparrow\uparrow}(N^{\uparrow\downarrow})$ is the number of events with nucleon and lepton spin parallel (anti-parallel). Events stand for a DIS scattering process with charmed hadron in the final state. $G(\eta, s)$ is the (known) unpolarised gluon distribution function which depends, as $\Delta G(\eta, s)$, on the momentum fraction η and the scale s. $\Delta\sigma(s)^{\gamma g \to c\bar{c}}$ ($\sigma(s)^{\gamma g \to c\bar{c}}$) are the polarised (unpolarised) cross sections of the partonic subprocess. The experimental asymmetry is diluted by the target polarisation, P_t, the beam polarisation, P_b, the dilution factor, f, which is defined as the fraction of polarisable material in the target and the depolarisation factor, D, which describes the polarisation transfer from the lepton to the virtual photon. A^{exp} is of the order of 2-3%.

A similar expression holds for the method with high p_T hadron pairs. But as mentioned above several background processes contribute to the asymmetry as well. They can be computed and subtracted. This leads to a larger systematic error compared to the method with charmed mesons.

2.2 The measurement of $\Delta q(x)$

The measurement of $\Delta q(x)$ can be performed in parallel to the measurement of ΔG. i.e. with longitudinal beam and target polarisation.

The double spin asymmetries of hadrons is a linear combination of all quark helicity distributions:

$$A^h(x, z) = P_t P_b f D \frac{\sum_q e_q^2 \Delta q(x) D_q^h(z)}{\sum_q e_q^2 q(x) D_q^h(z)} \quad q = u, d, s, \bar{u}, \bar{d}, \bar{s}$$

where $q(x)$ are the unpolarised quark distributions and $D_q^h(z)$ the fragmentation functions. Both are known. Thus measuring asymmetries for different hadrons one obtains a system of linear equations which can be solved for the $\Delta q(x)$'s.

2.3 The measurement of $\Delta_T q(x)$

The transverse quark distribution can be accessed via single spin asymmetries when only the target is polarised perpendicular to the beam momentum. The

asymmetry considered in this case is

$$A_T^h = \frac{N^\uparrow(\Phi_S) - N^\downarrow(\Phi_S + \pi)}{N^\uparrow(\Phi_S) + N^\downarrow(\Phi_S + \pi)} = D_{NN}|P_t|f\frac{\sum_q e_q^2 \Delta_T q(x) \Delta_T D_q^h(z)}{e_q^2 \Delta q(x) D_q^h(z)} \cdot \sin(\Phi_H + \Phi_S) \,. \quad (2)$$

$N^\uparrow(N^\downarrow)$ is the number of events with target spin pointing upwards (downwards). Φ_H and Φ_S are the azimuthal angle of the leading hadron and the target spin with respect to the lepton scattering plane. $D_{NN}(y)$ is a depolarisation factor.

3 The COMPASS Experiment

The requirements for the measurements discussed above are

- a polarised high energy lepton beam
- a polarised target
- a spectrometer with particle identification and a large acceptance down to $Q^2 \approx 0$

The COMPASS experiment fulfils these requirements. COMPASS is a fixed target experiment located at the muon beam-line of the CERN-SPS accelerator.

The muon beam energy can be varied between 100 and 200 GeV. The muons originating from a parity violating π-decay are naturally polarised to $P_b \approx -80\%$. The beam intensity is about 2×10^8 muons per spill of 5 s every 14.4 s.

The target is a two cell solid state target polarised by Dynamic Nuclear Polarisation. NH_3 will be used as a proton target. The dilution factor is $f \approx 3/(3+14) = 0.17$. ^{6}LiD serves as a deuteron target. In ^{6}LiD the lithium can be considered as ^{4}He + D so that the dilution factor f is 50%. With 60 cm long target cells the nominal luminosity is $5 \times 10^{32} \mathrm{cm}^{-2}\mathrm{s}^{-1}$.

COMPASS uses a two stage forward spectrometer, shown in Fig. 2. Both stages consist of a bending magnet and particle identification provided by an electro-magnetic and a hadronic calorimeter, a Ring Imaging Cherenkov Counter (RICH) and an iron absorber to identify muons. The magnets have a bending power of 1 Tm (5 Tm). The two RICHs provide a $K - \pi$ separation in the momentum range 3-50 GeV and 20-120 GeV, respectively for the two stages. The overall acceptance of the spectrometer is ± 200 mrad and 1-200 GeV. Tracking is provided by different types of detectors. The beam region is covered by scintillating fiber hodoscopes and silicon detectors. Small area tracking is provided by Micromeagas, Gas Electron Multipliers (GEMs) and MWPCs. For large area tracking drift chambers with a size up to 320×240 cm^2 are used.

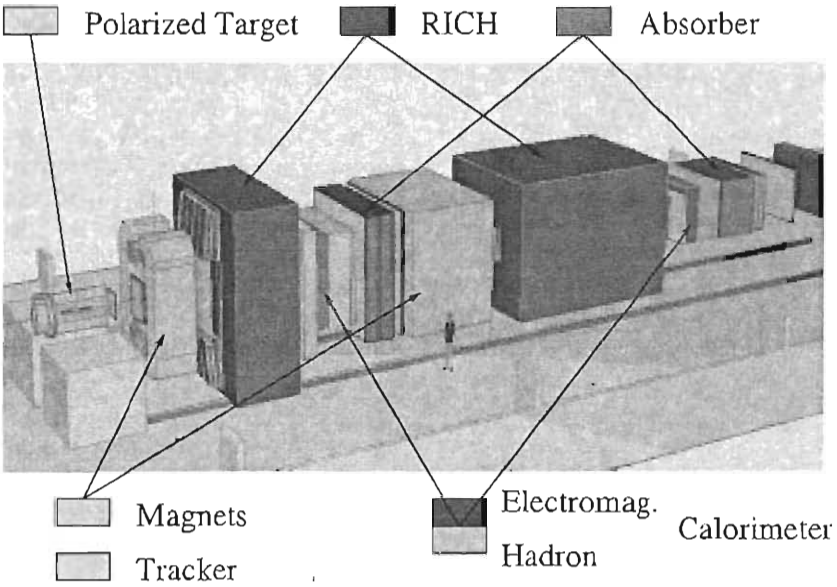

Figure 2: The COMPASS experiment

Among the detectors mentioned above the second RICH and the electromagnetic calorimeters are not yet installed. Their presence is not essential for the measurements discussed here.

Coincidences between two hodoscope planes at different positions along the beam serve as a trigger for the scattered muon. Compared to previous experiments the kinematic range is extended to very low Q^2. This corresponds to a small scattering angle of the muon so that the trigger hodoscopes have to be positioned close to the beam region. To trigger efficiently on these DIS events, a certain energy deposition in the hadron calorimeters is demanded in addition to the coincidence in the two hodoscope planes.

3.1 The 2002 Data Taking

After an engineering run in 2001 COMPASS had its first physics run in 2002. Out of the 100 days of beam time, 76 days could be used to take physics data. The other 24 days were needed for setup and tuning. 80% of the physics data were taken with a longitudinal polarised target the rest with a transversely polarised target. In total 300 TByte of data were collected.

The performances of a few components of the experiment will be discussed. Fig. 3 shows the measurement of the target polarisation as a function of time for the 10 NMR coils, 5 in each target cells. To cancel systematic effects the two target halves are polarised oppositely. The build up time of the polarisation is approximately two days. During the 2002 run target polarisation of about 50% were routinely reached.

In Fig. 4 the reconstructed vertex position along the beam direction is shown. One clearly distinguishes the two target halves. The reduced number of reconstructed vertices in the upstream target half is explained by the absorption of hadrons in the target material. Hadrons are mandatory to find the vertex position since the data is dominated by events where the scattering angle of the muon is small.

Fig. 5 shows the Cherenkov angle measured in the RICH vs. the particle momentum determined by the tracking detectors. Besides the electron and pion ridges a kaon ridge is clearly visible.

3.2 Error Estimates from the 2002 data

In the following statistical error estimates are given for the three physics topics discussed in section 2.

For the measurement of ΔG we anticipated a statistical error of $\delta\Delta G/G = 0.3$ from the method with high p_T hadron pairs. The following cuts were applied to reduce the background:

- $p_T > 0.7\text{GeV}^2$,

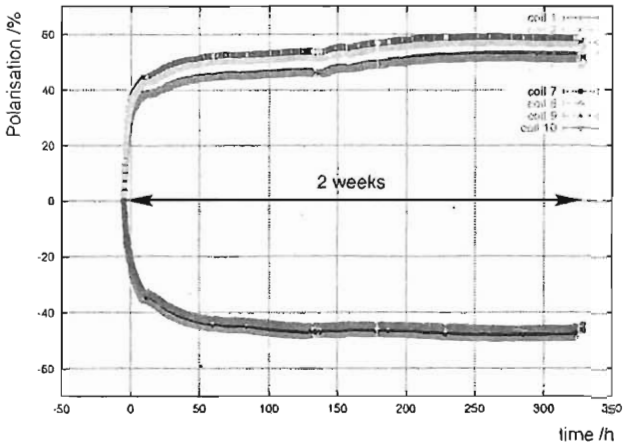

Figure 3: The target polarisation as a function of time measured with 10 NMR coils.

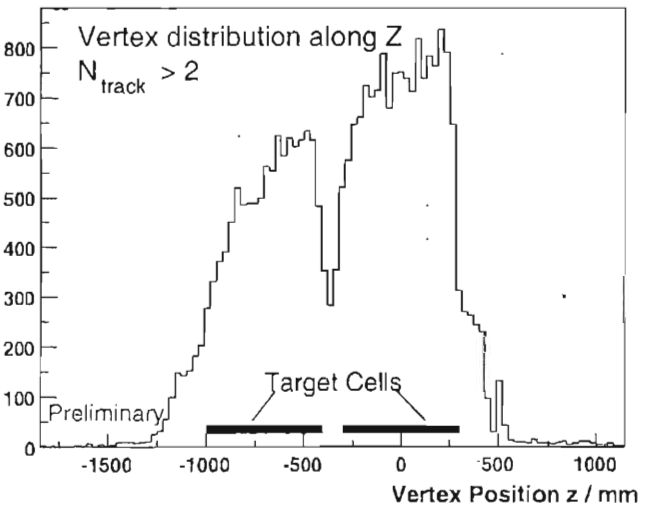

Figure 4: Vertex distribution along the beam direction.

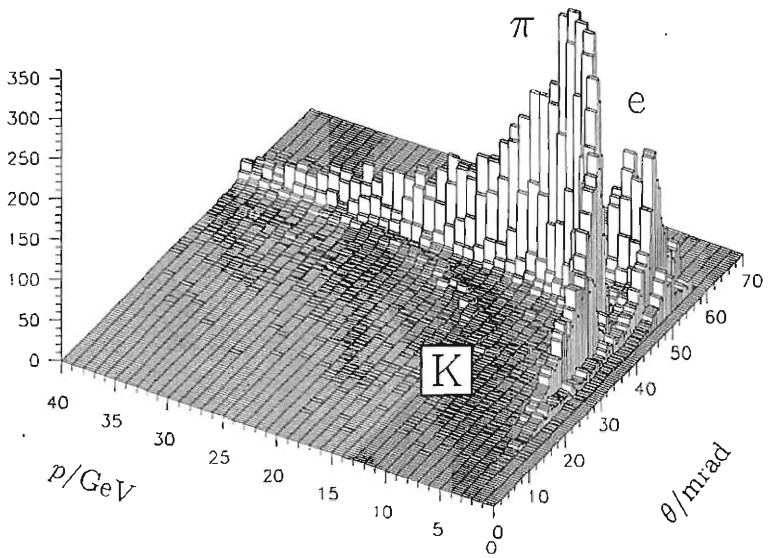

Figure 5: The Cherenkov angle, θ, measured with the RICH vs. the particle momentum, p, determined by tracking.

- $p_{1,T}^2 + p_{2,T}^2 > 2.5\text{GeV}^2$,
- $Q^2 > 1$ GeV^2.

Figs. 6 shows the statistical error estimates on Δs. The inclusive asymmetry and asymmetries from positive, negative hadrons, K^+, K^- and K_s entered this estimate. Cuts on $Q^2 > 1$ GeV^2 and $z > 0.2$ were imposed.

Finally, Fig. 7 shows an error estimate for the transverse polarised quark distributions $\Delta_T q(x)$. The asymmetry A_{UT} shown is a linear combination of the $\Delta_T q(x)$'s:

$$A_{UT} = \frac{\sum_q e_q^2 \Delta_T q(x) \Delta_t D_q^h(z)}{e_q^2 \Delta q(x) D_q^h(z)} .$$

The curve is a model prediction from Efremov.

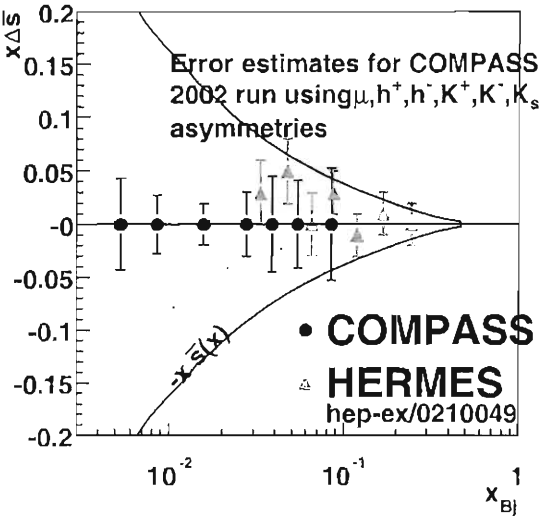

Figure 6: The estimated statistical error on Δs.

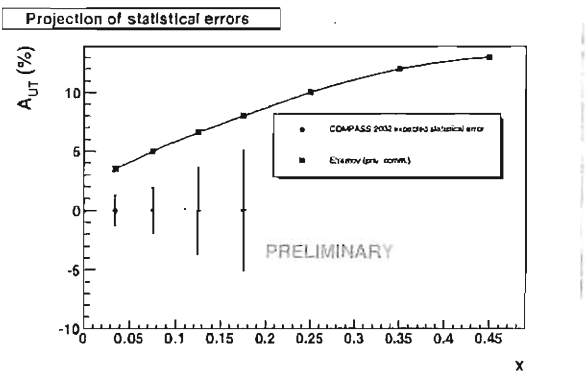

Figure 7: The estimated statistical error on $A_{UT} = \frac{\sum_q e_q^2 \Delta_T q(x) \Delta_t D_q^h(z)}{e_q^2 \Delta q(x) D_q^h(z)}$.

4 The Future

The next steps are the production of the full 2002 data set and the reconstruction of D^0's. The 2003 run started in May. Another run with a muon beam is scheduled for 2004 as well as a first short hadron run. COMPASS plans to continue running after the SPS shutdown in 2005.

References

1. COMPASS proposal, CERN/SPSLC 96-14,SPSLC/P297, 1996

JET STUDIES AT CDF IN RUN 2

Robert Snihur
University College London

Written contribution not received

JET PHYSICS AT LEP AND QCD

I.M. Dremin
Lebedev Physical Institute, Moscow 119991, Russia

Abstract

With the advent of LEP we discovered jets and at its last years we learned a lot about intermediate vector bosons. All that strongly supports our belief in QCD. Jet physics is briefly described in this talk. Experimental results are compared with QCD predictions. It is shown that the perturbative QCD has been able not only to *describe* the existing data but also to *predict* many bright phenomena.

The main process of e^+e^--annihilation at LEP looks like two jets moving in the opposite directions. These jets are considered in QCD as (initiated by quarks and collimated) cascades of consecutive emissions of partons each of which produces observed hadrons due to soft confinement.

1 Early days

Jets were discovered in 1975. Their angular collimation was demonstrated in studies of such kinematical properties as sphericity, spherocity, thrust etc. They show that the transverse momenta are small compared to the total momenta if the proper coordinate axes are chosen. The collimation increases with energy increase.

The jet axes were defined from these characteristics. It has been shown that the angular (θ) distribution of jet axes in e^+e^--annihilation follows the dependence $\propto (1 + \cos^2\theta)$ expected for spin 1/2 objects.

The quark origin of jets was proven in studies of the ratio of e^+e^--annihilation cross sections to hadrons and to $\mu^+\mu^-$-pairs. QCD predicts that this ratio should be equal to the sum of squared charges of the objects initiating jets. In experiment, this ratio equals just its value for quarks and increases with energy at the thresholds for heavier quarks.

Thus, these early findings assured us that QCD is on the right way. Later, numerous data supported this conclusion as is shown in what follows in brief. To shorten the presentation, only some of most impressive results have been chosen and no Figures are presented. More complete list with a detailed survey and Figures demonstrating comparison with experiment can be found in the books [1, 2] and in recent review papers [3, 4, 5, 6, 7].

2 Theory

According to QCD, the primary quarks emit gluons which, in their turn, can emit e^+e^--pairs and gluons. Thus the branching process of jet evolution appears. The gluons with high enough transverse momenta can create gluon jets. QCD pretends to describe jets of both quark and gluon origin. Many hadrons are created when partons become confined.

Analytical QCD pretends to start with asymptotical values and proceed to lower energies accounting for conservation laws, higher order perturbative and non-perturbative effects. The perturbative approach is justified at high transferred momenta due to the asymptotic freedom property of QCD which states that the coupling strength becomes smaller with increase of transferred momenta. The perturbative evolution is terminated at some low scale $Q_0 \sim 1\text{GeV}$

for transverse momenta or virtualities of partons. Here, the transition between partonic degrees of freedom at short distances to hadronic degrees of freedom at long distances (i.e., from weak to strong coupling) begins. Every experiment encodes this transition. To deal with it in practice, the local parton-hadron duality (LPHD) is assumed which declares that the distributions at the parton level describe the hadron observables up to some constant factor. This concept originates from the preconfinement property of quarks and gluons to form colorless clusters. In this framework, the perturbative QCD has demonstrated its very high predictive power. It works surprisingly well when applied for comparison with experiment.

The most general approach starts from the equation for the generating functional. The generating functional contains complete information about any multiparticle process. It is defined as

$$G(\{u\},\kappa_0) = \sum_n \int d^3k_1 ... d^3k_n u(k_1) ... u(k_n) P_n(k_1,...,k_n;\kappa_0), \qquad (1)$$

where $P_n(k_1,...,k_n;\kappa_0)$ is the probability density for exclusive production of particles with momenta $k_1,...,k_n$ at the initial virtuality (energy) κ_0, and $u(k)$ is an auxiliary function. For $u(k)$ =const, one gets the generating function of the multiplicity distribution $P_n(\kappa_0)$. The variations of $G(\{u\})$ over $u(k)$ (or differentials for constant u) provide any inclusive distributions and correlations of arbitrary order, i.e. complete information about the process. The general structure of the equation for the generating functional describing the jet evolution for a single species partons can be written symbolically as

$$G' \sim \int \alpha_S K[G \otimes G - G] d\Omega. \qquad (2)$$

It shows that the evolution of G indicated by its variation (derivative) G' is determined by the cascade process of the production of two partons by a highly virtual time-like parton (the term $G \otimes G$) and by the escape of a single parton (G) from a given phase space region $d\Omega$. The weights are determined by the coupling strength α_S and the splitting function K defined by the interaction Lagrangian. The integral runs over all internal variables, and the symbol $\otimes$ shows that the two partons share the momentum of their parent. This is a non-linear integrodifferential probabilistic equation with shifted arguments in the $G \otimes G$ term under the integral sign.

For quark and gluon jets, one writes down the system of two coupled equations. Their solutions give all characteristics of quark and gluon jets and allow for the comparison with experiment to be done. Let us write them down explicitly for the generating functions now.

$$G'_G = \int_0^1 dx K_G^G(x) \gamma_0^2 [G_G(y + \ln x) G_G(y + \ln(1-x)) - G_G(y)]$$

$$+ \quad n_f \int_0^1 dx K_G^F(x)\gamma_0^2[G_F(y+\ln x)G_F(y+\ln(1-x)) - G_G(y)], \quad (3)$$

$$G'_F = \int_0^1 dx K_F^G(x)\gamma_0^2[G_G(y+\ln x)G_F(y+\ln(1-x)) - G_F(y)], \quad (4)$$

where $G'(y) = dG/dy$, $y = \ln(p\Theta/Q_0) = \ln(2Q/Q_0)$, p is the initial momentum, Θ is the angle of the divergence of the jet (jet opening angle), assumed here to be small, Q is the jet virtuality, $Q_0 = \text{const}$, n_f is the number of active flavors,

$$\gamma_0^2 = \frac{2N_c\alpha_S}{\pi}, \quad (5)$$

the running coupling constant in the one-loop approximation is

$$\alpha_S(y) = \frac{6\pi}{(11N_c - 2n_f)y}, \quad (6)$$

the labels G and F correspond to gluons and quarks, and the kernels of the equations are

$$K_G^G(x) = \frac{1}{x} - (1-x)[2 - x(1-x)], \quad (7)$$

$$K_G^F(x) = \frac{1}{4N_c}[x^2 + (1-x)^2], \quad (8)$$

$$K_F^G(x) = \frac{C_F}{N_c}\left[\frac{1}{x} - 1 + \frac{x}{2}\right], \quad (9)$$

where N_c=3 is the number of colours, and $C_F = (N_c^2 - 1)/2N_c = 4/3$ in QCD. The variable u has been omitted in the generating functions.

Let us note that these equations can be exactly solved [8] if the coupling strength is assumed fixed, i.e. independent of y. For the running coupling strength, the Taylor series expansion can be used [9] to get the modified perturbative expansion of physically measurable quantities. The asymptotical results are obtained in the so-called double-logarithmic (DLA) or leading order (LO) approximation when the terms $(\alpha_S \ln^2 s)^n$ are summed. Here s is the cms energy squared. The emitted gluons are assumed so soft that the energy-momentum conservation is neglected. The corrections accounting for conservation laws in the $G \otimes G$ term and in limits of the integration as well as the higher order terms in the weight $\alpha_S K$ (in particular, the non-singular terms of the kernels K) appear first in the next-to-leading (NLO or MLLA - modified leading logarithm approximation) and then in higher (2NLO,...) orders. Formally, these equations have been proven only for the next-to-leading (NLO) order of the perturbative QCD. However, one can try to consider them as kinetic equations in higher orders and/or generalize them including the above-mentioned effects in a more rigorous way than it is usually implied.

3 QCD predictions and their comparison with experiment

The theoretical results have been successfully compared with available experimental data. The main bulk of the data is provided by e^+e^--processes at Z^0 energy.

The energy dependence of mean multiplicity

The equations for the average multiplicities in jets are obtained from the system of equations (3), (4) by expanding the generating functions in $u-1$ and keeping the terms with q=0 and 1 according to the definition

$$\frac{dG}{du}\Big|_{u=1} = \sum nP_n = \langle n \rangle. \tag{10}$$

¿From their solutions one learns about the energy evolution of the ratio of multiplicities in quark and gluon jets r and of the QCD anomalous dimension γ (the slope of the logarithm of average multiplicity in a gluon jet) defined as

$$r = \frac{\langle n_G \rangle}{\langle n_F \rangle}, \qquad \gamma = \frac{\langle n_G \rangle'}{\langle n_G \rangle} = (\ln\langle n_G \rangle)'. \tag{11}$$

They have been represented by the perturbative expansion at large y as

$$\gamma = \gamma_0(1 - a_1\gamma_0 - a_2\gamma_0^2 - a_3\gamma_0^3) + O(\gamma_0^5), \tag{12}$$

$$r = r_0(1 - r_1\gamma_0 - r_2\gamma_0^2 - r_3\gamma_0^3) + O(\gamma_0^4). \tag{13}$$

Using the Taylor series expansion of $\langle n \rangle$ at large y in the corresponding equations with (12), (13) one gets the coefficients a_i, r_i.

One of the most spectacular predictions of QCD states that in the leading order approximation, where $\gamma = \gamma_0$, average multiplicities should increase with energy [10, 11, 12, 13] like $\exp[c\sqrt{\ln s}]$, i.e., in between the power-like and logarithmic dependences predicted by hydrodynamical and multiperipheral models. Next-to-leading order results account for the term with a_1 in Eqn. (12) [14, 15, 16] and contribute the logarithmically decreasing factor to this behavior whereas the higher order terms do not practically change this dependence [17, 18]. The fitted parameters in the final expression are an overall constant normalization factor which is defined by confinement and a scale parameter Q_0. The e^+e^--data are well fitted by such an expression. Let us note here that the expansion parameter γ is rather large at present energies being about 0.4 - 0.5.

Let us stress here that the perturbative expansion in Eq. (12) leads to the modification of the perturbative expansion for $\langle n \rangle$. Since γ exponentiates in $\langle n \rangle$, the so called modified perturbative expansion shows up in $\langle n \rangle$.

Difference between quark and gluon jets

The system of two equations for quark and gluon jets predicts that asymptotically the energy dependence of mean multiplicities in them should be identical. However, normalization differs, and gluon jets are more "active" so that the ratio $r = \langle n_G \rangle / \langle n_F \rangle$ of average multiplicities in gluon and quark jets should tend at high energies [19] to the ratio of Casimir operators $C_A/C_F = 9/4$. Once again, this prediction shows how far are we now from the true asymptotics because in experiment this ratio is about 1.5 at Z^0 energy and even smaller at lower energies. The higher order terms [20, 14, 18] (calculated now up to 3NLO) improve the agreement and approach the experimental value with an accuracy about 15%. The higher order terms change slightly also the energy behavior of quark jets compared to gluon jets as observed in experiment. However, the simultaneous fit of quark and gluon jets with the same set of fitted parameters is still not very accurate. This failure is again due to insufficiently precise description of the ratio r.

Let us stress here that LO and NLO terms in energy dependence of mean multiplicities cancel in the ratio r. Thus, this is the most sensitive measure of higher order corrections which pushes us to work at the limits of our knowledge. Moreover, due to this cancellation the γ_0^3-terms in r-expansion correspond to γ_0^4-terms in expansion of γ itself, i.e. to 4NLO and not to 3NLO-terms there. And they have been calculated analytically [18]. Therefore the slight disagreement with experiment should not surprise us very much when we work at (and, may be, even outside!) the limits of applicability of the whole approach.

Moreover, QCD predicted [18] that the ratio of multiplicities r should be smaller than the ratio of their slopes (first derivatives) which, in turn, is smaller than the ratio of their curvatures (second derivatives), and all of them are smaller than 2.25 and tend to this limit in asymptotics. This has been confirmed by experiment as well.

Oscillations of cumulant moments

The shape of the multiplicity distribution can be described by its higher moments related to the width, the skewness, the kurtosis etc. The q-th derivative of the generating function corresponds to the factorial moment F_q, and the derivative of its logarithm defines the so-called cumulant moment K_q. The latter ones describe the genuine (irreducible) correlations in the system (it reminds the connected Feynman graphs).

$$F_q = \frac{\sum_n P_n n(n-1)...(n-q+1)}{(\sum_n P_n n)^q} = \frac{1}{\langle n \rangle^q} \cdot \frac{d^q G(z)}{du^q}\Big|_{u=1}, \qquad (14)$$

$$K_q = \frac{1}{\langle n \rangle^q} \cdot \frac{d^q \ln G(z)}{du^q}\Big|_{u=1}. \qquad (15)$$

These moments are not independent. They are connected by definite relations that can easily be derived from their definitions in terms of the generating function. In that sense, cumulants and factorial moments are equally suitable.

Solving the Eqns. (3), (4), one gets quite naturally the predictions [9, 8, 21] for the behavior of the ratio $H_q = K_q/F_q$. At asymptotically high energies, this ratio is predicted to behave as q^{-2}. However, the asymptotics is very far from our realm. At present energies, according to QCD, this ratio should reveal the minimum at $q \approx 5$ and subsequent oscillations. This astonishing qualitative prediction has been confirmed in experiment (for the first time in Ref. [22]). Moreover, the oscillations of the moments with their rank have been observed. The quantitative analytical estimates are not enough accurate but the numerical computer solution [23] reproduces oscillations quite well. These new laws differ from all previously attempted distributions of the probability theory.

The hump-backed plateau

Dealing with inclusive distributions, one should solve the equations for the generating functional. It has been done up to NLO approximation. As predicted by QCD, the momentum (rapidity y) spectra of particles inside jets should have the shape of the hump-backed plateau [24, 12, 13, 25]. This striking prediction of the perturbative QCD differs from the previously popular flat plateau advocated by Feynman. It has been found in experiment. The depletion between the two humps is due to angular ordering and color coherence in QCD. The humps are of the approximately Gaussian shape near their maxima if the variable $\xi = -\ln x$; $x = p/E_j$ is used. Here p is the particle momentum, E_j is the jet energy. This prediction was first obtained in the LO QCD, and more accurate expressions were derived in NLO [26]. Moments of the distributions up to the fourth rank have been calculated. The drop of the spectrum towards small momenta becomes more noticeable in this variable. The comparison with experimental data at different energies has revealed good agreement both on the shape of the spectrum and on the energy dependence of its peak position and width.

Difference between heavy- and light-quark jets

Another spectacular prediction of QCD is the difference between the spectra and multiplicities in jets initiated by heavy and light quarks. Qualitatively, it corresponds to the difference in bremsstrahlung by muons and electrons where the photon emission at small angles is strongly suppressed for muons because

of the large mass in the muon propagator. Therefore, the intensity of the radiation is lower in the ratio of masses squared. The coherence of soft gluons also plays an important role in QCD. For heavy quarks the accompanying radiation of gluons should be stronger depleted in the forward direction (dead-cone or ring-like emission). It was predicted [27, 28] that it should result in the energy-independent difference of companion mean multiplicities for heavy- and light-quark jets of equal energy. The naive model of energy rescaling [29, 30, 31] predicts the decreasing difference. The experimental data support this QCD conclusion.

Color coherence in 3-jet events

When three or more partons are involved in hard interaction, one should take into account color-coherence effects. Several of them have been observed. In particular, the multiplicity can not be represented simply as a sum of flows from independent partons. QCD predicts that the particle flows should be enlarged in the directions of emission of partons and suppressed in between them. Especially interesting is the prediction that this suppression is stronger between $q\bar{q}$-pair than between gq and $g\bar{q}$ in $e^+e^- \to q\bar{q}g$ event if all angles between partons are large (the "string" [32] or "drag" [33] effect). All these predictions have been confirmed by experiment. In $q\bar{q}g$ events the particle population values in the qg valleys are found larger than in the $q\bar{q}$ valley by a factor 2.23±0.37 compared to the theoretical prediction of 2.4. Moreover, QCD predicts that this shape is energy-independent up to an overall normalization factor.

Let us note that for the process $e^+e^- \to q\bar{q}\gamma$ the emission of additional photons would be suppressed both in the direction of a primary photon and in the opposite one. In the case of an emitted gluon, we observe the string (drag) effect of enlarged multiplicity in its direction and stronger suppression in the opposite one. This suppression is described by the ratio of the corresponding multiplicities in the $q\bar{q}$ region which is found to be equal 0.58±0.06 in experiment whereas the theoretical prediction is 0.61.

The color coherence reveals itself as inside jets as in inter-jet regions. It should suppress both the total multiplicity of $q\bar{q}g$ events and the particle yield in the transverse to the $q\bar{q}g$ plane for decreasing opening angle between the low-energy jets. When hard gluon becomes softer, color coherence determines, e.g., the azimuthal correlations of two gluons in $q\bar{q}gg$ system. In particular, back-to-back configuration ($\varphi \sim 180^0$) is suppressed by a factor ~ 0.785 in experiment, 0.8 in HERWIG Monte Carlo and 0.93 in analytical pQCD. In conclusion, color coherence determines topological dependence of jet properties.

Some proposals have been promoted for a special two-scale analysis of 3-jet events when the restriction on the transverse momentum of a gluon jet is

imposed [34, 35]. They found also support from experiment.

Intermittency and fractality

The self-similar parton cascade leads to special multiparton correlations. Its structure with "jets inside jets inside jets..." provoked the analogy with turbulence and the ideas of intermittency [36]. Such a structure should result in the fractal distribution in the available phase space [37]. The fractal behavior would display the linear dependence of logarithms of factorial moments on the logarithmic size of phase space windows. The moments are larger in smaller windows, i.e. the fluctuations increase in smaller bins in a power-like manner (see the review paper [38]).

In QCD, the power dependence appears for a fixed coupling regime [8]. The running property of the coupling strength in QCD flattens [39, 40, 41] this dependence at smaller bins, i.e. the multifractal behavior takes over there. The slopes for different ranks q are related to the Renyi dimensions. Both the linear increase at comparatively large but decreasing bins and its flattening for small bins have been observed in experiment. However, only qualitative agreement with analytical predictions can be claimed here. The higher order calculations are rather complicated and mostly the results of LO with some NLO corrections are yet available. In experiment, different cuts have been used which hamper the direct comparison. However, Monte Carlo models where these cuts can be done agree with experiment better. The role of partonic and hadronization stages in this regime is still debatable.

Subjet multiplicities

A single quark-antiquark pair is initially created in e^+e^--annihilation. With very low angular resolution one observes two jets. A three-jet structure can be observed when a gluon with large transverse momentum is emitted by the quark or antiquark. However such a process is suppressed by an additional factor α_S, which is small for large transferred momenta. It can be calculated perturbatively. At relatively low transferred momenta, the jet evolves to angular ordered subjets ("jets inside jets..."). Different algorithms have been proposed to resolve subjets. By increasing the resolution, more and more subjets are observed. For very high resolution, the final hadrons are resolved. The resolution criteria are chosen to provide infrared safe results.

In particular, one can predict the asymptotical ratio of subjet multiplicities in 3- and 2-jet events if one neglects soft gluon coherence:

$$\frac{n_3^{sj}}{n_2^{sj}} = \frac{2C_F + C_A}{2C_F} = \frac{17}{8}. \tag{16}$$

Actually, the coherence reduces this value to be below 1.5 in experiment for all acceptable resolution parameters. Theoretical predictions [16] agree only qualitatively with experimental findings.

Subjet multiplicities have also been studied in separated quark and gluon jets. The analytical results [42] represent the data fairly well for large values of the subjet resolution scale y_0.

Jet universality

According to QCD, jets produced in processes initiated by different colliding particles (ep, pp, AA etc) should be universal and depend only on their own parent (gluon, light or heavy quark) if not modified by the secondary interactions. This prediction has been confirmed by many experiments.

4 Conclusions and outlook

A list of successful analytical and Monte-Carlo QCD predictions can be made longer. In particular, much work was done on the energy dependence of higher moments of multiplicity distributions, on forward-backward multiplicity correlations, on Bose-Einstein correlations, on various shape parameters of jets (and, in general, on event shape distributions), on non-perturbative corrections etc. QCD serves not only as a powerful tool for studies of multiparticle production processes but as a background for new physics as well.

The new era will be opened with the advent of new generations of linear colliders like TESLA.

Acknowledgements

We should praise LEP and experimentalists from ALEPH, DELPHI, L3 and OPAL collaborations for numerous results which allowed to enlarge our knowledge of physics of multiparticle production. I regret that the available space for the written version did not allow me to refer to all these papers and I had to omit Figures and cite mostly the theoretical predictions. In oral presentation, I tried to avoid these shortcomings.

References

1. I.V. Andreev, Chromodynamics and hard processes at high energies (Nauka, Moscow, 1981) (in Russian).

2. Yu.L. Dokshitzer *et al*, Basics of Perturbative QCD, Ed. J. Tran Thanh Van (Editions Frontieres, Gif-sur-Yvette, 1991).

3. I.M. Dremin, Phys.-Uspekhi **37**, 715 (1994).

4. V.A. Khoze *et al* , Int. J. Mod. Phys. **A 12**, 2949 (1997).

5. I.M. Dremin *et al*, Phys. Rep. **349**, 301 (2001).

6. V.A. Khoze *et al*, in: At the Frontier of Particle Physics: Handbook of QCD, Boris Ioffe Festschrift, Vol.2 (Ed. M. Shifman) (Singapore: World Scientific, 2001) p. 1101.

7. I.M. Dremin, Phys.-Uspekhi **43** (2002).

8. I.M. Dremin *et al*, Phys. Rev. **D 49**, 5805 (1994); Phys. Lett. **B 324** 477 (1994).

9. I.M. Dremin, Phys. Lett. **B 313**, 209 (1993).

10. A.H. Mueller, Phys. Lett. **B 104**, 161 (1981).

11. J.B. Gaffney *et al*, Nucl. Phys. **B 250**, 109 (1985).

12. Yu. L. Dokshitzer *et al*, Z. Phys. **C 15**, 335 (1982); **C 18**, 83 (1983).

13. A. Bassetto *et al*, Nucl. Phys. B **207**, 189 (1982).

14. B.R. Webber, Phys. Lett. **B 143**, 501 (1984).

15. Yu.L. Dokshitzer *et al*, Int. J. Mod. Phys. **A 7**, 1875 (1992).

16. S. Catani *et al*, Nucl. Phys. **B 377**, 445 (1992).

17. I.M. Dremin *et al*, Phys. Lett. **B 459**, 341 (1999).

18. A. Capella *et al*, Phys. Rev. **D 61**, 074009 (2000).

19. S.J. Brodsky *et al*, Phys. Rev. Lett. **37**, 402 (1976).

20. A.H. Mueller, Nucl. Phys. **B 241**, 141 (1984).

21. I.M. Dremin *et al*, Mod. Phys. Lett. **A 9**, 1471 (1994); JETP Lett. **58**, 881 (1993).

22. I.M. Dremin *et al*, Phys. Lett. **B 336**, 119 (1994).

23. S. Lupia, Phys. Lett. **B 439**, 150(1998).

24. Ya.I. Azimov *et al*, Pis'ma v ZhETP **35**, 390 (1982); JETP Lett. **35**, 482 (1982).

25. Ya.I. Azimov *et al*, Z. Phys. C **27**, 65 (1985); **31**, 213 (1986).

26. C.P. Fong *et al*, Phys. Lett. B **229**, 289 (1989); **B 241**, 255 (1990); Nucl. Phys. B **355**, 54 (1991).

27. Yu.L. Dokshitzer *et al*, J. Phys. G **17**, 1481, 1602 (1991).

28. B.A. Schumm *et al*, Phys. Rev. Lett. **69**, 3025 (1992).

29. Ya.I. Azimov *et al*, Sov. J. Nucl. Phys. **36**, 878 (1982).

30. A.V. Kisselev *et al*, Z. Phys. C **41**, 521 (1988).

31. V.A. Petrov *et al*, Z. Phys. C **66**, 453 (1995).

32. B. Andersson *et al*, Phys. Lett. B **94**, 211 (1980).

33. Ya. I. Azimov *et al*, Phys. Lett. **B 165**, 147 (1985); Sov. J. Nucl. Phys. **43**, 95 (1986).

34. P. Eden *et al*, JHEP **9809**, 015 (1998).

35. P. Eden *et al*, Eur. Phys. J. C **11**, 345 (1999).

36. A. Bialas *et al*, Nucl. Phys. B **273**, 703 (1986).

37. I.M. Dremin, JETP Lett. **45**, 643 (1987).

38. E.A. DeWolf *et al*, Phys. Rep. **270**, 1 (1996).

39. Yu.L. Dokshitzer *et al*, Nucl. Phys. B **402**, 139 (1993).

40. W. Ochs *et al*, Phys. Lett. **B 289**, 159 (1992); **B 304**, 144 (1993).

41. Ph. Brax *et al*, Z. Phys. C **62**, 649 (1994).

42. M.H. Seymour, Phys. Lett. B **378**, 279 (1996).

A TIME VARIATION OF THE QCD COUPLING CONSTANT

Harald Fritzsch
Ludwig-Maximilians-University Munich, Sektion Physik

May 6, 2003

Abstract

Astrophysical indications that the fine structure constant has undergone a small time variation during the cosmological evolution are discussed within the framework of the standard model of the electroweak and strong interactions and of grand unification. A variation of the electromagnetic coupling constant could either be generated by a corresponding time variation of the unified coupling constant or by a time variation of the unification scale, of by both. The various possibilities, differing substantially in their implications for the variation of low energy physics parameters like the nuclear mass scale, are discussed. The case in which the variation is caused by a time variation of the unification scale is of special interest. It is supported in addition by recent hints towards a time change of the proton-electron mass ratio.

The Standard Model of the electroweak and strong interactions has at least 18 parameters, which have to be adjusted in accordance with experimental observations. These include the three electroweak coupling strengths g_1, g_2 g_3, the scale of the electroweak symmetry breaking, given by the universal Fermi constant, the 9 Yukawa couplings of the six quarks and the three charged leptons, and the four electroweak mixing parameters. One parameter, the mass of the hypothetical scalar boson, is still undetermined. For the physics of stable matter, i.e. atomic physics, solid state physics and a large part of nuclear physics, only six constants are of importance: the mass of the electron, setting the scale of the Rydberg constant, the masses of the u and d-quarks setting the scale of the breaking of isotopic spin, and the strong interaction coupling constant α_s. The latter, often parametrized by the QCD scale parameter Λ, sets the scale for the nucleon mass. The mass of the strange quark can also be included since the mass term of the s-quarks is expected to contribute to the nucleon mass, although the exact amount of strangeness contribution to the nucleon mass is still being discussed - it can range from several tenth of MeV till more than 100 MeV. As far as macro-physical aspects are concerned, Newton's constant must be added, which sets the scale for the Planck units of energy, space and time.

Since within the Standard Model the number of free parameters cannot be reduced, and thus far theoretical speculations about theories beyond the model have not led to a well-defined framework, in view of lack of guidance by experiment, one may consider the possibility that these parameters are time and possibly also space variant on a cosmological scale. Speculations about a time-change of coupling constants have a long history, starting with early speculations about a cosmological time change of Newton's constant G [1-4]. Since in particular the masses of the fermions as well as the electroweak mass scale are related to the vacuum expectation values of a scalar field, time changes of these parameters are conceivable. In some theories beyond the Standard Model also the gauge coupling constants are related to expectation values of scalar fields which could be time dependent [5].

Recent observations in astrophysics concerning the atomic fine-structure of elements in distant objects suggest a time change of the fine structure constant [6]. The data suggest that α was lower in the past, at a redshift of $z \approx 0.5 \ldots 3.5$:

$$\Delta\alpha/\alpha = (-0.72 \pm 0.18) \times 10^{-5}. \tag{1}$$

If α is indeed time dependent, the other two gauge coupling constants of the Standard Model are also expected to depend on time, as pointed out recently [7] (see also [8,9]), if the Standard Model is embedded into a grand unified theory. Moreover the idea of a grand unification of the coupling constants leads to a relation between the time variation of the electromagnetic coupling constant and the QCD scale parameter Λ, implying a physical time variation of the nucleon mass, when measured in units given by an energy scale independent of QCD, like the electron mass or the Planck mass. The main assumption is that the physics responsible for a cosmic time evolution of the coupling constants takes place at energies above the unification scale. This allows to use the usual relations from grand unified theories to evolve the unified coupling constant down to low energy.

Considering the six basic parameters mentioned above plus Newton's constant G, one can in general consider seven relative time changes: $\dot{G}/G$, $\dot{\alpha}/\alpha$, $\dot{\Lambda}/\Lambda$, $\dot{m}_e/m_e$, $\dot{m}_u/m_u$, $\dot{m}_d/m_d$ and $\dot{m}_s/m_s$. Thus in principle seven different functions of time do enter the discussion. However not all of them could be measured, even not in principle. Only dimensionless ratios e.g. the

ratio Λ/m_e or the fine-structure constant could be considered as reasonable candidates for a time variation.

The time derivative of the ratio Λ/m_e describes a possible time change of the atomic scale in comparison to the nuclear scale. In the absence of quark masses there is only one mass scale in QCD, unlike in atomic physics, where the two parameters α and m_e enter. The parameter α is directly measurable by comparing the energy differences describing the atomic fine structure (of order $m_e c^2 \alpha^4$) to the Rydberg energy $hcR_\infty = m_e c^2 \alpha^2/2 \approx 13.606$ eV.

Both astrophysics experiments as well as high precision experiments in atomic physics in the laboratory could in the future give indications about a time variation of three dimensionless quantities: α, M_p/m_e and $(M_n - M_p)/m_e$. The time variation of α reported in [6] implies, assuming a simple linear extrapolation, a relative rate of change per year of about 1.0×10^{-15}/yr. This poses a problem with respect to the limit given by an analysis of the remains of the naturally occurring nuclear reactor at Oklo in Gabon (Africa), which was active close to 2 billion years ago. One finds a limit of $\dot{\alpha}/\alpha = (-0.2 \pm 0.8) \times 10^{-17}$/yr. This limit was derived in [11] under the assumption that other parameters, especially those related to the nuclear physics, did not change during the last 2 billion years. It was recently pointed out [7,10], that this limit must be reconsidered if a time change of nuclear physics parameters is taken into account. In particular it could be that the effects of a time change of α are compensated by a time change of the nuclear scale parameter. For this reason we study in this paper several scenarios for time changes of the QCD scale, depending on different assumptions about the primary origin of the time variation.

Without a specific theoretical framework for the physics beyond the Standard Model the relative time changes of the three dimensionless numbers mentioned above are unrelated. We shall incorporate the idea of grand unification and assume for simplicity the simplest model of this kind, consistent with present observations, the minimal extension of the supersymmetric version of the Standard Model (MSSM), based on the gauge group $SU(5)$. In this model the three coupling constants of the Standard Model converge at high energies at the scale Λ_G. In particular the QCD scale Λ and the fine structure constant α are related to each other. In the model there are besides the electron mass and the quark masses three further scales entering, the scale for the breaking of the electroweak symmetry Λ_w, the scale of the onset of supersymmetry Λ_s and the scale Λ_G where the grand unification sets in.

According to the renormalization group equations, considered here in lowest order, the behaviour of the coupling constants changes according to

$$\alpha_i(\mu)^{-1} = \left(\frac{1}{\alpha_i^0(\Lambda_G)} + \frac{1}{2\pi} b_i^S \ln\left(\frac{\Lambda_G}{\mu}\right) \right) \theta(\mu - \Lambda_S) + \left(\frac{1}{\alpha_i^0(\Lambda_S)} + \frac{1}{2\pi} b_i^{SM} \ln\left(\frac{\Lambda_S}{\mu}\right) \right) \theta(\Lambda_S - \mu), \tag{2}$$

where the parameters b_i are given by $b_i^{SM} = (b_1^{SM}, b_2^{SM}, b_3^{SM}) = (41/10, -19/6, -7)$ below the supersymmetric scale and by $b_i^S = (b_1^S, b_2^S, b_3^S) = (33/5, 1, -3)$ when $\mathcal{N} = 1$ supersymmetry is restored, and where

$$\frac{1}{\alpha_i^0(\Lambda_S)} = \frac{1}{\alpha_i^0(M_Z)} + \frac{1}{2\pi} b_i^{SM} \ln\left(\frac{M_Z}{\Lambda_S}\right) \tag{3}$$

where M_Z is the Z-boson mass and $\alpha_i^0(M_Z)$ is the value of the coupling constant under consideration measured at M_Z. We use the following definitions for the coupling constants:

$$\begin{aligned} \alpha_1 &= 5/3g_1^2/(4\pi) = 5\alpha/(3\cos^2(\theta)\overline{\rm MS}) \\ \alpha_2 &= g_2^2/(4\pi) = \alpha/\sin^2(\theta)\overline{\rm MS} \\ \alpha_s &= g_3^2/(4\pi). \end{aligned} \tag{4}$$

Assuming $\alpha_u = \alpha_u(t)$ and $\Lambda_G = \Lambda_G(t)$, one finds:

$$\frac{1}{\alpha_i}\frac{\dot{\alpha}_i}{\alpha_i} = \left[\frac{1}{\alpha_u}\frac{\dot{\alpha}_u}{\alpha_u} - \frac{b_i^S}{2\pi}\frac{\dot{\Lambda}_G}{\Lambda_G}\right] \tag{5}$$

which leads to

$$\frac{1}{\alpha}\frac{\dot{\alpha}}{\alpha} = \frac{8}{3}\frac{1}{\alpha_s}\frac{\dot{\alpha}_s}{\alpha_s} - \frac{1}{2\pi}\left(b_2^S + \frac{5}{3}b_1^S - \frac{8}{3}b_3^S\right)\frac{\dot{\Lambda}_G}{\Lambda_G}. \tag{6}$$

One may consider the following scenarios:

1) Λ_G invariant, $\alpha_u = \alpha_u(t)$. This is the case considered in [7] (see also [8]), and one finds

$$\frac{1}{\alpha}\frac{\dot{\alpha}}{\alpha} = \frac{8}{3}\frac{1}{\alpha_s}\frac{\dot{\alpha}_s}{\alpha_s} \tag{7}$$

and

$$\frac{\dot{\Lambda}}{\Lambda} = -\frac{3}{8}\frac{2\pi}{b_3^{SM}}\frac{1}{\alpha}\frac{\dot{\alpha}}{\alpha}. \tag{8}$$

2) α_u invariant, $\Lambda_G = \Lambda_G(t)$. One finds

$$\frac{1}{\alpha}\frac{\dot{\alpha}}{\alpha} = -\frac{1}{2\pi}\left(b_2^S + \frac{5}{3}b_1^S\right)\frac{\dot{\Lambda}_G}{\Lambda_G}, \tag{9}$$

with

$$\Lambda_G = \Lambda_S\left[\frac{\Lambda}{\Lambda_S}\exp\left(-\frac{2\pi}{b_3^{SM}}\frac{1}{\alpha_u}\right)\right]^{\left(\frac{b_3^{SM}}{b_3^S}\right)} \tag{10}$$

which follows from the extraction of the Landau pole using (2). One obtains

$$\frac{\dot{\Lambda}}{\Lambda} = \frac{b_3^S}{b_3^{SM}}\left[\frac{-2\pi}{b_2^S + \frac{5}{3}b_1^S}\right]\frac{1}{\alpha}\frac{\dot{\alpha}}{\alpha} \approx -30.8\frac{\dot{\alpha}}{\alpha} \tag{11}$$

3) $\alpha_u = \alpha_u(t)$ and $\Lambda_G = \Lambda_G(t)$. One has

$$\begin{aligned} \frac{\dot{\Lambda}}{\Lambda} &= -\frac{2\pi}{b_3^{SM}}\frac{1}{\alpha_u}\frac{\dot{\alpha_u}}{\alpha_u} + \frac{b_3^S}{b_3^{SM}}\frac{\dot{\Lambda}_G}{\Lambda_G} \\ &= -\frac{3}{8}\frac{2\pi}{b_3^{SM}}\frac{1}{\alpha}\frac{\dot{\alpha}}{\alpha} - \frac{3}{8}\frac{1}{b_3^{SM}}\left(b_2^S + \frac{5}{3}b_1^S - \frac{8}{3}b_3^S\right)\frac{\dot{\Lambda}_G}{\Lambda_G} \\ &\cong 46\frac{\dot{\alpha}}{\alpha} + 1.07\frac{\dot{\Lambda}_G}{\Lambda_G} \end{aligned} \tag{12}$$

where thecretical uncertainties in the factor $R = (\dot{\Lambda}/\Lambda)/(\dot{\alpha}/\alpha) = 46$ have been discussed in [7]. The actual value of this factor is sensitive to the inclusion of the quark masses and the associated thresholds, just like in the determination of Λ. Furthermore higher order terms in the QCD evolution of α_s will play a role. In ref. [7] it was estimated: $R = 38 \pm 6$.

The case in which the time variation of α is not related to a time variation of the unified coupling constant, but rather to a time variation of the unification scale, is of particular interest. Unified theories, in which the Standard Model arises as a low energy approximation, might well provide a numerical value for the unified coupling constant, but allow for a smooth time variation of the unification scale, related in specific models to vacuum expectation values of scalar fields. Since the universe expands, one might expect a decrease of the unification scale due to a dilution of the scalar field. A lowering of Λ_G implies according to (9)

$$\frac{\dot{\alpha}}{\alpha} = -\frac{1}{2\pi}\alpha\left(b_2^S + \frac{5}{3}b_1^S\right)\frac{\dot{\Lambda}_G}{\Lambda_G} = -0.014\frac{\dot{\Lambda}_G}{\Lambda_G}. \tag{13}$$

If $\dot{\Lambda}_G/\Lambda_G$ is negative, $\dot{\alpha}/\alpha$ increases in time, consistent with the experimental observation. Taking $\Delta\alpha/\alpha = -0.72 \times 10^{-5}$, we would conclude $\Delta\Lambda_G/\Lambda_G = 5.1 \times 10^{-4}$, i.e. the scale of grand unification about 8 billion years ago was about 8.3×10^{12} GeV higher than today. If the rate of change is extrapolated linearly, Λ_G is decreasing at a rate $\frac{\dot{\Lambda}_G}{\Lambda_G} = -7 \times 10^{-14}/\text{yr}$. If this is indeed the case, it would imply that proton decay is faster in the distant future.

According to (11) the relative changes of Λ and α are opposite in sign. While α is increasing with a rate of $1.0 \times 10^{-15}/\text{yr}$, Λ and the nucleon mass is decreasing, e.g. with a rate of $1.9 \times 10^{-14}/\text{yr}$. The magnetic moments of the proton μ_p as well of nuclei would increase according to

$$\frac{\dot{\mu}_p}{\mu_p} = 30.8\frac{\dot{\alpha}}{\alpha} \approx 3.1 \times 10^{-14}/\text{yr}. \tag{14}$$

The effect can be seen by monitoring the ratio $\mu = M_p/m_e$. Measuring the vibrational lines of H_2, a small effect was seen [12] recently. The data allow two different interpretations:

a) $\Delta\mu/\mu = (5.7 \pm 3.8) \times 10^{-5}$

b) $\Delta\mu/\mu = (12.5 \pm 4.5) \times 10^{-5}$.

The interpretation b) agrees essentially with the expectation based on (11):

$$\frac{\Delta\mu}{\mu} = 22 \times 10^{-5}. \tag{15}$$

It is interesting that the data suggest that μ is indeed decreasing, while α seems to increase. If confirmed, this would be a strong indication that the time variation of α at low energies is caused by a time variation of the unification scale.

The time variation of the ratio M_p/m_e and α discussed here are such that they could by discovered by precise measurements in quantum optics. The wave length of the light

emitted in hyperfine transitions, e.g. the ones used in the cesium clocks being proportional to $\alpha^4 m_e/\Lambda$ will vary in time like

$$\frac{\dot{\lambda}_{hf}}{\lambda_{hf}} = 4\frac{\dot{\alpha}}{\alpha} - \frac{\dot{\Lambda}}{\Lambda} \approx 3.5 \times 10^{-14}/\mathrm{yr} \tag{16}$$

taking $\dot{\alpha}/\alpha \approx 1.0 \times 10^{-15}/\mathrm{yr}$ [6]. The wavelength of the light emitted in atomic transitions varies like α^{-2}:

$$\frac{\dot{\lambda}_{at}}{\lambda_{at}} = -2\frac{\dot{\alpha}}{\alpha}. \tag{17}$$

One has $\dot{\lambda}_{at}/\lambda_{at} \approx -2.0 \times 10^{-15}/\mathrm{yr}$. A comparison gives:

$$\frac{\dot{\lambda}_{hf}/\lambda_{hf}}{\dot{\lambda}_{at}/\lambda_{at}} = -\frac{4\dot{\alpha}/\alpha - \dot{\Lambda}/\Lambda}{2\dot{\alpha}/\alpha} \approx -17.4. \tag{18}$$

At present the time unit second is defined as the duration of 6.192.631.770 cycles of microwave light emitted or absorbed by the hyperfine transmission of cesium-133 atoms. If Λ indeed changes, as described in (11), it would imply that the time flow measured by the cesium clocks does not fully correspond to the time flow defined by atomic transitions.

It remains to be seen whether the effects discussed in this paper can soon be observed in astrophysics or in quantum optics. A determination of the double ratio $(\dot{\Lambda}/\Lambda)/(\dot{\alpha}/\alpha) = R$ would be of crucial importance, both in sign and in magnitude. If one finds the ratio to be about -20, it would be considered as a strong indication of a unification of the strong and electroweak interactions based on a supersymmetric extension of the Standard Model. In any case the numerical value of R would be of high interest towards a better theoretical understanding of time variation of the fundamental constants and unification.

Acknowledgements

I would like to thank A. Albrecht, J. D. Bjorken, E. Bloom, G. Boerner, S. Brodsky, P. Chen, S. Drell, G. Goldhaber, T. Haensch, M. Jacob, P. Minkowski, A. Odian, H. Walther and A. Wolfe for useful discussions.

References

[1] P. M. Dirac, Nature 192, 235 (1937).

[2] E. A. Milne, Relativity, Gravitation and World Structure, Clarendon press, Oxford, (1935), Proc. Roy. Soc. A, 3, 242 (1937).

[3] P. Jordan, Naturwiss., 25, 513 (1937); Z. Physik, 113, 660 (1939).

[4] L. D. Landau, in W. Pauli, ed., Niels Bohr and the Development of Physics, McGraw-Hill, NY, p.52, (1955).

[5] M. B. Green, J. H. Schwarz and E. Witten, Superstring Theory, Vol. 1 and 2, T. Damour and A. M. Polyakov, Nucl. Phys. B 423, 532 (1994) [arXiv:hep-th/9401069].

[6] J. K. Webb *et al.*, Phys. Rev. Lett. 87 091301 (2001) [arXiv:astro-ph/0012539].

[7] X. Calmet and H. Fritzsch, arXiv:hep-ph/0112110, to appear in Eur.Phys. J. C.

[8] P. Langacker, G. Segre and M. J. Strassler, Phys. Lett. B 528, 121 (2002) [arXiv:hep-ph/0112233]; T. Dent and M. Fairbairn, arXiv:hep-ph/0112279.

[9] H. Fritzsch, "Fundamental constants at high energy," arXiv:hep-ph/0201198, Invited talk at Symposium on 100 Years Werner Heisenberg: Works and Impact, Bamberg, Germany, 26-30 Sep 2001; S. J. Landau and H. Vucetich, arXiv:astro-ph/0005316; V. V. Flambaum and E. V. Shuryak, arXiv:hep-ph/0201303; C. Wetterich, arXiv:hep-ph/0203266; Z. Chacko, C. Grojean and M. Perelstein, arXiv:hep-ph/0204142.

[10] V. V. Flambaum and E. V. Shuryak, in [9].

[11] T. Damour and F. Dyson, Nucl. Phys. B 480, 37 (1996) [arXiv:hep-ph/9606486].

[12] A. V. Ivanchik, E. Rodriguez, P. Petitjean and D. A. Varshalovich, arXiv:astro-ph/0112323.

SESSION VIII - SEARCH FOR PHYSICS BEYOND THE SM

Philip Bambade	Four–Fermion Production and Limits on Anomalous Couplings at LEP–2
Pablo Garć ia*	Higgs Results and Searches for New Physics at LEP
Lorenzo Bellagamba	Searches for New Physics at HERA
Emmanuel Sauvan	Lepton Production in *ep* Collisions at HERA
Luca Scodellaro	Searches for New Phenomena in CDF
Wyatt Merritt	Recent New Phenomena Results from the Searches at D0 Experiment
Victor Novikov	Z-Lineshape versus 4th Generation Masses

* The trasparencies of the missing contributions are available on the web site http://www.pi.infn.it/lathuile/lathuile_2003.html

FOUR-FERMION PRODUCTION AND LIMITS ON ANOMALOUS COUPLINGS AT LEP-2

Philip Bambade
LAL, Université Paris-Sud, Bât. 200, BP 34, F-91898 Orsay Cédex, France

Abstract

Electroweak processes with four fermions in the final state were measured extensively at LEP-2 in e+e- collisions with centre-of-mass energies up to 209 GeV. By combining the results obtained by Aleph, Delphi, L3 and Opal, the predictions from the Standard Model were probed at the level of their present accuracy. An important outcome was the possibility to measure the predicted charged triple gauge boson self-couplings with a precision of a few percent. Moreover studies of four-fermion processes allowed new physics to be searched for by looking for anomalous gauge boson self-couplings. The measurements reported are also relevant to direct searches for new particles at LEP-2, as four-fermion processes contribute an important background in several cases. The latest results from the LEP experiments - some of which are now available in finalized form - and their combination are reviewed and discussed.

1 Introduction

During the second part of the LEP program in 1995-2000, the centre-of-mass energy of the e^+e^- collisions was raised above the Z boson mass, reaching up to 209 GeV in the last year of operation. Integrated luminosities of about 700 pb^{-1} were collected by each of the four LEP collaborations ALEPH, DELPHI, L3 and OPAL, mostly above the W and Z-pair production thresholds. This allowed a comprehensive measurement program of boson pair production in e^+e^- collisions and more generally of all possible four-fermion ($4f$) final states. Two of the principal aims of LEP, directly validating the non-Abelian gauge structure of the standard model (SM) and searching for anomalous gauge boson self-couplings to reveal new physics beyond the SM (NP), could be pursued.

Most of the measured $4f$ final states result from processes seen at LEP for the first time. Initially some of the theoretical predictions and modelling were crude. Improvements were needed to match the experimental accuracy and were challenging, especially in the case of W-pair production [1]. The LEP measurements stimulated important work to compute radiative corrections and to devise appropriate ways to choose the scales of coupling constants when several were involved. The results were also included in practical event generators, where numerical divergences resulting from the small electron mass and the handling of the full set of graphs both had to be dealt with efficiently.

The experience gained at LEP in measuring $4f$ final states and the progress in the theoretical description and modelling were also important in the context of many new particle searches. In several cases the experimental signatures are very similar to those of the signal searched for, thus providing a useful environment to test the corresponding analysis techniques[1]. In the longer term, the improvements in the calculations will also benefit similar work at a future e^+e^- linear collider, where very high precision will be needed.

This report has two sections. Firstly, the latest measurements of $4f$ final states arising via the production processes $e^+e^- \to WW$, ZZ, $Z\gamma^*$, $ee Z/\gamma^*$ and $e\nu W$ are described. Secondly, interpretations of these measurements in terms of constraints on gauge boson self-couplings are presented, covering both charged and neutral triple gauge couplings (TGC) and the more recently studied quartic gauge couplings (QGC). For each channel, salient experimental, technical or theoretical features are highlighted and results from combining the LEP data-sets are presented when available. The main achievements are assessed after each section, comparing cross-section measurements to present theoretical predictions, and constraints on gauge boson self-couplings to estimates of effects in scenarios for NP, and to sensitivities expected in the future. A general conclusion is given with prospects to finalize and publish all results.

[1] A good example is the Z-pair production process, for which event rates and topologies were almost identical to those in the Higgs boson search.

2 Four-fermion processes

2.1 Signal definition in the simulation

The expected cross-sections of the production processes $e^+e^- \rightarrow WW$, ZZ, $Z\gamma^*$, eeZ/γ^* and $e\nu W$ are shown for illustration in fig.1. When combining the measurements of different sub-channels or experiments, it is important to establish common conventions. Two ways of defining a signal to be measured were used, either as the total cross-section in a kinematic region where it is dominant or as that corresponding exclusively to the relevant Feynman graphs. In both cases a sub-set of events was pre-selected in the simulation with high purity and efficiency in terms of relative contribution of the studied process. The selected rates were then scaled into those of the studied process, taking into account interference effects for identical final states. In the first method cuts were chosen in view of theory uncertainties affecting both the studied and other contributing processes in the different regions.

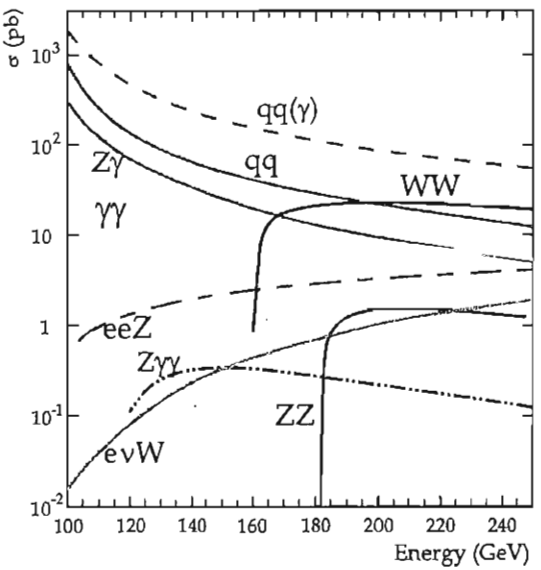

Figure 1: *Cross-sections of the main two and four-fermion processes at LEP-2.*

2.2 WW production

W-boson pairs are produced via the doubly-resonant graphs shown in fig.2 at tree level. Measurements of cross-sections and decay branching ratios, using a total of about 40000 events selected by the four LEP collaborations in the data collected in 1996-2000, are reported in [2]. All decay topologies $q\bar{q}q\bar{q}$, $l\nu q\bar{q}$ and $l\nu l\bar{\nu}$ were analysed. The separation achieved by ALEPH between signal and background is illustrated in fig.3.

The cross-sections obtained by combining all LEP results are shown in fig.4 as a function of the centre-of-mass energy, with a comparison to theoretical expectations [3]. The results clearly favour the SM prediction where the graphs in fig.2 involving TGCs are included, hence providing strong evidence for the non-Abelian gauge group structure of the theory. The highest precision was achieved by combining the results from all energies normalised to respective expectations. The best agreement was obtained using the new YFSWW [4] and RacoonWW [5] predictions. In these two calculations all $O(\alpha)$ electroweak (EW) radiative corrections relevant to the graphs in fig.2 were included through expansions about the W-pole (in the so-called leading and double pole approximations, respectively). They were introduced into "complete" $4f$ generators such as KoralW [6] and Wphact [7] by reweighting the relevant matrix elements, to achieve a consistent description of all processes in the full phase space[2]. The result obtained using YFSWW and combining the data from all energies was

$$\frac{\sigma_{\rm WW}}{\sigma_{\rm YFSWW}} = 0.997 \pm 0.007(stat) \pm 0.009(syst). \qquad (1)$$

Results with RacoonWW differed by only 0.2%, well within the estimated theory uncertainty of 0.5%. On the contrary a set of previously used predictions which did not include all EW radiative corrections were too high by 2%, illustrating the sensitivity to loop effects achieved in these results [1].

The main source of uncertainty was from limited precision in the modelling of QCD fragmentation and hadronization, which could bias selection efficiencies in the semi-leptonic and fully hadronic sub-channels and in the latter, background levels from $q\bar{q}(\gamma)$ final states with four or more jets. Such effects being correlated among experiments and energies and of similar magnitude as the statistical errors, a careful treatment was important in the combination [3]. All systematic errors were grouped in four classes (100% correlated or uncorrelated among experiments or energies) and the full covariance matrix for the measurements at each experiment and energy was built for the χ^2-minimisation. This procedure was applied to all LEP cross-section combinations described in

[2]The matching to the two-photon generation was also studied in Wphact.

this report. For the result quoted in eq.1 it gave $\chi^2 = 35.4$ for 31 degrees of freedom.

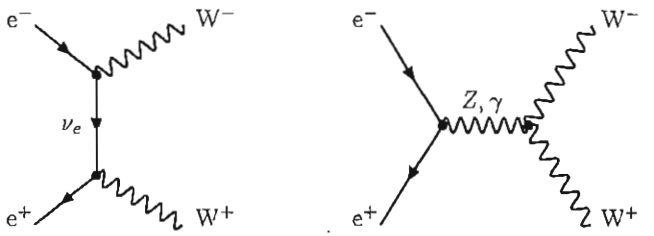

Figure 2: *Feynman graphs for on-shell WW production.*

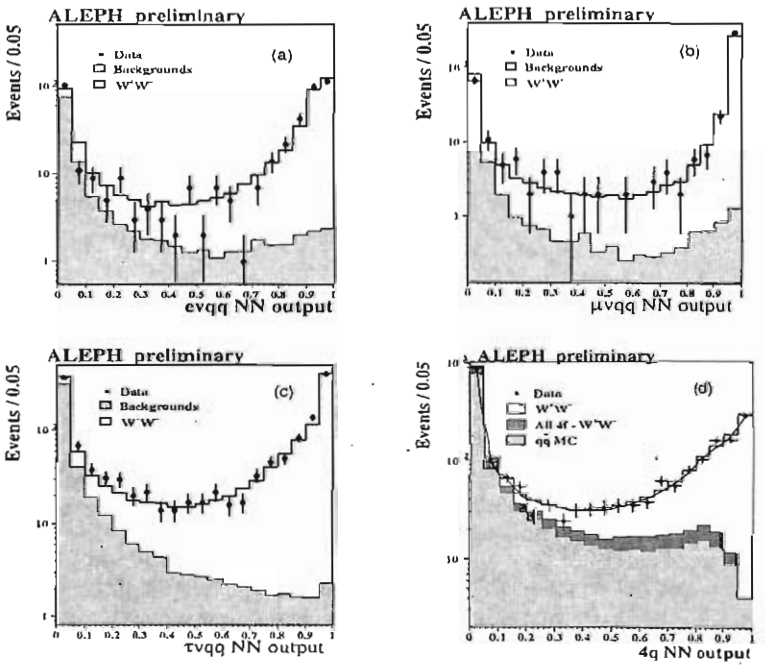

Figure 3: *Outputs from the neural networks used to isolate the W-boson pair signal in the fully hadronic and in the three semi-leptonic sub-channels.*

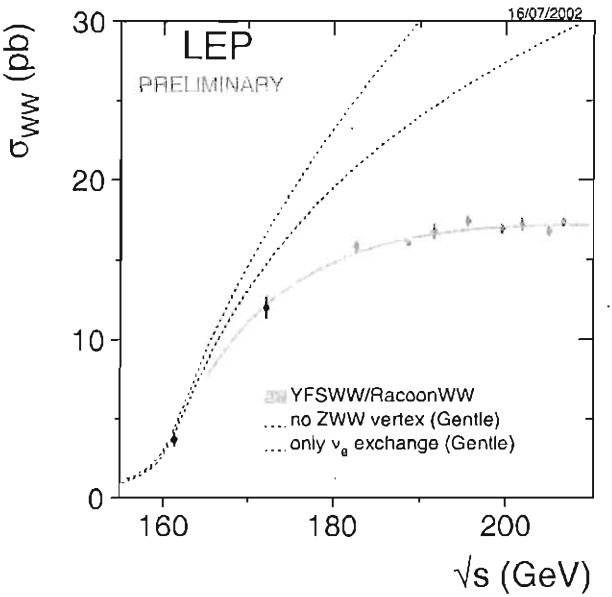

Figure 4: *Combined WW cross-section measurements compared with the SM predictions from YFSWW and RacoonWW. The dashed curves correspond to removing one or both of the graphs with triple gauge boson couplings in fig.2.*

2.3 ZZ production

Z-boson pair production occurs at tree level in the SM only via graphs with a t-channel electron (similar to that with a ν in fig.2). The cross-section was measured by the four LEP collaborations with data collected in 1997-2000 using all visible decays $q\bar{q}q\bar{q}$, $\nu\bar{\nu}q\bar{q}$, $ll q\bar{q}$, $llll$ and $\nu\bar{\nu}ll$ [8]. The combined result [3] shown in fig.5 agrees well with the SM predictions [1]. Combining all energies gave

$$\frac{\sigma_{ZZ}}{\sigma_{ZZTO}} = 0.969 \pm 0.047(stat) \pm 0.028(syst), \qquad (2)$$

using ZZTO, one of the calculations. The theoretical uncertainty, estimated to be 2%, was higher than for W-pairs (because radiative corrections were not fully included) but sufficient given measurement errors. The main correlated systematic errors, arising from the background modelling, were smaller than the statistical ones.

This measurement constrained potential anomalous production from NP, as described in sec.3.3 in the case of potential neutral TGCs. The reconstruction of the Z-boson polar angle achieved by DELPHI in this context is shown in the lower plot of fig.13.

Reconstructing the Z-boson pairs at LEP-2 was also an important test for the Higgs searches, since the analysed topologies were quasi-identical and cross-sections similarly small. L3 measured the $ZZ \to b\bar{b}X$ cross-section specially with this in mind [9].

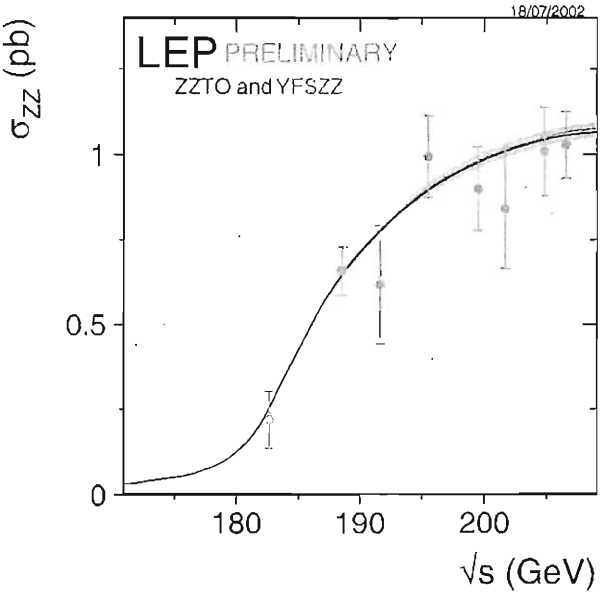

Figure 5: *Combined ZZ cross-section measurements compared with the SM predictions from ZZTO and YFSZZ. The band shows the theory uncertainty.*

2.4 $Z\gamma^*$ production

Measurements of neutral boson pairs were also extended to include an off-shell photon intead of a Z. The process can then be described as a "virtual radiative return to the Z", with characteristic forward-peaked production and quasi mono-energetic γ^* at the lower masses. Resulting topologies are distinctive and gave sizeable backgrounds in several searches for NP, which needed checking. They also led to an original search for anomalous production via neutral TGCs, using a new parametrization extended to include off-shell terms (see sec.3.3).

DELPHI analysed the $\mu\mu q\bar{q}$, $eeq\bar{q}$, $\nu\bar{\nu}q\bar{q}$, llll and $q\bar{q}q\bar{q}$ final states and OPAL the $\mu\mu q\bar{q}$ and $eeq\bar{q}$ ones [10]. Good agreement was found. Fig.6 shows the di-quark and di-lepton mass spectra obtained by OPAL. The suppression at low di-quark mass comes from the smaller leptonic Z-boson decay branching ratio. In final states with electrons, t-channel single-boson processes $ee(Z/\gamma^*)$ with both electron seen (see sec.2.5) enhanced the cross-section at high and low di-electron mass.

Another interesting final state, $\nu\bar{\nu}q\bar{q}$ has a mono-jet topology because the γ^* mass distribution peaks at low values. The corresponding energy-averaged cross-section was measured by DELPHI

$$\sigma_{Z\gamma^* \to \nu\bar{\nu}q\bar{q}} = 0.129 \pm 0.035(stat) \pm 0.015(syst) \text{ pb.} \quad (3)$$

The expected value was 0.088 pb. Uncertainties in the hadronization at low $q\bar{q}$ mass and in the way to set α_{em} given the different scales involved were shown to affect predictions by up to 5% [11]. Effects can be reduced by carefully treating the t-channel component in final states with electrons, and via phase space cuts. This should be good enough for the partial combination of three LEP experiments now planned.

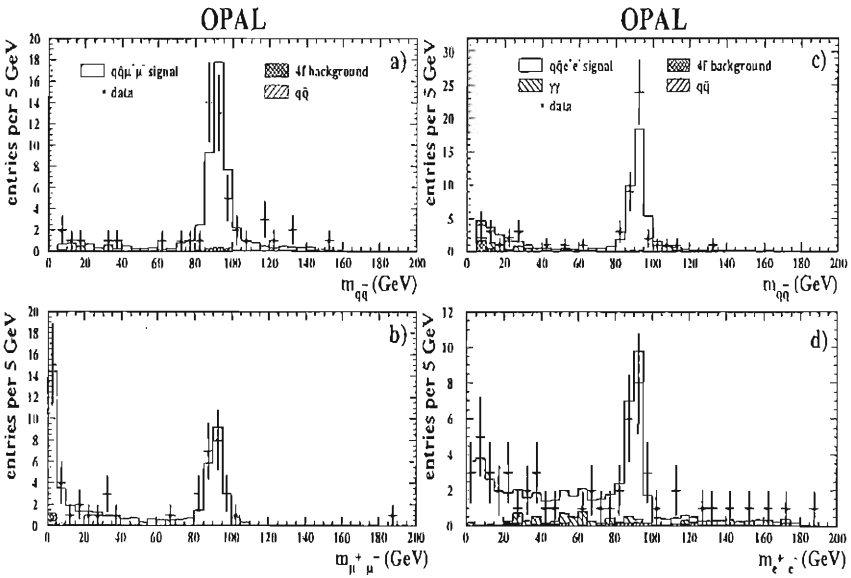

Figure 6: *Di-fermion invariant masses obtained in the* $Z\gamma^* \to llq\bar{q}$ *sub-channel after kinematic fitting with constraints from four-momentum conservation.*

2.5 eeZ/γ^* production

Neutral bosons can be produced singly via the so-called EW Compton scattering process $e^+\gamma \rightarrow e^+\gamma^*/Z$, where a quasi-real photon radiated from one of the beam electrons scatters off the opposite one (see fig.7). The signature of such events is an electron in the detector with moderate energy recoiling against the γ^*/Z system, with the other "spectator" electron mostly lost in the beam-pipe. LEP collaborations measured the $ee q\bar{q}$ and $ee\mu\mu$ final states with one electron lost using data collected in 1997-2000 [12]. Competing "single-tag" contributions from two-photon processes were suppressed using correlations between the tag electron charge and direction. The reconstruction of single-Z or γ^* components is illustrated in fig.8, where the hadronic mass spectrum from DELPHI is shown. The excess of data below the Z-boson mass is assumed to come from biases in the two-photon background. A combination of cross-sections using the ALEPH, DELPHI and L3 results [3] was performed in the high mass single-Z region, giving good agreement with expectations. The signal was defined as the cross-section from all graphs in the kinematic region: $m_{f\bar{f}} > 60$ GeV/c^2 (f = q, μ), $12^\circ < \theta_{e^-} < 120^\circ$, $\theta_{e^+} < 12^\circ$, $E_{e^-} > 3$ GeV/c^2 (with implicit charge conjugation). Averaging over energies gave

$$\frac{\sigma_{Zee}}{\sigma_{WPHACT}} = 0.951 \pm 0.068(stat) \pm 0.048(syst), \qquad (4)$$

using WPHACT, one of the calculations. Uncertainties in the way to set α_{em} and from treating initial state radiation given the different scales involved affected the predictions at the 5% level [11]. This matched the experimental errors, though some differential effects may need to be included.

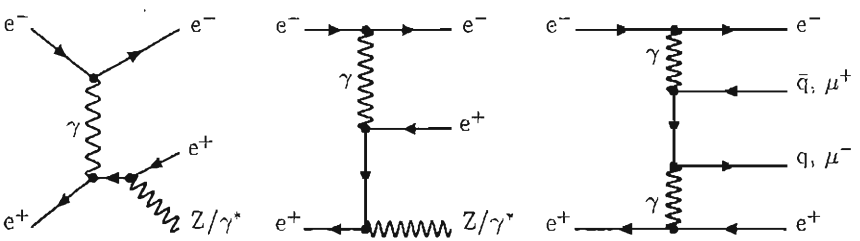

Figure 7: *Examples of tree level Feynman graphs for single neutral boson production (left and middle) and for the competing two-photon process (right).*

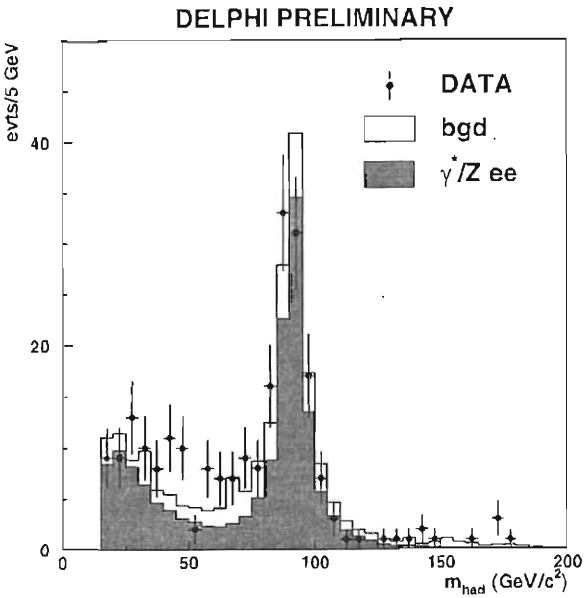

Figure 8: *Hadronic invariant mass obtained in the reconstruction of the* eeZ/γ^* *process after kinematic fitting with constraints from four-momentum conservation and assuming an electron lost along the beam-line.*

2.6 $\mathrm{e}\nu_\mathrm{e}\mathrm{W}$ production

W-bosons can also be produced singly via EW Compton scattering processes $\mathrm{e}^+\gamma \to \bar{\nu}_\mathrm{e}\mathrm{W}^+$ as depicted in fig.9. The middle graph involves charged TGCs which can be probed measuring this process (see sec.3.2). As for single Z-boson production, the spectator electron is mostly lost in the beam-pipe.

LEP collaborations measured all the possible final states $\mathrm{e}\nu_\mathrm{e}\mathrm{q}\bar{\mathrm{q}}$, $\mathrm{e}\nu_\mathrm{e}\mathrm{l}\nu_\mathrm{l}$ ($\mathrm{l} = \mathrm{e}, \mu, \tau$) with the electron lost using data collected in 1997-2000 [13]. The main signature was the large missing energy and either a pair of acoplanar jets with mass close to m_W or a single energetic lepton. The reconstruction achieved by L3 is illustrated in fig.10. The signal was defined as the complete t-channel sub-set of $4f$ graphs within kinematic cuts specified to reduce theoretically poorly known multiperipheral contributions from graphs such as the last one in fig.9: $\mathrm{e}\nu_\mathrm{e}\mathrm{q}\bar{\mathrm{q}}$: $m_{\mathrm{q}\bar{\mathrm{q}}} > 45$ GeV/c^2; $\mathrm{e}\nu_\mathrm{e}\mathrm{l}\nu_\mathrm{l}$ ($\mathrm{l} = \mu, \tau$): $E_\mathrm{l} > 20$ GeV; $\mathrm{e}\nu_\mathrm{e}\mathrm{e}\nu_\mathrm{e}$: $|\cos\theta_{\mathrm{e}^+}| < 0.95$ and $E_\mathrm{e}^+ > 20$ GeV. All results [3] agreed with SM expectations [1]. Combining the cross-sections measured by all experiments at

all energies gave

$$\frac{\sigma_{e\nu_e W}}{\sigma_{\mathrm{GRACE}}} = 0.949 \pm 0.067(stat) \pm 0.040(syst), \qquad (5)$$

using GRACE, one of the calculations. Uncertainties similar to those described in sec.2.5 for single Z-bosons affected single W-bosons. Even though for the (gauge-invariant) t-channel graphs defining the single W-boson signal, complete fermionic one-loop corrections exist [14], allowing the correct scale for α_{em} to be set, a 5% error was estimated [1], also here matching the experimental precision.

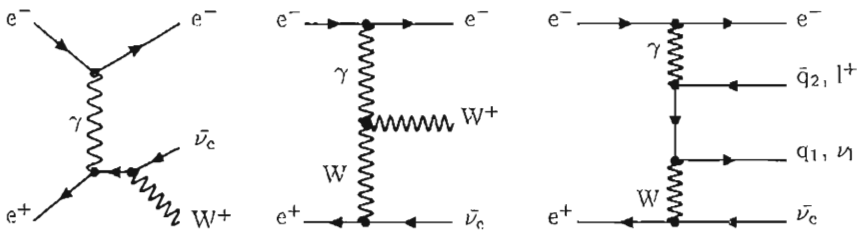

Figure 9: *Examples of tree level Feynman graphs for single W-boson production (left and middle) and for the multiperipheral contribution (right).*

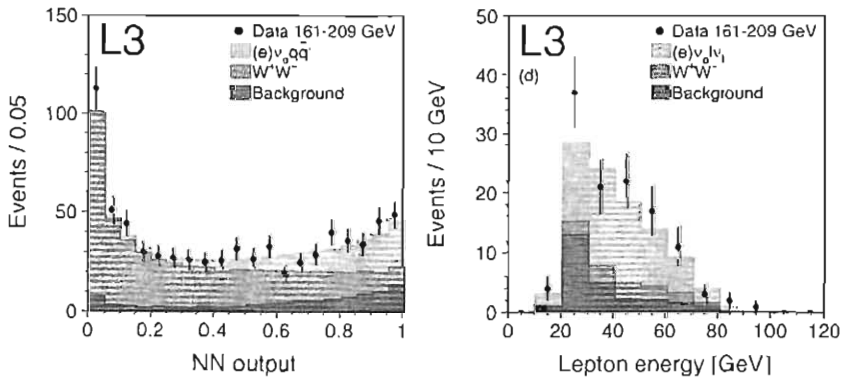

Figure 10: *Output from the neural network used to isolate the single W-boson signal in the hadronic sub-channel (left) and combined reconstructed lepton energy spectrum in the fully leptonic sub-channel (right).*

2.7 Summary

The comprehensive $4f$ measurement program conducted at LEP has been a success. It provided a large set of original results and established experimentally the SM environment where NP searches were carried out. The experimental precision achieved was matched by the accuracy of theory, as recalled in tab.1, in some cases after substantial work by the theoretical community [1].

In the case of the W-pairs the non-Abelian gauge group structure of the SM was clearly confirmed. The accuracy obtained, close to 0.5%, even allowed the SM calculation at loop level to be probed. In the case of the Z-pairs, a valuable experimental cross-check of the Higgs search at LEP-2 was made. In the case of the single-resonant boson processes SM predictions were tested in several yet unexplored regions.

Not all topics covered by the $4f$ sub-group of the LEP EW working group or by individual experiments could be reviewed in this report, for instance the measurements of the production polar angle, decay branching ratios, polarisation and spin correlations in the W-boson pair production process, and of the $Z\gamma\gamma$ cross-section[3].

Table 1: *Overview of experimental results and estimated theory errors for the production processes $e^+e^- \to WW$, ZZ, eeZ/γ^* and $e\nu W$. The predictions in the quoted ratios were obtained with the event generators YFSZZ, ZZTO, WPHACT and GRACE, respectively* [1].

physical process	measurement / prediction	theoretical precision
$e^+e^- \to WW$	$0.997 \pm 0.007(stat) \pm 0.009(syst)$	0.005
$e^+e^- \to ZZ$	$0.969 \pm 0.047(stat) \pm 0.028(syst)$	0.02
$e^+e^- \to eeZ/\gamma^*$	$0.951 \pm 0.068(stat) \pm 0.048(syst)$	0.05
$e^+e^- \to e\nu_e W$	$0.949 \pm 0.067(stat) \pm 0.040(syst)$	0.05

3 Gauge boson self-couplings

3.1 Overview

Couplings between the SM gauge bosons were measured at LEP by analysing $4f$ (and other) final states. Deviations from tree level values are predicted in NP scenarios and arise also from radiative corrections. If large enough to be

[3] A first partial combination of $WW\gamma$ cross-section measurements is shown in fig.14 in the context of the search for QGCs described in sec.3.4.

measured, such deviations can help to probe NP at energy scales beyond the kinematic range of direct searches for new particles.

Anomalous self-couplings were searched for at three and four boson vertices, involving both charged and neutral gauge bosons. Charged TGCs exist in the SM due to the non-Abelian gauge group structure (see sec.2.2). On the contrary neutral TGCs vanish at tree level. The SM predicts QGCs, but their size is very small. In the two latter cases one can only hope to detect anomalous contributions.

3.2 Charged triple gauge couplings

Parametrizations for the tree level VWW vertices (V=Z,γ) in the right and middle graphs of fig.2 and 9 involve in their most general form a Lorentz invariant Lagrangian with fourteen independent complex couplings [15]. Restricting the search to models with symmetries as in the SM (C, P, $U(1)_{em}$ and $SU(2)_L \times U(1)_Y$) the number of independent couplings reduces to three: g_1^Z, κ_γ and λ_γ. In the SM the two first couplings are equal to 1 and the latter vanishes. They can be related to the weak charge, magnetic dipole and electric quadrupole moments of the W-boson.

Deviations from the SM values can be probed in a complementary way via effects induced on the single and pair production processes (see sec.2.6 and 2.2), the former being sensitive mainly to κ_γ and the latter mainly to g_1^Z and λ_γ[4]. Results obtained by the four LEP collaborations using the data collected in 1996-2000 are reported in [17]. To maximize the sensitivity, the cross-sections, boson production polar angles, decay polar and azimuthal angles and average polarisation were exploited, using several adapted combination methods, based for example on "optimal observables" [18]. The reconstruction performed by L3 for the boson production and decay angles in semi-leptonic W-boson pairs is illustrated in fig.11.

The measurement of charged TGCs obtained by combining all LEP results is shown in fig.12 [3] with the negative log likelihoods provided by each experiment for each coupling, and their sums. Each coupling was minimized independently with the two others kept at their SM values[5]. Good agreement with the tree-level SM expectations was found within errors of 2-5%.

The main source of correlated systematic uncertainty was of theoretical nature, from the recent inclusion of $O(\alpha)$ EW radiative corrections in the W-pair production process (see sec.2.2). This source of error was estimated conservatively as the full difference between results using Monte Carlo samples

[4]The $\nu\nu\gamma$ final state also has some sensitivity to κ_γ and λ_γ through the WW fusion process [16].

[5]Two and three-parameter analyses resulted in weak correlations.

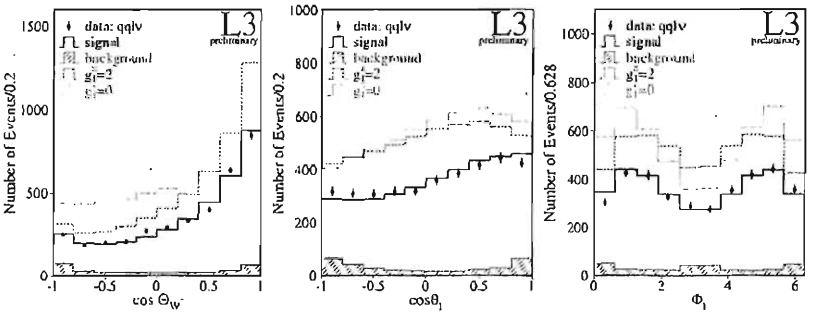

Figure 11: *Measured production polar angles (left), decay polar angles (middle) and decay azimuthal angles (right) of the W-bosons in the sub-channel* $WW \to l\nu q\bar{q}$. *The sensitivity to deviations from the SM prediction* $g_1^Z = 1$ *is indicated.*

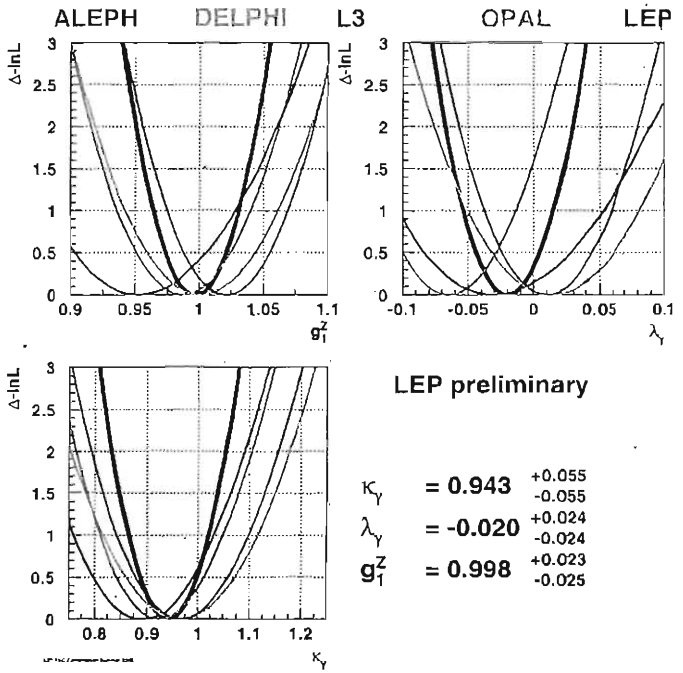

Figure 12: *Measurement of the charged TGC parameters* g_1^Z, κ_γ *and* λ_γ.

with and without these new corrections, yielding negative shifts of -0.015 for g_1^Z and λ_γ and -0.04 for κ_γ. Although these shifts are sizeable, it can be seen from their signs and from the values found for the couplings that the agreement with the SM is as good with or without them. This is different from the cross-section measurement, where the improvement from the new corrections was clear. This feature is perhaps a little surprising, since more information is used to extract the charged TGCs, like angles and the single W-boson channel.

Since these shifts had similar sizes as the statistical errors and were fully correlated between energies and experiments, a careful treatment was implemented in the combination, expressing the likelihoods as functions of each coupling and of additional free parameters, to represent each error weighted by its sensitivity in each experiment, and by then performing a simultaneous minimization [3].

3.3 Neutral triple gauge couplings

There are no self-couplings involving exclusively neutral gauge bosons at tree level in the SM.

For NP satisfying Lorentz invariance and preserving the $U(1)_{em}$ and Bose symmetries for identical particles, the most general parametrization for the ZZZ, ZZγ and Z$\gamma\gamma$ vertices has twelve independent parameters, six of which are CP-conserving: $h_{3,4}^{Z/\gamma}$ and $f_5^{Z/\gamma}$, while the other six are CP-violating: $h_{1,2}^{Z/\gamma}$ and $f_4^{Z/\gamma}$ [15]. The h and f terms describe the Vγ and VZZ vertices, respectively, where $V = Z, \gamma$ is off-shell but the two other bosons are on-shell.

These two classes of neutral TGCs can be probed via effects induced on the production processes $e^+e^- \to Z\gamma$ and ZZ, respectively (see sec.2.3 for the measurement of the latter). Results obtained by the four LEP collaborations using the data collected in 1996-2000 are reported in [19]. The cross-sections and boson production angles were exploited, as well as, for the $e^+e^- \to Z\gamma \to q\bar{q}\gamma$ process the Z decay angle in its rest frame and, for the $e^+e^- \to Z\gamma \to \nu\bar{\nu}\gamma$ process the photon energy. The reconstruction performed by DELPHI for the two angles just described is illustrated in fig.13.

The constraints on neutral TGCs obtained combining all LEP results are shown in tab.2 [3]. The precision was dominated by statistical errors. There was lower sensitivity to f than to h terms because of the less favourable kinematics at the threshold for Z-boson pair production.

The analysis done treated h and f terms separately, though it has recently been shown that using the $SU(2)_L \times U(1)_Y$ symmetry as in the charged case relates the Vγ and VZZ vertices for some classes of operators and can lead to fewer independent couplings [20]. Although some generality may be lost, this will now be done as well. It is expected that the more precise $e^+e^- \to Z\gamma$

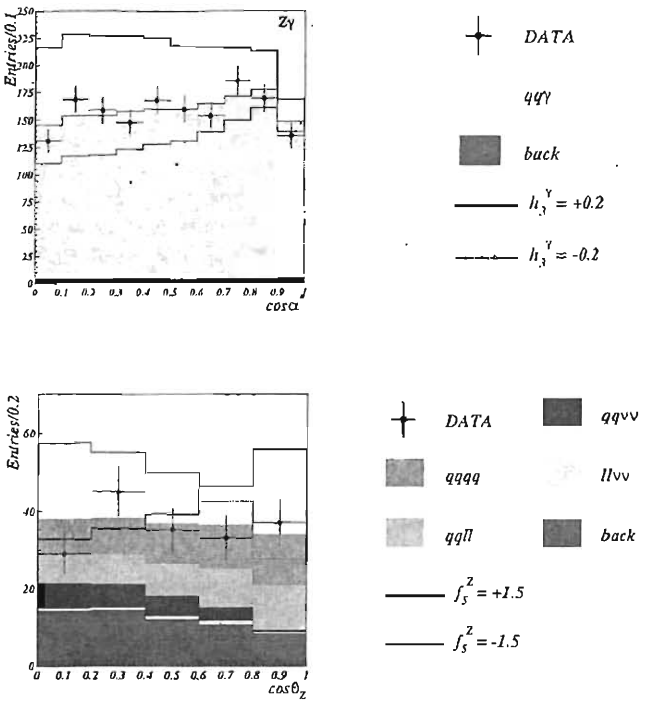

Figure 13: *Measured decay angle of the Z in its rest frame in the* $e^+e^- \to Z\gamma \to q\bar{q}\gamma$ *process (upper plot). Measured production angle in Z-boson pairs for the main final states studied by DELPHI* [8] *(lower plot). The sensitivity to the presence of CP-conserving* h_3^γ *and* f_5^Z *couplings, respectively at the* $\gamma Z\gamma$ *and ZZZ vertices, is indicated.*

measurements will dominate the constraints from such a combined analysis.

Another recent theoretical development has enabled a generalization of the description by including off-shell bosons [21]. It was argued that the resulting effects cannot be ignored in detailed experiments, especially if data measured outside the strictly on-shell regions of the Z-pair and $Z\gamma$ processes are also used. A first study in this direction has been presented by DELPHI, based on the $Z\gamma^*$ production measurement (see sec.2.4) [19].

Table 2: *Combined 95 % confidence level probability intervals for the neutral TGCs probed by measuring the* $e^+e^- \to Z\gamma$ *and ZZ processes. The constraints shown on h and f terms result from the single and two-parameter analyses, respectively. Some correlation between h terms was observed in a two-parameter analysis done combining results from three experiments* [3]. *The two latter bosons at each listed vertex correspond to the final state produced and are on-shell.*

vertex	CP	parameter	95 % CL limits
$\gamma Z\gamma$	odd	h_1^γ	[-0.056, +0.055]
$\gamma Z\gamma$	odd	h_2^γ	[-0.045, +0.025]
$\gamma Z\gamma$	even	h_3^γ	[-0.049, +0.008]
$\gamma Z\gamma$	even	h_4^γ	[-0.002, +0.034]
$ZZ\gamma$	odd	h_1^Z	[-0.13, +0.13]
$ZZ\gamma$	odd	h_2^Z	[-0.078, +0.071]
$ZZ\gamma$	even	h_3^Z	[-0.20, +0.07]
$ZZ\gamma$	even	h_4^Z	[-0.05, +0.12]
γZZ	odd	f_4^γ	[-0.17, +0.19]
ZZZ	odd	f_4^Z	[-0.30, +0.28]
γZZ	even	f_5^γ	[-0.34, +0.38]
ZZZ	even	f_5^Z	[-0.36, +0.38]

3.4 Quartic gauge couplings

The couplings predicted in the SM at the WWWW, WWZZ, WW$\gamma\gamma$ and WWZγ vertices are below LEP-2 sensitivities. The searches performed probed potential anomalous contributions arising from NP, concentrating on operators which do not simultaneously cause anomalous TGCs. It has been argued that such operators, often referred to as "genuine" QGCs, can be related more directly to the scalar sector of the theory [22]. The parametrization used involves four CP-conserving terms at the WW$\gamma\gamma$ and ZZ$\gamma\gamma$ vertices, $a_{0,c}^{W,Z}$, and a CP-violating one at the WWZγ vertex, a_n [23]. By convention these terms are usually normalised to Λ^2, the square of the energy scale at which the NP responsible for them appears.

Experimentally these terms were probed by measuring the three boson final state processes $e^+e^- \to WW\gamma$ (for $a_{0,c}^W$ and a_n) and $e^+e^- \to Z\gamma\gamma$ (for $a_{0,c}^Z$), using both the rates and energy spectra of the photons [24]. The presence of $a_{0,c}^{W,Z}$ terms was also studied through their influence on the $e^+e^- \to \nu\nu\gamma\gamma$ process, via a contributing graph with WW fusion and another one involving neu-

trino pair production mediated by a Z boson which radiates two photons [25]. Both the rate and the photon pair recoil mass spectrum were exploited.

Only the L3 $Z\gamma\gamma$ and OPAL $\nu\nu\gamma\gamma$ results were combined so far, allowing to set the following 95% CL limits on the $ZZ\gamma\gamma$ vertex: $-0.033 < a_0^Z \times GeV^2/\Lambda^2 < 0.046$ and $-0.009 < a_c^Z \times GeV^2/\Lambda^2 < 0.026$ [3]. A combination of the cross-sections obtained by DELPHI and L3 for the $WW\gamma$ final state was also performed[6] and is illustrated in fig.14, together with the SM prediction of EEWWG [26] and the sensitivity to the CP-violating a_n coupling. No combined constraints on $a_{0,c}^W$ and a_n QGCs were yet obtained from this limited cross-section information, but individual results have been published, for example the L3 one: $-0.015 < a_0^W \times GeV^2/\Lambda^2 < 0.015$ and $-0.048 < a_c^W \times GeV^2/\Lambda^2 < 0.026$ (using also the information from the $\nu\nu\gamma\gamma$ final state), and $-0.14 < a_n \times GeV^2/\Lambda^2 < 0.13$.

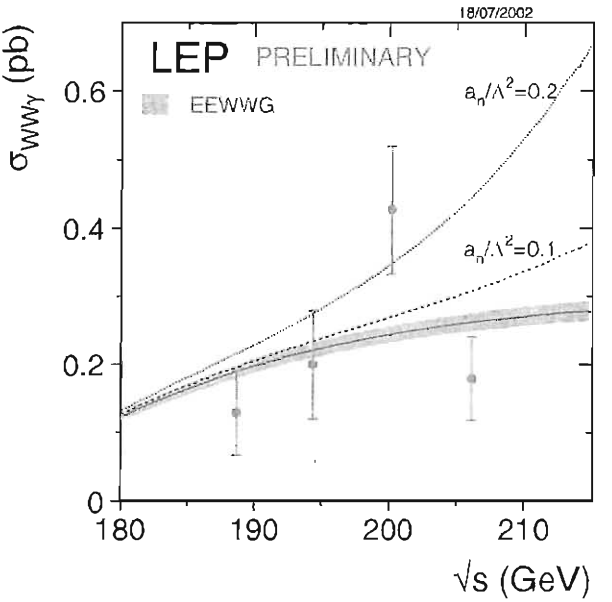

Figure 14: *Combination of $WW\gamma$ cross-section measurements by DELPHI and L3 compared with the SM prediction. The sensitivity to the presence of a CP-violating a_n coupling at the $WWZ\gamma$ vertex is indicated by the predicted distribution for two values of a_n/Λ^2 (in units of GeV^{-2}).*

[6]The signal was defined as the cross-section from all graphs in the kinematic region: $|m_{f\bar{f}} - m_W| < 2\Gamma_W$, $\cos\theta_{\gamma,f} < 0.90$, $|\cos\theta_\gamma| < 0.95$ and $E_\gamma > 5$ GeV.

3.5 Summary

The charged TGCs were measured within a few 0.01 of their predicted values in the SM, confirming again the non-Abelian gauge group structure. NP giving anomalous contributions of the order of these errors could be excluded. The sensitivity was not enough to probe SM loop effects, which are predicted to be at the 0.003 level. It was also barely enough to sense effects from SUSY even in the most optimistic scenarios with sparticles not far above the kinematic limit. A Z′ with a low mass would on the other hand have produced visible effects, but would also have been strongly felt in di-fermion cross-section measurements [27].

Some improvement to the precision is still expected from on-going work to estimate the uncertainty on the $O(\alpha)$ corrections in a better way than just quoting their full effect, for instance by varying assumptions in the theoretical treatments used. This could help to understand why there was some sensitivity to SM loop effects when measuring the total cross-section (see sec.2.2) but not the charged TGCs (see sec.3.2). Further ahead experiments at higher energies will improve the sensitivity. The TeVatron with 10 fb^{-1} and the LHC with 300 fb^{-1} should for example pin down λ_γ to about ± 0.005 and ± 0.0003, respectively. A good sensitivity to all TGCs is expected at a future e^+e^- linear collider. For instance TESLA should reach a precision of a few ± 0.0001 after collecting 1500 fb^{-1} at $\sqrt{s} = 800$ GeV [28].

The neutral TGCs were found to be zero as expected, but within larger error ranging from ± 0.05 to ± 0.30. In the case of perturbative NP, anomalous contributions to neutral TGCs are expected to be depressed by at least one more power of $m^2_{W,Z}/\Lambda^2$ compared to charged ones, because operators with higher dimension are involved. Neutral TGCs expected from several scenarios for NP have for example been studied in [29]. The overall conclusion reached was that potential effects were generally below experimental sensitivities, except in cases of new particles with masses just above the kinematic reach, or of NP which is not perturbative.

The QGCs were also found to be close to zero as expected. Here the expected "natural" size of couplings at LEP-2 is about 1 for NP with an energy scale $\Lambda = 3$ TeV, which is far below the experimental sensitivity [30].

Even though effects on gauge couplings from the NP scenarios that were investivated turned out to be too small to be detected, the systematic search program carried out at LEP-2 was certainly justified to demonstrate the validity of the SM, and to show that there is no evidence of new physics from totally unexpected sources. The analyses done are also a useful preparation for similar work at future high energy colliders.

Recent measurements and analyses of spin density matrix elements in the W-boson pair production process are not covered here.

4 Conclusions and prospects

The results on the measurements of $4f$ final states and gauge boson self-couplings are an important part of the LEP legacy. The present work is to complete the documentation promptly, while the main physicists involved are still available. All final experimental results and combinations are expected during 2003. At the time of this writing, only the measurements by DELPHI of Z-boson pair production, by L3 of single boson production and quartic couplings, and by OPAL of $Z\gamma^*$ production are considered truly "final" in the sense of being described in a refereed CERN-EP preprint note or journal publication. It is important to ensure a high quality and an appropriate level of detail in the descriptions of the analyses and final results to facilitate future reading.

5 Acknowledgements

The beautiful experimental results presented in this report are one of the cherries on the LEP-2 cake: a long chain of prior tasks was required. The accelerator physicists and operators achieved energies and luminosities in excess of expectations. The experimental teams took quality data with ever rising efficiencies. Alignment and calibration procedures were carried out. Huge sets of Monte Carlo simulations were produced and checked. And more... All this detailed work and the people involved must be recognised.

The work of the $4f$ and Gauge Couplings LEP working groups should also be acknowledged. Such common inter-collaboration groups provide a competitive and stimulating environment where the best experts from each experiments can share their knowledge, discuss approaches, compare and cross-scrutinize each others results and methods. They were an important ingredient which enhanced the scientific quality and can serve as example for the future.

Personally, I would like to thank my colleagues in the DELPHI $4f$ team for collaborating over the years and for the good spirit, in particular Sandro Ballestrero, Marcia Begalli, Maurizio Bonesini, Guennadi Borisov, Roberto Contri, Niels Kjaer, Esther Ferrer, Enrico Graziani, Anna Lipniacka, Ernesto Migliore, Rosy Nikolaidou, Hywel Phillips, Maria Elena Pol, Jens Rehn, Robert Sekulin, Alessandra Tonazzo, Valerio Verzi, Ivo van Vulpen and Mariusz Witek. Special thanks also to the successive DELPHI spokesmen Daniel Treille, Wilbur Venus, Tiziano Camporesi and Jan Timmermans, who supported our work and to Roberto Chierici, Ulrich Parzefall and Robert Sekulin, who helped me prepare this review. Jan, Robert, Roberto and Sandro also kindly proof-read this text.

References

1. E. Accomando *et al*, *Four-fermion production in e^+e^- collisions*, Reports of the working groups on precision calculations for LEP2 Physics, S. Jadach, G. Passarino, R. Pittau (eds.) CERN 2000-009 (2000), 1.
2. LEP collaboration public notes ALEPH 2001-013, DELPHI 2002-054, L3 note 2756, OPAL PN-469 with preliminary results and references therein.
3. The LEP collaborations ALEPH, DELPHI, L3 and OPAL, the LEP EW working group and SLD heavy flavours and electroweak groups, *A combination of preliminary electroweak measurements and constraints on the standard model*, CERN-EP/2002-091 (also hep-ex/0212036).
4. S. Jadach *et al*, Comput. Phys. Commun. **140**, 432 (2001).
5. A. Denner *et al*, Nucl. Phys. **B587**, 67 (2000).
6. S. Jadach *et al*, Comput. Phys. Commun. **140**, 475 (2001).
7. A. Ballestrero *et al*, Comput. Phys. Commun. **152**, 175 (2003).
8. DELPHI collaboration, J. Abdallah *et al*, CERN-EP/2003-009.
   LEP collaboration public notes ALEPH 2001-006, L3 note 2770, OPAL PN-482 with preliminary results and references therein.
9. L3 collaboration, M. Acciarri *et al*, Phys. Lett. **B497**, 23 (2001).
10. OPAL collaboration, G. Abbiendi *et al*, Phys. Lett. **B544**, 259 (2002).
    DELPHI collaboration public note 2001-096 with preliminary results.
11. E. Accomando *et al*, Comput. Phys. Commun. **150**, 166 (2003).
    For the hadronization of low mass systems, see M. Boonekamp, hep-ph/0111213.
12. OPAL collaboration, G. Abbiendi *et al*, Phys. Lett. **B438**, 391 (1998).
    L3 collaboration, P. Achard *et al*, CERN-EP/2002-103.
    LEP collaboration public notes ALEPH 2002-029 and DELPHI 2002-057 with preliminary results and references therein.
13. L3 collaboration, P. Achard *et al*, Phys. Lett. **B547**, 151 (2002).
    LEP collaboration public notes ALEPH 2001-017, DELPHI 2002-057 and OPAL PN-427 with preliminary results and references therein.
14. E. Accomando *et al*, Phys. Lett. **B479**, 209 (2000).
    G. Passarino *et al*, Nucl. Phys. **B574**, 451 (2000).

15. K. Hagiwara *et al*, Nucl. Phys. **B282**, 253 (1987).

16. OPAL collaboration public note PN-508 with preliminary results and references therein.

17. LEP collaboration public notes ALEPH 2001-027, DELPHI 2002-016, L3 note 2734, OPAL PN-501 with preliminary results and references therein. The L3 publication in [13] also includes a determination of κ_γ.

18. M. Diehl *et al*, Z. Phys. **C62**, 397 (1994).

19. OPAL collaboration, G. Abbiendi *et al*, Eur. Phys. J. **C17**, 13 (2000). LEP collaboration public notes ALEPH 2001-061, DELPHI 2001-097, L3 notes 2672 and 2696, OPAL reference in [8] with preliminary results and references therein.

20. G. Gounaris *et al*, Phys. Rev. **D65**, 017302 (2002). J. Alcaraz, Phys. Rev. **D65**, 075020 (2002).

21. G. Gounaris *et al*, Phys. Rev. **D62**, 073012 (2000).

22. S. Godfrey, *Quartic Gauge Boson Couplings*, hep-ph/9505252.

23. G. Bélanger *et al*, Phys. Lett. **B288**, 210 (1992). W. Stirling *et al*, J. Phys. **G21**, 517 (1995).

24. OPAL collaboration, G. Abbiendi *et al*, Phys. Lett. **B471**, 293 (1999). L3 collaboration, P. Achard *et al*, Phys. Lett. **B527**, 29 (2000). L3 collaboration, P. Achard *et al*, Phys. Lett. **B540**, 43 (2002). DELPHI collaboration public note 2002-059 with preliminary results.

25. OPAL collaboration public note PN-510 with preliminary results.

26. W. Stirling *et al*, Eur. Phys. J. **C14**, 103 (2000).

27. G. Gounaris *et al*, *Triple Gauge Boson Couplings Working Group*, Physics at LEP2, G. Altarelli, T. Sjostrand, F. Zwirner (eds.) CERN Report 96-01 (1996).

28. R. Heuer *et al* (eds.), *Part III: Physics at an e^+e^- linear collider*, TESLA Technical Design Report (2001).

29. G. Gounaris *et al*, Phys. Rev. **D62**, 073013 (2000).

30. G. Bélanger *et al*, Eur. Phys.J. **C13**, 283 (2000).

HIGGS RESULTS AND SEARCHES FOR NEW PHYSICS AT LEP

Pablo García
CIEMAT, Madrid

Written contribution not received

SEARCHES FOR NEW PHYSICS AT HERA

L. Bellagamba
INFN Bologna
on behalf of the H1 and ZEUS Collaborations

Abstract

A review of recent results on search for physics beyond the Standard Model at the *ep* collider HERA is presented. Due to the peculiarity of the *ep* collisions, which have both lepton and baryon numbers in the initial state, the presented results for contact interactions, leptoquarks, squarks in R parity violating SUSY and excited fermions, are, to large extent, complementary to those of LEP and TEVATRON.

1 Introduction

At HERA 27.5 GeV electrons or positrons collide against 920 GeV (820 GeV before 1998) protons, resulting in a center-of-mass energy, $\sqrt{s}$, of 318 (300) GeV. The maximum square momentum transfer reached, Q^2, is few times 10^4 GeV^2, allowing to probe the proton structure at the level of 10^{-16} cm.
The luminosity collected by the two experiments, H1 and ZEUS, in the years 1994-2000 was approximately 110 pb^{-1} with e^+p and 15 pb^{-1} with e^-p. High energy ep collisions offer a unique environment to search for new physics. In this report we review the status of the search for contact interactions, leptoquarks, squarks in R parity violating supersymmetric (SUSY) models and excited fermions.

2 Contact interactions

New physics at very high energy scale can produce, via virtual processes, sizeable effect at the energy range accessible at HERA. Four-fermion contact interaction model is a convenient way to parameterize the virtual effects of new physics that could produce deviations from the Standard Model (SM) expectations at high Q^2. As strong limit have already been placed for scalar and tensor couplings [1], we considered here only the vector cases which can be represented adding the following extra-terms to the SM lagrangian:

$$L_{CI} = \sum_{\alpha,\beta=L,R}^{q=u,d} \eta^q_{\alpha\beta}(\bar{e_\alpha}\gamma^\mu e_\alpha)(\bar{q_\beta}\gamma^\mu q_\beta) \qquad (1)$$

where the coefficients $\eta^q_{\alpha\beta} = \epsilon_{\alpha\beta} g^2_{CI}/\Lambda^2$ characterize the different CI scenarios defining their chiral properties via the sign of the interference with the SM, $\epsilon_{\alpha\beta}$, their strength via the coupling g_{CI} (by convention set to $g_{CI} = \sqrt{4\pi}$) and their effective mass scale via the parameter Λ (α and β are the electron and quark helicity, respectively and q is the quark flavor). The measurement of the high-Q^2 Neutral Current cross section, performed by both collaborations [2, 3], show good agreement with the SM; limits on the scale Λ were hence derived for several CI scenarios. Table 1 shows 95% confidence level (CL) limits for few scenarios for HERA experiments, CDF and OPAL collaborations. Models which foresee large extra dimensions could also produce sizeable deviations from SM expectations if the extra-dimensions are compactified to a size of the order of the millimeter. In these models the graviton, differently from the other SM particles, can propagate also through the extra-dimensions and the effective Plank scale, M_S, could be comparable to the electro-weak scale. The specific model [6] have been considered and a limit $M_S > 0.8$ TeV [7, 8] have been set at 95% CL.

	H1 (Prel.)	ZEUS (Prel.)	CDF	OPAL
VV+	5.3	6.5	5.0	3.8
VV-	5.5	7.0	6.3	4.9
AA+	2.5	4.6	4.5	3.4
AA-	4.1	5.3	5.6	4.5

Table 1: 95% *CL limits on* Λ *(TeV) for the* $VV\pm$ *(*$\eta_{LL} = +\eta_{LR} = +\eta_{RL} = +\eta_{RR} = \pm 4\pi/\Lambda^2$*) and* $AA\pm$ *(*$\eta_{LL} = \eta_{LR} = \eta_{RL} = +\eta_{RR} = \pm 4\pi/\Lambda^2$*) CI scenarios. CDF* [4] *and OPAL* [5] *results are also shown*

3 Leptoquarks and squarks

Leptoquarks (LQs) are color-triplet bosons carrying both leptonic (L) and baryonic (B) numbers. They are foreseen by several SM extensions which connect the lepton and the quark sectors. These states can be directly produced at HERA via the fusion of the initial state electron with a quark in the proton, the production cross section depending on the unknown Yukawa coupling λ. The results have been interpreted in the framework of the Buchmüller-Rückl-Wyler [9] model, which foresees 14 LQ types (7 scalar and 7 vector) with fixed branching ratios to eq and νq. The LQs are characterized by the fermionic number, $F \quad 3B + L = 0, \pm 2$. F=0 LQs couple a particle with an anti-particle and are therefore better tested in e^+p collisions while $|F| = 2$ LQs, coupling two particles or two anti-particles, are better tested in $e \ p$ collisions. The LQ, decaying to lepton-quark pair, produces a final state which is, event by event, indistinguishable from SM deep inelastic scattering (DIS), on the other hand the x and y distributions are different. LQs with a mass M_{LQ} below the HERA center of mass energy are predominantly produced as a s-channel resonance peaked at $x = M_{LQ}^2/s$ while dependence on the inelasticity variable y, which is related to the lepton decay angle in the LQ rest frame (θ^*, with $cos\theta^* = 1 \quad 2y$), is different for scalar LQs (flat in y), vector LQs ($\sim (1 \quad y)^2$) and SM DIS ($\sim 1/y^2$). A cut in y is therefore used to enhance the LQ signal over the DIS background. No evidence of signal has been found by either collaboration [10, 11, 12]. limits on λ as a function of M_{LQ} have been derived and shown in fig. 1 compared to Tevatron and LEP limits. A more general LQ model have also been considered, treating the branching ratios to electron and neutrino, β_e and β_ν, as free parameters, with the constraints $\beta_e + \beta_\nu = 1$. In this case combining the e (NC) and the ν (CC) channels, the limits obtained are largely independents of the branching ratios. HERA experiments have unique sensitivity for $\beta_e \ll 1$.

Leptoquarks could also mediate lepton-flavor violating (LFV) processes if, be-

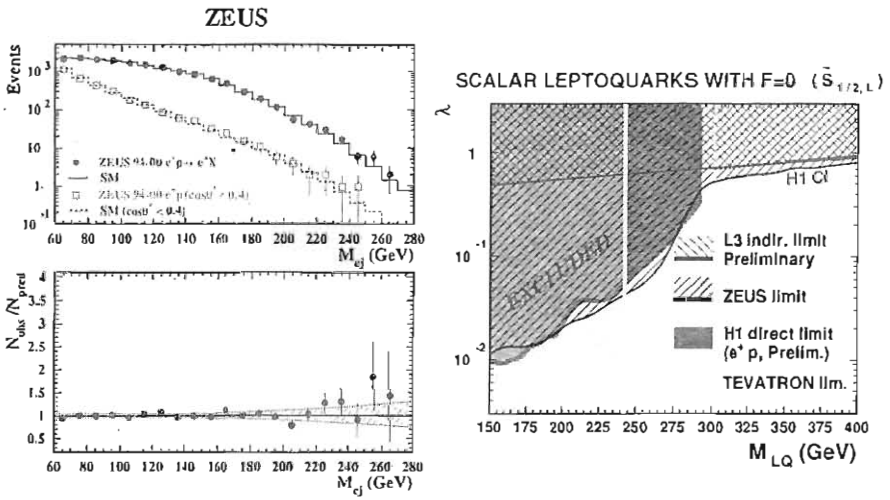

Figure 1: *Left plot: e-jet invariant mass spectrum for ZEUS and comparison with SM expectation. Right plot: exclusion limits at 95% CL on the Yukawa coupling λ as a function of the mass for a scalar LQ with $F = 0$ for ZEUS and H1. The region above the curves are excluded. LEP and TEVATRON limits are also shown.*

side the eq coupling, they have also a coupling to higher generation leptons. Both ZEUS and H1 [13, 11] have studied such a possibility. In some cases, when higher generation quarks are involved and especially for the τ channel, HERA constraints improve on bounds from rare decays.

Squarks in R parity violating SUSY models can also be directly produced at HERA. The H1 collaboration [14] considered the direct production of single squarks of any generation in eq fusion via a Yukawa coupling λ', taking into account R parity violating and conserving decays of the squarks. No significant deviation from the SM expectations was found and the results have been interpreted in term of constraints within the Minimal Supersymmetric Standard Model (MSSM) and the minimal Supergravity Model (mSUGRA). The left plot of fig. 2 shows the 95% CL limit for the λ' coupling involved in stop production. The indirect bound from atomic parity violation is also reported. The right plot shows, within the mSUGRA framework, the domain of the plane $(m_0, m_{\frac{1}{2}})$ excluded by H1, assuming a coupling of electro-weak strength. Squarks of the first two family, up to a mass of 260 GeV, are excluded. Limit from D0 is also reported.

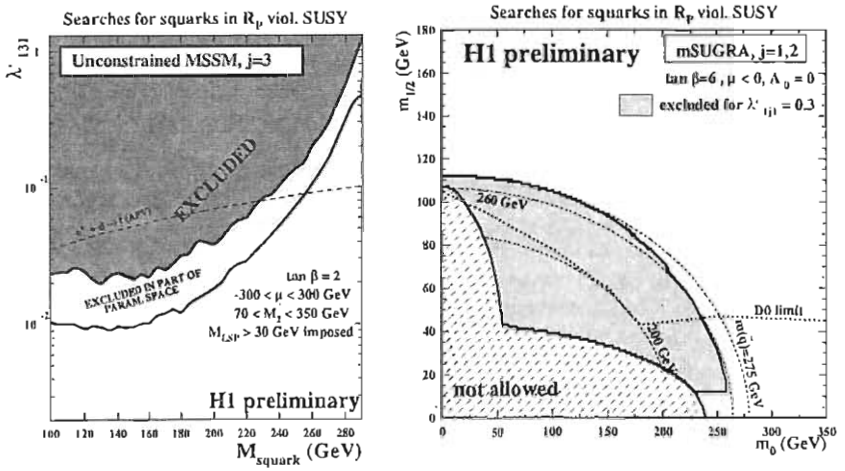

Figure 2: *Left plot: upper limit at 95% CL for the λ' coupling involved in stop production as a function of the stop mass for* $\tan\beta = 2$. *For each stop mass a scan of the MSSM parameters M_2 and μ have been performed and the largest (lowest) value of the coupling limit is shown by the upper (lower) full curve. Bound from APV is also shown. Right plot: excluded region in m_0, $m_{\frac{1}{2}}$ plane within the mSUGRA framework, for the first two squark families, assuming $\lambda' = 0.3$, $\tan\beta = 6$, $\mu < 0$ and $A_0 = 0$. Limit from D0 is also reported.*

4 Excited fermions

In this section searches for excited electrons and neutrinos are presented, more details on the following results are reported in [15, 16, 17]. At HERA excited electrons (neutrinos) could be singly produced through t-channel γ and Z (W) boson exchange. Their production cross-section and partial decay width have been calculated using an effective lagrangian [18, 19] which depends on a compositness scale Λ and on form factors f and f', reduced here to constants, describing the relative coupling strengths of the excited leptons to the $SU(2)_L$ and $U(1)_Y$ gauge bosons, respectively. Usually these coupling parameters are assumed to be of comparable strength and the relationships $f = +f'$ and $f = -f'$ are considered. In this case the production cross sections and partial decay widths depend only on the excited lepton mass and the ratio f/Λ. All the decay channels $e^*(\nu^*) \rightarrow e(\nu)\gamma$, $e^*(\nu^*) \rightarrow \nu(e)W$ and $e^*(\nu^*) \rightarrow e(\nu)Z$ have been searched for, considering the subsequent W and Z hadron decay (the ZEUS collaboration also considered in the e^* case the $Z \rightarrow \nu\bar{\nu}$ decay). The signature of such processes is very clear: a high energetic electrons and/or large missing transverse momentum beside a peak in the invariant mass of the lepton and the gauge boson. Such clear signatures allowed to select the signal with high efficiency. For the e^* decay in $e\gamma$ the efficiency was in the range

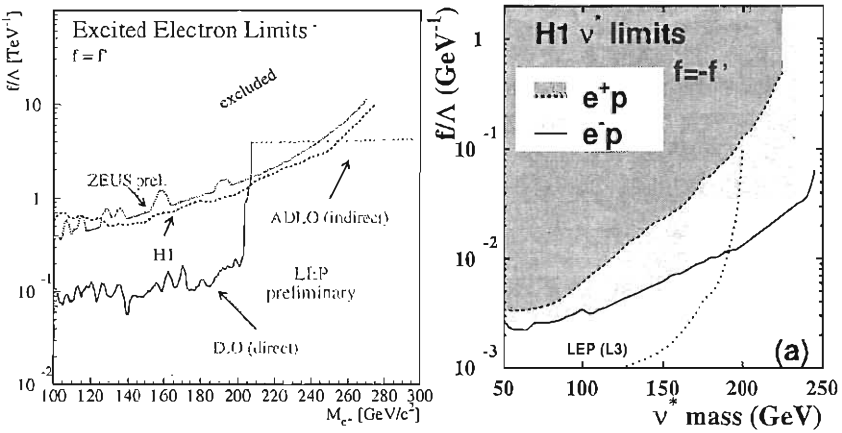

Figure 3: *Exclusion limit on f/Λ at 95% CL as a function of the mass for e^* in case of $f = +f'$ (left plot) and for ν^* in case of $f = f'$ (right plot). In the e^* case, exclusion limit are reported for H1 (full statistics), ZEUS (e^+p data collected in 1994-1997) and LEP experiments. In the ν^* case, exclusion limit by H1 refers to e p and e^+p data collected in 1998-1999 and in 1994-1997, respectively.*

70 80%, while in the other cases it was typically 30 60% for masses in the range 130 250 GeV. The most important sources of backgrounds are the NC and CC DIS and the W production. Since no excess over the SM expectations was found, limits at 95% CL were set on f/Λ as a function of e^* and ν^* masses. Fig. 3 show the HERA and LEP results for e^* in the case of $f = +f'$ and H1 and L3 [20] results for ν^* in the case $f = f'$ (the ZEUS collaboration has similar results [15]). The HERA limits extends the excluded region to higher masses than reached in previous direct searches.

5 Conclusions

A review have been presented of the searches for physics beyond SM at HERA. The results are in general comparable/complementary to those of LEP and TEVATRON.

In the next few years H1 and ZEUS will increase considerably the data statistics, thus a very interesting program for the searches of new physics will be thus pursue by the HERA experiments, waiting for the first LHC collisions.

References

1. W. Buchmüller and D. Wyler, Phys. Lett. **B 177**, 377 (1996).
2. H1 Coll., Eur. Phys. J. **C 19**, 269 (2001).
   H1 Coll., hep-ex/0304003, Accepted by Eur. Phys. J.
3. ZEUS Coll., Eur. Phys. J. **C 21**, 443 (2001).
   ZEUS Coll., Eur. Phys. J. **C 28** 175 (2003).
4. CDF Coll., Phys. Rev. Lett. **79**, 2191 (1997).
5. OPAL Coll., Phys. Lett. **B 387**, 432 (1996).
6. N. Arkani-Hamed, S. Dimopulos and G. Dvali, Phys. Lett. **B 429**, 263 (1998) and Phys. Rev. **D 59**, 086004 (1999).
7. H1 Coll., Phys. Lett. **B 479** 358 (2000).
   H1 Coll., hep-ex/0305015, Accepted by Phys Lett B.
8. ZEUS Coll., Abstract 602 submitted to EPS01, Budapest.
9. W. Buchmüller R. Rückl and D. Wyler, Phys. Lett. **B 191**, 442 (1987).
   Erratum ibid. **B 448**, 320 (1999).
10. H1 Coll., Phys. Lett. **B 523** 234 (2001).
11. H1 Coll., Eur. Phys. J. **C 11** 447 (1999).
12. ZEUS Coll., hep-ex/0304008, accepted by Phys. Rev. D.
13. ZEUS Coll., Phys. Rev. **D 65** 092004 (2002).
    ZEUS Coll., paper 906 submitted to ICHEP02, Amsterdam.
    ZEUS Coll., paper 605 submitted to EPS01, Budapest.
14. H1 Coll., Eur. Phys. J. **C 20** 4 (2001).
15. ZEUS Coll., Phys. Lett. **B 549** 32 (2002).
16. H1 Coll., Phys. Lett. **B 525**, 9 (2002).
17. H1 Coll., Phys. Lett. **B 548** 35 (2002).
18. K. Hagiwara, D. Zeppenfeld and S. Komamiya, Z. Phys. **C 29**, 115 (1993).
19. U. Baur, M. Spira and P. M. Zerwas, Phys. Rev. **D 42**, 815 (1990).
20. L3 Coll., Phys. Lett. **B 502**, 37 (2001).

LEPTON PRODUCTION IN EP COLLISIONS AT HERA

Emmanuel Sauvan
on behalf of H1 and ZEUS Collaborations
Centre de Physique des Particules de Marseille
163 Avenue de Luminy, F-13288 Marseille cedex 9, France
e-mail: sauvan@cppm.in2p3.fr

Abstract

High transverse momentum (P_T) lepton production has been studied in ep scattering at HERA. Two classes of events have been investigated. The first contains an isolated lepton, a hadronic system and large missing P_T, the second contains two or three leptons. The measurements use all the HERA data taken before the high luminosity upgrade. The H1 isolated lepton measurements lie somewhat above the Standard Model (SM) expectation when the isolated lepton is a muon or an electron and the hadronic P_T is large whereas ZEUS only observes such an excess for isolated τ leptons. These measurements allow stringent limits to be placed on a possible flavour changing neutral current $t - u - \gamma$ coupling, which would lead to the production of single top quarks and hence isolated leptons, hadronic activity and missing P_T. The rate with which multi-lepton evens are produced is found to be in good overall agreement with the SM. H1 observes somewhat more events than expected in both the di-electron and tri-electron samples at large di-electron masses.

1 Isolated lepton events

Events containing both an isolated lepton (l) with high transverse momentum and missing transverse momentum (P_T^{miss}) have been searched for at HERA by the H1 and ZEUS experiments. Within the Standard Model (SM) the dominant source of such events is the production of W bosons whose cross-section is of the order of 1 pb.

The selection is based on the signature of missing transverse momentum correlated with a high energy lepton ($e^{\pm}$ or $\mu^{\pm}$). The events may also contain a hadronic system X with transverse momentum P_T^X. The H1 selection [1] is optimised for W-like topologies starting at $P_T^X > 12$ GeV whereas ZEUS performed an inclusive analysis [2] dominated by non-W processes and a search optimised for top quark at high P_T^X.

In e^+p data (101.6 pb^{-1}), 10 candidate events have been observed by H1 in the electron channel while 9.85±1.31 are expected and 8 events for an expectation of 2.55±0.45 in the muon channel. One event is observed in e^-p data (13.6 pb^{-1}) for 2.06±0.28 events expected. A good agreement with SM predictions can be observed at low transverse momentum P_T^X of the hadronic system. As shown in Fig. 1 the distribution of the lepton-neutrino transverse mass is also in agreement with the SM distribution which is dominated by W production. But at high $P_T^X > 25$ GeV more events than expected are found by H1 (Fig. 1 and tab. 1). This deviation at high P_T^X of the H1 data is present in both e^+p data samples from the years 1994-1997 and 1999-2000.

The ZEUS experiment observed 24 electron events while $20.6\ ^{+1.7}_{-4.6}$ events are predicted and 12 muon events compared to $11.9\ ^{+0.6}_{-0.7}$ expected from the SM in $e^{\pm}p$ data corresponding to an integrated luminosity of 130 pb^{-1}. In contrast to H1 data, a good agreement with the SM prediction is observed for $P_T^X > 25$ GeV (Tab. 1).

The τ decay channel of the W boson has been recently investigated by the ZEUS experiment [3]. This analysis relies on the search for isolated tracks with associated calorimetric patterns characteristic of hadronic τ decay. A multivariable technique based on a likelihood discriminator was used to separate one-prong decays of the τ decay of the W from the background caused by Charge Current Deep Inelastic Scattering (CC-DIS). Two τ candidates have been observed in a region at high transverse momentum of the hadronic system $P_T^X > 25$ GeV where 0.12±0.02 events are expected.

2 Anomalous top production at HERA

Within the SM the rate of top quark production is negligible in $e^{\pm}p$ collisions at HERA energies. An anomalous $\gamma - u - t$ coupling would allow top production

Table 1: *Isolated lepton event yields compared to SM predictions for the ZEUS and H1 experiments. The fraction in percent coming from W production is quoted in parenthesis.*

Selection e^+p	Electrons Data/SM (W)	Muons Data/SM (W)
H1 (101.6 pb^{-1}) e^+p		
full sample	10 / 9.88 ± 1.69 (73 %)	8 / 2.55 ± 0.45 (87 %)
$P_T^X > 25$ GeV	4 / 1.49 ± 0.25 (85 %)	6 / 1.54 ± 0.41 (84 %)
$P_T^X > 40$ GeV	3 / 0.54 ± 0.11 (83 %)	3 / 0.55 ± 0.12 (93 %)
ZEUS (130 pb^{-1}) $e^\pm p$		
full sample	24 / 20.6 $^{+1.7}_{-4.6}$ (17 %)	12 / 11.9 $^{+0.6}_{-0.7}$ (16 %)
$P_T^X > 25$ GeV	2 / 2.9 $^{+0.59}_{-0.32}$ (45 %)	5 / 2.75 $^{+0.21}_{-0.21}$ (50 %)
$P_T^X > 40$ GeV	0 / 0.94 $^{+0.11}_{-0.10}$ (61 %)	0 / 0.95 $^{+0.14}_{-0.10}$ (61 %)

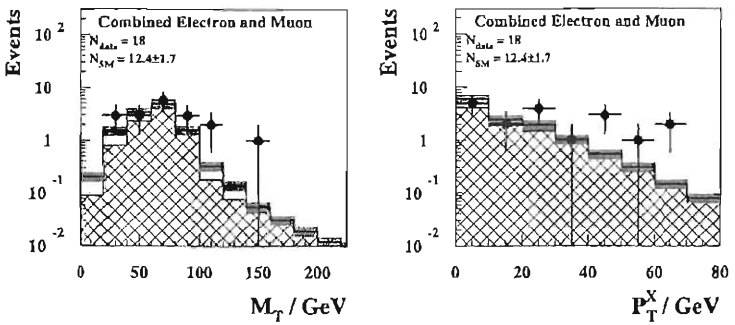

Figure 1: *Lepton-neutrino transverse mass (left) and hadronic transverse momentum (right) distributions of the H1 isolated lepton events, compared to the SM predictions.*

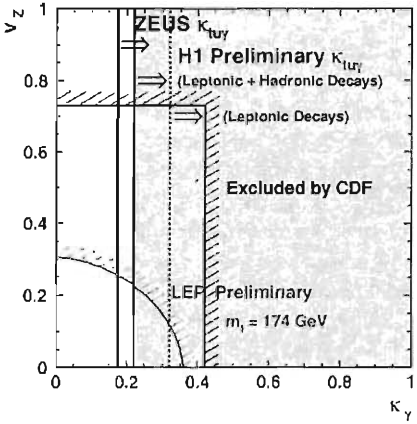

Figure 2: *Present limits of LEP, TEVATRON and HERA on anomalous couplings of the top quark to other quarks and neutral gauge bosons.*

through Flavour Changing Neutral Currents (FCNC's) [5]. Searches for such a process have been performed by the ZEUS [2] and H1 [4] experiments for both semi-leptonic and hadronic decays of the top quark. The top quark can decay into a b-quark jet and a W boson followed by hadronic or leptonic decay. $W \to lX$ decay which leads to events with a high energy lepton, missing transverse momentum and high P_T hadronic jets.

In the leptonic channel, the selections of Section 1 were further tightened to select top candidates, adding a threshold in P_T^X of 40 GeV (ZEUS) or 25 GeV (H1). A positive lepton charge and M_T higher than 10 GeV was also required by H1. With these cuts, 5 events are observed by H1 where 1.77 ± 0.46 are expected, whereas no event is seen by ZEUS in both electron and muon channels while one event is expected in each channel.

If the W produced in the top decay itself decays hadronically, events with three high P_T jets are produced, one high P_T jet being associated with the secondary b-quark and two high P_T jets with the W decay. The experimental selection therefore requires three jets with P_T's above 40, 25 and 14 GeV (ZEUS) or 40, 25 and 20 GeV (H1). Both experiments further reduce the QCD photoproduction background by requiring the 3-jet mass and one of the 2-jet masses to be compatible with the top and W masses, respectively. An additional cut on the angle between the two jets from the W decay in the top rest frame is applied by H1. The searches were performed on data sets corresponding to integrated luminosities of 130.1 pb^{-1} (ZEUS) and 115.2 pb^{-1}

(H1). The observed event yields are 14 for an expectation of 17.6 $^{+2.5}_{-1.5}$ (ZEUS) and 14 for an expectation of 19.6 ± 7.8 (H1). Both experiments find no excess compared to SM predictions. This does not favour the interpretation of the H1 high P_T^X lepton events as single top production. This interpretation is however not ruled out since 95% C.L. upper limits on the top cross-section derived from the hadronic channel would correspond to 5.4 events in the leptonic channel while 5 are observed.

Combining the leptonic and hadronic channels, an upper limit on the effective $\kappa_{\gamma ut}$ coupling has been calculated using the effective lagrangian of [6]. The upper bounds on $\kappa_{\gamma ut}$ at 95% C.L. of 0.174 (ZEUS) and 0.22 (H1) are competitive with those obtained at LEP [7] and the Tevatron [8] (Fig. 2). The ZEUS limit is more stringent than the H1 limit because they do not observed any excess of data in the leptonic channel.

3 Multi-lepton events

Both H1 and ZEUS have studied multi-electron and multi-muon production [9, 10] in *ep* collisions. Within the SM the production of multilepton events in *ep* collisions is possible mainly through photon-photon interactions, where quasi-real photons radiated from the incident electron and proton interact to produce a pair of leptons $\gamma\gamma \rightarrow l^+l^-$ [11]. For multi-electron final states the background comes mainly from Neutral Current Deep Inelastic Scattering (NC-DIS) or elastic Compton scattering, while for multi-muon final state the background is negligible.

The selection for multi-electron events is done by requiring at least two central electrons ($20° < \theta_e < 150°$ for H1 and $17° < \theta_e < 167°$ for ZEUS) with $P_T^{e_1}/P_T^{e_2} > 10/5$ GeV (H1) or $P_T^{e_1}/E^{e_2} > 10/5$ GeV (ZEUS). An isolated charged track has to be associated with the calorimeter energy deposit. Any other third electron is allowed to be present in a wider angular range ($5° < \theta_e < 175°$). The selected events are classified by the number of identified electrons in di- and tri-electron samples.

The results of both experiments are presented in Tab. 2. The di-electron sample is dominated by pair production with 15-20% contribution from other SM processes. In the tri-electron sample, the background contribution is negligible. Both H1 and ZEUS observations are in good agreement with the predicted yields. The main difference between H1 and ZEUS predictions for the signal is due to different angular range for the central electrons. A few events with invariant mass of the two highest P_T electrons $M_{12} > 100$ GeV are observed in a region where the SM prediction is low (Fig. 3 and 4). Three di-electron events are measured by H1 where 0.25 are expected and 2 by ZEUS for an expectation of 0.77. In the tri-electron sample 3 events are observed by

H1 compared to an expectation of 0.23 while no events are observed by ZEUS where 0.37 are expected.

Table 2: *Observed and predicted multi-electron event yields for all selected events and for events with masses $M_{12} > 100$ GeV.*

Selection	Data	SM	Lepton Pairs	NC-DIS + Compton
H1 (115 pb^{-1})				
2e	105	118.2 ± 12.8	93.3 ± 11.5	25.0 ± 5.5
3e	16	21.6 ± 3.0	21.5 ± 3.0	0.1 ± 0.0
2e $M_{12} > 100$ GeV	3	0.25 ± 0.05	0.21 ± 0.04	0.04 ± 0.03
3e $M_{12} > 100$ GeV	3	0.23 ± 0.04	0.23 ± 0.04	0.0 ± 0.0
ZEUS (130 pb^{-1})				
2e	191	213.9 ± 3.9	182.2 ± 1.2	31.7 ± 3.7
3e	26	34.7 ± 0.5	34.7 ± 0.5	–
2e $M_{12} > 100$ GeV	2	0.77 ± 0.08	0.47 ± 0.05	0.30 ± 0.07
3e $M_{12} > 100$ GeV	0	0.37 ± 0.04	0.37 ± 0.04	–

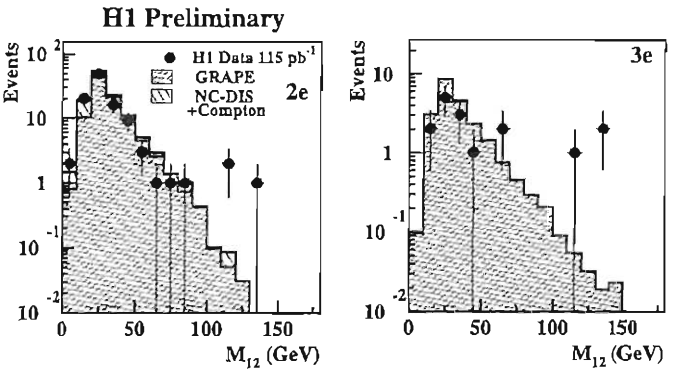

Figure 3: *Distribution of the invariant mass M_{12} of the two highest P_T electrons for the H1 analysis. Events classified as di-electrons (left) and tri-electrons (right) are shown.*

A search for multi-muon events has also been performed by both experiments. Muons are identified using central tracker reconstructed tracks,

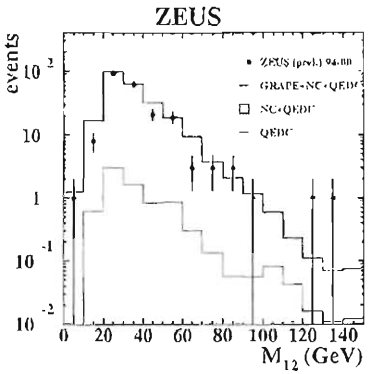

Figure 4: *Distribution of the invariant mass M_{12} of the two highest P_T electrons for the ZEUS analysis. All observed events with more than two electrons are shown.*

calorimetric deposits and muon chamber signals. At least two muons with $P_T^{\mu_1}/P_T^{\mu_2} > 2$ GeV and $P_T^{\mu_1}/P_T^{\mu_2} > 5$ GeV in the angular range $20° < \theta_\epsilon < 160°$ are required in H1 and ZEUS analyses, respectively. With an analysed data sample corresponding to an integrated luminosity of 105 pb^{-1} 200 events are detected by ZEUS where $213 \pm 11_{stat.}$ are expected. Using an integrated luminosity of 70 pb^{-1}, 1242 multi-muon events are observed in the H1 analysis in good agreement with the expectation of $1253 \pm 125_{stat.+syst.}$. No event with two muons at high mass $M_{\mu\mu} > 100$ GeV is observed by either experiment. The 3 high mass di-electron events observed by H1 would correspond to one di-muon event expected with $M_{\mu\mu} > 100$ GeV because of the lower efficiency and luminosity in the multi-muon channel.

4 Conclusions and outlook

Events with an isolated high P_T lepton and missing transverse momentum have been observed in ep collisions at HERA. The most probable interpretation in the SM framework is real W production with subsequent leptonic decay. This mechanism produces a relatively low P_T hadronic system. Intriguing events containing a high P_T hadronic system and an isolated electron or muon have been observed by H1 while no deviation from the SM prediction was observed by ZEUS. Two events containing an isolated τ and missing transverse momentum have been identified by ZEUS at high P_T^X while 0.12 ± 0.02 are predicted.

The interpretation of these electron and muon events in terms of anomalous single top quark production has been explored and competitive limits on the $\kappa_{\gamma ut}$ effective coupling determined.

High P_T multi-electron and di-muon production has also been measured. Good general agreement with the Standard Model expectation has been found. However few multi-electron events with an invariant mass of the two highest P_T electrons above 100 GeV have been observed in excess compared to the SM prediction. No event with two muons at high mass $M_{\mu\mu} > 100$ GeV is observed by either experiment.

A new high luminosity phase of the HERA collider is now starting with the goal of accumulating an integrated luminosity of 1 fb^{-1}. This will clarify the origin of the isolated lepton and multi-electron events observed by H1. Enhanced b-tagging capabilities provided by the new H1 and ZEUS vertex detectors will also make the identification of new phenomena such as anomalous top production easier.

References

1. V. Andreev *et al.* (H1 Collaboration), Phys. Lett. **B561**, 241 (2003).
2. S. Chekanov *et al.* (ZEUS Collaboration), Phys. Lett. **B559**, 153 (2003).
3. ZEUS Collaboration, contributed paper 909 to XXXIst ICHEP, July 2002, Amsterdam.
4. H1 Collaboration, contributed paper 1024 to XXXIst ICHEP, July 2002, Amsterdam.
5. H. Fritzsch and D. Holtmannspötter, Phys. Lett. **B457**, 1199 (1999).
6. T. Han and J.L. Hewett, Phys. Rev. **D60**, 074015 (1999).
7. ALEPH, DELPHI, L3, OPAL and the LEP EXOTICA working group, contributed paper sbmitted to Summer 2001 Conferences, LEP Exotica WG 2001-01.
8. F. Abe *et al.* (CDF Collaboration), Phys. Rev. Lett. 80, 2525 (1998).
9. H1 Collaboration, contributed paper 1019 and 1021 to XXXIst ICHEP, July 2002, Amsterdam.
10. ZEUS Collaboration, contributed paper 910 to XXXIst ICHEP, July 2002, Amsterdam.
11. J.A.M. Vermaseren, Nucl. Phys. **B229**, 347 (1983);
    N. Artega-Romero, C. Carimalo and P. Kessler, Zeit.f.Phys **C52**, 289 (1991).

SEARCH FOR NEW PHENOMENA IN CDF

Luca Scodellaro (for the CDF collaboration)
Padova University & INFN, Italy

Abstract

We present the most recent results and perspectives of the searches for new phenomena at the CDF experiment of the Tevatron collider.

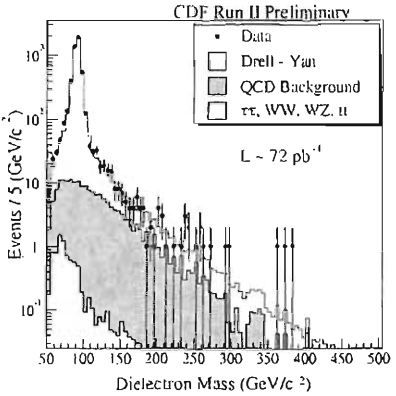

Figure 1: *Dielectrum mass spetrum.*

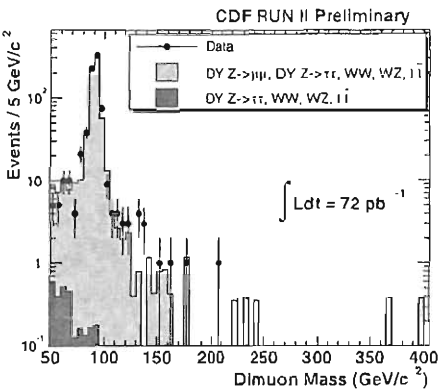

Figure 2: *Dimuon mass spetrum.*

1 Introduction

The Run II of the Tevatron collider began in spring 2001. The accelerator provides $p\bar{p}$ collisions at a center-of-mass energy $\sqrt{s}$ of 1.96 GeV. The CDF detector has undergone substantial upgrades since the end of Run I. A detailed description of the new devices can be found in reference [1].

2 Drell-Yan Dilepton Production

High mass dileptons allow to search for new particle production. In particular, the CDF collaboration has recently looked for new neutral gauge boson Z' and Randall-Sundrum gravitons in approximately 72 pb^{-1} of Run II data.

2.1 Search for New Neutral Gauge Boson Z' in Dielectron Channel

High P_T electron data have been used to search for Z' boson decaying into an electron pair $q\bar{q} \rightarrow Z' \rightarrow e^+e^-$. The event selection is based on the detection of a good central electron with $E_T > 25$ GeV and a second good electron with $E_T > 25$ GeV either in the central or in the plug calorimeter. A cut on the missing transverse energy significance, $\not\!\!E_T/\sqrt{\Sigma E_T} < 2.5$, is also applied to remove W+*jets* background. The observed dielectron mass spectrum agrees with background expectation (fig.1). 95% CL upper limit on the production cross section times branching ratio into electrons is set as a function of Z' mass. When Standard Model couplings are assumed, a 95% CL lower limit on the Z' mass is established at 650 GeV/c^2.

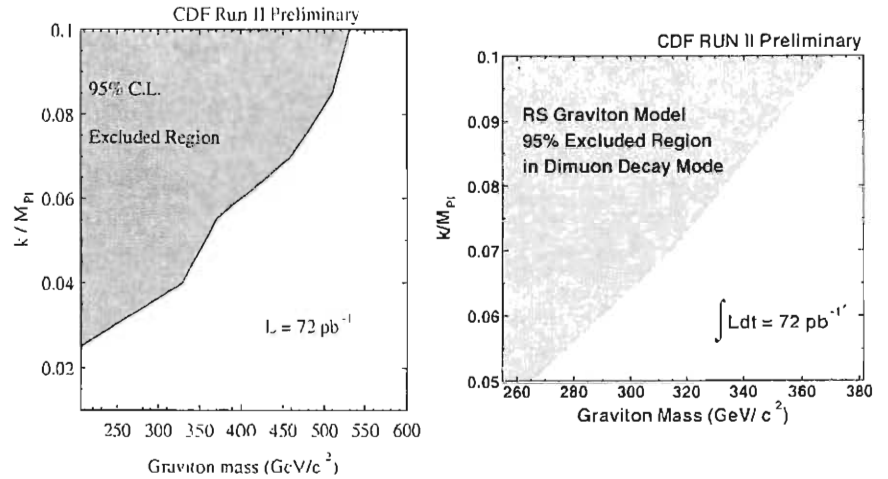

Figure 3: 95% *CL excluded regions in the mass-coupling parameter plan for Randall-Sundrum gravitons in the dielectron (left) and dimuon (right) channels.*

2.2 Search for New Neutral Gauge Boson Z' in Dimuon Channel

The search of Z' boson production in the dimuon channel is based on the selection of two good muons with transverse momentum $P_T > 20\ GeV/c$. Cuts on the track impact parameter and isolation are applied to remove cosmic ray and QCD background respectively. No excess over the Standard Model prediction is observed in the dimuon mass distribution (fig.2), and 95% CL upper limit on the production cross section times branching ratio into muons is set as a function of the Z' boson mass. Finally, by assuming Standard Model couplings, a 95% CL lower limit on the Z' mass is set at 455 GeV/c^2.

2.3 Results for Graviton Searches

The Randall-Sundrum model provides a small extra-dimension solution to the hierarchy problem by means of a non-factorizable geometry [2, 3]. Excited gravitons in 5 dimensions are expected to be observable. Results for resonance searches in high mass dileptons have also been used to draw excluded regions in the graviton mass-coupling parameter k/M_{Pl} plan (fig.3).

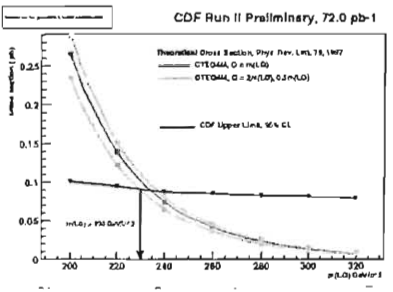

Figure 4: *95% CL upper limit cross section as a function of the leptoquark mass compared with NLO theoretical expectations.*

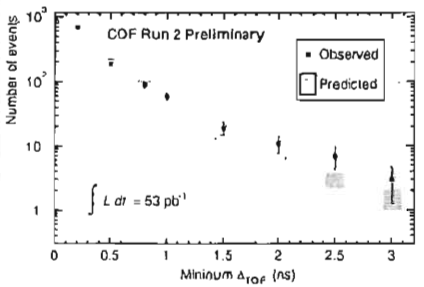

Figure 5: *Event maximum Δt distribution compared with background expectation.*

3 Leptoquark Searches in Run II

Leptoquarks are generally pair produced in $p\bar{p}$ collisions [4]. They decay into a lepton-quark pair, with generation mixing suppressed by FCNC constraints [5]. A search for first generation leptoquark has been recently performed in the dielectron+jets channel at CDF. 72 $pb-1$ of inclusive electron data have been selected by requiring two central electrons with $E_T > 5\ GeV$ and two jets ($E_T >$ 30 GeV and 15 GeV respectively). No events are observed after kinematic cuts. 95% CL upper limits on the production cross section as a function of the leptoquark mass are set (fig.4). By assuming $Br(LQ \rightarrow lq) = 1$ and using the NLO theoretical estimate, a scalar leptoquark with mass below 230 GeV/c^2 is excluded.

4 CHArged Massive Particles

Physics theories extending the Standard Model usually predicts new conserved quantum numbers leading to stable particles. Long-lived CHArged Massive ParticleS (CHAMPS) escaping CDF detector can be detected by high-P_T muon triggers. Moreover, due to their large mass, these particles are expected to move slowly, leading to long Time-Of-Flight (TOF) through the detector. CHAMP production has been investigated by exploiting the new TOF system, providing sensitivity to higher $\beta\gamma$ values than the dE/dx measurement used in Run I analyses. 52 pb^{-1} of high-P_T muon data have been used. In order to have full tracking efficiency on CHAMPS with mass larger than 100 GeV/c^2, a cut at 40 GeV/c is applied on the transverse momentum of the candidate tracks. The time t_0 at which the interaction is occurred is estimated by averaging

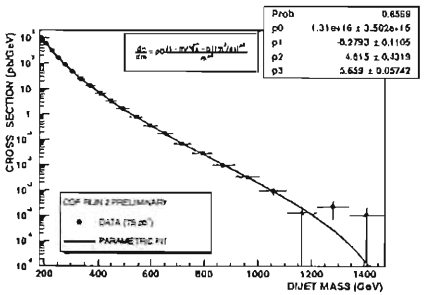

Figure 6: *Dijet mass distribution presented as a differential cross section in* 10% *wide mass bins.*

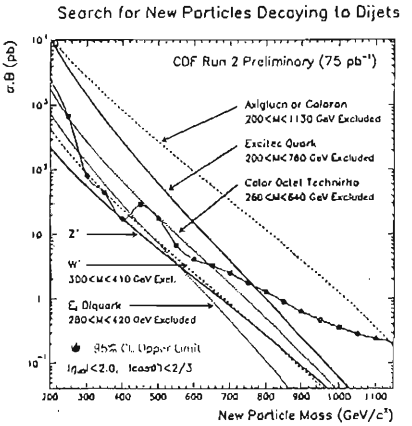

Figure 7: 95% *CL upper limits on the cross section times branching ratio for new particles decaying into dijets.*

the measured time for tracks with $P_T < 20\ GeV/c$. Tracks with high time of flight difference Δt with respect to t_0 are looked for. The maximum probability of discovery has been found to be guaranteed by a cut $\Delta t > 2.5\ ns$. Tracks with $20 < P_T < 40\ GeV/c$ are used to predict the background (fig.5): $2.9 \pm 0.7(stat.) \pm 3.1(sys.)$ events are expected, while 7 events are observed. Production cross section upper limits are established for a stable stop model [6]. By assuming NLO predictions, a 95% CL lower limit on the stop mass is set at 107 GeV/c^2.

5 Dijet Mass Bumps

75 pb^{-1} of inclusive jet samples have been used to search for new particles decaying into dijets. The two highest E_T jets in each event are used to compute the dijet invariant mass spectrum (fig.6). QCD production in the t-channel pole is suppressed by requiring the dijet satisfies

$$|tanh(\Delta\eta/2)| < 2/3. \quad (1)$$

No evidence for new particles is observed, and excluded mass regions for several models are drawn (fig.7).

Table 1: *Missing E_T and photon triggers.*

Missing E_T Triggers	
MET45	$\not\!\!E_T > 45\ GeV$
MET_L3PS100	$\not\!\!E_T > 25\ GeV$ & prescale 100
MET35+2JETS	$\not\!\!E_T > 35\ GeV$ & 2 jets w/ $E_T > 10\ GeV$
MET+BJET	$\not\!\!E_T > 20\ GeV$ & 2 displaced tracks ($\|d_0\| > 100\ \mu m$)
Photon Triggers	
INCLUSIVE PHOTON	$E_T^\gamma > 25$ or 50 or 70 GeV
DIPHOTON	$E_T^\gamma > 12$ or 18 GeV
TRIPHOTON	$E_T^\gamma > 10\ GeV$
PHOTON+BJET	$E_T^\gamma > 10\ GeV$ & 1 displaced track ($\|d_0\| > 120\ \mu m$)
PHOTON+MUON	$E_T^\gamma > 16\ GeV$ & $P_T^\mu > 4\ GeV/c$
PHOTON−DIJET	$E_T^\gamma > 18\ GeV$ & $E_T^{jet1} > 18\ GeV$, $E_T^{jet2} > 10\ GeV$

Table 2: *Observed and expected number of diphoton events with additional electron or muon.*

	Obs.	Exp. $E_T^\gamma > 13\ GeV$	Exp.
$e\gamma\gamma$	0	$0.27 \pm 0.10 \pm 0.14$	$0.04 \pm 0.03 \pm 0.02$
$\mu\gamma\gamma$	0	$0.04 \pm 0.007 \pm 0.02$	$0.007 \pm 0.005 \pm 0.004$

6 Exclusive Missing E_T + Jets Searches in Run I

Missing transverse energy signature has been recently used to test extra dimension solution to the hierarchy problem [7] with Run I data. Gravitons are expected to be produced in association with an extra parton. Required experimantal signature is large missing E_T ($\not\!\!E_T > 80\ GeV$) plus an extra jet: 284 events are observed while 271 ± 16 events are expected mainly from $Z \rightarrow \nu\bar{\nu}$ background. By assuming a number of 2, 4 or 6 extra dimension, an effective Plank scale below 1.0, 0.77 and 0.71 TeV respectively has been excluded at 95% CL.

7 Inclusive Missing E_T and Photon Searches in Run II

Several triggers have been implemented to study weakly interacting particle production and new phenomena leading to photons in the final states (tab.1). Large samples are being collected and tested. In particular, the diphoton sample has been deeply studied: 1365 events have been selected by requiring two

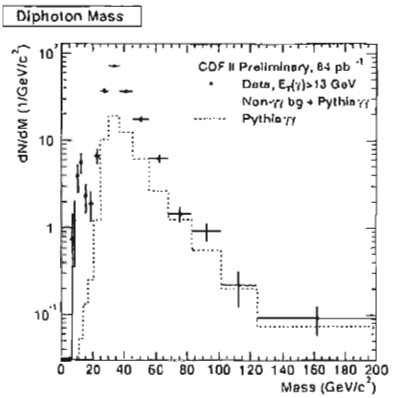

Figure 8: *Observed diphoton mass spetrum.*

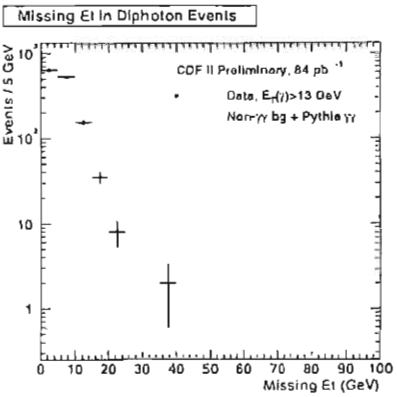

Figure 9: *Missing E_T distribution in diphoton events.*

central photons with $E_T > 13\ GeV$ (95 events with $E_T > 25\ GeV$). Diphoton mass spectrum and missing transverse energy have been investigated (fig.8 and 9). The number of events with additional electron or muon has also been studied (tab.2). Background expectation agrees with data. These samples provide an important testing bench for new physics beyond the Standard Model.

8 Tau Lepton Based Searches

Tau leptons provide an other crucial experimental signature for new phenomena searches. In particular, large cross sections into final states with τ are expected for supersymmetric Higgs production at large β values. Tau detection has been largely improved in RunII and specific $\tau+\not\!\!E_T$ and ditau triggers have been implemented. Improved tau reconstruction also offers interesting perspectives for supersymmetric searches like for example R-parity violating stop decays

$$p\bar{p} \rightarrow \tilde{t}\bar{\tilde{t}} + X \rightarrow (b\tau^+)(\bar{b}\tau^-) + X \tag{2}$$

and Chargino-Neutralino production

$$p\bar{p} \rightarrow W^{\pm} \rightarrow \tilde{\chi}_1^{\pm}\tilde{\chi}_2^0 \rightarrow (\tau^{\pm}\nu\tilde{\chi}_1^0)(\tau^{\pm}\tau^{\mp}\tilde{\chi}_1^0). \tag{3}$$

9 R-Parity Violating Decaying Particles

The CDF collaboration has recently performed two searches for new particles decaying via R-parity violating interactions with RunI data.

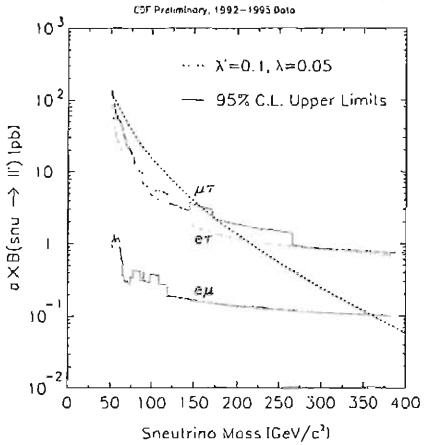

Figure 10: *95% CL upper limits on cross section times branching ratio as a function of sneutrino mass, together with NLO cross section for the referenced parameters.*

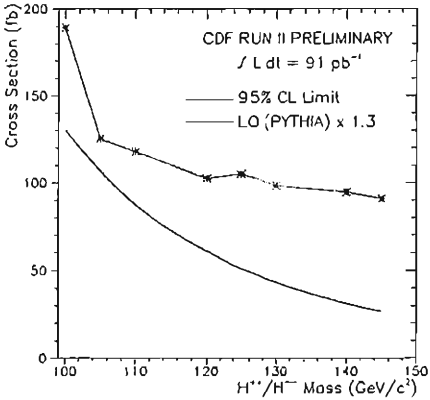

Figure 11: *95% CL upper limits on cross section times branching ratio into electrons as a function of doubly-charged Higgs mass, compared with theoretical expectation.*

In the first analysis, stop pair production has been considered, with both the stop quarks decaying into τb [8]. A tau is required to decay leptonically, while the second tau is required to decay hadronically: the searched signature is an opposite sign lepton-tau pair plus two jets. After kinematic cuts, no events are observed, while $3.2^{\pm 1.4}_{\pm 0.3}$ events are predicted by Standard Model processes. by assuming $Br(\tilde{t} \rightarrow b\tau) = 1$ and NLO cross sections, a 95% CL lower limit on the stop mass is set at 122 GeV/c^2.
In the second search, R_p-production of a scalar neutrino $\tilde{\nu}$ is considered. Flavour-violating $\tilde{\nu}$ decays into opposite sign leptons are looked for. Events are selected by requiring an opposite sign muon-electron pair, back to back in the azimuthal direction. No excess over the background expectation is observed, and 95% CL upper limits on the production cross section times the branching ratio are derived (fig.10).

10 Search for Doubly-Charged Higgs

The observed lack of symmetry between left- and right-handed weak interactions suggests a more fundamental left-right symmetric lagrangian spontaneously broken at higher energies [9, 10, 11]. The see-saw mechanism, designed

in the context of the left-right symmetric model, successfully predicts light neutrino mass [12], providing a powerful motive to that model. Finally, supersymmetric extensions [13, 14] suggest low mass doubly-charged Higgs, whose same-sign lepton decay mode provides a strong experimental signature.
95 pb^{-1} of inclusive electron data have been recently used at CDF to search for doubly-charged Higgs production via same-sign central electron pair observation. No events are observed in a search reagion of $\pm 10\%$ of the Higgs mass around each Higgs mass considered, and 95% CL upper limits on the production cross section are established (fig.11). We remark that this experimental search is sensitive to the production of any new doubly-charged particle decaying to dielectrons.

11 Conclusions

CDF detector is collecting data from March 2001. Run II searches for new phenomena have already started. First limits using dileptons and dijet mass spectra have been set for various phenomena and specific theories beyond the Standard Model have been tested. Moreover, the new Time-Of-Flight system has been exploited to search for CHAMPS. Results are already improving Run I ones. Larger samples are being collected and tested for searches based on tau lepton, missing transverse energy and photon signature. High integrated luminosity will provide the best opportunity for new physics discovery until LHC starts to run.

References

1. R. Blair *et al* [CDF-II collaboration], FERMILAB-PUB-96-390-E (1996).
2. L. Randall *et al*, Phys. Rev. Lett. **83**, 3370 (1999).
3. L. Randall *et al*, Phys. Rev. Lett. **83**, 4690 (1999).
4. M. Kramer *et al*, Phys. Rev. Lett. **79**, 341 (1997).
5. W. Buchmuller *et al*, Phys. Lett. B **177**, 337 (1986).
6. R. Barbieri *et al*, Phys. Rev. D **63**, 105007 (2001).
7. N. Arkani-Hamed *et al*, Phys. Lett. B **429**, 263 (1998).
8. D. Acosta *et al*, FERMILAB-PUB-03-070-E (2003).
9. R.N. Mohapatra *et al*, Phys. Rev. D 11, 566 (1975).
10. R.N. Mohapatra *et al*, Phys. Rev. D **12**, 1502 (1975).

11. R.N. Mohapatra *et al*, Phys. Rev. D **23**, 165 (1981).

12. R.N. Mohapatra *et al*, Phys. Rev. Lett. **44**, 912 (1980).

13. C.S. Aulakh *et al*, Phys. Rev. D **57**, 4174 (1998).

14. Z. Chacko *et al*, Phys. Rev. D **58**, 015003 (1998).

RECENT NEW PHENOMENA RESULTS FROM THE D0 EXPERIMENT

Wyatt Merritt
Fermilab, P.O. Box 500, Batavia, IL 60510 USA
For the D0 collaboration

Abstract

Results are described from seven analyses from the New Phenomena group in the D0 experiment, using datasets of 30-50 pb^{-1} of data collected in Run II of the Fermilab Tevatron, at a center-of-mass energy of 1.96 TeV. These analyses are: a search for charginos and neutralinos in the trilepton channel; a search for GMSB SUSY in the 2 γ + missing E_T channel; a search for SUSY in the jets + missing E_T channel; a search for new physics in the e-μ channel; a search for leptoquarks in the muon + jets channel; and searches for extra dimensions with dielectrons, diphotons, and dimuons. Also presented are two searches for the Z resonance in τ-τ decays.

1 Introduction

The D0 experiment at the the Fermilab Tevatron is now analyzing first results from a number of searches for phenomena outside the standard model, using data collected from Run II at 1.96 TeV in the center of mass. These results are beginning to rival Run I results in sensitivity, and are clearly demonstrating the physics capabilities for D0 in Run II. As part of this demonstration, we also describe in this article the emerging evidence for Z decaying to τ pairs, which will be a significant Standard Model channel against which to benchmark various New Phenomena searches.

2 $Z \rightarrow \tau$-τ analyses

Taus are often a significant part of the phenomenology of theories beyond the Standard Model. In Higgs searches, SUSY searches via trileptons, and in third generation leptoquark searches, detection of τs is important. However, we need a Standard Model channel to give confidence in our modeling and detection efficiencies. Two searches at D0 are seeing evidence for the decay $Z \rightarrow \tau$-τ.

The first analysis searches for the mode in which one τ has decayed to an electron, and the second τ has decayed hadronically. A collinear approximation is used to calculate the τ-τ invariant mass. First, a preselection is made of a sample containing a good electron with $E_T > 12$ GeV and a jet which is a τ candidate (a very loose requirement).

The daughter particles from the τ (the jet and electron) are assumed to give the τ direction. The measured missing E_T is used to project the neutrino momentum along the τ direction. This approximation will have reasonable resolution only because of the application of a cut in $\Delta\phi$, excluding the region $3.0 < \Delta\phi < 3.3$, where $\Delta\phi$ is the difference in azimuth between the two (approximate) tau directions.

Other cuts are applied for background rejection : $M_T(e\nu) < 60$ GeV and $M(e\tau) < 60$ GeV. Neural nets are used to further tighten the τ ID of the jet candidate. Different nets are used for $\tau \rightarrow \pi^{\pm}\ \nu$ (type 1)and $\pi^{\pm}\ \pi^0\ \nu$ (type 2); three prong decays are not included. The distributions of τ candidates in the data and of τ signal Monte Carlo in the neural net variables are shown in Fig. 1. The cut requires the NN output to be > 0.95.

A like sign sample with the same cuts is used as an estimator of the background. The subtracted distribution of opposite sign events minus like sign events in the τ-τ invariant mass is shown, compared with the signal Monte Carlo, in Fig. 2. The number of events in the distributions is given in Table 1.

The second Z to τ-τ analysis utilizes the channel when one τ decays to a muon, and the other hadronically. For this analysis, the sample contains a central, isolated muon with tight quality cuts and $p_T > 7$ GeV, and a jet flagged as a τ candidate with $E_T > 15$ Gev. The τ candidate jet must have

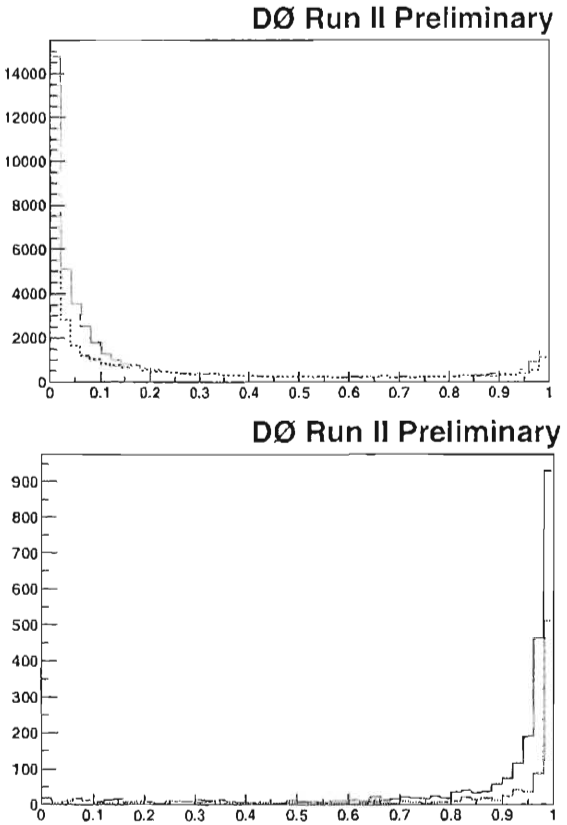

Figure 1: (a) The distribution of the neural net outputs for τ candidates in the data, for the two types of one-prong event (type 1 and type 2,described in text). (b) The distribution of the neural net outputs for τ candidates in the signal Monte Carlo, for the same two types.

a single matching isolated central track. The muon and τ are required to be separated in ϕ by at least 2.5 radians.

A quantity called the profile can be used to help distinguish τs from QCD background. The profile is defined as the sum of the two leading E_T towers divided by the total E_T for the τ candidate jet. In order to extract a signal, the 2-dimensional distributions of profile vs isolation are formed for opposite and like sign events in the sample. The subtracted distribution should contain the $Z \rightarrow \tau\ \tau$ signal. These distributions are shown in Fig. 3.

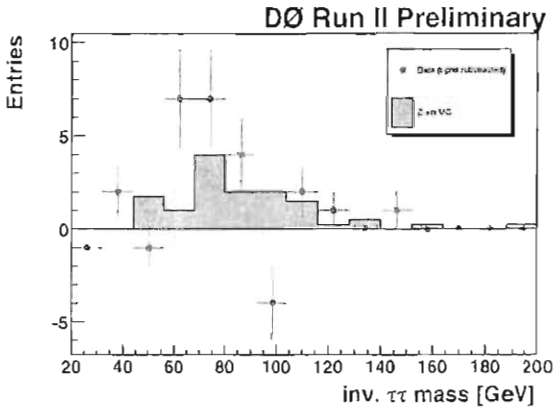

Figure 2: *Distribution vs $\tau\tau$ invariant mass of opposite sign events minus like sign events, from the data (shown as points with errors), compared with the signal Monte Carlo (shown as a filled histogram).*

Table 1: *Number of events from the $\tau\tau$ invariant mass distributions.*

Data	
No. Opposite sign events	49
No. Like sign events	35
Difference	14 ± 9
$\tau\tau$ MC norm. to $50pb^{-1}$	13 ± 4

3 Chargino-Neutralino search

For the first of the SUSY searches reported here, an analysis is performed within the mSUGRA framework to look for chargino-neutralino pair prodcution with both SUSY particles decaying leptonically. The channel searched for is 2 electrons + a third lepton (identified with an isolated high p_T track) + missing E_T. The luminosity of the sample which was examined was $40\ \mathrm{pb}^{-1}$.

The sample is taken from both single and dielectron triggers. The selection asks that the standard EM ID cuts on each electron be satisfied; that they have $E_T > 15$ GeV and 10 GeV respectively; and that both have a matching central track. Further cuts imposed are 10 GeV $< M_{ee} <$ 70 GeV, and $M_{T(e\nu)}$ > 15 GeV. The requirement of an additional track with $p_T > 5$ GeV, well isolated in both ϕ and η from the other two leptons, and with $\eta < 3$, completes

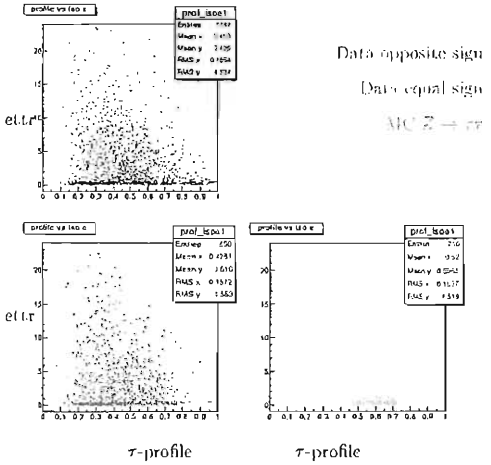

Figure 3: *Distribution of isolation vs profile for opposite sign data(upper left), like sign data (lower left), and $Z \rightarrow \tau\tau$ Monte Carlo (lower right).*

the specification of the trilepton sample. Background estimates are made from two kinds of source: Standard Model processes with real missing E_T, and QCD background with fake missing E_T from measurement errors. The first type of source is estimated with PYTHIA followed by a full detector simulation, for all contributing processes. The second source is estimated from data using samples with inverted ID cuts. Table 2 shows the number of events in the total background and in the data at each successive stage of the application of cuts. The final entry describes the complete set of cuts, which results in no events in data or in the background estimate. From this analysis, we can not yet exclude the two mSugra points which were simulated for the signal. The cross section $\times$ branching ratio exclusion level was 3.5(2.4) pb^{-1}. for the efficiencies at the simulated small (large) mSugra mass points.

4 GMSB SUSY Search

The second SUSY search is looking in the 2γ + missing E_T channel for a characteristic signature of gauge-mediated symmetry breaking models. It uses a luminosity of 40 pb^{-1}.

Table 2: *Comparison of background with data in chargino-neutralino search.*

	Total Background	Data
ID + kinem + trk	3216 ± 43	3132
$10 < M_{ee} < 70GeV$	660 ± 19	721
$M_T > 15GeV$	96 ± 8	123
3rd trk	3.2 ± 2.3	3
$ME_T > 15GeV$	0.0 ± 1.4	0

Table 3: *Comparison of background with data in $2\gamma + ME_T$ search.*

Missing E_T cut	QCD-Dominated Data Sample	2γ Data	QCD Sample Normalized to 2γ Data
< 20 GeV	5841	535	Normalized to be equal
> 25 GeV	65	3	6.0 ± 0.8
> 30 GeV	27	1	2.5 ± 0.5
> 35 GeV	18	0	1.6 ± 0.4

The triggers used are single or diEM triggers, and have been determined to be > 97% efficient for 2 photons with $E_T > 20$ GeV. The first selection requires 2 EM objects in the central η region, with standard EM ID requirements, no matched tracks, and $E_T > 20$ GeV. The topological and data quality cuts were chosen to minimize QCD background and the non-Gaussian tails for missing E_T. It was required to have no jets in the intercryostat region. Also, the leading jet and the missing E_T were required to be separated by > 2.5 radians in ϕ. Missing E_T for this analysis is calculated using cells, but only cells inside jets are used in the coarse outer region of the calorimeters, to avoid some instrumental problems.

Background comes from QCD processes and is estimated by using a sample with inverted EM quality cuts. The comparison of the background estimate and the 2γ data is shown in Table 3. The missing E_T distributions for data and background estimate are compared in Fig. 4. The data are compared with GMSB SUSY theory, using a model in which the neutralino is the NLSP, and Λ is the scale of SUSY breaking. Using the parameters $N_5 = 1$, $tan\beta = 15$, and the sign of μ positive [1], a limit on Λ of 51 TeV can be established, and this is shown in Fig. 5. This is close to the Run I limits on this parameter.

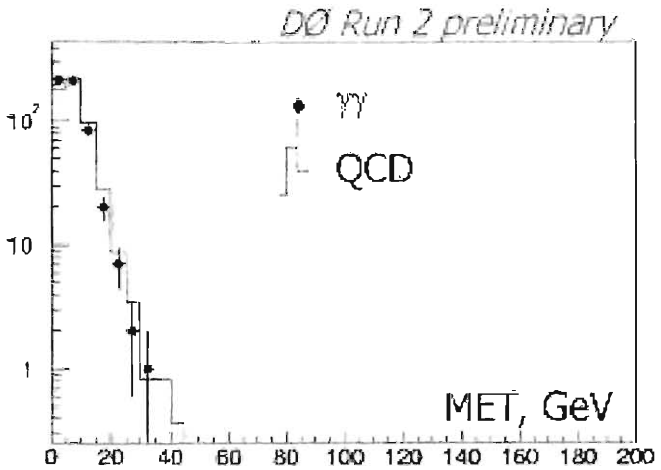

Figure 4: *Distribution of missing E_T for data and background estimate in the 2γ + missing* E_T *channel.*

5 Jets + missing E_T Search

The next search uses the jets + missing E_T channel. The sample encompassed 4 pb^{-1} of luminosity. The trigger required a single high p_T jet above 65 GeV. The analysis required 2 jets found with cone 0.7 algorithm. Missing E_T was calculated from the calorimeter towers. The standard jet energy scale corrections were applied. The selection cuts included jet quality cuts, cuts to remove electrons, data quality cuts, angular separation cuts between the two leading jets, and between each of the three leading jets and the missing E_T vector. Also, the leading jet E_T was required to be > 100 GeV to insure full trigger efficiency.

Backgrounds were estimated for the physics background channels, with real missing E_T, using PYTHIA generation and full detector simulation. For the background due to mismeasured missing E_T, a fit to the low missing E_T region was used to extrapolate into the higher missing E_T region. Fig. 6 shows the distribution of missing E_T in the data sample, compared with the fits, using different choices for the fit region. Table 4 gives the results of the analysis, including the limits obtained on cross section times efficiency.

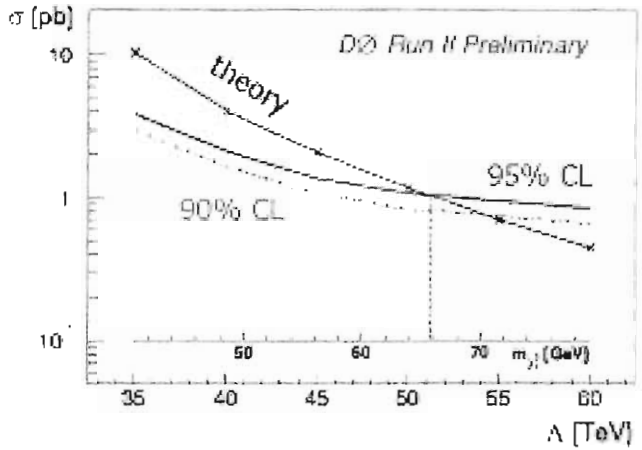

Figure 5: *Limit on* Λ, *the GMSB SUSY breaking scale, established in the* $2\gamma +$ *missing*E_T *channel.*

Table 4: *Comparison of background with data in jets +* $\not\!\!E_T$ *search.*

Missing $\not\!\!E_T$ cut	QCD Fit	Total Background	Data	$95\% CL\epsilon \times \sigma(pb)$
> 70 GeV	$17.4 \pm 7.9 \pm 2.7$	$18.4 \pm 7.9 \pm 2.7$	7	4.18
> 80 GeV	$8.5 \pm 5.0 \pm 1.7$	$9.5 \pm 5.0 \pm 1.7$	6	3.76
> 90 GeV	$4.2 \pm 3.0 \pm 1.0$	$5.1 \pm 3.0 \pm 1.0$	4	3.12
> 100 GeV	$2.0 \pm 1.7 \pm 0.6$	$2.7 \pm 1.7 \pm 0.6$	3	2.69

6 Search in the e-μ channel

In this analysis, the e-μ channel was examined, because it has low background and high discovery potential. The goal was to provide a model-independent limit on the cross section for new physics. The analysis used data from 30 pb^{-1} of data.

The trigger for this analysis required 1 electron with $E_T > 20$ GeV and 1 muon inside $\eta = 2$. The offline selection for the muon required that it be identified by the muon system scintillators, matched to a central track, be isolated using both the calorimeter and the track criteria, and pass the cosmic veto timing criteria. The electron offline selection requirements were: identification by isolated EM cluster, matched with a central track. Both electron

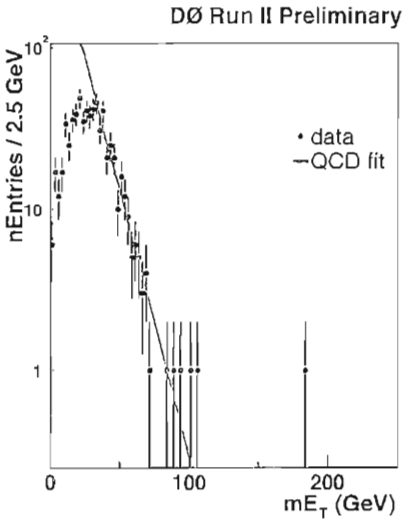

Figure 6: *Distribution of missing E_T for data, compared with the background fits, in the jets + missing* E_T *channel.*

Table 5: *Comparison of background with data in eμ search.*

Missing E_T cut	Data	Total Background
> 0 GeV	13	$9.6 \pm 0.6 \pm 2.6$
> 10 GeV	10	$7.3 \pm 0.5 \pm 2.1$
> 15 GeV	7	$4.6 \pm 0.4 \pm 1.6$
> 20 GeV	6	$3.0 \pm 0.3 \pm 1.3$
> 25 GeV	3	$2.3 \pm 0.3 \pm 1.1$
> 30 GeV	3	$1.9 \pm 0.2 \pm 0.9$
> 35 GeV	2	$1.6 \pm 0.2 \pm 0.8$
> 40 GeV	0	$1.4 \pm 0.2 \pm 0.7$
> 45 GeV	0	$1.1 \pm 0.1 \pm 0.5$

and muon were required to have $p_T > 20$ GeV. The misidentification probabilities for electron and muon were measured from the data. The Standard Model contributions to the background were calculated using PYTHIA plus a full detector simulation. The SM processes simulated were WW, ttbar, and Z $\rightarrow \tau\tau$. The comparison of data with total background is shown in Table 5. The cross section limits obtained, as a function of a missing E_T cut, are shown in Fig. 7.

7 Second generation leptoquark search

This search used the channel 2 muons + 2 jets to search for a second generation scalar leptoquark, using 30 pb^{-1} of data.

The trigger required 2 muons at Level 1, 1 muon at Level 2, and no further rejection at Level 3. A sample was preselected using the requirements: 2 muons, isolated in both the calorimeter and the central tracker, oppositely charged, each with $p_T > 15$ GeV, and with $m_{\mu\mu} > 60$ GeV. This sample was compared with the Drell Yan simulation, and a correction was made based on the observed jet multiplicity in the μ-μ mass window [60-110] GeV. Then, the LQ sample was defined to be the preselection + 2 cone 0.5 jets, each with $E_T > 20$ GeV and $\eta < 2.4$, passing standard jet quality cuts, and with the $m_{\mu\mu} > 110$ GeV. The cross section limit obtained with these cuts is shown in Fig. 8.

8 Large Extra Dimensions search with electrons and photons

In string theories in which the Standard Model processes are restricted to the D3 brane, but in which gravity can propagate in 'extra' dimensions, virtual graviton diagrams can contribute to dilepton and diboson production [2]. D0

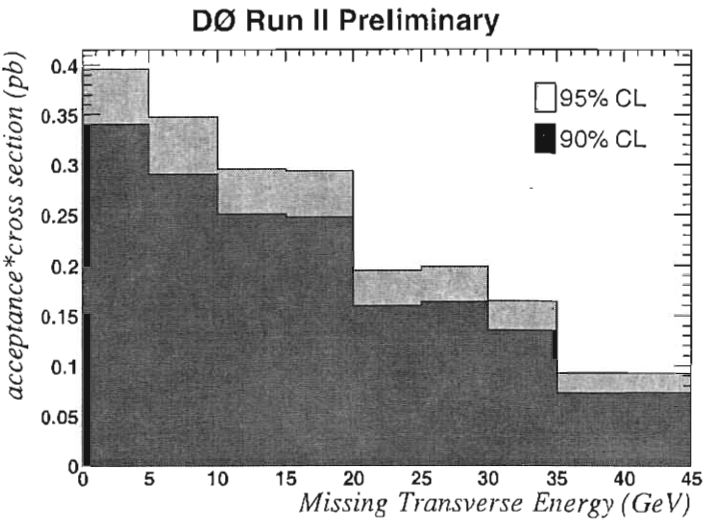

Figure 7: *Cross section limits for the eμ analysis, as a function of the cut in missing E_T.*

has searched for such a signature in the ee + $\gamma\gamma$ channel, using 50 pb^{-1} of data.

The analysis required either a single or diEM trigger to fire. The selection required 2 EM objects, each with $E_T > 25$ GeV and standard EM quality cuts, and a missing $E_T < 25$ GeV. Background was estimated from a fast Monte Carlo for Drell Yan and diphoton production. The misidentification probabilities were estimated from data. The 2-D distributions in the diEM mass and $cos(\theta^*)$ were fitted to obtain three terms: the SM contribution, the direct gravity term, and the interference term. Only the topologies with at least one of the EM objects in the central calorimeter were used. The results of these fits were translated into lower limits on the Planck scale M_s, given different assumptions about F (a dimensionless parameter which incorporates the dependence of the virtual G_{KK} exchange on the number of extra dimensions) [3]. These limits are shown in Table 6.

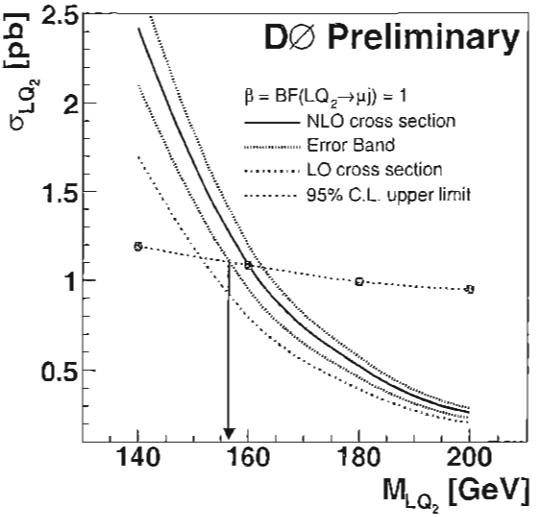

Figure 8: *Cross section limits for the second generation leptoquark analysis.*

Table 6: *Results of extra dimensions analyses: limits on M_s in TeV.*

	GRW	HLZ n=2	HLZ n=7	Hewett $\lambda = +1$
diEM	1.12	1.16	0.89	1.00
diμ	0.79	0.68	0.63	0.71

9 Large Extra Dimensions search with muons

A very similar search for large extra dimensions using the 2μ channel has also been performed. This is the first such search to be reported at the Tevatron. It used 30 pb^{-1} of data.

The trigger used was the same as in the second generation leptoquark search. The offline selection required 2 isolated muons, each with a central track match and $p_T > 15$ GeV. Cosmics were removed. A cut of $m_{\mu\mu} > 40$ GeV was applied. Background was estimated from a fast Monte Carlo for Drell Yan production. The muon misidentification probability was estimated from data. A 2-D fit procedure like the one described in the EM search above was carried out, and the resulting M_s limits are also given in Table 6.

10 Conclusion

D0 is continuing to pursue searches for New Phenomena vigorously in Run II of the Tevatron. New search channels are being introduced, and our search reach and capabilities are expanding. As Run II's luminosity accumulates, the discovery potential continues to rise.

References

1. P3 Summary Report, *Proceedings of the Snowmass Workshop* (2001).

2. N. Arkani-Hamed, S. Dimopoulos, G. Dvali, Phys. Lett. **B429**, 263 (1998); I. Antoniadis, N. Arkani-Hamed, S. Dimopoulos, G. Dvali, Phys. Lett. **B436**, 257 (1998); N. Arkani-Hamed, S. Dimopoulos, G. Dvali, Phys. Rev. **D59**, 086004 (1999); N. Arkani-Hamed, S. Dimopoulos, J. March-Russell, SLAC-PUB-7949, e-Print Archive: hep-th/9809124.

3. G. Guidice *et al.*, Nucl. Phys. **B544**, 3 (1999); T. Han *et al.*, Phys. Rev. **D59**, 105006 (1999); J. Hewett, Phys. Rev. Lett. **82**, 4765 (1999).

Z-LINESHAPE VERSUS 4TH GENERATION MASSES

V.A. Novikov
ITEP, Moscow, Russia

Abstract

The dependence of the Z-boson shape on the location of the $N\bar{N}$ threshold (N is the 4th generation neutrino) is analyzed. The bounds on the existence of 4th generation are derived from the comparison of the theoretical expression for the Z-lineshape with experimental data. The 4th generation is excluded at 95% C. L. for $m_N < 46.7 \pm 0.2$ GeV.

My talk is based on the results of the paper written in collaboration with S.S.Bulanov, L.Okun, A.Rozanov and M.Vysotsky [1].

1 Introduction

I consider a simple and straightforward generalization of the Standard Model (SM), namely the SM with extra chiral generations of heavy leptons (N, E) and quarks (U, D). This model was studied in detail in a number of papers [2–11]. It is important that in such extension of the SM the radiative corrections due to new particles to the SM predictions are finite in the limit of very high masses of extra generations, i.e. heavy generations do not decouple from the low-energy observables. Thus they can be found or excluded by comparing precision electroweak data with one-loop theoretical predictions. Such indirect search for heavy generations from the analysis of the electroweak data fit were performed in [7, 12–15].

The very interesting result of these exercises is that two and more partially heavy extra generations with $m_N \approx m_Z/2$ are not excluded by existing experimental data. It happens that large corrections due to "light" N compensate corrections due to heavy U, D, E. In this case we have a sample of conspiracy of New Physics. (The reason to have large corrections for "light" N is simple - for $m_Z \approx 2m_N$ we have approximately degenerate states (Z boson and pair $(N\bar{N})$) and even small perturbation produces large mixing between degenerate states.)

The existence of semi-heavy neutrino N can be checked directly. One way is to study the reaction $e^+e^- \to \gamma N\bar{N}$. The result of this search can be found in ref. [13]. In this talk I consider another way of the direct search for N: we study the Z-lineshape near the threshold of $N\bar{N}$ production. The energy dependence of $e^+e^- \to Z \to hadrons$ cross section near Z-resonance exhibits a characteristic behavior near the threshold, a cusp. Such behaviour of cross sections in quantum mechanics was discovered by Wigner, Baz and Breit decades ago and is discussed in textbooks, e.g. see [19]. In particle physics analogous phenomenon was considered in [20]. Unlike the general quantum mechanical cases, Z-boson physics is purely perturbative and allows to get explicit formulae for cross section. We found that the variations of cross section because of the cusp are small. Nevertheless, high precision of experimental data on Z production allows us to bound N mass from below. We compare the theoretical expression for the Z-lineshape with the experimental data, presented in [21], and find that the 4th generation is excluded at 95% C. L. for $m_N < 46.7 \pm 0.2$ GeV.

2 Cusps

Consider the scattering of two particles A and B into final state F near the resonance R. Let the mass of the resonance R be near the threshold of $N\bar{N}$ production. The decay rate of $R \to N\bar{N}$ is proportional to the phase-space volume $\sqrt{s-4m_N^2}$, where $\sqrt{s}$ is the energy of the process. Due to unitarity the same factor $\sqrt{s-4m_N^2}$ appears in the amplitude for $A+B \to F$ reaction as well

$$T_0 + iT_1\sqrt{s-4m_N^2}, \tag{1}$$

where T_0 and T_1 are smooth functions of s. Thus the cross-section of $A+B \to F$ is proportional to [19]

$$\begin{aligned} \sigma \sim |T_0|^2 + 2\sqrt{s-4m_N^2}\Im[T_0T_1^*], \qquad s > 4m_N^2 \\ |T_0|^2 - 2\sqrt{4m_N^2-s}\Re[T_0T_1^*], \qquad s < 4m_N^2. \end{aligned} \tag{2}$$

The form of the cross-section energy behavior near threshold depends on the value of the difference $arg(T_0) - arg(T_1)$ (see Fig. 1) [19]. In all cases there are two branches lying on both sides of common vertical tangent. Thus, the existence of the threshold leads to the appearance of the characteristic energy dependence of the cross section. The cross section near threshold is the linear function of $\sqrt{s-4m_N^2}$ with different slopes under and above threshold.

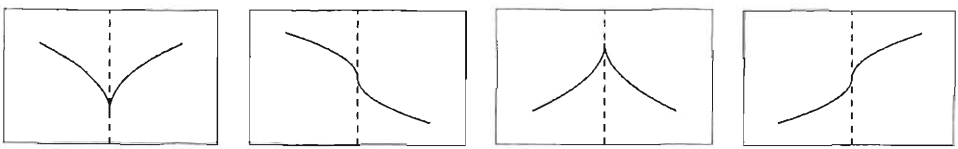

Figure 1: Different cases of cross section behavior near threshold. Vertical axis is σ, while horizontal one is s; dashed line crosses horizontal axis at $4m_N^2$

Below we will consider the case when $R \equiv Z$.

3 Z-lineshape in the presence of 4th generation

The cross-section of $e^+e^- \to Z \to hadrons$ near Z-resonance is well described by the Breit-Wigner formula [22]

$$\sigma_h^{SM} = \frac{12\pi\Gamma_e\Gamma_h}{|p^2 - m_Z^2 + i\Gamma_Z^{SM}p^2/m_Z|^2}\frac{p^2}{m_Z^2}, \tag{3}$$

where $p = p_1 + p_2$, p_1 and p_2 are momenta of initial electron and positron, m_Z is the mass of Z boson, Γ_e is the width of $Z \to e^+e^-$ decay, Γ_h is the width of $Z \to hadrons$, Γ_Z^{SM} is the total width of Z in the SM.

The 4th generation contributes to the Z-boson polarization operator. This contribution can be accounted for in the expression (3) by replacing the denominator:

$$|p^2 - m_Z^2 + i\Gamma_Z^{SM} p^2/m_Z|^2 \to$$
$$|p^2 - m_Z^2 + i\Gamma_Z p^2/m_Z + \Sigma_Z^{(4th)}(p^2) - \Re[\Sigma_Z^{(4th)}(m_Z^2)]|^2. \qquad (4)$$

Thus the real part of the polarization operator is subtracted at $p^2 = m_Z^2$ in order to avoid the shifting of Z-boson mass. The contribution of the $N\bar{N}$ channel into Z width is taken into account by the imaginary part of $\Sigma_Z^{(N)}(p^2)$. The amplitude of $e^+e^- \to hadrons$ is proportional to

$$A_h \sim \left[p^2 - m_Z^2 + i\Gamma_Z p^2/m_Z + (\Sigma_Z^{(N)}(p^2) - \Re[\Sigma_Z^{(N)}(m_Z^2)])\right]^{-1}. \qquad (5)$$

Expanding this expression near the threshold of $N\bar{N}$ production ($p^2 = 4m_N^2$, $A_h \sim T_0 + iT_1\sqrt{p^2 - 4m_N^2}$) we obtain for the cross section the following behaviour

$$\sigma_{p^2<4m_N^2} \sim \frac{1}{\gamma}\left(1 + \frac{\bar{f}^2 m_Z^2}{64\pi}\frac{(4m_N^2 - m_Z^2)\sqrt{\frac{4m_N^2}{p^2} - 1}}{\gamma}\right), \qquad (6)$$

$$\sigma_{p^2>4m_N^2} \sim \frac{1}{\gamma}\left(1 - \frac{\bar{f}^2 m_Z^2}{64\pi}\frac{m_Z\Gamma_Z\sqrt{1 - \frac{4m_N^2}{p^2}}}{\gamma}\right), \qquad (7)$$

where $\gamma = (4m_N^2 - m_Z^2)^2 + (m_Z\Gamma_Z)^2$ and the second terms in the brackets in eqns. (6, 7) are proportional to $\Re[T_0T_1^*]$ and $\Im[T_0T_1^*]$ respectively. As it was mentioned in section 2 the form of the p^2 dependence of the cross section near the threshold is determined by the relative phase of T_0 and T_1. In our case we have two types of cusps (see Figs. 2), which correspond to $arg T_0 - arg T_1$ lying in the third quadrant for $4m_N^2 < m_Z^2$ and in fourth quadrant for $4m_N^2 > m_Z^2$, or to $\Re[T_0T_1^*]$ and $\Im[T_0T_1^*]$ being negative for $4m_N^2 < m_Z^2$ and $\Re[T_0T_1^*]$ being positive, while $\Im[T_0T_1^*]$ being negative for $4m_N^2 > m_Z^2$. It can also be seen from Figs. 2 that the cross section of $e^+e^- \to hadrons$ decreases above the threshold in accordance with the unitarity.

Though the change of Z-lineshape due to these cusps is very small compared to the pure Breit-Wigner curve, as it is shown in Fig. 2, this effect may manifest itself when comparing the theoretical predictions with the experimental data. It is due to the fact, that Z-lineshape is measured with very high

Table 1.
The experimental values of the $e^+e^- \to hadrons$ cross section, obtained by ALEPH, DELPHI, L3 and OPAL collaborations, extracted from Fig. 2 of [21]. $\sqrt{s}$ is presented in GeV, σ_h in nanobarns. The 1993-1995 data set.

Table 1.1 ALEPH

$\sqrt{s}$	89.4316	89.4400	91.1860	91.1980	91.2200	91.2840
σ_h	9.891	9.980	30.500	30.43	30.458	30.555
$\delta\sigma_h$	0.043	0.044	0.078	0.032	0.067	0.13

$\sqrt{s}$	91.2950	91.3030	92.9685	93.0140
σ_h	30.678	30.660	14.300	14.04
$\delta\sigma_h$	0.078	0.090	0.060	0.056

Table 1.2 DELPHI

$\sqrt{s}$	89.4307	89.4378	91.186	91.2	91.203	91.28
σ_h	9.87	9.93	30.392	30.50	30.46	30.65
$\delta\sigma_h$	0.044	0.056	0.065	0.044	0.19	0.13

$\sqrt{s}$	91.292	91.304	92.966	93.014
σ_h	30.67	30.46	14.35	13.89
$\delta\sigma_h$	0.098	0.086	0.044	0.045

Table 1.3 L3

$\sqrt{s}$	89.4497	89.4515	91.206	91.222	91.297	91.309
σ_h	10.088	10.08	30.358	30.547	30.525	30.545
$\delta\sigma_h$	0.034	0.034	0.067	0.034	0.087	0.067

$\sqrt{s}$	92.983	93.035
σ_h	14.231	13.91
$\delta\sigma_h$	0.046	0.053

Table 1.4 OPAL

$\sqrt{s}$	89.4415	89.45	91.207	91.222	91.285	92.973	93.035
σ_h	9.980	10.044	30.445	30.46	30.64	14.27	13.85
$\delta\sigma_h$	0.044	0.034	0.053	0.025	0.098	0.046	0.046

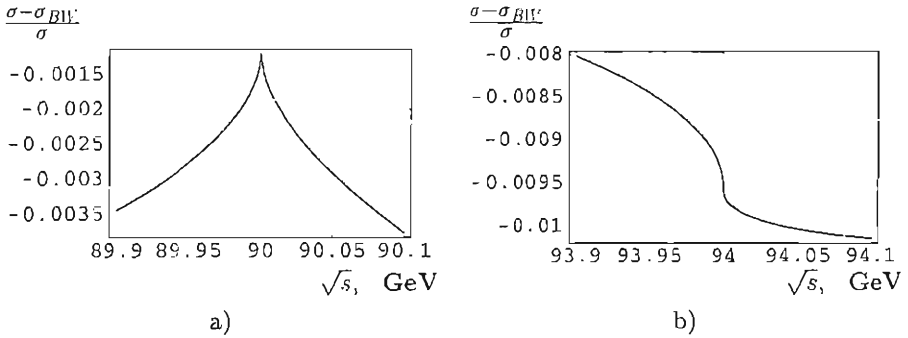

Figure 2: The dependence of relative departure of the $e^+e^- \to hadrons$ cross section in the presence of 4th generation from the SM prediction on the c.m. energy of e^+e^- for $m_N = 45$ GeV (a) and $m_N = 47$ GeV (b).

precision. In the next section we will compare the theoretical cross section with the experimental data.

4 Comparison with the experimental data

The experimental data on the cross section of $e^+e^- \to hadrons$ reaction is usually presented in the form, that includes the electromagnetic corrections, i. e. initial and final state interactions and photon emission [21]. In order to compare our formulae for the cross section with experimental ones, we use the ZFITTER code [22], which takes into account these corrections. We use the following inputs:

$$m_Z = 91.1882(22) \text{ GeV}, \quad m_t = 175(4.4) \text{ GeV}, \quad \bar{\alpha} = 1/128.918(45),$$

$$\alpha_s = 0.1182(27), \quad m_H = 120 \text{ GeV}.$$

With the reasonable assumption that the initial and final state radiation effects are not significantly modified by fourth generation we can calculate the cross section

$$\sigma_h^{4th} = \sigma_h \frac{\sigma_h^{ZF}}{\sigma_h^{SM}}, \tag{8}$$

where σ_h^{ZF} is the result of ZFITTER code and

$$\sigma_h = \frac{12\pi\Gamma_e\Gamma_h}{|p^2 - m_Z^2 + i\Gamma_Z p^2/m_Z + (\Sigma^{(4th)}(p^2) - \Re[\Sigma^{(4th)}(m_Z^2)])_{FP}|^2} \frac{p^2}{m_Z^2}, \tag{9}$$

at values of c. m. energy, at which the experimental values of cross section were measured [21]. There are 35 experimental points from 1995 data, which we use. These points are extracted from Fig. 2 of [21] and presented in Table 1. We took only the points corresponding to 1993-1995 set, due to the fact that they are measured with higher precision than the 1991-1993 set. Then we calculate the $\chi^2/n_{d.o.f.}$, where $n_{d.o.f.} = 35 - N$, N is the number of fitted parameters[1], and

$$\chi^2 = \sum_{i=1}^{35} \left(\frac{\sigma_h^{th} - \sigma_h^{exp}}{\delta\sigma_h^{exp}} \right)^2, \qquad (10)$$

σ_h^{exp} is the experimental value of cross section and $\delta\sigma_h^{exp}$ is its error, in order to determine at what confidence level the 4th generation is excluded by the experimental data. However, the bound on N mass from below depends on the higgs mass and mass splittings between U and D quarks and between E and N leptons. The effects of varying m_H, $|m_U - m_D|$, and $|m_E - m_N|$ are not independent. As it was shown in [15], the increase of $|m_U - m_D|$ or $|m_E - m_N|$ can be compensated by the increase of higgs mass. This leads to the appearance of χ^2_{min} valleys. It can be seen from Figs. 4a) and 4b), where the dependence of χ^2 on $m_H, |m_U - m_D|$ (a) and $m_H, |m_E - m_N|$ (b) is shown for $m_N = 49$ GeV.

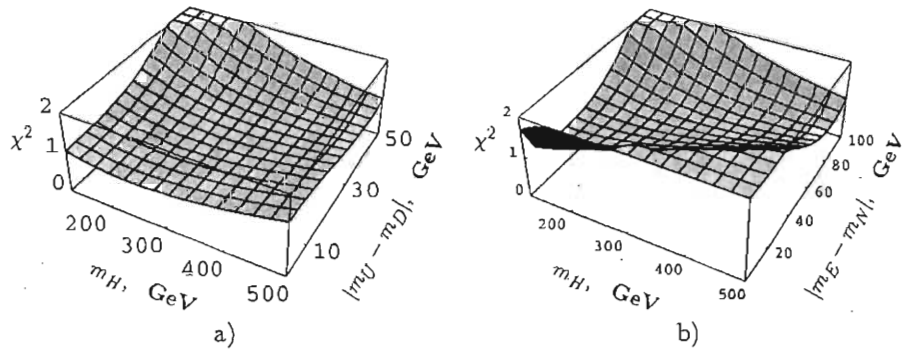

Figure 3: The dependence of χ^2 on $m_H, |m_U - m_D|$ (a) and on $m_H, |m_E - m_N|$.

If we use then the LEP II bound $m_E > 100$ GeV and the results of [15], that the best fit of electroweak data corresponds to the light E near the bound and $m_N \approx 50$ GeV, then we have only two parameters, m_H and $|m_U - m_D|$ that affect the bound on m_N. As it can be seen from Fig. 5a) the best fit is

[1]In our case $N = 1$, because only heavy neutrino mass is a free parameter, all other parameters are fixed.

acquired for $0.11m_H - 19.7 < |m_U - m_D| < 0.12m_H - 9.2$. In this region of masses we calculate χ^2 and find that the 4th generation is excluded at 95% C. L. for $m_N < 46.7 \pm 0.2$ GeV. The theoretical uncertainty is caused by the varying of $|m_U - m_D|$ from 0 to 50 GeV, as well as by the uncertainties of the input parameters of ZFITTER, which were also used when calculating σ_h and σ_h^{SM}. The main contribution to the theoretical uncertainty comes from m_t and α_S. The variation from 0 to 50 GeV is chosen, because the quality of the fit is fast worsening for $|m_U - m_D| > 50$ GeV.

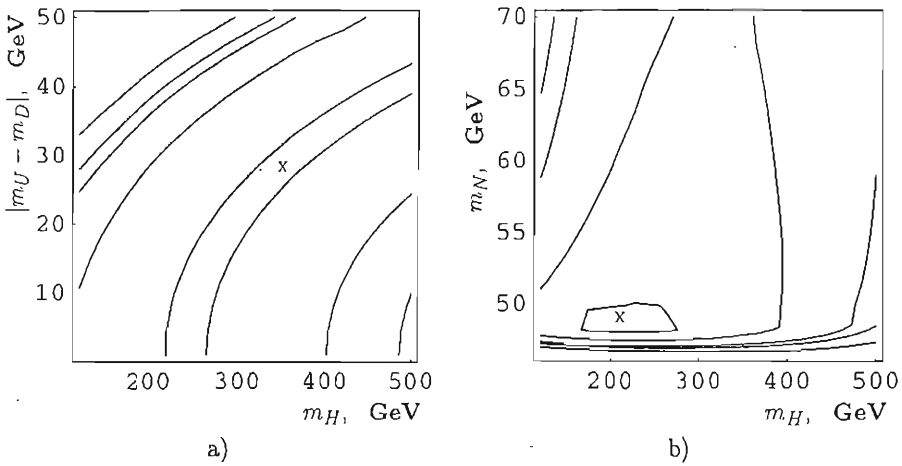

Figure 4: a) Exclusion plot on the plane m_H, $|m_U - m_D|$ for $m_N = 49$ GeV; $\chi^2_{min} = 0.85$ denoted by cross b) Exclusion plot on the plane m_H, m_N for $|m_U - m_D| = 10$ GeV; $\chi^2_{min} = 0.85$ denoted by cross. Solid lines represents the borders of 1σ, 2σ, 3σ, 4σ and 5σ regions.

In order to illustrate the dependence of the fit quality on the higgs mass we study $\chi^2(m_N, m_H)$ (see Fig. 5b)). From this figure it is seen that the 95% C. L. bound lies below 50 GeV and slightly varies with the increase of the higgs mass near $m_N = 47$ GeV. In this figure we take $|m_U - m_D| = 10$ GeV. It can be seen from Figs. 4 a) and b) that for certain region of 4th generation particles and higgs masses the quality of the fit can be even better than in SM. According to the results of [21] the $\chi^2/n_{d.o.f.}(SM) = 1.09$, which corresponds to 2σ level, while in the presence of 4th generation it is $\chi^2_{min}/n_{d.o.f.} = 0.88$, which is inside 1σ region.

We should note, that the direct search of heavy neutrinos in e^+e^- annihilation into a pair of heavy neutrinos with the emission of the initial state bremsstrahlung photon ($e^+e^- \to \gamma + Nothing$) could result in the bound $m_N \geq 50$ GeV [13, 14] if all four LEP experiments will make a combined

analysis [16].

Though this bound on m_N would be slightly better than the one, obtained in the present paper, the data and the procedure used to extract the bounds are completely different and independent.

5 Conclusions

We study the dependence of Z-lineshape on the location of the threshold of $N\bar{N}$ production. We compare the theoretical predictions for the Z-lineshape with the experimental data, using the exact formulae for Z polarization operator, instead of expanding it into a Taylor series near m_Z as it is done in the standard renormalization procedure.

We found that the bound on N mass depends on the higgs mass and on the splittings of 4th generation quark and lepton masses ($|m_U - m_D|$ and $|m_E - m_N|$). However, the effects caused by them are not independent, because the increase of mass splittings can be compensated by the increase of the higgs mass, as it was shown in [15]. Using the results of [15] we fixed $m_E = 100$ GeV. Then we used the fact that $|m_U - m_D|$ and m_H are not independent. Thus, we had one free parameter left: $|m_U - m_D|$. We varied $|m_U - m_D|$ from 0 to 50 GeV and found that the 4th generation is excluded by the experimental data at 95% C. L. for $m_N < 46.7 \pm 0.2$ GeV. The theoretical uncertainty is caused by the varying of $|m_U - m_D|$, as well as by the uncertainties of the input parameters of ZFITTER, which were also used when calculating σ_h and σ_h^{SM}.

Acknowledgments

I would like to thank the organizers of La Thuile conference, particular Mario Greco, for their warm hospitality and for excellent conference.

References

1. S.S.Bulanov *et al.* ,hep-ph/0301268.
2. J. Erler, P. Langacker, Review of Particle Physics. The European Physical Journal **C15** (2000) 95, chapter 10.6.
3. A. Masiero *et al.*, Phys. Lett. **B355** (1995) 329.
4. T. Inami *et al.*, Mod. Phys. Lett. **A10** (1995) 1471.
5. N. Evans, Phys. Lett. **B340** (1994) 81.
6. P. Bamert and C. P. Burgess, Z. Phys. **C66** (1995) 495.

7. V. A. Novikov *et al.*, Mod. Phys. Lett. **A10** (1995) 1915.

8. D.Fargion *et al.*, Phys. Rev. **D52** (1995) 1828;
D.Fargion *et al.*, Phys. Rev. **D54** (1996) 4684;
K. Belotsky *et al.*, hep-ph/0210153;
D.Fargion *et al.*, JETP Lett. **68** (1998) 685;
D.Fargion *et al.*, JETP Lett. **69** (1999) 434;
K. Belotsky *et al.*, Phys. Atom. Nucl. **65** (2002) 382;
K. Belotsky *et al.*, Phys. Lett. **B529** (2002) 10.

9. C. D. Froggatt and J. E. Dubicki, Proceedings to the workshops "What comes beyond the Standard model 2000, 2001" vol. 1.

10. A. Borstnic Bracic and N. Mankoc Borstnik, Proceedings to the workshops "What comes beyond the Standard model", 2000, 2001, 2002, vol 2;
D. Lukman, A Kleppe, N. Mankoc Borstnik, Proceedings to the workshops "What comes beyond the Standard model", 2000, 2001, 2002, vol 2.

11. E. Arik *et al.*, Phys. Rev. **D66** (2002) 116006;
E. Arik *et al.*, Phys. Rev. **D66** (2002) 033003.

12. M. Maltoni, V. A. Novikov, L. B. Okun, A. N. Rozanov, and M. I. Vysotsky, Phys. Lett. **B476** (2000) 107.

13. V.A. Ilyin *et al.*, Phys. Lett., **B503** (2001) 126; hep-ph/0006324;
V.A. Ilyin *et al.*, Proceedings ICHEP2000 Osaka conference; hep-ph/0009167.

14. V. A. Novikov *et al.*, Phys. Lett. **B529** (2002) 111; hep-ph/0111028.

15. V. A. Novikov *et al.*, JETP Lett. **76** (2002) 119; hep-ph/0203132.

16. The ALEPH Collaboration, ALEPH 2001-010; CONF 2001-007 (2001);
P.Abreu *et al.*, DELPHI Collaboration, Eur. Phys. J. **C16** (2000) 53;
M. Acciari *et al.*, L3 Collaboration, Phys. Lett. **B470** (1999) 268;
G. Abbiendi *et al.*, OPAL Collaboration, Eur. Phys. J. **C14** (2000) 73.

17. H.-J. He, N. Polonsky and S. Su, Phys. Rev. **D64** (2001) 053004; hep-ph/0102144.

18. V. A. Novikov *et al.*, Rep. Prog. Phys. **62** (1999) 1275.

19. L. D. Landau, E. M. Lifshitz, Quantum Mechanics (Moscow, Nauka, 1974) par. 147.

20. A. I. Baz, L. B. Okun, JETP **8** (1959) 526.

21. LEP collaborations, Combination procedure for the precise determination of Z boson parameters from results of the LEP experiments, CERN-EP/2000-153; hep-ex/0101027.

22. D. Bardin *et al.*, Comput. Phys. Commun., **133** (2001) 229.

23. ALEPH Coll., Phys. Lett., **B429** (1998) 201.

SESSION IX – FUTURE EXPERIMENTS AND PROJECTS

Makoto Tomoto	Prospects for DØ Higgs Search
Marco Grassi*	A Sensitive Search for the $\mu \to e\gamma$ Decay: the MEG Experiment
Massimo Masera	Perspectives of the ALICE Experiment

* The trasparencies of the missing contributions are available on the web site http://www.pi.infn.it/lathuile/lathuile_2003.html

PROSPECTS FOR DØ HIGGS SEARCH

Makoto Tomoto
Fermi National Accelerator Laboratory
(For DØ collaboration)

Abstract

The DØ experiment has been taking data at RunII of the Tevatron since March 2001. The DØ Higgs group started analysis towards discovery of the Higgs boson. The results presented here are based on the data from an integrated luminosity of 50 pb^{-1} collected from August 2002 to January 2003. We have focused on initial analysis of W or Z plus jets, the first steps towards Higgs searches in the WH or ZH channel and on $H \rightarrow WW$ production. We also present prospects for DØ Higgs searches.

1 Introduction

The highest priority of high energy physics is discovery of the Higgs boson and understanding the mechanism of the electroweak symmetry breaking. It is the last piece of the Standard Model (SM), and also the key to understanding any beyond the standard model physics.

The direct measurements at the LEP experiments [1] and indirect global fits [2] from theory indicate that the Higgs mass lies roughly between 115 GeV and 200 GeV. The Higgs search at Tevatron covers this mass range. The DØ and CDF experiments are currently the only experiments which have capability of discovering Higgs bosons in this mass range. A previous Monte Carlo study by the SUSY Higgs Working Group (SHWG) [3] at Fermilab suggests that a 3 to 5 sigma discovery of the Higgs boson can be made in most of this mass region. In order to achieve this, large integrated luminosity is required and we have to combine all possible Higgs production and decay channels measured by both DØ and CDF experiments. The SHWG also concluded that it is vital to improve our understanding of the signal and background processes and the detector performance. Especially vital are b tagging of jets and mass resolution of two b-tagged jets.

At the Tevatron, the Higgs is produced via gluon fusion ($gg \to H$), associated production with W or Z boson ($p\bar{p} \to HW$ or HZ), and associated production with $q\bar{q}$ ($p\bar{p} \to Hq\bar{q}$) in order of decreasing production rate. The branching ratio of the Higgs decay channel is dominated by pair production of b quarks ($H \to b\bar{b}$) in the small Higgs mass region ($m_H \leq 130$ GeV) and by pair production of W boson ($H \to WW^{(*)}$) in the large Higgs mass region (≥ 130 GeV). Events from HZ or HW production in which H decays to $b\bar{b}$ and the W or Z decays leptonically are the most promising channel in the low Higgs mass region. In the large Higgs mass regions, on the other hand, the decay chain of the gluon fusion and Higgs decay to WW is most prospective. Finally, $Hb\bar{b}$ production is analyzed in order to search for SUSY Higgs model, because this production rate is enhanced by one of the supersymmetric parameter, $\tan\beta$.

2 Higgs searches at DØ

The current activities of the DØ Higgs group [4] are Monte Carlo and a trigger studies for $WH \to l\nu b\bar{b}$ (l=e or μ), $ZH \to ll b\bar{b}$ (l=e, μ, or ν), $H \to WW^{(*)}$, $H \to \gamma\gamma$, and SUSY Higgs searches for the $\phi b(b\bar{b})$ decay channel. The data analysis on Higgs searches has been also started using data collected by the DØ experiment from August 2002 to January 2003. The results presented here are based on 50 pb^{-1} of integrated luminosity Two kinds of data analyses towards are presented here. One is inclusive W or Z plus jets production in the $p\bar{p}$ collision. This is a study of the background sources for the WH or

ZH production searches and thus is the first step towards Higgs searches. The second topic is search for WW decays of the Higgs produced by gluon fusion. This channel is very interesting for not only Higgs searches but also electroweak physics and new phenomena.

3 W/Z + jets analysis

Looking at W or Z plus inclusive jets is the first step towards Higgs searches via WH or ZH production. In addition, this analysis is a background study of the $Wb\bar{b}$ or $Zb\bar{b}$ production, which is the largest background source of WH or ZH channel, because the properties of the di b-jets from $Wb\bar{b}$ or $Zb\bar{b}$ can be related to ones of the W or Z plus jets [5].

The analysis was performed for $W(Z)$ decay to both electron(s) and muon(s). The integrated luminosity of the data we used in this analysis was 35 pb^{-1}. The events were triggered by an isolated lepton with high transverse momentum (p_T). Using isolated lepton triggers allows us to analyze jet properties without any biases. The electron identification was based on the calorimeter shower shape χ^2, electromagnetic energy fraction, and an E/p requirement with an associated track. The muon was identified by track segments reconstructed in the muon system, isolation from significant energy deposition in the calorimeter and an associated track from the central tracking system. The muon momentum is taken from the tracking system. The selection criteria are summarized in Tab. 1. In addition, W or Z inclusive samples were

Table 1: *The selection for reconstructing W or Z*

channel	electron	muon
W plus jets	$p_T > 20$ GeV $\|\eta\| < 0.8$ missing $E_T > 25$ GeV	$p_T > 25$ GeV $\|\eta\| < 1.5$ missing $E_T > 20$ GeV
Z plus jets	$p_T > 20$ GeV $\|\eta\| < 2.3$ 60 GeV $< M_{ee} <$ 120 GeV	$p_T > 15$ GeV $\|\eta\| < 2.0$ 60 GeV $< M_{\mu\mu} <$ 120 GeV

required to have at least one jet which satisfies $p_T > 20$ GeV and $|\eta| < 2.5$. The standard DØ calorimeter energy calibration, called the Jet Energy Scale (JES) was applied.

Fig.1 and Fig.2 are the p_T distributions of the leading (left) and the second leading (right) jet for W plus jets and Z plus jets, respectively. Both electron and muon channels were combined. The error is dominated by systematic error from JES.

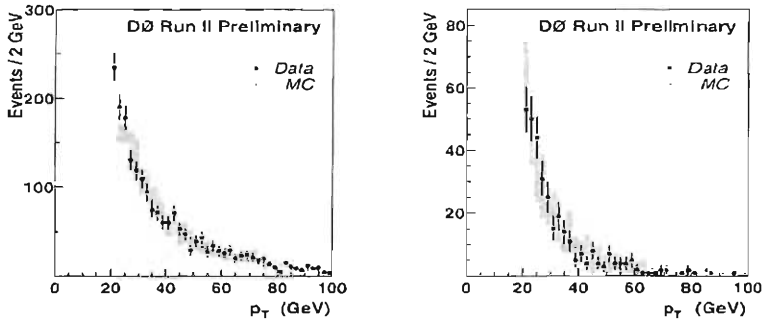

Figure 1: *Transverse momentum of the leading jet (left) and next leading jet (right) for W plus jets channel. Dots are collider data, hatched bars are Monte Carlo expectations extracted from* PYTHIA. *Two distributions were normalized to the same area. The bar indicates a statistical error and a main systematic error coming from the JES.*

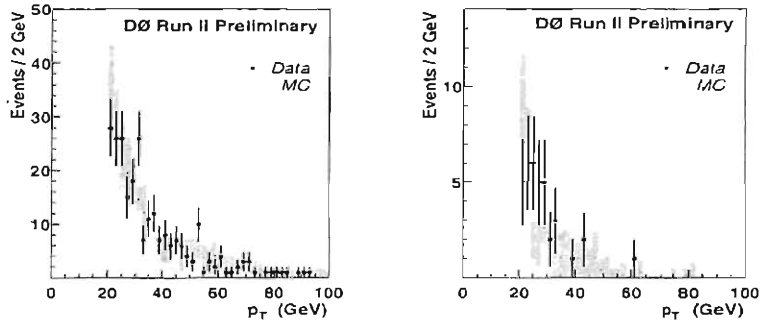

Figure 2: *Transverse momentum of the leading jet (left) and next leading jet (right) for W plus jets channel. Dots are collider data, hatched bars are Monte Carlo expectations extracted from* PYTHIA. *Two distributions were normalized to the same area. The bar indicates a statistical error and a main systematic error coming from the JES.*

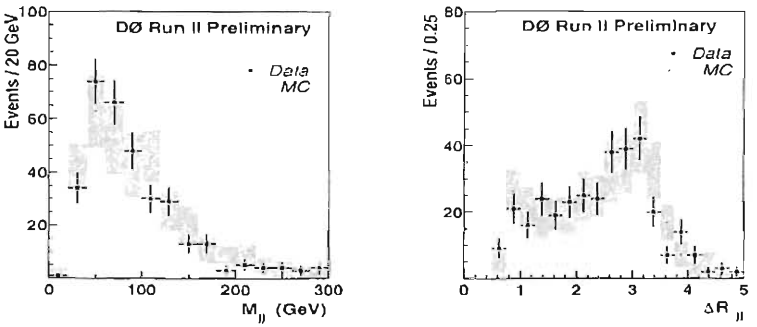

Figure 3: *The di-jet mass (left) and separation of 2 leading jets (right) for W plus jets channel. Dots are collider data, hatched bars are Monte Carlo expectations extracted from* PYTHIA. *Two distributions were normalized to the same area. The bar indicates a statistical error and a main systematic error coming from the JES.*

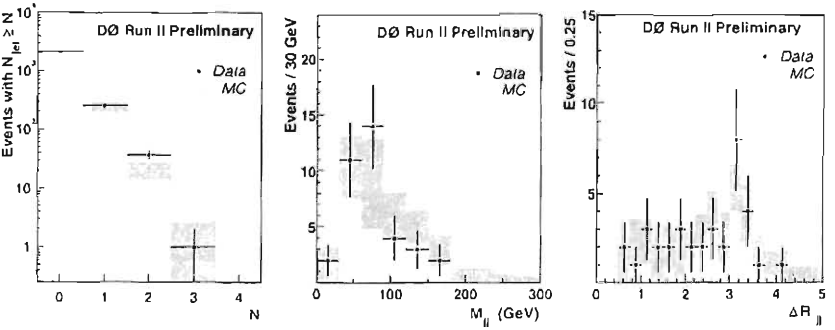

Figure 4: *The number of the jets(left) and di-jet mass (center) and separation of 2 leading jets (right) for Z plus jets channel. Dots are collider data, hatched bars are Monte Carlo expectations extracted from* PYTHIA. *Two distributions were normalized to the same entries of the first bin for left plot and the same area for center and right plots, respectively. The bar indicates a statistical error and a main systematic error coming from the JES.*

Fig.3 is the distribution of the di jet mass (left) and the separation (right) between leading and second leading jets, which is defined by $\Delta R = \sqrt{\Delta\eta^2 + \Delta\phi^2}$ for the W plus jets channel. Fig.4 (center and right) are same plots for the Z plus jets channel. Fig.4 also includes the jet multiplicity distribution. All plots indicated that the PYTHIA [6] Monte Carlo and data show good shape agreement, indicating an understanding of jet properties and detector response.

4 Comments on b tagging

The next step in searches for WH or ZH would be b-jet identification. The b jet identification is critical to keep efficiency of the $H(\rightarrow b\bar{b})$ signal high and to suppress non-b jets. The performance is largely determined by Impact Parameter (IP) resolution. The DØ tracking system, which consists of the silicon detector and the eight layers fiber tracker, was built to provide good b jet identification performance, and the IP resolution was measured to be less than 20 μm for tracks with $p_T > 10$ GeV. The results agreed with Monte Carlo expectation. The b tagging performance is demonstrated by using a signed IP significance method. Fig.5 shows the signed IP significance (i.e., the distance of closest approach (dca) divided by its error) for the muon plus jet sample. The sign of IP significance is negative (positive), if the muon track crosses jet axis before (after) the primary vertex. The negative side of this distribution should be indicative of the resolution, and its mirror image has been superimposed on the positive side of the distribution (hatched histogram). The excess on positive side was due to muons from long-lived particles. The b jets enhance this excess and we clearly identify b jets with IP significance method. Further studies are in progress and we will be able to report b tagging efficiency plots, in the near future.

5 WW production

WW production in $p\bar{p}$ collisions is interesting for number of the reasons. This is the most promising channel for SM Higgs searching in the high mass region ($m_H > 130$ GeV). If a 4th fermion family exists, the SM Higgs cross section is enhanced [7]. And if the Higgs couples to only bosons or the top quark, the branching ratio of this production is increased (i.e, Fermiophobic/Topcolor Higgs) [8].

One final state of this channel is very simple; a high p_T di-lepton pair with large missing E_T. The background is expected to be mostly direct WW production, Drell-Yan process, $t\bar{t}$, and QCD backgrounds. The disadvantage of the analysis is that the direct reconstruction of the Higgs mass cannot be made. Instead, we use the transverse mass, defined as $M_T = \sqrt{(E_T^{\ell\ell} + E_T^{\nu\nu})^2 - (p_T^{\ell\ell} + p_T^{\nu\nu})^2)}$

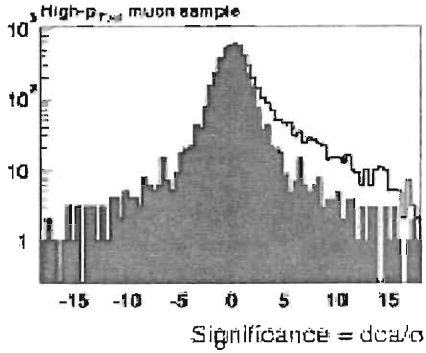

Figure 5: *Impact parameter significance. The sign of IP significance was defined negative (positive), if muon track crosses jet axis before (after) primary vertex. The negative side of this distribution should be indicative of the resolution, and its mirror image was also superimposed on the positive side of the distribution (hatched histogram). The excess on positive side was due to muons from long-lived particles.*

,where $E_T^{\ell\ell} = \sqrt{(p_T^{\ell\ell})^2 + (m_{\ell\ell})^2}$ and $E_T^{\nu\nu} = \sqrt{(E_T^{miss})^2 + (m_{\ell\ell})^2}$. The opening angle between leptons ($\Delta\Phi_{\ell\ell}$) is a useful discriminating variable, because two leptons from the Higgs tend to move in parallel (i.e., small $\Delta\Phi_{\ell\ell}$) due to spin correlation in $H \to WW$ decay products. On the other hand, two leptons from Drell-Yan and multi-jets processes are emitted back to back (i.e., large $\Delta\Phi_{\ell\ell}$).

The di-electron and electron plus muon channels are reported here. The integrated luminosity of the data we used in di-electron channel and electron plus muon channel was 44.5 pb^{-1} and 35 pb^{-1}, respectively . At least two leptons in an event were required with the p_T of leading lepton and second leading lepton required to be greater than 20 GeV and 10 GeV, respectively. The missing E_T was required to be greater than 20 GeV. Requiring $\Delta\phi(E_T^{miss}, jets) > 0.5$ and $|\vec{E}_T^{miss} + \vec{p}_T| > 50$ GeV rejects events where the missing transverse momentum is caused by a mismeasurement of jet energy in the detector. For the di-electron channel, the di-lepton mass and transverse mass were required to be less than $m_H/2$ and less than m_H+20 GeV, respectively, to reject Drell-Yan process. Finally as discussed above, requiring the opening angle between leptons ($\Delta\Phi_{\ell\ell}$) less than 2.0 reduces the background. The selections were optimized for 4 different mass points (i.e.,m_H =120 GeV, 140 GeV, 160 GeV, and 180 GeV) and Tab.2 is number of events remaining after the successive application of all selections for di-electron channel optimized for m_H =120 GeV. The $\Delta\Phi_{\ell\ell}$ distributions for the di-electron channel are shown in Fig.6. The left

Table 2: *Number of expected backgrounds and remained data for $H \to WW \to e^+e^-\nu\bar{\nu}$ channel.*

	Expected background	DATA
ID, p_T	2748±42±245	2753
$m_{ee} < m_H/2$	264±18.6±4.3	262
missing E_T >20 GeV	12.3±2.5±0.7	11
mass cut	3.6±1.4±0.2	1
$\Delta\Phi_{\ell\ell}$ <2.0	0.7±1.4±0.1	0

and right figures show $\Delta\Phi_{\ell\ell}$ distributions after basic kinematic cuts and all selections except $\Delta\Phi_{\ell\ell}$, respectively. The background from multi-jets, Drell-Yan, W plus jet, $W\gamma$, WW, and $t\bar{t}$ processes were estimated using Monte Carlo. The predictions agree with data distribution very well. The signal distribution, multiplied by factor 50, is overlaid in the right figure. Similar results for the

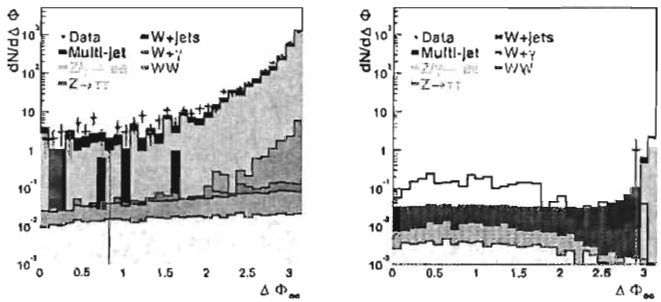

Figure 6: *The $\Delta\Phi_{\ell\ell}$ distributions for $H \to WW \to ee\nu\nu$ channel. The selection is optimized for m_H=120 GeV. The left and right figures show $\Delta\Phi_{\ell\ell}$ distributions after basic kinematic cuts and all selections except $\Delta\Phi_{\ell\ell}$, respectively. The background from multi-jets, Drell-Yan, $Z \to \tau\tau$, W plus jet, $W\gamma$, WW, and $t\bar{t}$ processes were overlaid. The signal distribution, multiplied by factor 50, was overlaid in the right figure.*

$H \to WW \to e\mu\nu\nu$ channel are shown in Tab.3 and Fig.7. The selection was optimized for m_H=160 GeV. Fig.8 shows one example of a $H \to WW \to ee$ candidate passing through all event selections.

Table 3: *Number of expected backgrounds events and observed data for* $H \to WW \to e\mu\nu\bar{\nu}$ *channel.*

	Expected background	DATA
ID, p_T	22±2.1±2.2	22
$m_{ee} < m_H/2$	3.1±1.7±0.1	4
missing E_T >20 GeV	1.4±1.5±0.1	2
$\Delta\Phi_{\ell\ell}$ <2.0	0.9±1.5±0.1	1

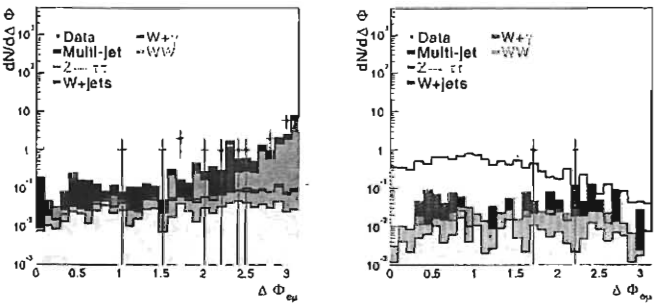

Figure 7: *The* $\Delta\Phi_{\ell\ell}$ *distributions for* $H \to WW \to e\mu\nu\nu$ *channel. The selection is optimized for* m_H=160 *GeV. The left and right figure was* $\Delta\Phi_{\ell\ell}$ *distributions after basic kinematic cuts and all selections except* $\Delta\Phi_{\ell\ell}$*, respectively. The background from multi-jets,* $Z \to \tau\tau$*,* W *plus jet,* $W\gamma$*,* WW*, and* $t\bar{t}$ *processes were overlaid. The signal distribution, multiplied by factor 20, was overlaid in the right figure.*

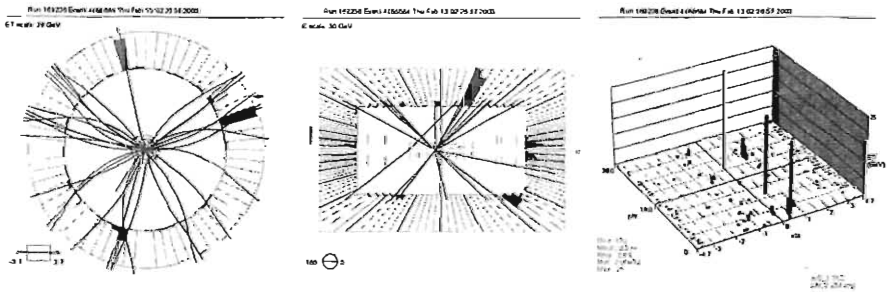

Figure 8: *One example of the event display for* $H \to WW \to ee\nu\nu$ *channel.*

6 Conclusion

DØ Run II has started taking physics quality data. Backgrounds to Higgs production are under study. We report analyses of W or Z plus jets and WW production. Additional Higgs channels not reported here are also being studied. We expect more results will be shown in the near future.

References

1. ALEPH, DELPHI, L3 and OPAL Collaborations, Search for the Standard Model Higgs Boson at LEP, CERN-EP/2003-011
2. The LEP Electroweak Working Group, A Combination of Preliminary Electroweak Measurements and Constraints on the Standard Model, hep-ex/0212036
3. M. Carena, J. S. Conway, H. E. Haber, J. D. Hobbs, *et al* . , Report of the Higgs Working Group of the Tevatron Run 2 SUSY/Higgs Workshop, hep-ph/0010338
4. DØ Higgs group, http://www-d0.fnal.gov/Run2Physics/higgs/
5. John Campbell, R. K. Ellis, Next-to-leading order corrections to W+2 jet and Z+2 jet production at hadron colliders, Phys.Rev. **D65**, 113007 (2002), hep-ph/0202176
6. Torbjorn Sjostrand, Leif Lonnblad, Stefan Mernna, and Peter Skands, PYTHIA 6.2 Physics and Manual, hep-ph/0108264
7. E. Arik *et al*, With four Standard Model families, the LHC could discover the Higgs Boson with a few fb^{-1}, SN-ATLAS-2001-006, hep-ph/0109037
8. L. Brücher, R. Santos, Experimental Signatures of Fermiophobic Higgs Bosons, hep-ph/9907434

A SENSITIVE SEARCH FOR THE $\mu \to e\gamma$ DECAY: THE MEG EXPERIMENT

Marco Grassi
INFN, Pisa

Written contribution not received

PERSPECTIVES OF THE ALICE EXPERIMENT

Massimo Masera, for the ALICE Collaboration
Dipartimento di Fisica Sperimentale and I.N.F.N., Torino (Italy)

Abstract

The Large Hadron Collider, now under contruction at the European Center for Nuclear Research, represents a unique opportunity for Heavy-Ion Physics. It will provide nuclear collisions at a center-of-mass energy of the order of 5.5 TeV per nucleon, $\sim$ 30 times higher then the present Relativistic Heavy Ion Collider at BNL, currently the highest energy nuclear accelerator. The LHC will represent a huge step forward in terms of both volume and energy density that can be attained in nuclear interactions: particle production will be dominated by hard processes. ALICE (A Large Ion Collider Experiment) is the only detector specifically designed for the physics of nuclear collisions at LHC, even though it can also study high cross section processes occurring in proton–proton collisions. ALICE is conceived as a general–purpose detector and will address most of the phenomena related to the QGP formation at LHC energies: to this purpose, a large fraction of the hadrons, leptons and photons produced in each interaction will be measured and identified. ALICE is developing rapidly: the R&D is essentially complete, and large parts of the main detectors are in production.

In the following, the experimental conditions at the LHC with nuclear beams will be summarized, the main detector components of ALICE will be described and the physics program of the experiment will be briefly discussed.

1 Introduction

Ultrarelativistic heavy-ion collisions have been studied for fifteen years with a rich experimental programme both at the AGS (Brookhaven National Laboratories) and at the SPS (CERN). It turned out that in these collisions very high energy densities can be reached and there are experimental evidences that in Pb-Pb collisions at the SPS a new state of matter in which quarks and gluons are deconfined was formed [1]. The Relativistic Heavy Ion Collider (RHIC) at BNL began its activity in 2000 opening a new horizon for studying nucleus-nucleus interactions. The centre of mass energy ($\sqrt{s} = 200\,GeV$ per nucleon) is one order of magnitude higher than what can be achieved at the SPS hence the temperature reached in the collision should well exceed the critical value for the phase transition to the QGP. The amount of available experimental results

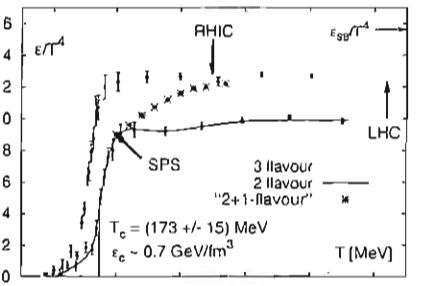

Figure 1: *Lattice QCD phase transition* [4]

from RHIC is impressive [2]. The next step towards really high energies will be made by the Large Hadron Collider (LHC) that will be ready for physics in the year 2007. The available centre of mass energy will be $5.5 TeV$ per nucleon with Pb beams, 27.5 times higher if compared to RHIC. In Fig. 1 the temperature dependence of the energy density ϵ as computed in lattice QCD is shown under different assumptions: two and three light quarks and two light quarks plus one heavier quark (s).

In Fig. 1 the expected behaviour is indicated by the stars: at temperatures $T \simeq T_c = 173 \pm 15 MeV$, the quark s does not contribute to the thermodynamics due to its mass whereas at high temperature the energy density is essentially given by 3-light flavour QCD. At the LHC, the colliding system is expected to be well within the plateau at $T \sim 3T_c$ with a vanishing baryochemical potential at $y \sim 0$. In this regime of $\mu_B << T$ the equation of state approaches the better understood case of $\mu_B = 0$. The ideal limit of a Stefan-Boltzmann gas of quarks and gluons is not reached even at the highest temperatures which

hints at a complex structure of quasi-particle excitations in the plasma phase.

The acceleration of nuclear beams is part of the initial program, and a Heavy Ion pilot run is foreseen for the first LHC year. The LHC will dedicate every year few weeks of running to Heavy Ions. Four experiments will operate at the LHC. One of these, ALICE, is dedicated to Heavy Ions, another one, CMS, is dedicated primarily to pp but features a well defined HI program, while a third, ATLAS, has expressed an interest in running with Heavy Ions. Being the only dedicated experiment for the study of nuclear collisions at the LHC, ALICE is essentially a "Heavy Ion Program" which covers in one experiment the full range of relevant observables, even though it is able to address relevant high cross section p–p phenomena [3]. CMS, on the other hand, is optimized for the study of high transverse momentum processes, and will therefore focus on these observables only.

2 Physics observables

The higher energy will improve by large factors, typically by an order of magnitude, all parameters relevant to the formation of the Quark-Gluon-Plasma: energy density, size and lifetime of the system. The initial temperatures will largely exceed the calculated critical temperature for QGP formation, therefore allowing the study of QGP in its asymptotic gas form. In the central region the net baryon number density will essentially vanish, improving the ease of comparison with lattice QCD calculations and the closeness to the conditions of the primordial universe. The region of x_{Bj} explored will extend singificantly towards smaller-x values, while particle production will be dominated by hard rather than soft processes. Moreover, it will be possibile to exploit a wider set of relevant observables as compared to previous accelerators, thus substantially enhancing the understanding of the properties of the system. First of all, the higher energy and the high luminosity will improve access to hard probes sensitive to the nature of the medium at the earliest stages. The study of jet production and therefore of the propagation of fast partons will find at the LHC its ideal environment, allowing the study of jet fragmentation functions up to well over 100 GeV/c of jet p_T[1] . The excellent PID capability and wide coverage in transverse momentum of ALICE will allow the detailed study of the fragmentation functions. The study of the jet recoiling against a photon will allow the measurement of the fast parton energy loss. The study of the heavy quark potential will benefit from the possibility to measure both the charmonium and bottomium families, which provide a wide range of radii and binding energies, and of the possibility of measuring in the same experiment the production of open charm and beauty mesons, and even of the contribution

[1] We expect to collect about 1000 jets with a $P_T \sim 200\,GeV/c$ per year

of B meson decays to the J/ψ yield. The temperature of the medium should be high enough to allow a precise direct measurement of the prompt photon spectrum, which would be a direct thermometer of the system.

In addition to the new wealth of information provided by the hard probes, the very high multiplicity, several thousands of charged partciles per unit η, will allow the measurement of a large number of observables on an event-by-event basis: impact parameter, multiplicity, particle composition and spectra and HBT parameters of the system. Therefore single event analysis, and in particular the study of non-statistical fluctuations associated to critical phenomena, can be effectively performed at the LHC.

The present ALICE design [5, 6, 7, 8]. is a multi-purpose one, addressing in a comprehensive way all the relevant observables, and foresees the measurement and identification of most of the produced hadrons, leptons and photons. The ALICE physics goals can be summarized, albeit not exhaustively, as follows:

- *Global event features.* Multiplicities, very forward energy flow (0 degree) and rapidity distributions allow to determine the centrality, the number of participants in the interaction and to specify the initial energy density.
- *The geometry and space–time evolution of the emitting source.* The space–time structure of the collision fireball will be studied with two-particle momentum correlations.
- *Degrees of freedom* as a function of temperature. Quantities related to the dynamical evolution of the hadronic phase like p_T spectra and particle ratios of identified hadrons ($\pi, \eta, \omega, \phi, p, K, \Lambda, \Xi, \Omega$) and direct photons will be measured.
- *Non statistical fluctuations and critical behaviour.* This topic will be addressed by event–by–event analyses, including some spectra and particle ratios. Distortions of $N_\gamma - N_{charged}$ correlations will be suitable for the detection of Disoriented Chiral Condensates (DCC). Searches for anomalies like the *Centauro* events will be also performed.
- *Chiral symmetry restoration.* It will be searched through the study of the resonance decays.
- *Collective effects*: elliptic and directed flow will be investigated by various sub detectors.
- *Hard probes.* Open charm and beauty, high p_T spectra, jets and jet quenching will be measured. Spectroscopy of the J/Ψ and Υ families will provide a tool particularly sensitive to deconfinement.

As a difference from the other LHC experiments, the sensitivity to low p_T particles is relevant for many of the physics issues addressed by ALICE. Therefore the main experimental challenge consists in tracking and identifying virtually all the produced stable particles in an environment in which these particles will be several thousands per unit of rapidity.

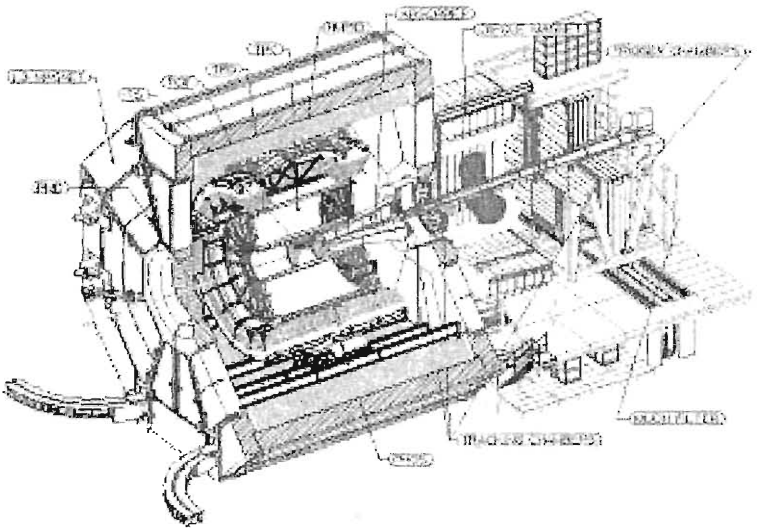

Figure 2: *Longitudinal view of the ALICE detector*

3 The Experimental apparatus

The experimental layout is represented in Fig. 2. The relatively low interaction rate expected with nuclear beams together with the high particle density lead to a solution based on a Time Projection Chamber (TPC) used for tracking in the central rapidity region. This detector, which is able to sustain the foreseen rate has a high granularity over a wide region. It extends longitudinally from $-2.5m$ to $2.5m$ and radially from $90cm$ up to $250cm$ in order to have a dE/dx resolution $< 10\%$ for electron identification. The design and the choice of the gas are optimised for a good double–track resolution. The total number of channels is $5.7\,10^5$ feeding the DAQ with an amount of information of $\sim 60\ MB$ for a central event, corresponding to 12000 tracks. The pseudorapididity coverage of the TPC and the other detectors of the central barrel is $|\eta| < 0.9$, which is adequate for studying particle ratios, p_T spectra and HBT correlations.

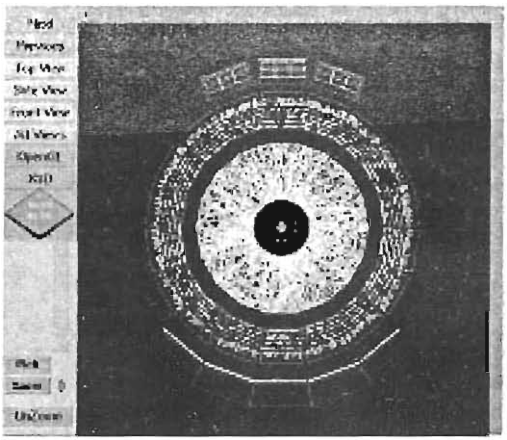

Figure 3: *ALICE event display. Particles are generated with a polar angle θ in the range $85 < \theta < 95$ with a density corresponding to the maximum foreseen value. Starting from the beam axis, ITS, TPC, TRD and TOF are displayed. PHOS and HMPID are below and above the beam axis respectively*

The magnetic field necessary for momentum measurements is provided by the magnet of the L3 experiment: it generates a weak solenoidal field ($B < 0.5\,T$) over the whole region of the barrel. This choice allows a low momentum cut-off ($\sim 100\ MeV/c$) and, at the same time, a good tracking efficiency and momentum resolution.

The six layers of silicon detectors forming the Inner Tracking System (ITS) are used for track reconstruction close to the vertex. The innermost layer is located at a radius $r = 4\,cm$, only $1\,cm$ from the beam pipe, while the sixth layer is located at $r = 44\,cm$. The main goal of the ITS is to reconstruct secondary vertices from hyperons, K_0^S and charmed mesons decays, hence the vertexing resolution must be $< 100\ \mu m$. This constraint, together with the high track density, led to the choice of detectors that provide a bidimensional information such as silicon pixels in the first two layers and silicon drift detector for the third and fourth layers. The last two layers, due to the relatively large surface to be equipped, employ double sided silicon strip detectors. The ITS is also needed for low momentum particle identification through dE/dx measurement.

4 Overview and expected performance

The ALICE rapidity acceptance has been chosen to be large enough to allow the study of particle ratios, p_T spectra and HBT (Hanbury-Brown-Twiss) radii on an event-by-event basis, meaning several thousand reconstructed particles per event. Detecting the decay products of particles at $p_T < m$ requires about 2 units in rapidity (for masses above 1–2 GeV/c^2) and a corresponding coverage in azimuth. A similar acceptance is necessary to collect a reasonable (few 10^3) sample of Υ in the dielectron channel, given the expected luminosity and running time. Again a similar value of acceptance is required to collect sufficient statistics to measure hadronic decays of charmed mesons with good significance. The coverage of the central detector ($|\eta| < 0.9$, full 2π in ϕ) has therefore been chosen as a compromise between acceptance requirements and cost.

ALICE has been specifically designed to maximize momentum coverage, from $\approx$ 100 MeV/c, the lowest values relevant for thermodynamical studies, to $\approx$ 100 GeV/c, the transverse momentum of the leading particles of jets with transverse energy well over 100 GeV. The measurement of numerous precision points over a long measured track length in a moderate magnetic field and with minimal material allows to satisfy both requirements.

4.1 Tracking

The design of the ALICE tracking system has primarily been driven by the requirement for safe and robust track finding. It uses mostly three-dimensional hit information and dense tracking with many points in a moderate magnetic field.

The main tracking detectors are the TPC and the ITS. The tracks are found in the TPC at first, then are followed inward to the ITS and finally extrapolated down to the vertex. A simulated central Pb–Pb event is shown in Fig. 3, where the hits produced in the barrel detectors are displayed. The hits in the TPC are so closely spaced that the tracks associated to charged particles are actually visible. Even at such high multiplicities, the track finding algorithms in TPC and ITS proved to be very effective: in Fig. 4, reconstructed tracks in the ITS with a transverse momentum higher than 1 GeV/c are displayed: the first five silicon layers are clearly visible. A candidate track is accepted when a cluster is found on each ITS layer. The found tracks can be followed outward to Transition Radiation Detector (TRD), which is devoted to the identification of electrons but has good tracking capabilities.

The overall performance of the ALICE tracking system has been simulated taking into account the details of the detector performance.

At target multiplicity the tracking efficiency in the TPC is better than 90% practically independent of p_T down to about 100 MeV/c. For lower multiplicities, the efficiency would rapidly improve, reaching values $\approx$ 97% below

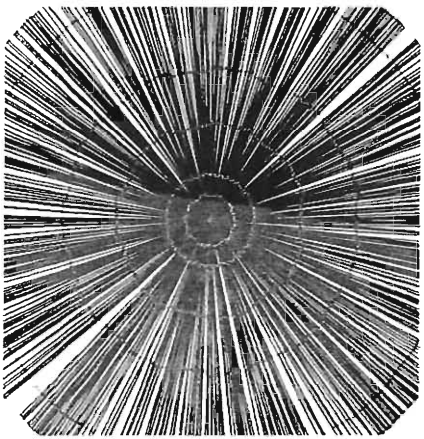

Figure 4: *Reconstructed tracks in the Inner Tracking System ($p_T > 1\,GeV/c$)*

4000 charged particles per unit of rapidity. For very low transverse momenta the ITS has the capability to function as a stand-alone tracker, providing tracking and PID down to below 100 MeV/c. This feature is particularly important to reconstruct the low-p_T decay products of Hyperons.

The momentum resolution, including ITS, TPC and TRD, is better than $\approx 1.5\%$ for momenta between 200 MeV/c and 2 GeV/c, and it is still close to $\approx 12\%$ at 100 GeV/c. The angular resolution is on average ≈ 0.5 mrad.

These momentum and angular resolutions, coupled with the excellent capability to disentangle close tracks, provide ALICE with the capability of measuring with good precision the HBT parameters for a source of radius well in excess of 10 fm.

The impact parameter resolution improves rapidly with transverse momentum, and it reaches 60 μm at 1 GeV/c. This value is adequate for efficient identification of the short-lived B and D mesons, which have $c\tau$ of the order of 100 to 300 μm.

4.2 Particle Identification

One of the distinctive features of ALICE is the particle identification capability, which is realized using a number of different techniques. This robust PID system allows the identification of a large number of protons, pions and kaons in each Pb-Pb event, so that their transverse momentum spectra can be studied on an event-by-event basis. Thanks also to the good momentum and angular resolution, the decay $\phi \rightarrow$K K can be measured with great precision, with

a mass resolution of about 2 MeV/c^2. Coupled with the excellent vertexing capability of the ALICE tracking system, Hyperons (including the rare Ω) and the hadronic decays of charmed mesons can be measured. The measurement of hadronic decays of charmed mesons is an ideal example of the combined power of the ALICE detector systems, using PID, tracking and vertexing. The result is a measurement of the neutral D meson decaying into $K\pi$ with a significance of about 37, which allows a direct study of the p_T dependence of charmed meson production down to 1 GeV/c of p_T (significance $\approx$12).

Hadron identification is provided over a large part of the phase space by the combination of dE/dx measurement in the silicon and in the TPC with a high-resolution ($< 100\,ps$) barrel TOF at r=3.7 m. The dE/dx resolution of the TPC is sufficient to provide good π identification in the relativistic rise region, thus providing an additional handle for the study of hard probes. The TOF uses innovative multigap resistive plate chambers (MRPC), featuring 160,000 precision readout channels.

A Ring Imaging Cherenkov detector of the proximity focusing type, using a liquid C_6F_{14} radiator, covering about 15% of the acceptance of the ALICE central detectors, allows the identification of hadrons up to higher momenta (π/K to 3 GeV/c and K/p to 5 GeV/c) .

4.3 Leptons

Both electrons and muons are measured in ALICE, the electrons in the central barrel and the muons in a dedicated forward arm. The acceptance and resolution are such as to allow the measurement of heavy quarkonia families down to $p_T \approx 0$ and with good separation of the different "onium" states for both ee and $\mu\mu$ channels. The electron measurement coupled with the vertexing capability allows the direct measurement of the yield of B and D mesons via their semileptonic decay, thus providing the natural reference for the "onium" measurements.

Electrons are identified in ALICE by combining the particle identification capability of ITS, TPC and TOF and complementing it with a dedicated Transition Radiation Detector. The TRD consists of six layers of radiator followed by Time Expansion Chambers filled with Xenon/CO_2, providing an e/π rejection power of 100 when operating in a high multiplicity environment. The TRD fast tracking capability is used to trigger on high-p_T leptons, thus enriching their statistical sample, and hadrons, thus providing an essential trigger for jet leading particles. The detector in its full configuration covers the central barrel region of ALICE, and consists of 540 modules organized in 36 azimuthal sectors, corresponding to the azimuthal segmentation of the TPC. The TRD needs therefore 800 m^2 of high-granularity readout chambers, equipped with over one million electronics channels.

The forward muon spectrometer allows the study of vector meson reso-

nances via their $\mu^+\mu^-$ decay. The signals appear on a continuum due to B and D meson decays and Drell-Yan processes. The spectrometer has an efficiency for dimuons better than 90% and a mass resolution better than 100 MeV/c^2 in the Υ region and better than 70 MeV/c^2 in the J/Ψ region. The momentum precision is about 1%. The muon spectrometer consists of a composite absorber ($\approx 10\lambda_{INT}$) starting close to the interaction point (one meter) to reduce the μ background due to π and K decays. A high-density small angle absorber with a central hole shields the spectrometer from the particles emitted at angles from 0 to 2 degrees and allows the LHC beams to traverse the spectrometer. At the end of the spectrometer is located a final muon identifier filter wall, consisting $\approx 10\lambda_{INT}$ of iron. The spectrometer magnet is a large warm dipole magnet with a field of 0.7 T, giving a 3 Tm field integral. The dipole accepts muons at angles smaller than 9 degrees. Ten planes of thin multiwire proportional chambers with cathode pad readout placed in front, inside and following the dipole measure the muon trajectories. Two single gap RPC planes detect the particles emerging from the muon filter and provide the trigger for the spectrometer.

4.4 Photons

Prompt photons, π^0's and η's are measured in a single-arm, high-resolution electromagnetic calorimeter. The accuracy of the single inclusive photon spectra will be determined by the systematic errors on photon-reconstruction efficiency and by the knowledge of the decay background. An acceptable systematic error can be obtained only at low channel occupancy and therefore requires a calorimeter with small Molière radius, R_M, at a large distance ($\approx$ 5 m) from the vertex. The acceptance has been defined such as to keep the statistical errors below the expected systematic ones. The PHOS is located 5 m vertically beneath the interaction region and is built from $PbWO_4$, a material with small Molière radius and high light output.

4.5 Jets

Jets are measured in ALICE by reconstructing charged particles in a cone around a "seed" particle of high p_T. The TRD triggering capability provides the possiblity to record $\approx 10^6$ events per standard Pb run with jet energy above 100 GeV (10^4 above 200 GeV). Therefore ALICE will collect sufficient statistics to exploit its excellent tracking and PID capability for the study of detailed jet fragmentation functions, which is a very sensitive tool for the study of jet quenching. Using the photon measured in the PHOS as a tag, ALICE can study photon-jet back-to-back pairs. In this way, the average jet energy is defined by the photon measurement, and the fast parton energy loss is directly accessible. The range of jet energies accessible with such a measurement would be greatly enhanced by the proposed large acceptance electromagnetic calorime-

ter. If available, the EMCal would also significantly improve the measurement of the jet energy, by complementing the measurement of the charged particles performed by the tracking system, and provide an improved jet trigger.

5 Conclusions

With the advent of the LHC it will be possible to study the QGP well above the energy density of the phase transition. There will be a sizeable improvement in all the parameters related to the quark gluon plasma formation and to the possiblity of studying it on a more stable theoretical ground. The ALICE experiment just ended its research and developement phase and entered the construction phase. The design of the apparatus is now well defined and the available simulation and analysis tools have reached a high level of accuracy and reliability: the Collaboration is making a great effort to study in detail the physics capabilities of the experiment. The results obtained so far are confirming that ALICE will be able to exploit the possibilities of studying strongly interacting matter available at the LHC.

References

1. U. Heinz and M. Jacob, nucl-th/0002042, 16/02/2000
2. S. White, these Proceedings
3. J.P. Revol, Pramàna J. Phys.: 60 (2003) pp.795-816
4. B. Alessandro et Al., ALICE physics, theoretical overview, CERN-ALI-2002-025, 2002
5. ALICE Technical Proposal N. Ahmad et al., CERN/LHCC/95-71 (1995).
6. ALICE TP addendum, S. Beolé et al., CERN/LHCC/96-32
7. ALICE TP addendum, G. Dellacasa et al., CERN/LHCC/99-13
8. P. Giubellino, Eur.Phys.J.direct C4S1:05, 2002

SPECIAL SESSION – PHYSICS AND SOCIETY

Judith Jackson	Global Communication Strategies for a Global Community
Francesco De Martini*	Trends and Perspectives in Quantum Information and Computation
Massimiliano Russo*	The Nuclear Terrorist Threats: Reality and Countermeasures
Giovanni Bignami*	Future Missions in Space

* The trasparencies of the missing contributions are available on the web site http://www.pi.infn.it/lathuile/lathuile_2003.html

GLOBAL COMMUNICATION FOR A GLOBAL COMMUNITY

Judith Jackson
Fermi National Accelerator Laboratory, Batavia, Illinois 60510, USA

Abstract

The InterAction Collaboration, organized in December 2001 by communicators from the world's particle physics laboratories, is dedicated to the development of a collaborative model of physics communication to reflect and to better serve the international character of the science of particle physics. Conference organizers for the XVIIme Rencontres de la Vallee d'Aoste in March 2003 invited the collaboration's members to hold a parallel meeting devoted to global particle physics communication. The Collaboration reported on the results of the meeting to the main conference and presented a strategic plan for global particle physics communication, "not only to help international particle physics stay alive, but also, in our field of activity, to set visible footprints for peaceful collaboration across all borders."

1 Physics Without Borders

The science of particle physics today is a worldwide collaborative endeavor. Experiments at the world's accelerator laboratories are carried out by collaborations of scientists from nearly every country of the globe. The size and scale of the accelerators and detectors required for research in this field dictate a degree of international cooperation that is perhaps greater than in any other field of research. Moreover, if international collaboration is important to the current success of the field, it will be crucial to the particle physics of the future. The discoveries of the future will require still greater cooperation among laboratories, among nations and across the fields of physics. The days when one laboratory or one national program could succeed at the expense of others has passed. For the science of particle physics to succeed, all must succeed. Particle physics will live or die by the capability for international collaboration.

In the field of particle physics, most communication resources are concentrated at the laboratories. The laboratories have the mission, the dedicated budgets, the professional staff, the expertise and the continuity required for ongoing and sustained communication of particle physics with key audiences. Just as collaboration is crucial to the future of particle physics research, it is equally important in the area of particle physics communication. It strengthens the current worldwide program by fostering the efficient use of resources, reducing parallel efforts and making the most of communication opportunities, and it is critical for the future. For example, for a large-scale future accelerator to be built somewhere in the world, the ability of the field of particle physics to communicate as one will be essential. If such a vision is to become reality, communication models and practices need to change now.

To achieve the kind of future that particle physicists envision for their field, the laboratories have begun to change the way they communicate. To strengthen and improve that effort, the InterAction Collaboration was established at a meeting in December 2001 at DESY Laboratory in Hamburg. The original members were communicators from Brookhaven National Laboratory, CERN, DESY, Fermilab, Gran Sasso Laboratory, and SLAC. Today, the collaboration's membership also includes communicators from the American Physical Society, Berkeley Lab, Cornell, Dubna, Frascati, INFN, IN2P3, KEK, Saclay and Thomas Jefferson Laboratory. Communicators from all particle physics laboratories are invited to join.

At the original meeting, collaborators decided to move forward on four projects: the creation of a common "Interactions Newswire," with international news from the world of particle physics; the development of a world particle physics "Image Bank" on a common website for the use of particle physics communicators; the coordination of press releases and other communication; and the effort to include communication on the agenda of physics conferences. The InterAction collaboration reported progress on all fronts.

2 Interactions Newswire

The Interactions Newswire sent its first particle physics news bulletin on September 17, 2002. In the six months of operation leading up to the La Thuile conference, 32 Newswires had appeared, originating from the particle physics laboratories of the world. The subscriber list included more than 500 members from 31 countries including reporters, representatives of funding agencies, government officials and members of the particle physics community.

3 Interactions Web Site

The InterAction collaboration presented a preview of the the Interactions Web Site http://209.242.196.11/cms/ scheduled to be rolled out publicly at the Lepton-Photon Conference at Fermilab in August 2003. The launch will introduce http://www.interactions.org as the official URL. The Web site includes particle physics news from the world's media, as well as a collection of more than 600 high-resolution images, an image bank of high-resolution photographs and illustrations from the world's physics laboratories. Designed as a resource for all who communicate about particle physics, the website includes sections on policy and funding, education, universities and the future of the field. It is open to all in the field of particle physics who need a central resource for making information available within the global field of particle physics.

4 ICFA Support

Following a presentation by the InterAction collaboration to the International Committee for Future Accelerators at its meeting in Tsukuba, Japan in February 2003, ICFA Chair Jonathan Dorfan sent the following letter to the collaboration organizers.

"At the recent ICFA meeting, the Committee appreciated your report on the need for better communication about particle physics, and ICFA endorses the efforts of the international collaboration of particle physics communicators, InterAction."

5 Strategic Plan for Global Particle Physics Communication

During the La Thuile conference meeting, the InterAction collaboration developed a strategic communication plan for international particle physics communication and presented the plan to the conference.

Goal:

Increase support around the world for fundamental particle physics research.

Strategy:

Strengthen collaboration among laboratory communicators in order to
- share resources
- speak with one voice
- develop a common science message

Actions:
- complete the first phase of the Interactions.org website and image bank for public rollout at the Lepton-Photon Conference at Fermilab August 11-16.
- develop and carry out a collaborative international media plan for press relations at the Lepton-Photon Conference.
- develop a collaborative InterAction plan for participation in the International Year of Physics in 2005.
- develop common materials and messages for the world's long-baseline neutrino experiments at Gran Sasso, KEK and Fermilab.
- research and write a Guide for the Perplexed to the various aspects and components of the data grid, defining terms, roles and interactions of grid projects around the world; explore developing common grid messages, press releases and materials.
- develop a joint statement of the science case for a linear collider in the LHC era.
- explore opportunities to collaborate at the CERN conference on :Science and the Information Society" associated with the World Summit on the Information Society to be held in December 2003 in Geneva.
- strengthen collaboration on press releases, policy papers, articles, and communication issues that affect worldwide particle physics.

TRENDS AND PERSPECTIVES IN QUANTUM INFORMATION AND COMPUTATION

Francesco De Martini
Università "la Sapienza and Sezione I.N.F.M., Roma

Written contribution not received

THE NUCLEAR TERRORIST THREATS: REALITY AND COUNTERMEASURES

Massimiliano Russo
CISAM, San Piero a Grado, Pisa

Written contribution not received

FUTURE MISSIONS IN SPACE

Giovanni Bignami
ASI, Pavia

Written contribution not received

Participants

Phil ADAMSON	London	pa@hep.ucl.ac.uk
Roberta ANTOLINI	LNGS	antolini@lngs.infn.it
Philip BAMBADE	LAL	bambade@lal.in2p3.fr
Antonio BARONCELLI	Roma	toni.baroncelli@roma3.infn.it
Franco BEDESCHI	Pisa	bed@fnal.gov
Lorenzo BELLAGAMBA	Bologna	lorenzo.bellagamba@bo.infn.it
Giorgio BELLETTINI	Pisa	giorgiob@fnal.gov
Enzo BERTOLINI	Corecom	bertolinienzo@tiscalinet.it
Giovanni BIGNAMI	Pavia/ASI	gfb@ifctr.mi.cnr.it
Halina BILOKON	LNF	halina.bilokon@lnf.infn.it
Roy BRIERE	Carnegie Mellon	rbriere@andrew.cmu.edu
Matteo CACCIARI	Parma	matteo.cacciari@cern.ch
Rino CASTALDI	Pisa	rino.castaldi@pi.infn.it
Heriberto CASTILLA	CINVESTAV-IPN	castilla@fnal.gov
Andrea CASTRO	Bologna	castro@bo.infn.it
Flavio CAVANNA	L'Aquila	cavanna@aquila.infn.it
Filippo CERADINI	Roma	ceradini@roma3.infn.it
Fabio CERUTTI	CERN	fabio.cerutti@cern.ch
Franco CERVELLI	Pisa	franco.cervelli@pi.infn.it
Giorgio CHIARELLI	Pisa	giorgio.chiarelli@pi.infn.it
Eugenio COCCIA	Roma	eugenio.coccia@roma2.infn.it
Marco CONTALBRIGO	Ferrara	contalbrigo@fe.infn.it
Flavio COSTANTINI	Pisa	flavio.costantini@pi.infn.it
Giancarlo D'AMBROSIO	Napoli	giancarlo.dambrosio@na.infn.it
Mikhail DANILOV	ITEP	danilov@mail.desy.de
Vittorio DE ALFARO	Torino	vda@to.infn.it
Francesco DE MARTINI	Roma	francesco.demartini@uniroma1.it
Alberto DE MIN	Padova	alberto.de.min@cern.ch
Alvaro DE RUJULA	CERN	alvaro.derujula@cern.ch
Aldo DEANDREA	IPN	deandrea@ipnl.in2p3.fr
Oleg DENISOV	Torino	denisov@to.infn.it
Paolo DESIATI	Wisconsin	desiati@amanda.physics.wisc.edu
Giordano DIAMBRINI PALAZZI	Roma	giordano.diambrini@roma1.infn.it
Alexander DOLGOV	Moscow/Ferrara	dolgov@fe.infn.it

Igor DREMIN	Moscow	dremin@td.lpi.ru
Alexey DRUTSKOY	Moscow	drutskoi@bmail.kek.jp
Boris ERMOLAEV	St.Petersburg	boris.ermolaev@cern.ch
Fabrizio FABBRI	Bologna	fabrizio.fabbri@bo.infn.it
Riccardo FACCINI	Roma	rfaccini@slac.stanford.edu
Alberto FERIANI	CISAM	alberto.feriani@cisam.it
Ruggero FERRARI	Milano	ruggero.ferrari@mi.infn.it
Fernando FERRONI	Roma	fernando.ferroni@roma1.infn.it
Petra FOLKERTS	DESY	petra.folkerts@desy.de
Harald FRITZSCH	Münich	fritzsch@mppmu.mpg.de
Ivan FURIC	MIT	ikfuric@mit.edu
Barbara GALLAVOTTI	LNF	barbara.gallavotti@presid.infn.it
Sergey GANZHUR	Saclay	ganzhur@hep.saclay.cea.fr
Pablo GARCIA ABIA	CIEMAT	pablo.garcia@ciemat.es
Ugo GASTALDI	LNL	gastaldi@lnl.infn.it
Gianpiero GERVINO	Torino	gervino@to.infn.it
James GILLIES	CERN	james.gillies@cern.ch
Paolo GIUSTI	Bologna	giusti@bo.infn.it
Ricardo GOMES	Fermilab	rgomes@fnal.gov
Alfred GOSHAW	Duke/Fermilab	goshaw@fnal.gov
Marco Grassi	Pisa	Marco.grassi@pi.infn.it
Mario GRECO	Roma	mario.greco@lnf.infn.it
Jean-Francois GRIVAZ	Orsay	grivaz@lal.in2p3.fr
Carlo GUSTAVINO	LNGS	gustavino@lngs.infn.it
Arthur HALPRIN	Delaware	halprin@udel.edu
Nicholas HASTINGS	KEK	hastings@bmail.kek.jp
Mattew HERNDON	John Hopkins	herndon@fnal.gov
Clemens A. HEUSCH	Santa Cruz	heusch@slac.stanford.edu
Takeo HIGUCHI	KEK	takeo.higuchi@kek.jp
Andrew HIME	Los Alamos	ahime@lanl.gov
Albino IMPERIAL	Geneva	
Mauro IODICE	Roma	mauro.iodice@roma3.infn.it
Taku ISHIDA	KEK	taku.ishida@kek.jp
Gino ISIDORI	LNF	gino.isidori@lnf.infn.it
Judith JACKSON	Fermilab	jjackson@fnal.gov

Patrick JANOT	CERN	Patrick.Janot@cern.ch
Marumi KADO	LBL	mmkado@lbl.gov
Takayuki KAWAMURA	CERN	takayuki.kawamura@cern.ch
Robert KEHOE	Michigan	kehoe@pa.msu.edu
Robert KEPHART	Fermilab	kephart@fnal.gov
Boris KHAZIN	Budker	b.i.khazin@inp.nsk.su
Sandrine LAPLACE	Orsay	laplace@lal.in2p3.fr
Andrea LAVAGNO	Torino	andrea.lavagno@polito.it
Jonathan LINK	Columbia	link@fnal.gov
Tony LISS	Urbana	tml@uiuc.edu
Claudio LUCI	Roma	claudio.luci@roma1.infn.it
Maurizio LUSIGNOLI	Roma/CERN	maurizio.lusignoli@roma1.infn.it
Giampaolo MANNOCCHI	CNR/LNF	giampaolo.mannocchi@cern.ch
Massimo MASERA	Torino	masera@to.infn.it
Takayuki MATSUI	KEK	takayuki.matsui@kek.jp
Wyatt K. MERRITT	Fermilab	wyatt@fnal.gov
Ivan MIKULEC	Wien/CERN	ivan.mikulec@cern.ch
Peter MINKOWSKI	Bern	mink@itp.unibe.ch
Charles A. NELSON	SUNY	cnelson@binghamton.edu
Victor NOVIKOV	ITEP	novikov@heron.itep.ru
Tokio OHSKA	KEK	tokio.ohska@kek.jp
Alexandre OLCHEVSKI	JINR/CERN	a.olchevski@cern.ch
Ornella PALAMARA	LNGS	ornella.palamara@lngs.infn.it
Luca PASSALACQUA	LNF	luca.passalacqua@lnf.infn.it
Joerg PRETZ	Bonn/CERN	jorg.pretz@cern.ch
Giovanni PUNZI	Pisa	giovanni.punzi@pi.INFN.IT
Heather RAY	Michigan	
Massimiliano RUSSO	CISAM	massimiliano.russo@cisam.it
Emmanuel SAUVAN	Marseille	sauvan@cppm.in2p3.fr
Thomas SCHOERNER SADENIUS	CERN	thomas.schoerner@cern.ch
Luca SCODELLARO	Padova	scodellaro@pd.infn.it
Evgeni SHABALIN	ITEP	shabalin@vitep5.itep.ru
Luca SILVESTRINI	Roma	luca.silvestrini@roma1.infn.it
Franco SIMONETTO	Padova	franco.simonetto@pd.infn.it
Alexei SISSAKIAN	JINR	sisakian@jinr.ru

Rob SNIHUR	London/Fermilab	snihur@fnal.gov
Paolo SPAGNOLO	Pisa	paolo.spagnolo@pi.infn.it
R. Wayne SPRINGER	Utah	springer@physics.utah.edu
Luca STANCO	Padova	stanco@padova.infn.it
Lawrence SULAK	Boston	sulak@physics.bu.edu
Giancarlo SUSINNO	Cosenza	susinno@cs.infn.it
Anyes TAFFARD	Liverpool	anyes@fnal.gov
Roberto TENCHINI	Pisa	roberto.tenchini@cern.ch
Makoto TOMOTO	Fermilab	tomoto@fnal.gov
Fabio TRUC	Aosta	truc@netvallee.it
Yoshi UCHIDA	Stanford	Yoshi.Uchida@Stanford.EDU
Anne Mieke VAN DEN BERGEN	Amsterdam	bergen@interactions.org
Silvia VANNUCCI GIROMINI	LNF	silvia.giromini@lnf.infn.it
Andrea VENTURI	Pisa	andrea.venturi@cern.ch
Francesco VISSANI	LNGS	francesco.vissani@lngs.infn.it
Mikhail VYSOTSKY	ITEP	vysotsky@heron.itep.ru
Wenfeng WANG	IHEP	wangwf@mail.ihep.ac.cn
Linda WARE	Jefferson Lab	ware@jlab.org
Sebastian N. WHITE	BNL	sebastian.white@cern.ch, white1@bnl.gov
Avi YAGIL	Fermilab	yagil@fnal.gov
Vladimir ZOLLER	ITEP	zoller@heron.itep.ru
Stefano ZUCCHELLI	Bologna	zucchelli@bo.infn.it

Frascati Physics Series Volumes

Volume I – *Heavy Quarks at Fixed Target*
Eds. S. Bianco and F.L. Fabbri
Frascati, May 31-June 2, 1993
ISBN 88-86409-00-1

Volume II –Special Issue, *Les Rencontres de Physique de la Vallée d'Aoste - Results and Perspectives in Particle Physics*
Ed. M. Greco
La Thuile, Aosta Valley, March 5 -11, 1995
ISBN 88-86409-03-6

Volume III – *Heavy Quarks at Fixed Target*
Ed. B. Cox
University of Virginia, Charlottesville
October 7-10, 1994,
ISBN 88-86409-04-4

Volume IV – *Workshop on Physics and Detectors for DAΦNE*
Eds. R. Baldini, F. Bossi, G. Capon, G. Pancheri
Frascati, April 4-7, 1995
ISBN 88-86409-05-2

Volume V – Special Issue, *Les Rencontres de Physique de la Vallée d'Aoste - Results and Perspectives in Particle Physics*
Ed. M. Greco
La Thuile, Aosta Valley, March 3-9, 1996
ISBN 88-86409-07-9

Volume VI – *Calorimetry in High Energy Physics*
Eds. A. Antonelli, S. Bianco, A. Calcaterra, F.L. Fabbri
Frascati, June 8-14, 1996
ISBN 88-86409-10-9

Volume VII – *Heavy Quarks at Fixed Target*
Ed. L. Köpke
Rhinefels Castle, St. Goar, October 3-6, 1996
ISBN 88-86409-11-7

Volume VIII – *ADONE a milestone on the particle way*
Ed. V. Valente –1997
ISBN 88-86409-12-5

Volume IX – Special Issue, *Les Rencontres de Physique de la Vallée d'Aoste – Results and Perspectives in Particle Physics*
Ed. M. Greco
La Thuile, Aosta Valley, March 2-8, 1997
ISBN-88-86409-13-3

Volume X – *Advanced ICFA Beam Dynamics Workshop on Beam Dynamics Issue for e^+e^- Factories*
Eds. L. Palumbo, G. Vignola
Frascati, October 20-25, 1997
ISBN 88-86409-14-1

Volume XI – *Proceedings of the XVIII International Conference on Physics in Collision*
Eds. S. Bianco, A. Calcaterra, P. De Simone, F. L. Fabbri
Frascati, June 17-19, 1998
ISBN 88-86409-15-X

Volume XII –*Special Issue, Les Rencontres de Physique de la Vallée d'Aoste - Results and Perspectives in Particle Physics*
Ed. M. Greco
La Thuile, Aosta Valley, March 1-7, 1998
ISBN 88-86409-16-8

Volume XIII –*Bruno Touschek and the Birth of the e^+e^-*
Ed. G. Isidori
Frascati, 16 November, 1998
ISBN 88-86409-17-6

Volume XIV – Special Issue, *Les Rencontres de Physique de la Vallée d'Aoste - Results and Perspectives in Particle Physics*
Ed. M. Greco
La Thuile, Aosta Valley, February 28-March 6, 1999
ISBN 88-86409-18-4

Volume XV –*Workshop on Hadron Spectroscopy*
Eds. T. Bressani, A. Feliciello, A. Filippi
Frascati, March 8–2 1999
ISBN 88-86409-19-2

Volume XVI –*Physics and Detectors for DAΦNE*
Eds. S. Bianco, F. Bossi, G. Capon, F.L. Fabbri, P. Gianotti, G. Isidori, F. Murtas
Frascati, November 16 -19, 1999
ISBN 88-86409-21-4

Volume XVII – *Special Issue, Les Rencontres de Physique de la Vallée d'Aoste - Results and Perspectives in Particle Physics*
Ed. M. Greco
La Thuile, Aosta Valley, February 27 –March 4, 2000
ISBN 88-86409-23-0

Volume XVIII – *LNF Spring School*
Ed. G. Pancheri
Frascati 15-20 May, 2000
ISBN 88-86409-24-9

Volume XIX – *XX Physics in Collision*
Ed. G. Barreira
Lisbon June 29-July1st. 2000
ISBN 88-86409-25-7

Volume XX – *Heavy Quarks at Fixed Target*
Eds. I. Bediaga, J. Miranda, A. Reis
Rio de Janeiro, Brasil, October 9-12, 2000
ISBN 88-86409-26-5

Volume XXI –*IX International Conference on Calorimetry in High Energy Physics*
Eds. B. Aubert, J. Colas, P. Nédélec, L. Poggioli
Annecy Le Vieux Cedex, France, October 9-14, 2000
ISBN 88-86409-27-3

Volume XXII –*Special Issue, Les Rencontres de Physique de la Vallée d'Aoste - Results and Perspectives in Particle Physics*
Ed. M. Greco
La Thuile, Aosta Valley, March 4-10 , 2001
ISBN 88-86409-28-1

Volume XXIII – *XXI Physics in Collision*
Ed. Soo-Bong Kim
Seoul, Korea, June 28 –30, 2001
ISBN 88-86409-30-3

Volume XXIV – *International School of Space Science –2001 Course on: Astroparticle and Gamma-ray Physics in Space*
Eds. A. Morselli, P. Picozza
L'Aquila, Italy, August 30 –September 7, 2000
ISBN 88-86409-31-1

Volume XXV – *TRDs for the 3rd Millennium Workshop on Advanced Transition Radiation Detectors for Accelerator and Space Applications*
Eds. N. Giglietto, P. Spinelli
Bari, Italy, September 20-23, 2001
ISBN 88-86409-32-X

Volume XXVI – *KAON 2001*
International Conference on CP Violation
Eds. F. Costantini, G. Isidori, M. Sozzi
Pisa Italy, June 12th –17th, 2001
ISBN 88-86409-33-8

Volume XXVII – *Special Issue, Les Rencontres de Physique de la Vallée d'Aoste - Results and Perspectives in Particle Physics*
Ed. M. Greco
La Thuile, Aosta Valley, March 3-9, 2002
ISBN 88-86409-34-6

Volume XXVIII – *Heavy Quarks at Leptons 2002*
Eds. G. Cataldi, F. Grancagnolo, R. Perrino, S. Spagnolo
Vietri sul mare (Italy), May 27th – June 1st, 2002
ISBN 88-86409-35-4

Volume XXIX –
Workshop on Radiation Dosimetry: Basic Technologies, Medical Applications, Environmental Applications
Ed. A. Zanini
Rome (Italy), February 5–6, 2002
88-86409-36-2